

# Motion tracking and deformation analysis in biomechanics

**Edited by**

Jiaqiu Wang, Zhiyong Li, Chi Wu and Liguozhao Zhao

**Coordinated by**

Ryan Huang and Ran He

**Published in**

Frontiers in Bioengineering and Biotechnology



## FRONTIERS EBOOK COPYRIGHT STATEMENT

The copyright in the text of individual articles in this ebook is the property of their respective authors or their respective institutions or funders. The copyright in graphics and images within each article may be subject to copyright of other parties. In both cases this is subject to a license granted to Frontiers.

The compilation of articles constituting this ebook is the property of Frontiers.

Each article within this ebook, and the ebook itself, are published under the most recent version of the Creative Commons CC-BY licence. The version current at the date of publication of this ebook is CC-BY 4.0. If the CC-BY licence is updated, the licence granted by Frontiers is automatically updated to the new version.

When exercising any right under the CC-BY licence, Frontiers must be attributed as the original publisher of the article or ebook, as applicable.

Authors have the responsibility of ensuring that any graphics or other materials which are the property of others may be included in the CC-BY licence, but this should be checked before relying on the CC-BY licence to reproduce those materials. Any copyright notices relating to those materials must be complied with.

Copyright and source acknowledgement notices may not be removed and must be displayed in any copy, derivative work or partial copy which includes the elements in question.

All copyright, and all rights therein, are protected by national and international copyright laws. The above represents a summary only. For further information please read Frontiers' Conditions for Website Use and Copyright Statement, and the applicable CC-BY licence.

ISSN 1664-8714  
ISBN 978-2-8325-6888-0  
DOI 10.3389/978-2-8325-6888-0

**Generative AI statement**

Any alternative text (Alt text) provided alongside figures in the articles in this ebook has been generated by Frontiers with the support of artificial intelligence and reasonable efforts have been made to ensure accuracy, including review by the authors wherever possible. If you identify any issues, please contact us.

**About Frontiers**

Frontiers is more than just an open access publisher of scholarly articles: it is a pioneering approach to the world of academia, radically improving the way scholarly research is managed. The grand vision of Frontiers is a world where all people have an equal opportunity to seek, share and generate knowledge. Frontiers provides immediate and permanent online open access to all its publications, but this alone is not enough to realize our grand goals.

**Frontiers journal series**

The Frontiers journal series is a multi-tier and interdisciplinary set of open-access, online journals, promising a paradigm shift from the current review, selection and dissemination processes in academic publishing. All Frontiers journals are driven by researchers for researchers; therefore, they constitute a service to the scholarly community. At the same time, the *Frontiers journal series* operates on a revolutionary invention, the tiered publishing system, initially addressing specific communities of scholars, and gradually climbing up to broader public understanding, thus serving the interests of the lay society, too.

**Dedication to quality**

Each Frontiers article is a landmark of the highest quality, thanks to genuinely collaborative interactions between authors and review editors, who include some of the world's best academicians. Research must be certified by peers before entering a stream of knowledge that may eventually reach the public - and shape society; therefore, Frontiers only applies the most rigorous and unbiased reviews. Frontiers revolutionizes research publishing by freely delivering the most outstanding research, evaluated with no bias from both the academic and social point of view. By applying the most advanced information technologies, Frontiers is catapulting scholarly publishing into a new generation.

**What are Frontiers Research Topics?**

Frontiers Research Topics are very popular trademarks of the *Frontiers journals series*: they are collections of at least ten articles, all centered on a particular subject. With their unique mix of varied contributions from Original Research to Review Articles, Frontiers Research Topics unify the most influential researchers, the latest key findings and historical advances in a hot research area.

Find out more on how to host your own Frontiers Research Topic or contribute to one as an author by contacting the Frontiers editorial office: [frontiersin.org/about/contact](https://frontiersin.org/about/contact)

# Motion tracking and deformation analysis in biomechanics

## Topic editors

Jiaqiu Wang — London South Bank University, United Kingdom

Zhiyong Li — Queensland University of Technology, Australia

Chi Wu — The University of Sydney, Australia

Liguo Zhao — Nanjing University of Aeronautics and Astronautics, China

## Topic coordinators

Ryan Huang — Queensland University of Technology, Australia

Ran He — University of Leicester, United Kingdom

## Citation

Wang, J., Li, Z., Wu, C., Zhao, L., Huang, R., He, R., eds. (2025). *Motion tracking and deformation analysis in biomechanics*. Lausanne: Frontiers Media SA.  
doi: 10.3389/978-2-8325-6888-0

## Table of contents

- 05 **Editorial: Motion tracking and deformation analysis in biomechanics**  
Jiaqiu Wang, Chi Wu, Qiuxiang Huang, Ran He, Zhiyong Li and Liguoz Zhao
- 09 **Determination of muscle shape deformations of the tibialis anterior during dynamic contractions using 3D ultrasound**  
Annika S. Sahrmann, Lukas Vosse, Tobias Siebert, Geoffrey G. Handsfield and Oliver Röhrle
- 21 **Biomechanical analysis of the tandem spinal external fixation in a multiple-level noncontiguous lumbar fractures model: a finite element analysis**  
Huarong Chen, Yu Kang, Yiguo Yan, Hu Wang, Wen Peng, Yijia Liao, Mingxiang Zou, Zhun Xu, Xizheng Song, Wenjun Wang and Cheng Wang
- 33 **Effect of orthopedic insoles on lower limb motion kinematics and kinetics in adults with flat foot: a systematic review**  
Hairong Chen, Dong Sun, Yufei Fang, Shunxiang Gao, Qiaolin Zhang, István Bíró, Viktória Tafferner-Gulyás and Yaodong Gu
- 47 **Finite element simulations of smart fracture plates capable of cyclic shortening and lengthening: which stroke for which fracture?**  
Michael Roland, Stefan Diebels, Kerstin Wickert, Tim Pohlemann and Bergita Ganse
- 61 ***In vivo* analysis of ankle joint kinematics and ligament deformation of chronic ankle instability patients during level walking**  
Yaokuan Ruan, Shengli Wang, Nan Zhang, Zhende Jiang, Nan Mei, Pu Li, Lei Ren, Zhihui Qian and Fei Chang
- 72 **Rotation of the hammer and performance in hammer throwing**  
Jiaru Huang, Leonardo A. Peyré-Tartaruga, Junlei Lin, Yu Shi and Wei Li
- 80 **Quantitative assessment of the oral microvasculature using optical coherence tomography angiography**  
Tianyu Zhang, Yilong Zhang, Jinpeng Liao, Simon Shepherd, Zhihong Huang, Michaelina Macluskey and Chunhui Li
- 94 **Correlation between the biomechanical characteristics and stability of the 143D movement during the balance phase in competitive Tai Chi**  
Ruifeng Huang, Yong Ma, Shijie Lin, Weitao Zheng, Lin Liu and Mengyao Jia



- 106 **Validation of the efficacy of the porous medium model in hemodynamic analysis of iliac vein compression syndrome**  
Lingling Wei, Ke Hu, Jiaqiu Wang, Shuang Zhang, Xiaoxiao Yang, Yuanli Chen, Chenshu Li, Xinwu Lu, Kaichuang Ye, Peng Qiu and Yanqing Zhan
- 117 **Effects of different microfracture drilling parameters on bone quality: a finite element analysis**  
Jiayi Luo, Zihao Zou, Qiang Zou, Siwei Luo, Jialin He and Chuan Ye
- 129 **Dynamic balance control in healthy young women during stair descent: a plantar pressure-based study**  
Ruiqin Wang, Jinfeng Cao, Haoran Xu, Panjing Guo, Yumin Li, Yuyi Fan, Yunfei Gui, Leqi Li, Roger Adams, Jia Han and Jie Lyu
- 138 **Non-contact tracking of shoulder bones using ultrasound and stereophotogrammetry**  
Ahmed Sewify, Maxence Lavaill, Dermot O'Rourke, Maria Antico, Peter Pivonka, Davide Fontanarosa and Saulo Martelli
- 150 **Biomechanical assessment of vulnerable plaque: from histological evidence to ultrasound elastography and image-based computational patient-specific modelling**  
Nicoletta Curcio, Michele Conti, Rosanna Cardani, Laura Valentina Renna, Giacomo Dell'Antonio, Vlasta Bari, Giovanni Nano, Giulia Matrone and Daniela Mazzaccaro
- 162 **Finite element analysis of the biomechanical effects of manipulation of lower limb hyperextension on the sacroiliac joint**  
Bangmin Luo, Yikai Li, Cheng Wang and Zhun Xu
- 172 **Unilateral chewing of foods. Analysis of energy balance and peak power of the mandibular elevator muscles**  
Przemysław Stróżyk and Jacek Batchanowski
- 187 **The evolution of three-dimensional knee kinematics after ACL reconstruction within one year**  
Lingchuang Kong, Huahao Lai, Xiaolong Zeng, Peng Gao, Wenhao Liang, Qi Gao, Zhiyuan Kong, Wu Wu, Xiaona Wu and Tao Zhang



## OPEN ACCESS

EDITED AND REVIEWED BY  
Markus O. Heller,  
University of Southampton, United Kingdom

\*CORRESPONDENCE  
Jiaqiu Wang,  
✉ jiaqiu.wang@hotmail.com

RECEIVED 23 August 2025  
ACCEPTED 27 August 2025  
PUBLISHED 08 September 2025

CITATION  
Wang J, Wu C, Huang Q, He R, Li Z and Zhao L  
(2025) Editorial: Motion tracking and  
deformation analysis in biomechanics.  
*Front. Bioeng. Biotechnol.* 13:1691342.  
doi: 10.3389/fbioe.2025.1691342

COPYRIGHT  
© 2025 Wang, Wu, Huang, He, Li and Zhao. This  
is an open-access article distributed under the  
terms of the [Creative Commons Attribution  
License \(CC BY\)](#). The use, distribution or  
reproduction in other forums is permitted,  
provided the original author(s) and the  
copyright owner(s) are credited and that the  
original publication in this journal is cited, in  
accordance with accepted academic practice.  
No use, distribution or reproduction is  
permitted which does not comply with these  
terms.

# Editorial: Motion tracking and deformation analysis in biomechanics

Jiaqiu Wang<sup>1,2,3\*</sup>, Chi Wu<sup>4</sup>, Qiuxiang Huang<sup>2,3</sup>, Ran He<sup>5</sup>,  
Zhiyong Li<sup>2,3,6</sup> and Liguo Zhao<sup>7</sup>

<sup>1</sup>School of Computer Science and Digital Technologies, London South Bank University, London, United Kingdom, <sup>2</sup>School of Mechanical, Medical and Process Engineering, Queensland University of Technology, Brisbane, QLD, Australia, <sup>3</sup>Centre for Biomedical Technologies, Queensland University of Technology, Brisbane, QLD, Australia, <sup>4</sup>School of Engineering, University of Newcastle, Callaghan, NSW, Australia, <sup>5</sup>School of Engineering, University of Leicester, Leicester, United Kingdom, <sup>6</sup>Faculty of Sports Science, Ningbo University, Ningbo, Zhejiang, China, <sup>7</sup>School of Energy and Power Engineering, Nanjing University of Aeronautics and Astronautics, Nanjing, Jiangsu, China

## KEYWORDS

biomechanics, kinematics, deformation, motion tracking, finite element analysis, computational model, ultrasound, optical coherence tomography

## Editorial on the Research Topic

### Motion tracking and deformation analysis in biomechanics

## Introduction

Biomechanical analysis plays a critical role in the clinical diagnosis and treatment of a wide range of diseases. At the whole-body level, it is essential for assessing movement, exercise performance, and sports biomechanics. At the tissue level, deformation and strain characteristics are closely linked to pathological changes in conditions such as cancer, cardiovascular disease, musculoskeletal disorders and etc.

This Research Topic aims to explore the forefront of innovative imaging, sensing, and computational modelling techniques in biomechanical analysis. It particularly highlights cutting-edge research that utilises non-invasive, contactless technologies and advanced algorithms to uncover biomechanical characteristics. Special emphasis is placed on the integration, clinical application, and validation of these methods using real-world patient data.

This Research Topic collects 16 high-quality publications, including one review article and 15 original research papers. Based on the focus areas, the contributions can be broadly categorised into the following groups: (1) biomechanics in sports and performance analysis; (2) kinematics and kinetics in rehabilitation evaluation; (3) musculoskeletal dynamics; (4) finite element analysis (FEA) in bone and joint; (5) biomechanical measurements in vascular system.

## Biomechanics in sports and performance analysis

Biomechanics, along with relevant imaging, sensing, and modelling techniques, provides the foundation for assessing human physical performance. These approaches help individuals improve their exercise outcomes and show great potential in enhancing athletes' professional skills in competitive sports.

Huang et al. presented an intriguing study sparked by the fusion of modern biomechanical analytical technologies with the traditional Chinese martial art of Tai Chi. Using measurement platforms for three-dimensional (3D) motion capture, force analysis, and electromyography, the study quantitatively investigated the correlations among kinematic, kinetic, and surface electromyography (sEMG) characteristics, as well as the stability index, during the balance phase of 143D, one of the most challenging movements in competitive Tai Chi. This work advances the understanding of movement characteristics and balance mechanisms from the biomechanical perspective, providing theoretical support to enhance training effectiveness and athletic performance.

Wang et al. investigated dynamic balance during step descent in 20 young women using F-Scan plantar-pressure insoles across four heights (5, 15, 25, 35 cm). They quantified landing strategy and center-of-pressure (COP) metrics and analyzed step height. With increasing height, COP velocities and ranges rose significantly ( $p < 0.001$ ), indicating greater balance demand; preferred landing shifted from hindfoot toward forefoot beginning at 5 cm. Dominant vs. non-dominant leading foot showed similar kinetics, except a smaller 95% COP area for the dominant foot (better stability;  $p = 0.013$ ). The study informs a practical stair design for fall-prevention guidance.

The study by Huang et al. investigated the effects of hammer rotation on the performance in hammer throwing of female athlete. By comparing each athlete's long and short competition trials and employing three-dimensional motion analysis, they found that longer throws featured greater release velocity, higher velocity gain during double support, shorter single-support phases, lower horizontal azimuth angles, and longer rotational radii at key instants. These findings offer insights for enhancing biomechanical efficiency and training strategies in the hammer throwing competition.

## Kinematics and kinetics in rehabilitation evaluation

In rehabilitation, biomechanical forces are key parameters for ensuring optimal outcomes, particularly for exercise-related conditions. Advanced biomechanical analytical approaches greatly enhance the effectiveness of rehabilitation through deeper insights and more precise interventions.

Orthopaedic insoles are commonly used to address flatfoot conditions, but their biomechanical effectiveness across different movements remains debated. Chen et al. published a systemic review exploring the impact of orthopaedic insoles on the kinematics and kinetics of lower limb motion, with a focus on evaluating their effectiveness and identifying future research directions in flatfoot biomechanics. The review comprehensively

analyses 19 studies filtered from 671 screened cohorts, and confirms the effectiveness of orthopaedic insoles in improving movement patterns in patients with flatfoot. It also highlights several current limitations and key directions for future research, including the need for further investigation into biomechanical effectiveness, the potential of personalised orthopaedic insoles, and the importance of conducting studies across diverse populations and movement types, as well as long-term interventions.

Ruan et al. used dynamic biplane radiography to assess ankle joint kinematics and ligament deformation in 12 patients with chronic ankle instability (CAI) during walking. Compared with the uninjured side, CAI ankles showed reduced tibiotalar dorsiflexion, greater talar displacement, and increased subtalar inversion. During stance, the anterior talofibular ligament (ATFL) elongated with plantarflexion and talar anterior translation, while the calcaneofibular ligament (CFL) shortened. The findings highlight the importance of sagittal alignment in ligament repair and underline biomechanical markers for targeted rehabilitation aimed at restoring balanced ankle stability in CAI patients.

Kong et al. presented a study involving a cohort of 49 patients who underwent anterior cruciate ligament reconstruction (ACLR), aiming at exploring dynamic changes in six degrees of freedom (6DoF) knee joint kinematics over a 1-year rehabilitation period. By combining kinematic analysis with clinical scoring systems, the study investigated functional recovery patterns and provided evidence to support the optimisation of postoperative rehabilitation strategies. The findings highlight the importance of individualised rehabilitation, emphasising joint stability and range of motion recovery during the early postoperative phase (0–6 months), and correction of rotational and flexion-extension functions during the later phase (6–12 months) to enhance knee function and prevent long-term adverse outcomes.

## Musculoskeletal dynamics

The musculoskeletal system provides humans with the power of motion. Although the underlying processes are highly complex, modern imaging and modelling techniques allow these processes to be quantitatively revealed and analysed.

Sewify et al. explored the feasibility of combining 3D ultrasound and motion capture for non-invasive tracking of shoulder bones. Through *in silico* simulations and cadaveric experiment, they compared two registration algorithms: Iterative-Closest-Point (ICP) and Coherent Point Drift (CPD), for aligning full bone models with 3D ultrasound-imaged surface patches. CPD showed higher accuracy but longer computation time, suggesting it may be more suitable for this task. The study highlights the promise of 3D ultrasound with motion capture for dynamic bone tracking.

Sahrmann et al. introduced a 3D ultrasound-based method to quantify shape deformations of the tibialis anterior (TA) muscle during dynamic contractions. They found that muscle volume remained constant across different muscle lengths, while mean cross-sectional area (CSA) increased during TA muscle shortening. Additionally, maximum CSA shifted proximally with shortening. Significant differences were found between active and passive movements, especially at higher velocities. Their approach

enables non-invasive, dynamic tracking of muscle morphology and provided new insights for future empirical studies and musculoskeletal modelling.

From the perspective of energy and power, [Stróżyk and Bałchanowski](#) analysed unilateral food chewing, a process involving complex biomechanical interactions within the masticatory system. Using experimentally derived food resistance patterns and a 3D kinematic-dynamic model of the masticatory system, they simulated unilateral chewing to quantify energy and peak power generated by the masseter, medial pterygoid, and temporalis muscles. This study provides biomechanical insights into mastication: food height and texture influence muscle energy demands, with greater energy from the masseter and medial pterygoid on the working side and higher temporalis activity on the non-working side. Food position more strongly affects peak muscle power for foods with high texture heterogeneity.

## Finite element analysis in bone and joint

Finite element analysis (FEA) is a powerful numerical method originally developed in engineering to solve mechanical problems. Applied to biomechanics, it has proven highly effective in analysing intricate biomechanical forces and deformations, particularly in scenarios such as disease condition assessment, treatment planning, and bespoke implant design.

[Luo et al.](#) used FEA to investigate the effects of different manipulations of lower limb hyperextension (MLLHs) on the sacroiliac joint (SIJ) and surrounding ligaments. A 3D pelvis model was constructed, and four types of MLLHs were simulated. The resulting stresses on the pelvis and SIJ, as well as SIJ displacements and ligament strains, were analysed to quantitatively characterise the biomechanical effects of MLLHs and to provide a reference for clinical practice.

[Chen et al.](#) conducted a FEA to simulate two different fixations, the long-segment spinal inner fixation (LSIF) and the tandem spinal external fixation (TSEF) in treating multilevel non-contiguous spinal fracture (MNSF), evaluating their biomechanical performance. They found that TSEF demonstrated outperformed biomechanical characteristics compared to LSIF, including better preservation of range of motion and more balanced disc stress distribution. TSEF also reduced stress concentration on connecting rods and minimized stress shielding of fractured vertebrae, suggesting it may be a more effective alternative for managing MNSF.

[Roland et al.](#) performed FEA on a fractured human tibial shaft to identify optimal axial stroke values for “smart” fracture plates that were capable of cyclic shortening/lengthening. In the study, the FE models were reconstructed from CT data and incorporated virtual implants, simulating various fracture gap sizes (1–3 mm), angles (5°–60°), and healing stages. Mechanical parameters, including strain measures and the “perfect healing window”, were calculated and examined using linear regression. The analyses identified optimal strokes of 0.10–0.25 mm in early healing, 0.10 mm in mid-healing, and 0.35–0.45 mm in late healing, with gap size showing the greatest influence. These findings offer quantitative design guidance for active implants to enhance fracture healing.

In another FEA-based study, [Luo et al.](#) evaluated the biomechanical effects of varying microfracture drilling parameters, including diameter, depth, and spacing, on bone stability at cartilage defect sites. A femoral medial condyle defect model with different drilling configurations was subjected to FEA under simulated standing-load conditions. The results indicated that all parameter combinations produced stresses below the bone’s yield strength, with smaller diameter drills and closer spacing yielding the lowest Von Mises stresses. These findings provide biomechanical insight to support the selection of optimised drilling parameters in microfracture surgery, helping to preserve bone stability.

## Biomechanical measurements in vascular system

As a whole-body system, vascular system is responsible to provide sources of pump blood to whole body. Its complexity is reflected in its intricate network, multi-level structure, and variations in flow, velocity, and pressure at different locations. Moreover, the interaction between pulsatile blood flow and the compliant vessel walls poses additional challenges for performing accurate biomechanical measurements in the vascular system.

[Curcio et al.](#) evaluated non-invasive biomechanical metrics, including ultrasound-based point shear wave elastography (p-SWE) and wall tracking stiffness assessment, as well as computed tomography angiography (CTA)-derived 3D modelling with patient-specific FEA, to classify vulnerable carotid plaques in 100 endarterectomy patients. Vulnerable plaques showed significant differences in both ultrasound-derived stiffness measures, such as Young’s modulus, and FEA-based stress parameters, including von Mises and maximum principal stress patterns. Both modalities effectively differentiated vulnerable from stable plaques, supporting their potential for non-invasive stroke risk assessment.

[Zhang et al.](#) developed an objective optical coherence tomography angiography (OCTA) workflow for quantifying oral microvasculature. They employed a swept-source OCT system to scan 37 volunteers across four intraoral sites and analyzed a benign ulcer. They introduced automatic depth-of-interest segmentation and four metrics, namely, vessel area density (VAD), vessel skeleton density (VSD), vessel diameter index (VDI), and a novel weighted tortuosity index (WTI). Repeat scans showed low coefficients of variation, and site-specific patterns emerged (e.g., hard palate: lower VAD/VSD; floor of mouth: larger VDI). The work establishes reproducible OCTA metrics and WTI for early diagnosis and monitoring.

[Wei et al.](#) validated a porous-medium (PM) model for improving accuracy of patient-specific computational fluid dynamics (CFD) results in analysing iliac vein compression syndrome (IVCS). They reconstructed bilateral iliac veins with collaterals, modelled laminar Newtonian blood flow, tuned PM viscous resistance, and used a discrete-phase model to reproduce Digital Subtraction Angiography (DSA) contrast transit via time-to-peak (TTP). The PM model transported over 80% of particles through collaterals and matched DSA TTP (92.4% concordance). Compared to a non-porous model, the proposed PM model cut stenotic-region velocity by 87.5%, increased the IVC–left iliac pressure gradient by 141 Pa, and shifted WSS >2.0 Pa to

collateral vessels. The approach aligns CFD with clinical hemodynamics and supports IVCS assessment and treatment planning.

## Outlook

This Research Topic integrates the latest advancements in deformation and biomechanical analysis, spanning from whole-body to tissue-level studies. It highlights innovations in imaging, sensing, computational analysis, and modelling techniques, and further identifies current limitations while outlining future research directions. Collectively, These contributions underscore the significance of the field in advancing toward real clinical impact.

## Author contributions

JW: Writing – review and editing, Writing – original draft. CW: Writing – original draft, Writing – review and editing. QH: Writing – review and editing, Writing – original draft. RH: Writing – original draft, Writing – review and editing. ZL: Writing – review and editing. LZ: Writing – review and editing.

## Funding

The author(s) declare that no financial support was received for the research and/or publication of this article.

## Conflict of interest

The authors declare that the research was conducted in the absence of any commercial or financial relationships that could be construed as a potential conflict of interest.

The author(s) declared that they were an editorial board member of Frontiers, at the time of submission. This had no impact on the peer review process and the final decision.

## Generative AI statement

The author(s) declare that no Generative AI was used in the creation of this manuscript.

Any alternative text (alt text) provided alongside figures in this article has been generated by Frontiers with the support of artificial intelligence and reasonable efforts have been made to ensure accuracy, including review by the authors wherever possible. If you identify any issues, please contact us.

## Publisher's note

All claims expressed in this article are solely those of the authors and do not necessarily represent those of their affiliated organizations, or those of the publisher, the editors and the reviewers. Any product that may be evaluated in this article, or claim that may be made by its manufacturer, is not guaranteed or endorsed by the publisher.



## OPEN ACCESS

## EDITED BY

Björn Rath,  
Clinic Wels-Grieskirchen, Austria

## REVIEWED BY

Francesco Cenni,  
University of Jyväskylä, Finland  
Heiko Stark,  
Friedrich Schiller University Jena, Germany

## \*CORRESPONDENCE

Annika S. Sahrman,  
✉ sahrmann@imsb.uni-stuttgart.de

RECEIVED 20 February 2024

ACCEPTED 22 May 2024

PUBLISHED 05 June 2024

## CITATION

Sahrman AS, Vosse L, Siebert T, Handsfield GG and Röhrle O (2024), Determination of muscle shape deformations of the tibialis anterior during dynamic contractions using 3D ultrasound.

*Front. Bioeng. Biotechnol.* 12:1388907.

doi: 10.3389/fbioe.2024.1388907

## COPYRIGHT

© 2024 Sahrman, Vosse, Siebert, Handsfield and Röhrle. This is an open-access article distributed under the terms of the [Creative Commons Attribution License \(CC BY\)](#). The use, distribution or reproduction in other forums is permitted, provided the original author(s) and the copyright owner(s) are credited and that the original publication in this journal is cited, in accordance with accepted academic practice. No use, distribution or reproduction is permitted which does not comply with these terms.

# Determination of muscle shape deformations of the tibialis anterior during dynamic contractions using 3D ultrasound

Annika S. Sahrman<sup>1,2\*</sup>, Lukas Vosse<sup>2,3</sup>, Tobias Siebert<sup>2,3</sup>,  
Geoffrey G. Handsfield<sup>4</sup> and Oliver Röhrle<sup>1,2</sup>

<sup>1</sup>Institute for Modelling and Simulation of Biomechanical Systems, University of Stuttgart, Stuttgart, Germany, <sup>2</sup>Stuttgart Center for Simulation Science, University of Stuttgart, Stuttgart, Germany, <sup>3</sup>Institute of Sport and Movement Science, University of Stuttgart, Stuttgart, Germany, <sup>4</sup>Auckland Bioengineering Institute, University of Auckland, Auckland, New Zealand

**Purpose:** In this paper, we introduce a novel method for determining 3D deformations of the human tibialis anterior (TA) muscle during dynamic movements using 3D ultrasound.

**Materials and Methods:** An existing automated 3D ultrasound system is used for data acquisition, which consists of three moveable axes, along which the probe can move. While the subjects perform continuous plantar- and dorsiflexion movements in two different controlled velocities, the ultrasound probe sweeps cyclically from the ankle to the knee along the anterior shin. The ankle joint angle can be determined using reflective motion capture markers. Since we considered the movement direction of the foot, i.e., active or passive TA, four conditions occur: slow active, slow passive, fast active, fast passive. By employing an algorithm which defines ankle joint angle intervals, i.e., intervals of range of motion (ROM), 3D images of the volumes during movement can be reconstructed.

**Results:** We found constant muscle volumes between different muscle lengths, i.e., ROM intervals. The results show an increase in mean cross-sectional area (CSA) for TA muscle shortening. Furthermore, a shift in maximum CSA towards the proximal side of the muscle could be observed for muscle shortening. We found significantly different maximum CSA values between the fast active and all other conditions, which might be caused by higher muscle activation due to the faster velocity.

**Conclusion:** In summary, we present a method for determining muscle volume deformation during dynamic contraction using ultrasound, which will enable future empirical studies and 3D computational models of skeletal muscles.

## KEYWORDS

3D ultrasound, image processing, dynamic movement, muscle deformation, contraction



# 1 Introduction

Muscles are the motors of human movement. During contraction, muscle deformation occurs as a result of changes in muscle length, changes in internal muscle architecture (particularly pennation angle and fascicle length), and constraints on muscle deformation by surrounding tissues and external forces (Lieber and Fridén, 2000; Reinhardt et al., 2016; Wick et al., 2018).

2D ultrasound is a widely-used and clinically established tool for investigating skeletal muscle architecture (Arampatzis et al., 2006; Ryan et al., 2019). In a systematic review, Hooren et al. (2020) showed the feasibility of 2D ultrasound for investigating fascicle length and pennation angle during dynamic contraction. However, with such examinations, 3D information is missing which may provide relevant information on the muscle's contractile behavior. A commonly used method to examine 3D muscle architecture and muscle volume relies on a combination of conventional magnetic resonance imaging (MRI) and diffusion tensor imaging (DTI) (van Donkelaar et al., 1999; Heemskerk et al., 2010; Hiepe et al., 2013). Compared to such methods, ultrasound is less expensive, enables faster acquisitions and is portable.

Thus, there have been recent efforts to generate 3D images from ultrasound data. In this regard, muscle volume is a useful morphological parameter to infer age, training level and growth processes of subjects (Albracht et al., 2008; Hanson et al., 2009; Siebert et al., 2017). In addition, the anatomical cross-sectional area (CSA) and its distribution on the muscle belly can provide information about the specific muscle shape and muscle adaptations (Albracht et al., 2008).

3D freehand ultrasound is an approach for acquiring muscle volumes from ultrasound imaging where the position of the ultrasound probe is recorded by, e.g., optical retroreflective motion capture markers or a magnetic sensor. The operator uses the equipped probe to scan along the longitudinal muscle axis, such that the image position and orientation for each cross-sectional 2D image is known. As a result, a stack of 2D cross-sectional images of the muscle is collected, from which a 3D volume can be reconstructed by applying a series of coordinate transformations (Barber et al., 2009; Rana and Wakeling, 2011; Raiteri et al., 2016; Weide et al., 2017). Furthermore, the reconstructed volumes obtained from 3D freehand ultrasound measurements can be used to determine in-plane fascicle lengths or pennation angles (Kurihara et al., 2005; Weide et al., 2017).

Previous studies which investigated volumetric muscle data using 3D ultrasound mainly focused on isometric contractions or resting states (Raiteri et al., 2016; Weide et al., 2017; Cenni et al., 2018). Isometric conditions are static and account only for a small part of movements in everyday life. There is a need for acquisition techniques that capture the dynamic contractile behavior of muscles that investigate 3D muscle deformation in dynamic conditions. Such a technique could record dynamic muscle shape changes during contraction which would capture essential information that could be used as inputs for the development and validation of 3D computational models of muscles (Röhrle et al., 2016; Seydewitz et al., 2019).

This study presents a novel approach for determining 3D deformation of the tibialis anterior (TA) muscle during dynamic

movement. The approach represents an extension of an automated 3D ultrasound system for acquisition of muscle volumes in static conditions (Sahrmann et al., 2024; Sahrmann et al., 2024), and a sophisticated implementation of the methods employed in Sahrmann et al. (2022). By using motion capture for determination of the ankle joint angle and encoder data for recording the ultrasound probe position and orientation, each 2D ultrasound image contains a corresponding probe position/orientation and an ankle joint angle. Reconstructing 3D ultrasound images while the foot is moving is possible by defining ankle joint angle intervals during repeated plantarflexion movements. In this study, we determine muscle volume and the anatomical CSA from the acquired information, i.e., the 2D images, as well as position and ankle joint angle information.

## 2 Materials and methods

This section describes the experimental methods for obtaining 3D ultrasound images in dynamic conditions, i.e., while the subject actively moves the foot under controlled conditions. The algorithm for reconstructing 3D volumes of the TA during motion is presented, which groups ankle joint angles into intervals of 1°.

### 2.1 Experimental setup

We used an automated 3D ultrasound system, with an Aixplorer MACH30 (Supersonic Imagine, Aix-en-Provence, France) and a linear probe (SuperLinear SL18-5), for acquisition of 3D ultrasound data, as further described in Sahrmann et al. (2024). The system consists of three axes along which the probe is moved and a built-in force control mechanism to ensure consistent tissue deformation. Simultaneously, eight infrared cameras (VICON, Oxford, United Kingdom) recorded positional data from reflective markers at a frame rate of 100 Hz. The system contains three movement directions, which allow positioning of the ultrasound probe in the 3D space. The first movement direction corresponds to the circular path of the two semicircles. The second movement axis corresponds to the horizontal axis between the two semicircles, which allows the movement along the shank (longitudinal muscle axis). The third movement axis corresponds to the vertical movement of the probe, perpendicular to the longitudinal axis. This vertical axis is realized as a direct linear motor and contains an included force control, such that the probe presses on the skin with the same force along the scanning trajectory. With this, there is no loss of skin contact due to the curved shape of the leg or inconsistent tissue deformation due to changes in the exerted contact force.

We collected the 2D ultrasound images with an HD frame grabber (USB3HDCAP, Star-Tech.com Ltd.) at a frame rate of 30 Hz. For synchronizing the encoder data of the axes of the system, the ultrasound images recorded with the frame grabber and the VICON motion capture markers, the automated 3D ultrasound system at first sent a 5 V signal to the VICON system once a movement at the axes is started or stopped. This signal serves as an external trigger for VICON to start or stop a measurement. Simultaneously, VICON sends out a User Datagram Protocol (UDP) message containing relevant information if a recording



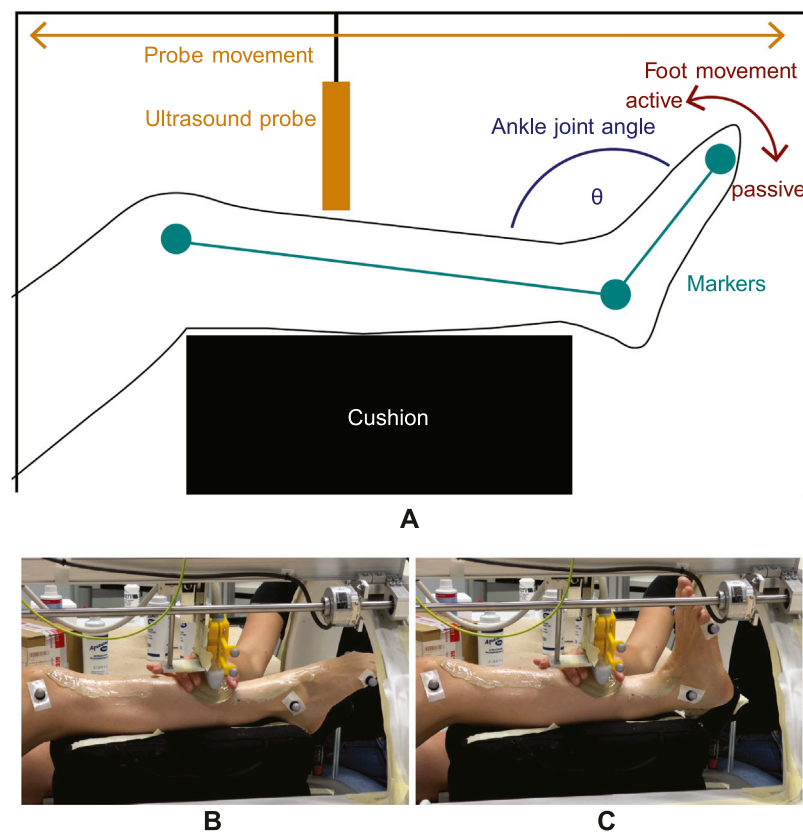


FIGURE 1

Experimental setup for dynamic imaging. (A) The lower leg is elevated and equipped with reflective markers (green) from which the ankle joint angle  $\theta$  (blue) can be computed. While the foot moves periodically from plantarflexion to neutral position (red arrow) and vice-versa, the transducer moves back and forth (orange arrow) from the distal to the proximal end of the TA. As the dorsiflexion movement direction is generated by TA contraction, it is defined as an *active* movement whereas opposite plantarflexion is defined as a *passive* movement. (B,C) show images of the setup with one subject during dynamic imaging at two different ankle joint angle positions. Here, the gel pad is moved alongside to ensure sufficient image quality.

starts or stops. A custom-written LabVIEW (version 2021.0) script receives the UDP message as a trigger for recording the image data. For computation of the ankle joint angle, reflective markers were placed at the following locations: lateral and medial epicondyle, lateral and medial malleolus, first and fifth metatarsal. We placed each subject's lower limb on a hard cushion. The positioning allowed movement of the foot and visibility of the reflective markers.

In total, 3D ultrasound images of the TA of the right leg were obtained from five subjects (2 male, three female). The experimental procedures involving human subjects described in this paper were approved by the University of Stuttgart's Committee on Responsibility in Research (number: Az. 21-011). All subjects provided written informed consent. The anthropometric characteristics of the subjects are: age  $27.8 \pm 3.1$  years, height  $177.2 \pm 7.9$  cm, weight  $68 \pm 10.9$  kg, body mass index  $21.52 \pm 1.93 \frac{\text{kg}}{\text{m}^2}$ .

As a first part of the study, participants were told to actively move their foot to two different positions: (1) plantarflexion and (2) neutral foot position, which is defined as the neutral standing position. One scan of each position was conducted per subject with an average scan time of 15–20 s. The probe movement velocity on the horizontal axis was set to  $20 \frac{\text{mm}}{\text{s}}$  for the static and dynamic trials. With a recording frame rate of 30 Hz, there are

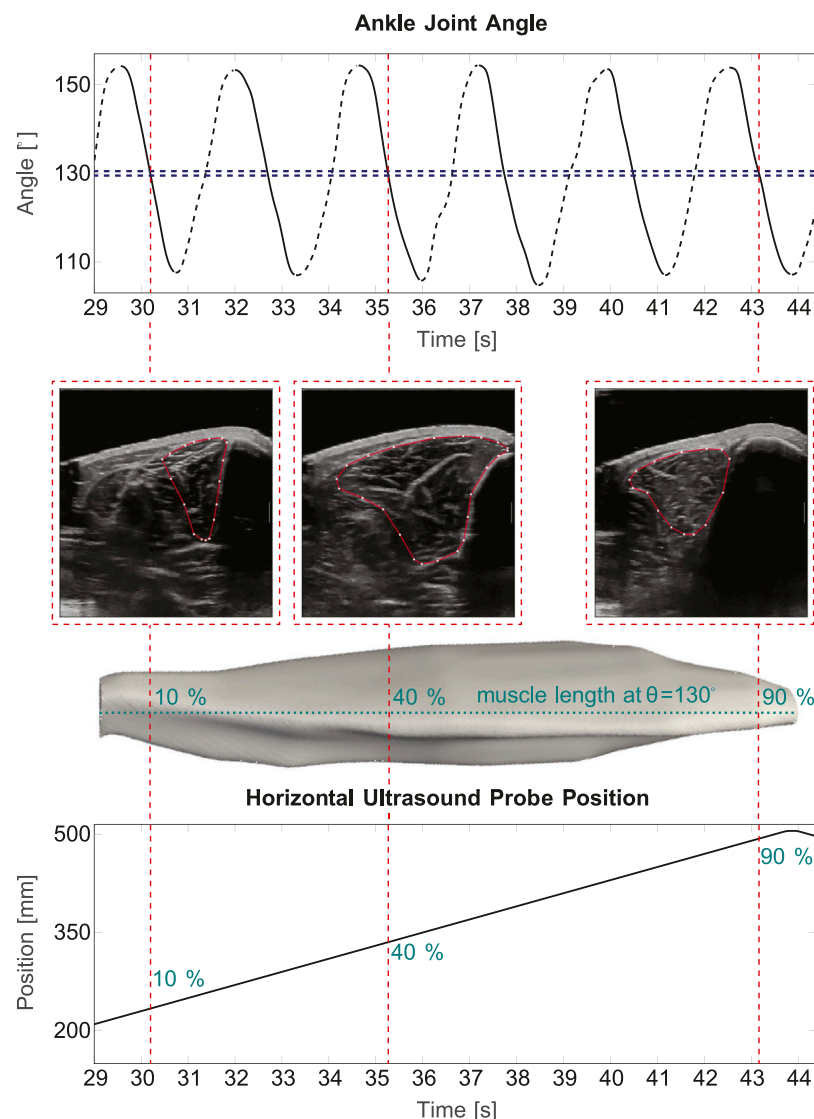
approximately 15 images collected per cm the average distance between two sequential collected 2D images is 0.67 mm.

For the second part of the study, the subject performed a cyclical movement consisting of a plantarflexion (neutral to plantarflexed position) and a dorsiflexion (from plantarflexed to neutral position) until a defined stop signal is given. Average joint angles for plantarflexion and the neutral position were  $157^\circ \pm 6^\circ$  and  $113^\circ \pm 9^\circ$ , respectively.

We used a metronome for visual and audio feedback for the subject to control their foot velocity. Moving velocity was set on the metronome to 45 and 100 beats per minute, which is referred to as *slow* and *fast*, respectively. This means that the foot was in plantarflexion on every second beat, and in the neutral position on each beat in between.

Simultaneously, the automated 3D ultrasound system moved the transducer periodically from the proximal to the distal end of the TA and vice-versa (along the horizontal axis, Figure 1).

The principle of the data acquisition method is illustrated in Figure 1. Since the repetitive foot movement is a monotonous task, it can be demanding in terms of coordination and concentration. Therefore, each subject's trial for a given velocity (which totaled 9 min) was split into 4 separate smaller trials of 2 min and 15 s each, in order to ensure a constant concentration level for the subjects



**FIGURE 2**  
3D ultrasound in cyclic movements. The top part of the figure shows a 15 s sequence of measured ankle joint angle during a cyclic *slow* velocity trail. Here, it is distinguished between *active* (solid lines) and *passive* (dashed lines) movement. A  $1^\circ$  interval at  $130^\circ$  ankle joint angle is illustrated exemplarily in blue, the red lines show three example image frames, which are extracted. Below, the corresponding 2D B-Mode ultrasound images and the corresponding position on the muscle are shown. The bottom part displays the ultrasound probe's position along the horizontal axis of the device.

during the measurements. To avoid loss of skin contact, a gel pad (Aquaflex, Parker Laboratories, Fairfield, United States of America) and ultrasound gel were used (see [Figures 1B, C](#)).

## 2.2 Angle intervals

After recording, encoder positions and motion capture data were sampled to the ultrasound frame rate. Four trials of one velocity were stitched to obtain a sufficient number of 2D images within one ankle joint angle interval for reconstruction. The ankle joint angle  $\theta$  was computed as the angle between the vector from lateral knee epicondyle to lateral malleolus and the vector from lateral malleolus to fifth metatarsal (see [Figure 1A](#)). Ultrasound measurements for a given ankle angle were binned into intervals of  $1^\circ$ , which means

$\theta - 0.5^\circ \leq \theta < \theta + 0.5^\circ$ . Furthermore, it was determined if the slope on the ankle angle curve was negative or positive. This was done to define the direction of the foot movement, i.e., if it is a dorsiflexion (negative slope) or plantarflexion (positive slope) movement. Since 3D ultrasound images of the TA were acquired, the dorsiflexion induced by TA contraction is referred to as *active* movement direction and the opposite plantarflexion movement direction is referred to as *passive* in the following. All frames and encoder positions belonging to one specific angle interval and movement direction were extracted.

[Figure 2](#) illustrates a cutout (of approximately 15 s) of one example trial with *slow* velocity. Three extracted frames at the same ankle joint angle  $\theta$  ( $130^\circ$ ), yet from different positions along the TA (10%, 40% and 90% of the muscle length), are shown exemplarily for *active* dorsiflexion.

If the distance between two images within one interval was smaller than 0.8 mm, the average of those images and corresponding position values was taken. The image stack and the corresponding encoder positions were exported to Matlab (R2020a, MathWorks, MA, United States of America) if they met the following criteria: 1) a minimum of 40 images are within the image stack of the interval with one movement position and 2) the maximum distance between two images within the stack is less than 25 mm.

A Stradwin (v6.02, University of Cambridge, United Kingdom) file was generated from the Matlab file containing all 2D images and position information for a given  $\theta$  interval. Stradwin is a freely available software tool developed by the Machine Intelligence Laboratory at the Cambridge University's Engineering Department. The program was developed mainly for data acquisition and visualization of 3D freehand ultrasound applications. Stradwin requires two different input files: a binary image file (.sxi) containing the collected images and a text file (.sw) comprising pixel scaling information for each image and associated position and orientation data. In the program, the 2D images are automatically positioned according to the position and orientation data in the sw file.

Since there are four different conditions (*slow active*, *slow passive*, *fast active*, *fast passive*), the maximum and minimum available  $\theta$  meeting the inclusion criteria was determined for each condition. For each subject, range of motion (ROM) was defined as the range from the larger value of the smallest available  $\theta$  value for *active* and *passive* movement to the smaller value of the largest available  $\theta$  value for *active* and *passive* movement. For each of the four conditions, the volume was reconstructed in 10% intervals of ROM. This means, that there are 11 reconstructions (0%–100% of ROM) for each subject and condition, so a total of 44 data sets (which describe the 3D muscle shape) per subject. The ROM intervals correspond to the muscle elongation caused by extension of the foot for plantarflexion, i.e., the 0% of ROM means the shortest TA muscle length and 100% of ROM refers to the longest one.

## 2.3 3D reconstruction and image segmentation

We used Stradwin for 3D reconstruction of the TA. The segmentation was done by manually outlining the muscle on 15–20 slices at approximately equidistant frames along the muscle's longitudinal axis. The selection of 15–20 segmented slices leads to a slightly larger distance between images in comparison to a study of Raiteri et al. (2016), investigating the TA in isometric conditions using 3D freehand ultrasound. Here, the TA cross-section was segmented in 5–15 mm intervals. Both the muscle volume and length and the fascicle orientations and lengths were investigated, whereas our study primarily focuses on the assessment of muscle volume, length and anatomical cross-sectional area (CSA). From the manually outlined slices, Stradwin interpolates a surface through the segmented image slices and creates a 3D volume (Treece et al., 1999; Treece et al., 2000). Surface creation settings in Stradwin were set to *low resolution* and *high smoothing* strength.

We used a weighted principal component analysis (PCA), as proposed in the study of Raiteri et al. (2016), to initially rotate the geometry into the coordinate system of its principal component axes. Volume was defined as the sum of the segmented voxels multiplied by their resolution in each dimension. Length is the euclidean distance from the centroids of the first and last segmented slice, e.g., the most proximal and most distal point of the TA. For each segmentation slice, the CSA is computed by the sum of pixels multiplied by the pixel size.

## 2.4 Ellipsoid prediction

An ellipsoid can be considered a highly simplified shape of a muscle which has been shown to allow reproduction of muscle shapes and gearing ratios (Siebert et al., 2012). For later comparison with experimental TA data, the equation for the volume of an ellipsoid was used for computing its CSA (Eq. (1)):

$$V = \frac{4}{3}\pi abc. \quad (1)$$

Here,  $a$ ,  $b$ ,  $c$  are the lengths of the semi-axes of the ellipsoid. The parameter  $c$  is defined as the longitudinal semi-axis of the ellipsoid (Eq. (2)),

$$c = \frac{1}{2}L_{Muscle}, \quad (2)$$

where  $L_{Muscle}$  is the muscle length at the corresponding  $\theta$  interval. The maximum CSA of an ellipsoid can be defined as (Eq. (3)):

$$CSA_{Ellipsoid} = \pi ab. \quad (3)$$

Muscle volume was assumed to stay constant (Baskin and Paolini, 1967; Böl et al., 2013), while  $c$  was considered to elongate as the muscle would be lengthened by moving the foot from neutral position to plantarflexion. Using the experimentally determined CSA values,  $CSA_{ellipsoid}$  can be determined as (Eq. (4)):

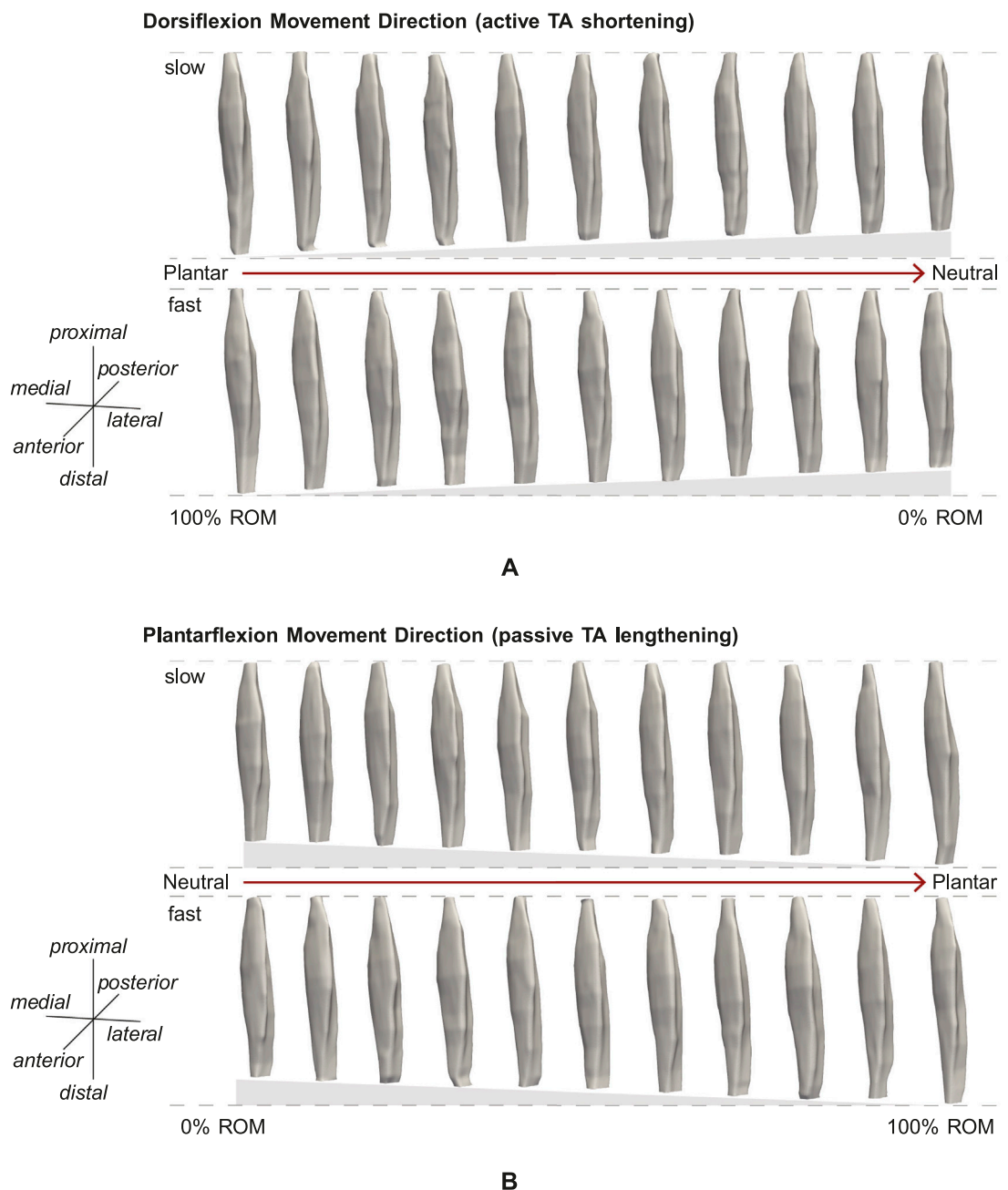
$$CSA_{Ellipsoid} = \frac{3}{4} \frac{V_{muscle}}{c}. \quad (4)$$

## 2.5 Statistical analysis

Shapiro-Wilk tests were used for testing the data for normal distribution. For comparison between groups, one way repeated analyses of variance (ANOVAs) were used for normally distributed data and Friedman tests were applied for non-normally distributed data. Analyses of covariance were employed for comparison between regression lines. The level of significance,  $\alpha$ , was set to 0.05.

## 3 Results

Figures 3A, B show examples of TA volume reconstructions for one representative subject for all 11 intervals of ROM, for *active* TA shortening and *passive* TA lengthening, respectively. As expected, muscle length decreases during *active* TA contraction with a



**FIGURE 3**  
Example reconstruction for 10% intervals of ROM for (A) active and (B) passive movement with slow and fast velocity. (A) Muscle shortening towards the neutral position can be observed. (B) Muscle lengthening and stretching towards the plantarflexion position are visible.

decrease in the ankle joint angle, i.e., a decrease in ROM (100% ROM to 0% ROM, see Figure 3A). Due to TA shortening the muscle gets thicker.

### 3.1 Muscle volume and length

The mean computed muscle volume of the five subjects for the static trials was  $89.0 \pm 28.1 \text{ cm}^3$ . For these trials, muscle volumes did not differ significantly between neutral position and plantarflexion for each subject. For the dynamic trials, the determined mean muscle

volume was  $89.2 \pm 26.4 \text{ cm}^3$ . Muscle volume did not differ significantly between the different ROM intervals. Also, no significant differences between the muscle volumes obtained from dynamic and static trials could be observed. Averaged over all subjects, the maximum differences of normalized muscle volume between different ROM intervals for dynamic trials were in a 2% range. The mean change in muscle length from neutral position to plantarflexion was  $20.0 \pm 3.7 \text{ mm}$  (9.6% increase) for static trials. For the dynamic trials, we found an overall length change of  $22.5 \pm 8.5 \text{ mm}$  (11.2% increase) from neutral to plantarflexion. We further computed the change in muscle length for the two movement

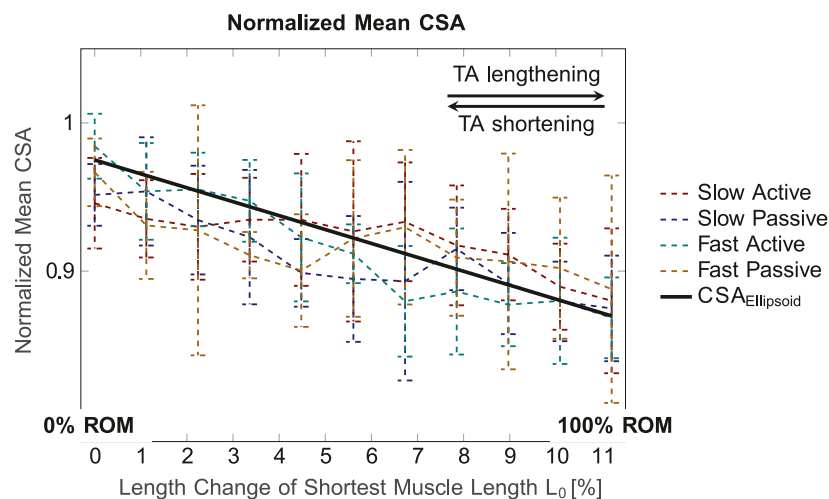


FIGURE 4

Mean normalized CSA (for the whole muscle) for the four conditions and different muscle lengths. The normalized volume value for the ellipsoid, which is defined as constant for all muscle lengths, was set to 1.3. In general, the normalized mean CSA decreases for increasing muscle length.

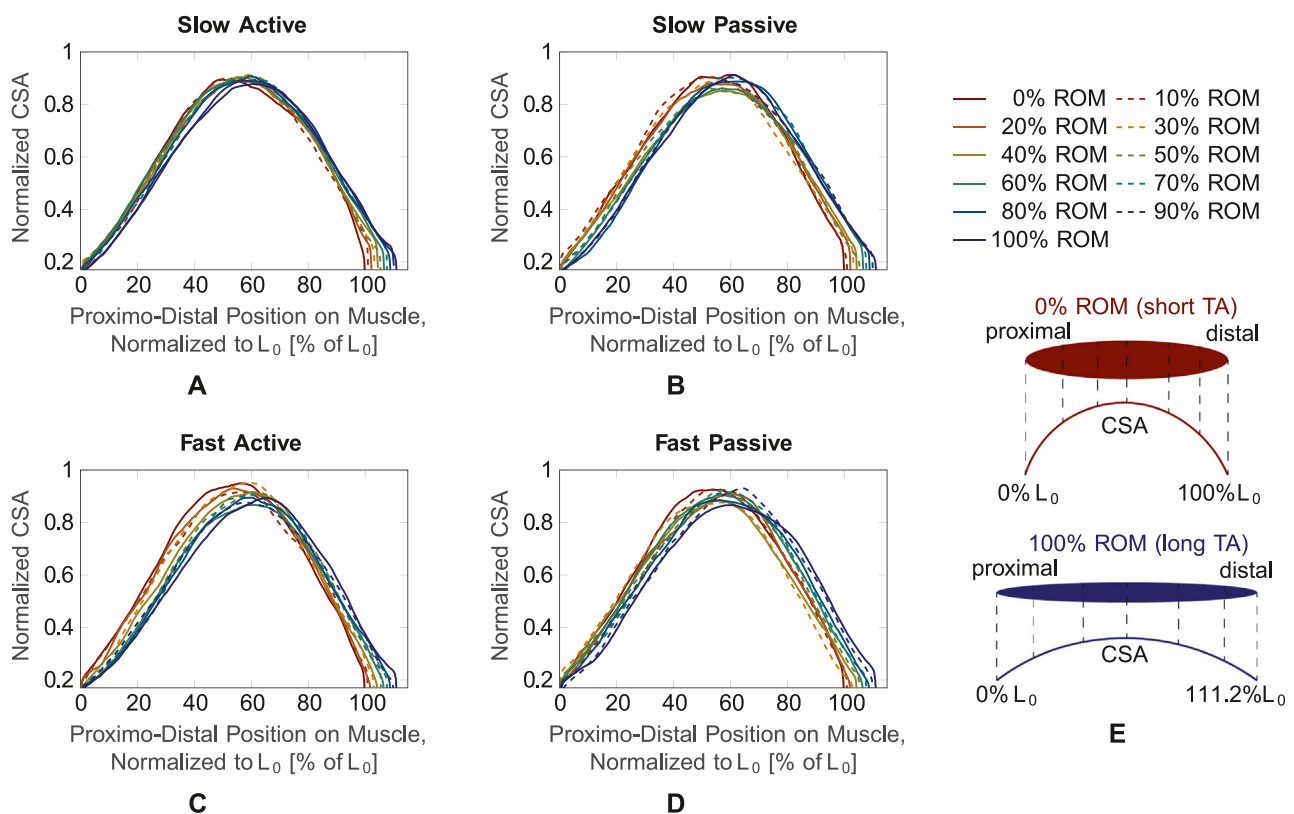


FIGURE 5

CSA over muscle length normalized to the shortest muscle length  $L_0$  for the four conditions. Different muscle lengths corresponding to different ROM values (0%–100% ROM) are plotted with different line types and colors. (A) *Slow active*, (B) *slow passive*, (C) *fast active*, (D) *fast passive*. As schematically shown in (E), 0% ROM and 100% ROM refer to the shortest and longest TA length, respectively. The muscle CSA (exemplary broken vertical lines in (E)) is plotted from the proximal to the distal end of the muscle, which corresponds to 111.2%  $L_0$  for the longest muscle.



directions separately. For the *active* condition, the muscle length decrease was  $23.0 \pm 5.6$  mm (11.5%) and for the *passive* condition, the muscle length increase was  $22.0 \pm 10.9$  mm (10.8%).

### 3.2 Cross-sectional area

The shortest muscle length, corresponding to 0% of ROM (Figure 3), was defined as 100% of the reference muscle length  $L_0$ . Muscle lengths of other ROM intervals were computed with regard to  $L_0$ . Thus, by increasing the ROM intervals to 100% of ROM, the maximum muscle length is 111.2% of  $L_0$ , corresponding to a mean stretch of 11.2%.

Figure 4 illustrates the mean normalized CSA values for the whole muscle for the four conditions (*slow active*, *slow passive*, *fast active*, *fast passive*), and the predicted ellipsoid cross sectional area  $CSA_{Ellipsoid}$ . Here,  $CSA_{Ellipsoid}$  shows a straight line with a negative slope, i.e., a decrease in CSA for elongation of the ellipsoid. The experimentally determined CSA shows a similar trend for all conditions. Significant differences in mean CSA between different muscle lengths, i.e., different ROM intervals, were found for *slow active* ( $p = 0.004$ ), *slow passive* ( $p < 0.001$ ) and *fast active* ( $p < 0.001$ ), and no significant differences for *fast passive* ( $p = 0.111$ ). Mean CSA was significantly different between *slow active* and *fast active* ( $p = 0.003$ ) and *fast active* and *fast passive* ( $p = 0.001$ ).

Figure 5 illustrates the mean normalized CSA of all subjects for the four different conditions (Figures 5A–D), plotted over the shortest muscle length  $L_0$  for the dynamic trials. The curves are color-coded according to  $L_0$ , i.e., from red (minimum muscle length, corresponding to 0% ROM) to blue (maximum muscle length, corresponding to 100% ROM). For better visualization, they are illustrated with alternating solid and dashed lines. For all four conditions, the curves show an increase in CSA in the middle region of the muscle, while they narrow towards the proximal and distal ends. This can be explained by the spindle-like shape of the muscle, i.e., the muscle belly is located in the middle part of the muscle and narrows towards the tendons at the proximal and distal part of the muscle (Figure 5E). It can be observed that the maximum value of the CSA is shifted in the left direction on the x-axis, i.e., towards the proximal side, for decreasing muscle length, which is especially visible for the *fast active* condition (Figure 5C). Thus, for the more proximal part of the muscle, the red curve (0% ROM) is above the blue curve (100% ROM). In the distal part of the muscle, the red curve is below the blue one. During *fast active* contractions (Figure 5C) there is a noticeable increase in the maximum CSA (blue line, representing 100% ROM to red line, representing 0% ROM) as the muscle shortens.

Due to slight fluctuations in the curves, which may be caused by movement and evaluation artifacts, assessments of the three other conditions (*slow active*, *slow passive*, *fast passive*) are difficult. To achieve a better understanding of the changes in maximum CSA and its position on the longitudinal axis of the muscle, we smoothed the curves by fitting them with a second degree polynomial function.

For testing of correlation between the curves and the polynomial fit, a Pearson correlation was applied and a mean correlation coefficient  $R = 0.981$  (ranging from 0.967 to 0.989) was found. Thus, the polynomial fit can be considered a reliable approximation. The resulting maximum CSA values and their corresponding

positions on the muscle's longitudinal axis for the four conditions (pale colored lines) are shown in Figures 6A, B, respectively. In general, for muscle shortening, the CSA seems to increase by approximately 5% (Figure 6A) and its position seems to shift from ~60% of  $L_0$  to ~55% of  $L_0$ , i.e., in proximal direction on the longitudinal muscle axis (Figure 6B). To confirm these statements statistically and to examine the differences between the four conditions, an analysis of covariance, which makes use of linear regressions, was employed (colored thick lines in Figure 6). Based on the analysis of covariance, we can conclude that in all four conditions a decrease in the maximum CSA for stretching the muscle can be observed.

Maximum CSA is significantly different between *slow active* and *fast active* ( $p = 0.005$ ), *slow passive* and *fast active* ( $p = 0.028$ ) and *fast active* and *fast passive* ( $p = 0.0014$ ). The position of the maximum CSA shifts to the proximal part for shorter muscle lengths for all four conditions. The position of the maximum CSA does not significantly differ between the four conditions.

## 4 Discussion

In this paper, we introduced a novel approach for obtaining 3D muscle volumes of the TA during movement. In general, the TA muscle consists mainly of type I muscle fibers (Henriksson-Larsén et al., 1983; Jakobsson et al., 1990). The contraction velocity and forces (~0N) required to perform the prescribed movement are notably lower than the muscle's capacity. Participants characterized the movement's difficulty as minimal, with no indication of perceived exhaustion. Consequently, muscular fatigue is not deemed a limiting factor. In both static and dynamic conditions, muscle volumes stayed constant while muscle lengthening was observed due to an increase of ROM. This is consistent with previous literature (Fry et al., 2003; Barber et al., 2009) and may indicate a low error of the proposed method for determining muscle shape and volume in dynamic conditions. So far, 3D freehand ultrasound imaging studies on skeletal muscles mainly focused on isometric contractions, i.e., static conditions, for obtaining 3D volumes (Barber et al., 2009; Weide et al., 2017; Cenni et al., 2018). With the proposed method, 3D reconstructions of the TA during periodic movements are possible. This may provide entirely new means to investigate the muscle's dynamic contraction behavior.

### 4.1 Comparison with a simple ellipsoidal muscle model

When the ankle joint angle decreases, the TA muscle shortens and the maximum CSA shifts towards the proximal origin of the muscle. Since the muscle volume stays constant, it has to redistribute along the shorter length of the muscle. The comparison of the CSA prediction by an ellipsoidal muscle model with experimentally obtained data shows a similar trend in decrease of CSA for increase in muscle length (Figure 4). This demonstrates that the proposed method can serve as a suitable tool for determining 3D muscle deformations during dynamic contractions.

Although an ellipsoid is a highly simplified shape of a skeletal muscle, it has been shown to be an appropriate geometric body for

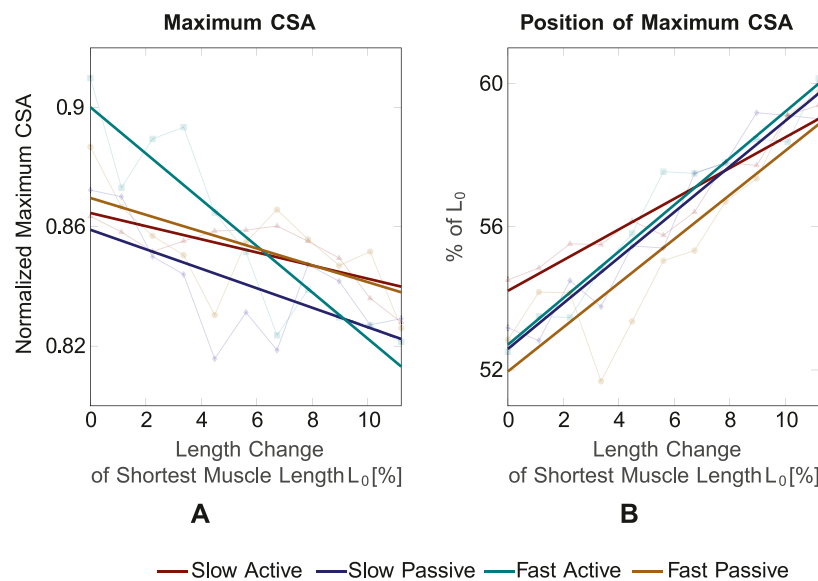


FIGURE 6

(A) Maximum CSA value and (B) position of maximum CSA for the four conditions and different muscle lengths. The maximum CSA decreases for increasing muscle length and its position shifts towards the distal part for increasing muscle length.

predicting muscle shape and contraction behavior (Siebert et al., 2012). However, the suitability for the ellipsoid as a representative muscle shape (Aubel and Thalmann, 2004) may vary between different muscles. This applies particularly to non-spindle-shaped muscles with more complex muscle geometries, such as the back and shoulder muscles (Stark et al., 2012; Tous et al., 2023). Thus, the proposed method enables the generation of more sophisticated input geometries for modeling skeletal muscle, compared to a simplified shape, such as an ellipsoid.

## 4.2 Comparison of 2D and 3D ultrasound

Franchi et al. (2017) found positive correlations between muscle thickness measured from 2D ultrasound images and anatomical CSA obtained from MRI. Investigating the TA by using 2D ultrasound, Maganaris and Baltzopoulos (1999) and Reeves and Narici (2003) did not find significant changes in TA muscle thickness at different ankle joint angles. Their results applied to resting conditions and maximum voluntary contraction (MVC). In the present study, we found an increase of the mean CSA (Figure 4) and maximum CSA (Figure 6) with a decrease of the ankle joint angle in *passive* and *active* conditions. In terms of the relationship between the anatomical CSA and muscle thickness (Franchi et al., 2017), this would not be consistent with the findings of Maganaris and Baltzopoulos (1999) and Reeves and Narici (2003). Hu et al. (2019) found, however, significant differences between muscle thickness for dorsiflexion and plantarflexion and Choi et al. (2019) observed increases in muscle thickness during contraction.

Such differences in findings may be explained by the different methods used in the studies or differences in TA architecture of the examined subject groups. The TA has a complex bipennate architecture and exhibits sexual dimorphisms in humans (Martin-Rodriguez et al., 2023). Furthermore, the TA presents

morphological asymmetries between its superficial and deep unipennate regions. For example, the superficial and deep TA regions differ in thickness and pennation angle (Martin-Rodriguez et al., 2023). Depending on their architecture, muscles and muscle compartments can deform differently in their width and thickness when shortened (Eng et al., 2018). Observed muscle deformations via 2D ultrasound may therefore depend on the positioning and orientation of the ultrasound probe. Thus, the existing differences in findings on 2D thickness indicate the need of a method for obtaining 3D volumes of muscles revealing deformation patterns during dynamic contractions, of which our proposed method is capable.

## 4.3 Impact of movement condition on CSA

Significant differences in mean CSA were observed for different ROM intervals for the *slow active*, *slow passive* and *fast active* conditions but not for the *fast passive* one (see Section 3.2 and Figure 4). Increasing the movement velocity during contractions against equal loads (in our case the inertia of the foot) requires higher muscle activations. Thus, it can be expected that the *fast passive* TA movements required a higher activation of the antagonistic plantar flexors (i.e., the gastrocnemius muscles and the soleus muscle) compared to *slow passive* TA movements. In previous studies on the human lateral gastrocnemius, a gradual increase in muscle activation from 10% to 100% resulted in different muscle thicknesses (Kelp et al., 2023). This is due to activation and force-dependent changes in the internal muscle architecture, especially the pennation angle. At higher contraction speeds there is greater muscle fiber rotation, i.e., change in pennation angle (Azizi et al., 2008; Eng et al., 2018). This can also lead to movement velocity dependent differences in CSA. Since the lower leg rested on the plantar flexors in our experimental setup (Figure 1), their higher



active deformation at increased cycle frequencies (100 beats per minute) led to a stronger vertical movement of the lower leg and the ultrasound transducer. Thus, artifacts in the ultrasound TA images may occur. Consequently, such vertical movement may induce the larger standard deviations in the computed CSA observed, as in Figure 4 (yellow broken line). Hence, the scatter of the data for the *fast passive* condition is larger, which is probably why statistically significant deviations do not occur.

We found significantly different maximum CSA values between the *fast active* and all other conditions. The observed differences are explainable and to be expected because the muscle shape differs between *active* and *passive* muscles with the same length (Böl et al., 2013). The linear regression of the maximum CSA curve (Figure 6A) shows the steepest slope for the *fast active* condition, where the highest TA muscle activation can be expected. This indicates a greater bulging of the muscle for the *fast active* condition. The findings are in agreement with those of Raiteri et al. (2016), who measured CSA changes of the TA during isometric contractions with different activation levels using 3D freehand ultrasound. For low activation levels in a range of 5%–10% MVC, the change in CSA compared to a resting state was in a range of 2%–4%, which is relatively small. Larger increases in CSA were observed for 25% and 50% MVC.

The increase in CSA for higher velocities can be related to the variable contraction behavior of a muscle and the architectural gearing ratio (AGR) (Brainerd and Azizi, 2005). The AGR is defined as the relation of the muscle shortening velocity to the fiber shortening velocity. When a muscle contracts, variable shape changes of the muscle can occur (Eng et al., 2018), i.e., the thickness can increase, decrease or stay constant. This is caused by the architectural changes in the muscle during dynamic contraction, as muscle fibers can both shorten and rotate. The combination of shortening and rotation enables changes in the pennation. Thus, changes in pennation angle allow the muscle belly to shorten faster than the fibers, which refers to an AGR greater than one. In this study, the increase in CSA for faster velocities may therefore be caused by a higher AGR.

## 4.4 Limitations

One limitation of the proposed method is that the leg of the subject was not fixed during scanning. Therefore, it was not possible to enable a fully controlled movement of the leg. This means that side movements of the foot during *active* or *passive* movement were possible. Further, some participants felt a moderate discomfort and needed to shift the leg's position between trials, even though the movement was relatively small, since the subjects stayed in the lying position and did not stand up in between. Thus, the stitched trials might not always be recorded at the exact same leg position. Moreover, the movement velocity of the foot was based on the metronome. This does not ensure that all movements were exerted with the exact same velocity. Therefore, in order to ensure more controlled conditions in terms of movement direction and velocity, future studies should include a fixture of the leg which enables only plantarflexion and dorsiflexion movements. The fixation of the leg and the kinematic control of a reproducible cyclic joint movement may be realized by using an isokinetic measurement system, such as

an ISOMED (Holzer et al., 2023). Through the possibility of more controlled measurements with less movement artifacts, the deformation gradient of the muscle may be computed. This means that 3D deformation changes can be determined between different muscle lengths during dynamic movements. By reducing the effects of movement and fixing the leg, it is possible to examine not only the external deformation of the muscle, but also its internal architecture, for which the method described in Sahrman et al. (2024) can be used. Furthermore, with our algorithm, 3D images were reconstructed if the maximum distance between two images did not exceed 25 mm. In our study, the main focus was to present a method for obtaining features such as muscle volume, length and CSA, where this distance was sufficient for segmentation. However, this distance could limit reconstructions in terms of fascicle features such as fascicle length or pennation angle. For also determining such fascicle characteristics, the maximum distance between two sequential images would need to be reduced. Therefore, with a decrease of the maximum distance and the previously mentioned solutions for avoiding artifacts due to unwanted subject movements, fascicle parameters such as fascicle length, pennation angle and the physiological cross-sectional area may be determined in future studies.

Another limitation is that no EMG was applied, therefore the activation level of the muscle was not measured. Arampatzis et al. (2006) stated that the TA is active during maximal plantarflexion efforts. In our case, however, the movement is a free movement without any resistance, therefore we can assume overall small activation levels of the dorsi- and plantarflexors. With regard to the plantar flexion movement, we can assume that we are at a low activation level of the plantarflexors and therefore also have minimal activation of the TA. Due to this very low activation of the TA, we assume that the TA has no influence here, thus we chose the terminologies *active* and *passive* based on these assumptions. Due to the low level of TA activation, differences in CSA between *active* and *passive*, and *slow* and *fast* velocities were comparably small. Consequently, it would be beneficial to include a force resistance and measurement of muscle activity, to also study effects of the CSA during higher muscle contraction levels. Thus, future studies should contain a mechanism, such that the foot moves against a controlled resistance, e.g., a dynamometer, and EMG electrodes. This would also enable measurements where to foot is moved passively.

Furthermore, since the aim of this work is to present a novel method to obtain and reconstruct 3D ultrasound images of the TA during dynamic movements, we employed the method on five human subjects. This number of subjects might be a limiting factor in this study, as a larger population can increase the level of confidence in our results and conclusions. In addition, due to the small number of subjects we did not examine our data for gender-specific differences that may affect musculature and height. Thus, in future studies a larger number of subjects should be investigated such that also gender-specific data can be examined.

## 5 Conclusion

In summary, we have proposed a method for determining muscle volume deformation during dynamic contraction. Constant muscle volumes during contraction indicate the

suitability of the method for determination of TA shape changes during dynamic movements. Moreover, we determined realistic changes in 3D muscle shape, such as the proximal shift in maximum CSA. Thus, an improved understanding of muscle contraction behavior, especially during dynamic movements, can be achieved with the proposed method. Since the acquisition of 3D deformation of skeletal muscle during dynamic movement is highly restricted with the current existing imaging methods, this study contributes significantly to the research area.

Data on changes in muscle shape during contraction are needed for the validation of 3D muscle models (Seydewitz et al., 2019). Therefore, the proposed method may help to enhance input data for existing computational models and to answer new research questions. In addition, new insights into the muscle geometry in dynamic conditions may help to establish new means to investigate skeletal muscles in healthy and pathological conditions. As such, further extensions may enable the development of new therapy approaches.

## Data availability statement

The raw data supporting the conclusion of this article will be made available by the authors, without undue reservation.

## Ethics statement

The studies involving humans were approved by the University of Stuttgart's Committee on Responsibility in Research (number: Az. 21-011). The studies were conducted in accordance with the local legislation and institutional requirements. The participants provided their written informed consent to participate in this study.

## Author contributions

AS: Conceptualization, Formal Analysis, Investigation, Methodology, Software, Visualization, Writing–original draft, Writing–review and editing. LV: Formal Analysis, Investigation, Writing–original draft, Writing–review and editing. TS: Formal Analysis, Investigation, Writing–original draft, Writing–review and editing. GH: Conceptualization, Formal Analysis,

Investigation, Methodology, Writing–original draft, Writing–review and editing. OR: Conceptualization, Formal Analysis, Funding acquisition, Investigation, Methodology, Writing–original draft, Writing–review and editing.

## Funding

The author(s) declare that financial support was received for the research, authorship, and/or publication of this article. This project has received funding from the German Research Foundation (DFG) as part of the International Research Training Group “Soft Tissue Robotics” (GRK 2198/1), the Stuttgart Center for Simulation Science (SimTech, EXC2075–390740016) and the Bundesministerium für Bildung und Forschung (BMBF, German Federal Ministry of Education and Research), Grant No. 01EC 1907B (“3DFoot”).

## Conflict of interest

The authors declare that the research was conducted in the absence of any commercial or financial relationships that could be construed as a potential conflict of interest.

The author(s) declared that they were an editorial board member of Frontiers, at the time of submission. This had no impact on the peer review process and the final decision.

## Publisher's note

All claims expressed in this article are solely those of the authors and do not necessarily represent those of their affiliated organizations, or those of the publisher, the editors and the reviewers. Any product that may be evaluated in this article, or claim that may be made by its manufacturer, is not guaranteed or endorsed by the publisher.

## Supplementary material

The Supplementary Material for this article can be found online at: <https://www.frontiersin.org/articles/10.3389/fbioe.2024.1388907/full#supplementary-material>

## References

- Albracht, K., Arampatzis, A., and Baltzopoulos, V. (2008). Assessment of muscle volume and physiological cross-sectional area of the human triceps surae muscle *in vivo*. *J. Biomechanics* 41, 2211–2218. doi:10.1016/j.jbiomech.2008.04.020
- Arampatzis, A., Karamanidis, K., Stafildis, S., Morey-Klapsing, G., DeMonte, G., and Brüggemann, G.-P. (2006). Effect of different ankle- and knee-joint positions on gastrocnemius medialis fascicle length and EMG activity during isometric plantar flexion. *J. Biomechanics* 39, 1891–1902. doi:10.1016/j.jbiomech.2005.05.010
- Aubel, A., and Thalmann, D. (2004). MuscleBuilder: a modeling tool for human anatomy. *J. Comput. Sci. Technol.* 19, 585–595. doi:10.1007/bf02945584
- Azizi, E., Brainerd, E. L., and Roberts, T. J. (2008). Variable gearing in pennate muscles. *Proc. Natl. Acad. Sci.* 105, 1745–1750. doi:10.1073/pnas.0709212105
- Barber, L., Barrett, R., and Lichtwark, G. (2009). Validation of a freehand 3d ultrasound system for morphological measures of the medial gastrocnemius muscle. *J. Biomechanics* 42, 1313–1319. doi:10.1016/j.jbiomech.2009.03.005
- Baskin, R., and Paolini, P. (1967). Volume change and pressure development in muscle during contraction. *Am. J. Physiology-Legacy Content* 213, 1025–1030. doi:10.1152/ajplegacy.1967.213.4.1025
- Böl, M., Leichsenring, K., Weichert, C., Sturmat, M., Schenk, P., Blickhan, R., et al. (2013). Three-dimensional surface geometries of the rabbit soleus muscle during contraction: input for biomechanical modelling and its validation. *Biomechanics Model. Mechanobiol.* 12, 1205–1220. doi:10.1007/s10237-013-0476-1
- Brainerd, E. L., and Azizi, E. (2005). Muscle fiber angle, segment bulging and architectural gear ratio in segmented musculature. *J. Exp. Biol.* 208, 3249–3261. doi:10.1242/jeb.01770
- Cenni, F., Schless, S.-H., Bar-On, L., Aertbeliën, E., Bruyninckx, H., Hanssen, B., et al. (2018). Reliability of a clinical 3d freehand ultrasound technique: analyses on healthy and pathological muscles. *Comput. Methods Programs Biomed.* 156, 97–103. doi:10.1016/j.cmpb.2017.12.023

- Choi, M.-S., Shin, J.-H., Park, H.-K., and Lee, W.-H. (2019). Reliability and validity of rehabilitative ultrasound images obtained using a hands-free fixed probe in measuring the muscle structures of the tibialis anterior and the gastrocnemius. *Phys. Ther. Rehabilitation Sci.* 8, 194–201. doi:10.14474/ptrs.2019.8.4.194
- Eng, C. M., Azizi, E., and Roberts, T. J. (2018). Structural determinants of muscle gearing during dynamic contractions. *Integr. Comp. Biol.* 58, 207–218. doi:10.1093/icb/icy054
- Franchi, M. V., Longo, S., Mallinson, J., Quinlan, J. I., Taylor, T., Greenhaff, P. L., et al. (2017). Muscle thickness correlates to muscle cross-sectional area in the assessment of strength training-induced hypertrophy. *Scand. J. Med. Sci. Sports* 28, 846–853. doi:10.1111/sms.12961
- Fry, N., Childs, C., Eve, L., Gough, M., Robinson, R., and Shortland, A. (2003). Accurate measurement of muscle belly length in the motion analysis laboratory: potential for the assessment of contracture. *Gait Posture* 17, 119–124. doi:10.1016/s0966-6362(02)00059-0
- Hanson, E. D., Srivatsan, S. R., Agrawal, S., Menon, K. S., Delmonico, M. J., Wang, M. Q., et al. (2009). Effects of strength training on physical function: influence of power, strength, and body composition. *J. Strength Cond. Res.* 23, 2627–2637. doi:10.1519/jsc.0b013e3181b2297b
- Heemskerk, A. M., Sinha, T. K., Wilson, K. J., Ding, Z., and Damon, B. M. (2010). Repeatability of DTI-based skeletal muscle fiber tracking. *NMR Biomed.* 23, 294–303. doi:10.1002/nbm.1463
- Henriksson-Larsén, K. B., Lexell, J., and Sjöström, M. (1983). Distribution of different fibre types in human skeletal muscles. i. method for the preparation and analysis of cross-sections of whole tibialis anterior. *Histochem. J.* 15, 167–178. doi:10.1007/BF01042285
- Hiepe, P., Herrmann, K.-H., Güllmar, D., Ros, C., Siebert, T., Blickhan, R., et al. (2013). Fast low-angle shot diffusion tensor imaging with stimulated echo encoding in the muscle of rabbit shank. *NMR Biomed.* 27, 146–157. doi:10.1002/nbm.3046
- Holzer, D., Millard, M., Hahn, D., Siebert, T., Schwirtz, A., and Seiberl, W. (2023). Tendon compliance and preload must be considered when determining the *in vivo* force–velocity relationship from the torque–angular velocity relation. *Sci. Rep.* 13, 6588. doi:10.1038/s41598-023-33643-9
- Hooren, B. V., Teratsias, P., and Hodson-Tole, E. F. (2020). Ultrasound imaging to assess skeletal muscle architecture during movements: a systematic review of methods, reliability, and challenges. *J. Appl. Physiology* 128, 978–999. doi:10.1152/jappphysiol.00835.2019
- Hu, C., Hu, H., Mai, X., Lo, W. L. A., and Li, L. (2019). Correlation between muscle structures and electrical properties of the tibialis anterior in subacute stroke survivors: a pilot study. *Front. Neurosci.* 13, 1270. doi:10.3389/fnins.2019.01270
- Jakobsson, F., Borg, K., and Edström, L. (1990). Fibre-type composition, structure and cytoskeletal protein location of fibres in anterior tibial muscle. Comparison between young adults and physically active aged humans. *Acta Neuropathol.* 80, 459–468. doi:10.1007/BF00294604
- Kelp, N. Y., Clemente, C. J., Tucker, K., Hug, F., Pinel, S., and Dick, T. J. M. (2023). Influence of internal muscle properties on muscle shape change and gearing in the human gastrocnemius. *J. Appl. Physiology* 134, 1520–1529. doi:10.1152/jappphysiol.00080.2023
- Kurihara, T., Oda, T., Chino, K., Kanehisa, H., Fukunaga, T., and Kawakami, Y. (2005). Use of three-dimensional ultrasonography for the analysis of the fascicle length of human gastrocnemius muscle during contractions. *Int. J. Sport Health Sci.* 3, 226–234. doi:10.5432/ijshs.3.226
- Lieber, R. L., and Fridén, J. (2000). Functional and clinical significance of skeletal muscle architecture. *Muscle & Nerve* 23, 1647–1666. doi:10.1002/1097-4598(200011)23:11<1647::aid-mus1>3.3.co;2-d
- Maganaris, C. N., and Baltzopoulos, V. (1999). Predictability of *in vivo* changes in pennation angle of human tibialis anterior muscle from rest to maximum isometric dorsiflexion. *Eur. J. Appl. Physiology* 79, 294–297. doi:10.1007/s004210050510
- Martin-Rodriguez, S., Gonzalez-Henriquez, J. J., Galvan-Alvarez, V., Cruz-Ramirez, S., Calbet, J. A., and Sanchis-Moysi, J. (2023). Architectural anatomy of the human tibialis anterior presents morphological asymmetries between superficial and deep unipennate regions. *J. Anat.* 243, 664–673. doi:10.1111/joa.13864
- Raiteri, B. J., Cresswell, A. G., and Lichtwark, G. A. (2016). Three-dimensional geometrical changes of the human tibialis anterior muscle and its central aponeurosis measured with three-dimensional ultrasound during isometric contractions. *PeerJ* 4, e2260. doi:10.7717/peerj.2260
- Rana, M., and Wakeling, J. M. (2011). *In-vivo* determination of 3d muscle architecture of human muscle using free hand ultrasound. *J. Biomechanics* 44, 2129–2135. doi:10.1016/j.jbiomech.2011.05.026
- Reeves, N. D., and Narici, M. V. (2003). Behavior of human muscle fascicles during shortening and lengthening contractions *in vivo*. *J. Appl. Physiology* 95, 1090–1096. doi:10.1152/jappphysiol.01046.2002
- Reinhardt, L., Siebert, T., Leichsenring, K., Blickhan, R., and Böl, M. (2016). Intermuscular pressure between synergistic muscles correlates with muscle force. *J. Exp. Biol.* 219, 2311–2319. doi:10.1242/jeb.135566
- Röhrle, O., Sprenger, M., and Schmitt, S. (2016). A two-muscle, continuum-mechanical forward simulation of the upper limb. *Biomechanics Model. Mechanobiol.* 16, 743–762. doi:10.1007/s10237-016-0850-x
- Ryan, D. S., Stutzig, N., Siebert, T., and Wakeling, J. M. (2019). Passive and dynamic muscle architecture during transverse loading for gastrocnemius medialis in man. *J. Biomechanics* 86, 160–166. doi:10.1016/j.jbiomech.2019.01.054
- Sahrman, A. S., Gizzi, L., Zanker, A., Handsfield, G. G., and Röhrle, O. (2022). “Dynamic 3d ultrasound imaging of the tibialis anterior muscle,” in 2022 44th Annual International Conference of the IEEE Engineering in Medicine & Biology Society (EMBC), China, 11–15 July 2022 (IEEE). doi:10.1109/embc48229.2022.9871352
- Sahrman, A. S., Handsfield, G. G., Gizzi, L., Gerlach, J., Verl, A., Besier, T. F., et al. (2024). A system for reproducible 3d ultrasound measurements of skeletal muscles. *IEEE Trans. Biomed. Eng.*, 1–12. doi:10.1109/tbme.2024.3359854
- Sahrman, A. S., Vosse, L., Siebert, T., et al. 3D ultrasound-based determination of skeletal muscle fascicle orientations. *Biomech Model Mechanobiol.* (2024). doi:10.1007/s10237-024-01837-3
- Seydewitz, R., Siebert, T., and Böl, M. (2019). On a three-dimensional constitutive model for history effects in skeletal muscles. *Biomechanics Model. Mechanobiol.* 18, 1665–1681. doi:10.1007/s10237-019-01167-9
- Siebert, T., Günther, M., and Blickhan, R. (2012). A 3d-geometric model for the deformation of a transversally loaded muscle. *J. Theor. Biol.* 298, 116–121. doi:10.1016/j.jtbi.2012.01.009
- Siebert, T., Tomalka, A., Stutzig, N., Leichsenring, K., and Böl, M. (2017). Changes in three-dimensional muscle structure of rabbit gastrocnemius, flexor digitorum longus, and tibialis anterior during growth. *J. Mech. Behav. Biomed. Mater.* 74, 507–519. doi:10.1016/j.jmbbm.2017.07.045
- Stark, H., Fröber, R., and Schilling, N. (2012). Intramuscular architecture of the autochthonous back muscles in humans. *J. Anat.* 222, 214–222. doi:10.1111/joa.12005
- Tous, C., Jodoin, A., Pontré, B., Grabs, D., Begon, M., Bureau, N. J., et al. (2023). Characterizing the myoarchitecture of the supraspinatus and infraspinatus muscles with mri using diffusion tensor imaging. *J. Magnetic Reson. Imaging* 59, 851–862. doi:10.1002/jmri.28840
- Treecce, G., Prager, R., Gee, A., and Berman, L. (2000). Surface interpolation from sparse cross sections using region correspondence. *IEEE Trans. Med. Imaging* 19, 1106–1114. doi:10.1109/42.896787
- Treecce, G. M., Prager, R. W., Gee, A. H., and Berman, L. (1999). Fast surface and volume estimation from non-parallel cross-sections, for freehand three-dimensional ultrasound. *Med. Image Anal.* 3, 141–173. doi:10.1016/s1361-8415(99)80004-8
- van Donkelaar, C. C., Kretzers, L. J. G., Bovendeerd, P. H. M., Lataster, L. M. A., Nicolay, K., Janssen, J. D., et al. (1999). Diffusion tensor imaging in biomechanical studies of skeletal muscle function. *J. Anat.* 194, 79–88. doi:10.1046/j.1469-7580.1999.19410079.x
- Weide, G., van der Zwaard, S., Huijting, P. A., Jaspers, R. T., and Harlaar, J. (2017). 3d ultrasound imaging: fast and cost-effective morphometry of musculoskeletal tissue. *J. Vis. Exp.*, 55943. doi:10.3791/55943
- Wick, C., Böl, M., Müller, F., Blickhan, R., and Siebert, T. (2018). Packing of muscles in the rabbit shank influences three-dimensional architecture of m. soleus. *J. Mech. Behav. Biomed. Mater.* 83, 20–27. doi:10.1016/j.jmbbm.2018.04.006



## OPEN ACCESS

## EDITED BY

Yang Liu,  
Hong Kong Polytechnic University, Hong Kong  
SAR, China

## REVIEWED BY

Sacha Cavelier,  
Queensland University of Technology, Australia  
Francesco Travascio,  
University of Miami, United States

## \*CORRESPONDENCE

Cheng Wang,  
✉ chengwang2013@foxmail.com

<sup>†</sup>These authors have contributed equally to  
this work

RECEIVED 03 March 2024

ACCEPTED 29 May 2024

PUBLISHED 19 June 2024

## CITATION

Chen H, Kang Y, Yan Y, Wang H, Peng W, Liao Y,  
Zou M, Xu Z, Song X, Wang W and Wang C  
(2024), Biomechanical analysis of the tandem  
spinal external fixation in a multiple-level  
noncontiguous lumbar fractures model: a finite  
element analysis.  
*Front. Bioeng. Biotechnol.* 12:1395197.  
doi: 10.3389/fbioe.2024.1395197

## COPYRIGHT

© 2024 Chen, Kang, Yan, Wang, Peng, Liao, Zou,  
Xu, Song, Wang and Wang. This is an open-  
access article distributed under the terms of the  
[Creative Commons Attribution License \(CC BY\)](https://creativecommons.org/licenses/by/4.0/).  
The use, distribution or reproduction in other  
forums is permitted, provided the original  
author(s) and the copyright owner(s) are  
credited and that the original publication in this  
journal is cited, in accordance with accepted  
academic practice. No use, distribution or  
reproduction is permitted which does not  
comply with these terms.

# Biomechanical analysis of the tandem spinal external fixation in a multiple-level noncontiguous lumbar fractures model: a finite element analysis

Huarong Chen<sup>1,2†</sup>, Yu Kang<sup>1,3†</sup>, Yiguo Yan<sup>1†</sup>, Hu Wang<sup>1</sup>,  
Wen Peng<sup>1</sup>, Yijia Liao<sup>1,4</sup>, Mingxiang Zou<sup>1</sup>, Zhun Xu<sup>1</sup>,  
Xizheng Song<sup>1</sup>, Wenjun Wang<sup>1</sup> and Cheng Wang<sup>1\*</sup>

<sup>1</sup>The First Affiliated Hospital, Department of Spine Surgery, Hengyang Medical School, University of South China, Hengyang, Hunan, China, <sup>2</sup>Central People's Hospital of Zhanjiang, Zhanjiang, Guangdong, China, <sup>3</sup>The Third Affiliated Hospital of Sun Yat-sen University, Department of Spine Surgery, Sun Yat-sen University, Guangzhou, Guangdong, China, <sup>4</sup>Luoyang Orthopedic-Traumatological Hospital of Henan Province (Henan Provincial Orthopedic Hospital), Luoyang, Henan, China

**Objective:** This study aimed to investigate the biomechanical characteristics of the tandem spinal external fixation (TSEF) for treating multilevel noncontiguous spinal fracture (MNSF) using finite element analysis and provide a theoretical basis for clinical application.

**Methods:** We constructed two models of L2 and L4 vertebral fractures that were fixed with the TSEF and the long-segment spinal inner fixation (LSIF). The range of motion (ROM), maximum stresses at L2 and L4 vertebrae, the screws and rods, and the intervertebral discs of the two models were recorded under load control. Subsequently, the required torque, the maximum stress at L2 and L4 vertebrae, the screws and rods, and the intervertebral discs were analyzed under displacement control.

**Results:** Under load control, the TSEF model reserved more ROM than the LSIF model. The maximum stresses of screws in the TSEF model were increased, while the maximum stresses of rods were reduced compared to the LSIF model. Moreover, the maximum stresses of L2 and L4 vertebrae and discs in the TSEF model were increased compared to the LSIF model. Under displacement control, the TSEF model required fewer moments (N·mm) than the LSIF model. Compared to the LSIF model, the maximum stresses of screws and rods in the TSEF model have decreased; the maximum stresses at L2 and L4 in the TSEF model were increased. In the flexion condition, the maximum stresses of discs in the TSEF model were less than the LSIF model, while the maximum stresses of discs in the TSEF model were higher in the extension condition.

**Conclusion:** Compared to LSIF, the TSEF has a better stress distribution with higher overall mobility. Theoretically, it reduces the stress concentration of the connecting rods and the stress shielding of the fractured vertebral bodies.

## KEYWORDS

tandem spinal external fixation, finite element analysis, multilevel noncontiguous spinal fracture, biomechanics, thoracolumbar fracture



## Introduction

The multilevel noncontiguous spinal fracture (MNSF) is a unique type of spinal fracture characterized by two or more fractured vertebral bodies separated by at least one normal vertebral body (Korres et al., 1981; Powell et al., 1989; Iencean, 2002; Lian et al., 2007). MNSF is primarily caused by high-energy injuries, such as traffic accidents and high falls (Wittenberg et al., 2002; Bensch et al., 2006; Kanna et al., 2016). Extreme pain, spinal instability, deformity, and neurological dysfunction are the frequent clinical features of MNSF. The most common treatment for MNSF is the LSIF system using open posterior surgery (Takami et al., 2017). However, it has been reported that the long-segment screw-rod fixation (usually five segments or more) exhibits many inherent defects, including loss of range of motion (ROM), stress concentration on the screws or rods, and stress shielding of the fractured vertebral bodies.

The external spinal fixation systems we utilized in previous studies have achieved satisfactory clinical outcomes in treating single-segment thoracolumbar fractures (Wang et al., 2011; Song et al., 2014; Wang C. et al., 2018). Spinal external fixation is a minimally invasive surgical technique that reduces the fractured vertebral body percutaneously. Generally, the external fixation is removed 3 months after the operation, thus reducing the risk of complications caused by prolonged rigid fixation (Wang et al., 2011). Inspired by the single-segment external fixation, we developed the tandem spinal external fixation (TSEF) for MNSF, which demonstrated no neurological symptoms (Figures 1A–D). The TSEF has many clinical advantages compared to the traditional long-segment spinal inner fixation (LSIF), but the potential mechanic characteristics of TSEF are yet to be explored.

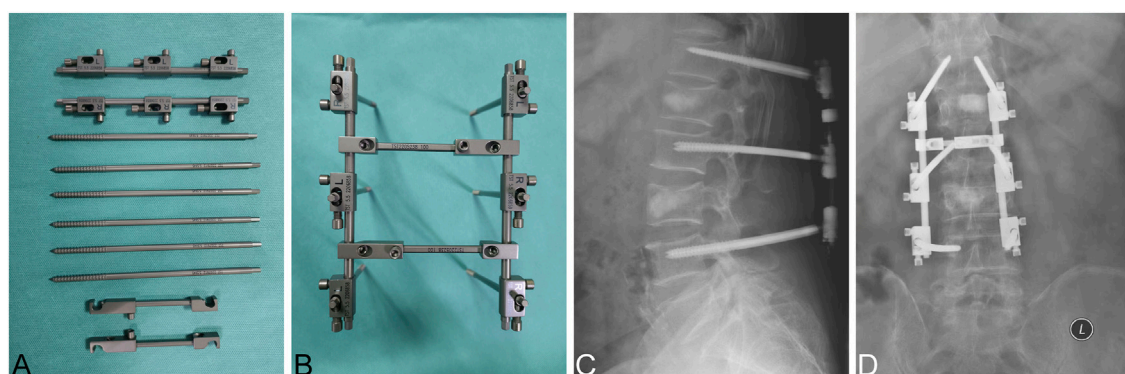
Finite element analysis (FEA) is a method for analyzing complex solid and structural mechanics systems and has been widely used in orthopedic biomechanics research. Complex spinal fractures can be reconstructed using FEA based on computed tomography (CT) technology. Moreover, the biomechanical characteristics of spinal implants can be well revealed using FEA (Xu et al., 2014a; Liao et al., 2017; Liao et al., 2022). This study evaluated the biomechanical characteristics of the TSEF in treating MNSF using FEA and

provided the corresponding theoretical basis for the clinical application in MNSF.

## Material and methods

### Construction and validation of finite element model of L1–L5 lumbar spine

The DICOM format files for the finite element model construction (L1–L5 lumbar spine) were obtained from a healthy volunteer (26 years old male weighing 71 kg and height of 173 cm) using a 64-slice spiral CT. After thresholding segmentation, dynamic growth, mask editing, and Boolean manipulation, the three-dimensional (3D) contour model of L1–L5 was extracted using the software Mimics 20.0 (Materialize, Belgium). Slices of the contour model were collected using Geomagic 12 (Geomagic Inc., United States) and then processed by smoothing, grinding, denoising, surface construction, and solidification. SolidWorks 2015 (Dassault, France) was used to reconstruct the intervertebral disc (matrix and nucleus pulposus) and articular surface. The reconstructed model vertebral bodies consisted of cortical bone, cancellous bone, and endplates. The intervertebral discs consisted of the nucleus pulposus and fibrous ring (3:7). The articular cartilage was set at 0.3 mm thickness, and the upper and lower articular cartilages were in frictional contact with a friction coefficient of 0.1. Seven paravertebral ligaments, including the anterior longitudinal ligament, posterior longitudinal ligament, ligamentum flavum, interspinous ligament, supraspinous ligament, capsular ligament, and intertransverse process ligament, were modeled. Intact L1–L5 lumbar model material and characteristics were assigned based on previous studies (Wang H. et al., 2018; Han et al., 2022), as shown in Table 1. The mesh sizes of 3 mm, 2 mm, 1.5 mm, 1 mm, and 0.5 mm were meshed using Ansys workbench 18.0 (Ansys, United States). The 5% change indicated that the mesh was converged. According to the mesh convergence results shown in Table 2, a final mesh size of 1 mm was selected for the subsequent analysis of this study (Figure 2A). The L1–L5 lumbar



**FIGURE 1**  
Clinical application of TSEF (A) Components of TSEF. (B) The overall diagram of TSEF. (C,D) X-Ray images of clinical application of TSEF. The bone substitute showed in this figure was Bicera™ (Wiltrom Ltd, Taiwan).

TABLE 1 Material properties of the finite element model (Wang H. et al., 2018; Han et al., 2022).

Component name	Young's modulus(MPa)	Poisson's ratio	Cross-sectional area(mm <sup>2</sup> )
Cortical bone	12,000	0.3	-
Cancellous bone	100	0.3	-
Injured cancellous bone	10	0.3	-
Cartilage	10	0.4	-
Bony endplate	1,000	0.4	-
Nucleus pulposus	1	0.499	-
Annulus fibrosus	4.2	0.3	-
ALL	20	0.3	63.7
PLL	20	0.3	20
LF	19.5	0.3	40
ISL	11.6	0.3	40
SSL	15	0.3	30
TL	58.7	0.3	3.6
CL	32.9	0.3	60
Instruments	110,000	0.3	-

ALL, anterior longitudinal ligament; PLL, posterior longitudinal ligament; LF, ligamentum flavum; ISL, interspinous ligament; SSL, supraspinal ligament; TL, transverse ligament; CL, capsular ligament.

TABLE 2 Parameters for mesh convergence.

Size of mesh (mm)	Element	Node	Stress on vertebra (MPa)
0.5	2,229,305	3,157,044	20.09
1	693,194	1,030,241	20.08
1.5	311,639	493,005	19.19
2	279,010	302,980	18.15
3	90,017	173,045	16.86

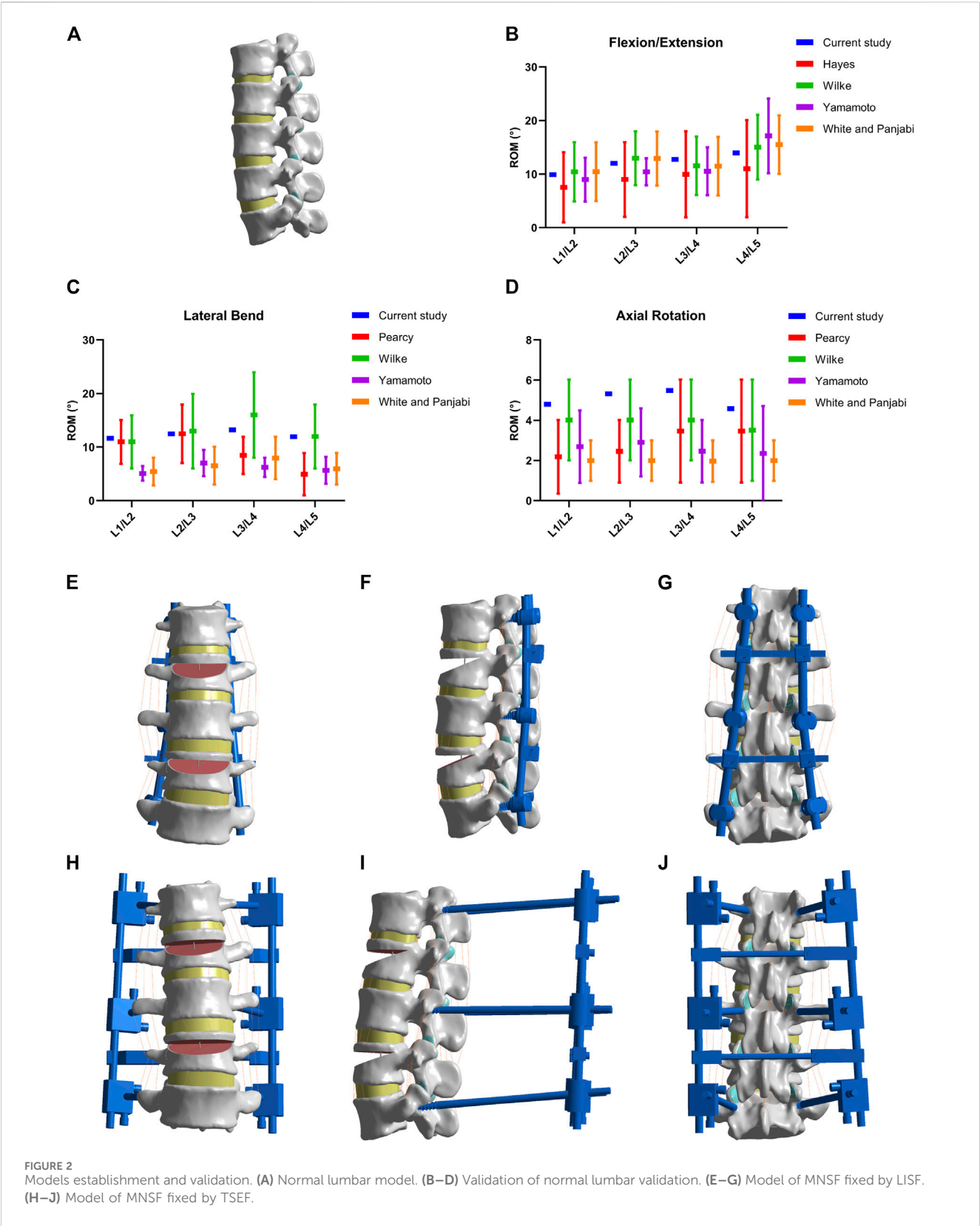
spine finite element model (FEM) was validated by comparing it with previous study data (White and Panjabi, 1976; Pearcy et al., 1985; Hayes et al., 1989; Yamamoto et al., 1989; Wilke et al., 1997) (Figures 2B–D).

### Model construction of MNSF

The L2 and L4 vertebral bodies were selected to simulate the fracture. The finite element model of MNSF was constructed as described in the previous literature (Liu et al., 2018; Zhou et al., 2020). Briefly, a line parallel to the upper endplate was made at 15% of the anterior edge of the L2 vertebral body to the posterior edge of the vertebral body. Then a diagonal line was made from the intersection of the line and the posterior edge of the vertebral body to 55% of the anterior edge of the vertebral body as a triangle. Then, the triangular part of the vertebral body was removed. The same procedure was performed on the L4 vertebral body.

### Model construction of MNSF fixed with LSIF and TSEF

Models of LSIF and TSEF were constructed using SolidWorks 2015 (Dassault, France). The diameter specifications of the pedicle screws and connection rods of LSIF were 6.5 mm and 6 mm, respectively. The diameter specifications of the pedicle screws and connection rods of TSEF were 5.5 mm and 5 mm, respectively. Pedicle screws were transpedicular and placed in L1, L3, and L5 vertebral bodies. Screws should be parallel to the upper endplate and implanted beyond the anterior 1/3 of the vertebral body. The pedicle screw holders of LSIF were partially attached to the bone surface, and the connecting rods were fixed with the screw holder U-groove. The predial apparatus fixed the connecting rods of TSEF on the body surface of L1–L5. The final normal model included 693,194 units and 1,030,241 nodes, the LSIF model included 694,386 units and 1,058,953 nodes, and the TSEF model included 739,105 units and 1,121,711 nodes



(Figures 2E–J). Given that the bone and implant remained within the range of small deformations under body load, a linear elastic constitutive model was assumed for both the implant and the bone components in the presenting analysis (Xu et al., 2014b). The linear elastic constitutive equation was described as followed:

$$\sigma = E \cdot \varepsilon$$



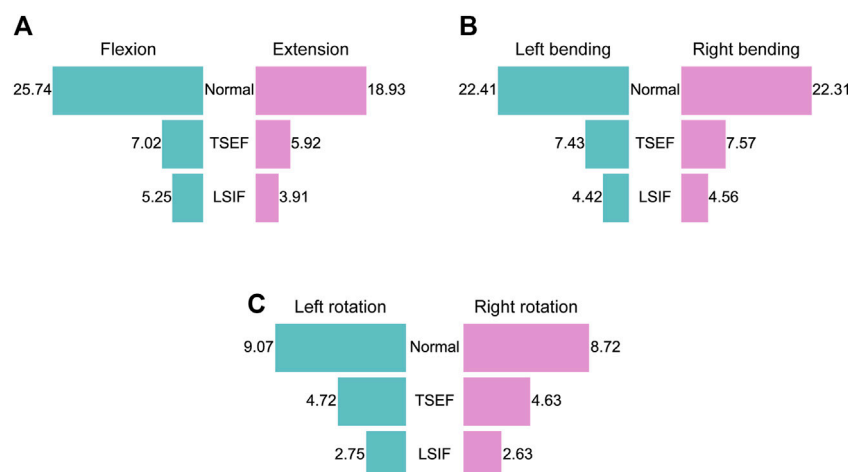


FIGURE 3

Restriction of two fixations on lumbar mobility under the six conditions. (A) ROM of the normal, TSEF and LSIF models under flexion and extension conditions. (B) ROM of the normal, TSEF and LSIF models under left and right bending conditions. (C) ROM of the normal, TSEF and LSIF models under left and right rotation conditions.

( $\sigma$  indicates stress, E indicates elasticity modulus,  $\epsilon$  indicates deformation)

## Control mode and boundary condition

Load control [500 N preload and 7500 N mm motion torque (Müller et al., 2021; Han et al., 2022)] was applied to the upper surface of the L1 vertebral body, while the bottom of the L5 vertebral body was fully fixed and restrained. The range of motion (ROM) of different models was recorded under six working conditions: flexion and extension, left and right lateral flexions, and left and right rotations. The maximum stresses on screws, rods, fractured vertebral bodies, and intervertebral discs in internal and external fixation models were compared and analyzed.

The maximum ROMs in flexion and extension conditions of the TSEF model were defined as the boundary conditions. The preload of 500 N was applied as described previously (Liao et al., 2022). An increasing motion torque was applied to the models gradually, and the values of motion torque that the two different models required to achieve boundary conditions were recorded and analyzed. Meanwhile, the maximum stresses of the screws, rods, fractured vertebral bodies and intervertebral discs were recorded.

## Results

### Load control

#### Range of motion (ROM)

The ROM of flexion, extension, left bending, right bending, left rotation and right rotation were 25.74°, 18.93°, 22.41°, 22.31°, 9.07°, and 8.72° for the normal model; were 7.02°, 5.92°, 7.43°, 7.57°, 4.72°, and 4.63° for the TSEF model; were 5.25°, 3.91°, 4.42°, 4.56°, 2.75°, and 2.63° for the LSIF model (Figures 3A–C). The ROM of the TSEF model was smaller than that of the normal lumbar model, which was

27.3%–53.1% of the normal lumbar model. The ROM of the LSIF model was smaller than that of the normal lumbar model, which was 19.7%–30.3% of the normal lumbar model. Thus, both TSEF and LSIF models significantly restricted the ROM of the lumbar spine.

### Von mises stress of pedicle screws and connecting rods

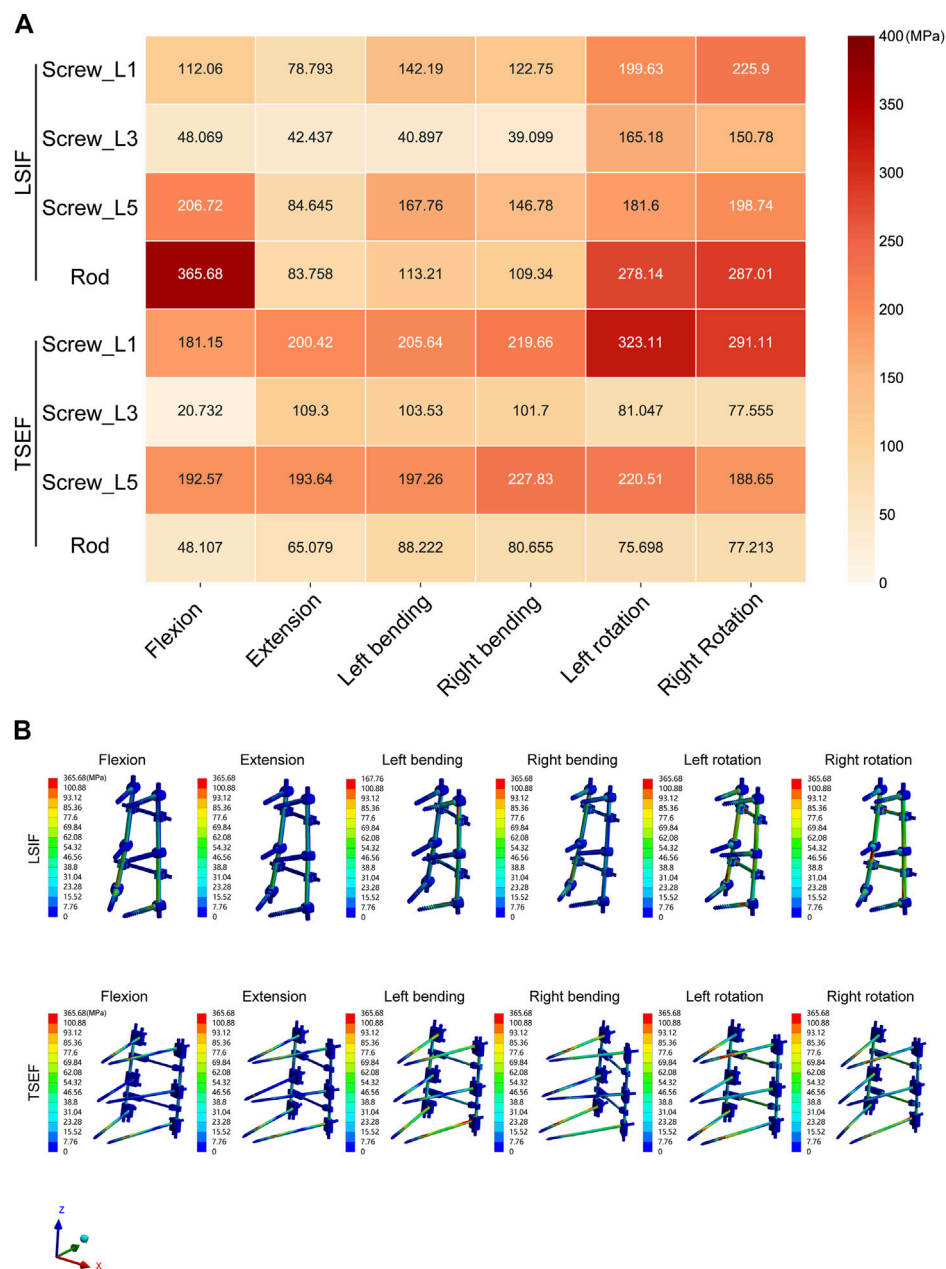
The maximum values of stress and cloud plots of pedicle screws and connecting rods of TSEF and LSIF models under the six operating conditions are shown in Figure 4. The maximum von Mises stress value of pedicle screws of LSIF and TSEF models were observed in the left and right rotation conditions. The maximum von Mises stress value of the LSIF model in the right rotation was 225.9 MPa, and the maximum von Mises stress value of the TSEF model in the left rotation was 323.11 MPa. The maximum stress of pedicle screws of the TSEF model was greater than that of the LSIF model except for flexion. The maximum stress of the connecting rod of the LSIF model was 365.68 MPa during the flexion, and that of the connecting rod of the TSEF model was 88.22 MPa during the left flexion. The maximum stress on connecting rod of the TSEF model was less than that of the LSIF model under all conditions. In the TSEF model, the uppermost and lowermost screws bore the higher stress. In the LSIF model, the uppermost and lowermost screws and the connecting rods primarily shared the stress.

### Maximum von mises stress of the fractured vertebral body

Under all working conditions, the maximum von Mises stress values of the L4 fractured vertebral body of the two groups of models were higher than that of the L2 fractured vertebral body. Moreover, the maximum von Mises stress values of the L2 and L4 fractured vertebral bodies of the TSEF model were higher than that of the LSIF model (Figure 5).

### Maximum von mises stress of intervertebral disc

In all working conditions, the maximum von Mises stress values of the intervertebral discs in the TSEF model were higher



**FIGURE 4** Maximum von mises stress analysis of LSIF and TSEF under the six conditions. **(A)** Heatmap of the Maximum von mises stress on LSIF and TSEF under the six conditions. **(B)** Cloud plots of the Maximum von mises stress on LSIF and TSEF under the six conditions.

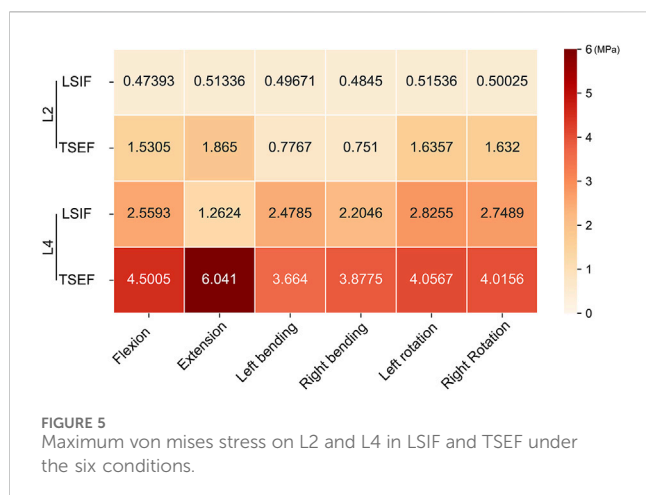
than that of the corresponding discs in the LSIF model (Figure 6A). In flexion, the maximum stress of the disc in the TSEF model was 1.22 MPa (L4/L5), while the LSIF model was 1.19 MPa (L4/L5). In extension, the maximum stress of the disc in the TSEF model was 1.18 MPa (L4/L5), while the LSIF model was 0.70 MPa (L1/L2). In left bending, the maximum stress of the disc in the TSEF model was 1.69 MPa (L4/L5), while the LSIF model was 0.52 MPa (L1/L2). In right bending, the maximum stress of the disc in the TSEF model was 1.65 MPa (L4/5), while the LSIF model was 0.63 MPa (L1/L2). In left rotation, the maximum stress of the disc in the TSEF model was 1.08 MPa (L1/2), while the LSIF model was 0.90 MPa (L1/L2). In the right

rotation, the maximum stress of the disc in the TSEF model was 1.20 MPa (L4/L5), while the LSIF model was 0.73 MPa (L4/L5). The cloud plots of the intervertebral discs of TSEF and LSIF models under the six operating conditions are shown in Figure 6B.

## Displacement control

### Motion torque required for the same ROM

Under load control, the maximum ROM of the TSEF model was 7.02° in flexion and 5.92° in extension, which was the target



value of displacement control. When the flexion activity reached 7.02°, the required torque for TSEF and LSIF were 7500 N·mm and 18,200 N·mm, respectively. When the extension activity reached 5.29°, the TSEF and LSIF models required 7500 N·mm and 21650 N·mm, respectively. The required motion torque of the LSIF model was higher than that of the TSEF model (Figure 7A).

### Maximum von mises stress of pedicle screws and connecting rods

Under displacement control, the maximum stress of screws and connecting rods in the LSIF model was higher than that in the TSEF model in flexion (screw: 380.51 vs. 192.57 MPa; rod: 564.73 vs. 48.11 MPa). The maximum stress of screws and connecting rods in the LSIF model was higher than that in the TSEF model in extension (screw: 421.81 vs. 200.42 MPa; rod: 341.84 vs. 65.08 MPa) (Figure 7B).

### Maximum von mises stress of fractured vertebral bodies

Under displacement control, the maximum stress of fractured vertebral bodies in the TSEF model was higher than that in the LSIF model in flexion (L2: 1.53 vs. 1.16 MPa; L4: 4.50 vs. 4.10 MPa). The maximum stress of fractured vertebral bodies in the TSEF model was higher than that in the LSIF model in the extension condition (L2: 1.87 vs. 1.27 MPa; L4: 6.04 vs. 5.65 MPa) (Figure 7C).

### Maximum von mises stress of intervertebral discs

Under displacement control, the maximum stress of intervertebral discs in the TSEF model was less than that in the LSIF model in flexion condition (L1/L2: 1.09 vs. 1.41 MPa; L2/L3: 0.94 vs. 1.31 MPa; L3/L4: 1.14 vs. 1.52 MPa; L4/L5: 1.22 vs. 1.57 MPa); the maximum stress of intervertebral discs in the TSEF model was higher than that in the LSIF model in extension condition (L1/L2: 1.07 vs. 0.84 MPa; L2/L3: 0.83 vs. 0.67 MPa; L3/L4: 0.90 vs. 0.74 MPa; L4/L5: 1.18 vs. 0.95 MPa). The variance was calculated to represent the degree of dispersion of the two sets of data. Variance in the TSEF model was less than that in the LSIF model (Figure 7D).

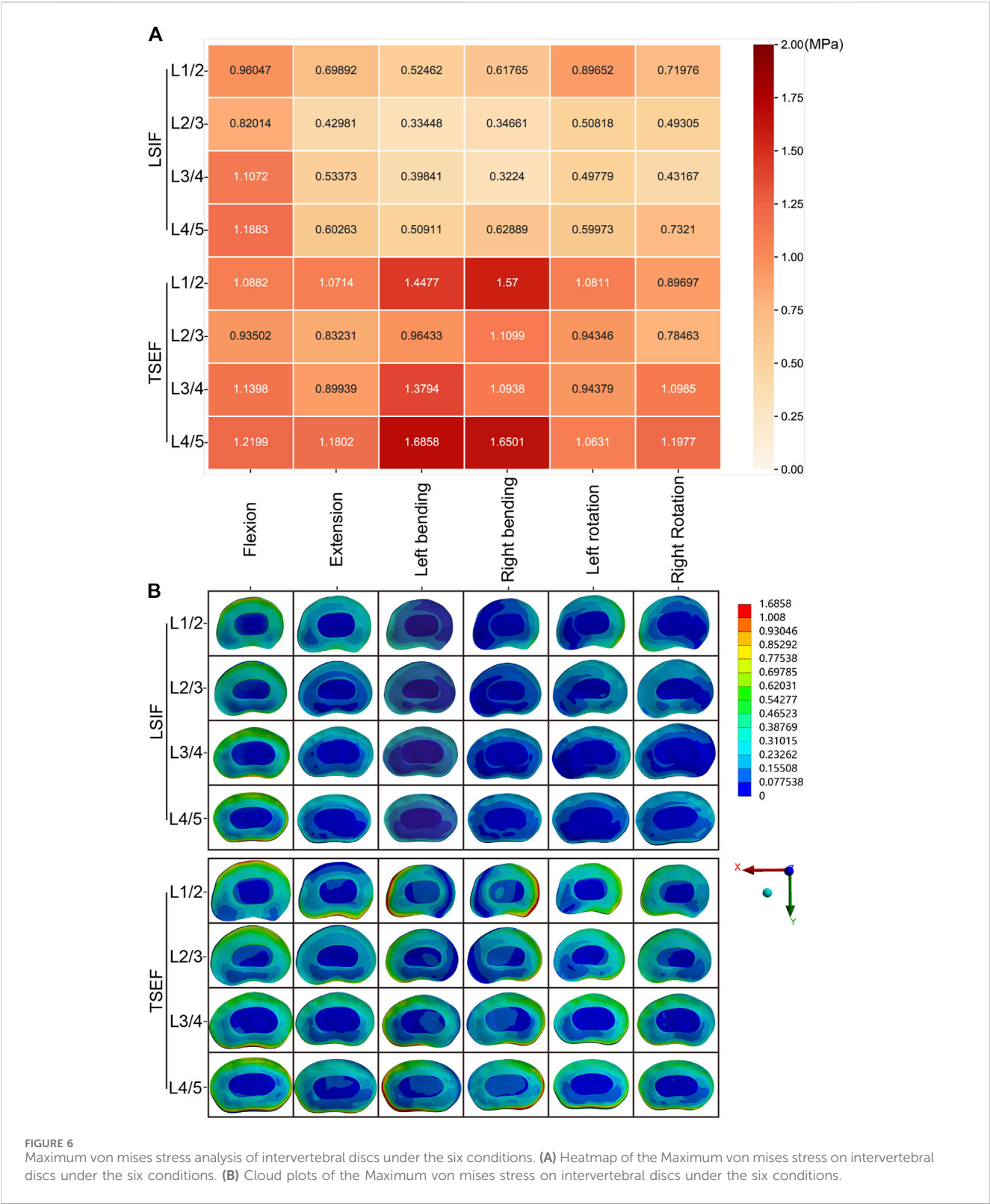
## Discussion

There are different ways to set a follower load on the spine model. The follower load parameters can be modified based on the target segments. In the study of Elmasry et al., the thoracolumbar spine models (T12-L2) were loaded with a 400 N follower load and 5000 N·mm moments (Elmasry et al., 2018). When selecting the lumbar spine as the subject of research, it is common practice to apply a follower load of 500 N at the L1 level, with a torque set at 7500 N·mm (Müller et al., 2021; Han et al., 2022). Therefore, the presenting lumbar model was loaded with a 500 N follower load and 7500 N·mm moments.

Under load control, the maximum ROM of the internal fixation model in six conditions ranged from 19.7% to 30.3% of the normal lumbar spine model. The result indicated that the entire lumbar spine was effectively fixed with the traditional long-segment spinal inner fixation, but the mobility of the lumbar spine was significantly limited. The maximum ROM of the TSEF was 27.3%–53.1% of the normal lumbar spine model. The TSEF model preserved more ROM compared to the LSIF model without losing stability. The overall ROM in the TSEF model was increased by 38.6%–75.2% compared to the LSIF model. Therefore, this might reduce the incidence of complications resulting from mobility loss of the thoracolumbar spine to a certain extent.

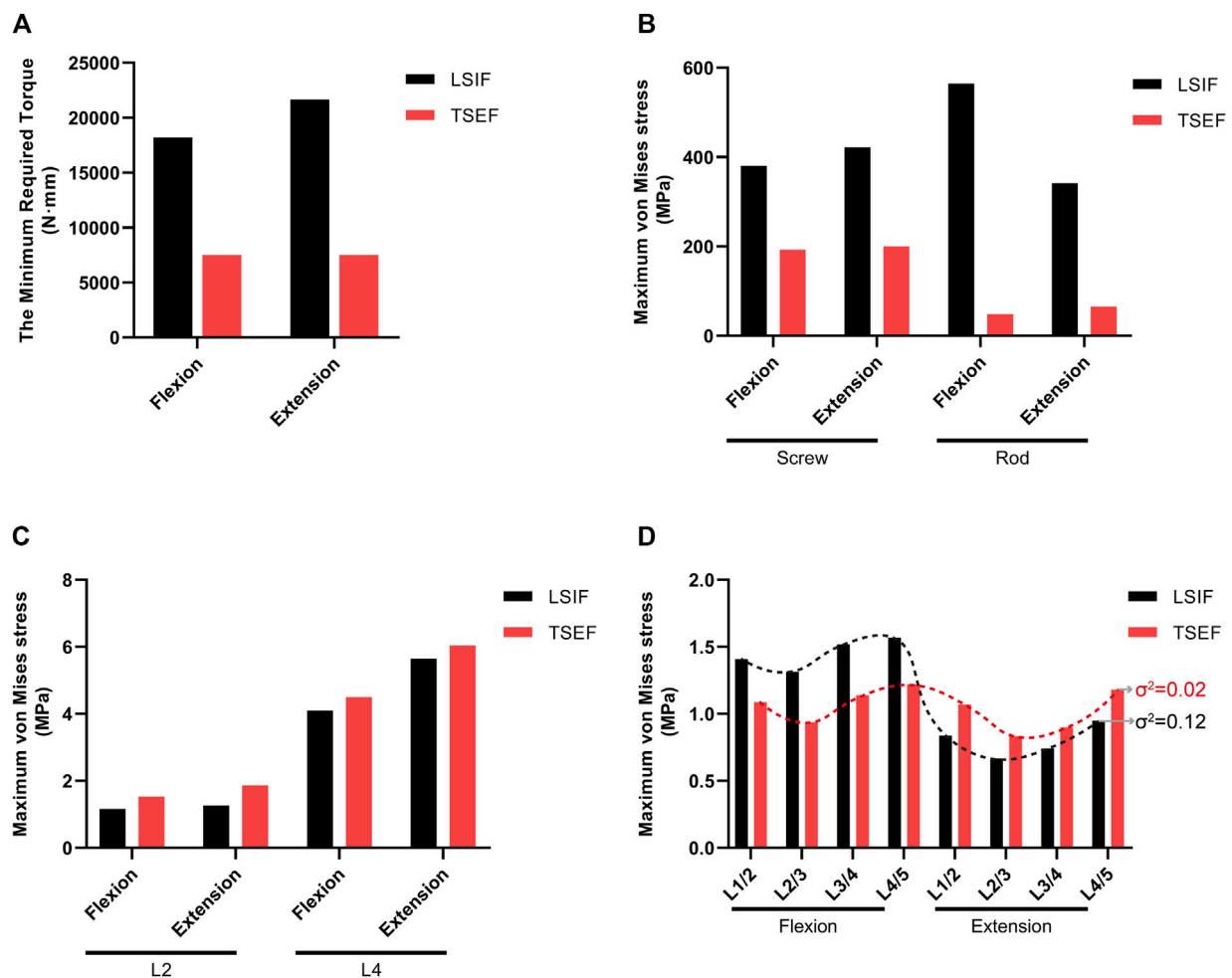
Additionally, we found that the maximum stress of the pedicle screw in the external fixation model was higher than that in the internal fixation model under all conditions except the flexion. However, the values of the stresses in the external fixation model were far below the fatigue threshold of 550 MPa, indicating the low risk of breakage of TSEF. Moreover, based on our previous experience, it is not adequate to analyze the stress of the screw-rod system purely using load control because the activity of the human spine is primarily achieved through displacement control (Liao et al., 2022). In order to simulate and analyze the specific stress situation of the nail bar system, we adopted the maximum activity of the external fixed model under flexion and extension conditions as the target. We achieved the same activity by increasing the load of the internal fixation model. In this case, we found that the load applied by the internal fixation system reached 242.7% and 288.7% of the initial load. Therefore, the patients treated with the LSIF system need to exert more force using the low back muscles to complete the same amplitude of movement under the same motion situation. Theoretically, it increases the burden on the tendon ligament complex of the lower back following the surgery.

At the same time, under the displacement control, the maximum stress of the LSIF model was significantly higher than that before, and the stress of the screw and the connecting rod was significantly higher than the maximum stress of the TSEF model. Even under the flexion condition, the stress value of the rod reached 564.73 MPa, which indicated there might be a fracture risk (Zhou et al., 2020). Our results reversely proved that the safety of the TSEF was significantly better than that of the long-segment screw-rod internal fixation system, and the safety of the screw-rod system was not significantly reduced due to the increase in its ROM. According to the clinical use of external spinal fixation, we usually remove the external fixation system 3 months after surgery, so no screw breakage occurs in clinical practice.



This study analyzed and compared the maximum stress of the fractured vertebral bodies. The maximum stress of the L4 vertebral body of the two models was higher than that of the L2 vertebral body under both load control and displacement control. Under load control, the maximum stress of the L2 and L4 fractured vertebral bodies of TSEF increased by 222.94% and 75.849% relative to LSIF in

flexion condition, and increased by 263.29% and 378.53% relative to LSIF in extension condition. However, when utilizing displacement control, which more accurately replicates real motion, the increments were significantly decreased. Under displacement control, the maximum stress of the L2 and L4 fractured vertebral bodies of TSEF increased by 31.53% and 9.82% relative to LSIF in



**FIGURE 7** Comparison of LSIF and TSEF under displacement control. **(A)** Required torque for the two fixations to reach the ROM of flexion 7.02° and extension 5.29°. **(B)** Maximum von mises stress on screws and rods of the LSIF and TSEF models under the displacement control. **(C)** Maximum von mises stress on fractured vertebra bodies (L2 and L4) in LSIF and TSEF under the displacement control. **(D)** Maximum von mises stress on discs in LSIF and TSEF under the displacement control.  $\sigma^2$ : variance.

flexion condition, and increased by 47.11% and 6.98% relative to LSIF in extension condition. Hence, it is our contention that the modest rise in stress under displacement control conditions should not, in theory, have a significant impact on the healing or exacerbation of the fracture. Previous studies have shown that rigid fixation may lead to stress shielding (Frost, 2004), which is not conducive to fracture healing, and long-segment fixation further increases this risk (Seçer et al., 2015). A certain degree of micromotion and stress stimulation may promote fracture healing (Uthoff et al., 2006; Bottlang et al., 2010; Augat et al., 2021; Duan and Lu, 2021; Travascio et al., 2021). According to experimental data, the maximum stress in the fractured vertebrae of the external fixation model increased slightly compared to the internal fixation model, and the TSEF model preserved more ROM compared to the LSIF model. Theoretically, the external fixation system has a potential in reducing the stress shading of the fractured vertebrae and promoting early healing of the fractured vertebrae. Similarly, the vast majority of the fractured vertebrae had already reached clinical healing at 3 months using external fixation

in our clinical setting. Under load control, the maximum stress of the intervertebral disc of the TSEF was smaller than that of the LSIF in flexion condition, while greater than that of the LSIF in extension condition. The variance, reflecting the discrete degree of a data set, was smaller in TSEF compared to LSIF. It indicated that TSEF exhibited a better biomechanical characteristic regarding discs stress distribution compared to LSIF.

In this study, we demonstrated the function of two fixation systems in the body through load control and displacement control, but there were some limitations. The lumbar model was constructed using the radiographic data from a healthy male volunteer, which discounted the influence of the morphological heterogeneity in lumbar spine. The cortical and cancellous bone were defined as homogeneous materials with different Young's modulus, and the intervertebral discs and cartilage are modeled as elastic elements. However, the morphology and density of cancellous bone play a significant role in determining the biomechanical properties of the vertebral body, with variations in bone density due to gender and age influencing surgical decision-making (Al-Barghouthi et al., 2020;



Garay et al., 2022). Additionally, complex muscle interactions and the viscoelastic behavior of disc fibers and ligaments are easily ignored in the discs computational model (Volz et al., 2022). Hence, the current model exhibits certain constraints in accurately replicating real motion scenarios. The incorporation of multiple models, encompassing a wide range of parameters including cancellous bone morphology, age, gender, and intervertebral disc metabolism characteristics, will significantly enhance its applicability.

On the other hand, the uniformed screws were utilized in the construction of two models (6.5 mm for LSIF, 5.5 mm for TSEF). If each screw model were constructed based on the SD/PW ratio (screw diameter/pedicle width) as previously documented (Solitro et al., 2019; Solitro et al., 2024), the model would more accurately reflect the variability in dimensions of the lumbar segments. In a study regarding the screw pullout load reported by Giovanni F. Solitro et al., given that the friction coefficient and shear stress are critical for screw pullout analysis, a layer surrounding the screw was modeled to include a failure for shear at a value of 1, and the bone-screw interface was modeled as surface-to-surface contact with a coefficient of friction of 2 (Solitro et al., 2024). In the present study, we focused on ROM of the lumbar spine and stresses on model elements in the TSEF and LSIF models, hence the bone-screw interface was defined as binding contact without modeling surrounding screws (Xu et al., 2014b).

The advancement of orthopedic implants has led to the exploration and application of emerging metal materials and screw insertion techniques. Michal Szczodry and others introduced a novel technique known as Increased Cortical Purchase (ICP) that demonstrates comparable accuracy to conventional methods and has the potential to enhance the long-term stability of pedicle screw fixations (Szczodry et al., 2018). A study conducted by Patrick A. Massey and co-authors presented biomechanical evidence suggesting that nitinol memory rods utilized in a posterior construct exhibit similar compression properties to titanium rods, but possess higher torsional failure load and torsional toughness (Massey et al., 2021). Sweetu Patel and others conducted research to develop and assess a biomedical Ti6Al4V rod aimed at enhancing the stability of the bone-rod interface (Patel et al., 2015). In order to broaden the scope of applicability of this model, which is now confined to the direct implantation mode of conventional titanium alloy implants, it is suggested that factors such as material properties, surface coating, and screw placement method be incorporated into the model construction parameters.

## Conclusion

MNSF is a unique type of spinal trauma commonly caused by high-energy injuries, and its global incidence was 1.6%–16.7% (Seçer et al., 2015). The surgical treatment of MNSF with spinal instability is still controversial (Lian et al., 2007; Seçer et al., 2015; Cho and Kim, 2019). Some studies reported treating MNSF using a long-segment screw-rod inner fixation system that fixed range could cover the entire lumbar spine (L1–L5) (Lian et al., 2007; Seçer et al., 2015; Cho and Kim, 2019). However, the traditional

long-segment spinal inner fixation (LSIF) would lead to extensive soft-tissue damage, loss of spinal ROM, stress concentration on fixation, stress shielding of fractured vertebral bodies, and adjacent segment degeneration (ASD) (Bastian et al., 2001; Park et al., 2004; Uthoff et al., 2006; Bottlang et al., 2010; Augat et al., 2021; Duan and Lu, 2021). We developed the TSEF based on our previous research and the single-segment external spinal fixation system to deal with the above problems. The TSEF has many advantages in managing MNSF due to its simpler structure, smaller surgical incision, faster rehabilitation, and better elastic properties (Wang et al., 2011; Song et al., 2014; Wang C. et al., 2018). Moreover, it has achieved satisfactory efficacy in early clinical application.

This study successfully simulated the surgical processes of MNSF treated using two different fixations (LSIF and TSEF). The maximum ROM and the maximum stresses on screws, rods, fractured vertebral bodies, and intervertebral discs of the two models were compared under six conditions (flexion, extension, left and right bending, and left and right rotation). In conclusion, we find that TSEF shows the better biomechanical characteristics in ROM preservation and discs stress distribution compared to LSIF. TSEF reduces the stress concentration of the connecting rods and the stress shielding of the fractured vertebral bodies. Therefore, the TSEF might be a better alternative for MNSF.

## Data availability statement

The original contributions presented in the study are included in the article/Supplementary material, further inquiries can be directed to the corresponding author.

## Ethics statement

Written informed consent was obtained from the individual(s) for the publication of any potentially identifiable images or data included in this article.

## Author contributions

HC: Writing—original draft. YK: Writing—review and editing. YY: Writing—review and editing. HW: Writing—review and editing. WP: Writing—review and editing. YL: Writing—review and editing. MZ: Writing—review and editing. ZX: Writing—review and editing. Writing—original draft. XS: Writing—review and editing. WW: Writing—review and editing. CW: Writing—review and editing.

## Funding

The author(s) declare that financial support was received for the research, authorship, and/or publication of this article. This work was supported by grants from the Natural Science Foundation in Hunan Province (2022JJ30537), the Key Laboratory in Hengyang

City (2018KJ115), and the Project of Health Commission in Hunan Province (20201961).

## Conflict of interest

The authors declare that the research was conducted in the absence of any commercial or financial relationships that could be construed as a potential conflict of interest.

## References

- Al-Barghouti, A., Lee, S., Solitro, G. F., Latta, L., and Travascio, F. (2020). Relationships among bone morphological parameters and mechanical properties of cadaveric human vertebral cancellous bone. *J. Bone Miner. Res.* 35 (5), e10351. doi:10.1002/jbm.b.35105
- Augat, P., Hollenstein, M., and von Rüden, C. (2021). The role of mechanical stimulation in the enhancement of bone healing. *Injury* 52 (Suppl. 2), S78–S83. doi:10.1016/j.injury.2020.10.009
- Bastian, L., Lange, U., Knop, C., Tusch, G., and Blauth, M. (2001). Evaluation of the mobility of adjacent segments after posterior thoracolumbar fixation: a biomechanical study. *Eur. spine J.* 10 (4), 295–300. doi:10.1007/s005860100278
- Bensch, F. V., Koivikko, M. P., Kiuru, M. J., and Koskinen, S. K. (2006). The incidence and distribution of burst fractures. *Emerg. Radiol.* 12 (3), 124–129. doi:10.1007/s0010140-005-0457-5
- Bottlang, M., Doornink, J., Lujan, T. J., Fitzpatrick, D. C., Marsh, J. L., Augat, P., et al. (2010). Effects of construct stiffness on healing of fractures stabilized with locking plates. *J. Bone Jt. Surg. Am. volume* 92 (Suppl. 2), 12–22. doi:10.2106/JBJS.J.00780
- Cho, Y., and Kim, Y. G. (2019). Clinical features and treatment outcomes of acute multiple thoracic and lumbar spinal fractures: a comparison of continuous and noncontinuous fractures. *J. Korean Neurosurg. Soc.* 62 (6), 700–711. doi:10.3340/jkns.2019.0093
- Duan, Z. W., and Lu, H. (2021). Effect of mechanical strain on cells involved in fracture healing. *Orthop. Surg.* 13 (2), 369–375. doi:10.1111/os.12885
- Elmasry, S. S., Asfour, S. S., and Travascio, F. (2018). Finite element study to evaluate the biomechanical performance of the spine after augmenting percutaneous pedicle screw fixation with kyphoplasty in the treatment of burst fractures. *J. Biomechanical Eng.* 140 (6). doi:10.1115/1.4039174
- Frost, H. M. (2004). A 2003 update of bone physiology and Wolff's Law for clinicians. *Angle Orthod.* 74 (1), 3–15. doi:10.1043/0003-3219(2004)074<0003:AUOBPA>2.0.CO;2
- Garay, R. S., Solitro, G. F., Lam, K. C., Morris, R. P., Albarghouthi, A., Lindsey, R. W., et al. (2022). Characterization of regional variation of bone mineral density in the geriatric human cervical spine by quantitative computed tomography. *PLoS one* 17 (7), e0271187. doi:10.1371/journal.pone.0271187
- Han, L., Li, Y., Li, Z., Ma, H., Wang, C., Chen, Q., et al. (2022). Biomechanical and clinical study of rod curvature in single-segment posterior lumbar interbody fusion. *Front. Bioeng. Biotechnol.* 10, 824688. doi:10.3389/fbioe.2022.824688
- Hayes, M. A., Howard, T. C., Gruel, C. R., and Kopta, J. A. (1989). Roentgenographic evaluation of lumbar spine flexion-extension in asymptomatic individuals. *Spine* 14 (3), 327–331. doi:10.1097/00007632-198903000-00014
- Iencean, S. M. (2002). Double noncontiguous cervical spinal injuries. *Acta Neurochir.* 144 (7), 695–701. doi:10.1007/s00701-002-0940-7
- Kanna, R. M., Gaik, C. V., Mahesh, A., Shetty, A. P., and Rajasekaran, S. (2016). Multilevel non-contiguous spinal injuries: incidence and patterns based on whole spine MRI. *Eur. spine J.* 25 (4), 1163–1169. doi:10.1007/s00586-015-4209-2
- Korres, D. S., Katsaros, A., Pantazopoulos, T., and Hartofilakidis-Garofalidis, G. (1981). Double or multiple level fractures of the spine. *Injury* 12 (3), 147–152. doi:10.1016/0020-1383(81)90050-4
- Lian, X. F., Zhao, J., Hou, T. S., Yuan, J. D., Jin, G. Y., and Li, Z. H. (2007). The treatment for multilevel noncontiguous spinal fractures. *Int. Orthop.* 31 (5), 647–652. doi:10.1007/s00264-006-0241-5
- Liao, J. C., Chen, W. P., and Wang, H. (2017). Treatment of thoracolumbar burst fractures by short-segment pedicle screw fixation using a combination of two additional pedicle screws and vertebroplasty at the level of the fracture: a finite element analysis. *BMC Musculoskelet. Disord.* 18 (1), 262. doi:10.1186/s12891-017-1623-0
- Liao, Y., Yan, Y., Kang, Y., Wang, W., Song, X., Peng, W., et al. (2022). Biomechanical analysis of the external fixation in a lumbar fracture model: a finite element study. *J. Med. Biol. Eng.* 42, 469–478. doi:10.1007/s40846-022-00727-2
- Liu, J., Yang, S., Lu, J., Fu, D., Liu, X., and Shang, D. (2018). Biomechanical effects of USS fixation with different screw insertion depths on the vertebrae stiffness and screw stress for the treatment of the L1 fracture. *J. back Musculoskelet. rehabilitation* 31 (2), 285–297. doi:10.3233/BMR-169692
- Massey, P. A., Hoge, S., Nelson, B. G., Ogden, A. L., Mody, M. G., Myers, M., et al. (2021). Nitinol memory rods versus titanium rods: a biomechanical comparison of posterior spinal instrumentation in a synthetic corpectomy model. *Glob. spine J.* 11 (3), 277–282. doi:10.1177/2192568220902401
- Müller, A., Rockenfeller, R., Damm, N., Kosterhohn, M., Kuntelhardt, S. R., Aiyangar, A. K., et al. (2021). Load distribution in the lumbar spine during modeled compression depends on lordosis. *Front. Bioeng. Biotechnol.* 9, 661258. doi:10.3389/fbioe.2021.661258
- Park, P., Garton, H. J., Gala, V. C., Hoff, J. T., and McGillicuddy, J. E. (2004). Adjacent segment disease after lumbar or lumbosacral fusion: review of the literature. *Spine* 29 (17), 1938–1944. doi:10.1097/01.brs.0000137069.88904.03
- Patel, S., Solitro, G. F., Sukotjo, C., Takoudis, C., Mathew, M. T., Amirouche, F., et al. (2015). Nanotopography and surface stress analysis of Ti6Al4V bioimplant: an alternative design for stability. *JOM* 67, 2518–2533. doi:10.1007/s11837-015-1341-8
- Pearcy, M., Portek, I., and Shepherd, J. (1985). The effect of low-back pain on lumbar spinal movements measured by three-dimensional X-ray analysis. *Spine* 10 (2), 150–153. doi:10.1097/00007632-198503000-00007
- Powell, J. N., Waddell, J. P., Tucker, W. S., and Transfeldt, E. E. (1989). Multiple-level noncontiguous spinal fractures. *J. trauma* 29 (8), 1146–1151. doi:10.1097/00005373-198908000-00013
- Seçer, M., Alagöz, F., Uçkun, O., Karakoyun, O. D., Uluş, M. Ö., Polat, Ö., et al. (2015). Multilevel noncontiguous spinal fractures: surgical approach towards clinical characteristics. *Asian spine J.* 9 (6), 889–894. doi:10.4184/asj.2015.9.6.889
- Solitro, G. F., Welborn, M. C., Mehta, A. I., and Amirouche, F. (2024). How to optimize pedicle screw parameters for the thoracic spine? A biomechanical and finite element method study. *Glob. spine J.* 14 (1), 187–194. doi:10.1177/21925682221099470
- Solitro, G. F., Whitlock, K., Amirouche, F., Mehta, A. I., and McDonnell, A. (2019). Currently adopted criteria for pedicle screw diameter selection. *Int. J. spine Surg.* 13 (2), 132–145. doi:10.14444/6018
- Song, X., Wang, W., Yan, Y., Zuo, J., Yao, N., and Lin, H. (2014). Clinical effect evaluation of percutaneous vertebroplasty combined with the spinal external fixator for the treatment of osteoporotic compressive fractures with posterior vertebral defect. *Eur. spine J.* 23 (12), 2711–2717. doi:10.1007/s00586-014-3346-3
- Szczodry, M., Solitro, G. F., Amirouche, F., and Patel, P. (2018). Pedicle screw with increased cortical purchase can be inserted with same accuracy as the screw in straightforward trajectory using 3D modeling landmarks. *Spine deform.* 6 (1), 20–27. doi:10.1016/j.jspd.2017.06.004
- Takami, M., Okada, M., Enyo, Y., Iwasaki, H., Yamada, H., and Yoshida, M. (2017). Noncontiguous double-level unstable spinal injuries. *Eur. J. Orthop. Surg. traumatology Orthop. traumatology* 27 (1), 79–86. doi:10.1007/s00590-016-1855-y
- Travascio, F., Buller, L. T., Milne, E., and Latta, L. (2021). Mechanical performance and implications on bone healing of different screw configurations for plate fixation of diaphyseal tibia fractures: a computational study. *Eur. J. Orthop. Surg. traumatology Orthop. traumatologie* 31 (1), 121–130. doi:10.1007/s00590-020-02749-5
- Uthoff, H. K., Poitras, P., and Backman, D. S. (2006). Internal plate fixation of fractures: short history and recent developments. *J. Orthop. Sci. official J. Jpn. Orthop. Assoc.* 11 (2), 118–126. doi:10.1007/s00776-005-0984-7
- Volz, M., Elmasry, S., Jackson, A. R., and Travascio, F. (2022). Computational modeling of intervertebral disc pathophysiology: a review. *Front. physiology* 12, 750668. doi:10.3389/fphys.2021.750668
- Wang, C., Que, Y. C., Song, X. Z., Yan, Y. G., Chen, Y., and Wang, W. J. (2018a). New external spinal skeletal fixation combined with percutaneous injury vertebra bone grafting for the treatment of two-segment thoracolumbar fractures. *China J. Orthop. traumatology* 31 (8), 714–717. doi:10.3969/j.issn.1003-0034.2018.08.006

## Publisher's note

All claims expressed in this article are solely those of the authors and do not necessarily represent those of their affiliated organizations, or those of the publisher, the editors and the reviewers. Any product that may be evaluated in this article, or claim that may be made by its manufacturer, is not guaranteed or endorsed by the publisher.



- Wang, H., Mo, Z., Han, J., Liu, J., Li, C., Zhou, Y., et al. (2018b). Extent and location of fixation affects the biomechanical stability of short- or long-segment pedicle screw technique with screwing of fractured vertebra for the treatment of thoracolumbar burst fractures: an observational study using finite element analysis. *Medicine* 97 (26), e11244. doi:10.1097/MD.00000000000011244
- Wang, W., Yao, N., Song, X., Yan, Y., and Wang, C. (2011). External spinal skeletal fixation combination with percutaneous injury vertebra bone grafting in the treatment of thoracolumbar fractures. *Spine* 36 (9), E606–E611. doi:10.1097/BRS.0b013e3181f92dac
- White, A. A., 3rd, and Panjabi, M. M. (1976). The clinical biomechanics of scoliosis. *Clin. Orthop. Relat. Res.* (118), 100–112. doi:10.1097/00003086-197607000-00018
- Wilke, H. J., Kirschak, S. T., Wenger, K. H., and Claes, L. E. (1997). Load-displacement properties of the thoracolumbar calf spine: experimental results and comparison to known human data. *Eur. spine J. official Publ. Eur. Spine Soc. Eur. Spinal Deformity Soc. Eur. Sect. Cerv. Spine Res. Soc.* 6 (2), 129–137. doi:10.1007/BF01358746
- Wittenberg, R. H., Hargus, S., Steffen, R., Muhr, G., and Bötzel, U. (2002). Noncontiguous unstable spine fractures. *Spine* 27 (3), 254–257. doi:10.1097/00007632-200202010-00010
- Xu, G., Fu, X., Du, C., Ma, J., Li, Z., and Ma, X. (2014a). Biomechanical effects of vertebroplasty on thoracolumbar burst fracture with transpedicular fixation: a finite element model analysis. *Orthop. traumatology, Surg. Res. OTSR* 100 (4), 379–383. doi:10.1016/j.otsr.2014.03.016
- Xu, G., Fu, X., Du, C., Ma, J., Li, Z., Tian, P., et al. (2014b). Biomechanical comparison of mono-segment transpedicular fixation with short-segment fixation for treatment of thoracolumbar fractures: a finite element analysis. *Proc. Institution Mech. Eng. Part H, J. Eng. Med.* 228 (10), 1005–1013. doi:10.1177/0954411914552308
- Yamamoto, I., Panjabi, M. M., Crisco, T., and Oxland, T. (1989). Three-dimensional movements of the whole lumbar spine and lumbosacral joint. *Spine* 14 (11), 1256–1260. doi:10.1097/00007632-198911000-00020
- Zhou, F., Yang, S., Liu, J., Lu, J., Shang, D., Chen, C., et al. (2020). Finite element analysis comparing short-segment instrumentation with conventional pedicle screws and the Schanz pedicle screw in lumbar 1 fractures. *Neurosurg. Rev.* 43 (1), 301–312. doi:10.1007/s10143-019-01146-9



## OPEN ACCESS

## EDITED BY

Jiaqiu Wang,  
London South Bank University, United Kingdom

## REVIEWED BY

Ryan (Qiuxiang) Huang,  
Queensland University of Technology, Australia  
Dusan Radivoje Mitic,  
University of Belgrade, Serbia  
Qiang Chen,  
Southeast University, China

## \*CORRESPONDENCE

Dong Sun,  
✉ [sundong@nbu.edu.cn](mailto:sundong@nbu.edu.cn)  
Yaodong Gu,  
✉ [guyaodong@hotmail.com](mailto:guyaodong@hotmail.com)

RECEIVED 20 May 2024

ACCEPTED 19 June 2024

PUBLISHED 09 July 2024

## CITATION

Chen H, Sun D, Fang Y, Gao S, Zhang Q, Bíró I, Tafferner-Gulyás V and Gu Y (2024), Effect of orthopedic insoles on lower limb motion kinematics and kinetics in adults with flat foot: a systematic review.  
*Front. Bioeng. Biotechnol.* 12:1435554.  
doi: 10.3389/fbioe.2024.1435554

## COPYRIGHT

© 2024 Chen, Sun, Fang, Gao, Zhang, Bíró, Tafferner-Gulyás and Gu. This is an open-access article distributed under the terms of the [Creative Commons Attribution License \(CC BY\)](https://creativecommons.org/licenses/by/4.0/). The use, distribution or reproduction in other forums is permitted, provided the original author(s) and the copyright owner(s) are credited and that the original publication in this journal is cited, in accordance with accepted academic practice. No use, distribution or reproduction is permitted which does not comply with these terms.

# Effect of orthopedic insoles on lower limb motion kinematics and kinetics in adults with flat foot: a systematic review

Hairong Chen<sup>1,2,3</sup>, Dong Sun<sup>2\*</sup>, Yufei Fang<sup>1</sup>, Shunxiang Gao<sup>2</sup>, Qiaolin Zhang<sup>2,3,4</sup>, István Bíró<sup>3</sup>, Viktória Tafferner-Gulyás<sup>5</sup> and Yaodong Gu<sup>2\*</sup>

<sup>1</sup>Ningbo No. 2 Hospital, Ningbo, China, <sup>2</sup>Faculty of Sports Science, Ningbo University, Ningbo, China, <sup>3</sup>Doctoral School on Safety and Security Sciences, Óbuda University, Budapest, Hungary, <sup>4</sup>Faculty of Engineering, University of Szeged, Szeged, Hungary, <sup>5</sup>John von Neumann Faculty of Informatics, Óbuda University, Budapest, Hungary

Flatfoot is characterized by the collapse of the medial longitudinal arch, eversion of the rearfoot and abduction of the loaded forefoot. Orthopedic insoles are the frequently recommended treatment to support the arch of the foot, adjust the structure of the foot, reduce pain, improve stability and new techniques have been applied to the design of orthopedic insoles in recent years. However, the effectiveness of orthopedic insoles in different motions is still debated from the perspective of biomechanics. Therefore, this study aimed to explore the impact of orthopedic insoles on the kinematics and kinetics of lower limb motion, and to verify effectiveness and propose possible future research directions. We conducted a literature search across three databases employing Boolean operations and filtered results based on eligibility criteria. A total of 671 relevant literature were searched in this review, and 19 literature meeting the requirements were finally included. The results showed that: 1) orthopedic insoles were effective when patients walk, run and jump from the perspective of biomechanics; 2) orthopedic insoles had different result on the change of ankle sagittal angle, moment and peak pressure in the metatarsal region; 3) Whether the effect of insoles, which uses new techniques such as different 3D printed technologies and adds various accessories, can be further improved remains to be further studied; 4) Follow-up studies can pay more attention to the differences between diverse populations, increase the breadth of running and jumping and other movements research and long-term intervention.

## KEYWORDS

orthopedic insoles, flatfoot, adults, lower limb motion, kinematics, kinetics

## 1 Introduction

Flat foot, also known as pes planus, is a condition where the medial longitudinal arch of the foot collapses, leading to a flat appearance of the sole when standing (Flores et al., 2019). This condition can affect one or both feet and results in a series of biomechanical changes including the eversion of the rearfoot and the abduction of the loaded forefoot (Arachchige et al., 2019). Such alterations in foot structure can have significant repercussions for an individual's overall posture and motor mechanics (Myerson, 1996; Van Boerum et al., 2003; Chinpeerasathian et al., 2024). Flat feet often lead to structural changes in the foot, causing

various painful symptoms (Toullec et al., 2015). One common issue is plantar fascia pain, resulting from the additional stress placed on this thick band of tissue that spans the bottom of the foot, due to the collapsed arch (Chen, 2020). Similarly, the altered mechanics may exacerbate stress on the Achilles tendon, leading to Achilles tendonitis (Vijayakumar et al., 2017). The ligamentous structures of the foot may also become overstretched or unstable, particularly under the load during weight-bearing activities, contributing to overall joint laxity and instability (Clement et al., 1984; Bertani et al., 1999). The instability and pain in the foot often lead to rapid fatigability, limiting physical activity and endurance (Franco, 1987). Medial instability can contribute to an uneven distribution of weight, which not only aggravates foot discomfort but can also lead to pain in the knees, hips, and lower back. These musculoskeletal pains occur as the body attempts to compensate for the uneven weight distribution and altered biomechanics caused by flat foot (Messier et al., 1988; Kaufman et al., 1999; Herchenröder et al., 2021). For many adults experiencing these symptoms, orthopedic insoles are a frequently recommended treatment. These insoles are designed to support the foot's arch, realign foot structure, alleviate pain, and enhance stability (Lusardi et al., 2012). The goal of using orthopedic insoles is to improve daily living and allow for greater physical activity without discomfort (Hume et al., 2008; Mills et al., 2010; Richter et al., 2011; Banwell et al., 2014).

At present, literature reviews have explored the effects of orthopedic insoles on the lower limbs. However, the impact of orthopedic insoles on flatfeet has been met with mixed conclusions in several systematic reviews (Michaudet et al., 2018; Choi et al., 2020). Assessing the effectiveness of orthotic devices is essential, considering their widespread prescription has considerable implications for healthcare expenses. For example, around 8% of the population, or five million people, were prescribed foot orthoses for medical reasons in Germany. This led to an increase of 466.6 million euros in statutory health insurance costs in 2019, attributable solely to these prescriptions (Herchenröder et al., 2021). Moreover, proof of either a beneficial or detrimental impact of orthoses on flatfeet can serve as a basis in orthopedic clinics to enhance the treatment strategies for patients suffering from flatfeet (Oerlemans et al., 2023).

Kinematic and radiological measurements have commonly been used as outcome measures in previous systematic reviews, with only a few focusing on kinetic parameters (Desmyttere et al., 2018; Choi et al., 2020; Hill et al., 2020). Moreover, most of the research concerns walking, whereas in daily activities people tend to wear orthopedic insoles for other movements such as running and jumping as well. There are few relevant reviews which focus on the effects of orthopedic insole on the kinematics and kinetics for different movements in population with flat feet.

Several new technological devices have been applied to the design and production of orthopedic insoles in the recent years, and biomechanical research on orthopedic insoles have also exploded. Against this background, my review systematically examines the biomechanical effects of orthopedic insoles on lower limb kinematics and kinetics in adults with flat feet, exploring their effectiveness and providing valuable references for future development and research directions in orthopedic insoles.

## 2 Materials and methods

This study was carried out in compliance with the PRISMA (systematic reviews and meta-analysis) preferred reporting items (Page et al., 2021; Zhou and Ugbohue, 2024; Feng and Song, 2017; Gao, 2022; Jiang, 2020).

### 2.1 Search strategy

To guarantee the reliability of the study findings, the search design was reviewed and endorsed by all the authors involved in the study. The electronic literature searches were conducted using the Web of Science, Scopus, and PubMed databases from 1 January 2019, to 26 March 2024. The selected time frame ensures that the study includes the most recent and relevant research, where newer studies can provide the latest insights and data. To enhance the comprehensiveness of our search, we employed a broad range of search terms and obtained a substantial number of results. We meticulously reviewed the retrieved literature to identify the studies that best met our criteria, ensuring the quality and validity of the included research. The search strategies were shown in Table 1.

### 2.2 Eligibility criteria

The inclusion criteria for screening the studies were as follows: 1) the articles must be published in English; 2) the article must appear in a peer-reviewed journal; 3) The participants must be adults (non-elderly and non-children); 4) the participants must suffer from flexible flatfoot; 5) the article must investigate lower limb motion kinematics and kinetics under insole intervention.

Articles were excluded if 1) articles were excluded if they were review articles; 2) Research subjects were excluded if they suffered from flexible flatfoot due to other diseases (e.g., rheumatoid arthritis, cerebral palsy); 3) articles were excluded if they focused solely on imaging research without addressing lower limb motion kinematics and kinetics; 4) articles were excluded if they focused on machine learning methods without direct examination of kinematics and kinetics; 5) articles were excluded if they only utilized finite element analysis or simulations without empirical data on human subjects.

### 2.3 Study risk of bias assessment

Two reviewers (H.C. and Y.G.) independently assessed the methodological quality of articles using the Combie criteria, which encompass seven domains (Kou et al., 2018). Based on the Combie evaluation tool, each article received a total possible score of 7.0 points, and quality of the articles was categorized as A, B, and C which indicated 6.0–7.0 points, 4.0–5.5 points, and 0–4.0 points, respectively. In the event of any disagreements during the quality assessment, an independent arbitrator would intervene to resolve them (I.B.).

TABLE 1 Search strategies in each electronic database.

Database	Search strategies	Result
PubMed	("flat foot" [All Fields] OR "flatfoot" [All Fields] OR "flat feet" [All Fields] OR "flatfeet" [All Fields] OR "plane foot" [All Fields] OR "platypodia" [All Fields] OR "pes planus" [All Fields] OR "talipes planus" [All Fields]) AND ("inner sole" [All Fields] OR "insole" [All Fields] OR "orthopedic insole" [All Fields]) AND ("biomechanics" [All Fields] OR "kinetic" [All Fields] OR "kinematic" [All Fields]) AND 2019/01/01:2024/03/26 [Date - Publication]	12
Web of Science	TS= (("flat foot" OR "flatfoot" OR "flat feet" OR "flatfeet" OR "plane foot" OR "platypodia" OR "pes planus" OR "talipes planus") AND ("inner sole" OR "insole" OR "orthopedic insole") AND ("biomechanics" OR "kinetic" OR "kinematic")) AND PY= (2019–2024)	20
Scopus	((("flat foot" OR "flatfoot" OR "flat feet" OR "flatfeet" OR "plane foot" OR "platypodia" OR "pes planus" OR "talipes planus") AND ("inner sole" OR "insole" OR "orthopedic insole") AND ("biomechanics" OR "kinetic" OR "kinematic"))) AND PUBYEAR >2018 AND PUBYEAR <2025	639

## 2.4 Data extraction and management

Table 1 illustrates those two reviewers (H.C. and Y.G.) independently extracted data from all chosen studies using a standardized form according to the principles of participants, interventions, comparisons, and outcomes (PICOS).

## 3 Results

In this section, we presented the findings of our systematic review based on the Prisma framework, which provided a structured approach to categorize and analyze the results, ensuring a comprehensive and systematic examination of the data. The characteristic information of included studies were detailed in Table 2. Only studies that met the inclusion and exclusion criteria and had a risk of bias score of 5.5 or above were analyzed. We analyzed the impact of orthopedic insoles on lower limb walking, running, and jumping kinematics and kinetics in adults and aimed to present a clear and organized synthesis of the existing literature, highlighting key trends, gaps, and insights that emerged from our analysis.

### 3.1 Literature selection

In the initial search, 671 articles were identified. After deduplication and pooling, 488 articles were advanced to the screening stage. Ultimately, 65 studies were chosen during the eligibility assessment, during which articles were excluded based on specific criteria if they suffered from flat feet due to other diseases (n = 2), imaging research (n = 18), children (n = 12), only used finite element analysis or simulations (n = 2), other foot orthotic interventions (n = 4), only used electromyogram analysis (n = 7), not lower limb motion kinematics and kinetics (n = 1), 19 articles were selected for the systematic review (Figure 1).

### 3.2 Original characteristics

This review of studies on biomechanics reveals a focus on several key parameters: joint kinematics (12 studies), joint kinetics (10 studies), plantar pressure and kinetics (8 studies), and ground reaction forces

(6 studies). Geographically, the distribution of these studies includes 47.4% from China, 15.8% from Iran and Canada, and 5.3% from South Korea, Australia, Czech Republic, and the United Arab Emirates. Sample sizes varied with 36.8% of studies including 15 to 20 participants, 36.8% including 10 to 15 participants, 10.5% including 5 to 10 participants, and 15.8% having more than 20 participants. In terms of participant gender, 10.5% of the studies exclusively involved males, 15.8% females, 52.6% a mix of both genders, and 21.1% did not describe. Most of the studies (78.9%) focused on walking, while 10.5% each focused on running and jumping (Figure 2).

### 3.3 Risk of bias

The risk of bias in all the selected studies was evaluated, and the outcomes are detailed in Table 3. Of the studies included, 94.7% scored above 5.5 points, which is categorized as quality A, while one study scored below 6.0 points, classified as quality B. Thus, the selected literature for this study is rated as high and moderate in quality.

### 3.4 Impact on walking

This part mainly covered the analysis of existing studies on the changes in joint kinematics, joint kinetics, plantar pressure and kinetics, and ground reaction forces when walking in orthopedic insoles conditions. A total of fifteen studies were analyzed.

#### 3.4.1 Joint kinematics

Eight studies investigated the effects of insole interventions on lower limb joint kinematics during walking. One study found that arch support insoles led to smaller peak everted position and reduced rearfoot motion compared to normal insoles (Han et al., 2019). Another study reported that orthotic insoles improved the arch index both before and after long-term intervention during walking on level surfaces and stairs (Zhai et al., 2019). In comparison to wearing shoes only, using 3D printed foot orthoses resulted in increased peak ankle dorsiflexion (Cheng et al., 2021). Additionally, rigid 3D printed foot orthoses reduced midfoot eversion and forefoot abduction, while 3D printed foot orthoses with posting decreased ankle eversion angle (Desmyttere et al., 2021). In terms of arch support, 3D printed orthoses showed a

TABLE 2 The characteristic information of included studies.

Author and year	Sample size (total)	Gender (Male/Female)	Experimental insole	Tests	Biomechanical parameters	Key findings
Han et al. (2019)	28	28/0	Normal insole (control) Type A (arch support function) Type B (arch support and cushion pads)	Walking speed: 80 beats per minute	Joint kinematics (Joint angle) Joint kinetics (Joint moment) GRF	Peak everted position (Type A, Type B↓VS Control) Range of rearfoot motion in the longitudinal axis (Type A↓VS Control) Peak evtor moment (Type A, Type B↓VS Control)
Ho et al. (2019)	26	26/0	Neutral flat insole Prefabricated foot orthose	Vertical countermovement jump (CMJ) Standing broad jump (SBJ)	Joint kinematics (Joint angle) Joint kinetics (Joint moment) GRF (Peak GRF)	CMJ take off: ankle eversion↓ SBJ take off: ankle eversion↓, peak horizontal GRF↓ peak ankle frontal moment↓
Karimi et al. (2019)	15	—	None Arch support foot insole	Walk with a comfortable speed	Joint kinematics Joint kinetics (Joint moment) GRF (Peak GRF)	First and second peaks of ankle adductor moment↓ Second peak of vertical force↓ First peak of anteroposterior↑ Mediolateral component↓
Lee et al. (2019)	12	—	None Customized arch support orthoses (CASO) Orthotic heel lift (HL)	Run on the runway at a self-selected speed	Joint kinematics (Joint angle) Joint kinetics (Joint moment, Achilles tendon force)	Peak dorsiflexion angle (CASO↑,HL↓VS None; CASO↑VS HL) Peak plantarflexion moment (CASO↓, HL↓VS None) Peak ATL (Achilles Tendon load) (CASO↓, HL↓VS None) Time to peak Achilles tendon force (CASO↑, HL↑VS None) Achilles tendon loading rate (CASO↓, HL↓VS None)
Lin et al. (2019)	12	4/8	Standard shoe (Shoe) Standard shoe with 3D Printed FOs (Shoe + FO)	Walk at a self-selected speed	Joint kinetics (Joint moment) GRF	Maximum ankle evtor moment↓ Peak external rotator moment↓ Maximum ankle plantar flexor moment↑
Xu et al. (2019)	90	—	3D printed customized (experimental group) Prefabricated insole (control group)	Walk at speed of 3.12 ± 1.95 km/h	Plantar pressure and kinetics (Peak pressure, Peak force)	Week 0: peak pressure in the 3rd metatarsal region↓ peak force in the 1st metatarsal↓,mid-foot pressure↑ Week 8: the peak pressure and force in mid-foot↑ Control group: the peak pressures of the 4th and 5th metatarsal areas↓, peak force of the 5th metatarsal area↓, peak force of 1st metatarsal area↑ (Week 8 VS Week 0) Experimental group: the peak pressure of the 2nd to 5th toe↑ the lateral heel area of the big toe↑ (Week 8 VS Week 0)
Zhai et al. (2019)	15	0/15	None Orthotic insole	Walk on level surface, walking up and down 10 cm and 20 cm stairs	Plantar pressure and kinetics (Peak force)	Plantar max force↓ (especially when walking downstairs)

(Continued on following page)



TABLE 2 (Continued) The characteristic information of included studies.

Author and year	Sample size (total)	Gender (Male/Female)	Experimental insole	Tests	Biomechanical parameters	Key findings
Huang et al. (2020)	15	0/15	Arch-support insole Flat insole	Walk on treadmill: 9-degree incline (uphill walking) 9-degree decline (downhill walking), a level surface (level walking) at 2.7 km/h speed for all slopes	Plantar pressure and kinetics (Peak pressure)	Peak pressure of the BT↑ on the uphill and level surface Peak pressure of the MH↓ on the uphill, downhill, and level surface Peak pressure of the M2, M3 and M4↑ while the LH↓
Cheng et al. (2021)	10	4/6	Reinforced and undercut arch support (R + U+) Reinforced without undercut arch support (R + U-) Without reinforced and undercut arch support (R-U+) Control without insole	Walk at their comfortable speed	Joint kinematics (Joint angle) Plantar pressure and kinetics (Peak pressure, Pressure-time integral) GRF	Peak ankle dorsiflexion↑ and peak pressure↑ at the medial midfoot region (insole vs. control) Peak pressure↓ at the hindfoot region (insole vs. control) Peak medial midfoot pressure↑ and medial hindfoot pressure↑ (R + U- vs. R+U+ and R-U+) Peak pressure at lateral forefoot↓, lateral midfoot↑ (R+U+ vs. R + U- and R-U+) Pressure-time integral at the medial midfoot region (R-U+↑ and R + U+↑ vs. control, R + U+↓ vs. R-U+)
Desmyttere et al. (2021)	19	6/13	Shoe only 3D printed flexible Fos +with posting 3D printed rigid Fos	Walk for 3 min at predetermined speed	Joint kinematics (Joint angle) Joint kinetics (Joint moment)	Midfoot eversion↓ and forefoot abduction↓ (rigid foot orthoses vs. other) Ankle eversion angle↓, inversion moment↓ and knee abduction moment↑ (posting vs. other)
Jiang et al. (2021)	10	8/2	Ordinary flat insole General orthotic insole Plantar pressure redistribution insole (PPRI)	Walk on the treadmill at speed 0.8 m/s, 1.0 m/s, and 1.2 m/s	Plantar pressure and kinetics (Peak pressure)	Peak pressure in T area at slow speed (PPRI↑ vs. flat insole) Peak pressure in M2 area at slow speed (PPRI↓ vs. orthotic insole) Peak pressure in MH area at all speed (PPRI↓ vs. flat insole) Peak pressure in MH area at slow speed (PPRI↓ vs. orthotic insole) Peak pressure in MH area at fast speed (orthotic insole↓ vs. flat insole) Peak pressure in LH area at normal speed (PPRI↓ vs. flat insole) Peak pressure in LH area at all speed (orthotic insole↓ vs. flat insole)
Khorasani et al. (2021)	18	8/10	Without insole Prefabricated soft insole Custom-molded rigid medical insole	Walk at a self-selected speed and rhythm	Plantar pressure and kinetics (Peak pressure, Peak force)	Mean pressure and force in the heel, MTP2,3 MTP4,5 (insole↓ vs. control) Pressure in the medial midfoot (insole↑ vs. control) No differences between two insoles

(Continued on following page)

TABLE 2 (Continued) The characteristic information of included studies.

Author and year	Sample size (total)	Gender (Male/Female)	Experimental insole	Tests	Biomechanical parameters	Key findings
Ataabadi et al. (2022)	20	12/8	SHOD Custom-made FOs with medial heel wedge LDT (Low-dye tape)	Run at running speed ( $7.9 \pm 0.6$ km/h)	Joint kinematics (Joint angle) Joint kinetics (Joint moment)	Dorsiflexion angle (Fos↓vs. SHOD) Ankle eversion (Fos↓vs. SHOD and LDT) Knee adduction angle (Fos↑vs. SHOD and LDT) Hip adduction angle (LDT↑vs. Fos and SHOD) Hip external rotation (Fos↑vs. LDT) Plantar flexor moment (Fos↓vs. SHOD) Knee extensor moment (Fos↑vs. SHOD) Knee external rotation moment (Fos↑vs. SHOD and LDT) Knee abductor moment (Fos↑vs. SHOD) Hip extensor moment (LDT↑vs. Fos and SHOD)
Cherni et al. (2022)	19	6/13	Shoe only 3D printed flexible Fos 3D printed flexible FOs with posting 3D printed rigid Fos	Walk as normal as possible	Plantar pressure and kinetics (Peak pressure)	Peak pressures, mean pressures in the midfoot area (Fos↑vs. control) The latter was reinforced by increasing the stiffness
Ho et al. (2022)	12	5/8	Shoe without Fos Shoe with 3D printed Shoe with traditionally made Fos	Walk within 5% of their preferred time	Joint kinematics (Arch height drop) Joint kinetics (Joint moment, Joint power) GRF (Peak GRF)	Arch height drop (3D printed↓vs. traditional) Ankle plantarflexion moment (3D printed and traditional↓vs. control) Ankle power absorption (3D printed and traditional↓vs. control) VGRF (3D printed and traditional↓vs. control)
Hsu et al. (2022)	10	5/5	Without insoles Auto-scan insole Total contact insole Medial wedge insole	Walk at a self-selected speed	Joint kinematics (Navicular height, Joint angle) Joint kinetics	Navicular height↑, ankle dorsiflexion angle↑and comfort↑with insole Wedge insole was the most efficient in navicular height↑and ankle dorsiflexion angle↑
Jandova et al. (2022)	18	—	Original insole (INS1) Customized thermoplastic (INS2) 3D printed insole (INS3)	Walk	Plantar pressure and kinetics (Peak pressure)	Pressure in middle foot (INS1↓vs. INS2 and 3) Peak pressure in middle foot (35% higher in INS2 and 23% higher in INS3 compared to INS1) Peak pressure in the rearfoot (INS2↓vs. INS1)
Alsaafin et al. (2023)	31	0/31	Shoes only Foot orthoses (15° inverted angle) Foot orthoses (25° inverted angle)	Walk	Joint kinematics (Joint angle)	Maximum ankle plantarflexion angle maximum ankle dorsiflexion angle (foot orthose↓vs. shoe) Maximum ankle external rotation angle maximum ankle internal rotation angle (foot orthose↓vs. shoe) Maximum ankle plantarflexion angle (25°inverted angle↓vs. 15° inverted angle and shoe) Maximum hip external rotation angle (foot orthose↑ vs. shoe)

(Continued on following page)

TABLE 2 (Continued) The characteristic information of included studies.

Author and year	Sample size (total)	Gender (Male/Female)	Experimental insole	Tests	Biomechanical parameters	Key findings
Dami et al. (2024)	15	—	Without Fos MWFOs (medially wedged Fos) TFOs (thin-flexible Fos)	Drop landing on the level surface Drop landing on the valgus inclined surface	Joint kinematics (Joint angle) Joint kinetics (Joint moment)	Level surface: midfoot dorsiflexion angle midfoot abduction angle (MWFOs↓vs. SHOD) Ankle eversion angle (MWFOs < TFOs < SHOD) Valgus inclined surface: midfoot dorsiflexion angle (MWFOs < TFOs < SHOD) Midfoot abduction angle (MWFOs↓ vs. TFOs and SHOD) Ankle eversion angle (MWFOs < TFOs < SHOD) Hip flexion angle (MWFOs↑vs. TFOs) Hip internal rotation angle (MWFOs↓vs. TFOs and SHOD) Hip abduction moment (MWFOs↓ and TFOs↓ vs. SHOD)

smaller arch height drop compared to traditional orthoses (Ho et al., 2022). Furthermore, insoles were found to increase navicular height, and 3D printed insoles specifically increased ankle dorsiflexion angle, with the wedge condition being most effective (Hsu et al., 2022). The maximum ankle dorsiflexion angle during mid-stance, the maximum ankle external and internal rotation angles, and the maximum ankle plantarflexion angle during loading response were all reduced under orthotic settings when compared to wearing shoes alone. Furthermore, when compared to the 15° inverted angle and shoes-alone situations, the maximal ankle plantarflexion angle at toe-off only reduced in the 25° inverted angle condition. In contrast, under orthotic settings, the maximal hip external rotation angle rose (Alsaafin et al., 2023). It is worth noting that one study by Karimi did not discover any appreciable variations in lower limb kinematics (Karimi et al., 2019).

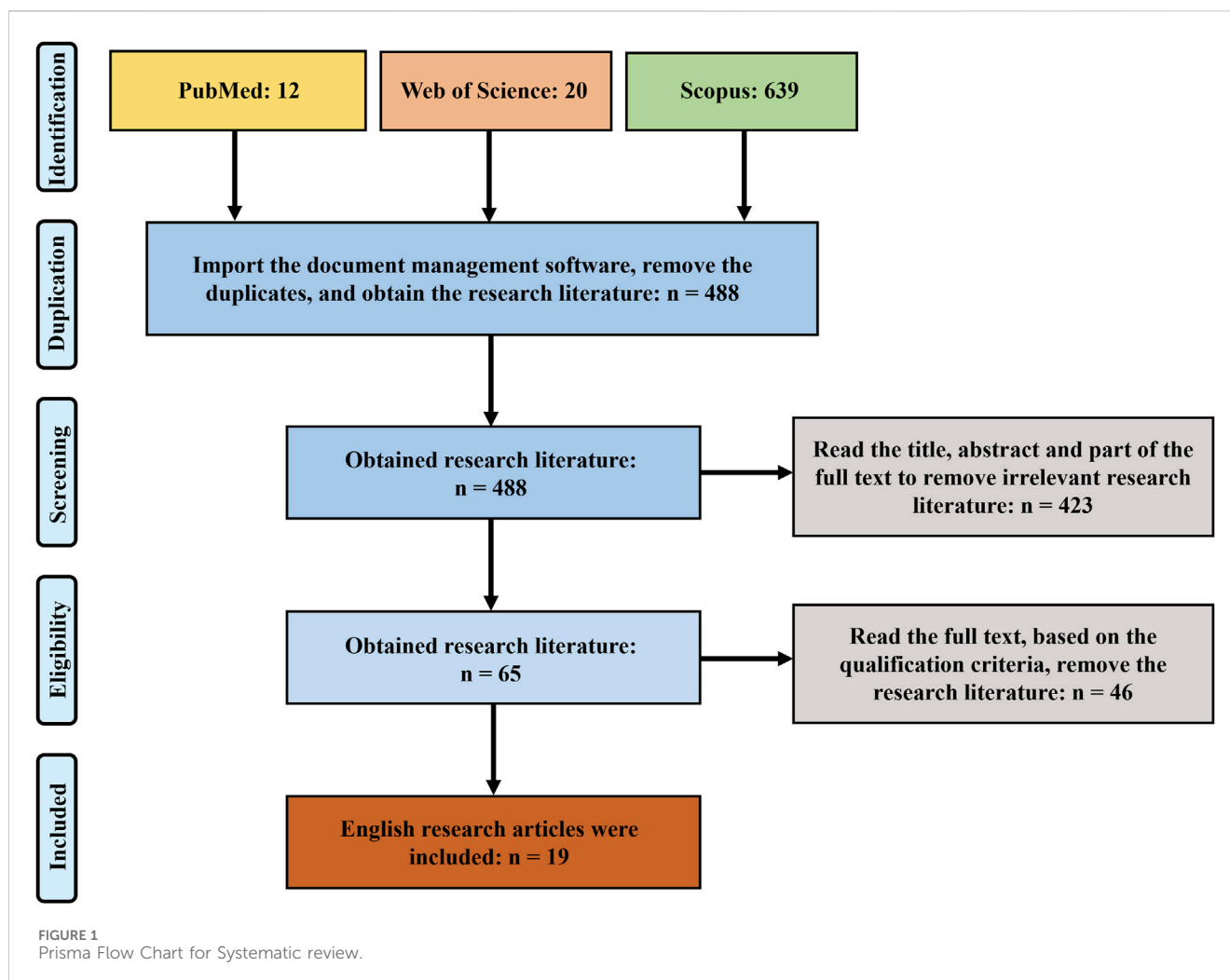
3.4.2 Joint kinetics

Six studies examined how insole interventions impact lower limb joint kinetics during walking (Han et al., 2019). Arch support insoles resulted in lower peak evtor moments compared to normal insoles (Karimi et al., 2019). Foot insoles decreased the first and second peaks of adductor moments on the ankle joint. 3D printed foot orthoses (FOs) reduced the maximum ankle evtor moment by an average of 35% and significantly decreased the peak external rotator moment by 16%. Additionally, the maximum ankle plantar flexor moment with 3D printed FOs was significantly higher than with regular shoes (Lin et al., 2019). FOs with posting reduced ankle inversion moment and increased knee abduction moment (Desmyttere et al., 2021). Traditional and 3D printed foot orthoses showed lower ankle plantar flexion moment during control conditions and higher power absorption compared to control and traditional conditions (Ho et al., 2022). The study of Hsu was the only one that did not find differences in lower limb kinetic (Hsu et al., 2022).

3.4.3 Plantar pressure and kinetics

Eight articles reported the impact of insole interventions on the planter pressure during walking. The long-term intervention study of insoles showed following. Peak force in the first metatarsal region and peak pressure in the third metatarsal region were initially lower in the tailored (EVA) insoles group than in the standard insoles group. By week 8, though, the group using the tailored (EVA) insoles had more midfoot force and peak pressure. Conversely, by week 8, the first metatarsal area’s peak force was greater and the fourth and fifth metatarsal areas’ peak pressures and forces were lower in the traditional insoles group than they had been in the previous week (Xu et al., 2019). Regarding flatfoot, orthotic insole treatment effectively decreased plantar pressure, especially during downhill walking (Zhai et al., 2019). In arch support insoles, the peak pressure of the big toe (BT) was higher on uphill and level surfaces compared to flat insoles, while the peak pressure of the mid-heel (MH) was lower on all surfaces. Additionally, the peak pressure of the second (M2), third (M3), and fourth (M4) metatarsals was higher in arch-support insoles than flat insoles, while the lateral heel (LH) pressure was lower in arch-support insoles (Huang et al., 2020). In comparison to the control, there was a rise in peak pressure at the medial midfoot region and a fall in the rearfoot region for the insole conditions. Additionally, at the medial midfoot and hindfoot regions, R+U– demonstrated a considerably higher peak pressure than R+U+ and R–U+. In comparison to R–U+ and R + U–, R+U+ exhibited a notably reduced peak pressure at the forefoot and a higher one at the midfoot on the lateral side. Only the medial midfoot region showed significant variations in the pressure-time integral, and paired comparisons revealed that R–U+ and R+U+ were different from the control. Moreover, compared to R–U+, R+U+ showed a substantially reduced pressure-time integral at the medial forefoot region (Cheng et al., 2021).

At modest walking speeds, the peak pressure of PPRI insoles in the T region was higher than the flat insole. Peak pressure in the



M2 region was lower when walking slowly with the PPRI insole than when using the orthotic insole. Peak pressure in the MH region was lower when walking at slow, normal, and rapid walking speeds with the PPRI insole than when walking at slow walking speeds with the orthotic insole. Furthermore, at a normal walking speed, the peak pressure in the LH area was lower while using the PPRI footbed than when using the flat insole. At normal, fast, and slow walking speeds, the peak pressure with the orthotic insole was lower than with the flat insole (Jiang et al., 2021). The mean pressure and force at the second, third, fourth, and fifth metatarsophalangeal (MTP2,3,4,5) joints as well as the heel decreased with the usage of insoles. Nevertheless, it was discovered that wearing insoles increased pressure in the medial midfoot. There were no discernible variations in plantar pressure and force between the rigid insole that was custom-molded and the prefabricated soft insole (Khorasani et al., 2021). Walking with foot orthoses caused the greatest alterations in the midfoot area, where peak pressures, mean pressures, and contact area all increased (Cherni et al., 2022). In terms of pressure on the middle foot, both INS2 and INS3 result in increased peak pressure when compared to INS1, with INS2 having a 35% higher peak pressure and INS3 showing a 23% higher peak pressure in the middle foot region. For the rearfoot pressure,

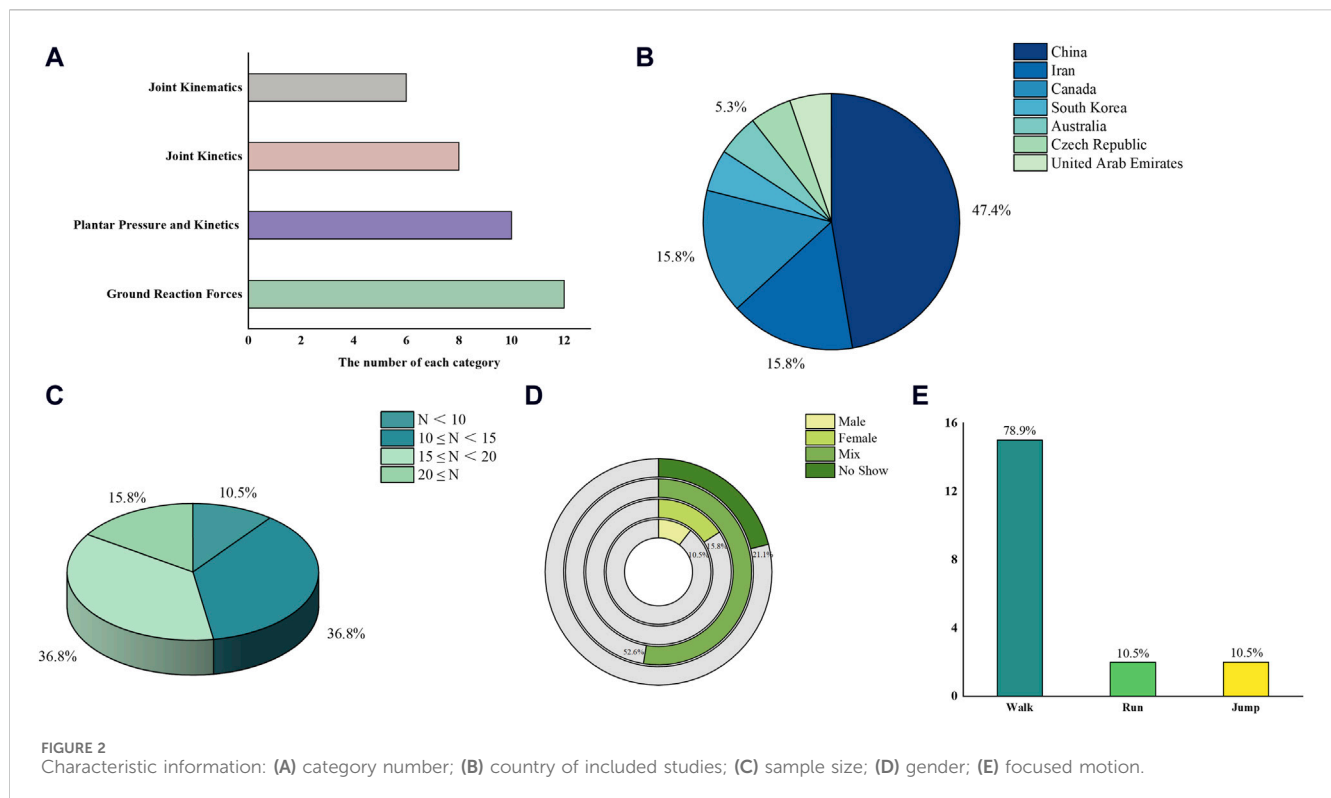
INS2 decreased the peak pressure when compared to the INS1 (Jandova et al., 2022).

### 3.4.4 Ground reaction force

Five articles investigated the effects of insole interventions on ground reaction forces during walking. One study discovered that using arch support insoles while walking led to a reduction in the second peak of vertical force, but an increase in the first peak of anteroposterior force. In addition, the sideways component of the force exerted by the ground decreased when participants utilized insoles, as opposed to walking without them (Karimi et al., 2019). Another study reported lower vertical ground reaction forces during walking with both Traditional and 3D printed insoles compared to a control condition (Ho et al., 2022). The studies of Han, Lin and Cheng did not find differences in ground reaction force (Han et al., 2019; Lin et al., 2019; Cheng et al., 2021).

## 3.5 Impact on running

This part mainly covered the analysis of existing studies on the changes in joint kinematics and joint kinetics when running in orthopedic insoles conditions. A total of two studies were analyzed.



### 3.5.1 Joint kinematics

Two articles investigated the effects of insole interventions on lower limb joint kinematics during running. In the first study, the use of Heel Lifts (HL) caused the peak dorsiflexion angle to drop in comparison to the control condition, whereas the use of Custom Arch Support Orthotics (CASO) increased it. Furthermore, when employing CASO, the peak dorsiflexion angle was greater than when using HL (Lee et al., 2019). In the second study, when compared to wearing standard shoes (SHOD), foot orthotics (FOs) decreased the dorsiflexion angle and decreased ankle eversion during the whole stance phase. During the stance phase, FOs increased the knee adduction angle at the knee joint. Furthermore, in comparison to the Low-Dye Taping (LDT) condition, FOs enhanced hip external rotation in the horizontal plane at the start of the stance phase (Ataabadi et al., 2022).

### 3.5.2 Joint kinetics

Two articles reported the impact of insole interventions on the kinetic of lower limb joints during running. The peak plantarflexion moment was reduced when running with both CASO and HL compared to the control condition. Additionally, peak Achilles tendon loading (ATL) was lower when using HL during running compared to the control. In comparison to the control, both the CASO and HL interventions demonstrated a marginally longer duration from initial contact to peak Achilles tendon force (duration to peak Achilles tendon force). Running with HL resulted in a lower Achilles tendon loading rate (ATLR) compared to the control group (Lee et al., 2019). The plantar flexor moment was lower with FOs compared to SHOD. Knee moments (extensor, external rotation, and abductor) were all higher with FOs. Additionally, the knee external rotation moment remained higher with FOs when compared to LDT. In contrast, the hip

extensor moment was higher with LDT than with FOs and SHOD (Ataabadi et al., 2022).

## 3.6 Impact on jumping

This part mainly covered the analysis of existing studies on the changes in joint kinematics, joint kinetics and ground reaction forces when jumping in orthopedic insoles conditions. A total of two studies were analyzed.

### 3.6.1 Joint kinematics

The impact of insole interventions on lower limb joint kinematics during jumping was examined in two articles. One study found that foot orthoses resulted in less ankle eversion during the take-off phase of a countermovement jump (CMJ) compared to an insole condition. Another study reported that during a standing broad jump (SBJ), foot orthoses were associated with less ankle eversion compared to the insole condition (Ho et al., 2019). Modified wedge foot orthoses (MWFOs) were found to reduce the midfoot dorsiflexion angle during the landing phase of drop landings on a level surface when compared to shoe wear. When using MWFOs as opposed to shoes, a reduced midfoot abduction angle was also observed. Furthermore, MWFOs and total contact foot orthoses (TFOs) both led to a smaller ankle eversion angle compared to shoes, with MWFOs also showing a smaller ankle eversion angle compared to TFOs. During drop landings on a valgus-inclined surface, both MWFOs and TFOs were associated with a smaller midfoot dorsiflexion angle compared to wearing shoes. Additionally, MWFOs showed a smaller midfoot dorsiflexion angle compared to TFOs. Moreover, MWFOs resulted



TABLE 3 Study risk of bias assessment.

Studies	①	②	③	④	⑤	⑥	⑦	Grade	Quality
Han et al. (2019)	Yes	Yes	Yes	Yes	Yes	Yes	Yes	7	A
Ho et al. (2019)	Yes	Yes	Yes	Yes	Yes	No	Yes	6	A
Karimi et al. (2019)	Yes	Yes	Yes	Yes	Yes	No	Yes	6	A
Lee et al. (2019)	Yes	Yes	Yes	Yes	Yes	Yes	Yes	7	A
Lin et al. (2019)	Yes	Yes	Yes	Yes	Yes	No	Yes	6	A
Xu et al. (2019)	Yes	Yes	Yes	Yes	Yes	No	Yes	6	A
Zhai et al. (2019)	Yes	Yes	Yes	Yes	Yes	No	Yes	6	A
Huang et al. (2020)	Yes	Yes	Yes	Yes	Yes	Yes	Yes	7	A
Cheng et al. (2021)	Yes	Yes	Yes	Yes	Yes	No	Yes	6	A
Desmyttere et al. (2021)	Yes	Yes	Yes	Yes	Yes	No	Yes	6	A
Jiang et al. (2021)	Yes	Yes	Yes	Unclear	Yes	Yes	Yes	6.5	A
Khorasani et al. (2021)	Yes	Yes	Yes	Yes	Yes	No	Yes	6	A
Ataabadi et al. (2022)	Yes	Yes	Yes	Yes	Yes	Yes	Yes	7	A
Cherni et al. (2022)	Yes	Yes	Yes	Yes	Yes	No	Yes	6	A
Ho et al. (2022)	Yes	Yes	Yes	Yes	Yes	Yes	Yes	7	A
Hsu et al. (2022)	Yes	Yes	Yes	Unclear	Yes	No	Yes	5.5	B
Jandova et al. (2022)	Yes	Yes	Yes	Yes	Yes	No	Yes	6	A
Alsaafin et al. (2023)	Yes	Yes	Yes	Yes	Yes	Yes	Yes	7	A
Dami et al. (2024)	Yes	Yes	Yes	Yes	Yes	Yes	Yes	7	A

**Note:** ①The study design was scientific and rigorous; ②The data collection strategy is reasonable; ③The research reports sample response rates; ④The total representativeness of samples was favorable; ⑤The research purpose and method are reasonable; ⑥The power of the test was reported; ⑦The statistical method was correct.

in a smaller midfoot abduction angle compared to TFOs and shoes. Both MWFOs and TFOs were associated with a smaller ankle eversion angle compared to shoes, with MWFOs also showing a smaller ankle eversion angle compared to TFOs. Compared to TFOs, MWFOs showed a larger hip flexion angle, and compared to TFOs and shoes, MWFOs showed a smaller hip internal rotation angle (Dami et al., 2024).

3.6.2 Joint kinetics

Two articles reported the impact of insole interventions on the kinetic of lower limb joints during jumping. Foot orthosis conditions was less peak ankle frontal moment than insole condition at standing broad jump (SBJ) (Ho et al., 2019). Dropping onto a level surface: A smaller ankle inversion moment was observed for individuals wearing minimal footwear (MWFOs) compared to those wearing shoes (shod). A smaller hip abduction moment was observed for individuals wearing toe-only footwear (TFOs) compared to MWFOs. Dropping onto a valgus inclined surface: A smaller hip abduction moment was observed for both TFOs and MWFOs compared to those wearing shoes (Dami et al., 2024).

3.6.3 Ground reaction force

One article reported the impact of insole interventions on GRF during jumping. Foot orthosis conditions was lower peak horizontal

GRF than insole condition at standing broad jump (SBJ) (Ho et al., 2019).

4 Discussion

In recent years, orthopedic insoles have received a lot of attention in the studies of lower limb biomechanics in motion. This systematic review categorized and sorted out the key information and findings of the studies, analyzed the effect of orthopedic insoles on lower limb motion kinematics and kinetics in adults with flatfoot including walking, running, and jumping movements, and aimed to reveal the effectiveness of orthopedic insoles in different motion forms and to provide a scientifically rigorous basis for the use of orthopedic insoles. In addition, the shortcomings of the existing studies were found to provide valuable directions for the future development and research direction of orthopedic insoles.

4.1 Characteristic information

From the perspective of the original characteristics, the countries of origin of selected articles were mainly concentrated in Asia and the sample size of the participants was mostly between 10 and 20. In

addition, for the gender selection of the participants, most of the studies were mixed gender, but there are anatomical characteristics differences between males and females such as the pelvis, which may have an impact on the effect produced by orthopedic insoles (Petrie et al., 2023). In terms of the type of orthopedic insoles, the main types of insoles were common customized insoles, 3D printed insoles of various designs, and various accessories added for assistance. In addition, the main motion studied was walking, with relatively few studies on running and jumping motions.

## 4.2 Walking

### 4.2.1 Kinematics

Almost overwhelmingly, studies had found that orthopedic insoles have an impact on walking kinematics. During walking, orthopedic insoles provided better arch support compared to no insoles and have a significant effect when walking up and down stairs (Ataabadi et al., 2022; Alsaafin et al., 2023). Orthopedic insoles reduced peak ankle eversion angle, maximum ankle external rotation angle, internal rotation angle, and increased maximum hip external rotation angle (Han et al., 2019; Jandova et al., 2022). These kinematic changes, which help to reduce the abnormal posture of flatfoot, help flatfoot patients to perform walking. However, the effects produced by different designs of orthopedic insoles on walking kinematics were controversial. Some studies had found that the use of 3D printed orthopedic insoles can reduce the arch height drop better compared to traditional orthopedic insoles, but the effect of different designs of 3D printed insoles on the reduction of the arch height drop was not consistent. The wedge insoles had the best effect, and the effect of the other designs of 3D printed insoles had no difference (Khorasani et al., 2021; Ataabadi et al., 2022). The effects of different designs of 3D printed insoles on reducing peak ankle eversion angle were also inconsistent. The 3D printed orthopedic insoles with posting was the most effective, but there was no difference in effect between the other designs of 3D printed insoles. The rigid 3D printed orthopedic insoles, compared to no insoles and other types of 3D printed insoles reduced midfoot eversion and forefoot abduction (Lee et al., 2019). These suggested that changing the design of the insole may increase its alteration of walking kinematics and better correction of abnormal foot posture.

However, there were also opposing trends in the effects of different designs of orthopedic insoles on walking kinematics. Orthopedic insoles reduced the range of motion in the sagittal plane of the rearfoot, maximum ankle plantarflexion and dorsiflexion angle, while angle orthopedic insoles with a 25° inverted further reduced the maximum ankle plantarflexion angle (Han et al., 2019; Jandova et al., 2022). However, 3D printed insoles increased peak ankle dorsiflexion angle and the effect of different designs of 3D printed insoles on increasing the peak ankle dorsiflexion angle was not consistent, with wedge insole increasing the most significantly but there was no disparity in the effect between other designs of 3D printed insoles (Ho et al., 2019; Ataabadi et al., 2022). There was still controversy about how ankle angles change to benefit population with flatfoot. One view was that flatfoot was due to excessive dorsiflexion and eversion resulting in

talus and tarsal subluxation and pronation, where dorsiflexion or hypermobility of the ankle should be controlled (Needleman and international, 2005). Another view was that the limited range of motion of the ankle leads to rearfoot inversion and that the range of motion of the ankle should be restored (Hösl et al., 2014). Therefore, it remained to be explored which design of orthopedic insoles was more effective in modifying ankle dorsiflexion and extension.

### 4.2.2 Kinetics

The vast proportion of studies had found that orthopedic insoles influenced walking joint kinetics. Orthopedic insoles exhibited smaller peak ankle eversion moment and ankle power absorption; 3D printed insoles similarly exhibited reduced maximal ankle eversion moment, peak external rotator moment, and ankle power absorption (Han et al., 2019; Khorasani et al., 2021; Ho et al., 2022). The magnitude of joint moments during walking can be considered key to preventing injury, and using fewer moments will reduce the likelihood of injury from overuse (Novacheck and posture, 1998). Increasing the stiffness of 3D printed Fos will reduce the ankle inversion moment and the functional demands on the inversion muscles will be reduced, which may result in overuse injuries to other compensatory muscles. However, a rise in the knee abduction moment, despite values within the safe range, may have an undesirable effect and lead to the development of osteoarthritis in the medial compartment knee (Lee et al., 2019). Like joint kinematics, opposing results existed in studies regarding ankle sagittal plane moment. 3D printed insole showed greater ankle plantarflexion moment, whereas traditionally made insoles and 3D printed insoles showed smaller ankle plantarflexion moment (Khorasani et al., 2021; Ho et al., 2022). The divergence of the studies lies in the understanding of muscle activation of the peroneus longus, peroneus brevis, soleus, medial peroneus, and lateral peroneus in patients with flatfoot during the stance phase, which can be further validated by electromyogram in subsequent studies.

### 4.2.3 Plantar pressure and kinetics

Orthopedic insoles affected plantar pressure and kinetics during walking. The impact of orthopedic insoles on plantar pressure and kinetics typically included a rise in peak pressure at the midfoot and a reduction in peak pressure at the heel (Ho et al., 2019; Xu et al., 2019; Jiang et al., 2021). Orthopedic insoles helped maintain the calcaneus in a normalized alignment, improving pressure distribution and absorption. With the addition of longitudinal arch support, these insoles shifted pressure from the rearfoot to the midfoot and decreased rearfoot pressure, ultimately reducing the risk of tibial stress fractures (Aminian et al., 2013). The intervention of orthopedic insoles can normalize plantar pressure distribution. Different designs of orthopedic insoles caused further effects on plantar pressure distribution. Customized insoles and 3D printed insoles resulted in a further increase in midfoot peak pressure, a decrease in rearfoot peak pressure, and a further increase in midfoot peak pressure after long term intervention (Ho et al., 2019; Cherni et al., 2022; Hsu et al., 2022). Peak pressure in the metatarsal region is still a controversial topic. According to recent research, using a medial longitudinal arch support may help to transfer pressure from the first metatarsal to the second and third metatarsals in the central forefoot. Additionally, this support may lessen forefoot pronation

and lessen strain on the first metatarsal by keeping the subtalar joint in a position that is similar to its usual state (Redmond et al., 2009). After long term intervention, 3D printed insoles reduced peak pressure and force in the medial metatarsal region (Hsu et al., 2022). However, it had been shown that orthopedic insoles had no impact on pressure and force distribution in the M1 region (Ho et al., 2019; Xu et al., 2019; Jiang et al., 2021). Subsequent studies should pay more attention to this point. Different walking styles and different walking speeds were also factors that influenced the alteration of plantar pressure by orthopedic insoles. Pressure distribution in the rearfoot and metatarsal region was altered as a result (Karimi et al., 2019; Lin et al., 2019; Alsaafin et al., 2023).

#### 4.2.4 Kinematics

There were not many studies related to the effect of orthopedic insoles on ground reaction forces during walking and most of them reported no difference existed (Han et al., 2019; Ho et al., 2019; Ho et al., 2022). Studies showed that aligning the foot structure with orthopedic insoles resulted in a decrease in the peak vertical GRF (Cheng et al., 2021; Khorasani et al., 2021). Further studies should follow to determine the effects.

### 4.3 Running

Orthopedic insoles had been shown to correct abnormal foot plantarflexion moment, decrease achillea tendon forces, and redress abnormal ankle eversion foot posture during running, but adding the medial heel wedge results in increased knee moment. Like walking, what effect orthopedic insoles have on the peak dorsiflexion angle still need to be further investigated, and different designs of orthopedic insoles affected the peak dorsiflexion angle differently (Huang et al., 2020; Desmyttere et al., 2021).

### 4.4 Jumping

In jumping and landing motions, orthopedic insoles can reduce foot and ankle eversion and increase foot stability. In addition, orthopedic insoles reduced ankle stress and enhance hip stability in landing motion. Different designs of orthopedic insoles have different effects on hip joint biomechanics (Zhai et al., 2019; Dami et al., 2024).

### 4.5 Limitations and directions

The review primarily focused on walking, running, and jumping, while overlooking other critical activities such as stair climbing, lateral movements, or sports-specific actions. Methodological variations among included studies, including differences in orthopedic insole types, could impact result comparability. The review may not adequately address outcome variations due to small sample sizes or limited diversity in study populations, including differences in age, weight, and activity levels. Most studies emphasized short-term effects of orthopedic insole usage,

neglecting long-term durability and sustained biomechanical impacts.

Future research should encompass a broader range of movements and activities to offer the more comprehensive assessment of effectiveness. Standardized protocols for biomechanical analysis and insole design would enhance cross-study comparisons. Long-term studies are essential to evaluate sustained effects on lower limb biomechanics and foot health. Studies should also encompass larger, more diverse populations to explore how factors such as age, gender, weight, and activity levels influence orthopedic insole efficacy. Lastly, investigating and comparing new technologies and materials in orthopedic insole design would advance understanding in this field.

Some specific examples of potential studies or experiments that could further advance. Recruit a diverse cohort that encompasses a wide range of ages, genders, weights, and physical activity levels, ensuring a robust sample size to boost the study's statistical strength. Implement a variety of orthopedic insole types, including traditional materials as well as innovative technologies like 3D printing and specialized accessories. Conduct longitudinal studies with follow-up periods from 6 months to 2 years to evaluate both the immediate and prolonged impacts of the insoles. Gather extensive kinematic and kinetic data during various activities, including walking, running, jumping, stair climbing, and lateral movements, utilizing standardized biomechanical assessment tools and protocols. Apply sophisticated statistical methods to dissect the effects of orthopedic insoles on lower limb biomechanics and perform subgroup analyses to identify differences based on gender, age, and other demographic variables. These strategic methodologies will enable future research to deliver more conclusive and relevant findings on the efficacy of orthopedic insoles for patients with flatfoot.

### 4.6 Summary

Overall, recent studies have demonstrated the effectiveness of orthopedic insoles during walking, running, jumping motions, correcting abnormal foot postures, and better protecting patients for these motions. However, there was still disagreement about changes in peak ankle eversion angle, ankle sagittal plane moment, and peak pressure in the metatarsal region. No consensus on whether the biomechanical effectiveness of the insole can be further enhanced using personalization, 3D printed, and the addition of a variety of accessories, which could be further explored in subsequent studies to find the most effective orthopedic insoles. In addition, follow up studies could focus more on diverse populations, jumping and other motions and long-term intervention, etc.

## 5 Conclusion

Based on the results of this systematic review we can conclude the effectiveness of orthopedic insoles for walking, running, and jumping. However, the changes of orthopedic insoles on the sagittal plane angle and moment of ankle joint and the peak pressure in the metatarsal region are still controversial. It is unknown whether the orthopedic insoles designed by the new technology can improve the effect. Besides, it is necessary to expand the depth of studies related

to the more diverse populations, the running, jumping and other motions and long-term intervention, etc. These are the directions for the development and research of orthopedic insoles in the future.

## Author contributions

HC: Writing—original draft. DS: Writing—original draft. YF: Writing—original draft. SG: Writing—original draft. QZ: Writing—review and editing. IB: Writing—review and editing. VT -G: Writing—review and editing. YG: Writing—original draft, Writing—review and editing.

## Funding

The author(s) declare that financial support was received for the research, authorship, and/or publication of this article. This study was sponsored by Zhejiang Province Science Fund for Distinguished Young Scholars (Grant number: LR22A020002), Ningbo Key Research and Development Program (Grant number: 2022Z196), Zhejiang Rehabilitation Medical Association Scientific Research Special Fund (ZKKY2023001), Research Academy of Medicine Combining Sports, Ningbo (No.2023001), the Project of Ningbo Leading Medical &Health

## References

- Alsaafin, N., Saad, N., Mohammad Zadeh, S. A., and Hegazy, F. A. J. J. o.M. H. (2023). Effect of different foot orthosis inverted angles on walking kinematics in females with flexible flatfeet. *J. Multidiscip. Healthc.* Vol. 16, 2613–2623. doi:10.2147/jmdh.s420003
- Aminian, G., Safaeepour, Z., Farhoodi, M., Pezeshk, A. F., Saeedi, H., Majddoleslam, B. J. P., et al. (2013). The effect of prefabricated and proprioceptive foot orthoses on plantar pressure distribution in patients with flexible flatfoot during walking. *Prosthetics Orthot. Int.* 37 (3), 227–232. doi:10.1177/0309364612461167
- Arachchige, S. N. K., Chander, H., and Knight, A. J. T. F. (2019). Flatfeet: biomechanical implications, assessment and management. *Foot* 38, 81–85. doi:10.1016/j.foot.2019.02.004
- Ataabadi, P. A., Abbassi, A., Letafatkar, A., Vanwanseele, B. J. G., and Posture (2022). The effects of foot orthosis and low-dye tape on lower limb joint angles and moments during running in individuals with pes planus. *Gait Posture* 96, 154–159. doi:10.1016/j.gaitpost.2022.05.024
- Banwell, H. A., Mackintosh, S., Thewlis, D. J. J. o.f., and research, a. (2014). Foot orthoses for adults with flexible pes planus: a systematic review. *J. foot ankle Res.* 7, 23–18. doi:10.1186/1757-1146-7-23
- Bertani, A., Cappello, A., Benedetti, M., Simoncini, L., and Catani, F. J. C. B. (1999). Flat foot functional evaluation using pattern recognition of ground reaction data. *Clin. Biomech.* 14 (7), 484–493. doi:10.1016/s0268-0033(98)90099-7
- Chen, L. (2020). *Biomechanics of the plantar fascia in running and the implication for plantar fasciitis*. Hong Kong Polytechnic University. Ph.D.
- Cheng, K.-W., Peng, Y., Chen, T.L.-W., Zhang, G., Cheung, J.C.-W., Lam, W.-K., et al. (2021). A three-dimensional printed foot orthosis for flexible flatfoot: an exploratory biomechanical study on arch support reinforcement and undercut. *Materials* 14 (18), 5297. doi:10.3390/ma14185297
- Cherni, Y., Desmyttere, G., Hajizadeh, M., Bleau, J., Mercier, C., and Begon, M. J. C. B. (2022). Effect of 3D printed foot orthoses stiffness on muscle activity and plantar pressures in individuals with flexible flatfeet: a statistical non-parametric mapping study. *Clin. Biomech.* 92, 105553. doi:10.1016/j.clinbiomech.2021.105553
- Chinpeerasathian, C., Sin Oo, P., Siriphorn, A., and Pensri, P. J. P. o. (2024). Effect of foot orthoses on balance among individuals with flatfoot: a systematic review and meta-analysis. *Plos one* 19 (3), e0299446. doi:10.1371/journal.pone.0299446
- Choi, J. Y., Hong, W. H., Suh, J. S., Han, J. H., Lee, D. J., Lee, Y. J. J. F., et al. (2020). The long-term structural effect of orthoses for pediatric flexible flat foot: a systematic review. *Foot ankle Surg.* 26 (2), 181–188. doi:10.1016/j.fas.2019.01.007
- Discipline (No.2022-F15, No.2022-F22), Ningbo Natural Science Foundation (Grant number: 2022J065, 2022J120) and K. C. Wong Magna Fund in Ningbo University, Ningbo No. 2 Hospital Hwa Mei Scientific Research Fund (2024HMKYA53), Hairong Chen is currently supported by the China Scholarship Council (202208330357), Qiaolin Zhang is currently supported by the China Scholarship Council (202208330356).
- ## Conflict of interest
- The authors declare that the research was conducted in the absence of any commercial or financial relationships that could be construed as a potential conflict of interest.
- ## Publisher's note
- All claims expressed in this article are solely those of the authors and do not necessarily represent those of their affiliated organizations, or those of the publisher, the editors and the reviewers. Any product that may be evaluated in this article, or claim that may be made by its manufacturer, is not guaranteed or endorsed by the publisher.
- Clement, D., Taunton, J., and Smart, G. J. T. A. j.o.s.m. (1984). Achilles tendinitis and peritendinitis: etiology and treatment. *Am. J. sports Med.* 12 (3), 179–184. doi:10.1177/036354658401200301
- Dami, A., Payen, E., Farahpour, N., Robb, K., Isabelle, P.-L., and Moisan, G. J. C. B. (2024). Medially wedged foot orthoses generate greater biomechanical effects than thin-flexible foot orthoses during a unilateral drop jump task on level and inclined surfaces. *Clin. Biomech.* 112, 106193. doi:10.1016/j.clinbiomech.2024.106193
- Desmyttere, G., Hajizadeh, M., Bleau, J., and Begon, M. J. C. B. (2018). Effect of foot orthosis design on lower limb joint kinematics and kinetics during walking in flexible pes planovalgus: a systematic review and meta-analysis. *Clin. Biomech.* 59, 117–129. doi:10.1016/j.clinbiomech.2018.09.018
- Desmyttere, G., Hajizadeh, M., Bleau, J., Leteneur, S., and Begon, M. J. C. B. (2021). Anti-pronator components are essential to effectively alter lower-limb kinematics and kinetics in individuals with flexible flatfeet. *Clin. Biomech.* 86, 105390. doi:10.1016/j.clinbiomech.2021.105390
- Feng, Y., and Song, Y. (2017). The categories of AFO and its effect on patients with foot impair: a systematic review. *Phys. Act. Health* 1 (1), 8–17. doi:10.5334/paah.3
- Flores, D. V., Mejía Gómez, C., Fernández Hernando, M., Davis, M. A., and Pathria, M. N. J. R. (2019). Adult acquired flatfoot deformity: anatomy, biomechanics, staging, and imaging findings. *Radiographics* 39 (5), 1437–1460. doi:10.1148/rg.2019190046
- Franco, A. H. J. P. t. (1987). Pes cavus and pes planus: analyses and treatment. *Phys. Ther.* 67 (5), 688–694. doi:10.1093/ptj/67.5.688
- Gao, Z. (2022). The effect of application of asymmetry evaluation in competitive Sports: A systematic review. *Phys. Act. Health* 6, 257–272. doi:10.5334/paah.215
- Han, K., Bae, K., Levine, N., Yang, J., Lee, J.-S. J. M. s.m.i.m.j.o.e., and research, c. (2019). Biomechanical effect of foot orthoses on rearfoot motions and joint moment parameters in patients with flexible flatfoot. *Med. Sci. Monit. Int. Med. J. Exp. Clin. Res.* 25, 5920–5928. doi:10.12659/msm.918782
- Herchenröder, M., Wilfling, D., Steinhäuser, J. J. J. o.f., and research, a. (2021). Evidence for foot orthoses for adults with flatfoot: a systematic review. *J. foot ankle Res.* 14, 57–11. doi:10.1186/s13047-021-00499-z
- Hill, M., Healy, A., Chockalingam, N. J. J. o.F., and Research, A. (2020). Effectiveness of therapeutic footwear for children: a systematic review. *J. Foot Ankle Res.* 13 (1), 23. doi:10.1186/s13047-020-00390-3
- Ho, M., Kong, P. W., Chong, L. J. Y., Lam, W. K. J. J. o.f., and research, a. (2019). Foot orthoses alter lower limb biomechanics but not jump performance in basketball players with and without flat feet. *J. foot ankle Res.* 12 (1), 24. doi:10.1186/s13047-019-0334-1



- Ho, M., Nguyen, J., Heales, L., Stanton, R., Kong, P. W., Kean, C. J. G., et al. (2022). The biomechanical effects of 3D printed and traditionally made foot orthoses in individuals with unilateral plantar fasciopathy and flat feet. *Gait Posture* 96, 257–264. doi:10.1016/j.gaitpost.2022.06.006
- Hösl, M., Böhm, H., Multerer, C., Döderlein, L. J. G., and posture (2014). Does excessive flatfoot deformity affect function? A comparison between symptomatic and asymptomatic flatfeet using the Oxford Foot Model. *Gait posture* 39 (1), 23–28. doi:10.1016/j.gaitpost.2013.05.017
- Hsu, C.-Y., Wang, C.-S., Lin, K.-W., Chien, M.-J., Wei, S.-H., and Chen, C.-S. J. B. (2022). Biomechanical analysis of the flatfoot with different 3D-printed insoles on the lower extremities. *Bioengineering-Basel* 9 (10), 563. doi:10.3390/bioengineering9100563
- Huang, Y.-p., Peng, H.-T., Wang, X., Chen, Z.-R., and Song, C.-Y. J. P. o. (2020). The arch support insoles show benefits to people with flatfoot on stance time, cadence, plantar pressure and contact area. *Plos One* 15 (8), e0237382. doi:10.1371/journal.pone.0237382
- Hume, P., Hopkins, W., Rome, K., Maulder, P., Coyle, G., and Nigg, B. J. S. M. (2008). Effectiveness of foot orthoses for treatment and prevention of lower limb injuries: a review. *Sports Med.* 38, 759–779. doi:10.2165/00007256-200838090-00005
- Jandova, S., Mendricky, R. J. D. P., and Manufacturing, A. (2022). Benefits of 3D printed and customized anatomical footwear insoles for plantar pressure distribution. *3D Print. Addit. Manuf.* 9 (6), 547–556. doi:10.1089/3dp.2021.0002
- Jiang, C. (2020). The effect of basketball shoe collar on ankle stability: a systematic review and meta-analysis. *Phys. Act. Health.* 4 (1), 11–18. doi:10.5334/paah.48
- Jiang, Y., Wang, D., Ying, J., Chu, P., Qian, Y., and Chen, W. J. S. (2021). Design and preliminary validation of individual customized insole for adults with flexible flatfeet based on the plantar pressure redistribution. *Sensors-Basel* 21 (5), 1780. doi:10.3390/s21051780
- Karimi, M., Tahmasebi, R. B., Satvati, B., Fatoye, F. J. J. o.M. i.M., and Biology (2019). Influence of foot insole on the gait performance in subjects with flat foot disorder. *J. Mech. Med. Biol.* 19 (06), 1950050. doi:10.1142/s0219519419500507
- Kaufman, K. R., Brodine, S. K., Shaffer, R. A., Johnson, C. W., and Cullison, T. R. J. T. A. j.o.s.m. (1999). The effect of foot structure and range of motion on musculoskeletal overuse injuries. *Am. J. Sports Med.* 27 (5), 585–593. doi:10.1177/03635465990270050701
- Khorasani, S. G. R., Cham, M. B., Sharifnezhad, A., Saeedi, H., and Farahmand, B. J. C. O. P. (2021). Comparison of the immediate effects of prefabricated soft medical insoles and custom-molded rigid medical insoles on plantar pressure distribution in athletes with flexible flatfoot: a prospective study. *Curr. Orthop. Pract.* 32 (6), 578–583. doi:10.1097/bco.0000000000001053
- Kou, W., Li, X., Yao, H., and Wei, P. J. I. J. o.P. O. (2018). Meta-analysis of the comorbidity rate of allergic rhinitis and asthma in Chinese children. *Int. J. Pediatr. Otorhinolaryngology* 107, 131–134. doi:10.1016/j.ijporl.2018.02.001
- Lee, K. K., Ling, S. K., and Yung, P. S. J. B. m.d. (2019). Controlled trial to compare the Achilles tendon load during running in flatfeet participants using a customized arch support orthoses vs an orthotic heel lift. *BMC Musculoskelet. Disord.* 20, 1–12. doi:10.1186/s12891-019-2898-0
- Lin, K.-W., Hu, C.-J., Yang, W.-W., Chou, L.-W., Wei, S.-H., Chen, C.-S., et al. (2019). “Biomechanical evaluation and strength test of 3D-printed foot orthoses,” in *Applied bionics and biomechanics 2019*.
- Lusardi, M. M., Jorge, M., and Nielsen, C. C. (2012). *Orthotics and prosthetics in rehabilitation*. Oxford, UK: Elsevier Health Sciences.
- Messier, S. P., Pittala, K. A. J. M., and sports, s.i. (1988). Etiologic factors associated with selected running injuries. *Med. Sci. Sports Exerc.* 20 (5), 501–505. and exercise. doi:10.1249/00005768-198810000-00012
- Michaudet, C., Edenfield, K. M., Nicolette, G. W., and Carek, P. J. J. F. e. (2018). Foot and ankle conditions: pes planus. *FP essentials* 465, 18–23.
- Mills, K., Blanch, P., Chapman, A. R., McPoil, T. G., and Vicenzino, B. J. B. j.o.s.m. (2010). Foot orthoses and gait: a systematic review and meta-analysis of literature pertaining to potential mechanisms. *Br. J. Sports Med.* 44 (14), 1035–1046. doi:10.1136/bjism.2009.066977
- Myerson, M. S. J. J. (1996). Instructional course lectures, the American academy of orthopaedic surgeons-adult acquired flatfoot deformity. treatment of dysfunction of the posterior tibial tendon. *J. Bone & Jt. Surg.* 78 (5), 780–792. doi:10.2106/00004623-199605000-00020
- Needleman, R. L. J. F., and international, a. (2005). Current topic review: subtalar arthroereisis for the correction of flexible flatfoot. *Foot ankle Int.* 26 (4), 336–346. doi:10.1177/107110070502600411
- Novacheck, T. F. J. G., and posture (1998). The biomechanics of running. *Gait posture* 7 (1), 77–95. doi:10.1016/s0966-6362(97)00038-6
- Oerlemans, L. N., Peeters, C. M., Munnik-Hagewoud, R., Nijholt, I. M., Witlox, A., and Verheyen, C. C. J. B. M. D. (2023). Foot orthoses for flexible flatfeet in children and adults: a systematic review and meta-analysis of patient-reported outcomes. *BMC Musculoskelet. Disord.* 24 (1), 16. doi:10.1186/s12891-022-06044-8
- Page, M. J., McKenzie, J. E., Bossuyt, P. M., Boutron, I., Hoffmann, T. C., Mulrow, C. D., et al. (2021). The PRISMA 2020 statement: an updated guideline for reporting systematic reviews. *BMJ* 372, n71. doi:10.1136/bmj.n71
- Petrie, K. A., Burbank, K., Sizer, P. S., James, C. R., and Zumwalt, M. (2023). “Considerations of sex differences in musculoskeletal anatomy between males and females,” in *The active female: health issues throughout the lifespan* (Springer), 3–24.
- Redmond, A. C., Landorf, K. B., Keenan, A.-M. J. J. o.F., and Research, A. (2009). Contoured, prefabricated foot orthoses demonstrate comparable mechanical properties to contoured, customised foot orthoses: a plantar pressure study. *J. Foot Ankle Res.* 2, 20–10. doi:10.1186/1757-1146-2-20
- Richter, R. R., Austin, T. M., and Reinking, M. F. J. J. o.a.t. (2011). Foot orthoses in lower limb overuse conditions: a systematic review and meta-analysis—critical appraisal and commentary. *J. Athl. Train.* 46 (1), 103–106. doi:10.4085/1062-6050-46.1.103
- Toullec, E. J. O., Surgery, T., and Research (2015). Adult flatfoot. *Orthop. Traumatol. Surg. Res.* 101 (1), S11–S17. doi:10.1016/j.otsr.2014.07.030
- Van Boerum, D. H., Sangeorzan, B. J. J. F., and clinics, a. (2003). Biomechanics and pathophysiology of flat foot. *Foot ankle Clin.* 8 (3), 419–430. doi:10.1016/s1083-7515(03)00084-6
- Vijayakumar, K., Kumar, S. S. J. I. J. o.P., and Therapy, O. (2017). Prevalence of flexible flatfoot (FFT) and rigid flatfoot (RFT) in relation with tightness of Achilles tendon and weakness of tibialis posterior tendon among the individuals of 40–60 Years of age. *Indian J. Physiother. Occup. Ther.* 11, 210–215. doi:10.5958/0973-5674.2017.00106.x
- Xu, R., Wang, Z., Ren, Z., Ma, T., Jia, Z., Fang, S., et al. (2019). Comparative study of the effects of customized 3D printed insole and prefabricated insole on plantar pressure and comfort in patients with symptomatic flatfoot. *Med. Sci. Monit. Int. Med. J. Exp. Clin. Res.* 25, 3510–3519. doi:10.12659/msm.916975
- Zhai, J., Qiu, Y., and Wang, J. J. J. o.t.A. P. M. A. (2019). Does flexible flatfoot require treatment? plantar pressure effects of wearing over-the-counter insoles when walking on a level surface and up and down stairs in adults with flexible flatfoot. *J. Am. Podiatric Med. Assoc.* 109 (4), 299–304. doi:10.7547/16-103
- Zhou, H., and Ugbole, C. (2024). Biomechanical analysis of lower limbs based on unstable condition sports footwear: a systematic review. *Phys. Act. Health.* 8 (1), 93–104. doi:10.5334/paah.332





## OPEN ACCESS

## EDITED BY

Chi Wu,  
The University of Sydney, Australia

## REVIEWED BY

Jingxiao Zhong,  
Max Planck Institute of Colloids and Interfaces,  
Germany  
Boyang Wan,  
The University of Sydney, Australia

## \*CORRESPONDENCE

Bergita Ganse,  
✉ Bergita.ganse@uks.eu

RECEIVED 19 April 2024

ACCEPTED 01 July 2024

PUBLISHED 23 July 2024

## CITATION

Roland M, Diebels S, Wickert K, Pohlemann T  
and Ganse B (2024), Finite element simulations  
of smart fracture plates capable of cyclic  
shortening and lengthening: which stroke for  
which fracture?  
*Front. Bioeng. Biotechnol.* 12:1420047.  
doi: 10.3389/fbioe.2024.1420047

## COPYRIGHT

© 2024 Roland, Diebels, Wickert, Pohlemann  
and Ganse. This is an open-access article  
distributed under the terms of the [Creative  
Commons Attribution License \(CC BY\)](#). The use,  
distribution or reproduction in other forums is  
permitted, provided the original author(s) and  
the copyright owner(s) are credited and that the  
original publication in this journal is cited, in  
accordance with accepted academic practice.  
No use, distribution or reproduction is  
permitted which does not comply with these  
terms.

# Finite element simulations of smart fracture plates capable of cyclic shortening and lengthening: which stroke for which fracture?

Michael Roland<sup>1</sup>, Stefan Diebels<sup>1</sup>, Kerstin Wickert<sup>1</sup>,  
Tim Pohlemann<sup>2</sup> and Bergita Ganse<sup>2,3\*</sup>

<sup>1</sup>Chair of Applied Mechanics, Saarland University, Saarbrücken, Germany, <sup>2</sup>Department of Trauma, Hand and Reconstructive Surgery, Departments and Institutes of Surgery, Saarland University, Homburg, Germany, <sup>3</sup>Werner Siemens-Endowed Chair for Innovative Implant Development (Fracture Healing), Departments and Institutes of Surgery, Saarland University, Homburg, Germany

**Introduction:** Bone healing can be improved by axial micromovement, as has been shown in animals and human patients with external fixators. In the development of smart fracture plates, the ideal amount of stroke for different fracture types in the different healing stages is currently unknown. It was hypothesized that the resulting strain in the fracture gap of a simple tibial shaft fracture does not vary with the amount of axial stroke in the plate, the fracture gap size, and the fracture angle.

**Methods:** With finite element simulations based on body donation computed tomography data, the second invariant of the deviatoric strain tensor (J2), strain energy density, hydrostatic strain, octahedral shear strain, and percentage of the fracture gap in the “perfect healing window” were computed for different gap sizes (1–3 mm), angles (5°–60°), and plate stroke levels (0.05–0.60 mm) in three healing stages. Multiple linear regression analyses were performed.

**Results:** Findings showed that an active fracture plate should deliver an axial stroke in the range of 0.10–0.45 mm. Different optimal stroke values were found for each healing phase, namely, 0.10–0.25 mm for the first, 0.10 mm for the second, and 0.35–0.45 mm for the third healing phase, depending on the fracture gap size and less on the fracture angle. J2, hydrostatic strain, octahedral shear strain and the strain energy density correlated with the fracture gap size and angle (all  $p < 0.001$ ). The influence of the fracture gap size and angle on the variability (adjusted  $R^2$ ) in several outcome measures in the fracture gap was shown to vary throughout healing. The contribution to the variability of the percentage of the fracture gap in the perfect healing window was greatest during the second healing phase. For J2, strain energy density, hydrostatic strain, and octahedral shear strain, the fracture gap size showed the greatest contribution in the third fracture healing phase, while the influence of fracture angle was independent of the healing phase.

**Discussion:** The present findings are relevant for implant development and to design clinical studies that aim to accelerate fracture healing using axial micromovement.

#### KEYWORDS

fracture healing, bone regeneration, computer simulation, smart implant, active implant, biomechanics, osteosynthesis, digital health

## 1 Introduction

Fracture healing is a physiological process that takes place in stages and involves numerous cellular components (Saul et al., 2023). Healing phases are the acute inflammatory response, recruitment of mesenchymal stem cells, generation of a cartilaginous and a periosteal bony callus, revascularization and neo angiogenesis at the fracture site, and mineralization and resorption of the cartilaginous callus, followed by bone remodeling (Marsell and Einhorn, 2011). The healing process usually requires several weeks to months, and in around 5%–10% of cases, fractures do not heal with the result of a non-union (Zura et al., 2016). Such healing problems are associated with massive socio-economic costs (Rupp et al., 2018; Leliveld et al., 2020). Factors associated with an elevated risk for non-union include open and more severe fractures, a high body mass index, smoking, and alcoholism (Zura et al., 2016). Excessive movement and forces in the fracture may also lead to non-union (Claes et al., 1998; Foster et al., 2021). To decrease costs, to bring patients back to work faster and to shorten immobilization time, it is desirable to reduce the incidence of non-union, as well as to shorten the healing time of bone fractures. In human tibial fractures, daily application of controlled cyclic micro-movement with an axial stroke of 0.5 mm via external fixators reduced the healing time by 21%–23% (Kenwright et al., 1986; Kershaw et al., 1993). In detail, Kenwright et al. (Kenwright et al., 1986) found faster healing by 7.1 weeks (23%, 30.8 weeks healing time without and 23.7 weeks with stimulation, 50 and 32 patients, respectively) and Kershaw et al. (Kershaw et al., 1993) reported a facilitation by 6 weeks (21%, 29 weeks healing time without and 23 weeks with stimulation, 23 and 22 patients, respectively). In addition, a decrease in the incidence of non-union was reported (8 non-union cases without and 2 cases with micro-movement) (Kenwright et al., 1986).

It is known that axial compression is better for fracture stimulation than translational shear or distraction (Augat et al., 2003; Hente et al., 2004; Bishop et al., 2006; Sigurdson et al., 2011). According to findings from animal and human studies, the ideal axial stroke in the fracture gap seems to be around 0.4–0.5 mm, depending on the fracture gap size (Kenwright and Goodship, 1989; Wolf et al., 1998). However, this has not yet been systematically studied *in silico* for different fracture types and healing phases. Changes in the ideal stroke value of an active plate over time have, to the authors' knowledge also never been determined for human bones. Increasing fracture gap sizes are known to delay the healing process (Claes et al., 1998). In addition, the angle of obliquity  $\theta$  of a fracture has significant effects on interfragmentary movement (IFM) and on octahedral shear strain (Miramini et al., 2016). Thus, the fracture gap size and the angle of obliquity might need to be considered when planning active

fracture stimulation with axial micromovement by an implant, and when determining the stroke, the implant needs to deliver. Claes & Heigele (Claes and Heigele, 1999) suggested that intramembranous bone formation occurs when strains smaller than  $\pm 5\%$  and hydrostatic pressures smaller than  $\pm 0.15$  MPa are present in the local tissue. In addition, endochondral ossification was suggested to be associated with compressive pressures larger than  $\pm 0.15$  MPa and strains smaller than  $\pm 15\%$ . Claes & Heigele proposed that all other conditions lead to the formation of connective tissue or fibrous cartilage instead of bone. Their idea of a so-called 'perfect healing window' was based on animal experiments, cell culture studies, and finite element models (Claes et al., 1998). The underlying mechanobiological mechanisms in bone regeneration include stimulation of mechano-sensitive Piezo channels that are involved in activating pathways in osteoblasts under cyclic stretching (Kang et al., 2024). Numerous cellular components, growth fractures and cytokines induce vascularization of the initially hypoxic fracture callus within 2–5 weeks, supporting ossification (Menger et al., 2022a). When forces and movement in the fracture gap are too high, the newly formed bony structures may be destroyed and need to be re-built, which is why excessive strains lead to the formation of connective tissue.

External fixators, as used in the named micro-movement studies, are frames that stabilize the fracture outside the skin and that are attached to screws and/or wires that connect them to the bone (Fernando et al., 2021). Among their disadvantages are a low patient comfort due to the external frame, risks of pin-site infections, and implant breakage or loosening. Ideally, it would be possible to provide the same stimuli through internal implants, similar to the nails and plates currently used as the gold standard in surgical fracture treatment. Furthermore, it would be desirable, if the implant had sensor functions, e.g., for stiffness changes and daily movement time in the fracture gap, and if it could process the data and act autonomously according to the individual current biomechanical needs (Ledet et al., 2018; Windolf et al., 2022). Smart implants with sensing and acting capabilities are currently under development to allow live monitoring of the fracture healing progress, as well as direct mechanical interventions (Ernst et al., 2021; Ganse et al., 2022). Technological advances in material science and systems engineering have recently opened up new opportunities to build smart fracture implants (Ganse et al., 2022). For example, shape memory alloys (SMA), such as Nitinol have the ability to shorten if warmed up, e.g., by an electric current, and it is possible to measure changes in their electrical resistance that correlate with the changes in length (Motzki et al., 2018). SMA wires embedded in a fracture plate or nail would allow the implant to shorten and to change its stiffness. This technology could not only be used to stimulate

bone healing at the fracture site by applying cyclic load, but it could also be applied to vary the implant stiffness during the course of healing, e.g., by moving stiffer and less stiff elements within the implant or by activating SMA wires embedded in composite materials. The right changes in implant stiffness during the healing process are known to enhance healing (Barcik and Epari, 2021; Fu et al., 2023).

As the authors are currently working on the development of an active fracture plate capable of shortening and lengthening, they needed to know which amount of axial stroke the mechanism needs to be able to deliver (Ganse et al., 2022). To be able to generate the optimal resulting cyclic movements in the fracture gap by an active plate, depending on fracture geometry, more or less stroke might be required in the plate. Currently, the amount of plate shortening needed for different fracture types and orientations is unknown. The authors are not aware of any previous papers that determined effects of an active fracture plate on the biomechanical environment in different fracture types. Therefore, the null-hypothesis of the present study was that the resulting strain in the fracture gap of a simple tibial shaft fracture does not vary with the amount of axial stroke in the plate, the fracture gap size, and the fracture angle.

## 2 Materials and methods

Ethical approval was obtained from the IRB of Saarland Medical Board (Aerztchamber des Saarlandes, Germany, application number 146/21). The study is part of the project Smart Implants, funded by the Werner Siemens Foundation. It is registered in the German Clinical Trials Register (DRKS-ID: DRKS00025108).

### 2.1 Model generation

As strain inside a fracture cannot be measured in experiments, it was decided to work with finite-element simulations. The authors have improved and validated their finite element simulations with numerous test stand experiments over the past years (Braun et al., 2021; Orth et al., 2023; Roland et al., 2023; Wickert et al., 2024). The workflow for model generation was divided into four main steps: 1) the bone model generation based on computed tomography data, 2) the design of a virtual twin of an active implant, 3) the generation of different fractures and 4) the assignment of material parameters representing different healing phases.

#### 2.1.1 Bone model

To obtain a realistic bone model, a computed tomography (CT) scan (SOMATOM Definition Edge, Siemens, Erlangen, Germany) of a human cadaveric specimen combined with a six-rod bone density calibration phantom (QRM-BDC/6, QRM GmbH Moehrendorf, Germany) was used. The donor was a female at the age of 74 years with a body height of 152.4 cm (60 in.) and a body weight of 81.65 kg (180 lbs.) without any known bone disease that could have had a lasting negative effect on bone quality. The CT scan was performed with a resolution of 0.541 mm of pixel spacing and 0.60 mm distance between two images, cf. Figure 1 A.

The image stack was segmented with an adaptive threshold procedure with respect to the calibration phantom, supplemented by a morphological close filter with isotropic values and a mask smoothing with a recursive Gaussian filter with anisotropic values. Afterwards, an island-removal, a cavity-fill and a fill-gaps filter with priority order procedure were applied, resulting in a high segmentation quality without detectable problems, cf. Figure 1 B. All image processing steps were performed in the software ScanIP (Synopsys, Mountain View, CA, United States).

In order to provide suitable material parameters in the finite element (FE) models, up to four steps are necessary: the first step is a densitometric relationship defining a mapping to convert raw CT attenuation to bone mineral density (BMD) values with the help of the six-rod calibration phantom. For this purpose, histograms were generated for the individual rods, representing the corresponding grayscale values from the raw CT data, given in Hounsfield units (HU), with respect to their number of voxels. The histogram curves were then smoothed with a robust local regression method in Matlab (Matlab 2021b; MathWorks, USA). Then, the maxima of each regression curve were used as calibration points for a least square fit defining a linear mapping of the CT data in HU to equivalent mineral density values ( $\rho_{eqm}$ ) also often referred to as quantitative CT values. The result of this calibration process is given by the linear mapping:

$$\rho_{eqm} = a \cdot HU + b, \text{ with } a = 7.939e-04 \text{ and } b = 0.014$$

The second step calculates the associated ash density ( $\rho_{ash}$ ) values from the calibrated equivalent mineral density values. For this purpose, the following relationship for hydroxyapatite phantoms was implemented (Eberle et al., 2013):

$$\rho_{ash} = 0.8772 \cdot \rho_{eqm} + (0.0789)$$

The third step is the conversion of the ash density into the apparent density ( $\rho_{app}$ ) which is used in the most relationships computing material parameters. Here, the conversion from (Edwards et al., 2013), originally defined by (Dalstra et al., 1993) was used:

$$\rho_{app} = \rho_{ash} / 0.626$$

The last step is the mapping from the apparent density ( $\rho_{app}$ ) to the Youngs modulus and Poisson ratio. Since most published formulas are only defined for the density range of the cancellous bone (Eberle et al., 2013), the formula of Rho et al. (Rho et al., 1995),

$$E = 6,570 \cdot \rho_{app}^{1.37}$$

with a Poisson ratio of 0.30 was used here. In accordance with (Cattaneo et al., 2001), for the bone 25 different material cards were generated via the described workflow and stored in the FEM model.

#### 2.1.2 Virtual twin of an active implant

Since there is currently no approved implant with active components on the market, a virtual implant of this kind was generated here. This enables the effects of such an implant on fracture healing to be tested by means of simulations and thus to gather initial experience for a later design of the components. To implement this concept, a CAD model of a standard implant

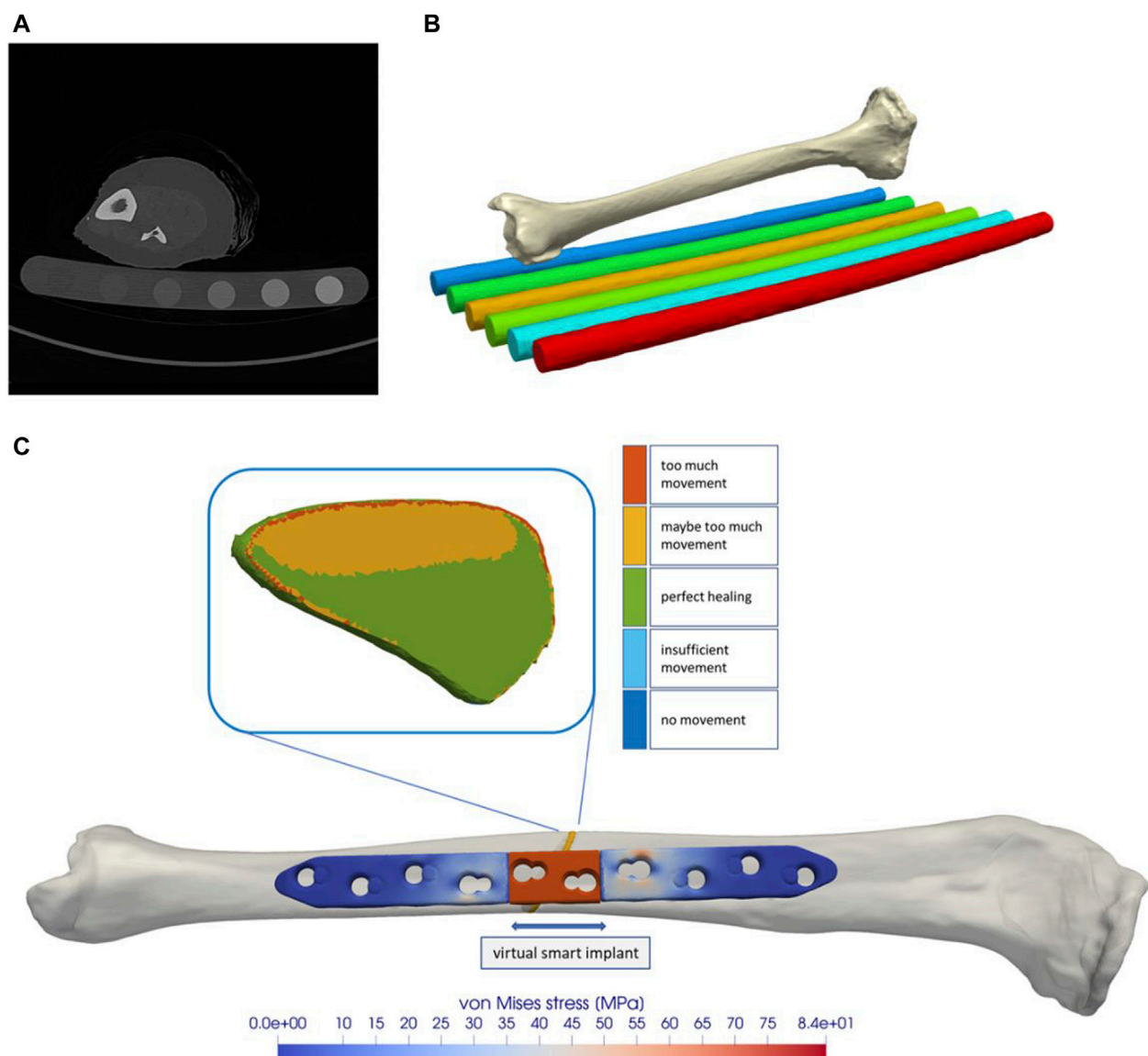


FIGURE 1

The tibial model was generated by processing computed tomography data that were recorded with a phantom for bone density estimation (A,B).

The model of a regular state-of-the-art bone plate was adapted to simulate shortening of the part depicted in red (C). The fracture gap and the healing-window classification are shown as an example.

(LCP locking compression plate) was created and an active element was added in the middle part. Afterwards, the virtual implant in the simulated environment was placed on the bone model by an orthopaedic trauma surgeon analogous to a real application in the software ScanIP using the CAD import module. Six screws, three on each side of the fracture, were additionally integrated into the model, cf. Figure 1 C. The virtual active element is realized in the simulation process by a suitable choice of boundary conditions. Therefore, the predefined stroke is set via Dirichlet boundary conditions on the distal side of the active element and complemented with fixed Dirichlet boundary conditions on the proximal side. Since this work focuses on the strain state of the fracture, we omitted the definition of contact conditions and rigidly connected the individual masks in the simulation. For the simulations, it was

assumed that the active implant is made from the standard material Ti6Al4V, with a Young's modulus of 108,000 MPa and a Poisson's ratio of 0.37.

### 2.1.3 Generation of different fractures

To investigate the influence of an active implant on fracture healing, different fractures were virtually generated and also placed by an orthopaedic trauma surgeon. For this purpose, a STL (stereolithography or standard triangle language) file of the bone surface was generated from the segmented bone model and processed in a free-form software (Geomagic Freeform Plus/Touch X, 3D Systems, Inc.). The freeform software is oriented on clay modelling and offers various analogue tools for editing the 3D objects. Therefore, clay-based modelling was chosen here and the 3D scraper tool was used to create the fractures in the 3D clay object based



on the STL file. The generated fractures were then saved again as independent STL files. They were then loaded into the ScanIP software to the segmented bone models and the CAD-based active implant. Using a surface-to-mask operation on the individual fractures and a subsequent Boolean operation between the masks for bone and fracture, the corresponding 3D models were created for each fracture.

### 2.1.4 Mapping of different healing phases

The FEM simulations were conducted as three separate static simulations and not as a longitudinal process. Three healing states were mapped virtually, as they may require different strokes of the active implant as a suitable mechanical stimulus. Starting from initial connective tissue with the material parameters Young's modulus  $E = 3.0$  MPa and Poisson ratio of 0.4 (Claes et al., 1998), the next class of fracture gap material considered here is fibrous cartilage with a Young's modulus of  $E = 200$  MPa and a Poisson ratio of 0.45 (Simon et al., 2011), and the last considered material is soft callus with Young's modulus of  $E = 1,000.0$  MPa and Poisson ratio of 0.3 (Claes et al., 1998).

### 2.1.5 Generation of the 3D FE meshes

Meshing of the 3D models was also performed in the ScanIP software. For this purpose, the segmented masks were placed in priority order, in ascending sequence from bone to fracture to implant. To increase the resolution of the fracture, an adaptive refinement was selected in all generated models, with the volume meshing parameter 'Coarseness' of  $-10$  for bone and implant and  $-5$  for the fracture area. This resulted in grids with around 1,000,000 mesh cells, whereby the number of mesh cells varied depending on thickness and angle of the fracture mask. Since all simulations were carried out in the simulation environment Abaqus (Dassault Systèmes, Velizy-Villacoublay, France), all meshes were generated using quadratic finite elements (C3D10, ten-node tetrahedral element with four integration points) with respect to the adaptive mesh resolution. At the beginning of the meshing process, two regions of interest (ROI) were marked on the active element of the implant and saved as node sets in the Abaqus input files to be able to apply the boundary conditions in the correct way. For every mesh, the software ScanIP checked the mesh statistic and the segmented masks for errors and all volume mesh generations were successful without detectable problems.

### 2.1.6 Biomechanical simulations

All simulations were performed in Abaqus using a standard workstation computer (Intel(R) Core(TM) i9-9920X CPU @ 3.50GHz, 128GB RAM, 64-Bit Windows 10 Pro) in sequential order in a queue driven by a Python script. The post-processing of the results, stored in Abaqus Odb (output database) files, was realized using Python in-house software. The relevant strain variables, which describe the mechanical stimulus or the interfragmentary movement, were read out for each integration point of the mesh cells of the fracture area and processed for statistical evaluation.

## 2.2 Statistics

The weighted means of the outcome measures described in Table 1 were calculated in the simulations. The perfect healing

window was computed according to the papers of Claes & Heigele (Claes and Heigele, 1999) and Claes et al. (Claes et al., 1998). In the tibial model, transverse fractures with different gap sizes (one to three mm) and simple fractures of different angles ( $5^{\circ}$ – $60^{\circ}$ ) were compared for several levels of plate stroke (0.05–0.60 mm) in three separate healing stages: 1. Initial connective tissue to fibro cartilage, 2. Fibro cartilage to soft callus, and 3. Soft callus to hard callus. All statistical tests were executed with IBM SPSS Statistics version 29 (IBM SPSS Statistics, Armonk, NY, United States). Significance was defined as  $p < 0.05$ . Normality tests were conducted using the Kolmogorov-Smirnov and Shapiro-Wilk tests. Multiple linear regression analyses were performed with forced entry for each of the named outcome measures as the dependent variable. Forced entry was chosen, as the number of independent variables is low and all variables have an explainable influence (Kucuk et al., 2016). The relationships of each of these parameters with the fracture gap size or angle, and the stroke of the plate as independent variables were explored. Two models were computed for each parameter, one for fracture gap size, and one for fracture angle. The reason why they could not be entered in the same model is that these are two separate data sets. The adjusted  $R^2$  for each dependent variable delivered by the multiple linear regression analysis indicates the percentage of the variability explained by the independent variables.

## 3 Results

All data were normally distributed. All multiple linear regression models were significant, which means they could be used.

### 3.1 Perfect healing window

Figure 2 shows the proportion of the fracture gap in the perfect healing window in relation to the fracture angle and the axial stroke performed by the implant. Based on the perfect healing window-data, the best axial plate-movement values for each fracture size (distance between bone ends) and healing phase are shown in Table 2. The ideal axial plate-movement values for different angles in oblique fractures are shown in Table 3. Findings indicate that an active fracture plate should deliver an axial stroke in the range of 0.1–0.45 mm to be able to cover the tested fracture types (Tables 2; 3; Figure 2 to 4). In addition, the highest adjusted  $R^2$ -values that indicate the percentage of the variability explained by fracture gap size and angle were found in the second healing phase (Tables 4; 5).

### 3.2 Fracture gap size

The fracture gap size affected all parameters in all healing phases (all  $p < 0.001$ ), except for octahedral shear strain in the third healing phase, and percent of fracture gap in the 'perfect healing window' in the first healing phase (Table 4). Figure 3 shows the relation of the outcome measures with the axial stroke of the plate and the fracture gap size (thickness of the fracture gap) for each healing phase. The smaller the fracture gap, the larger was the effect on the outcome measures. Results of the multiple linear regression analysis are



TABLE 1 Outcome measures in the fracture gap computed with finite element simulations.

Outcome measure	Description	Unit
J2	The second invariant of the deviatoric strain tensor, usually labelled J2, was identified as key quantity to describe the influence of strain on fracture healing (Garcia et al., 2003; Doblaré et al., 2004). It reflects the interplay of local volume change and local shape distortion. This was experimentally underpinned in the work of Bishop and colleagues (Bishop et al., 2003)	-
Strain energy density (SED)	In general, the strain energy density is a measure of how much energy a material can store and release when it is deformed. In the modelling of fracture healing and even more for bone remodelling, SED is often interpreted as a form of stimulus that causes adaptations (Weinans et al., 1992)	N/mm2
Hydrostatic strain (HS)	Hydrostatic strain is the average of the three normal strains of any strain tensor and contributes to the volume change (Ghiasi et al., 2017)	-
Octahedral shear strain (OSS)	The maximum shear strain in any plane for a 3D state of strain. OSS, derived from the deviatoric part, contributes to shape distortion (Ghiasi et al., 2017)	-
Percentage of fracture gap in the 'perfect healing window'	Percentage of elements in the fracture gap with a deformation state corresponding to the mechanical stimulus identified as promoting healing (Claes and Heigele, 1999; Shefelbine et al., 2005), as used in (Braun et al., 2021; Orth et al., 2023)	Percent

shown in Table 4. The highest adjusted  $R^2$ -values that indicate the percentage of the variability of J2, SED, HS, and OSS explained by fracture gap size and plate stroke were found in the last healing stage (Table 4). However, this was different for the percentage of the fracture gap in the perfect healing window, where  $R^2$  for fracture gap size and plate stroke was highest in the second healing phase.

3.3 Fracture angle

The fracture angle affected all parameters in all healing phases ( $p < 0.001$ ), except for the percentage of the fracture gap in the 'perfect healing window', that did not correlate with the fracture angle in the first two healing phases (Table 5). Figure 4 shows the relation of the outcome measures with the axial stroke of the plate and the fracture angle for each healing phase. For J2 and octahedral shear strain, a greater fracture angle led to a greater effect, while for SED and HS, the opposite was found (Figure 4). The adjusted  $R^2$ -values for fracture angle and plate stroke were equally distributed throughout healing phases for J2, SED, HS, and OSS, while the adjusted  $R^2$  for the percentage of the fracture in the perfect healing window was highest in the second healing phase (Table 5).

3.4 Healing phases

The ideal axial stroke in the plate was 0.10–0.25 mm for the first, 0.10 mm for the second, and 0.35–0.45 mm for the third healing phase when considering the finding of both analyses combined (Tables 2, 3). For each of the computed parameters, Figures 2–4 show differences in the scales on the Y-axes, which reflects changes in the local mechanical properties with fracture healing. The influence of fracture gap size and plate stroke on the adjusted  $R^2$  for J2, SED, HS, and OSS was greatest in the last healing phase, while fracture angle and plate stroke did not show a peak at any healing phase (Tables 4, 5). For the percentage of the fracture in the perfect healing window, adjusted  $R^2$  was greatest in the second healing phase for both fracture gap size and fracture angle.

4 Discussion

The present study showed that an active fracture plate should be able to deliver an axial stroke in the range of 0.10–0.45 mm to cover the tested fracture types. Different optimal stroke values are required for each healing phase, namely, 0.10–0.25 mm for the first, 0.10 mm for the second, and 0.35–0.45 mm for the third healing phase, depending on the fracture gap size (distance between bone ends), but less dependent of the fracture angle. The computed strain values and the strain energy density correlated with the fracture gap size and angle. In detail, analyses revealed that both fracture gap size and fracture angle had the greatest contribution to the variability of the percentage of the fracture gap in the perfect healing window during the second healing phase. For the other biomechanical parameters, the fracture gap size showed the greatest contribution in the third fracture healing phase, and the influence of fracture angle was independent of the healing phase. Based on the presented findings, the null-hypothesis that the resulting strain in the fracture gap of a simple tibial shaft fracture does not vary with the amount of axial stroke in the plate, the fracture gap size, and the fracture angle, was rejected.

It has long been known that the biomechanical requirements for rapid fracture healing vary with the stage of healing (Wolf et al., 1981). The dimensions of movement in the present study are in the range of experimental findings from Kenwright & Goodship (Kenwright and Goodship, 1989), who showed that 0.5 mm of axial micromovement was better than 2 mm. The present study would recommend 0.25 mm for the first, 0.15 mm for the second, and 0.45 mm for the third phase for a 3-mm transverse fracture gap. This is the first time that the required movement has been calculated to such detail. The present paper therefore opens up and demonstrates the methodology and which data such calculations can provide. It also showcases the non-linearity and complexities of determining the ideal stroke of an active plate. While the present simulations only covered the fracture angle and fracture gap type, this could in the future be expanded to more complex fracture types, such as wedge fractures, where the rotation of the wedge will likely play a major role. An increasing fracture gap size also leads to a longer duration of the healing process, which is another factor that may be addressed in future simulations (Claes et al., 1998). Comminuted fractures (several

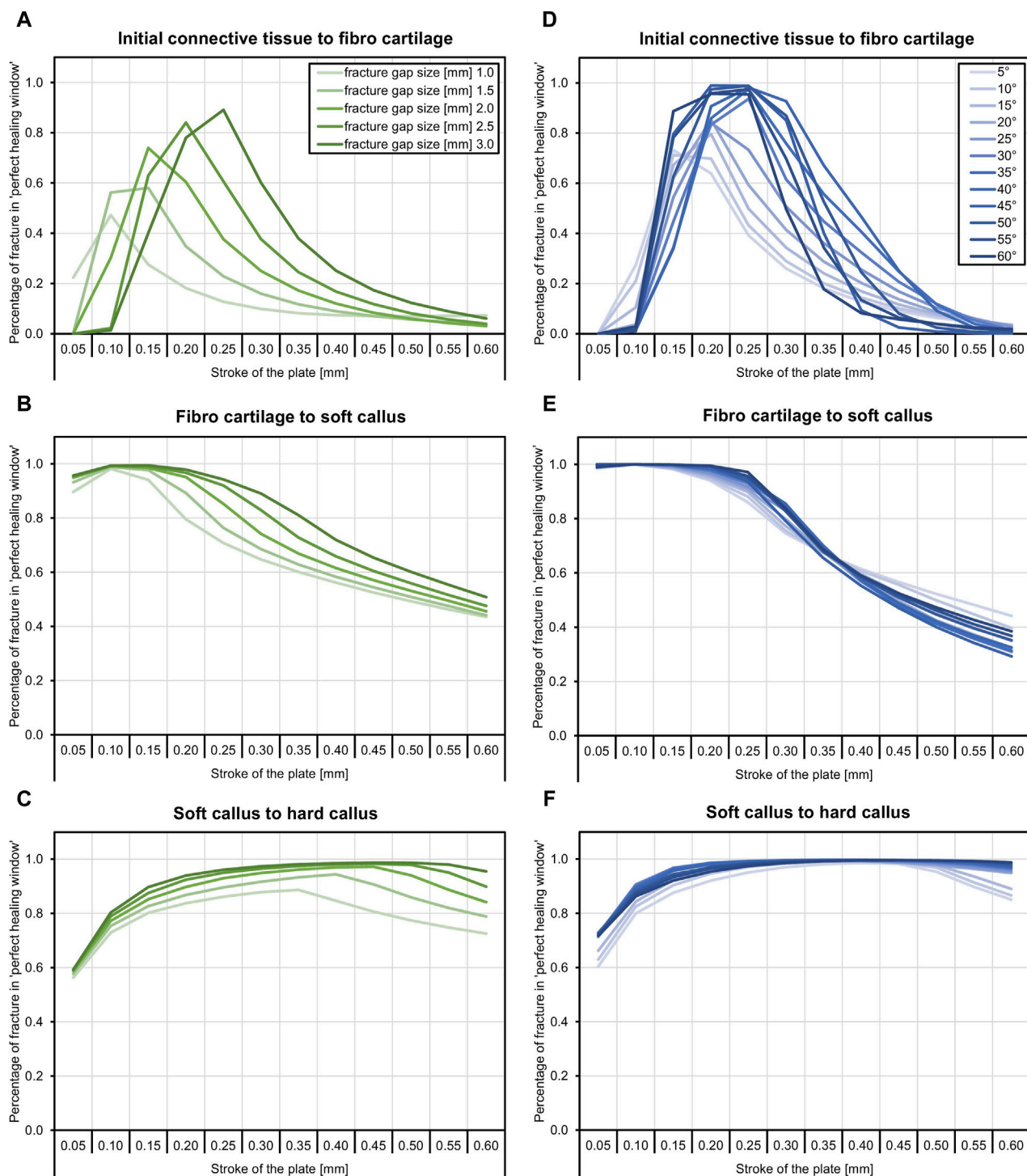


FIGURE 2

The proportion of the fracture gap in the perfect healing window depends on the fracture gap size, fracture angle, the axial stroke of the active implant, and the healing stage. The plate stroke and angle leading to the highest proportion of the fracture gap in the perfect healing window depends on the fracture gap size or fracture angle and healing stage. (A) In the early fracture healing phase, results indicate that, depending on the fracture gap size, an axial plate stroke of around 0.1 mm–0.25 mm is ideal (see Table 2). This is around 10% of the fracture gap size. (B) In the fibro cartilage to soft callus-phase, the ideal stroke is between 0.1 mm and 0.15 mm for all fracture gap sizes. (C) In the late healing phase, the ideal stroke increases with the fracture gap size and is between 0.35 mm and 0.45 mm. (D) With fracture obliquity, in the initial healing phase, the ideal stroke increases with pronounced maxima between 0.15 mm and 0.25 mm. (E) The second healing phase shows only small differences between fracture angles and very low ideal stroke values of 0.05 mm and 0.1 mm, while ideal values increase to 0.3 mm–0.45 mm in the last healing phase (F).

TABLE 2 Axial plate-movement values that delivered the highest percentage of the fracture gap in the ‘perfect healing window’ in mm for each fracture size (distance between bone ends) and healing phase, based on the perfect healing window-data. Results shown are for transverse tibial shaft fractures. See Figure 2 for visualization.

Healing phase	Fracture gap size [mm]					Range
	1.0	1.5	2.0	2.5	3.0	
Initial connective tissue to fibro cartilage	0.10	0.15	0.15	0.20	0.25	0.10–0.25
Fibro cartilage to soft callus	0.10	0.10	0.10	0.10	0.15	0.10–0.15
Soft callus to hard callus	0.35	0.40	0.45	0.45	0.45	0.35–0.45

TABLE 3 Axial plate-movement values that delivered the highest percentage of the fracture gap in the ‘perfect healing window’ in mm for each fracture angle (degree the fracture is tilted) and healing phase, based on the perfect healing window-data. Data shown are for oblique tibial shaft fractures with a 2-mm fracture gap size. See Figure 2 for visualization.

Healing phase	Fracture angle [degrees]												Range
	5°	10°	15°	20°	25°	30°	35°	40°	45°	50°	55°	60°	
Initial connective tissue to fibro cartilage	0.15	0.15	0.20	0.20	0.20	0.25	0.25	0.25	0.20	0.25	0.25	0.25	0.15–0.25
Fibro cartilage to soft callus	0.10	0.10	0.10	0.05	0.10	0.10	0.10	0.10	0.05	0.10	0.10	0.10	0.05–0.10
Soft callus to hard callus	0.40	0.40	0.40	0.30	0.35	0.35	0.40	0.40	0.45	0.45	0.45	0.45	0.30–0.45

fracture gaps and bone fragments) will be able to tolerate relatively greater motion since the strain is applied over a larger surface area of fracture fragments (Glatt et al., 2017). Shear movement is known to have negative effects on fracture healing (Augat et al., 2003), but while this was considered in the present simulations, results still indicated that the fracture angle did not matter as much as the fracture gap size. The fracture angle could have affected other biomechanical variables, such as shear stress and contact pressure, but at least shear stress does not seem to have influenced the findings to a larger degree. The present results also indicate that the influence of the fracture gap size and angle on the variability in several biomechanical parameters in the fracture gap varies throughout healing. This was previously known and recently increasingly considered, but not yet to this extent (Barcik and Epari, 2021).

The tibial load during movement and gait is influenced by anthropometric parameters such as age, body height, body weight, and hand grip strength, and has an influence on the fracture gap mechanics (Wolff et al., 2023; Wickert et al., 2024). Moreover, muscle contractions (Yang et al., 2015) and behavioral aspects influence the load, such as whether a patient adheres to the partial weight bearing instructions (Ganse et al., 2016), and by how much and how the person moves in daily life (Warmerdam et al., 2023; Warmerdam et al., 2024). In intact bone, the *in-vivo* deformation of the proximal in relation to the distal tibia in terms of bending and torsion during walking and running in humans amounts to up to 0.38°–0.90° of medial bending, 0.15°–1.30° of posterior bending, and 0.67°–1.66° of external torsion (Yang et al., 2014). It is therefore crucial to provide sufficient stiffness by the active implant when the patient walks to shield the fracture gap from excess movement and strain. In addition, the fracture callus stiffens throughout healing, which needs to be considered (Seide et al., 2012; Barcik and Epari, 2021). Therefore, fracture plates with adjustable stiffness have been suggested and introduced (Epari et al., 2021; Ganse et al., 2022). It is, however, due to play unlikely that such an implant will be able to stop all movement in the fracture gap when the patient walks. Thus, it seems of interest to measure the actual movement in the

fracture, i.e., indirectly by measuring bending and strain in the fracture plate (Hente et al., 2003; Wickert et al., 2024). When combined with electronics, the patient could then be warned of the excess load, and in a control loop, the implant stiffness could, at least to a certain degree, be adapted. Such warning systems have already been studied using instrumented insoles, but to date, the authors are not aware of any fracture implant with this capability (Abbott et al., 2019; Zhang et al., 2023). Moreover, the axial micromovement would only be needed, if these loads did not already exceed the strain and stimulation time considered optimal for healing. Fracture healing seems to underlie a circadian rhythm and requires daily stimulation, as well as sufficient recovery times of unloading (Barcik and Epari, 2021; Windolf et al., 2022). It also requires stimulation immediately after the injury to gain the best healing results (Barcik et al., 2023). Therefore, it seems desirable to combine sensing and acting capabilities in a smart implant for fracture healing.

The motivation for the present study was the need to know the amount of axial stroke an active implant would need to provide, as the authors required this information for their implant design and construction process. For computer simulations, the suitability and validity of simulation results are often questioned. In this case, however, test stand or animal experiments were not an option, as they would not have been able to provide the needed information that is true for human patients *in-vivo*. Among computer simulation methods, finite element simulations and rigid body assumptions are currently the gold standard for implant development (Mühling et al., 2021). When selecting the outcome measures, the authors sought to cover a variety of aspects that are known to matter in fracture healing. Future *in silico* studies may consider further implant-related factors, such as stress shielding, or soft tissue mechanics including the pull of muscles. In addition, instead of simulating separate healing phases, with more computing power, continuous simulations over the entire healing period may be beneficial. These could include loading data from real patients.

**TABLE 4** Findings from the multiple linear regression analysis for fracture gap size. Adjusted  $R^2$  values are shown for each dependent variable, and indicate the percentage of the variability explained by the independent variables. As an example, 59.4% of the variability of J2 in the first healing phase is explained by the fracture gap size and the stroke of the plate.  $p$ -values, non-standardized and standardized (Beta) coefficients of the computed parameters are listed for each parameter and healing phase, if significant. Healing phases: 1 = Initial connective tissue to fibro cartilage, 2 = Fibro cartilage to soft callus, 3 = Soft callus to hard callus.

Parameter	Healing phase	Adjusted $R^2$	Fracture gap size	Stroke of plate
J2	1	0.594	<0.001, 0.654, 0.443	<0.001, -6.601, -0.641
	2	0.751	<0.001, 0.048, 0.361	<0.001, -0.734, -0.793
	3	0.817	<0.001, 0.004, 0.307	<0.001, -0.069, -0.854
SED	1	0.680	<0.001, -0.020, -0.460	<0.001, 0.213, 0.692
	2	0.848	<0.001, -0.043, -0.330	<0.001, 0.795, 0.863
	3	0.925	<0.001, -0.011, -0.157	<0.001, 0.457, 0.950
HS	1	0.893	<0.001, 0.007, 0.449	<0.001, -0.088, -0.834
	2	0.952	<0.001, 0.000, 0.329	<0.001, -0.009, -0.919
	3	0.986	<0.001, 0.000, 0.180	<0.001, -0.004, -0.977
OSS	1	0.942	<0.001, -0.017, -0.316	<0.001, 0.344, 0.919
	2	0.996	<0.001, -0.001, -0.087	<0.001, 0.097, 0.994
	3	1.000	0.450	<0.001, 0.031, 1.000
Percent of fracture gap in the 'perfect healing window'	1	0.206	0.054	<0.001, -0.578, -0.425
	2	0.933	<0.001, 0.036, 0.226	<0.001, -1.055, -0.940
	3	0.368	<0.001, 0.037, 0.397	<0.001, 0.314, 0.481

**TABLE 5** Findings from the multiple linear regression analysis for fracture angle. Adjusted  $R^2$  values are shown for each dependent variable, and indicate the percentage of the variability explained by the independent variables. As an example, 89.6% of the variability of J2 in the first healing phase is explained by the fracture angle and the stroke of the plate.  $p$ -values, non-standardized and standardized (Beta) coefficients of the computed parameters are listed for each parameter and healing phase, if significant. Healing phases: 1 = Initial connective tissue to fibro cartilage, 2 = Fibro cartilage to soft callus, 3 = Soft callus to hard callus.

Parameter	Healing phase	Adjusted $R^2$	Fracture angle	Stroke of plate
J2	1	0.896	<0.001, -0.011, -0.217	<0.001, -4.871, -0.922
	2	0.933	<0.001, -0.001, -0.137	<0.001, -0.538, -0.957
	3	0.929	<0.001, -0.000, -0.152	<0.001, -0.061, -0.952
SED	1	0.908	<0.001, 0.000, -0.231	<0.001, 0.113, 0.925
	2	0.905	<0.001, -0.002, -0.249	<0.001, 0.569, 0.919
	3	0.908	<0.001, -0.001, -0.238	<0.001, 0.344, 0.924
HS	1	0.897	<0.001, 0.000, 0.585	<0.001, -0.046, -0.746
	2	0.889	<0.001, 0.000, 0.563	<0.001, -0.005, -0.757
	3	0.824	<0.001, 0.000, 0.644	<0.001, -0.002, -0.641
OSS	1	0.990	<0.001, 0.001, 0.157	<0.001, 0.399, 0.982
	2	0.994	<0.001, 0.000, 0.126	<0.001, 0.122, 0.989
	3	0.992	<0.001, 0.000, 0.143	<0.001, 0.040, 0.986
Percent of fracture gap in the 'perfect healing window'	1	0.120	0.165	<0.001, -0.664, -0.346
	2	0.938	0.677	<0.001, -1.393, -0.969
	3	0.344	0.026, 0.001, 0.153	<0.001, 0.282, 0.575

Once an active fracture plate has made it to the market, large-scale randomized clinical trials should be conducted systematically to determine the ideal stimulation setting (frequency, stroke, time) for

each fracture type and fracture size. Apart from the parameters considered in the present study, findings may also differ with, i.e., patient age and sex (Tang et al., 2022). Since diseases such as

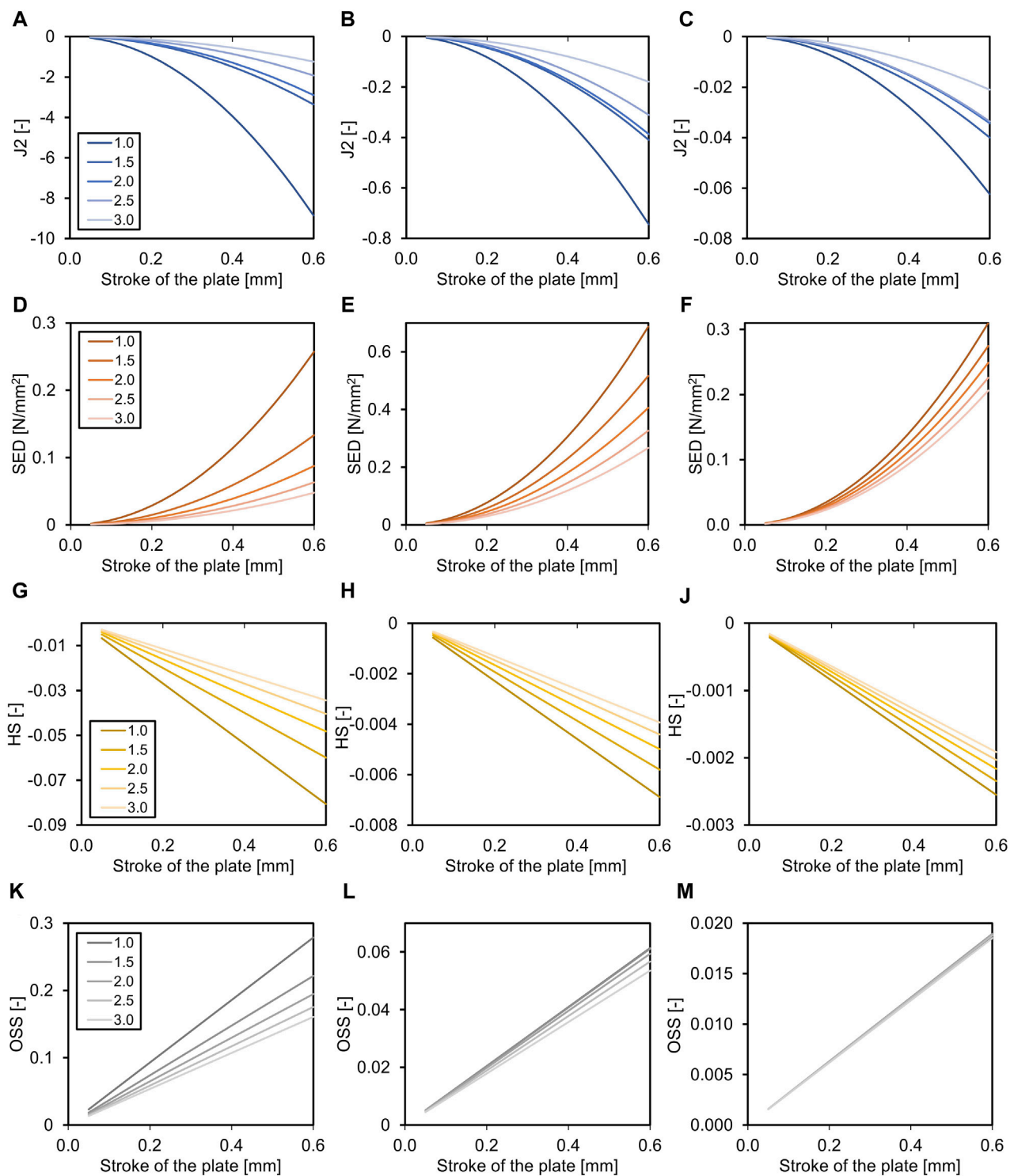


FIGURE 3

Effects of the fracture gap size (for transverse fracture, legend shows mm fracture gap) on the required axial stroke in the plate. Relation of the mean J2 (A–C), the mean strain energy density (SED, D–F), the hydrostatic strain (HS, G–I), and the octahedral shear strain (OSS, K–M) with the axial stroke of the plate and the fracture gap size (distance between bone ends). While the relation is non-linear for J2 and SED, it is linear for HS and OSS. Data are shown for the three analyzed phases of fracture healing separate, initial connective tissue to fibro cartilage (A,D,G,K), fibro cartilage to soft callus (B,E,H,L), and soft callus to hard callus (C,F,I,M). Note the different dimensions on the Y-axes throughout healing.

diabetes and osteoporosis are known to delay fracture healing (Nikolaou et al., 2009), it would be desirable to adjust the stimulation pattern individually, and to find ways to assess the fracture healing phases based

on measurements. Such studies would require a multi-centre setup and a large number of patients to accommodate for the many different options when varying the settings. The findings of the present study



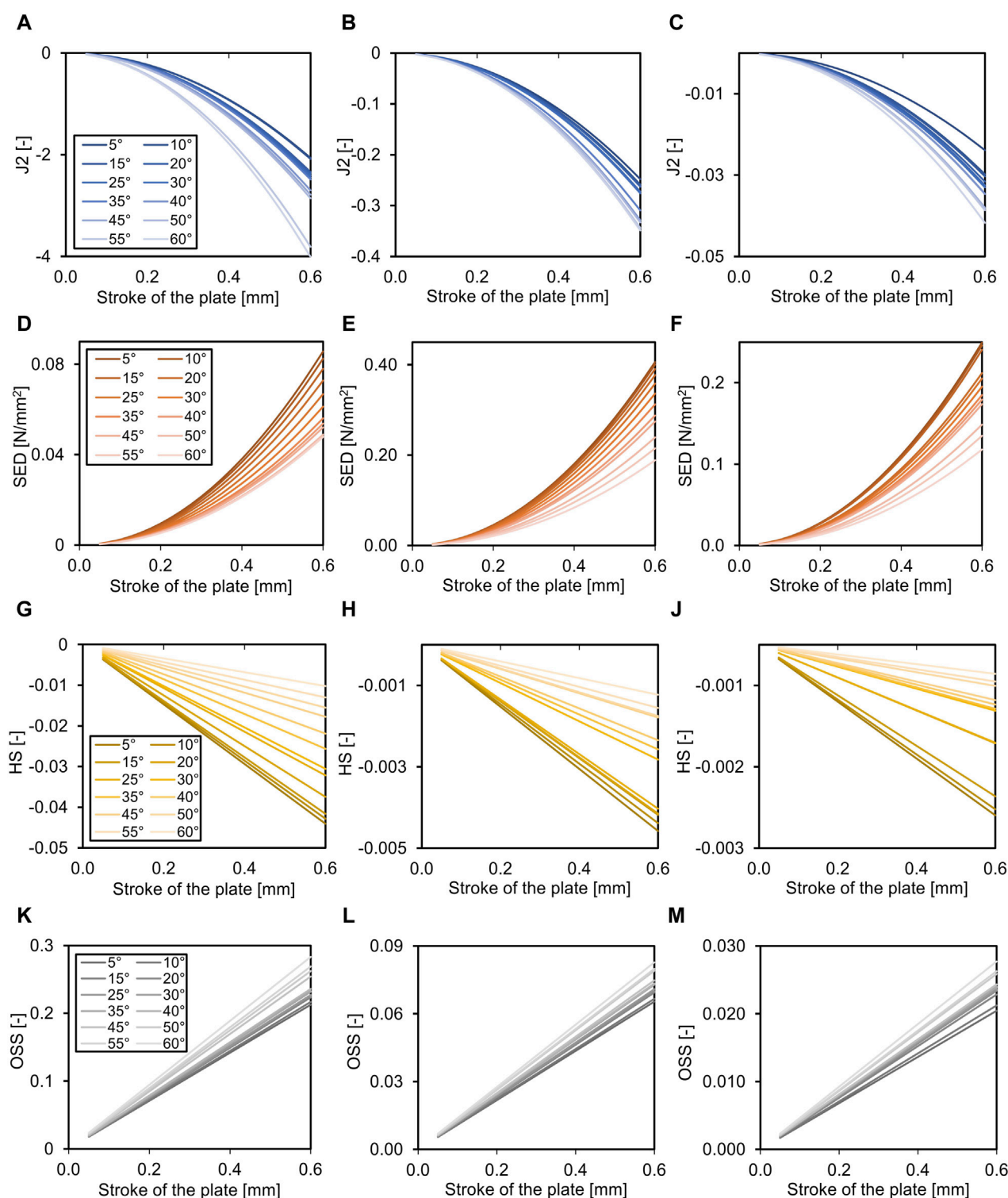


FIGURE 4

Effects of the fracture angle (for oblique fracture, legend shows degrees fracture angle) on the required axial stroke in the plate. Relation of the mean J2 (A–C), the mean strain energy density (SED, D–F), the hydrostatic strain (HS, G–I), and the octahedral shear strain (OSS, K–M) with the axial stroke of the plate and the fracture angle. While the relation is non-linear for J2 and SED, it is linear for HS and OSS. Data are shown for the three analyzed phases of fracture healing separate, initial connective tissue to fibro cartilage (A,D,G,K), fibro cartilage to soft callus (B, E, H, L), and soft callus to hard callus (C, F, J, M). Note the different dimensions on the Y-axes throughout healing.

then may serve as a first indication of what to look at. This study also showed that the demand for the amount of axial stroke in the implant and also the contribution of the movement to the variability in

biomechanical parameters in the fracture gap changes throughout healing. This should be taken into account when planning the interventions for such studies.

Limitations of this study were as follows: The assumption of three healing stages instead of a continuous, longitudinal simulation is certainly a simplification. However, since the present study already generated 768 simulation results with approximately 1.47 TB of data volume and required a long computing time, longitudinal simulations were not realistic at this level of detail with the simulation methods and hardware used. The concept of the ‘perfect healing window’ invented by Lutz Claes (Claes et al., 1998; Claes and Heigele, 1999) was chosen for the present study, but it is also a simplification of a more complex process. Only one bone of one patient was used to generate the model in this study, while running the simulations on a diverse set of many bones may have delivered a better view on the applicability to the overall population, making results more generalizable. The general rules described in the present findings are likely to be transferrable, while details in the actual stroke values may differ and show variation among patients, fractures and implants. The presented findings are likely only valid for the tibial diaphysis and may differ considerably for other bones, and the metaphyseal and epiphyseal regions. Limitations are also generally present in *in silico* studies that never fully represent the complexities of the real world, and therefore, experiments in animals and humans are required to confirm the findings. One limitation of our *in silico* study is the choice of an isotropic material model instead of an anisotropic model for the bone. However, this is a common simplification in literature due to computing time and the very few published works on anisotropic models (Knowles et al., 2016). A second simplification made in our *in silico* study is the rigid connection between the bone and screws instead of defining contact conditions. This approach is justified because it significantly reduces the computational complexity and time required for the simulations.

Another aspect of *in silico* studies based on FEA results is the question of validation. This is particularly challenging in our case because, on the one hand, the active implant exists only virtually, making experimental verification and validation impossible. On the other hand, the study relies on the bone of a donor, which was scanned via CT and then used for experiments in a different study, so the bone was no longer available at the time of this *in silico* study. Despite these challenges, an initial study (Wickert et al., 2024) has been published that compares the simulation workflow used here with experiments conducted on a testing device. This device applies the forces that occur during a forward step on a bone-implant system, providing an initial validation of the simulation process.

## 5 Conclusion

Based on finite element simulations, recommendations for the axial stroke of an active fracture plate were given for each healing phase, fracture size and angle. Results showed that an active fracture plate should deliver an axial stroke in the range of 0.10–0.45 mm. Different optimal stroke values were found for each healing phase, namely, 0.10–0.25 mm for the first, 0.10 mm for the second, and 0.35–0.45 mm for the third healing phase, depending on the fracture gap size and less on the fracture angle. The influence of the fracture gap size and angle on the variability in several outcome measures in the fracture gap was shown to vary throughout healing. The present findings may be useful for the development of smart fracture implants and to design clinical studies that will be needed to confirm the optimal settings for clinical use.

## Data availability statement

The datasets generated and analyzed for this study are available from the authors upon reasonable request. The raw data supporting the conclusions of this article will be made available by the authors, without undue reservation.

## Ethics statement

The studies involving humans were approved by Saarland Medical Board (Ärzttekammer der Saarlandes). The studies were conducted in accordance with the local legislation and institutional requirements. The participants provided their written informed consent to participate in this study.

## Author contributions

MR: Conceptualization, Data curation, Formal Analysis, Methodology, Writing–original draft, Writing–review and editing. SD: Funding acquisition, Writing–review and editing. KW: Data curation, Methodology, Writing–review and editing. TP: Funding acquisition, Writing–review and editing. BG: Conceptualization, Formal Analysis, Investigation, Project administration, Visualization, Writing–original draft, Writing–review and editing.

## Funding

The author(s) declare that financial support was received for the research, authorship, and/or publication of this article. This work was supported by the Werner Siemens Foundation [Smart Implants 2.0]. The funding source was not involved in the study design; in the collection, analysis and interpretation of data; in the writing of the report; or in the decision to submit the article for publication.

## Conflict of interest

TP is president and board member of the AO Foundation, Switzerland, and extended board member of the German Society of Orthopaedic Trauma Surgery (DGU), the German Society of Orthopaedic Surgery and Traumatology (DGOU), and the German Society of Surgery (DGCH). TP is also the speaker of the medical advisory board of the German Ministry of Defence.

The remaining authors declare that the research was conducted in the absence of any commercial or financial relationships that could be construed as a potential conflict of interest.

## Publisher’s note

All claims expressed in this article are solely those of the authors and do not necessarily represent those of their affiliated organizations, or those of the publisher, the editors and the reviewers. Any product that may be evaluated in this article, or claim that may be made by its manufacturer, is not guaranteed or endorsed by the publisher.

## References

- Abbott, C. A., Chatwin, K. E., Foden, P., Hasan, A. N., Sange, C., Rajbhandari, S. M., et al. (2019). Innovative intelligent insole system reduces diabetic foot ulcer recurrence at plantar sites: a prospective, randomised, proof-of-concept study. *Lancet Digit. Health* 1 (6), e308–e318. doi:10.1016/S2589-7500(19)30128-1
- Augat, P., Burger, J., Schorlemmer, S., Henke, T., Peraus, M., and Claes, L. (2003). Shear movement at the fracture site delays healing in a diaphyseal fracture model. *J. Orthop. Res.* 21 (6), 1011–1017. doi:10.1016/S0736-0266(03)00098-6
- Barcik, J., and Epari, D. R. (2021). Can optimizing the mechanical environment deliver a clinically significant reduction in fracture healing time? *Biomedicine* 9 (6), 691. doi:10.3390/biomedicine9060691
- Barcik, J., Ernst, M., Buchholz, T., Constant, C., Mys, K., Epari, D. R., et al. (2023). The absence of immediate stimulation delays bone healing. *Bone* 175, 116834. doi:10.1016/j.bone.2023.116834
- Bishop, N. E., Tami, I., Schneider, E., and Ito, K. (2003). *In vivo* comparison of early fracture healing under deviatoric and volumetric deformations. *Acta Bioeng. Biomech.* 4, 754–755.
- Bishop, N. E., van Rhijn, M., Tami, I., Corveleijn, R., Schneider, E., and Ito, K. (2006). Shear does not necessarily inhibit bone healing. *Clin. Orthop. Relat. Res.* 443, 307–314. doi:10.1097/01.blo.0000191272.34786.09
- Braun, B. J., Orth, M., Diebels, S., Wickert, K., Andres, A., Gawlitza, J., et al. (2021). Individualized determination of the mechanical fracture environment after tibial exchange nailing-A simulation-based feasibility study. *Front. Surg.* 8, 749209. doi:10.3389/fsurg.2021.749209
- Cattaneo, P. M., Dalstra, M., and Frich, L. H. (2001). A three-dimensional finite element model from computed tomography data: a semi-automated method. *Proc. Inst. Mech. Eng. H* 215 (2), 203–212. doi:10.1243/0954411011533760
- Claes, L. E., and Heigele, C. A. (1999). Magnitudes of local stress and strain along bony surfaces predict the course and type of fracture healing. *J. Biomech.* 32 (3), 255–266. doi:10.1016/S0021-9290(98)00153-5
- Claes, L. E., Heigele, C. A., Neidlinger-Wilke, C., Kaspar, D., Seidl, W., Margevicius, K. J., et al. (1998). Effects of mechanical factors on the fracture healing process. *Clin. Orthop. Relat. Res.* 355 (Suppl. 1), S132–S147. doi:10.1097/00003086-199810001-00015
- Dalstra, M., Huiskes, R., Odgaard, A., and van Erning, L. (1993). Mechanical and textural properties of pelvic trabecular bone. *J. Biomech.* 26 (4–5), 523–535. doi:10.1016/0021-9290(93)90014-6
- Doblaré, M., García, J. M., and Gómez, M. J. (2004). Modelling bone tissue fracture and healing: a review. *Eng. Fract. Mech.* 71 (13–14), 1809–1840. doi:10.1016/j.engfracmech.2003.08.003
- Eberle, S., Göttinger, M., and Augat, P. (2013). An investigation to determine if a single validated density-elasticity relationship can be used for subject specific finite element analyses of human long bones. *Med. Eng. Phys.* 35 (7), 875–883. doi:10.1016/j.medengphys.2012.08.022
- Edwards, W. B., Schnitzler, T. J., and Troy, K. L. (2013). Torsional stiffness and strength of the proximal tibia are better predicted by finite element models than DXA or QCT. *J. Biomech.* 46 (10), 1655–1662. doi:10.1016/j.jbiomech.2013.04.016
- Epari, D. R., Gurgun, R., Hofmann-Fliri, L., Schwyn, R., Schuetz, M., and Windolf, M. (2021). Biphasic plating improves the mechanical performance of locked plating for distal femur fractures. *J. Biomech.* 115, 110192. doi:10.1016/j.jbiomech.2020.110192
- Ernst, M., Richards, R. G., and Windolf, M. (2021). Smart implants in fracture care - only buzzword or real opportunity? *Injury* 52 (Suppl. 2), S101–S105. doi:10.1016/j.injury.2020.09.026
- Fernando, P. L. N., Abeygunawardane, A., Wijesinghe, P., Dharmaratne, P., and Silva, P. (2021). An engineering review of external fixators. *Med. Eng. Phys.* 98, 91–103. doi:10.1016/j.medengphys.2021.11.002
- Foster, A. L., Moriarty, T. F., Zalavras, C., Morgenstern, M., Jaiprakash, A., Crawford, R., et al. (2021). The influence of biomechanical stability on bone healing and fracture-related infection: the legacy of Stephan Perren. *Injury* 52 (1), 43–52. doi:10.1016/j.injury.2020.06.044
- Fu, R., Liu, Y., Song, F., Fu, J., Du, T., Liu, Y., et al. (2023). Effects of dynamization timing and degree on bone healing of different fracture types. *J. Orthop. Res.* 41 (11), 2394–2404. doi:10.1002/jor.25583
- Ganse, B., Orth, M., Roland, M., Diebels, S., Motzki, P., Seelecke, S., et al. (2022). Concepts and clinical aspects of active implants for the treatment of bone fractures. *Acta Biomater.* 146, 1–9. doi:10.1016/j.actbio.2022.05.001
- Ganse, B., Yang, P. F., Gardlo, J., Gauger, P., Kriechbaumer, A., Pape, H. C., et al. (2016). Partial weight bearing of the tibia. *Injury* 47 (8), 1777–1782. doi:10.1016/j.injury.2016.06.003
- García, J. M., Kuiper, J. H., Doblaré, M., and Richardson, J. B. (2003). A numerical model to study the mechanical influences on bone fracture healing. *Acta Bioeng. Biomech.* 4, 394–395.
- Ghiassi, M. S., Chen, J., Vaziri, A., Rodriguez, E. K., and Nazarian, A. (2017). Bone fracture healing in mechanobiological modeling: a review of principles and methods. *Bone Rep.* 6, 87–100. doi:10.1016/j.bonr.2017.03.002
- Glatt, V., Evans, C. H., and Tetsworth, K. (2017). A concert between biology and biomechanics: the influence of the mechanical environment on bone healing. *Front. Physiol.* 7, 678. doi:10.3389/fphys.2016.00678
- Hente, R., Cordey, J., and Perren, S. M. (2003). *In vivo* measurement of bending stiffness in fracture healing. *Biomed. Eng. Online* 2, 8. doi:10.1186/1475-925X-2-8
- Hente, R., Füchtmeier, B., Schlegel, U., Ernstberger, A., and Perren, S. M. (2004). The influence of cyclic compression and distraction on the healing of experimental tibial fractures. *J. Orthop. Res.* 22 (4), 709–715. doi:10.1016/j.jorthres.2003.11.007
- Kang, T., Yang, Z., Zhou, M., Lan, Y., Hong, Y., Gong, X., et al. (2024). The role of the Piezo1 channel in osteoblasts under cyclic stretching: a study on osteogenic and osteoclast factors. *Arch. Oral Biol.* 163, 105963. doi:10.1016/j.archoralbio.2024.105963
- Kenwright, J., and Goodship, A. E. (1989). Controlled mechanical stimulation in the treatment of tibial fractures. *Clin. Orthop. Relat. Res.* 241, 36–47. doi:10.1097/00003086-198904000-00006
- Kenwright, J., Richardson, J. B., Goodship, A. E., Evans, M., Kelly, D. J., Spriggins, A. J., et al. (1986). Effect of controlled axial micromovement on healing of tibial fractures. *Lancet* 2, 1185–1187. doi:10.1016/S0140-6736(86)92196-3
- Kershaw, C. J., Cunningham, J. L., and Kenwright, J. (1993). Tibial external fixation, weight bearing, and fracture movement. *Clin. Orthop. Relat. Res.* 293, 28–36. doi:10.1097/00003086-199308000-00005
- Knowles, N. K., Reeves, J. M., and Ferreira, L. M. (2016). Quantitative Computed Tomography (QCT) derived Bone Mineral Density (BMD) in finite element studies: a review of the literature. *J. Exp. Orthop.* 3 (1), 36. doi:10.1186/s40634-016-0072-2
- Kucuk, U., Kucuk, H. O., Eyuboglu, M., and Dogan, M. (2016). eComment. The importance of choosing a proper predictor variable selection method in logistic regression analyses. *Interact. Cardiovasc. Thorac. Surg.* 22 (3), 258. doi:10.1093/icvts/ivv403
- Ledet, E. H., Liddle, B., Kradinova, K., and Harper, S. (2018). Smart implants in orthopedic surgery, improving patient outcomes: a review. *Innov. Entrep. Health* 5, 41–51. doi:10.2147/IEH.S133518
- Leliveld, M. S., Polinder, S., Panneman, M. J., Verhofstad, M. H., and van Lieshout, E. M. (2020). Health care and productivity costs for isolated tibia shaft fracture admissions in The Netherlands. *Acta Orthop. Belg* 86 (2), 320–326.
- Marsell, R., and Einhorn, T. A. (2011). The biology of fracture healing. *Injury* 42 (6), 551–555. doi:10.1016/j.injury.2011.03.031
- Menger, M. M., Körbel, C., Bauer, D., Bleimehl, M., Tobias, A. L., Braun, B. J., et al. (2022a). Photoacoustic imaging for the study of oxygen saturation and total hemoglobin in bone healing and non-union formation. *Photoacoustics* 28, 100409. doi:10.1016/j.pacs.2022.100409
- Miramini, S., Zhang, L., Richardson, M., Mendis, P., and Ebeling, P. R. (2016). Influence of fracture geometry on bone healing under locking plate fixations: a comparison between oblique and transverse tibial fractures. *Med. Eng. Phys.* 38 (10), 1100–1108. doi:10.1016/j.medengphys.2016.07.007
- Motzki, P., Gorges, T., Kappel, M., Schmidt, M., Rizzello, G., and Seelecke, S. (2018). High-speed and high-efficiency shape memory alloy actuation. *Smart Mater. Struct.* 27, 075047. doi:10.1088/1361-665X/aac9e1
- Mühling, M., Winkler, M., and Augat, P. (2021). Prediction of interfragmentary movement in fracture fixation constructs using a combination of finite element modeling and rigid body assumptions. *Comput. Methods Biomech. Biomed. Engin* 24 (15), 1752–1760. doi:10.1080/10255842.2021.1919883
- Nikolaou, V. S., Efstathiopoulos, N., Kontakis, G., Kanakaris, N. K., and Giannoudis, P. V. (2009). The influence of osteoporosis in femoral fracture healing time. *Injury* 40 (6), 663–668. doi:10.1016/j.injury.2008.10.035
- Orth, M., Ganse, B., Andres, A., Wickert, K., Warmerdam, E., Müller, M., et al. (2023). Simulation-based prediction of bone healing and treatment recommendations for lower leg fractures: effects of motion, weight-bearing and fibular mechanics. *Front. Bioeng. Biotechnol.* 11, 1067845. doi:10.3389/fbioe.2023.1067845
- Rho, J. Y., Hobatho, M. C., and Ashman, R. B. (1995). Relations of mechanical properties to density and CT numbers in human bone. *Med. Eng. Phys.* 17 (5), 347–355. doi:10.1016/1350-4533(95)97314-F
- Roland, M., Diebels, S., Orth, M., Pohlemann, T., Bouillon, B., and Tjardes, T. (2023). Reappraisal of clinical trauma trials: the critical impact of anthropometric parameters on fracture gap micro-mechanics-observations from a simulation-based study. *Sci. Rep.* 13, 20450. doi:10.1038/s41598-023-47910-2
- Rupp, M., Biehle, C., Budak, M., Thormann, U., Heiss, C., and Alt, V. (2018). Diaphyseal long bone nonunions - types, aetiology, economics, and treatment recommendations. *Int. Orthop.* 42 (2), 247–258. doi:10.1007/s00264-017-3734-5
- Saul, D., Menger, M. M., Ehnert, S., Nüssler, A. K., Histing, T., and Laschke, M. W. (2023). Bone healing gone wrong: pathological fracture healing and non-unions-overview of basic and clinical aspects and systematic review of risk factors. *Bioeng. (Basel)* 10 (1), 85. doi:10.3390/bioengineering10010085
- Seide, K., Aljudaibi, M., Weinrich, N., Kowald, B., Jürgens, C., Müller, J., et al. (2012). Telemetric assessment of bone healing with an instrumented internal fixator: a

- preliminary study. *J. Bone Jt. Surg. Br.* 94 (3), 398–404. doi:10.1302/0301-620X.94B3.27550
- Shelfelbine, S. J., Augat, P., Claes, L., and Simon, U. (2005). Trabecular bone fracture healing simulation with finite element analysis and fuzzy logic. *J. Biomech.* 38 (12), 2440–2450. doi:10.1016/j.jbiomech.2004.10.019
- Sigurdson, U., Reikeras, O., and Utvag, S. E. (2011). The influence of compression on the healing of experimental tibial fractures. *Injury* 42 (10), 1152–1156. doi:10.1016/j.injury.2010.08.018
- Simon, U., Augat, P., Utz, M., and Claes, L. (2011). A numerical model of the fracture healing process that describes tissue development and revascularisation. *Comput. Methods Biomech. Biomed. Engin* 14, 79–93. doi:10.1080/10255842.2010.499865
- Tang, C. Q. Y., Chiow, S. M., Lai, S. H. S., and Chia, D. S. Y. (2022). The effect of hand dominance, age, gender, fracture comminution and ASA status on time to fracture healing following surgical fixation of distal radius fractures. *J. Hand Surg. Asian Pac* 27 (3), 459–465. doi:10.1142/S2424835522500461
- Warmerdam, E., Orth, M., Pohlemann, T., and Gansse, B. (2023). Gait analysis to monitor fracture healing of the lower leg. *Bioeng. (Basel)* 10 (2), 255. doi:10.3390/bioengineering10020255
- Warmerdam, E., Wolff, C., Orth, M., Pohlemann, T., and Gansse, B. (2024). Long-term continuous instrumented insole-based gait analyses in daily life have advantages over longitudinal gait analyses in the lab to monitor healing of tibial fractures. *Front. Bioeng. Biotechnol.* 12, 1355254. doi:10.3389/fbioe.2024.1355254
- Weinans, H., Huiskes, R., and Grootenboer, H. J. (1992). The behavior of adaptive bone-remodeling simulation models. *J. Biomech.* 25 (12), 1425–1441. doi:10.1016/0021-9290(92)90056-7
- Wickert, K., Roland, M., Andres, A., Diebels, S., Gansse, B., Kerner, D., et al. (2024). Experimental and virtual testing of bone-implant systems equipped with the AO Fracture Monitor with regard to interfragmentary movement. *Front. Bioeng. Biotech.* 12, 1370837. doi:10.3389/fbioe.2024.1370837
- Windolf, M., Varjas, V., Gehweiler, D., Schwyn, R., Arens, D., Constant, C., et al. (2022). Continuous implant load monitoring to assess bone healing status-evidence from animal testing. *Med. Kaunas* 58 (7), 858. doi:10.3390/medicina58070858
- Wolf, J. W. Jr, White, A. A. 3rd, Panjabi, M. M., and Southwick, W. O. (1981). Comparison of cyclic loading versus constant compression in the treatment of long-bone fractures in rabbits. *J. Bone Jt. Surg. Am.* 63 (5), 805–810. doi:10.2106/00004623-198163050-00016
- Wolff, S., Janousek, A., Pfeil, J., Veith, W., Haas, F., Duda, G., et al. (1998). The effects of external mechanical stimulation on the healing of diaphyseal osteotomies fixed by flexible external fixation. *Clin. Biomech. Bristol, Avon.* 13 (4-5), 359–364. doi:10.1016/s0268-0033(98)00097-7
- Wolff, C., Steinheimer, P., Warmerdam, E., Dahmen, T., Slusallek, P., Schlinkmann, C., et al. (2023). Effects of age, body height, body weight, body mass index and handgrip strength on the trajectory of the plantar pressure stance-phase curve of the gait cycle. *Front. Bioeng. Biotechnol.* 11, 1110099. doi:10.3389/fbioe.2023.1110099
- Yang, P. F., Kriebbaumer, A., Albracht, K., Sanno, M., Gansse, B., Koy, T., et al. (2015). On the relationship between tibia torsional deformation and regional muscle contractions in habitual human exercises *in vivo*. *J. Biomech.* 48 (3), 456–464. doi:10.1016/j.jbiomech.2014.12.031
- Yang, P. F., Sanno, M., Gansse, B., Koy, T., Brüggemann, G. P., Müller, L., et al. (2014). Torsion and antero-posterior bending in the *in-vivo* human tibia loading regimes during walking and running. *PLOS ONE* 9 (4), e94525. doi:10.1371/journal.pone.0094525
- Zhang, Z., Dai, Y., Xu, Z., Grimaldi, N., Wang, J., Zhao, M., et al. (2023). Insole systems for disease diagnosis and rehabilitation: a review. *Biosens. (Basel)* 13 (8), 833. doi:10.3390/bios13080833
- Zura, R., Xiong, Z., Einhorn, T., Watson, J. T., Ostrum, R. F., Prayson, M. J., et al. (2016). Epidemiology of fracture nonunion in 18 human bones. *JAMA Surg.* 151, e162775. doi:10.1001/jamasurg.2016.2775





## OPEN ACCESS

## EDITED BY

Zhiyong Li,  
Queensland University of Technology, Australia

## REVIEWED BY

Shaobai Wang,  
Shanghai University of Sport, China  
Peimin Yu,  
Ningbo University, China

## \*CORRESPONDENCE

Fei Chang,  
✉ changfei@jlu.edu.cn  
Zhihui Qian,  
✉ zhqian@jlu.edu.cn

<sup>†</sup>These authors have contributed equally to this work and share first authorship

RECEIVED 30 May 2024

ACCEPTED 22 July 2024

PUBLISHED 06 August 2024

## CITATION

Ruan Y, Wang S, Zhang N, Jiang Z, Mei N, Li P, Ren L, Qian Z and Chang F (2024), *In vivo* analysis of ankle joint kinematics and ligament deformation of chronic ankle instability patients during level walking. *Front. Bioeng. Biotechnol.* 12:1441005. doi: 10.3389/fbioe.2024.1441005

## COPYRIGHT

© 2024 Ruan, Wang, Zhang, Jiang, Mei, Li, Ren, Qian and Chang. This is an open-access article distributed under the terms of the [Creative Commons Attribution License \(CC BY\)](#). The use, distribution or reproduction in other forums is permitted, provided the original author(s) and the copyright owner(s) are credited and that the original publication in this journal is cited, in accordance with accepted academic practice. No use, distribution or reproduction is permitted which does not comply with these terms.

# *In vivo* analysis of ankle joint kinematics and ligament deformation of chronic ankle instability patients during level walking

Yaokuan Ruan<sup>1†</sup>, Shengli Wang<sup>2†</sup>, Nan Zhang<sup>3</sup>, Zhende Jiang<sup>1</sup>, Nan Mei<sup>4,5</sup>, Pu Li<sup>5</sup>, Lei Ren<sup>2</sup>, Zhihui Qian<sup>2\*</sup> and Fei Chang<sup>1\*</sup>

<sup>1</sup>Department of Orthopedics, The Second Hospital of Jilin University, Changchun, China, <sup>2</sup>Key Laboratory of Bionic Engineering (Ministry of Education, China), Jilin University, Changchun, China, <sup>3</sup>Department of Radiology, The Second Hospital of Jilin University, Changchun, China, <sup>4</sup>Orthopaedic Surgeon Department of Orthopaedic Surgery, Nara Medical University, Nara, Japan, <sup>5</sup>Health Technology College, Jilin Sport University, Changchun, China

**Introduction:** Chronic ankle instability (CAI) carries a high risk of progression to talar osteochondral lesions and post-traumatic osteoarthritis. It has been clinically hypothesized the progression is associated with abnormal joint motion and ligament elongation, but there is a lack of scientific evidence.

**Methods:** A total of 12 patients with CAI were assessed during level walking with the use of dynamic biplane radiography (DBR) which can reproduce the *in vivo* positions of each bone. We evaluated the uninjured and CAI side of the tibiotalar and subtalar joint for three-dimensional kinematics differences. Elongation of the anterior talofibular ligament (ATFL), calcaneofibular ligament (CFL), and posterior talofibular ligament (PTFL) were also calculated bilaterally.

**Results:** For patients with CAI, the dorsiflexion of the tibiotalar joint had reduced ( $21.73^\circ \pm 3.90^\circ$  to  $17.21^\circ \pm 4.35^\circ$ ), displacement of the talus increased ( $2.54 \pm 0.64$  mm to  $3.12 \pm 0.55$  mm), and the inversion of subtalar joint increased ( $8.09^\circ \pm 2.21^\circ$  to  $11.80^\circ \pm 3.41^\circ$ ). Mean ATFL elongation was inversely related to mean dorsiflexion angle (CAI:  $\rho = -0.82$ ,  $P < 0.001$ ; Control:  $\rho = -0.92$ ,  $P < 0.001$ ), mean ATFL elongation was related to mean anterior translation (CAI:  $\rho = 0.82$ ,  $P < 0.001$ ; Control:  $\rho = 0.92$ ,  $P < 0.001$ ), mean CFL elongation was related to mean dorsiflexion angle (CAI:  $\rho = 0.84$ ,  $P < 0.001$ ; Control:  $\rho = 0.70$ ,  $P < 0.001$ ), and mean CFL elongation was inversely related to mean anterior translation (CAI:  $\rho = -0.83$ ,  $P < 0.001$ ; Control:  $\rho = -0.71$ ,  $P < 0.001$ ). Furthermore, ATFL elongation was significantly (CAI:  $\rho = -0.82$ ,  $P < 0.001$ ; Control:  $\rho = -0.78$ ,  $P < 0.001$ ) inversely correlated with CFL elongation.

**Discussion:** Patients with CAI have significant changes in joint kinematics relative to the contralateral side. Throughout the stance phase of walking, ATFL increases in length during plantarflexion and talar anterior translation whereas the elongation trend of CFL was the opposite. This understanding can inform the development of targeted therapeutic exercises aimed at balancing ligament tension during different phases of gait. The interrelationship between two ligaments is that when one ligament shortens, the other lengthens. The



occurrence of CAI didn't change this trend. Surgeons might consider positioning the ankle in a neutral sagittal plane to ensure optimal outcomes during ATFL and CFL repair.

#### KEYWORDS

chronic ankle instability, lateral ligament, kinematics, biomechanics, ligament elongation, dynamic biplane radiography

## 1 Introduction

Ankle sprains are one of the most common injuries in sports and daily life (Soboroff et al., 1984). Up to 40% of patients who suffer from lateral ankle sprains develop long-term symptoms, such as frequent sensations of ankle instability and recurring sprains (Fong et al., 2007; Yu et al., 2023). These lingering symptoms are often referred to as chronic ankle instability (CAI) (Freeman, 1965; van Rijn et al., 2008). Clinical findings suggest that there is a correlation between CAI and degenerative changes in the ankle joint, which may increase the incidence of osteochondral lesions of the talus as well as osteoarthritis of the ankle joint (Deleu et al., 2021; Lalevée et al., 2023; Mousavi et al., 2023). Many researchers believe that abnormal joint motion and elongation of ligaments are significant factors contributing to the progression of osteoarthritis in patients with CAI (Caputo et al., 2009; Deleu et al., 2021; Ye et al., 2021).

Current research suggests that patients with CAI exhibit different kinematic outcomes compared to healthy persons, such as increased plantarflexion and inversion of the ankle joint (Balasukumaran et al., 2020a; Herb C. and Shank K., 2023; Mousavi et al., 2023). These changes in kinematics result in the ankle being positioned in a more open state, which decreases the mechanical stability of the joint and increases the risk of recurrent sprains (De Ridder et al., 2013; Li et al., 2019; Yu et al., 2024). To gain a deeper understanding of the phenomenon, numerous studies have utilized motion capture systems to reveal the kinematic differences between the ankle joints of patients with CAI and those of healthy individuals (Monaghan et al., 2006; Piming et al., 2023). However, this method considers the ankle joint as a whole and is unable to distinguish between the tibiotalar and subtalar joints (Wu et al., 2002; Lenz et al., 2020). Analyzing the tibiotalar and subtalar joints separately will help understand the kinematic changes within the patient's joints and lead to a deeper understanding of the disease.

Kinematic changes also affect ligament deformation (Agostinone et al., 2021). In particular, the lateral collateral ligament, including the anterior talofibular ligament (ATFL), calcaneofibular ligament (CFL), and posterior talofibular ligament (PTFL), which are often injured clinically (Yu et al., 2022). Many researchers have employed methods such as cadaveric experiments or simulation analysis to study the impact of lateral collateral ligament injury on joint stability and the deformation of the ATFL, CFL, and PTFL (Nigg et al., 1990; Zhang et al., 2014; Chang et al., 2021; Boey et al., 2022). These studies qualitatively explored the correlation between joint motion and ligament elongation. However, there is limited *in vivo* data describing how the ligament functions to stabilize the ankle joint during dynamic loading activities. A more thorough

comprehension of the *in vivo* role of ligaments in patients with CAI is necessary to enhance current treatment strategies and rehabilitation programs.

As a method of directly tracking the position of the skeleton, dynamic biplane radiography (DBR) overcomes the limitations of previous methods. The accuracy of DBR in measuring kinematics has been confirmed, with documented discrepancies of less than 1 mm and less than 1° (Wang et al., 2015; Kessler et al., 2019). Combined with MRI data, the DBR enables *in vivo* assessment of ligament deformation during dynamic activities (Englander et al., 2019; Chiba et al., 2021). A recent study used the DBR to analyze the ankle's kinematics in seven key poses during the stance phase and obtained similar results (Cao et al., 2019). However, using fewer key poses may make it difficult to accurately represent the complete dynamic cycle of joint kinematics.

This study aimed to analyze the impact of CAI on tibiotalar and subtalar joint motion and determine ligament elongation during the stance phase of walking by DBR. The correlation between the elongation of the lateral collateral ligament and kinematics was examined during walking, as well as the correlation between the elongation of the ligaments. We hypothesize that patients with CAI will exhibit altered joint kinematics and ligament elongation patterns compared to healthy controls, which may contribute to the observed instability and increased injury risk. The results may deepen the understanding of the dynamic changes in ankle kinematics and ligament deformation for patients with CAI, and therefore supply inspiration for the corresponding clinical practice.

## 2 Materials and methods

### 2.1 Subject recruitment

This research was granted approval by the Ethics Committee of our hospital, and informed consent was obtained from all participants. The data were obtained from a convenience sample of 12 patients selected, with an average age (and standard deviation) of  $35.4 \pm 13.0$  years and an average body mass index of  $23.9 \pm 3.1$  kg/m<sup>2</sup>. The demographic characteristics of the recruited subjects are detailed in [Supplementary Material \(Supplementary Table S1\)](#).

The inclusion criteria for CAI patients were as follows: (1) an initial ankle sprain occurring more than 12 months prior; (2) recurrent ankle sprain (at least two sprains in the same ankle), episodes of giving way (more than twice in the recent 3 months); (3) positive results on the talar tilt test and anterior drawer test; (4) MRI reveals the presence of ATFL injury with or without PTFL and CFL injury; (5) Foot and Ankle Outcome Score (FAOS): <75% in 3 or

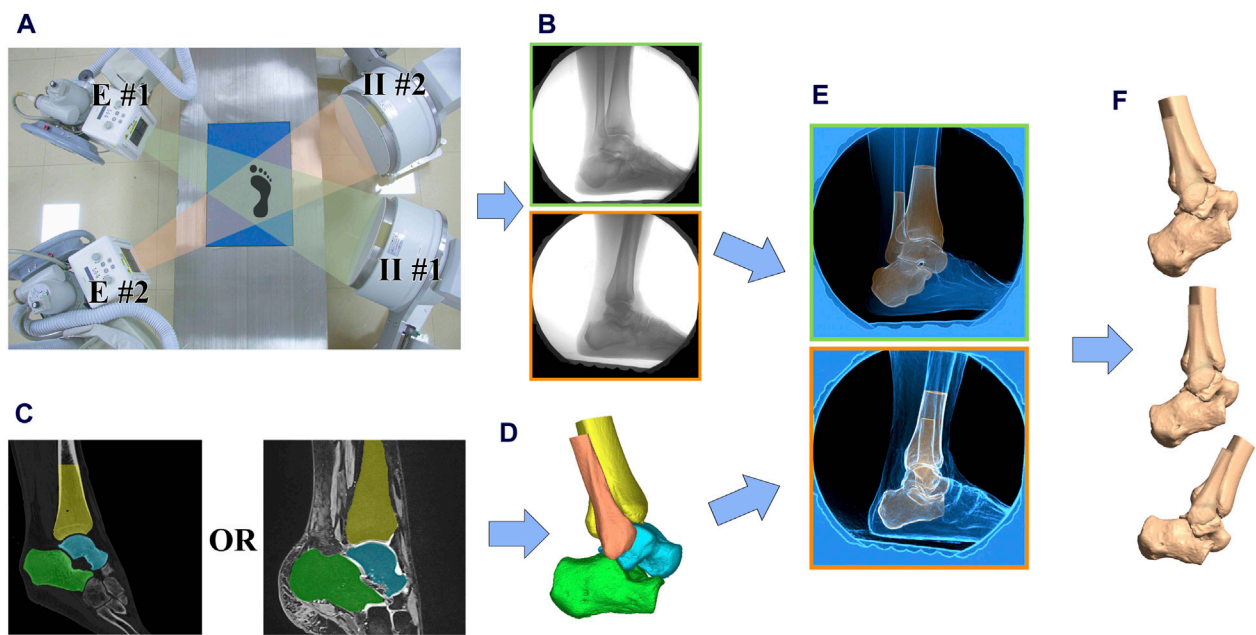


FIGURE 1

Data collection and processing workflow. (A) The image intensifiers (II #1 and II #2) processed images created by x-rays from the emitters (E #1 and E #2); (B) Participants performed 3–5 trials of walking at a self-selected pace within the biplane radiographic imaging system which collected at 120 Hz; (C) CT or 3D MR scans were collected and used to create subject-specific 3D bone models; (D) 3D model of the ankle joint with ligament origins and endpoints labeled; (E) 3D bone models were matched to the biplane radiographs using a validated process; (F) Relative translations, rotations and ligament elongation were calculated.

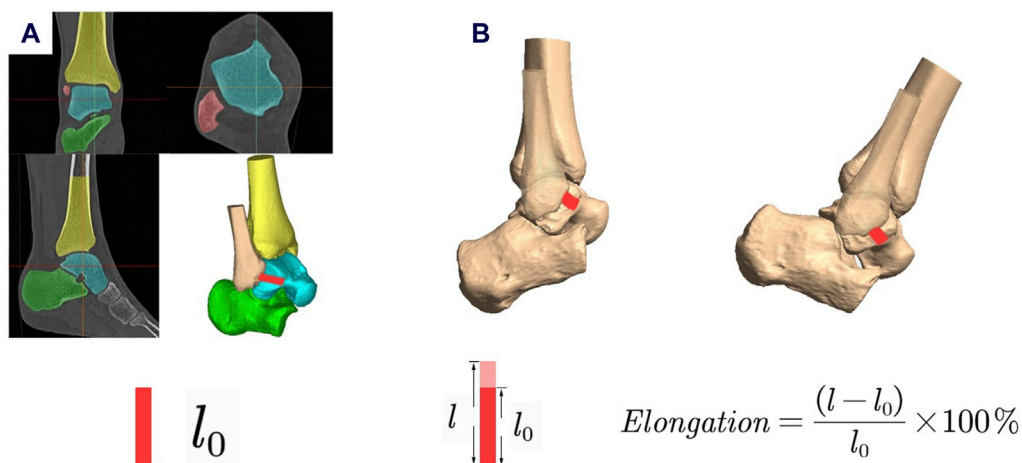


FIGURE 2

Measurement of ligament elongation. (A)  $l_0$  was determined as the length of the ligaments calculated from the MRI in its relaxed state during the MR scan; (B) Ligament elongation was calculated using the formula.

more categories. Exclusion criteria in the study were: (1) fractures and surgical history of the hindfoot; (2) patients who had suffered acute trauma in either lower extremity within the past 1 month or had experienced a sprain less than 1 month prior; (3) those diagnosed with osteoarthritis in either lower extremity, or other medical conditions that could impact normal gait; (4) patients with poor balance, or at risk of falling when walking on the raised laboratory walkway.

## 2.2 DBR motion capture

A previously employed DBR system (Imaging Systems and Service Inc., United States) was utilized to measure the kinematics of the tibiotalar and subtalar joints (Wang et al., 2023). Participants walked at a self-selected speed on a raised laboratory walkway. Three valid trials were recorded for each ankle (Figure 1A).

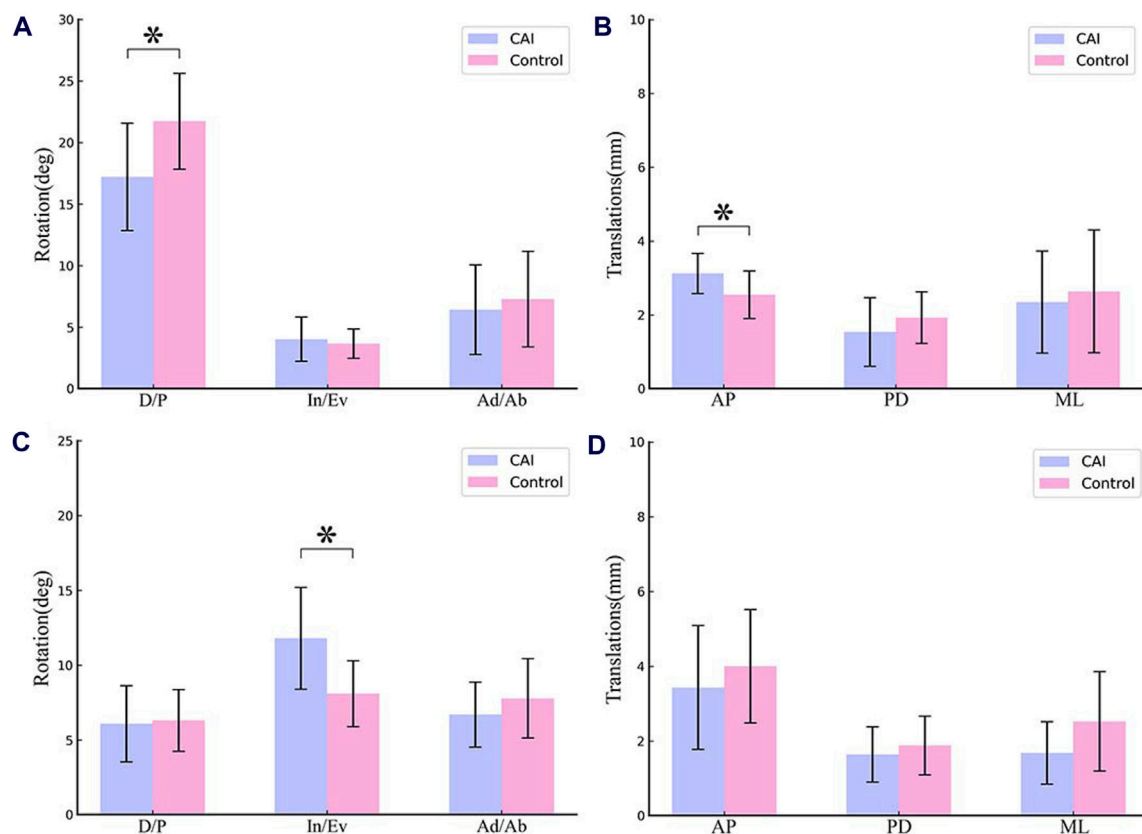


FIGURE 3

Mean RoM of the tibiotalar joint and subtalar joint during the stance phase of walking. (A) Rotation of tibiotalar joint; (B) Translation of tibiotalar joint; (C) Rotation of subtalar joint; (D) Translation of subtalar joint. (D/P, Dorsiflexion/Plantarflexion; In/Ev, Inversion/Eversion; Ad/Ab, Adduction/Abduction; AP, Anterior/Posterior; PD, Proximal/Distal; ML, Medial/Lateral).

Biplane radiographs of the ankle were obtained for a duration of 1–2 s in order to capture the stance phase at a rate of 120 frames/s (imaging parameters: 54–56 kV, 80–100 mA, 0.9 ms pulse width) (Figure 1B).

## 2.3 Imaging data and model-based markerless tracking

Quantification of *in vivo* joint kinematics from DBR images requires three-dimensional (3D) reconstruction data for each bone. In order to reduce the radiation exposure of the patients, a 3 T magnetic resonance imaging (MRI) scanner (Prisma, Siemens Medical, Solutions United States) was used to reconstruct bone models in three dimensions. Sagittal, coronal, and axial images were obtained from the participants' ankles while in a state of relaxation, using a double-echo steady-state sequence (DESS) and a 16-channel ankle coil (resolution:  $0.5 \times 0.5 \times 0.5$  mm; flip angle:  $25^\circ$ , repetition time: 17 ms, echo time: 6 ms) (Figure 1C) (Englander et al., 2019). Previous literature indicates that both CT and 3D MRI can be used for 2D–3D alignment. However, using MRI for alignment typically results in lower data accuracy and higher time costs. For more precise 2D–3D alignment, we utilized CT for 3D reconstruction and alignment for patients with CT images collected for clinical diagnostic needs (Akbari-

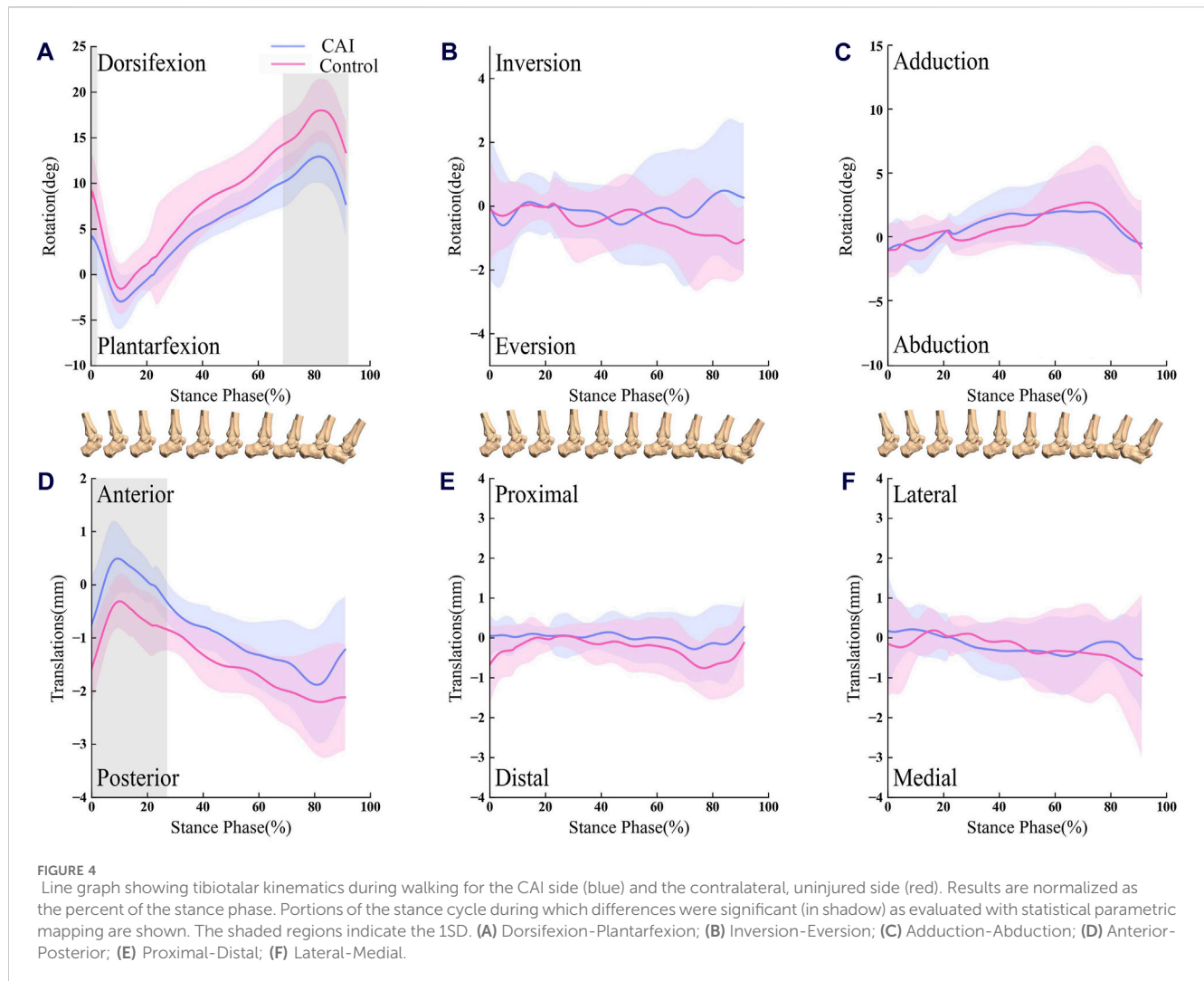
Shandiz et al., 2019). For other subjects, to avoid additional radiation exposure, we used 3D MRI for alignment. The ligament attachment points were located using MRI and matched to the 3D reconstructed model from CT scans (Figure 1D).

The DBR was calibrated during each test session in order to prevent distortion and reconstruct the virtual 3D environment (Knörlein et al., 2016). Autoscooper (Brown University, United States) was used to semi-automatically track and align digitally reconstructed radiographs with synchronized biplane radiographs for each bone (Figure 1E) (Akhbari et al., 2019; Maharaj et al., 2020).

## 2.4 Calculation of ligament elongation

The study involved measuring the lengths of the ligaments by determining the shortest distances between the centroids of the attachment areas on bones. The locations and configurations of ligaments attachment sites (ATFL/CFL/PTFL) were marked in the three perpendicular imaging planes based on MRI. Ligaments elongation (%) was calculated as

$$\text{Elongation} = \frac{(l - l_o)}{l_o} \times 100\%$$



where the reference length  $l_0$  was determined as the length of the ligaments calculated from the MRI in its relaxed state during the MR scan (Figure 2) (de Asla et al., 2009; Nukuto et al., 2023).

## 2.5 Joint kinematics calculation

The anatomical coordinate system (ACS) for each bone was determined using a combination of geometric measurements and anatomical landmarks, as outlined in previously established methodologies (Chen Wang et al., 2016; Lenz et al., 2021). The anatomical coordinate system was established as follows: For the tibia, the center of the distal articular surface was used as the origin of the coordinate system. For the talus, the center of the talus was used as the origin of the coordinate system. For the calcaneus, the center of the subtalar joint surface was used as the origin of the coordinate system. The positive directions of the axes were defined as follows: the lateral direction was defined as the positive x-axis, the anterior direction as the positive y-axis, and the proximal direction as the positive z-axis. Combining the ACS and skeletal spatial positions from DBR, we can quantify the kinematics of the tibiotalar and subtalar joints (Figure 1F). Joint angles and

translations were described as relative motion of the distal bone relative to the proximal. Dynamic tibiotalar and subtalar joints angles were computed using previously established methods (Wang et al., 2023).

The foot-strike and toe-off timing were utilized to calculate the percentage of the support phase. It was noted that during the late push-off phase, the ankle and hindfoot bones were not fully captured within the view volume of the biplane radiography system for certain subjects. We retained 92% of the data from the standing phase of walking, which is the period during which all subjects were collected.

## 2.6 Statistical analysis

Variations in tibiotalar and subtalar RoM during the stance phase were detected through the utilization of paired Student's t-tests. One-dimensional statistical parametric mapping (SPM) was employed to execute a time-domain-specific analysis of joint angles at each point of normalized percent stance. The benefit of SPM lies in its ability to conduct temporal comparisons and provide cluster-based p values (Dewig et al., 2023; Hu et al., 2023;



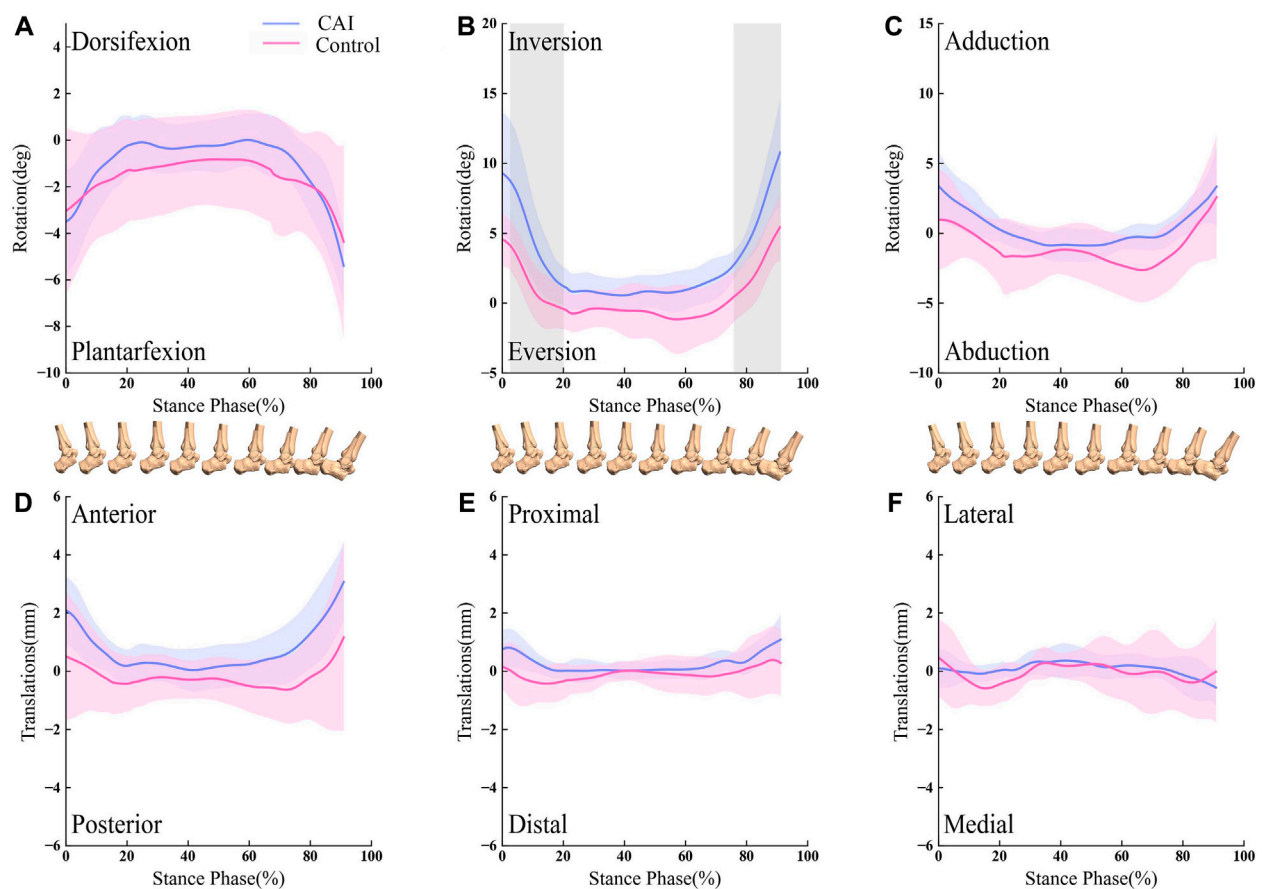


FIGURE 5

Line graph showing subtalar kinematics during walking for the CAI side (blue) and the contralateral, uninjured side (red). Results are normalized as the percent of the stance phase. Portions of the stance cycle during which differences were significant (in shadow) as evaluated with statistical parametric mapping are shown. The shaded regions indicate the 1SD. (A) Dorsiflexion-Plantarflexion; (B) Inversion-Eversion; (C) Adduction-Abduction; (D) Anterior-Posterior; (E) Proximal-Distal; (F) Lateral-Medial.

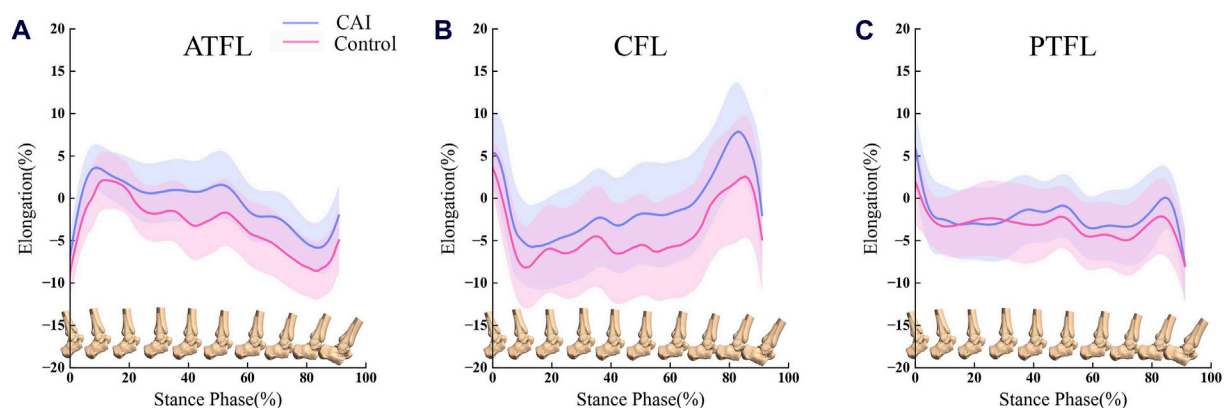


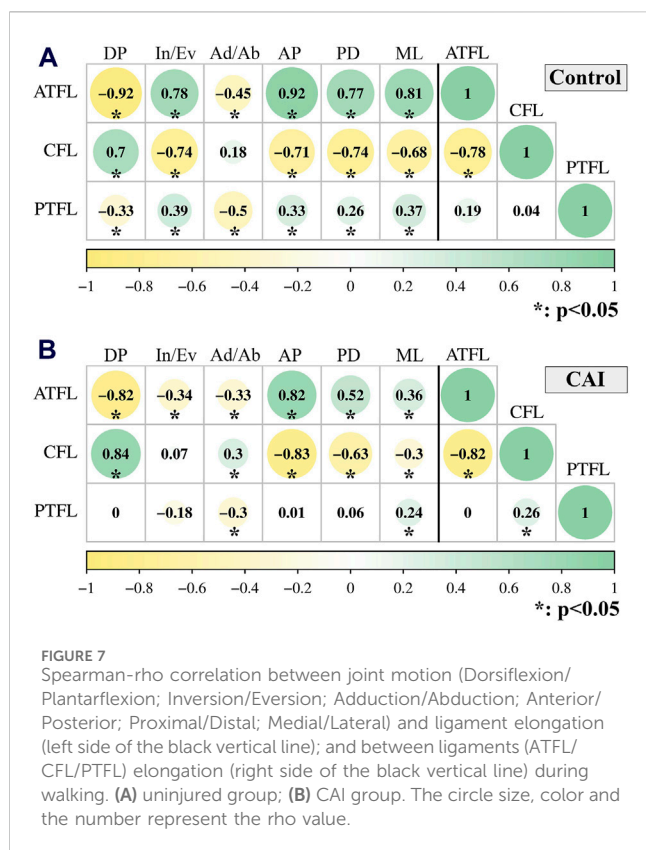
FIGURE 6

Comparison of ligament elongation between the CAI side (blue) and the contralateral, uninjured side (red). (A) ATFL elongation during the stance phase of walking; (B) CFL elongation during the stance phase of walking; (C) PTFL elongation during the stance phase of walking. Error bars represent 1SD.

Wattananon et al., 2023). A previous implementation of SPM (1d version 0.4, python-based open source software: [www.spm1d.org](http://www.spm1d.org)) was applied (Pataky, 2012; Pataky et al., 2016). With use of paired

t-tests, SPM evaluated whether kinematics and ligament elongation were statistically different between the CAI groups and contralateral, uninjured groups.





A Spearman-rho rank correlation was performed to test for a relationship between mean kinematics data (dorsiflexion, inversion, adduction, anterior, proximal, medial) and mean ligament elongation (ATFL/CFL/PTFL) for both groups. Furthermore, the relationships between ligaments elongation were quantified similarly. All statistical tests were performed in Python (3.9.1). Significance was set at  $P < 0.05$  for all tests.

## 3 Results

### 3.1 Kinematics of tibiotalar and subtalar joints

During the stance phase, the side with CAI showed a decrease in dorsiflexion ( $21.73^\circ \pm 3.90^\circ$  to  $17.21^\circ \pm 4.35^\circ$ ,  $p = 0.01$ ) and an increase in anterior translation of the talus ( $2.54 \pm 0.64$  mm to  $3.12 \pm 0.55$  mm,  $p = 0.02$ ) at the tibiotalar joint. Furthermore, the side affected by CAI showed an increase in inversion ( $8.09^\circ \pm 2.21^\circ$  to  $11.80^\circ \pm 3.41^\circ$ ,  $p = 0.02$ ) at the subtalar joint (Figure 3).

For the tibiotalar joint, CAI ankle had a reduced dorsiflexion angle from 0% to 2.07% and 68.81%–92% of the stance phase ( $p < 0.05$ ; maximum difference: 5.67°) (Figure 4A). The talus was more anterior relative to the tibia from 0% to 27.35% of the stance phase ( $p < 0.05$ ; maximum difference: 0.83 mm) (Figure 4D).

For the subtalar joint, the ankle with CAI exhibited a significant increase in the inversion angle, with the phase of the stance from

2.85% to 20.24%, and 76.52%–92% ( $p < 0.05$ ; maximum difference: 5.34°) as depicted in Figure 5B.

### 3.2 Ligaments elongation

In the stance phase, the ligaments (ATFL/CFL/PTFL) of CAI patients on the healthy and injured sides exhibit a similar tendency for elongation (Figure 6). Ankles with CAI experienced an average of 2.66% more elongation in the ATFL, 3.18% more elongation in the CFL, and 1.02% more elongation in the PTFL compared to their healthy side. However, these differences were not statistically significant.

There is a dynamic correlation between tibiotalar joint motion and ligament elongation, as well as the correlation between ligaments (ATFL/CFL/PTFL) deformation (Figure 7).

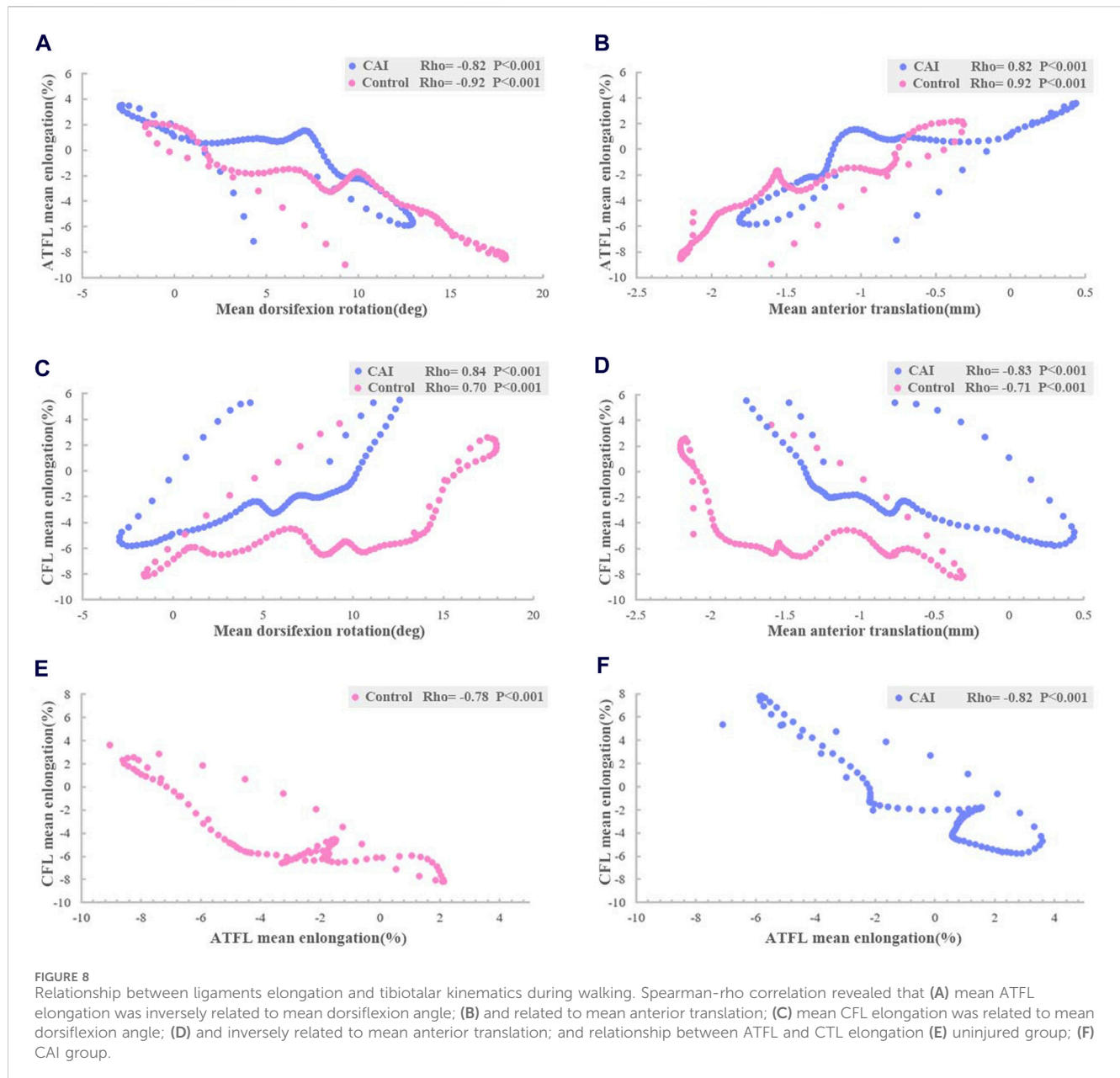
The relative elongation of the ATFL decreased as tibiotalar dorsiflexion (CAI:  $\rho = -0.82$ ,  $P < 0.001$ ; Control:  $\rho = -0.92$ ,  $P < 0.001$ ) and increased as anterior translation of talus occurred (CAI:  $\rho = 0.82$ ,  $P < 0.001$ ; Control:  $\rho = 0.92$ ,  $P < 0.001$ ) (Figures 8A, B). However, the relative elongation of the CFL increased as tibiotalar dorsiflexion (CAI:  $\rho = 0.84$ ,  $P < 0.001$ ; Control:  $\rho = 0.70$ ,  $P < 0.001$ ) and decreased with anterior translation of talus (CAI:  $\rho = -0.83$ ,  $P < 0.001$ ; Control:  $\rho = -0.71$ ,  $P < 0.001$ ) (Figures 8C, D).

Furthermore, the elongation of the ATFL was significantly inversely correlated with the elongation of the CFL (CAI:  $\rho = -0.82$ ,  $P < 0.001$ ; Control:  $\rho = -0.78$ ,  $P < 0.001$ ) (Figures 8E, F).

## 4 Discussion

In this study, we utilized DBR to calculate the *in vivo* motion of tibiotalar and subtalar joints, as well as ligament deformation in patients with CAI. This study found that there was less dorsiflexion and more anterior displacement of the talus in the tibiotalar joint, and more inversion in the subtalar joint was present on the affected side of the CAI compared to the healthy side, especially at the beginning and end of the stance phase. Furthermore, we identified a correlation between ligament elongation and tibiotalar joint motion. The elongation of the ATFL was significantly inversely correlated with the CFL, regardless of CAI. These findings may offer new insights into the motion patterns of ankle joints and connective ligaments during walking in patients with CAI.

There was less tibiotalar dorsiflexion and more subtalar inversion were found in the group with CAI. We distinguished the contribution of the tibiotalar and subtalar joints to these kinematic changes *in vivo*, although previous studies have obtained similar changes in ankle kinematics employing traditional optical motion capture methods (Tavakoli et al., 2016; Herb C. C. and Shank K., 2023; Piming et al., 2023). Inversion of the ankle mainly occurs at the subtalar joint. Previous studies have concluded that for patients with CAI, during inversion of the ankle the medial aspect of the talus likely impacts the tibial plafond, which may result in a talar osteochondral lesion and osteoarthritis (Delco et al., 2017; Yu et al., 2022; Nishimura et al., 2024). Interestingly, the present study found a significant inversion of the subtalar joint



rather than the tibiotaral joint during gait. This indicates that it does not seem to provide a significant contribution to the development of ankle osteoarthritis during walking.

In this study, it was shown that kinematics differences primarily appeared during the heel strike to foot flat phase and heel off to toe off phase. It has been reported that abnormal joint kinematics are generally associated with ligament injury and muscle strength alterations in patients with CAI (Caputo et al., 2009; Herb and Hertel, 2014). Koldenhoven et al. (2016) reported that activation of the tibialis anterior in patients resulted in increased ankle plantarflexion during heel strike. We believe that the ankle joints of patients in these phases are more unstable due to ligament injury and neuromuscular abnormality, which enables them to better demonstrate the differences compared to healthy ankles.

To our knowledge, the present study is the first to conduct an *in vivo* investigation to assess the elongation of the lateral ankle

ligament. This study found a high correlation between dorsiflexion angle and ATFL and CFL elongation. Numerous cadaveric studies have shown that the elongation of the ATFL increases with the plantarflexion angle, while the elongation of the CFL decreases (Ozeki et al., 2002; Takeuchi et al., 2021). However, cadaveric research cannot predict the effects of neuromuscular adaptation or dynamic loading on *in vivo* biomechanics (Canton et al., 2021). This *in vivo* evidence explains why ATFL is more vulnerable in plantarflexion, while the CFL might be more susceptible to injury in dorsiflexion.

de Asla et al. (2009) assessed the length of the lateral collateral ligament during dorsiflexion, plantarflexion, inversion, and eversion in healthy individuals using static biplane radiography. They observed a reciprocal correlation between the length of the ATFL and CFL. In this study, we refined the

motion patterns of the ATFL and CFL during continuous walking measurement and found two ligaments exhibit dynamically inversely correlated elongation characteristics. A dynamic complementary relationship between these two ligaments is essential for maintaining ankle stability. Currently, ankle sagittal plane angles are not considered during ligament repair, which may affect ATFL and CFL tension. We believe that the patient's ankle should be in a neutral position in the sagittal plane when repairing the ATFL and CFL to maintain balanced ligamentous tension.

Despite no significant differences being found, ligament elongation in the CAI group was greater than in the control group, especially in the ATFL and CFL. This may be related to the fact that the walking task may not be sufficient to reveal changes in ligament elongation in patients with CAI. In the study, only level walking was selected for the motion measurement because it is one of the most common daily activities and can be performed with low risk by CAI patients. In the future, more activities that require RoM, balance, and stability can be considered to further investigate the differences in ligament elongation in the population with CAI (Balasukumaran et al., 2020b; Canton et al., 2020). This may provide more information and insights on ankle positions that increase injury vulnerability and injury-related changes in biomechanics, therefore benefiting the design of surgical protocols.

The study had certain limitations that require further discussion. During the tracking process, it was noted that the hindfoot bones were outside the imaging range of the DBR for certain subjects at the late stage of the push-off phase. Therefore, we obtained dynamic data for 92% of the entire duration of the standing phase of the gait. This may lose valuable information at the end of the stance phase. This study focused on the lateral ligaments of the ankle *in vivo* and did not investigate the elongation of the deltoid ligament, which is also critical for ankle stability. Moreover, this study employed a convenience sample with a higher proportion of female participants due to the higher clinical incidence of CAI in females. This sampling may limit the generalizability of our findings to male patients. Future research should aim to investigate the potential kinematic and ligament elongation differences between genders with a larger and more balanced sample size.

In conclusion, patients with CAI have significant changes in joint kinematics relative to the contralateral side. Throughout the stance phase of walking, ATFL increases in length during plantarflexion and talar anterior translation whereas the elongation trend of CFL was the opposite. The interrelationship between the two ligaments is that when one ligament shortens, the other lengthens. In the future, further longitudinal research with a larger participant pool and more motion activities are necessary to determine whether the observed changes in movement and ligament stretching lead to successful postoperative outcomes.

## Data availability statement

The raw data supporting the conclusions of this article will be made available by the authors, without undue reservation.

## Ethics statement

The studies involving humans were approved by the Ethics Committee of the Second Hospital of Jilin University. The studies were conducted in accordance with the local legislation and institutional requirements. The participants provided their written informed consent to participate in this study. Written informed consent was obtained from the individual(s) for the publication of any potentially identifiable images or data included in this article.

## Author contributions

YR: Data curation, Methodology, Writing–original draft. SW: Methodology, Validation, Writing–original draft. NZ: Visualization, Writing–original draft. ZJ: Conceptualization, Writing–review and editing. NM: Data curation, Writing–original draft. PL: Data curation, Writing–original draft. LR: Methodology, Validation, Writing–review and editing. ZQ: Conceptualization, Methodology, Writing–review and editing. FC: Methodology, Writing–review and editing.

## Funding

The author(s) declare that financial support was received for the research, authorship, and/or publication of this article. This work was supported financially by the National Key R&D Program of China (Grant No. 2022YFE0107700), the National Natural Science Foundation of China (No. 52175270), and the Project of Scientific (No 20210402006GH).

## Conflict of interest

The authors declare that the research was conducted in the absence of any commercial or financial relationships that could be construed as a potential conflict of interest.

The author(s) declared that they were an editorial board member of Frontiers, at the time of submission. This had no impact on the peer review process and the final decision.

## Publisher's note

All claims expressed in this article are solely those of the authors and do not necessarily represent those of their affiliated organizations, or those of the publisher, the editors and the reviewers. Any product that may be evaluated in this article, or claim that may be made by its manufacturer, is not guaranteed or endorsed by the publisher.

## Supplementary material

The Supplementary Material for this article can be found online at: <https://www.frontiersin.org/articles/10.3389/fbioe.2024.1441005/full#supplementary-material>

## References

- Agostinone, P., Di Paolo, S., Grassi, A., Pinelli, E., Bontempi, M., Bragonzoni, L., et al. (2021). ACL deficiency influences medio-lateral tibial alignment and knee varus-valgus during *in vivo* activities. *Knee Surg. Sports Traumatol. Arthrosc.* 29 (2), 389–397. doi:10.1007/s00167-020-05979-6
- Akbari-Shandiz, M., Lawrence, R. L., Ellingson, A. M., Johnson, C. P., Zhao, K. D., and Ludewig, P. M. (2019). MRI vs CT-based 2D-3D auto-registration accuracy for quantifying shoulder motion using biplane video-radiography. *J. Biomech.* 82, 375–380. doi:10.1016/j.jbiomech.2018.09.019
- Akhbari, B., Morton, A. M., Moore, D. C., Weiss, A.-P. C., Wolfe, S. W., and Crisco, J. J. (2019). Accuracy of biplane videoradiography for quantifying dynamic wrist kinematics. *J. Biomechanics* 92, 120–125. doi:10.1016/j.jbiomech.2019.05.040
- Balasukumaran, T., Gottlieb, U., and Springer, S. (2020a). Spatiotemporal gait characteristics and ankle kinematics of backward walking in people with chronic ankle instability. *Sci. Rep.* 10 (1), 11515. doi:10.1038/s41598-020-68385-5
- Balasukumaran, T., Gottlieb, U., and Springer, S. (2020b). Spatiotemporal gait characteristics and ankle kinematics of backward walking in people with chronic ankle instability. *Sci. Rep.* 10 (1), 11515. doi:10.1038/s41598-020-68385-5
- Boey, H., van Rossom, S., Verfaillie, S., Sloten, J. V., and Jonkers, I. (2022). Maximal lateral ligament strain and loading during functional activities: model-based insights for ankle sprain prevention and rehabilitation. *Clin. Biomech. (Bristol, Avon)* 94, 105623. doi:10.1016/j.clinbiomech.2022.105623
- Canton, S., Anderst, W., and Hogan, M. V. (2020). *In vivo* ankle kinematics revealed through biplane radiography: current concepts, recent literature, and future directions. *Curr. Rev. Musculoskelet. Med.* 13 (1), 77–85. doi:10.1007/s12178-020-09601-7
- Canton, S. P., Gale, T., Onyekwu, C., Hogan, M. V., and Anderst, W. (2021). Syndesmosis repair affects *in vivo* distal interosseous tibiofibular ligament elongation under static loads and during dynamic activities. *J. Bone Jt. Surg. Am.* 103 (20), 1927–1936. doi:10.2106/jbjs.20.01787
- Cao, S., Wang, C., Zhang, G., Ma, X., Wang, X., Huang, J., et al. (2019). *In vivo* kinematics of functional ankle instability patients during the stance phase of walking. *Gait Posture* 73, 262–268. doi:10.1016/j.gaitpost.2019.07.377
- Caputo, A. M., Lee, J. Y., Spritzer, C. E., Easley, M. E., DeOrio, J. K., Nunley, J. A., et al. (2009). *In vivo* kinematics of the tibiotalar joint after lateral ankle instability. *Am. J. Sports Med.* 37 (11), 2241–2248. doi:10.1177/0363546509337578
- Chang, S. H., Morris, B. L., Saengsin, J., Tourné, Y., Guillo, S., Guss, D., et al. (2021). Diagnosis and treatment of chronic lateral ankle instability: review of our biomechanical evidence. *JAAOS - J. Am. Acad. Orthop. Surg.* 29 (1), 3–16. doi:10.5435/jaaos-d-20-00145
- Chen Wang, M. D., Geng, X., Wang, S., Xin Ma, M. D., Xu Wang, M. D., Jiazhang Huang, M. D., et al. (2016). *In vivo* kinematic study of the tarsal joints complex based on fluoroscopic 3D-2D registration technique. *Gait Posture* 49, 54–60. doi:10.1016/j.gaitpost.2016.06.009
- Chiba, D., Gale, T., Nishida, K., Suntaxi, F., Lesniak, B. P., Fu, F. H., et al. (2021). Lateral extra-articular tenodesis contributes little to change *in vivo* kinematics after anterior cruciate ligament reconstruction: a randomized controlled trial. *Am. J. Sports Med.* 49 (7), 1803–1812. doi:10.1177/03635465211003298
- de Asla, R. J., Kozánek, M., Wan, L., Rubash, H. E., and Li, G. (2009). Function of anterior talofibular and calcaneofibular ligaments during *in-vivo* motion of the ankle joint complex. *J. Orthop. Res. Res.* 4, 7. doi:10.1186/1749-799x-4-7
- Delco, M. L., Kennedy, J. G., Bonassar, L. J., and Fortier, L. A. (2017). Post-traumatic osteoarthritis of the ankle: a distinct clinical entity requiring new research approaches. *J. Orthop. Res.* 35 (3), 440–453. doi:10.1002/jor.23462
- Deleu, P. A., Leemrijse, T., Chêze, L., Naaim, A., Dumas, R., Devos Bevernage, B., et al. (2021). Post-sprain versus post-fracture post-traumatic ankle osteoarthritis: impact on foot and ankle kinematics and kinetics. *Gait Posture* 86, 278–286. doi:10.1016/j.gaitpost.2021.03.029
- De Ridder, R., Willems, T., Vanrenterghem, J., Robinson, M., Pataky, T., and Roosen, P. (2013). Gait kinematics of subjects with ankle instability using a multisegmented foot model. *Med. Sci. Sports Exerc* 45 (11), 2129–2136. doi:10.1249/MSS.0b013e31829991a2
- Dewig, D. R., Evans-Pickett, A., Pietrosimone, B. G., and Blackburn, J. T. (2023). Comparison of discrete and continuous analysis approaches for evaluating gait biomechanics in individuals with anterior cruciate ligament reconstruction. *Gait Posture* 100, 261–267. doi:10.1016/j.gaitpost.2023.01.012
- Englander, Z. A., Baldwin, E. L., 3rd, Smith, W. A. R., Garrett, W. E., Spritzer, C. E., and DeFrate, L. E. (2019). *In vivo* anterior cruciate ligament deformation during a single-legged jump measured by magnetic resonance imaging and high-speed biplanar radiography. *Am. J. Sports Med.* 47 (13), 3166–3172. doi:10.1177/0363546519876074
- Fong, D. T., Hong, Y., Chan, L. K., Yung, P. S., and Chan, K. M. (2007). A systematic review on ankle injury and ankle sprain in sports. *Sports Med.* 37 (1), 73–94. doi:10.2165/00007256-200737010-00006
- Freeman, M. A. (1965). Instability of the foot after injuries to the lateral ligament of the ankle. *J. Bone Jt. Surg. Br.* 47 (4), 669–677. doi:10.1302/0301-620x.47b4.669
- Herb, C., and Shank, K. (2023a). Ankle kinematics during a drop-vertical jump in patients with chronic ankle instability and healthy controls: a bivariate confidence interval comparison. *Gait Posture* 104, 147–150. doi:10.1016/j.gaitpost.2023.06.007
- Herb, C. C., and Hertel, J. (2014). Current concepts on the pathophysiology and management of recurrent ankle sprains and chronic ankle instability. *Curr. Phys. Med. Rehabilitation Rep.* 2 (1), 25–34. doi:10.1007/s40141-013-0041-y
- Herb, C. C., and Shank, K. (2023b). Ankle kinematics during a drop-vertical jump in patients with chronic ankle instability and healthy controls: a bivariate confidence interval comparison. *Gait Posture* 104, 147–150. doi:10.1016/j.gaitpost.2023.06.007
- Hu, Y., Teng, P., Wu, T.-L., Clark, R., Pua, Y.-H., Yong, J., et al. (2023). Association between standing and walking biomechanical parameters in knee osteoarthritis patients using statistical parametric mapping. *Osteoarthr. Cartil.* 31, S130–S131. doi:10.1016/j.joca.2023.01.086
- Kessler, S. E., Rainbow, M. J., Lichtwark, G. A., Cresswell, A. G., D'Andrea, S. E., Konow, N., et al. (2019). A direct comparison of biplanar videoradiography and optical motion capture for foot and ankle kinematics. *Front. Bioeng. Biotechnol.* 7, 199. doi:10.3389/fbioe.2019.00199
- Knörlein, B. J., Baier, D. B., Gates, S. M., Laurence-Chasen, J. D., and Brainerd, E. L. (2016). Validation of XMA Lab software for marker-based XROMM. *J. Exp. Biol.* 219 (Pt 23), 3701–3711. doi:10.1242/jeb.145383
- Koldenhoven, R. M., Feger, M. A., Fraser, J. J., Saliba, S., and Hertel, J. (2016). Surface electromyography and plantar pressure during walking in young adults with chronic ankle instability. *Knee Surg. Sports Traumatol. Arthrosc.* 24 (4), 1060–1070. doi:10.1007/s00167-016-4015-3
- Lalevée, M., Anderson, D. D., and Wilken, J. M. (2023). Current challenges in chronic ankle instability: review and perspective. *Foot Ankle Clin.* 28 (1), 129–143. doi:10.1016/j.fcl.2022.11.003
- Lenz, A. L., Nichols, J. A., Roach, K. E., Foreman, K. B., Barg, A., Saltzman, C. L., et al. (2020). Compensatory motion of the subtalar joint following tibiotalar arthrodesis: an *in vivo* dual-fluoroscopy imaging study. *J. Bone Jt. Surg. Am.* 102 (7), 600–608. doi:10.2106/jbjs.19.01132
- Lenz, A. L., Strobel, M. A., Anderson, A. M., Fial, A. V., MacWilliams, B. A., Krzak, J. J., et al. (2021). Assignment of local coordinate systems and methods to calculate tibiotalar and subtalar kinematics: a systematic review. *J. biomechanics* 120, 110344. doi:10.1016/j.jbiomech.2021.110344
- Li, L., Gollhofer, A., Lohrer, H., Dorn-Lange, N., Bonsignore, G., and Gehring, D. (2019). Function of ankle ligaments for subtalar and talocrural joint stability during an inversion movement - an *in vitro* study. *J. Foot Ankle Res.* 12, 16. doi:10.1186/s13047-019-0330-5
- Maharaj, J. N., Kessler, S., Rainbow, M. J., D'Andrea, S. E., Konow, N., Kelly, L. A., et al. (2020). The reliability of foot and ankle bone and joint kinematics measured with biplanar videoradiography and manual scientific roscoping. *Front. Bioeng. Biotechnol.* 8, 106. doi:10.3389/fbioe.2020.00106
- Monaghan, K., Delahunt, E., and Caulfield, B. (2006). Ankle function during gait in patients with chronic ankle instability compared to controls. *Clin. Biomech. (Bristol, Avon)* 21 (2), 168–174. doi:10.1016/j.clinbiomech.2005.09.004
- Mousavi, S. H., Khorramroo, F., Minoonejad, H., and Zwerver, J. (2023). Effects of biofeedback on biomechanical factors associated with chronic ankle instability: a systematic review with meta-analysis. *BMC Sports Sci. Med. Rehabil.* 15 (1), 168. doi:10.1186/s13102-023-00780-7
- Nigg, B. M., Skarvan, G., Frank, C. B., and Yeadon, M. R. (1990). Elongation and forces of ankle ligaments in a physiological range of motion. *Foot Ankle* 11 (1), 30–40. doi:10.1177/107110079001100107
- Nishimura, A., Senga, Y., Fujikawa, Y., Takegami, N., Akeda, K., Ogura, T., et al. (2024). Prevalence and risk factors of ankle osteoarthritis in a population-based study. *Foot Ankle Surg.* 30 (5), 389–393. doi:10.1016/j.fas.2024.02.009
- Nukuto, K., Gale, T., Yamamoto, T., Musahl, V., and Anderst, W. (2023). Bone morphology features associated with knee kinematics may not be predictive of ACL elongation during high-demand activities. *Knee Surg. Sports Traumatol. Arthrosc.* 31 (11), 5096–5103. doi:10.1007/s00167-023-07560-3
- Ozeki, S., Yasuda, K., Kaneda, K., Yamakoshi, K., and Yamanoi, T. (2002). Simultaneous strain measurement with determination of a zero strain reference for the medial and lateral ligaments of the ankle. *Foot Ankle Int.* 23 (9), 825–832. doi:10.1177/107110070202300909
- Pataky, T. C. (2012). One-dimensional statistical parametric mapping in Python. *Comput. Methods Biomech. Biomed. Engin* 15 (3), 295–301. doi:10.1080/10255842.2010.527837
- Pataky, T. C., Robinson, M. A., and Vanrenterghem, J. (2016). Region-of-interest analyses of one-dimensional biomechanical trajectories: bridging 0D and 1D theory, augmenting statistical power. *PeerJ* 4, e2652. doi:10.7717/peerj.2652
- Piming, G., Yaming, Y., Hai, S., Xia, L., and Xiaobing, L. (2023). Three-dimensional ankle kinematics of the full gait cycle in patients with chronic ankle instability: a case-control study. *Heliyon* 9 (11), e22265. doi:10.1016/j.heliyon.2023.e22265



- Soboroff, S. H., Pappius, E. M., and Komaroff, A. L. (1984). Benefits, risks, and costs of alternative approaches to the evaluation and treatment of severe ankle sprain. *Clin. Orthop. Relat. Res.* 183, 160–168. doi:10.1097/00003086-198403000-00026
- Takeuchi, Y., Inokuchi, R., Takao, M., Glazebrook, M., Martin Oliva, X., Yamazaki, T., et al. (2021). Three-dimensional analysis of anterior talofibular ligament strain patterns during cadaveric ankle motion using a miniaturized ligament performance probe. *BMC Musculoskelet. Disord.* 22 (1), 208. doi:10.1186/s12891-021-04058-2
- Tavakoli, S., Forghany, S., and Nester, C. (2016). The effect of dual tasking on foot kinematics in people with functional ankle instability. *Gait Posture* 49, 364–370. doi:10.1016/j.gaitpost.2016.07.302
- van Rijn, R. M., van Os, A. G., Bernsen, R. M., Luijsterburg, P. A., Koes, B. W., and Bierma-Zeinstra, S. M. (2008). What is the clinical course of acute ankle sprains? A systematic literature review. *Am. J. Med.* 121 (4), 324–331.e7. doi:10.1016/j.amjmed.2007.11.018
- Wang, B., Roach, K. E., Kapron, A. L., Fiorentino, N. M., Saltzman, C. L., Singer, M., et al. (2015). Accuracy and feasibility of high-speed dual fluoroscopy and model-based tracking to measure *in vivo* ankle arthrokinematics. *Gait Posture* 41 (4), 888–893. doi:10.1016/j.gaitpost.2015.03.008
- Wang, S., Qian, Z., Liu, X., Song, G., Wang, K., Wu, J., et al. (2023). Intrinsic kinematics of the tibiotalar and subtalar joints during human walking based on dynamic biplanar fluoroscopy. *J. Bionic Eng.* 20 (5), 2059–2068. doi:10.1007/s42235-023-00368-4
- Wattananon, P., Kongoun, S., Chohan, A., and Richards, J. (2023). The use of statistical parametric mapping to determine altered movement patterns in people with chronic low back pain. *J. Biomechanics* 153, 111601. doi:10.1016/j.jbiomech.2023.111601
- Wu, G., Siegler, S., Allard, P., Kirtley, C., Leardini, A., Rosenbaum, D., et al. (2002). ISB recommendation on definitions of joint coordinate system of various joints for the reporting of human joint motion—part I: ankle, hip, and spine. *J. Biomech.* 35 (4), 543–548. doi:10.1016/s0021-9290(01)00222-6
- Ye, D., Sun, X., Zhang, C., Zhang, S., Zhang, X., Wang, S., et al. (2021). *In vivo* foot and ankle kinematics during activities measured by using a dual fluoroscopic imaging system: a narrative review. *Front. Bioeng. Biotechnol.* 9, 693806. doi:10.3389/fbioe.2021.693806
- Yu, P., Cen, X., Mei, Q., Wang, A., Gu, Y., and Fernandez, J. (2024). Differences in intra-foot movement strategies during locomotive tasks among chronic ankle instability, copers and healthy individuals. *J. Biomech.* 162, 111865. doi:10.1016/j.jbiomech.2023.111865
- Yu, P., Cen, X., Xiang, L., Mei, Q., Wang, A., Gu, Y., et al. (2023). Regional plantar forces and surface geometry variations of a chronic ankle instability population described by statistical shape modelling. *Gait Posture* 106, 11–17. doi:10.1016/j.gaitpost.2023.08.007
- Yu, P., Mei, Q., Xiang, L., Fernandez, J., and Gu, Y. (2022). Differences in the locomotion biomechanics and dynamic postural control between individuals with chronic ankle instability and copers: a systematic review. *Sports Biomech.* 21 (4), 531–549. doi:10.1080/14763141.2021.1954237
- Zhang, M., Zhang, Y., Davies, T. C., and Xie, S. (2014). An *in-vivo* lateral ankle ligament strain behavior assessment technique for potential use in robot-assisted therapy. *Annu. Int. Conf. IEEE Eng. Med. Biol. Soc.* 2014, 4022–4025. doi:10.1109/embc.2014.6944506





## OPEN ACCESS

## EDITED BY

Zhiyong Li,  
Queensland University of Technology, Australia

## REVIEWED BY

Jen Rowson,  
The University of Sheffield, United Kingdom  
Jean Slawinski,  
Institut National du Sport, de l'Expertise et de la  
Performance (INSEP), France

## \*CORRESPONDENCE

Wei Li,  
✉ liweiwin@sina.com

RECEIVED 15 June 2024

ACCEPTED 12 August 2024

PUBLISHED 27 August 2024

## CITATION

Huang J, Peyré-Tartaruga LA, Lin J, Shi Y and  
Li W (2024) Rotation of the hammer and  
performance in hammer throwing.  
*Front. Bioeng. Biotechnol.* 12:1449465.  
doi: 10.3389/fbioe.2024.1449465

## COPYRIGHT

© 2024 Huang, Peyré-Tartaruga, Lin, Shi and Li.  
This is an open-access article distributed under  
the terms of the [Creative Commons Attribution  
License \(CC BY\)](#). The use, distribution or  
reproduction in other forums is permitted,  
provided the original author(s) and the  
copyright owner(s) are credited and that the  
original publication in this journal is cited, in  
accordance with accepted academic practice.  
No use, distribution or reproduction is  
permitted which does not comply with these  
terms.

# Rotation of the hammer and performance in hammer throwing

Jiaru Huang<sup>1</sup>, Leonardo A. Peyré-Tartaruga<sup>2,3</sup>, Junlei Lin<sup>1</sup>, Yu Shi<sup>1</sup>  
and Wei Li<sup>1\*</sup>

<sup>1</sup>School of Strength and Conditioning Training, Beijing Sport University, Beijing, China, <sup>2</sup>Human Locomotion Laboratory (LocoLab), Department of Public Health, Experimental Medicine and Forensic Sciences, University of Pavia, Pavia, Italy, <sup>3</sup>LaBiodin Biodynamics Laboratory, Escola de Educação Física, Fisioterapia e Dança, Universidade Federal do Rio Grande do Sul, Porto Alegre, Brazil

**Objective:** The purpose of this study was to determine the effects of hammer rotation on performance in hammer throwing.

**Methods:** The hammer's velocity increment at different stages, the duration of rotations at different phases, and the horizontal azimuth angle and rotation radius at critical instants were calculated and compared between the long and short trials for 26 female athletes in actual competitions.

**Results:** Compared to short trials, female throwers' long trials exhibited significantly larger release velocity ( $p < 0.001$ ,  $ES = 1.42$ ), greater velocity increment during the double support phase ( $p = 0.006$ ,  $ES = 0.59$ ), shorter duration during the single support phase ( $p \leq 0.043$ ,  $ES = 0.42-0.83$ ), lower horizontal azimuth angle ( $p \leq 0.027$ ,  $ES = 0.46-0.57$ ), and longer rotational radius at critical instants ( $p \leq 0.021$ ,  $ES = 0.48-0.73$ ).

**Conclusion:** During the process from the hammer head's low point to high point, athletes should focus on increasing the rotation radius of the hammer head and accelerating the right foot's landing speed during the single support phase. This approach aims to reduce the hammer's horizontal azimuth angle at the right foot touchdown, enhance the acceleration performance during the double support phase, and increase the release speed.

## KEYWORDS

female, velocity increment, rotation radius, horizontal azimuth angle, duration

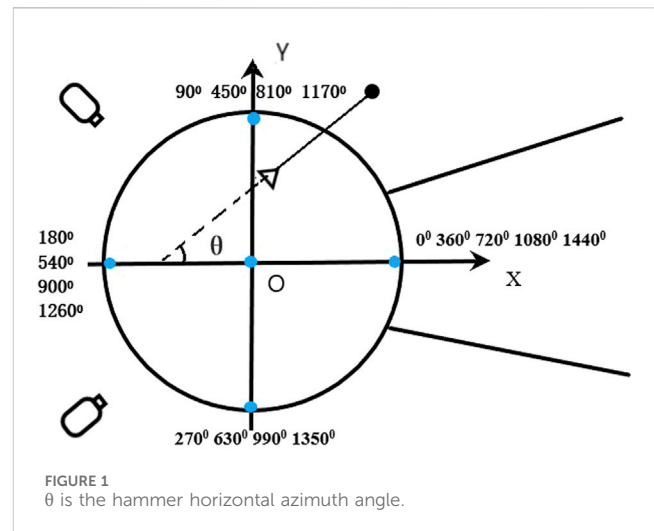
## Introduction

Hammer throwing is one of the four throwing events in track and field. Hammer throwers throw a hammer weighing 7.26 kg and 121.5 cm in length for men or 4 kg and 119.5 cm for women at a high speed in a throwing circle that is 7 feet in diameter (Murofushi et al., 2017). The throwing movement can be divided into three stages: the preliminary winds, the turns, and the delivery (Murofushi et al., 2017). In the preliminary winds, the athlete stands at the back edge of the throwing circle, facing away from the throwing direction, and rotates the hammer 2–3 times around the body with both feet in contact with the ground. Then, the athlete enters the phase of the turn, pivoting on one foot's heel and ball, continuously rotating and moving rapidly toward the throwing direction, creating a combined translational and rotational motion (Maheras, 2018; Murofushi et al., 2005). For an athlete rotating to the left, the left foot maintains contact with the ground throughout the rotation, while the right foot alternates between leaving and touching the ground, forming double support and single support phases in each turn (Castaldi et al., 2022). When the

athlete reaches the front edge of the throwing circle, they forcefully release the hammer, completing the throw (Dapena, 1984; Dapena, 1986; Dapena and Feltner, 1989; Otto, 1992).

The release velocity, which is the sum of the velocity increments from the three stages (preliminary winds, turns, and delivery), is the primary factor affecting the throwing distance, with a high linear correlation between the two (Knudson, 2007; Ruiz and Dávila, 2009). To maximize the release speed, athletes must be able to continuously accelerate the hammer during the turns and delivery phases following the completion of the preliminary winds. In each turn, the hammer speed exhibits a periodic fluctuation, increasing during the double support phases and decreasing during the single support phases, but generally trending upward (Brice et al., 2015; Brice et al., 2018; Murofushi et al., 2007). Compared to the single support phase, the athlete maintains a more stable body posture during the double support phase, which is more conducive to increasing the hammer speed (Bartoniets, 2000; Brice et al., 2008). Therefore, many coaches and scholars recommend that throwers prolong the double support duration by shortening the single support phase (Bartoniets, 2000; Otto, 1992). To effectively shorten the single support (SS) phase duration and extend the double support (DS) phase duration, athletes need to plant their right foot earlier (Hay, 1978). This helps extend the DS phase but also aids in forming a “wound-up position,” where both feet’ axes lead the hips axis, the hips axis leads the shoulder axis, and the hammer lags far behind these three, thus facilitating greater hammer acceleration (Hay, 1978). The radius of rotation of the hammer is another critical factor influencing changes in hammer speed. According to the equation  $v = \omega \cdot r$ , theoretically, maintaining a longer radius is conducive to increasing the hammer speed, because a longer radius allows the thrower-hammer system to have a slower angular velocity at any given linear speed of the hammer (Dapena and Feltner, 1989). In that situation, muscles can exert greater forces at slower speeds, which is expected to facilitate an increase in the system’s angular momentum (Hill, 1922). However, as the rotation progresses, the rotation radius of the hammer tends to decrease, which is closely related to changes in the athlete’s posture (Dapena, 1986).

Scientific research on the hammer throw is limited, and the few existing studies have small sample sizes, with some findings still needing clarification (Brice et al., 2018; Castaldi et al., 2022). The hammer velocity curve shows that the double-support phase is the primary phase for speed increase in turn, this does not necessarily mean that the differences in release velocity at varying throwing distances are mainly derived from this phase. Identifying the specific phases that lead to differences in performance can provide more targeted guidance for athletes’ training practices. The notion that extending the duration of the double support phase is more beneficial for improving throwing performance has been questioned (Dapena, 1984; Dapena, 1989; Hirose et al., 2016). In fact, some high-level athletes have achieved longer throwing distances with significantly shorter double support phases (Bartoniets, 2000; Maheras, 2010). Additionally, while a longer rotation radius is generally more conducive to improving throwing performance, the hammer’s rotation radius fluctuates during each turn, and previous studies have yet to clearly identify the specific phases that lead to differences in performance. Moreover, due to variations in athletes’ arm lengths, directly comparing the radius graphs of different throwers may not be reasonable (Dapena and McDonald, 1989). While previous studies



have advanced our understanding of hammer throw techniques, variations in athletes’ technical skills, body morphology, and physical fitness make it difficult to establish definitive guidelines for adjusting these factors to achieve the best performance. Therefore, we can only accurately identify and prescribe the adjustments needed to optimize hammer-throwing performance by comprehending the interference of these variable factors.

This study was to determine the effects of hammer rotation on performance in hammer throwing. It was hypothesized that 1) Compared to trials with the shortest official distances, the speed increment during the double support phase is greater in trials with the longest official distances. 2) Compared to trials with the shortest official distances, the duration of the double support phase is longer, and the duration of the single support phase is shorter in trials with the longest official distances. 3) Compared to trials with the shortest official distances, the horizontal azimuth of the hammer is smaller at critical instants in trials with the longest official distances among elite hammer throwers. 4) Compared to trials with the shortest official distances, the radius of rotation of the hammer is longer at critical instants in trials with the longest official distances among elite hammer throwers.

## Methods

### Participants

Comparisons of kinematic variables between the trials with the longest and shortest official distances were conducted for each participant in the same competition. This study analyzed the two trials with the greatest distance difference for the same athlete in the same competition from national competitions held in 2022, 2023, and 2024. If an athlete participated in multiple competitions, the competition with the greatest difference between their longest and shortest throws was selected. From 11 national competitions, after excluding trials with poor video quality caused by lighting and weather conditions and those where the hammer hit the net after release, a total of 26 athletes were chosen for the study. All athletes rotated to the left with the left foot keeping contact with the ground, and completed four turns.

## Data collection

The data of this study were collected from the 2022, 2023, and 2024 China Athletics World Championships Trials, the China Athletics Open, and the National Championships. Two high-speed cameras (ZcamE2, Shenzhen Vision Technology Co., Ltd.) were set at a height of 1.5 m, were connected using a synchronization cable, and were positioned on the right and left side of the throwing circle, respectively, with the 90-degree optical axes of the two video camcorders and 5–6 m horizontally distance from the center of throwing circle (Figure 1). All trials were recorded at 60 frames per second, a shutter speed of 1/1,600 s, and 1,920 × 1,080 resolution. Before the competition, a 28-point calibration frame (2.5 m long, 2 m wide, 2.5 m high) was used to calibrate camera positions and orientations. During calibration, five global reference frame markers were placed around the throwing circle to establish a global reference frame for data reduction.

For each trial, the two-dimensional coordinates of 21 body landmarks, the center of the hammerhead, and the intersection point of the handle and chain were manually digitized from video images. The digitization of each trial started five frames before the athlete's right foot first left the ground and ended five frames after the hammer was released. The 3D positions of 21 body landmarks and two specific points on the hammer were calculated from synchronized 2D data using the direct linear transformation technique (Abdel-Aziz et al., 2015). The mean calibration error for each calibration was under 10 mm, with the maximum error not exceeding 10 mm. These coordinates were then converted into the global reference frame, with the  $x$ -axis pointing in the throwing direction, the  $y$ -axis pointing to the athlete's left when facing the throwing direction, and the  $z$ -axis pointing upward (Figure 1). This conversion provided a detailed spatial representation of the athlete and equipment. The calculation of the 3D positions was performed using the digital processing software Fastmove Pose Creator (Dalian Sharp Motion Technology Co., Ltd.), and the 3D coordinates were then filtered using a Butterworth low-pass digital filter with an estimated optimal cutoff frequency of 7.14 Hz (Yu et al., 1999). The filtering was done using MATLAB R2022b.

## Data reduction

This study used the velocity of the center of the hammer head to represent the hammer's velocity. Although there is a difference between the two, both reflect the athlete's acceleration performance. The velocity-time curve of the hammer head's center was obtained by calculating the first-time derivative of the smoothed coordinate-time curve using the central numerical differentiation method (Equation 1).

$$\begin{aligned} v_{x,n} &= \frac{x_{n+1} - x_{n-1}}{2} \times F_s \\ v_{y,n} &= \frac{y_{n+1} - y_{n-1}}{2} \times F_s \\ v_{z,n} &= \frac{z_{n+1} - z_{n-1}}{2} \times F_s \end{aligned} \quad (1)$$

Where  $x_{n-1}$ ,  $y_{n-1}$ ,  $z_{n-1}$  are the coordinates of the hammer head's center at the point immediately before the sampling point  $n$ ;  $x_{n+1}$ ,

$y_{n+1}$ ,  $z_{n+1}$  are the coordinates of the hammer head's center at the point immediately after the sampling point  $n$ ;  $F_s$  is the sampling frequency (60fps). The resultant velocity of the hammerhead at the given sampling point  $n$  is (Equation 2):

$$v_n = \sqrt{v_{x,n}^2 + v_{y,n}^2 + v_{z,n}^2} \quad (2)$$

**Hammer velocity increment:** The hammer velocity increment for a given phase is defined as the final velocity at the end of the phase minus the initial velocity at the beginning.

**Hammer horizontal azimuth angle:** The vector from the intersection of the hammer handle and chain towards the center of the hammerhead is projected onto the X-O-Y plane of the global reference frame. The angle formed between the projected vector and the negative Y-axis is the horizontal azimuth angle of the hammer, which is the  $\theta$  angle shown in Figure 1.

**Hammer rotation radius:** In this study, the hammer's rotation radius in this study was calculated as the distance from the center of the hammer head to the midpoint of the line connecting the centers of both shoulders. Research indicates that trunk posture has a direct impact on the rotation radius. A 1-degree backward trunk tilt reduces the hammer rotation radius by approximately 4.6 mm (Dapena and McDonald, 1989). The calculations for the data above were performed using MATLAB R2022b.

## Data analysis

Based on the right foot's takeoff and touchdown, the turns and delivery were divided into single support (SS) and double support (DS) phases. Each of the first three turns includes four critical instants: 1) right foot takeoff (Ron); 2) hammer head's highest point (HP); 3) right foot touchdown (Roff); and 4) hammer head's lowest point (LP). In the fourth turn, the point of release (Rel) is also added. The highest and lowest points of the hammerhead are defined as the positions of the highest and lowest points in each turn.

## Statistical procedures

Paired sample t-tests were used to compare the differences between the longest and the shortest trials in terms of velocity increments at various stages, the duration of single/double support phases, the horizontal azimuth angle of the hammer, and the rotation radius of the hammer at critical instants.

Statistical analyses were performed using IBM SPSS Statistics 27. To indicate statistical significance, a Type I error rate of less than or equal to 0.05 was chosen.

## Results

### The average throw distance

Table 1 presents the average throwing distance for the selected trials, revealing a significant difference between the two trials ( $p < 0.001$ , ES = 3.28).

TABLE 1 Means and standard deviations of official distance.

Trial	Official distance
Long (m)	62.404 ± 6.153
Short (m)	57.111 ± 5.821
<i>P</i> -value	<0.001
Cohen's d	3.277

Long, the long distance trials.  
Short, the short distance trials.

### Difference in hammer speed

Figure 2A shows the hammer velocity curve from the instant the right foot first takes off to the instant the hammer is released. It demonstrates that the hammer velocity curves of the two trials began to diverge following the first turn. Figure 2B shows a statistically significant difference ( $p < 0.05$ ,  $ES = 1.42$ ) was observed in the hammer velocity at the instant of hammer release and in the total velocity increment during the double support phase. A non-significant difference ( $p > 0.05$ ,  $ES = 0.06$ – $0.24$ ) was observed in velocity increment during the preliminary wind and the total single support phase between the long and short trials.

### Difference in hammer rotation duration

Table 2 presents the differences in rotation duration between single and double support phases in each turn. There were no significant differences in the duration during the double support phase in any turn between the long and short trials ( $p > 0.05$ ,  $ES =$

$0.08$ – $0.23$ ). The long trials had a significant ( $p < 0.05$ ,  $ES = 0.42$ – $0.83$ ) shorter duration in the 1<sup>st</sup> and 4<sup>th</sup> turn and the total of single support phases, compared to the shorter trials.

### Difference in hammer horizontal azimuth angle

Table 3 displays the differences in the horizontal azimuth angle of the hammer at critical instants during the 1st to the 4th turns. The non-significant difference was observed in the horizontal azimuth angle between long and short trials at the right foot takeoff, the highest point, and the lowest point of the hammerhead ( $p > 0.05$ ,  $ES = 0.06$ – $0.36$ ). At the right foot touchdown, the long trials had a significantly lower angle in the 2nd, 3rd, and 4th turns compared to the short trials ( $p < 0.05$ ,  $ES = 0.46$ – $0.57$ ).

### Difference in hammer rotation radius

Table 4 shows the differences in the hammer rotation radius at critical instants from the 1st to the 4th turns. At the right foot takeoff, the hammer rotation radius of the long trials was significantly larger in the 2nd turn compared to the short trials ( $p < 0.05$ ,  $ES = 0.48$ ). At the highest point of the hammerhead, the hammer rotation radius in the long trials was significantly larger from the 1st to the 3rd turns compared to the short trials ( $p < 0.05$ ,  $ES = 0.52$ – $0.73$ ). At the right foot touchdown, the hammer rotation radius in the long trials was significantly larger in the 2nd turn compared to the short trials ( $p < 0.05$ ,  $ES = 0.51$ ). There was no significant difference in the hammer rotation radius at the lowest point of the hammer head between the long and short trials ( $p > 0.05$ ,  $ES = 0.05$ – $0.21$ ).

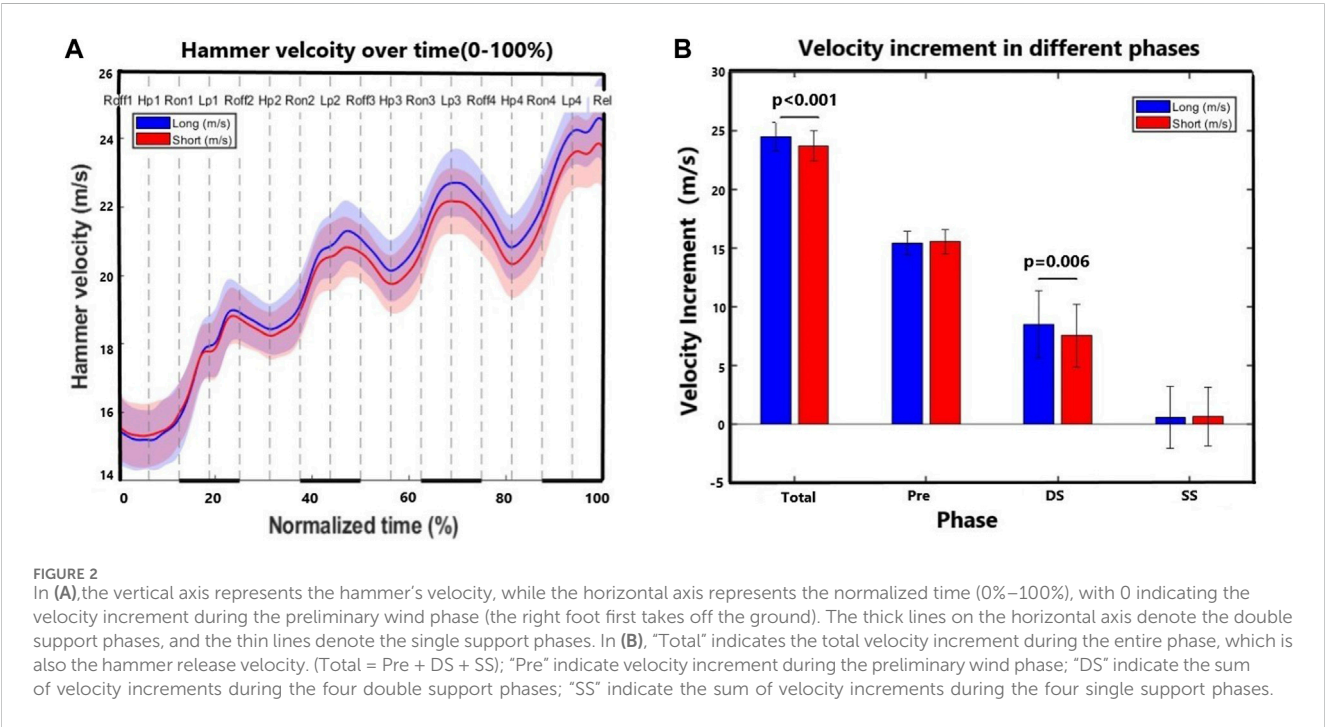


TABLE 2 Duration in the single and double support phases for each rotation

Phase	Trial	1st turn	2nd turn	3rd turn	4th turn	Sum
SS (s)	Long	0.306 ± 0.033	0.251 ± 0.027	0.235 ± 0.023	0.231 ± 0.023	1.037 ± 0.081
	Short	0.314 ± 0.035	0.257 ± 0.019	0.241 ± 0.022	0.239 ± 0.024	1.103 ± 0.080
	<i>P</i> -value	<b>0.038</b>	0.142	0.106	<b>0.043</b>	<b>&lt;0.001</b>
	<i>Cohen's d</i>	0.429	0.297	0.329	0.418	0.834
DS (s)	Long	0.339 ± 0.038	0.265 ± 0.024	0.240 ± 0.029	0.255 ± 0.026	1.099 ± 0.082
	Short	0.335 ± 0.035	0.272 ± 0.030	0.242 ± 0.028	0.258 ± 0.029	1.106 ± 0.078
	<i>P</i> -value	0.433	0.259	0.694	0.395	0.478
	<i>Cohen's d</i>	0.156	0.226	0.078	0.17	0.141

SS, the single support phase; DS, the double support phase.  
Bold values means Significant Difference.

TABLE 3 Horizontal azimuth angle at critical instants for each turn.

	Trial	1st turn	2nd turn	3rd turn	4th turn
Right foot takeoff (°)	Long	−7.683 ± 22.750	361.412 ± 20.728	718.373 ± 20.579	1,078.157 ± 20.547
	Short	−8.228 ± 23.534	363.961 ± 19.940	723.142 ± 23.030	1,082.967 ± 24.058
	<i>P</i> -value	0.717	0.217	0.110	0.077
	<i>Cohen's d</i>	0.072	0.248	0.325	0.361
High point (°)	Long	66.172 ± 15.784	438.255 ± 11.699	807.894 ± 10.719	1,175.025 ± 10.519
	Short	68.198 ± 14.707	439.839 ± 13.730	809.133 ± 14.692	1,174.101 ± 14.588
	<i>P</i> -value	0.092	0.263	0.449	0.576
	<i>Cohen's d</i>	0.344	0.225	0.151	0.111
Right foot Touchdown (°)	Long	147.900 ± 23.362	520.539 ± 13.426	884.641 ± 18.199	1,249.560 ± 15.248
	Short	151.840 ± 23.925	524.938 ± 16.577	891.625 ± 17.867	1,255.642 ± 20.754
	<i>P</i> -value	0.054	<b>0.020</b>	<b>0.008</b>	<b>0.027</b>
	<i>Cohen's d</i>	0.397	0.486	0.565	0.462
Low point (°)	Long	250.350 ± 14.138	623.964 ± 11.171	992.250 ± 10.913	1,354.978 ± 10.582
	Short	251.538 ± 14.445	624.904 ± 12.817	994.861 ± 10.947	1,354.301 ± 14.333
	<i>P</i> -value	0.362	0.623	0.195	0.782
	<i>Cohen's d</i>	0.182	0.098	0.261	0.055

Bold values means Significant Difference.

## Discussion

This study employed a distinctive design. Each participant's longest and shortest trials were selected from the same competition, typically occurring within an hour. This strategy aimed to minimize the influence of individual physical conditions and environmental factors on their performance. Consequently, the differences in official distance between the long and short trials observed in this study are primarily attributed to variations in the technique (Liu and Yu, 2022). The statistically significant differences in this study reflect a general pattern for the given variable between long and short trials among most participants.

We found that the difference in release speed between long and short trials was primarily attributed to the velocity increment during

the double support phase rather than the preliminary wind and single support phase, supporting our 1st hypothesis. Although the velocity increment during the preliminary wind constitutes the largest proportion of the hammer throw release velocity, and many technical articles on hammer throwing highlight the crucial role of the preliminary wind on a successful throw (Gutienez-Davila and Rojas-Ruiz, 2005; Kelley, 2014; Rozhkov et al., 2020), this study did not observe differences in velocity increment between the two trials in this stage. There might be two reasons for this. Firstly, the trials we selected were performed by the same athlete within the same competition. Athletes tend to maintain a relatively stable speed rhythm during the preliminary wind when their physical condition remains unchanged. Secondly, athletes maintain a stable stance with both feet in contact with the ground during this stage, and the



TABLE 4 Hammer rotation radius at critical instants for each rotation.

	Trial	1st turn	2nd turn	3rd turn	4th turn
Right foot takeoff (m)	Long	1.786 ± 0.040	1.804 ± 0.040	1.794 ± 0.038	1.796 ± 0.038
	Short	1.777 ± 0.037	1.789 ± 0.035	1.794 ± 0.038	1.789 ± 0.033
	<i>P-value</i>	0.170	<b>0.021</b>	0.948	0.108
	<i>Cohen's d</i>	0.277	0.482	0.013	0.327
High point (m)	Long	1.801 ± 0.046	1.792 ± 0.039	1.772 ± 0.040	1.760 ± 0.040
	Short	1.787 ± 0.037	1.772 ± 0.035	1.760 ± 0.037	1.749 ± 0.040
	<i>P-value</i>	<b>0.003</b>	<b>0.001</b>	<b>0.013</b>	0.176
	<i>Cohen's d</i>	0.565	0.728	0.524	0.273
Right foot touchdown (m)	Long	1.765 ± 0.043	1.770 ± 0.035	1.764 ± 0.037	1.763 ± 0.041
	Short	1.760 ± 0.043	1.757 ± 0.038	1.758 ± 0.032	1.758 ± 0.038
	<i>P-value</i>	0.227	<b>0.015</b>	0.219	0.384
	<i>Cohen's d</i>	0.203	0.512	0.247	0.174
Low point (m)	Long	1.710 ± 0.039	1.734 ± 0.040	1.748 ± 0.041	1.754 ± 0.046
	Short	1.705 ± 0.045	1.732 ± 0.039	1.746 ± 0.041	1.753 ± 0.042
	<i>P-value</i>	0.299	0.777	0.614	0.799
	<i>Cohen's d</i>	0.208	0.056	0.100	0.050

Bold values means Significant Difference.

velocity of the hammer is relatively slow, making it easier to control (Hay, 1978). Thus, even if there are technical deviations between the long and the short trials, athletes are able to accelerate the hammer. Once entering the turning stage, the increase in hammer velocity and the instability of body posture during the single support phase make it more difficult for athletes to control both their body and the hammer (Castaldi et al., 2022). Technical issues arising during the preliminary wind can easily affect the acceleration of the hammer during the double support phase, thereby diminishing its acceleration effect. The lack of significant differences in velocity increment during the single support phase may be related to the technical objective of this phase, which is to “surpass the equipment” in preparation for accelerating the hammer during the double support phase (Bartonietz, 2000). Hence, it becomes evident that when an athlete’s physical condition remains unchanged, ensuring a velocity increment during the double support phase is critical to maximizing their performance. From the analysis above, enhancing the hammer’s release velocity can be understood as increasing the velocity increment during the double support phase.

The results do not support our 2nd hypothesis totally, given that the duration of the double support phase did not differ significantly between the long and short trials, whereby the single support phase was indeed considerably shorter in the long trials. According to the momentum principle, we initially assumed that a longer duration of the double support phase would benefit the hammer’s acceleration. However, our findings indicate that the duration of the double support phase may be a minor factor contributing to the discrepancy in distance between short and long trials. This may be due to the difficulty in further accelerating the hammer after the hammerhead passes the lowest point in each turn, as the parallel alignment of the

shoulder and hip axes makes additional acceleration challenging (Brice et al., 2018). The hammer velocity curves also show that the hammer begins to decelerate from the low point after the second turn (Figure 2A). Therefore, deliberately extending the duration of the double support phase is of limited significance. Intriguingly, previous findings have shown that the muscle power from the upper limbs was not related to performance in hammer throw analyzing athletes from different athletic modalities (Zhao et al., 2023). Our results highlight the importance of analyzing the performance specifically in athletes from the same modality to get deeper insights into the performance determinants.

The results support our 3<sup>rd</sup> hypothesis that the horizontal azimuth angle of the hammer is smaller at critical instants (only at the right foot touchdown) in the long trials compared to the short trials. At the beginning of the double support phase, forming a maximally “wound-up” posture (with the hammer trailing far behind the feet, hips, and shoulders) is essential for effectively utilizing body power to accelerate the hammer (Hay, 1978). In this study, we define the horizontal azimuth angle of the hammer as the angle between the projection of the hammer in the horizontal plane and the negative *y*-axis. This angle gradually increases from the right foot takeoff to the right foot touchdown. A smaller azimuth angle at the right foot touchdown indicates that the hammer is more delayed in its spatial position (closer to the hammer’s high point), which may be more conducive to forming a wound-up posture where the body surpasses the hammer. Additionally, a smaller azimuth angle of the hammer at the right foot touchdown may also help extend the azimuthal angle covered by the hammer during the double support phase. Some researchers believe that expanding the range of azimuth angle covered by the hammer during the

double support phase, rather than the time spent, is key to enhancing the velocity increment of the hammer during this phase (Sedykh and Strelnitski, 2018).

The results support our 4th hypothesis that the radius of the hammer rotation is larger at the critical instants in the long trials compared to the short trials. In the previous paragraph, we discussed the advantages of a smaller hammer azimuth angle at the right foot touchdown for increasing the velocity increment during the double support phase. Athletes need to pay particular attention to certain technical aspects during the single support phase to achieve a smaller azimuth angle at this critical instant (Hay, 1978). As the hammer's horizontal azimuth angle increases continuously from the right foot takeoff to touchdown (during the single support phase), the horizontal azimuth angle of the hammer at the right foot touchdown is influenced by two factors: 1) The right foot landing speed: The shorter the time between the right foot takeoff and touchdown, the more the hammer head may lag relative to the body, which helps to reduce the hammer's horizontal azimuth angle. Table 2 shows that the long trials have a significantly shorter duration in the single support phase of the first and fourth turn, as well as a significantly shorter total single support duration, compared to the short trials; 2) The rotational radius of the hammer head during the single support phase: when the linear velocity remains constant, a larger rotational radius of the hammer head results in a lower angular velocity (Dapena, 1984), which may also cause the hammer head to lag more relative to the body at the instants of right foot touchdown. Table 4 shows that the rotational radius of the hammerhead at the instants of the right foot taking off and the hammerhead's highest point is significantly larger in the long trials compared to the short trials.

In comparing the difference in techniques between long and short trials, although differences in the velocity increment occurred during the double support phases, the single support phase indirectly influences the hammer head's acceleration performance during the double support phase. This reaffirms the primary technical objective of the single support phase to create space for accelerating the hammer during the double support phase. These findings suggest that athletes' shoulders should be relaxed and pulled well forward from the hammer head's lowest points to the instants the right foot taking off (Hay, 1978), with the torso slightly leaning towards the hammer to avoid sudden backward force applied through the shoulder and hip axes. Upon entering the single support phases, athletes should maintain their right foot close to the ground, move it alongside the left leg to reduce rotational inertia, and quickly land it.

One of the limitations of this study is the low sampling frequency, and the common differences in body movements among different throwers are still not fully understood. Further studies should employ within-subject designs with relatively large sample sizes to identify discrepancies in body characteristics. This will provide additional insights to improve understanding of hammer throwing techniques. In addition, we did not combine male athletes, who may have different biomechanics characteristics from female athletes (Konz and Hunter, 2015). Future research could compare male and female athletes to get a deeper insight into hammer throwing.

## Conclusion

During the process from the hammer head's lowest to highest points, athletes should focus on increasing the hammer head's rotational radius and accelerating the right foot's landing speed during the single support phase. This approach aims to reduce the hammer's horizontal azimuth angle at the right foot touchdown, enhance the acceleration performance during the double support phase, and increase the release speed.

## Data availability statement

The original contributions presented in the study are included in the article/supplementary material, further inquiries can be directed to the corresponding author.

## Ethics statement

The studies involving humans were approved by Beijing Sport University Research Ethics Review Board. The studies were conducted in accordance with the local legislation and institutional requirements. Written informed consent for participation in this study was provided by the participants' legal guardians/next of kin. The manuscript presents research on animals that do not require ethical approval for their study. Written informed consent was obtained from the individual(s) for the publication of any potentially identifiable images or data included in this article.

## Author contributions

JH: Writing—original draft, Writing—review and editing. LP: Writing—review and editing. JL: Writing—review and editing. YS: Software, Writing—review and editing. WL: Writing—review and editing.

## Funding

The author(s) declare that no financial support was received for the research, authorship, and/or publication of this article.

## Conflict of interest

The authors declare that the research was conducted in the absence of any commercial or financial relationships that could be construed as a potential conflict of interest.

## Publisher's note

All claims expressed in this article are solely those of the authors and do not necessarily represent those of their affiliated organizations, or those of the publisher, the editors and the reviewers. Any product that may be evaluated in this article, or claim that may be made by its manufacturer, is not guaranteed or endorsed by the publisher.

## References

- Abdel-Aziz, Y. I., Karara, H. M., and Hauck, M. (2015). Direct linear transformation from comparator coordinates into object space coordinates in close-range photogrammetry. *Photogrammetric Eng. and Remote Sens.* 81 (2), 103–107. doi:10.14358/PERS.81.2.103
- Bartonietz, K. (2000). “Hammer throwing: problems and prospects,” in *Biomechanics in sport: performance enhancement and injury prevention*. Editor V. Zatsiorsky (Wiley), 458–486.
- Brice, S. M., Ness, K. F., Everingham, Y. L., Rosemond, D., and Judge, L. W. (2018). Analysis of the separation angle between the thorax and pelvis, and its association with performance in the hammer throw. *Int. J. Sports Sci. and Coach.* 13 (6), 993–1000. doi:10.1177/1747954118787490
- Brice, S. M., Ness, K. F., and Rosemond, D. (2015). Validation of a method to predict hammer speed from cable force. *J. Sport Health Sci.* 4 (3), 258–262. doi:10.1016/j.jshs.2013.11.005
- Brice, S. M., Ness, K. F., Rosemond, D., Lyons, K., and Davis, M. (2008). Development and validation of a method to directly measure the cable force during the hammer throw. *Sports Biomech.* 7 (2), 274–287. doi:10.1080/14763140701841902
- Castaldi, G. M., Borzuola, R., Camomilla, V., Bergamini, E., Vannozzi, G., and Macaluso, A. (2022). Biomechanics of the hammer throw: narrative review. *Front. Sports Act. Living* 4, 853536. doi:10.3389/fspor.2022.853536
- Dapena, J. (1984). The pattern of hammer speed during a hammer throw and influence of gravity on its fluctuations. *J. Biomechanics* 17 (8), 553–559. doi:10.1016/0021-9290(84)90086-1
- Dapena, J. (1986). A kinematic study of center of mass motions in the hammer throw. *J. Biomechanics* 19 (NO.2), 147–158. doi:10.1016/0021-9290(86)90144-2
- Dapena, J. (1989). Some biomechanical aspects of hammer throwing. *Athl. Coach* 23 (3), 12–19.
- Dapena, J., and Feltner, M. E. (1989). Influence of the direction of the cable force and of the radius of the hammer path on speed fluctuations during hammer throwing. *J. Biomechanics* 22 (6–7), 565–575. doi:10.1016/0021-9290(89)90008-0
- Dapena, J., and McDonald, C. (1989). A three-dimensional analysis of angular momentum in the hammer throw. *Med. Sci. Sports Exerc.* 21 (2), 206–220. doi:10.1249/00005768-198904000-00015
- Gutiérrez-Davila, M., and Rojas-Ruiz, F. (2005). Comparative biomechanical analysis between hammer throwers of different performance levels. *J. Hum. Mov. Stud.* 49 (1), 31–48.
- Hay, J. (1978). *The biomechanics of sports techniques*. Prentice-Hall.
- Hill, A. V. (1922). The maximum work and mechanical efficiency of human muscles, and their most economical speed. *J. Physiology* 56 (1–2), 19–41. doi:10.1113/jphysiol.1922.sp001989
- Hirose, K., Byun, K. O., Maeda, K., and Ogata, M. (2016). “The relationship between the duration time of turn and the throwing record in the men’s hammer throw,” in ISBS-Conference Proceedings Archive, Tsukuba, Japan, July 18–22, 2016.
- Kelley, J. (2014). A camera calibration method for a hammer throw analysis tool. *Procedia Eng.* 72, 74–79. doi:10.1016/j.proeng.2014.06.002
- Knudson, D. (2007). *Fundamentals of biomechanics* (vol. 183). Springer.
- Konz, S. M., and Hunter, I. (2015). “Technique comparison of male and female hammer throwers,” in ISBS-Conference Proceedings Archive, Poitiers, France, June 29 – July 03, 2015.
- Liu, H., and Yu, B. (2022). Rotation of the thrower-discus system and performance in discus throwing. *Sports Biomech.* 23 (5), 624–639. doi:10.1080/14763141.2021.1880619
- Maheras, A. (2010). Reassessing velocity generation in hammer throwing. *IAAF. New Stud. Athl.* 24 (4), 71–80.
- Maheras, A. (2018). Biomechanical observations in hammer throwing. *Tech. Track Field and Cross Ctry.* 11 (3), 19–30.
- Murofushi, K., Babbitt, D., and Ohta, K. (2017). Supplemental exercises for core stability which utilize the concept of parametric oscillation in the hammer throw. *Strength and Cond. J.* 39 (4), 71–81. doi:10.1519/ssc.0000000000000299
- Murofushi, K., Sakurai, S., Umegaki, K., and Kobayashi, K. (2005). Development of a system to measure radius of curvature and speed of hammer head during turns in hammer throw. *Int. J. Sport Health Sci.* 3, 116–128. doi:10.5432/ijshs.3.116
- Murofushi, K., Sakurai, S., Umegaki, K., and Takamatsu, J. (2007). Hammer acceleration due to thrower and hammer movement patterns. *Sports Biomech.* 6 (3), 301–314. doi:10.1080/14763140701489843
- Otto, R. (1992). Sedykh photo sequence. *New Stud. Athl.* 7 (3), 51–65.
- Rozhkov, V., Pavlenko, V., Okun, D., Shutieiev, V., Shutieieva, T., and Lenska, O. (2020). Relationship between the biomechanical parameters technique for preliminary swings among elite hammer throwers. *J. Phys. Educ. Sport* 20, 2258–2262. doi:10.7752/jpes.2020.s3303
- Ruiz, F. J. R., and Dávila, M. G. (2009). The relation between angular displacement of the hammer in the double support phase and its velocity in the hammer throw. *J. Hum. Sport Exerc.* 4 (3), 254–261. doi:10.4100/jhse.2009.43.07
- Sedykh, Y., and Strelnitski, V. (2018). *Art and Science of hammer throw*. Los Altos, CA: Bookbaby.
- Yu, B., Gabriel, D., Noble, L., and An, K.-N. (1999). Estimate of the optimum cutoff frequency for the Butterworth low-pass digital filter. *J. Appl. Biomechanics* 15 (3), 318–329. doi:10.1123/jab.15.3.318
- Zhao, K., Siener, M., Zhao, Y., and Hohmann, A. (2023). Physical fitness and motor competence performance characteristics of Chinese elite youth athletes from four track and field throwing disciplines—a cross-sectional study. *Front. Physiology* 14, 1267804. doi:10.3389/fphys.2023.1267804



## OPEN ACCESS

## EDITED BY

Sabine Kling,  
University of Bern, Switzerland

## REVIEWED BY

Adrian Podoleanu,  
University of Kent, United Kingdom  
Jiaqiu Wang,  
London South Bank University, United Kingdom

## \*CORRESPONDENCE

Chunhui Li,  
✉ c.li@dundee.ac.uk

RECEIVED 14 July 2024

ACCEPTED 05 September 2024

PUBLISHED 20 September 2024

## CITATION

Zhang T, Zhang Y, Liao J, Shepherd S, Huang Z,  
Macluskey M and Li C (2024) Quantitative  
assessment of the oral microvasculature using  
optical coherence tomography angiography.  
*Front. Bioeng. Biotechnol.* 12:1464562.  
doi: 10.3389/fbioe.2024.1464562

## COPYRIGHT

© 2024 Zhang, Zhang, Liao, Shepherd, Huang,  
Macluskey and Li. This is an open-access article  
distributed under the terms of the [Creative  
Commons Attribution License \(CC BY\)](#). The use,  
distribution or reproduction in other forums is  
permitted, provided the original author(s) and  
the copyright owner(s) are credited and that the  
original publication in this journal is cited, in  
accordance with accepted academic practice.  
No use, distribution or reproduction is  
permitted which does not comply with these  
terms.

# Quantitative assessment of the oral microvasculature using optical coherence tomography angiography

Tianyu Zhang<sup>1,2</sup>, Yilong Zhang<sup>1</sup>, Jinpeng Liao<sup>2</sup>, Simon Shepherd<sup>3</sup>,  
Zhihong Huang<sup>2</sup>, Michaelina Macluskey<sup>3</sup> and Chunhui Li<sup>1\*</sup>

<sup>1</sup>Centre for Medical Engineering and Technology (CMET), School of Science and Engineering, University of Dundee, Dundee, United Kingdom, <sup>2</sup>Healthcare Engineering, School of Physics and Engineering Technology, University of York, York, United Kingdom, <sup>3</sup>School of Dentistry, University of Dundee, Dundee, United Kingdom

**Introduction:** Early diagnosis of oral squamous cell carcinoma can greatly improve treatment success rate and patient survival. Although Optical Coherence Tomography (OCT) based Angiography (OCTA) is a promising in vivo technique in oral imaging, there is a need for objective assessment of oral microvasculature.

**Methods:** This study aimed to demonstrate a comprehensive methodology of quantitative assessing OCTA intraoral scanning results to provide measurable, reproducible data and to avoid subjective visual interpretations. Data were collected from 37 healthy subjects in total across four intraoral sites—buccal mucosa (n = 32), labial mucosa (n = 24), floor of the mouth (n = 13), and hard palate (n = 8)—using a non-invasive swept-source OCT system. Four quantitative metrics—vessel area density, vessel skeleton density, vessel diameter index, and a newly proposed weighted Tortuosity Index—were used to assess OCTA images in oral applications.

**Results:** The quadruple quantitative assessment's repeatability was evaluated to be reliable. Analysis of a benign ulcer case revealed differences in these metrics compared to healthy cases.

**Discussion/Conclusion:** In conclusion, we demonstrated a comprehensive method to quantify microvasculature in the oral cavity, showing considerable promise for early diagnosis and clinical management of oral diseases.

## KEYWORDS

optical coherence tomography, angiography, quantitative analysis, oral squamous cell carcinoma, OCTA, intraoral imaging, oral microcirculation

## 1 Introduction

Oral squamous cell carcinoma (OSCC) represents a significant health concern due to its aggressive nature and adverse outcomes (Chamoli et al., 2021). Early diagnosis is crucial in managing OSCC, as it greatly reduces morbidity and improves the chances of successful treatment and patient survival (Sciubba, 2001; Feller and Lemmer, 2012; Mortazavi et al., 2014). The unique vascular patterns associated with tumor growth provide critical insights into the malignancy's progression and status (Macluskey et al., 2000; Sasahira and Kiritani,

2018; Tirelli et al., 2018). Specifically, vessel density, diameter, and tortuosity were found related to oral diseases (Ravi et al., 1998; Djaberli et al., 2013; Sasahira and Kirita, 2018). In this context, the study of microvasculature within OSCC lesions has emerged as a promising diagnostic avenue. Imaging modalities for assessing the oral microvasculature have seen significant developments in past decade, and has included high-frequency ultrasound (Huang et al., 2017; Fogante et al., 2022), real-time optical vascular imaging (RTOVI) (Bastos et al., 2022) and video-capillaroscopy (Scardina et al., 2007). However, high-frequency ultrasound is limited by its resolution compared to optical imaging techniques, while RTOVI is challenged by a restricted field of view. Video-capillaroscopy has only a shallow penetration depth due to using visible light for imaging. These limitations may impact on the ability of these techniques to capture the nuanced vascular changes at the earliest stages of OSCC. Therefore, there is a pressing need for more advanced, non-invasive imaging technologies that can accurately visualize and quantify microvascular alterations in OSCC, facilitating early and more effective diagnosis.

Optical coherence tomography (OCT) based angiography (OCTA) is a relatively recent innovation in imaging technology which has been developed for applications in oral diagnostics (Choi and Wang, 2014; Chen and Wang, 2017; Tsai et al., 2017; Le et al., 2018; 2022; Wei et al., 2018; Zhang et al., 2023). As a non-invasive imaging technique, OCTA offers high-resolution, three-dimensional views of microvascular structures without the need for contrast agents (Kashani et al., 2017). This technology operates on the principle of capturing the motion contrast of red blood cells, thereby providing detailed images of blood flow within tissues (Chen and Wang, 2017). These emerging applications highlight OCTA's growing significance in oral healthcare, providing a new frontier in the imaging-based assessment of oral diseases.

While OCTA, this non-invasive functional imaging technique has shown promises in oral imaging, there remains a need for objective assessment techniques of captured oral angiograms. Quantitative assessments of OCT angiograms have been implemented in other applications, e.g., in cardiology (Xie et al., 2024), dermatology (Untracht et al., 2021; Manfredini et al., 2023) and ophthalmology (Reif et al., 2012; Agemy et al., 2015; Jia et al., 2015; Chu et al., 2016; Engberg et al., 2020; Untracht et al., 2021; Wang et al., 2022), which can avoid subjective visual interpretations and provide measurable, reproducible data. For the analysis of microvascular structures, the aforementioned studies introduced several parameters, such as vessel area density (VAD) (Reif et al., 2012; Jia et al., 2015), vessel skeleton density (VSD) (Reif et al., 2012; Agemy et al., 2015), vessel diameter index (VDI) (Chu et al., 2016), and tortuosity index (TI) (Lee et al., 2018; Martelli and Giacomozzi, 2021). These metrics could bring advancements in characterizing the various vascular diseases. VAD offers insights into the density of the vascular network by measuring the area occupied by vessels (Reif et al., 2012; Jia et al., 2015; Chu et al., 2016), while VSD focuses on the length of these vessels, providing a different perspective on vascular distribution (Reif et al., 2012; Agemy et al., 2015; Chu et al., 2016). The VDI can contribute further by analyzing the average diameter of vessels (Chu et al., 2016). These parameters are vital in identifying and quantifying subtle vascular changes that may indicate disease presence or progression. However, it is important to note that each of these parameters, while valuable, might only

provide a partial view of the vascular landscape. For instance, VAD and VSD might not fully capture the dynamic aspects of blood flow or the functional status of the vessels (Chu et al., 2016). Similarly, VDI, dependent on image resolution and quality, might have limitations in accurately portraying the intricate details of microvascular architecture. Despite these limitations, these metrics collectively offer a comprehensive framework for assessing and understanding vascular alterations in various pathological states using OCTA (Chu et al., 2016). In addition, the tortuosity of the blood vessels is a significant factor for physiological features in diseases, which has been studied since Leonardo Da Vinci's works (Ciurică et al., 2019; Wells and Crowe, 2004; Kemp, 2019). A number of medical conditions or biological processes, such as aging, atherosclerosis, hypertension, genetic defects, and diabetes mellitus, can contribute to the development of increased or severe vessel tortuosity according to clinical studies (Del Corso et al., 1998; Pancera et al., 2000; Hiroki et al., 2002; Owen et al., 2008; Kahe et al., 2020). Although several metrics, TI, average TI and Vessel Complex Index (VCI), have been introduced for assessing vasculature tortuosity, none of these metrics include the factor of the vessel diameter, which is crucial for understanding the varying physiological significance of blood vessels of different diameters (Han, 2012; Yoon et al., 2023). Therefore, a novel approach to assess the vascular tortuosity factoring in the vessel diameter is necessary for quantitative assessment of microvasculature.

In our research, we have employed a set of quantitative metrics, VAD, VSD, and VDI, to assess OCTA images in oral applications. In addition, we have applied a weighted Tortuosity Index (WTI) calculation to assess the tortuosity of the blood vessels. These metrics have been chosen to provide a multi-dimensional understanding of the microvascular structures within the oral cavity to enhance the diagnostic capabilities and to offer clinicians a more nuanced view of vascular changes associated with various oral diseases. This approach enhances a detailed assessment of microvascular structures, which has the potential to contribute to improved monitoring and treatment of oral disease. In addition, to ensure that OCTA using these metrics can be effective as a diagnostic tool for diseases, it is crucial to understand the imaging within the context of healthy tissues.

## 2 Methods and materials

### 2.1 OCT system

The OCT system used in this study was introduced previously (Zhang et al., 2023), which was a lab-built, portable and non-invasive swept-source OCT (SS-OCT) system with a handheld scanning probe. The diagram of the SS-OCT system is shown in Figure 1. The laser source of this SS-OCT system is a vertical-cavity surface-emitting laser (VCSEL) source (SL132120, Thorlabs Inc., Newton, MA, United States), with a central wavelength of 1,300 nm, and a bandwidth of 100 nm. The imaging lens system was a two-lens system (AC127-075-C and AC254-125-C, Thorlabs Inc., Newton, MA, United States) designed for intraoral imaging, providing a lateral resolution of 39  $\mu\text{m}$ . The theoretical axial resolution was 7.5  $\mu\text{m}$  in air. The field of view was 5.25 mm  $\times$  5.25 mm for the intraoral scanning probe.



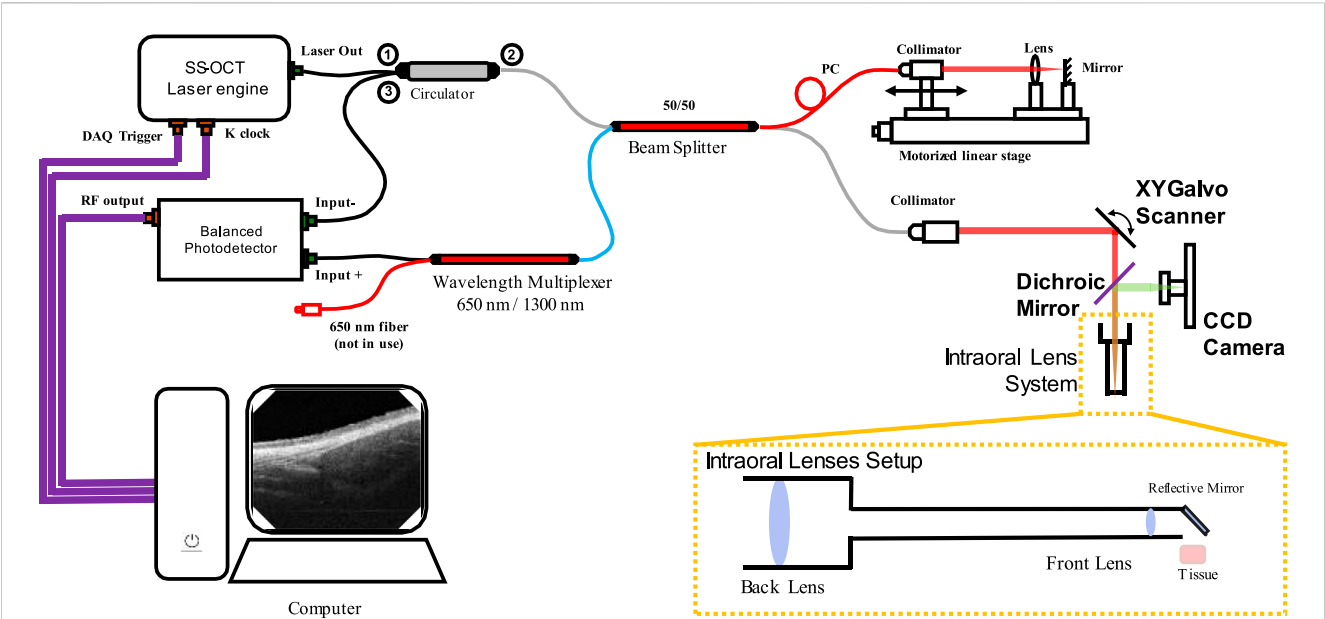


FIGURE 1  
The optical diagram of the SS-OCT system used in this study. (CCD: Charge-coupled device).

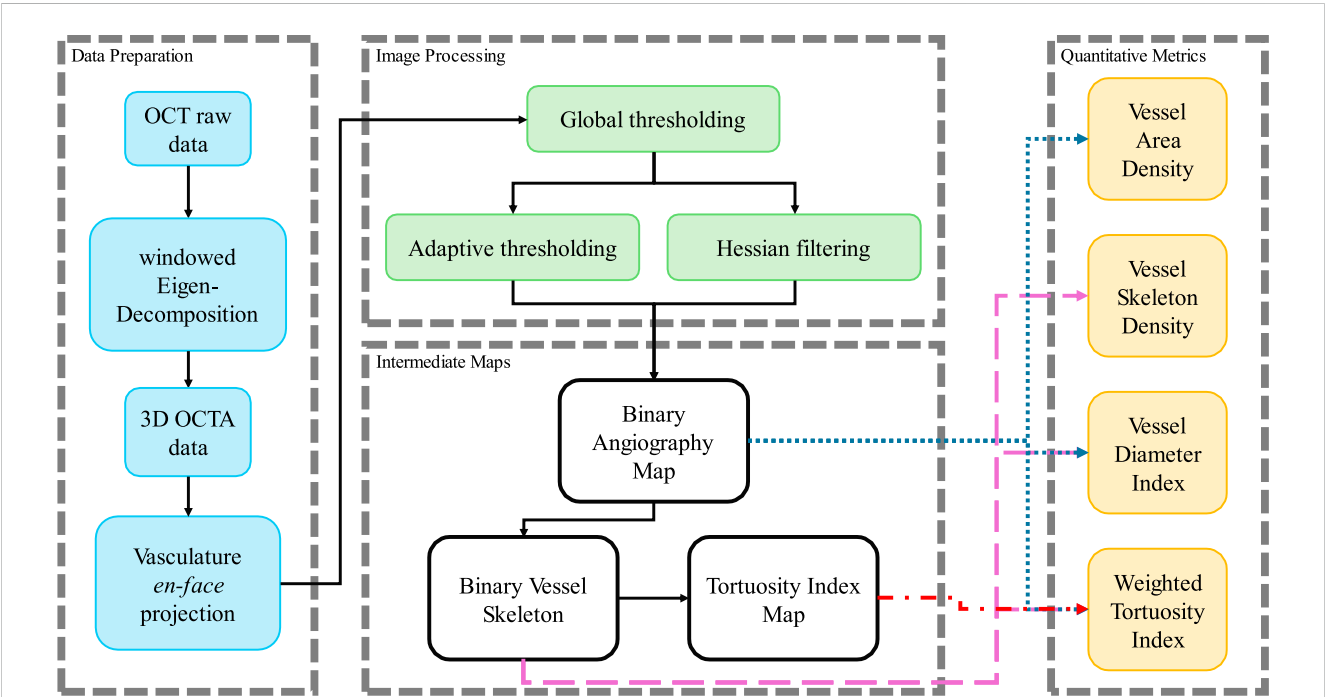


FIGURE 2  
The processing flow chart in this study to process the OCTA data and calculate the quantitative metrics.

## 2.2 Data collection

In this study, a total of 37 healthy participants were involved in the intraoral acquisition, which included four different intraoral sites, buccal mucosa, labial mucosa, floor of the mouth and hard palate. Due to different acceptances of the intraoral acquisition among participants, each scanning location had different numbers

of datasets. Specifically, the buccal mucosa acquisitions involved 32 participants. The labial mucosa acquisitions involved 24 participants. The acquisition of the floor of the mouth involved 13 participants. Lastly, the hard palate acquisitions involved eight participants. This study was reviewed and approved by the Research Ethics Committee of the University of Dundee (UOD-SSREC-RPG-BioEng-2022-001).

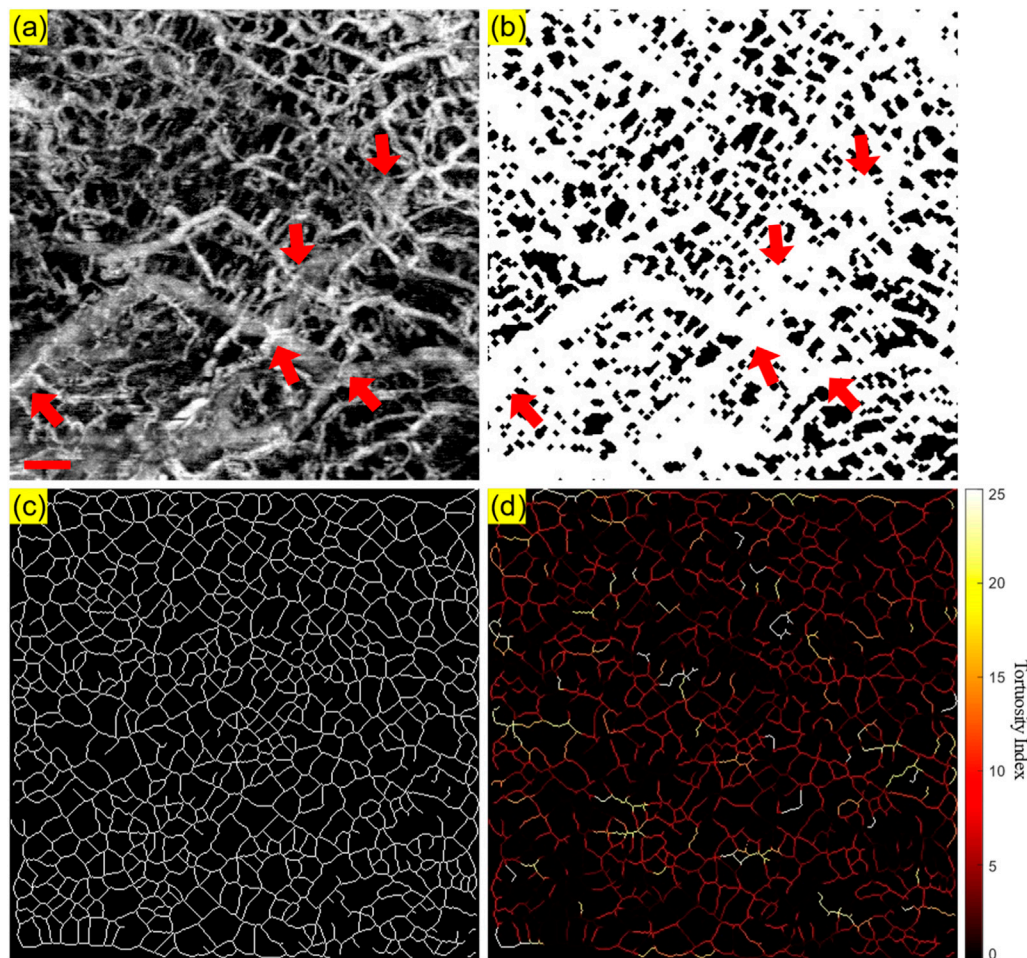


FIGURE 3

An illustrative OCTA dataset (healthy labial tissue) processed to generate the projection image and the three intermediate maps used for quantitative assessment: (A) The OCTA *en face* projection image with a red scale bar of 500 μm; (B) The binary angiography mask (BAM); (C) The binary vessel skeleton (BVS); (D) The Tortuosity Index (TI) map. The red arrows highlight the overlapping of blood vessels.

## 2.3 Data processing

The datasets acquired by this SS-OCT system contained four dimensions (4D), including three spatial dimensions and one temporal dimension. The size of the datasets was  $950 \times 400 \times 400 \times 4$  ( $Z \times X \times Y \times N$  in pixels, where  $Z$  was the axial dimension,  $X$  and  $Y$  were the lateral dimensions, and  $N$  was the temporal dimension). Several processing steps of data preparation were required to generate the intermediate maps, which would be needed for the quantification evaluation. The preparation flowchart is shown in Figure 2.

Firstly, the angiography reconstruction method, windowed Eigen-Decomposition (wED) (Zhang et al., 2022), was applied to the acquired 4D datasets, generating 3D volumes of angiography signals. Then, the 3D volumes would be compressed using Maximum Intensity Projection (Sato et al., 1998; Wang et al., 2018) to produce the *en face* projections. With the projection results of angiogram, the areas of angiography signals can be selected using global thresholding (Otsu, 1979), adaptive thresholding (Bradley and Roth, 2007), and Hessian Filter

(Frangi et al., 1998; Reif et al., 2012). The Otsu's method was used to determine the global threshold (Otsu, 1979). And then, after the combination of the adaptive thresholding (Bradley and Roth, 2007; Reif et al., 2012) and Hessian Filter (Frangi et al., 1998), the binary angiography masks (BAM) were generated and prepared for the OCTA quantification. With the BAM, the binary vessel skeletons (BVS) were generated (Lee et al., 1994; Kerschnitzki et al., 2013) while the BVS was processed to separate vessel segments and calculate the TI which generated the Tortuosity Index skeleton map. The intermediate maps are demonstrated in Figure 3. As shown in Figure 3B, BAM had the blood vessel areas as 1s, and the rest areas as 0s. BVS in Figure 3C where each blood vessel appeared as a distinct, one-pixel-wide line, contained the skeletons of the blood vessels in 1s, while the Tortuosity Index map in Figure 3D had the distribution of the TI for all vessel segments.

As shown in Figure 3, some overlapping of blood vessels can be observed, which can cause inaccurate quantitative assessments, especially for BVS. Therefore, an automatic Depth of Interest (DOI) selection algorithm was developed to divide one OCTA

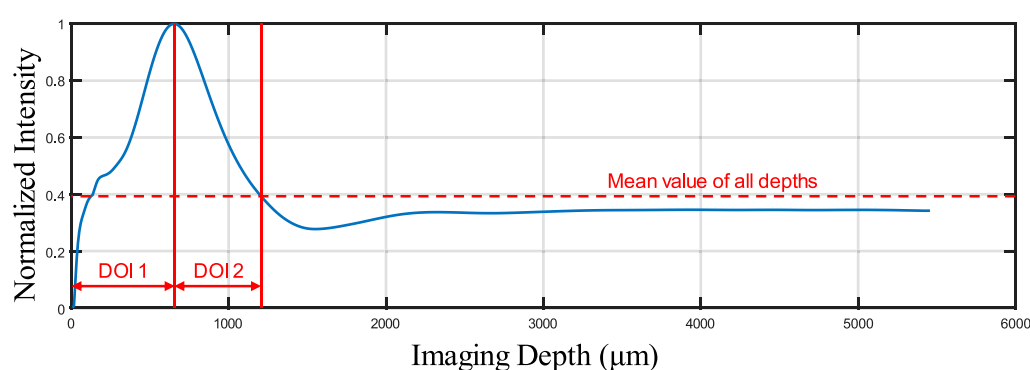


FIGURE 4  
The normalized signal intensity distribution on all imaging depths.

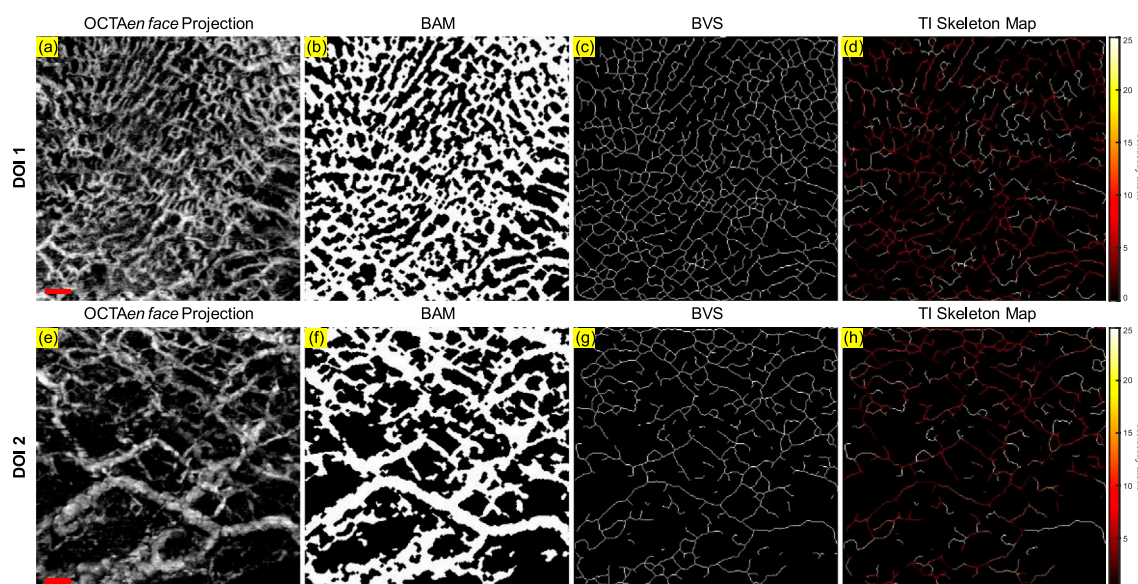


FIGURE 5  
The projection image and the three intermediate maps used for quantitative assessment for both DOI 1 and DOI 2: (A) The OCTA *en face* projection image of DOI 1 with a red scale bar of 500  $\mu\text{m}$ ; (B) The BAM of DOI 1; (C) The BVS of DOI 1; (D) The TI skeleton map of DOI 1; (E) The OCTA *en face* projection image of DOI 2 with a red scale bar of 500  $\mu\text{m}$ ; (F) The BAM of DOI 2; (G) The BVS of DOI 2; (H) The TI skeleton map of DOI 2.

dataset into two individual layers. As each volunteer will have different oral tissue thickness and signal attenuation, employing fixed-depth layer separation was considered an inappropriate method for solving this problem. In order to adapt to the different situations for all participants, the DOI was selected automatically depending on the average OCTA signal intensity at various depths. Specifically, for each 3D OCTA dataset of  $Z \times X \times Y$  in pixels, the averaging processing was applied on the  $X$  and  $Y$  axis, which can output an array of  $Z \times 1$ , the intensity distribution at all imaging depths as shown in Figure 4.

This automatic algorithm firstly would detect the end depth, where all OCTA signals attenuated and only noise remained, by finding the deepest location with the same intensity of the mean intensity of all depths. The layer separation depth was considered to be the location of the maximum intensity peak. Therefore, DOI 1 was selected from the top to the layer separation depth, while

DOI 2 was selected from the layer separation depth to the end depth. With two layers separated as DOI 1 and 2, both can be used to generate the intermediate maps for quantitative assessments which is shown in Figure 5. The OCTA quantitative metrics would be calculated from the intermediate maps for both DOIs.

As shown in Figure 2, the binary images were generated from the image processing, and then were used to calculate the OCTA quantitative metrics. For VAD, the area of the blood vessels divided by the whole area of the field of view was utilized as the density of the vascular area, which can be shown as Equation 1,

$$\text{VAD} = \frac{\sum_{x=1}^X \sum_{y=1}^Y \text{BAM}_{(x,y)}}{X \times Y} \times 100\% \quad (1)$$

where  $X$  and  $Y$  are the number of pixels on two axes of the *en face* projection images,  $x$  and  $y$  are the coordinates of the binary mask



(Reif et al., 2012; Jia et al., 2015). VSD was the density of the vessel skeleton areas, which can be calculated as Equation 2.

$$VSD = \frac{\sum_{x=1}^X \sum_{y=1}^Y BVS_{(x,y)}}{X \times Y} \times 100\% \quad (2)$$

As metrics of density, VAD and VSD were both presented in percentages (Reif et al., 2012; Agemy et al., 2015; Chu et al., 2016). Both the BAM and BVS were used to calculate the VDI. The ratio of the blood vessels' areas to the vessel skeletons was defined as VDI which is shown in Equation 3,

$$VDI = \frac{\sum_{x=1}^X \sum_{y=1}^Y (BVS_{(x,y)} \times dis_{Eu(x,y)} \times 2)}{\sum_{x=1}^X \sum_{y=1}^Y (BVS_{(x,y)})} \quad (3)$$

where  $dis_{Eu(x,y)}$  is the shortest Euclidean distance from the pixel  $(x, y)$  to the vessel edge for all pixels on the vessel skeletons (Maurer et al., 2003). The unit of VDI is pixels, while it can further be converted into micrometers using the pixel transverse size, which was done for all results in this study (Chu et al., 2016). TI represents the tortuosity of the blood vessels, which can be calculated by the average ratio of the vessel length divided by the Euclidean distance for all vessel segments (Lee et al., 2018; Martelli and Giacomozzi, 2021), which is shown in Equation 4,

$$TI = \left( \frac{SegmentLength}{EuclideanDistance} - 1 \right) \times 100 \quad (4)$$

where *SegmentLength* and *EuclideanDistance* are respectively the length and the Euclidean distance of each vessel segment. After calculating the TI values for all vessel segments, a TI skeleton map can be generated. However, in the analysis of vascular tortuosity, it is essential to account for the varying physiological significance of blood vessels of different diameters (Han, 2012; Yoon et al., 2023). This approach aligns with established practices in vascular research where the relative contribution of each vessel is proportionate to its diameter, reflecting its functional importance (Han, 2012; Yoon et al., 2023). Therefore, we utilized a weighted TI (WTI) method, that uses the diameter of each vessel segment as a weight parameter during the averaging which is shown in Equation 5,

$$WTI = \frac{\sum_{n=1}^N VDI_n \times \left( \frac{SegmentLength_n}{EuclideanDistance_n} - 1 \right)}{\sum_{n=1}^N VDI_n} \times 100 \quad (5)$$

where  $VDI_n$  is the VDI of the  $n$ th separated vessel segment,  $N$  is the total number of the vessel segments,  $SegmentLength_n$  and  $EuclideanDistance_n$  are respectively the length of the  $n$ th vessel segment and the Euclidean distance of the two endpoints of the  $n$ th vessel segment. WTI does not have a unit. To the best of our knowledge, this is the first instance where WTI has been employed to quantify the morphological characteristics of the oral microvasculature using OCT, although other metrics, such as vessel complex index, fractal dimension, and VI have been previously used in ophthalmological applications (Reif et al., 2012; Chu et al., 2016; Lee et al., 2018; Martelli and Giacomozzi, 2021). The proposed metric, WTI, to assess the tortuosity of blood vessels was evaluated, which was introduced in the Appendix.

## 3 Results

### 3.1 Quantitative maps in a healthy case

A clinically healthy labial mucosa dataset was shown in Figure 6 as a demonstration of the quantitative assessments of oral tissue OCTA imaging. Figure 6A shows the gray-scale OCTA *en face* projection of DOI 1, which was segmented by the automatic DOI selection algorithm. Figure 6B illustrates the quantitative heatmap of vessel density of Figure 6A, which was generated by using a moving kernel calculating the average vessel density within the kernel. All quantitative heatmaps were generated using the same method. Figure 6C displays the quantitative heatmap of vessel diameter in micrometers of Figure 6A, while Figure 6D shows the quantitative heatmap of TI of Figure 6A. Similarly, Figures 6E–H presents the same quantitative results of DOI 2.

Using the quantitative assessment methods above, VAD, VSD, VDI, and WTI were calculated from the OCTA projection images. For DOI 1, this healthy labial mucosa dataset output VAD of 53.26%, VSD of 7.00%, VDI of 91.04  $\mu$ m, and WTI of 20.30. Within DOI 2, the VAD and VSD decreased to 46% and 5.40%, which corresponded to the visual observation of the grayscale OCTA projection. An increase in the vessel diameter in DOI 2 also saw the VDI's rise, while the WTI decreased to 18.36 in DOI 2.

### 3.2 Evaluation of repeatability

As a demonstration for the repeatability of the quantitative assessment of OCTA imaging on oral tissues, a side-by-side comparison of two successive OCTA acquisitions was shown in Figure 7. The grayscale OCTA *en face* projection of DOI 1 is shown in Figures 7A, B, corresponding to Scan 1 and Scan 2 respectively. The corresponding quantitative heatmaps of vessel density are illustrated in Figures 7C, D. The BAMs of these scans are depicted in Figures 7E, F. Additionally, the quantitative heatmaps of vessel diameter for Scan 1 and Scan 2 are presented in Figures 7G, H, respectively. The TI skeleton maps of Scan 1 and Scan 2 are shown in Figures 7I, J, with the quantitative heatmaps of TI for these scans illustrated in Figures 7K, L. Similarly, the grayscale OCTA *en face* projections and quantitative results of DOI 2 are displayed in Figures 7M–X.

The quantitative maps shared the visual similarity between two successive scans. The quantitative metrics were calculated for both Scan 1 and Scan 2 as well, which were listed in Table 1. In addition, the coefficient of variation for each metric was calculated between two scans, which was considered to have reliable repeatability according to published standard (Chu et al., 2016).

### 3.3 Building database for healthy subjects

Aggregating a database of normal oral tissue OCTA ran concurrently within this study. A large database can be used for quantitative assessment to establish a guideline of the quantitative metrics for healthy oral tissue, which can be used to compare diseased cases in future studies. Currently, 32 healthy participants have been enrolled for buccal mucosa acquisitions. The quantitative

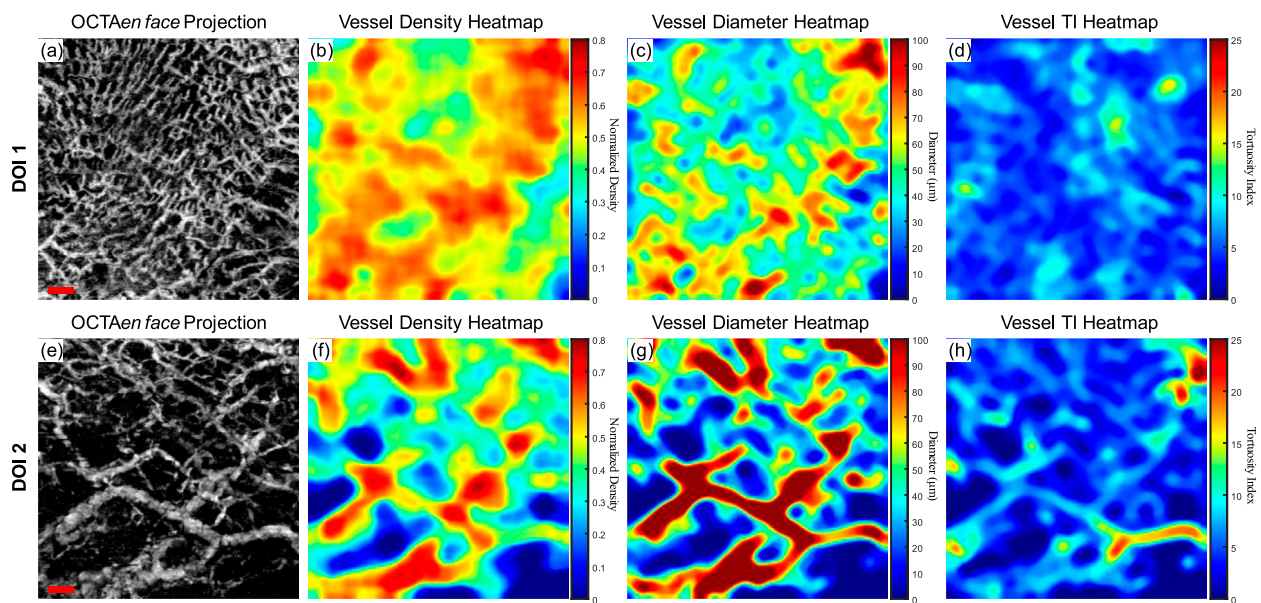


FIGURE 6

The quantitative maps of a normal labial mucosa dataset. (A) The gray-scale OCTA *en face* projection of the DOI 1 segmented by the automatic DOI selection algorithm with a scale bar of 500  $\mu\text{m}$ ; (B) The quantitative heatmap of vessel density of (A), which was calculated using a moving kernel; (C) The quantitative heatmap of vessel diameter in micrometers of (A) using a moving kernel; (D) The quantitative heatmap of TI of (A) using a moving kernel; (E) The gray-scale OCTA *en face* projection of the DOI 2 segmented by the automatic DOI selection algorithm with a scale bar of 500  $\mu\text{m}$ ; (F) The quantitative heatmap of vessel density of (E), which was calculated using a moving kernel; (G) The quantitative heatmap of vessel diameter in micrometers of (E) using a moving kernel; (H) The quantitative heatmap of TI of (E) using a moving kernel.

metrics of buccal mucosa datasets were listed in Table 2. In addition, 24 healthy individuals have participated in the collection of labial mucosa datasets, and the corresponding quantitative metrics are provided in Table 3. Furthermore, 13 healthy subjects have been included in the acquisition of datasets from the floor of the mouth, with the metrics outlined in Table 4. Lastly, eight healthy participants have been involved in the acquisition of hard palate datasets, with the quantitative metrics presented in Table 5.

### 3.4 Quantitative analysis of microvascular in benign labial ulcer

Although a large database of oral mucosal tissue in diseased states would be needed in future, an abnormal dataset was presented below in comparison with the quantitative results of normal database. Figure 8 shows the quantitative heatmaps of a labial mucosa dataset from a participant who developed a benign oral ulcer at the time of acquiring the dataset in Figure 8. The ulcer area was highlighted with the dashed lines. The 3D OCTA dataset was separated into two DOIs, and generated heatmaps of vessel density, vessel diameter, and vessel TI, in the same way of Figure 6.

Compared to the healthy labial mucosa dataset results, the ulcer metrics reveal distinct differences across various parameters. For DOI 1, the ulcer's VAD of 35.07% is lower than the healthy mean VAD of 49.97%, indicating a reduced density of blood vessels in the ulcerated tissue which can also be visually observed in the grayscale OCTA projection. For DOI 2, the ulcer's VAD of 46.24% is closer to the healthy mean of 44.11%, but still slightly elevated, suggesting a potential increase in vascular proliferation in the ulcerated region at

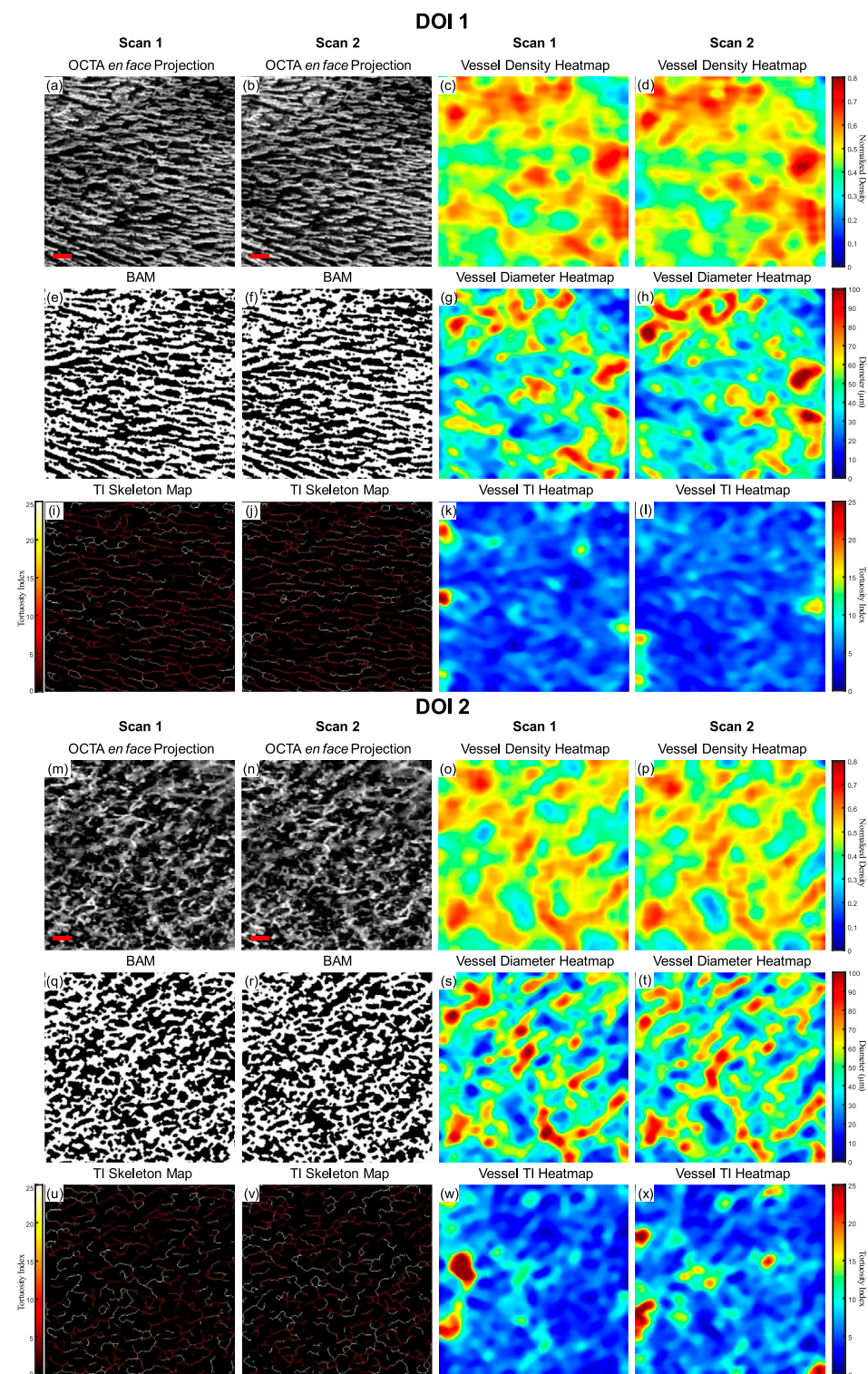
greater depths. The VSD for DOI 1 in the ulcer case is 5.10%, which is lower than the healthy mean of 6.64%, reflecting fewer vessel segments in the ulcerated tissue which corresponds to the OCTA projection. For DOI 2, the ulcer's VSD of 5.60% is higher than the healthy mean of 4.89%, suggesting an increased segmentation in the vessel network at this depth. The ulcer's VDI for DOI 1 is 77.37  $\mu\text{m}$ , lower than the healthy mean of 87.76  $\mu\text{m}$ , indicating narrower vessel diameters in the ulcerated area. Similarly, for DOI 2, the ulcer's VDI of 101.71  $\mu\text{m}$  is lower than the healthy mean of 108.41  $\mu\text{m}$ . The WTI for DOI 1 in the ulcer dataset is 22.13, higher than the healthy mean of 18.86, suggesting increased vessel tortuosity in the ulcerated tissue. For DOI 2, the ulcer's WTI of 25.02 is higher than the healthy mean of 16.82, indicating even greater tortuosity in the deeper vessels of the ulcerated region.

These detailed comparisons reveal that the ulcerated labial mucosa exhibits alterations in microvascular metrics compared to healthy tissue, with notable differences in vessel density, diameter, and tortuosity, reflecting the pathological changes associated with ulceration. However, to reach a statistical conclusion, more datasets of ulceration would be required to perform a statistical analysis. This ulceration case only demonstrates the diagnostic potential of quantitative assessment methods for oral microvasculature in this study.

## 4 Discussion

In this study, we demonstrated the use of OCTA to image and quantify microvasculature in *in vivo* human healthy and abnormal oral cavity. Four metrics, including vessel area density (VAD), vessel



**FIGURE 7**

A repeatability test for two repeated scans with buccal mucosa. (A) The greyscale OCTA *en face* projection of DOI 1 in Scan 1; (B) The greyscale OCTA *en face* projection of DOI 1 in Scan 2; (C) The quantitative heatmap of vessel density of (A); (D) The quantitative heatmap of vessel density of (B); (E) The BAM of (A); (F) The BAM of (B); (G) The quantitative heatmap of vessel diameter of (A); (H) The quantitative heatmap of vessel diameter of (B); (I) The TI skeleton map of (A); (J) The TI skeleton map of (B); (K) The quantitative heatmap of TI of (A); (L) The quantitative heatmap of TI (B); (M) The greyscale OCTA *en face* projection of DOI 2 in Scan 1; (N) The greyscale OCTA *en face* projection of DOI 2 in Scan 2; (O) The quantitative heatmap of vessel density of (M); (P) The quantitative heatmap of vessel density of (N); (Q) The BAM of (M); (R) The BAM of (N); (S) The quantitative heatmap of vessel diameter of (M); (T) The quantitative heatmap of vessel diameter of (N); (U) The TI skeleton map of (M); (V) The TI skeleton map of (N); (W) The quantitative heatmap of TI of (M); (X) The quantitative heatmap of TI of (N). All scale bars represent 500  $\mu\text{m}$ .

TABLE 1 Quantitative analysis of two repeated scans with buccal mucosa.

Depth of interest	DOI 1				DOI 2			
Quantitative Metrics	VAD	VSD	VDI [μm]	WTI	VAD	VSD	VDI [μm]	WTI
Scan 1	49.58%	7.12%	85.65	12.86	47.58%	6.27%	91.89	21.34
Scan 2	50.05%	7.38%	84.95	12.40	47.59%	6.26%	91.48	20.77
Coefficient of variation	0.0047	0.0179	0.0041	0.0257	0.0001	0.0008	0.0022	0.0194

TABLE 2 The quantitative metrics of buccal mucosa datasets. (n = 32).

Depth of interest	DOI 1				DOI 2			
Quantitative Metrics	VAD	VSD	VDI [μm]	WTI	VAD	VSD	VDI [μm]	WTI
Mean	43.32%	6.55%	74.50	20.45	41.17%	5.64%	83.09	22.17
Standard Deviation	8.12%	1.33%	10.79	3.16	6.73%	1.04%	9.64	2.23
Lower 95%	40.39%	6.08%	70.61	19.31	38.75%	5.27%	79.61	21.37
Upper 95%	46.25%	7.03%	78.38	21.59	43.60%	6.02%	86.57	22.97

TABLE 3 The quantitative metrics of labial mucosa datasets. (n = 24).

Depth of interest	DOI 1				DOI 2			
Quantitative Metrics	VAD	VSD	VDI [μm]	WTI	VAD	VSD	VDI [μm]	WTI
Mean	49.97%	6.64%	87.76	18.86	44.11%	4.89%	108.41	16.82
Standard Deviation	5.18%	0.86%	9.20	3.16	5.46%	0.79%	13.48	2.62
Lower 95%	47.78%	6.28%	83.88	17.53	41.81%	4.55%	102.71	15.71
Upper 95%	52.16%	7.00%	91.65	20.20	46.42%	5.23%	114.10	17.92

TABLE 4 The quantitative metrics of the floor of the mouth datasets. (n = 13).

Depth of interest	DOI 1				DOI 2			
Quantitative Metrics	VAD	VSD	VDI [μm]	WTI	VAD	VSD	VDI [μm]	WTI
Mean	52.00%	5.68%	120.21	17.18	53.98%	4.64%	161.67	15.41
Standard Deviation	5.28%	1.09%	23.07	2.05	5.93%	0.61%	31.62	2.07
Lower 95%	48.81%	5.02%	106.27	15.94	50.40%	4.27%	142.57	14.09
Upper 95%	55.19%	6.33%	134.15	18.41	57.57%	5.01%	180.78	16.73

TABLE 5 The quantitative metrics of the hard palate datasets. (n = 8).

Depth of interest	DOI 1				DOI 2			
Quantitative Metrics	VAD	VSD	VDI [μm]	WTI	VAD	VSD	VDI [μm]	WTI
Mean	33.19%	4.33%	85.25	23.39	35.83%	3.94%	114.90	19.69
Standard Deviation	6.07%	1.25%	8.88	4.89	4.92%	0.96%	26.53	3.87
Lower 95%	28.12%	3.29%	77.82	19.30	31.71%	3.13%	92.72	16.45
Upper 95%	38.27%	5.37%	92.67	27.48	39.95%	4.74%	137.07	22.93

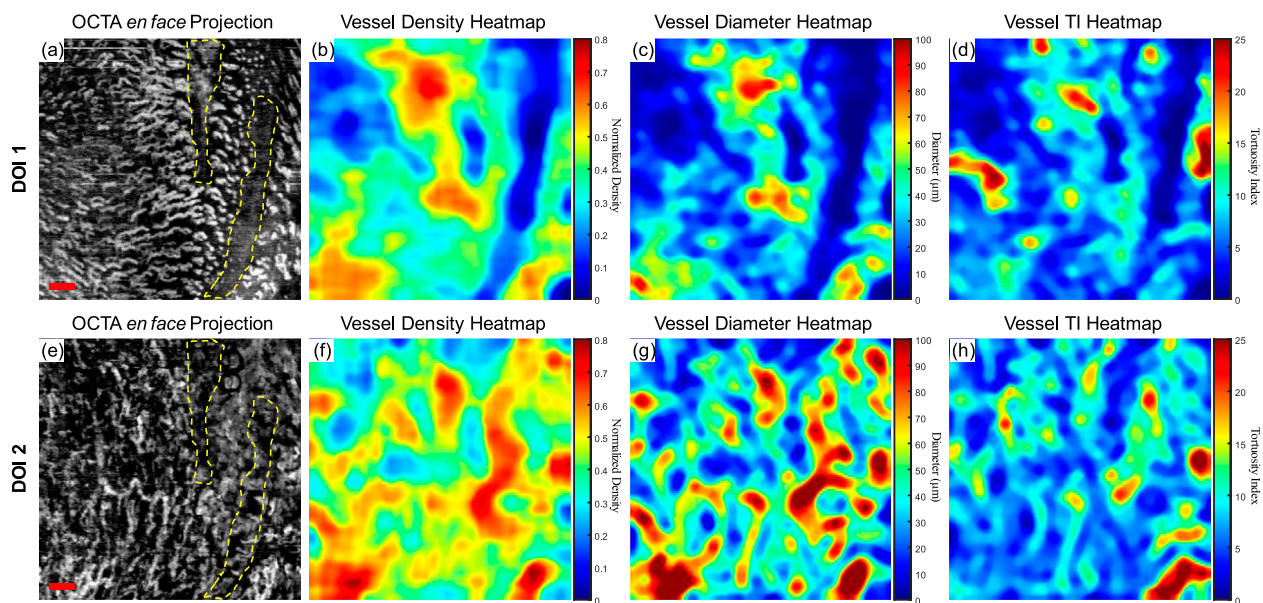


FIGURE 8

The quantitative maps of a labial mucosa dataset with a benign ulcer. (A) The gray-scale OCTA *en face* projection of the DOI 1 segmented by the automatic DOI selection algorithm with a scale bar of 500  $\mu\text{m}$ ; (B) The quantitative heatmap of vessel density of (A), which was calculated using a moving kernel; (C) The quantitative heatmap of vessel diameter in micrometers of (A) using a moving kernel; (D) The quantitative heatmap of TI of (A) using a moving kernel; (E) The gray-scale OCTA *en face* projection of the DOI 2 segmented by the automatic DOI selection algorithm with a scale bar of 500  $\mu\text{m}$ ; (F) The quantitative heatmap of vessel density of (E), which was calculated using a moving kernel; (G) The quantitative heatmap of vessel diameter in micrometers of (E) using a moving kernel; (H) The quantitative heatmap of TI of (E) using a moving kernel.

skeleton density (VSD), vessel diameter index (VDI), and the newly proposed weighted tortuosity index (WTI) were employed for the quantitative assessment of oral OCT angiograms. The microvasculature in the superficial layer (DOI 1) and deeper layer (DOI 2) of four intraoral sites, involving buccal mucosa, labial mucosa, floor of the mouth and hard palate, were quantified and contributed to the construction of a database from healthy participants. Additionally, a microvasculature analysis of a benign labial ulcer indicated that the metrics differed from those in the healthy dataset.

This study has several achievements. Firstly, we developed a robust method to automatically segment the superficial and deep layers of the oral cavity OCTA volume. Secondly, we introduced the WTI metric for accurate tortuosity quantification. Thirdly, we showcased the repeatability of our quantitative metrics results using a normal buccal mucosa case scanned successively at the same location. Lastly, and importantly, to the best of our knowledge, this is the first study to provide quantitative metrics for *in vivo* healthy and abnormal oral OCT angiograms. This work has the potential to offer clinicians a rapid and comprehensive strategy for interpreting angiograms.

Microvasculature has been shown to differ significantly between tissue layers, with clear boundaries typically segmented layers in dermatology studies (Men et al., 2017; Meiburger et al., 2019) and retinal studies (Garrity et al., 2017; Zhou et al., 2020). However, in the oral cavity, particularly within mucosal tissues, the epithelium and lamina propria are not well differentiated under OCT imaging (Feldchtein et al., 1998), posing challenges for segmentation and subsequent blood vessel overlapping, which causes inaccurate quantification. In addition, the epithelial thickness in oral soft

and hard tissues can vary largely, even within the same site (Di Stasio et al., 2019). Manual segmentation of these tissues is often impractical for large datasets due to its labor-intensive nature (Hill et al., 2024). In our study, we proposed a depth segmentation method based on the maximum OCTA intensity value derived from the overall mean intensity across all depths. With the proposed method, the overlapping issue in Figure 3 was reduced, which was shown in Figure 5. Although the proposed method was based on the OCTA intensity, not biological features, we are developing a deep-learning tool capable of automatically segmenting the epithelial layer for future work, which will enhance efficiency and accuracy.

Quantitative metrics play an important role in understanding OCT angiograms. Many studies employed only a single index to analyze the angiogram, such as VAD (Men et al., 2017), vessel diameter index (VDI) (Yao et al., 2021), or tortuosity index (TI) (Martelli and Giacomozzi, 2021). In contrast, our study utilized multiple metrics, providing a more comprehensive understanding of vasculature from various perspectives. Additionally, we proposed and evaluated a new metric, the vessel tortuosity index (WTI), which considered the factor of vessel diameter. To understand the quantitative metrics for a healthy oral database, we found that the VAD in the buccal mucosa (DOI1: 43.32%; DOI 2:41.17%), labial mucosa (DOI 1: 49.97%; DOI 2: 44.11%), and floor of the mouth (DOI 1: 52.00%; DOI 2: 53.98%) were similar, while the VSD of the buccal mucosa (DOI 1: 6.55%; DOI: 5.64%), labial mucosa (DOI 1: 6.64%; DOI 2: 4.89%), and floor of the mouth (DOI 1: 5.68%; DOI 2: 4.64%) were found in close values, suggesting these areas had comparable blood vessel density and distribution. This similarity was likely due to their roles as oral mucosa with similar



functions in protecting the underlying tissue and facilitating oral movements (Berkovitz, 2009; Nanci, 2012). The hard palate exhibited the smallest VAD (DOI 1: 33.19%; DOI 2: 35.83%) and VSD (DOI 1: 4.33%; DOI 2: 3.94%) in four oral sites, along with a higher vessel diameter (DOI 1: 85.25  $\mu\text{m}$ ; DOI 2: 114.90  $\mu\text{m}$ ) and lower tortuosity (DOI 1: 23.39; DOI 2: 19.69) in its deep layer compared to the superficial layer. These characteristics are possibly related to its specific anatomical features and the presence of numerous minor salivary glands between the mucosal surface and the underlying bone (Berkovitz, 2009; Nanci, 2012). The floor of the mouth had the largest VDI (DOI 1: 120.21  $\mu\text{m}$ ; DOI 2: 161.67  $\mu\text{m}$ ) but the smallest WTI (DOI 1: 17.18; DOI 2: 15.41), which may be attributed to its larger vasculature and unique structural characteristics. In comparison, the ulcer dataset showed a decrease in superficial capillary VAD (DOI 1: 35.07%) and VDI (DOI 1: 77.37  $\mu\text{m}$ ), indicating structural damage (Xie et al., 2024). The WTI in the ulcer (DOI 1: 22.13; DOI 2: 25.02) was higher than in healthy labial mucosa (DOI 1: 18.86; DOI 2: 16.82), suggesting increased vessel tortuosity in the ulcerated tissue. This increased tortuosity may indicate a response to inflammation and tissue repair mechanisms (Chong et al., 2017). A common early clinical state of OSCC is an ulcerated lesion (Pires et al., 2013). Therefore, our quantification framework could offer valuable insights into microvascular differences among multiple oral sites and changes during the progression of oral disease.

In addition to comprehensively identifying quantitative differences from the OCTA images among the healthy database and pathological condition of the oral cavity, the repeatability test of metrics exhibited high consistency of our methods. The low coefficient of variation (CV) values indicate that our quantification method was relatively repeatable between scans (CV < 5%), and the common indexes were smaller than previously published quantification works (Chu et al., 2016; Xie et al., 2024). Therefore, our methods should provide a high level of accuracy when using OCTA for monitoring oral disease progression and treatment response.

A few limitations of this study need to be addressed. First, since this study was using *in vivo* OCTA imaging, there is a lack of histological validation. Histological analysis, such as using Griffonia simplicifolia lectin (GSL) to visualize vascular lumens (Xie et al., 2024), could be conducted on biopsies from diseased patients. Additionally, to achieve more accurate descriptive statistics for healthy subjects, a larger sample size will be necessary. This limitation aligns with our intended future work, which aims to better understand normal tissue compared with biopsy proven clinically abnormal tissues. Larger sample sizes of both healthy and diseased tissue will enable us to conduct more robust statistical analyses and more accurately determine the utility of OCTA in oral diagnostics using our methods. A minimum of sample sizes of patients and healthy volunteers of 90 and 180 respectively would be ideal to yield 80% power with a significance level of 0.05. While our proposed depth segmentation method was reliable for OCTA quantification, the segmentation of actual layers in the oral cavity can reveal structural differences of multiple oral sites and structural changes caused by oral diseases. Considering the challenges of using conventional image processing to differentiate layers, deep-learning methods have the potential to accurately segment the oral cavity (Hill et al., 2024).

## 5 Conclusion

In this study, we demonstrated a comprehensive method to quantify the microvasculature in the oral cavity, including buccal mucosa, labial mucosa, floor of the mouth and hard palate. From the intraoral scanning results, we assessed four metrics: VAD, VSD, VDI, and the newly proposed WTI. These metrics were calculated in both superficial and deeper layers across four intraoral sites, using an automatic layer separation method. We also analyzed a benign ulcerated labial tissue. The four metrics collectively revealed differences from healthy tissue. Therefore, proposed quantitative assessment of OCTA imaging holds considerable promise for future research and clinical management of oral diseases.

## Data availability statement

The datasets presented in this article are not readily available because of ethical restrictions. Requests to access the datasets should be directed to Chunhui Li, c.li@dundee.ac.uk.

## Ethics statement

The studies involving humans were approved by Research Ethics Committee of the University of Dundee. The studies were conducted in accordance with the local legislation and institutional requirements. The participants provided their written informed consent to participate in this study.

## Author contributions

TZ: Conceptualization, Data curation, Formal Analysis, Investigation, Methodology, Resources, Software, Visualization, Writing—original draft. YZ: Formal Analysis, Investigation, Writing—original draft, Writing—review and editing. JL: Formal Analysis, Resources, Visualization, Writing—review and editing, Investigation. SS: Funding acquisition, Investigation, Project administration, Validation, Writing—review and editing. ZH: Funding acquisition, Project administration, Resources, Supervision, Writing—review and editing. MM: Funding acquisition, Project administration, Validation, Writing—review and editing. CL: Funding acquisition, Project administration, Supervision, Writing—review and editing.

## Funding

The author(s) declare that financial support was received for the research, authorship, and/or publication of this article. Dental School, University of Dundee (Tattersall Scholarships (2023)).

## Conflict of interest

The authors declare that the research was conducted in the absence of any commercial or financial relationships that could be construed as a potential conflict of interest.

## Publisher's note

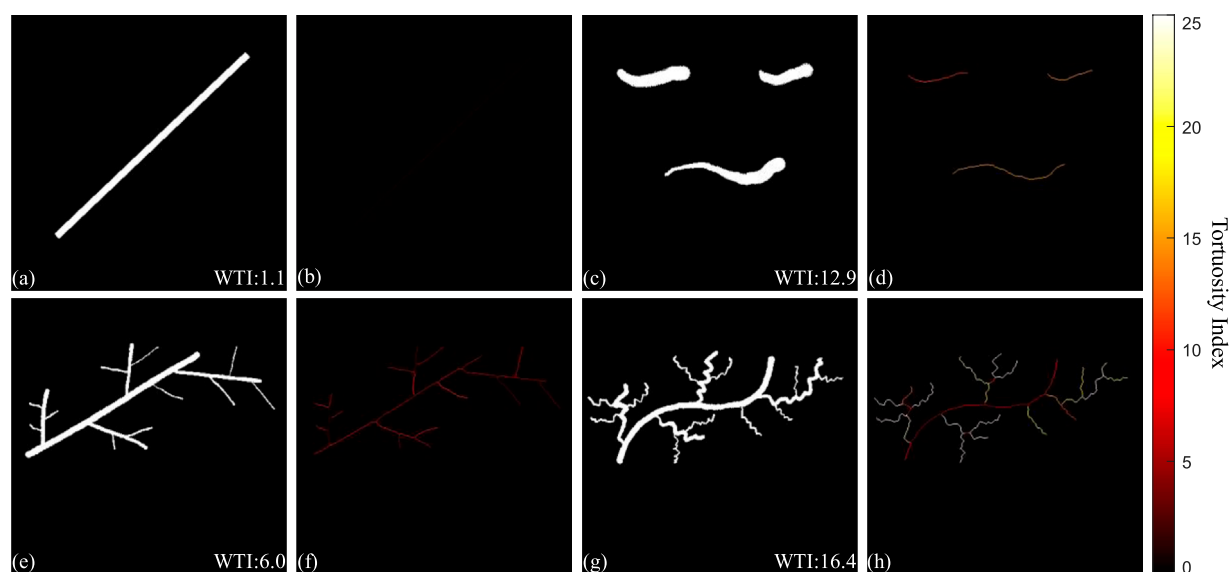
All claims expressed in this article are solely those of the authors and do not necessarily represent those of their affiliated

## References

- Agemy, S. A., Scripsema, N. K., Shah, C. M., Chui, T., Garcia, P. M., Lee, J. G., et al. (2015). Retinal vascular perfusion density mapping using optical coherence tomography angiography in normals and diabetic retinopathy patients. *Retina* 35, 2353–2363. doi:10.1097/IAE.0000000000000862
- Bastos, P., Carpentier, G., Patel, V., Papy-Garcia, D., Watson, T., and Cook, R. (2022). Real-Time Optical Vascular Imaging, a new method for the diagnosis and monitoring of oral diseases. *J. Microsc.* 288, 73–86. doi:10.1111/JMI.12975
- Berkovitz, B. K. B. (2009). *Oral anatomy, histology, and embryology*. Edinburgh, London: Mosby, 462.
- Bradley, D., and Roth, G. (2007). Adaptive thresholding using the integral image. *J. Graph. Tools* 12, 13–21. doi:10.1080/2151237X.2007.10129236
- Chamoli, A., Gosavi, A. S., Shirwadkar, U. P., Wangdale, K. V., Behera, S. K., Kurrey, N. K., et al. (2021). Overview of oral cavity squamous cell carcinoma: risk factors, mechanisms, and diagnostics. *Oral Oncol.* 121, 105451. doi:10.1016/J.ORALONCOLOGY.2021.105451
- Chen, C.-L., and Wang, R. K. (2017). Optical coherence tomography based angiography [Invited]. *Biomed. Opt. Express* 8 (2), 1056–1082. doi:10.1364/BOE.8.001056
- Choi, W. J., and Wang, R. K. (2014). *In vivo* imaging of functional microvasculature within tissue beds of oral and nasal cavities by swept-source optical coherence tomography with a forward/side-viewing probe. *Biomed. Opt. Express* 5, 2620. doi:10.1364/BOE.5.002620
- Chong, D. C., Yu, Z., Brighton, H. E., Bear, J. E., and Bautch, V. L. (2017). Tortuous microvessels contribute to wound healing via sprouting angiogenesis. *Arterioscler. Thromb. Vasc. Biol.* 37, 1903–1912. doi:10.1161/ATVBAHA.117.309993
- Chu, Z., Lin, J., Gao, C., Xin, C., Zhang, Q., Chen, C.-L., et al. (2016). Quantitative assessment of the retinal microvasculature using optical coherence tomography angiography. *J. Biomed. Opt.* 21, 066008. doi:10.1117/1.JBO.21.6.066008
- Ciurică, S., Lopez-Sublet, M., Loeys, B., Ibtissem, R., Nalin, N., Miikka, V., et al. (2019). Arterial tortuosity: novel implications for an old phenotype. *Am. Heart Assoc. Sci. Ciurică* 73 (5), 951–960. doi:10.1161/HYPERTENSIONAHA.118.11647
- Del Corso, L., Moruzzo, D., Conte, B., Agelli, M., Romanelli, A. M., Pastine, F., et al. (1998). Tortuosity, kinking, and coiling of the carotid artery: expression of atherosclerosis or aging? *Angiology* 49, 361–371. doi:10.1177/000331979804900505
- Di Stasio, D., Lauritano, D., Iquebal, H., Romano, A., Gentile, E., and Lucchese, A. (2019). Measurement of oral epithelial thickness by optical coherence tomography. *Diagnostics* 9, 90. doi:10.3390/diagnostics9030090
- Djaberi, R., Schuijff, J. D., de Koning, E. J., Wijewickrama, D. C., Pereira, A. M., Smit, J. W., et al. (2013). Non-invasive assessment of microcirculation by sidestream dark field imaging as a marker of coronary artery disease in diabetes. *Diab. Vasc. Dis. Res.* 10, 123–134. doi:10.1177/1479164112446302
- Engberg, A. M. E., Erichsen, J. H., Sander, B., Kessel, L., Dahl, A. B., and Dahl, V. A. (2020). Automated quantification of retinal microvasculature from OCT angiography using dictionary-based vessel segmentation. *Commun. Comput. Inf. Sci.* 1065 CCIS, 257–269. doi:10.1007/978-3-030-39343-4\_22
- Feldchtein, F. I., Gelikonov, G. V., Gelikonov, V. M., Iksanov, R. R., Kuranov, R. V., Sergeev, A. M., et al. (1998). *In vivo* OCT imaging of hard and soft tissue of the oral cavity. *Opt. Express* 3, 239. doi:10.1364/OE.3.000239
- Feller, L., and Lemmer, J. (2012). Oral squamous cell carcinoma: epidemiology, clinical presentation and treatment. *J. Cancer Ther.* 2012, 263–268. doi:10.4236/JCT.2012.34037
- Fogante, M., Carboni, N., and Argalia, G. (2022). Clinical application of ultra-high frequency ultrasound: discovering a new imaging frontier. *J. Clin. Ultrasound* 50, 817–825. doi:10.1002/JCU.23255
- Frangi, A. F., Niessen, W. J., Vincken, K. L., and Viergever, M. A. (1998). Multiscale vessel enhancement filtering. *Lect. Notes Comput. Sci. Incl. Subser. Lect. Notes Artif. Intell. Lect. Notes Bioinforma.* 1496, 130–137. doi:10.1007/bfb0056195
- Garrity, S. T., Iafe, N. A., Phasukkijwatana, N., Chen, X., and Sarraf, D. (2017). Quantitative analysis of three distinct retinal capillary plexuses in healthy eyes using optical coherence tomography angiography. *Invest. Ophthalmol. Vis. Sci.* 58, 5548–5555. doi:10.1167/IOVS.17-22036
- Han, H. C. (2012). Twisted blood vessels: symptoms, etiology and biomechanical mechanisms. *J. Vasc. Res.* 49, 185–197. doi:10.1159/000335123
- Hill, C., Malone, J., Liu, K., Ng, S. P. Y., MacAulay, C., Poh, C., et al. (2024). Three-dimension epithelial segmentation in optical coherence tomography of the oral cavity using deep learning. *Cancers* 16, 2144. doi:10.3390/CANCERS16112144
- Hiroki, M., Miyashita, K., and Oda, M. (2002). Tortuosity of the white matter medullary arterioles is related to the severity of hypertension. *Cerebrovasc. Dis.* 13, 242–250. doi:10.1159/000057850
- Huang, C. C., Chen, P. Y., Peng, P. H., and Lee, P. Y. (2017). 40 MHz high-frequency ultrafast ultrasound imaging. *Med. Phys.* 44, 2185–2195. doi:10.1002/MP.12244
- Jia, Y., Bailey, S. T., Hwang, T. S., McClintic, S. M., Gao, S. S., Pennesi, M. E., et al. (2015). Quantitative optical coherence tomography angiography of vascular abnormalities in the living human eye. *Proc. Natl. Acad. Sci.* 112, E2395–E2402. doi:10.1073/pnas.1500185112
- Kahe, F., Sharfaei, S., Pitliya, A., Jafarizade, M., Seifirad, S., Habibi, S., et al. (2020). Coronary artery tortuosity: a narrative review. *Coron. Artery Dis.* 31, 187–192. doi:10.1097/MCA.0000000000000769
- Kashani, A. H., Chen, C. L., Gahm, J. K., Zheng, F., Richter, G. M., Rosenfeld, P. J., et al. (2017). Optical coherence tomography angiography: a comprehensive review of current methods and clinical applications. *Prog. Retin Eye Res.* 60, 66–100. doi:10.1016/J.PRETEYERES.2017.07.002
- Kemp, M. (2019). Leonardo's philosophical anatomies. *Lancet* 393, 1404–1408. doi:10.1016/S0140-6736(19)30584-7
- Kerschnitzki, M., Kollmannsberger, P., Burghammer, M., Duda, G. N., Weinkamer, R., Wagermaier, W., et al. (2013). Architecture of the osteocyte network correlates with bone material quality. *J. Bone Min. Res.* 28, 1837–1845. doi:10.1002/jbmr.1927
- Le, N., Lu, J., Tang, P., Chung, K.-H., Subhash, H., Kilpatrick-Liverman, L., et al. (2022). Intraoral optical coherence tomography and angiography combined with autofluorescence for dental assessment. *Biomed. Opt. Express* 13, 3629. doi:10.1364/BOE.460575
- Le, N. M., Song, S., Zhou, H., Xu, J., Li, Y., Sung, C. E., et al. (2018). A noninvasive imaging and measurement using optical coherence tomography angiography for the assessment of gingiva: an *in vivo* study. *J. Biophot.* 11, e201800242. doi:10.1002/JBIO.201800242
- Lee, H., Lee, M., Chung, H., and Kim, H. C. (2018). Quantification of retinal vessel tortuosity in diabetic retinopathy using optical coherence tomography angiography. *Retina* 38, 976–985. doi:10.1097/IAE.0000000000001618
- Lee, T. C., Kashyap, R. L., and Chu, C. N. (1994). Building skeleton models via 3-D medial surface Axis thinning algorithms. *CVGIP Graph. Models Image Process.* 56, 462–478. doi:10.1006/cgip.1994.1042
- Macluskey, M., Chandrachud, L. M., Pazouki, S., Green, M., Chisholm, D. M., Ogden, G. R., et al. (2000). Apoptosis, proliferation, and angiogenesis in oral tissues. Possible relevance to tumour progression. *J. Pathol.* 191, 368–375. doi:10.1002/1096-9896(2000)9999:9999::AID-PATH652>3.0.CO;2-Y
- Manfredini, M., Sticchi, A., Lippolis, N., Pedroni, G., Giovani, M., Ciardo, S., et al. (2023). Characterization of acne-prone skin with reflectance confocal microscopy and optical coherence tomography and modifications induced by topical treatment and probiotic supplementation. *J. Clin. Med.* 12, 4787. doi:10.3390/JCM12144787
- Martelli, F., and Giacomozzi, C. (2021). Tortuosity index calculations in retinal images: some criticalities arising from commonly used approaches. *Inf. Switz.* 12, 466. doi:10.3390/info12110466
- Maurer, C. R., Qi, R., and Raghavan, V. (2003). A linear time algorithm for computing exact Euclidean distance transforms of binary images in arbitrary dimensions. *IEEE Trans. Pattern Anal. Mach. Intell.* 25, 265–270. doi:10.1109/TPAMI.2003.1177156
- Meiburger, K. M., Chen, Z., Sinz, C., Hoover, E., Minneman, M., Ensher, J., et al. (2019). Automatic skin lesion area determination of basal cell carcinoma using optical coherence tomography angiography and a skeletonization approach: preliminary results. *J. Biophot.* 12, e201900131. doi:10.1002/JBIO.201900131
- Men, S. J., Chen, C. L., Wei, W., Lai, T. Y., Song, S. Z., and Wang, R. K. (2017). Repeatability of vessel density measurement in human skin by OCT-based microangiography. *Skin. Res. Technol.* 23, 607–612. doi:10.1111/SRT.12379
- Mortazavi, H., Baharvand, M., and Mehdipour, M. (2014). Oral potentially malignant disorders: an overview of more than 20 entities. *J. Dent. Res. Dent. Clin. Dent. Prospects* 8, 6–14. doi:10.5681/JODDD.2014.002
- Nanci, A. (2012). *Ten cate's oral histology: development, structure, and function*. Elsevier. Available at: <http://www.sciencedirect.com/5070/book/9780323078467/ten-cates-oral-histology> (Accessed July 4, 2024).



- Otsu, N. (1979). A threshold selection method from gray-level histograms. *IEEE Trans. Syst. Man. Cybern.* 9, 62–66. doi:10.1109/TSMC.1979.4310076
- Owen, C. G., Newsom, R. S. B., Rudnicka, A. R., Barman, S. A., Woodward, E. G., and Ellis, T. J. (2008). Diabetes and the tortuosity of vessels of the bulbar conjunctiva. *Ophthalmology* 115, e27–e32. doi:10.1016/J.OPHTHA.2008.02.009
- Pancera, P., Ribul, M., Presciuttini, B., and Lechi, A. (2000). Prevalence of carotid artery kinking in 590 consecutive subjects evaluated by Echocolor Doppler. Is there a correlation with arterial hypertension? *J. Intern. Med.* 248, 7–12. doi:10.1046/J.1365-2796.2000.00611.X
- Pires, F. R., Ramos, A. B., Oliveira, J. B. C. de, Tavares, A. S., Luz, P. S. R. da, and Santos, T. C. R. B. dos (2013). Oral squamous cell carcinoma: clinicopathological features from 346 cases from a single Oral Pathology service during an 8-year period. *J. Appl. Oral Sci.* 21, 460–467. doi:10.1590/1679-775720130317
- Ravi, D., Ramadas, K., Mathew, B. S., Nalinakumari, K. R., Nair, M. K., and Pillai, M. R. (1998). Angiogenesis during tumor progression in the oral cavity is related to reduced apoptosis and high tumor cell proliferation. *Oral Oncol.* 34, 543–548. doi:10.1016/S1368-8375(98)00054-2
- Reif, R., Qin, J., An, L., Zhi, Z., Dziennis, S., and Wang, R. (2012). Quantifying optical microangiography images obtained from a spectral domain optical coherence tomography system. *Int. J. Biomed. Imaging* 2012, 1–11. doi:10.1155/2012/509783
- Sasahira, T., and Kiritani, T. (2018). Hallmarks of cancer-related newly prognostic factors of oral squamous cell carcinoma. *Int. J. Mol. Sci.* 19, 2413. doi:10.3390/IJMS19082413
- Sato, Y., Shiraga, N., Nakajima, S., Tamura, S., and Kikinis, R. (1998). Local maximum intensity projection lmp: a new rendering method for vascular visualization. *J. Comput. Assist. Tomogr.* 22, 912–917. doi:10.1097/00004728-199811000-00014
- Scardina, G. A., Picone, V., Cacioppo, A., and Messina, P. (2007). Study of microcirculation in oral lichen planus by video-capillaroscopy. *Oral Surg. Oral Med. Oral Pathology, Oral Radiology, Endodontology* 103, e30–e34. doi:10.1016/J.TRIPLEO.2006.10.022
- Sciubba, J. J. (2001). Oral cancer: the importance of early diagnosis and treatment. *Am. J. Clin. Dermatol.* 2, 239–251. doi:10.2165/00128071-200102040-00005
- Tirelli, G., Marcuzzo, A. V., and Boscolo Nata, F. (2018). Narrow-band imaging pattern classification in oral cavity. *Oral Dis.* 24, 1458–1467. doi:10.1111/ODI.12940
- Tsai, M.-T., Chen, Y., Lee, C.-Y., Huang, B.-H., Trung, N. H., Lee, Y.-J., et al. (2017). Noninvasive structural and microvascular anatomy of oral mucosae using handheld optical coherence tomography. *Biomed. Opt. Express* 8, 5001. doi:10.1364/BOE.8.005001
- Untracht, G. R., Matos, R. S., Dikaio, N., Bapir, M., Durrani, A. K., Butsabong, T., et al. (2021). OCTAVA: an open-source toolbox for quantitative analysis of optical coherence tomography angiography images. *PLoS One* 16, e0261052. doi:10.1371/JOURNAL.PONE.0261052
- Wang, J., Jia, Y., Hwang, T. S., Bailey, S. T., Huang, D., and Hormel, T. T. (2018). Maximum value projection produces better en face OCT angiograms than mean value projection. *Biomed. Opt. Express* 9, 6412–6424. doi:10.1364/BOE.9.006412
- Wang, X. ning, Cai, X., Li, S. wei, Li, T., Long, D., and Wu, Q. (2022). Wide-field swept-source OCTA in the assessment of retinal microvasculature in early-stage diabetic retinopathy. *BMC Ophthalmol.* 22, 473–511. doi:10.1186/s12886-022-02724-0
- Wei, W., Choi, W. J., and Wang, R. K. (2018). Microvascular imaging and monitoring of human oral cavity lesions *in vivo* by swept-source OCT-based angiography. *Lasers Med. Sci.* 33, 123–134. doi:10.1007/s10103-017-2350-3
- Wells, F., and Crowe, T. (2004). Leonardo da Vinci as a paradigm for modern clinical research. *Jtvs. Org.* 127, 929–944. doi:10.1016/j.jtvs.2004.02.002
- Xie, Z., Zeinstra, N., Kirby, M. A., Le, N. M., Murry, C. E., Zheng, Y., et al. (2024). Quantifying microvascular structure in healthy and infarcted rat hearts using optical coherence tomography angiography. *IEEE Trans. Med. Imaging* 43, 2878–2887. doi:10.1109/TMI.2024.3381934
- Yao, X., Ke, M., Ho, Y., Lin, E., Wong, D. W. K., Tan, B., et al. (2021). Comparison of retinal vessel diameter measurements from swept-source OCT angiography and adaptive optics ophthalmoscope. *Br. J. Ophthalmol.* 105, 426–431. doi:10.1136/BJOPHTHALMOL-2020-316111
- Yoon, H. S., Oh, J., and Kim, Y. C. (2023). Assessing machine learning models for predicting age with intracranial vessel tortuosity and thickness information. *Brain Sci.* 13, 1512. doi:10.3390/BRAINSCI13111512
- Zhang, T., Shepherd, S., Huang, Z., Li, C., and Macluskey, M. (2023). Development of an intraoral handheld optical coherence tomography-based angiography probe for multi-site oral imaging. *Opt. Lett.* 48 (18), 4857–4860. doi:10.1364/OL.497080
- Zhang, T., Zhou, K., Roccliffe, H. R., Pellicoro, A., Cash, J. L., Wang, W., et al. (2022). Windowed eigen-decomposition algorithm for motion artifact reduction in optical coherence tomography-based angiography. *Appl. Sci.* 2023 13, 378. doi:10.3390/AP13010378
- Zhou, K., Song, S., Legocki, A., Cheng, Y., Ding, L., Rezaei, K. A., et al. (2020). Quantitative handheld swept-source optical coherence tomography angiography in awake preterm and full-term infants. *Transl. Vis. Sci. Technol.* 9, 19. doi:10.1167/TVST.9.13.19



**FIGURE A1**  
Demonstration of the quantitative assessment of vasculature tortuosity. Figure (A, C, E, G) are hand-drawn binary images with vessel-like shapes, with WTI values calculated and displayed at the bottom-right corner. Figure (B, D, F, H) are the TI skeleton maps of the binary images respectively.

## Appendix

To evaluate the robustness of the WTI and better demonstrate WTI, four hand-drawn binary images which essentially can simulate the simplified binarized *en face* OCTA projections, BAM, were used to calculate the WTI and generate TI skeleton maps (Figure A1). Figures A1A, C, E, H are the hand-drawn binary images with vessel-like shapes to evaluate the tortuosity quantification. The WTI values were calculated and displayed at the bottom-right corner on each sub-figure. The first two images, Figures A1A, C were designed to assess separated segments, where one was a straight line and another consisted of curved lines. Figures A1B, D were the

TI skeleton maps of Figures A1A, C respectively. Besides the separated segments, connected vessel-like binary images in Figures A1E, G were applied to the same process. Figure A1E was a connected vessel branch with relatively straight lines, while Figure A1G was the same structured vessel branch with visually more tortuous vessels. Figures A1F, H were the TI skeleton maps of the binary images in Figures A1E, G. In comparisons of either separated segments or connected vessel branches, a positive relationship between the visual tortuosity and the WTI values was found in this demonstration. Therefore, the WTI can be considered as a useful tool to quantitatively assess the tortuosity of the microvasculature networks.



## OPEN ACCESS

## EDITED BY

Jiaqiu Wang,  
London South Bank University, United Kingdom

## REVIEWED BY

Andrea Tigrini,  
Marche Polytechnic University, Italy  
Shaobai Wang,  
Shanghai University of Sport, China  
Ryan Huang,  
Queensland University of Technology, Australia

## \*CORRESPONDENCE

Yong Ma,  
✉ mayong@whsu.edu.cn

RECEIVED 14 June 2024

ACCEPTED 16 September 2024

PUBLISHED 09 October 2024

## CITATION

Huang R, Ma Y, Lin S, Zheng W, Liu L and Jia M  
(2024) Correlation between the biomechanical  
characteristics and stability of the 143D  
movement during the balance phase in  
competitive Tai Chi.  
*Front. Bioeng. Biotechnol.* 12:1449073.  
doi: 10.3389/fbioe.2024.1449073

## COPYRIGHT

© 2024 Huang, Ma, Lin, Zheng, Liu and Jia. This  
is an open-access article distributed under the  
terms of the [Creative Commons Attribution  
License \(CC BY\)](https://creativecommons.org/licenses/by/4.0/). The use, distribution or  
reproduction in other forums is permitted,  
provided the original author(s) and the  
copyright owner(s) are credited and that the  
original publication in this journal is cited, in  
accordance with accepted academic practice.  
No use, distribution or reproduction is  
permitted which does not comply with these  
terms.

# Correlation between the biomechanical characteristics and stability of the 143D movement during the balance phase in competitive Tai Chi

Ruifeng Huang<sup>1,2,3</sup>, Yong Ma<sup>1,2,3\*</sup>, Shijie Lin<sup>4</sup>, Weitao Zheng<sup>1,2,3</sup>,  
Lin Liu<sup>1,2,3</sup> and Mengyao Jia<sup>1,2,3</sup>

<sup>1</sup>Engineering Research Center of Sports Health Intelligent Equipment of Hubei Province, Wuhan Sports University, Wuhan, China, <sup>2</sup>Research Center of Sports Equipment Engineering Technology of Hubei Province, Wuhan Sports University, Wuhan, China, <sup>3</sup>Key Laboratory of Sports Engineering of General Administration of Sports of China, Wuhan Sports University, Wuhan, China, <sup>4</sup>Department of Physical Education, Intelligent Sports Engineering Research Center, Northwest Polytechnical University, Xi'an, China

**Objective:** To explore the biomechanical factors affecting the stability of athletes in the 143D balance phase of competitive Tai Chi.

**Method:** The Vicon 3D motion capture system, Kistler 3D force platform, and Noraxon surface electromyography (sEMG) system were used to measure the joint angle, joint moment, center of gravity, ground reaction force, and sEMG data of athletes. The stability index was then calculated according to the formula. Pearson's or Spearman's correlation tests were used to analyze the associations between the biomechanical factors and stability index.

**Results:** (1) Medial lateral stability index (MLSI): A significant negative correlation was found between the ankle inversion angle of the supporting leg (SL) and MLSI ( $p < 0.05$ ). (2) Anterior posterior stability index (APSI): Significant negative correlations were observed between the ankle intorsion angle, integrated electromyography (iEMG) of the gastrocnemius, and muscle contribution rates of the tibialis anterior, external oblique, and gastrocnemius of the non-supporting leg (NL) with the APSI ( $p < 0.05$ ). The ankle dorsiflexion moment, iEMG of the rectus femoris and tibialis anterior, muscle contribution rate of the biceps femoris, and root mean-squared (RMS) amplitude of the gluteus maximus of the SL also showed significant negative correlations with the APSI ( $p < 0.05$ ). Strong and significant negative correlations were also identified between the hip intorsion angle, iEMG of the tibialis anterior, and RMS amplitude of the rectus femoris of the NL with the APSI ( $p < 0.01$ ). Further strong and significant negative correlation was also found between the RMS amplitude of the biceps femoris of the SL and APSI ( $p < 0.01$ ). The knee extorsion angle of the NL was positively correlated with the APSI ( $p < 0.05$ ). (3) Dynamic postural stability index (DPSI): The

**Abbreviations:** APSI, anterior posterior stability index; BF, biceps femoris; CTC, competitive Tai Chi; DPSI, dynamic postural stability index; EO, external oblique; ES, erector spinae; GA, lateral gastrocnemius; GM, gluteus maximus; GRF, ground reaction force; iEMG, integrated electromyography; MARCR, Martial Arts Routine Competition Regulation; MLSI, medial lateral stability index; MVC, maximum voluntary contraction; NL, non-supporting leg; RF, rectus femoris; RMS, root mean-squared; sEMG, surface electromyography; SL, supporting leg; TA, tibialis anterior.

knee adduction angle, iEMG of the tibialis anterior, and RMS amplitude of the erector spinae of the NL were significantly positively correlated with the DPSI ( $p < 0.05$ ). The knee abduction and hip extension moments of the SL were also significantly positively correlated with the DPSI ( $p < 0.05$ ).

**Conclusion:** The ankle inversion angle of the SL impacts left–right stability, while the NL’s hip and ankle intorsion angles, knee extorsion angle, and exertion on the core muscle and SL’s main muscles, as well as exertion of specific muscles of the NL affect anterior–posterior stability. The hip extension and knee abduction moments of the SL, knee adduction angle, exertion on the tibialis anterior, and activation of the erector spinae of the NL significantly affect the overall stability of an athlete.

#### KEYWORDS

joint angle, joint moment, integrated electromyography, root mean-squared amplitude, stability index

## 1 Introduction

Tai Chi is one of the most important traditional Chinese martial arts. It is characterized by its principles of using softness to overcome hardness, neutralizing and issuing energy, and its philosophical emphasis on harmonious integration (Yang et al., 2022; Yang and Yang, 2017). Practicing Tai Chi has been shown to promote physical health (Gatts and Woollacott, 2007). Since the introduction of the Martial Arts Routine Competition Regulation (MARCR) in 1958, Tai Chi has evolved into a competitive martial art form known as competitive Tai Chi (CTC). CTC is a sports event that features continuous, complex, and high-intensity Tai Chi movements performed to music. In recent years, given the continuous updates to the MARCR and improvement of CTC levels, the inclusion of designated and innovative difficult-level movements has driven CTC toward more advanced, newer, more intricate, and more exquisite practices (Wang and Qiu, 2012).

The difficulty levels of the balance movements in CTC are categorized into four types as A, B, C, and D, with the difficulty increasing gradually from A to D. In the latest MARCR issued in 2023, the code number of the low-balance with cross of back leg movement was assigned as 143D, indicating that this is the most challenging and also one of the highest scoring balance movements. Athletes frequently incorporate the 143D movement in CTC because it helps improve their competition scores and is crucial for connecting the one movement to the next (Sun, 2023). According to MARCR, when performing the 143D movement, CTC athletes can only use one of their legs as the supporting leg (SL) to execute the single-leg squat. The balance phase of the 143D movement begins when the athlete squats to the point where the thigh of the SL is no higher than horizontal, while the non-supporting leg (NL) is crossed behind the SL. During this phase, the NL is prohibited from touching the ground. Research indicates that whole-body stability significantly impacts the sports performances of CTC athletes, and point deductions are commonly applied as penalties during the phase that requires maintaining balance (Yi et al., 2019). Muscle exertion and joint biomechanics are critical factors that affect the stability of the athlete and also represent the ability of the athlete to maintain posture control (Gribble and Robinson, 2009; Borghuis et al., 2011; Brough et al., 2021).

The dynamic postural stability index (DPSI) is an effective method of evaluating body stability through calculation of the

ground reaction force (GRF); it was first proposed by Wikstrom et al. (2005) and can be used to evaluate not only the posture control abilities of patients with functional ankle instabilities (Brown et al., 2010) but also the balancing abilities of athletes practicing different sports (Frisch et al., 2011). Previous studies on other types of sports have demonstrated that biomechanical indicators significantly impact postural stability (Booysen et al., 2015; Robinson and Gribble, 2008; Borghuis et al., 2011). However, there is currently limited research on the impacts of the biomechanical indicators on the postural stabilities of CTC athletes when performing movements from A to D levels. Further investigations are thus required on the posture control and muscle exertion strategies of CTC athletes during execution of the 143D movements. Therefore, the Vicon motion capture system, Kistler force platform, and Noraxon surface electromyography (sEMG) system were used in this study to analyze the correlations between the kinematic, kinetic, and sEMG characteristics as well as DPSI during the balance phase of the CTC 143D movements. The present work aims to deepen the understanding regarding the movement characteristics and balance mechanisms of the 143D movements by providing theoretical support for improving the training effectiveness and sports performance in CTC.

## 2 Methods

### 2.1 Participants

G Power 3.1.9.2 was used in this study to calculate the predicted sample size. A larger effect size of 0.8 was set for the correlation analysis, and at least nine subjects are required with an  $\alpha$  of 0.05 and a power of 0.8 (Kang, 2021). Thus, 10 male athletes at or above the first level of CTC were recruited for this study from Hubei Province. All subjects have participated in at least provincial-level CTC events and their bodies are in good health; further, they did not have any conditions affecting their sports performance.

Among the participants, three athletes were at the elite level while the remaining seven were first-level athletes; the average age of the participants was  $19.00 \pm 0.81$  years, average height was  $177.50 \pm 3.75$  cm, average bodyweight was  $66.30 \pm 2.45$  kg, and average training period was  $9.71 \pm 2.43$  years. The dominant side of the lower limbs of all subjects was the right side. All participants were

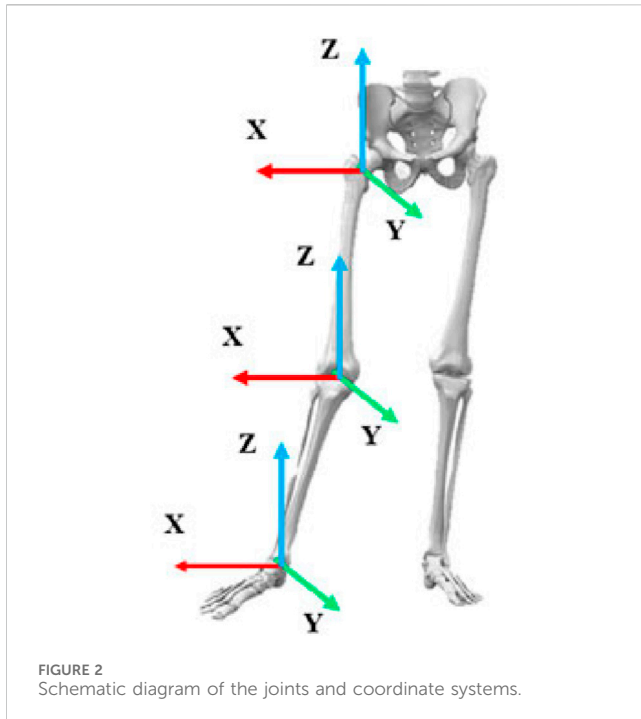


Position	Muscle	Abbreviation
Bilateral lower limbs	Rectus femoris	RF
	Tibialis anterior	TA
	Biceps femoris	BF
	Lateral gastrocnemius	GA
	Gluteus maximus	GM
Both sides of the torso	External oblique	EO
	Erector spinae	ES

The subjects ran slowly on a treadmill at a speed of 5 m/s and a slope of 0% for 5 min as the warm-up session, followed by stretching for 5 min based on their pretraining routines. Before testing, all participants underwent warm-up running sessions to enable them to complete the 143D movement efficiently. They practiced the 143D movement







in advance so as to adapt to the position and size of the force table in the laboratory and sat quietly for 2 min. Then, sEMG electrodes were attached to subjects as follows: the skin surface was first disinfected with alcohol; then, two electrodes were applied at the belly muscle; next, the Noraxon wireless sEMG collector was applied and secured with muscle tape. Because the 143D is a single-leg squat balance movement, the main muscles of the lower limbs and core muscles were the main targets in this study. The names and positions of the muscles monitored in the study are shown in Table 1.

Reflective markers were then applied to the bodies of the athletes. According to the plug-in-gait marker placement labeling scheme in the Vicon technical manual, at least 39 markers are required. Given the characteristics of Tai Chi movements and the need to analyze the indicators, the number of reflective markers was increased to 70, as shown in Figure 1.

### 2.2.2 Procedure

According to the sEMG operation manual, the maximum voluntary contraction (MVC) of the muscles was measured using the Noraxon wireless sEMG collector (Ultium EMG, Noraxon, United States, sampling frequency of 1,500 Hz). The subjects were instructed to perform MVC for 5 s, with three tests per muscle and a 60 s rest interval between each test.

The Vicon 3D motion capture system was used in this study for kinematic data collection using nine infrared cameras (T40, Vicon, UK, sampling frequency of 250 Hz). The kinetic data were collected using a Kistler 3D force platform (9260AA6, Switzerland, sampling frequency of 1,500 Hz). The sEMG signals were recorded from the lower limbs and core muscles of the subjects using the Noraxon system. Initially, the subjects stood on two force platforms on both feet in an anatomical position and maintained this posture for 2 s before performing the 143D movements according to the competition routines. The data were successfully collected at least three times from each athlete. The

success criterion for the 143D movement is as follows: an on-site professional referee awards a full score, meaning that the subjects must maintain the balanced posture for 2 s during the 143D balance phase. Additionally, the trials were considered successful if there were no noticeable losses from the markers and the sEMG signals were collected without issues. The trials that did not meet these criteria were deemed unsuccessful, and all failed trials were recorded as well.

## 2.3 Indicators

Based on the characteristics of the 143D movement, biomechanical research on difficult-level movements in CTC, and biomechanical research on balance movements in other sports events (Zhao et al., 2020; Li et al., 2020; Ma et al., 2016), the knee, ankle, and hip joint moments ( $\text{Nm}\cdot\text{kg}^{-1}$ ) were selected as the kinetic indicators along with the elevation of the human center of gravity (COG; m) as well as hip, knee, and ankle joint angles ( $^{\circ}$ ). The joint coordinate system used for the calculations is shown in Figure 2. The flexion and extension movements are performed around the X-axis, while adduction and abduction movements are considered around the Y-axis, and intorsion and extorsion movements are considered around the Z-axis.

The sEMG indicators include integrated electromyography (iEMG) (%s) and root mean-squared (RMS) (%) values (Zhao et al., 2020; Li et al., 2020). The stability indexes of the GRFs in the anterior–posterior and medial–lateral directions were calculated using specific formulas (Wikstrom et al., 2005); these indexes serve as one of the indicators for evaluating balance stability in sports performance. The formulas for the different indexes are as follows.

Medial lateral stability index (MLSI): When describing the 143D movement, this index represents the stability in the left-to-right direction of the body. The Equation 1 is as follows.

$$MLSI = \sqrt{\frac{\sum (0 - GRF_x)^2}{NDP}} \div BW, \quad (1)$$

Anterior posterior stability index (APSI): This refers to the stability of the body in the anterior-to-posterior direction. The Equation 2 is as follows

$$APSI = \sqrt{\frac{\sum (0 - GRF_y)^2}{NDP}} \div BW. \quad (2)$$

Dynamic postural stability index (DPSI): This refers to the overall stability of the body. The Equation 3 is as follows

$$DPSI = \sqrt{\frac{\sum (0 - GRF_x)^2 + \sum (0 - GRF_y)^2 + \sum (BW - GRF_z)^2}{NDP}} \div BW. \quad (3)$$

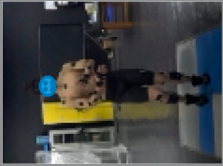

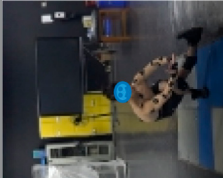
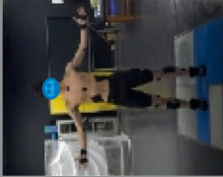
Here,  $NDP$  refers to the total number of frames recorded in the Vicon motion capture system;

$BW$  is the bodyweight;

$GRF_x$ ,  $GRF_y$ , and  $GRF_z$  are the GRFs in the anterior–posterior, medial–lateral, and vertical directions, respectively.

The larger the values of the MLSI, APSI, and DPSI, the poorer is the balance stability; contrarily, the smaller the values, the better is the balance stability.

TABLE 2 Event divisions in the 143D movement.

			
E1→E2	E2→E3	E3→E4	
Preparation Moment E1	Balance Moment E2	Retraction Moment E3	Ending Moment E4
When the NL is lifted off the ground	When the knee of the NL starts to undergo extension	When the knee of the NL starts to undergo flexion	When the NL is placed on the ground
Squat Phase P1	Balance Phase P2	Retract Phase P3	

2.4 Data processing

The coordinates of the markers captured by the Vicon 3D motion capture system were used for modeling. The c3D files were first exported to Visual 3D software for skeleton modeling, following which the kinetic motion files were imported into the static model for matching. The data collected with the 3D force platform were standardized, and the GRF was normalized to a multiple of the bodyweight. The kinetic indicators were calculated through inverse kinetics analysis.

The sEMG data were preprocessed in MR 3.6 software; initially, the three MVCs collected were processed using the Make MVC function, and the best data were selected for further analyses. The 14 processed MVC datasets were combined into a single file, and the channel order of the MVC file was adjusted to match the order in the 143D movement file for subsequent analyses. The 143D movement files were then processed for signal filtering, rectification, smoothing, and MVC normalization to generate a data report, in which the iEMG and RMS values were selected for further analyses.

2.5 Event division

In this study, the process of a complete 143D movement is defined as the period from the NL lifting off the ground to the NL touching the ground again. This process is divided into four events and three phases, as shown in Table 2. The focus of this study is on investigating the biomechanical characteristics of the 143D movements in the balance phase.

2.6 Statistical analysis

The Shapiro–Wilk test was conducted using IBM SPSS statistics 25 (IBM Corporation, Armonk, New York, United States) to assess the normality of the data distribution. The outliers were removed, and the Spearman or Pearson correlation test was applied accordingly thereafter to analyze the correlations between the biomechanical indicators and stability indexes. A *p*-value <0.05 was considered a significant correlation between the datasets. Moreover, the strength of the data correlation was categorized based on the magnitude of the correlation coefficient; a correlation coefficient between 0.8 and 1 is considered a robust correlation, and a value between 0.6 and 0.8 is considered a strong correlation (Salkind and Frey, 2019).

3 Results

3.1 Correlations between the kinematic indicators and stability indexes

According to Table 3, the MLSI of the 143D movement is significantly positively correlated with the adduction angle of the ankle joint in the SL (*p* < 0.05, *r* = 0.681). The APSI is significantly positively correlated with the intorsion angles of the ankle joint in the NL (*p* < 0.05, *r* = 0.692) and hip joint in the NL (*p* < 0.01, *r* = 0.817). Conversely, the extorsion angle of the knee joint in the NL is significantly negatively correlated with the APSI (*p* < 0.01, *r* = −0.824). The DPSI is significantly negatively correlated with the abduction angle of the knee joint in the NL (*p* < 0.05, *r* = −0.697).

TABLE 3 Correlations between the kinematic indicators and stability indexes.

Indicators		MLSI		APSI		DPSI	
		CC	Sig (two-tailed)	CC	Sig (two-tailed)	CC	Sig (two-tailed)
NL	KJA-X	−0.108	0.782	−0.328	0.389	0.242	0.531
	KJA-Y	−0.318	0.404	0.401	0.285	−.697*	0.037
	KJA-Z	0.022	0.956	−0.824**	0.006	0.298	0.437
	AJA-X	0.427	0.326	0.329	0.387	−0.228	0.555
	AJA-Y	0.469	0.203	0.692*	0.039	−0.258	0.503
	AJA-Z	−0.583	0.099	−0.191	0.622	0.395	0.293
	HJA-X	−0.431	0.247	−0.092	0.814	−0.007	0.986
	HJA-Y	−0.204	0.598	−0.102	0.793	−0.328	0.393
	HJA-Z	0.231	0.550	0.817**	0.007	−0.418	0.263
COG	COG-X	−0.333	0.381	0.033	0.932	0.421	0.286
	COG-Y	0.512	0.170	−0.301	0.433	0.067	0.865
	COG-Z	−0.606	0.084	−0.386	0.305	0.398	0.289
SL	KJA-X	−0.367	0.331	−0.012	0.975	−0.164	0.674
	KJA-Y	0.163	0.675	0.281	0.464	−0.006	0.987
	KJA-Z	0.536	0.137	−0.236	0.542	0.271	0.482
	AJA-X	0.434	0.243	−0.121	0.757	0.446	0.229
	AJA-Y	−0.317	0.406	0.352	0.356	−0.483	0.187
	AJA-Z	0.681*	0.043	0.029	0.941	0.111	0.775
	HJA-X	−0.359	0.139	−0.329	0.461	0.401	0.765
	HJA-Y	−0.533	0.342	0.283	0.387	−0.117	0.285
	HJA-Z	−0.608	0.083	−0.206	0.596	0.397	0.291

Notes: \* represents  $p < 0.05$ ; \*\* represents  $p < 0.01$ ; NL, non-supporting leg; SL, supporting leg; KJA, knee joint angle; AJA, ankle joint angle; HJA, hip joint angle; COG, center of gravity; ‘−’ represents a negative correlation; CC, correlation coefficient.

### 3.2 Correlations between the kinetic indicators and stability indexes

According to Table 4, none of the kinetic indicators are significantly associated with the MLSI of the 143D movement. However, the ankle dorsiflexion moment of the SL is significantly positively correlated with the APSI ( $p < 0.05$ ,  $r = 0.717$ ), while the APSI is significantly negatively correlated with the ankle intorsion moment of the SL ( $p < 0.01$ ,  $r = -0.850$ ). Additionally, the knee abduction moment ( $p < 0.05$ ,  $r = -0.709$ ) and the hip extension moment ( $p < 0.05$ ,  $r = -0.726$ ) of the SL are both significantly negatively correlated with the DPSI.

### 3.3 Correlations between the iEMG and stability indexes

As shown in Table 5, there are no significant positive correlations with the MLSI of the 143D movement. The APSI

is significantly positively correlated with the iEMG values of the RF of the SL ( $p < 0.05$ ,  $r = 0.783$ ), TA of the NL ( $p < 0.01$ ,  $r = 0.812$ ), TA of the SL ( $p < 0.05$ ,  $r = 0.672$ ), and GA of the NL ( $p < 0.05$ ,  $r = 0.758$ ). The DPSI is significantly negatively correlated with the iEMG value of only the TA of the NL ( $p < 0.01$ ,  $r = -0.779$ ).

### 3.4 Correlations between the muscle contribution rates and stability indexes

As shown in Table 6, the APSI of the 143D movement is significantly positively correlated with the muscle contribution rates of the TA of the NL ( $p < 0.05$ ,  $r = 0.682$ ), BF of the SL ( $p < 0.05$ ,  $r = 0.750$ ), and GA of the NL ( $p < 0.05$ ,  $r = 0.732$ ). In contrast, the muscle contribution rate of the EO in the NL is significantly negatively correlated with the APSI of the 143D movement ( $p < 0.05$ ,  $r = -0.777$ ). The muscle contribution rates on either side are not significantly correlated with the MLSI of the 143D movements.

TABLE 4 Correlations between the kinetic indicators and stability indexes.

Indicators		MLSI		APSI		DPSI	
		CC	Sig (two-tailed)	CC	Sig (two-tailed)	CC	Sig (two-tailed)
NL	KJM-X	−0.531	0.142	−0.205	0.597	0.354	0.351
	KJM-Y	0.215	0.579	−0.583	0.101	0.277	0.473
	KJM-Z	0.105	0.789	−0.267	0.487	0.388	0.303
	AJM-X	−0.611	0.081	−0.182	0.639	0.261	0.499
	AJM-Y	−0.639	0.064	0.026	0.947	0.055	0.89
	AJM-Z	−0.137	0.726	0.469	0.203	−0.484	0.188
	HJM-X	−0.532	0.141	−0.197	0.611	0.581	0.113
	HJM-Y	0.184	0.636	−0.035	0.929	−0.179	0.644
	HJM-Z	0.141	0.717	0.189	0.627	−0.109	0.781
SL	KJM-X	−0.281	0.464	−0.131	0.737	0.64	0.063
	KJM-Y	0.073	0.853	0.135	0.732	−0.708*	0.033
	KJM-Z	−0.117	0.765	0.317	0.406	−0.133	0.732
	AJM-X	−0.050	0.898	0.717*	0.031	−0.466	0.207
	AJM-Y	0.172	0.659	−0.850**	0.004	0.646	0.061
	AJM-Z	−0.347	0.360	0.181	0.641	−0.16	0.683
	HJM-X	0.424	0.256	0.547	0.127	−0.726*	0.027
	HJM-Y	0.094	0.809	−0.057	0.885	−0.539	0.134
	HJM-Z	0.399	0.287	−0.385	0.306	0.429	0.252

Notes: \* represents  $p < 0.05$ ; \*\* represents  $p < 0.01$ ; NL, non-supporting leg; SL, supporting leg; KJM, knee joint moment; AJM, ankle joint moment; HJM, hip joint moment; ‘−’ represents a negative correlation; CC, correlation coefficient.

### 3.5 Correlations between the RMS values and stability indexes

As shown in Table 7, there are no significant positive correlations with the MLSI of the 143D movement. The APSI is significantly positively correlated with the RMS values of the RF of the SL ( $p < 0.01$ ,  $r = 0.842$ ), GM of the SL ( $p < 0.05$ ,  $r = 0.761$ ), and BF of the SL ( $p < 0.01$ ,  $r = 0.917$ ). The DPSI is significantly negatively correlated with the RMS value of only the ES in the NL ( $p < 0.05$ ,  $r = -0.708$ ).

## 4 Discussion

This study explores the relationships of the kinematic, kinetic, and muscle exertion characteristics with the stability of the 143D movements during the balance phase. The results show a significant negative correlation between the ankle joint adduction angle of the SL and stability in the left–right directions of CTC athletes. The ankle joint intorsion angle of the NL; dorsiflexion moment of the SL; iEMG values of the RF and TA of the SL as well as GA of the NL; muscle contribution rates of the TA, EO, and GA of the NL as well as BF of the SL; and RMS value of the GM of the SL have significant negative correlations with the stability in the anteroposterior

direction. Additionally, the hip intorsion angle of the NL, iEMG value of the TA of the NL, and RMS values of the RF and BF of the SL are strongly and significantly negatively correlated with the stability in the anteroposterior direction. Conversely, the knee extension angle of the NL is positively correlated with the stability in the anteroposterior direction. The knee adduction angle of the NL; knee abduction and hip extension moments of the SL; iEMG value of the TA of the NL; and RMS value of the ES of the NL are significantly positively correlated with the overall stability of an athlete.

### 4.1 Correlations between the MLSI and biomechanical indicators

During the balance phase of the 143D movement, CTC athletes must maintain the single-leg squat position using only their SLs, while ensuring that their thighs do not rise above the horizontal level. The NL must then be crossed below the thigh of the SL, with the anterior aspect of the thigh of the NL being in contact with the posterior aspect of the thigh of the SL. The NL must be extended maximally, and the ankle joint should be in a dorsiflexed state to prevent the foot from touching the ground to avoid a penalty.

The results reveal a significant negative correlation between the adduction angle of the ankle joint of the SL and MLSI, indicating

TABLE 5 Correlations between the iEMG values and stability indexes.

iEMG		MLSI		APSI		DPSI	
		CC	Sig (two-tailed)	CC	Sig (two-tailed)	CC	Sig (two-tailed)
NL	RF	0.517	0.154	−0.117	0.765	−0.033	0.932
	TA	0.488	0.182	0.812**	0.008	−0.779*	0.013
	ES	0.238	0.538	0.042	0.915	−0.589	0.095
	GM	0.134	0.732	−0.393	0.295	−0.27	0.482
	BF	0.113	0.772	−0.154	0.691	0.296	0.441
	GA	0.335	0.379	0.758*	0.018	−0.254	0.513
	EO	0.629	0.069	0.439	0.238	−0.067	0.864
SL	RF	0.475	0.196	0.783*	0.013	−0.299	0.435
	TA	−0.43	0.248	0.672*	0.047	−0.442	0.234
	ES	0.07	0.859	−0.351	0.356	−0.179	0.644
	GM	0.327	0.432	0.552	0.156	−0.605	0.112
	BF	0.608	0.083	0.605	0.084	−0.218	0.573
	GA	0.188	0.628	−0.156	0.688	−0.29	0.449
	EO	0.516	0.155	−0.009	0.982	0.19	0.624

Notes: \* represents  $p < 0.05$ ; \*\* represents  $p < 0.01$ ; NL, non-supporting leg; SL, supporting leg; ‘−’ represents a negative correlation; CC, correlation coefficient.

TABLE 6 Correlations between the muscle contribution rates and stability indexes.

Muscle contribution rate		MLSI		APSI		DPSI	
		CC	Sig (two-tailed)	CC	Sig (two-tailed)	CC	Sig (two-tailed)
NL	RF	0.544	0.163	0.012	0.977	0.481	0.228
	TA	0.394	0.294	0.682*	0.043	−0.653	0.057
	ES	−0.206	0.595	0.345	0.363	−0.521	0.151
	GM	0.043	0.913	−0.556	0.122	−0.017	0.966
	BF	−0.001	0.999	−0.151	0.699	0.404	0.281
	GA	0.147	0.706	0.732*	0.025	−0.208	0.591
	EO	0.486	0.185	0.032	0.934	0.204	0.598
SL	RF	−0.008	0.985	0.601	0.087	−0.121	0.757
	TA	−0.591	0.123	0.432	0.285	−0.206	0.624
	ES	−0.231	0.549	−0.398	0.289	−0.209	0.589
	GM	−0.057	0.904	0.469	0.288	−0.322	0.481
	BF	0.017	0.966	0.750*	0.022	−0.567	0.112
	GA	−0.011	0.979	−0.211	0.586	−0.224	0.562
	EO	0.182	0.699	−0.777*	0.041	0.597	0.157

Notes: \* represents  $p < 0.05$ ; \*\* represents  $p < 0.01$ ; NL, non-supporting leg; SL, supporting leg; ‘−’ represents a negative correlation; CC, correlation coefficient.

that a larger ankle adduction angle of the SL is associated with reduced stability in the left–right direction. According to Kibele et al. (2015), the body during balance can be described as a continuously fluctuating inverted pendulum system. An athlete can maintain balance when the vertical projection of the COG of their body remains within the base of support (BoS) (Hof, 2007). An increased



TABLE 7 Correlations between the RMS values and stability indexes.

RMS		MLSI		APSI		DPSI	
		CC	Sig (two-tailed)	CC	Sig (two-tailed)	CC	Sig (two-tailed)
NL	RF	0.346	0.362	−0.076	0.847	0.521	0.151
	TA	0.602	0.086	0.435	0.242	−0.106	0.784
	ES	0.083	0.832	0.151	0.698	−.708*	0.033
	GM	−0.027	0.945	−0.314	0.411	−0.291	0.451
	BF	0.017	0.966	0.321	0.433	0.017	0.966
	GA	0.274	0.475	0.59	0.094	0.011	0.983
	EO	0.532	0.143	0.527	0.144	0.005	0.992
SL	RF	0.262	0.535	0.842**	0.009	−0.058	0.889
	TA	−0.507	0.163	0.642	0.062	−0.264	0.491
	ES	−0.213	0.583	−0.431	0.247	−0.036	0.931
	GM	0.048	0.911	0.761*	0.028	−0.616	0.103
	BF	−0.112	0.798	0.917**	0.001	−0.517	0.154
	GA	0.013	0.974	−0.503	0.168	0.233	0.544
	EO	0.328	0.389	0.153	0.695	0.221	0.568

Notes: \* represents  $p < 0.05$ ; \*\* represents  $p < 0.01$ ; NL, non-supporting leg; SL, supporting leg; ‘−’ represents a negative correlation; CC, correlation coefficient.

adduction angle of the ankle joint of the SL reduces the contact area between the sole and ground. Since the foot of the SL serves as the BoS, a smaller BoS decreases the distance (moment arm) from the vertical line of gravity to both edges of the BoS. This reduction in the moment arm diminishes the stabilizing moment generated by gravity, thereby impairing the ability to resist the tilting moment (Brough et al., 2021). Therefore, it is more challenging for CTC athletes to maintain stability in their left–right directions under these conditions.

## 4.2 Correlations between the APSI and biomechanical indicators

In the 143D movement, maintaining stability during the single-leg squat through the SL is crucial, and the TA of the SL plays a vital role in maintaining the dorsiflexed position of the ankle joint (Harput et al., 2013) supported by the other calf muscle groups to ensure that the COG of the body remains within the BoS (Krkelj, 2018). Additionally, muscles like the BF and RF of the thigh also help stabilize the knee joint of the SL (Iacono et al., 2016; Booysen et al., 2015).

The plantar flexion of the ankle joint is mainly achieved through concentric contractions of the GA and TA of the NL. However, our results reveal significant negative correlations between the stability in the anteroposterior direction and sEMG characteristics of the TA, GM, RF, and BF of the SL. Similarly, there are significant negative correlations with the sEMG characteristics of the TA and GA of the NL, suggesting that the excessive activities and activation levels of these muscles impair the stability of the athletes in the anteroposterior direction. Although previous studies have

demonstrated that co-activation of the thigh muscles during squatting increases knee joint stiffness and maintains stability, the effects of co-activation on stability remain unclear (Kean et al., 2006). Therefore, high-level co-activation may not be an effective strategy as it can unnecessarily stiffen the joints and reduce knee flexion ability (Booyesen et al., 2015); this could explain why the activity and activation of the main thigh muscle group in the SL in this study negatively affect stability in the anteroposterior direction.

Moreover, during isometric contraction of the TA of the SL, increased co-activation of the agonist muscle generates a higher net moment from these muscles (Behrens et al., 2015). Consequently, the TA activity level in the SL directly influences the dorsiflexion moment of the ankle joint. An excess dorsiflexion moment can cause the SL to tilt forward, thereby compromising the stability of the athlete in the anteroposterior direction.

This study reveals significant negative correlations of the hip and ankle intorsion angles of the NL with the stability of the athlete in the anteroposterior direction, while the knee extorsion angle is significantly positively correlated with the stability of the athlete in the same direction. To prevent the lateral side of the NL’s foot from touching the ground, the athlete must control the ankle joint of the NL to execute an intorsion movement. According to kinetic chain theory, body movements are transmitted sequentially from the proximal to the distal joints, meaning that the intorsion of the NL’s ankle is influenced by the movements of both the knee and hip joints (Prieske et al., 2015). To avoid the penalty for foot contact with the ground, CTC athletes often increase the hip intorsion angles of the NL, thereby increasing the distance between the lateral side of the foot and the ground. However, this adjustment decreases the knee extorsion angle, leading to overall intorsion of the NL. This overall

intorsion of the entire NL toward the lower left contradicts the requirements of the 143D movement, where the NL should remain behind the knee joint of the SL. Consequently, the support force provided by the NL to the SL decreases, requiring the SL to increase muscle exertion to maintain the single-leg squat posture and thereby affecting the athlete's stability in the anteroposterior direction. Additionally, the TA and GA mainly control the knee and ankle joint movements, which also explains why the force exerted by these muscle groups may negatively impact the stability of the athlete in the anteroposterior direction.

The results also reveal a significant positive correlation between the ankle intorsion moment of the SL and stability of the athlete in the anteroposterior direction, indicating that a smaller ankle intorsion moment of the SL is associated with poorer stability of the athlete in this direction. The intorsion state of the ankle joint, determined by the moment around the vertical axis of the SL, is influenced by both the lower limb muscle groups and position of the NL. Specifically, when the thigh of the NL is positioned on the lower left side of the SL's knee, it provides a supportive force toward the upper right side. However, as mentioned previously, when the NL rotates inward, the supportive force provided to the SL decreases. In the absence of SL foot movements, the calf may exhibit a counterclockwise rotation tendency, reducing the intorsion moment of the SL ankle joint. Studies on individuals with functional ankle instability (FAI) show that FAI can impair motion control, often forcing the individuals to adopt non-ankle strategies to maintain balance (Wikstrom et al., 2007). Such alterations in an athlete's motion control strategy can cause changes in technical movements, potentially explaining why the ankle joint moment of the SL and muscle exertion observed in this study are associated with reduced anteroposterior stability.

Lastly, we found that a higher contribution rate from the SL's EO is correlated with better stability in the anteroposterior direction. When an athlete maintains a single-leg squat position, the distribution of the bodyweight plays a crucial role in stability. Specifically, the lower body contributes more to the anterior aspect of the COG, while the upper body contributes more to the posterior aspect as it is heavier. To counterbalance this, the athlete must tilt their torso forward, shifting the weight toward the front to better align their COG and enhance the anteroposterior stability. The core muscle group, including the EO, is vital in achieving sagittal stability of the upper body during the balance phase (Borghuis et al., 2011). Given that the thigh of the SL must remain below the horizontal line during the squat, the distance between the abdomen and thigh of the SL is shorter when the torso is tilted forward, resulting in uneven distribution of mass on the left and right sides of the body. Behrens et al. (2015) explored the muscle activities in squatting exercises under different load distributions and found that uneven mass distribution of the squatting load places a greater demand on the trunk flexor muscles; this finding is aligned with the observations of this study, where the EO of the SL must be involved more when maintaining a forward tilting posture during the 143D movement.

### 4.3 Correlations between the DPSI and biomechanical indicators

The DPSI is a comprehensive measure of the stability of an athlete in multiple directions (Sell, 2012). We found that higher

activity levels of the TA in the NL are associated with improved overall stability in CTC athletes. This finding appears to contradict the earlier results, where increased iEMG values of the TA in the NL were linked to reduced stability in the anteroposterior direction. However, since the DPSI reflects the overall stability, it is suggested that although the higher iEMG value of the TA of the NL may negatively impact stability in the anteroposterior direction, it could still contribute positively to the overall stability. Therefore, athletes should maintain the force exerted by this muscle group during the balance phase of the 143D movement to ensure overall body balance.

A significant positive correlation was observed between the SL's hip joint extension moment and dynamic posture stability, indicating that a greater hip joint extension moment is related with better dynamic postural stability. Given the closed kinetic chain movement of the SL and the lack of significant impacts of the hip, knee, and ankle flexion–extension angles on dynamic postural stability, these effects may be attributed to changes in the hip joint extension moment caused by the torso, which in turn affects the dynamic postural stability of the body (Norris and Trudelle-Jackson, 2011).

A significant positive correlation was also found between the activation level of the ES of the NL and dynamic posture stability, revealing the importance of core muscle activation in maintaining overall postural stability. This aligns with the findings of Kibler et al. (2006) and Prieske et al. (2015), which suggests that the trunk muscle group achieves a proximal-to-distal force exertion pattern, effectively controlling and protecting the distal joints. Additionally, preactivation of the proximal muscle group may enhance the muscle activation of the limbs, thereby improving the dynamic postural stability. Currently, research on the correlations between knee joint adduction/abduction and dynamic postural stability is limited. However, in the context of the 143D movement, the position of the NL relative to the SL's knee joint influences the knee adduction angle of the NL. The closer the NL is to the posterior aspect of the knee joint of the SL, the greater is the outward support force exerted on the SL's knee joint, resulting in a larger abduction moment.

### 4.4 Limitations

This study has some notable limitations. First, the 143D movement is divided into three phases, each of which is very important. Future research will focus on investigating the variations in muscle states across the different phases of the 143D movement using OpenSim. Second, the present study mainly entails the biomechanical factors affecting the stability of the athlete during the 143D balance phase. Hence, there is scope for future research on the biomechanical factors affecting the performances of athletes in the other phases of CTC.

## 5 Conclusion

In summary, the ankle inversion angle of the SL significantly contributes to the stability of the athlete in the left–right direction.

The stability in the anteroposterior direction is significantly influenced by the ankle and hip intorsion angles as well as knee extorsion angle of the NL, in addition to exertion on the core muscles, lower limb muscles of the SL, and partial muscle groups of the NL. Additionally, the hip extension and knee abduction moments of the SL, knee adduction angle of the NL, exertion on the TA of the NL, and activation of the ES are critical factors affecting the overall stability of the athlete.

## Data availability statement

The original contributions presented in this study are included in the article/[Supplementary Material](#), and any further inquiries may be directed to the corresponding authors.

## Ethics statement

The studies involving humans were approved by the Wuhan Sports University Medical Ethics Committee. The studies were conducted in accordance with all local legislations and institutional requirements. The participants provided their written informed consent to participate in this study.

## Author contributions

RH: conceptualization, investigation, methodology, and writing—original draft. YM: data curation, funding acquisition, methodology, and writing—review and editing. SL: conceptualization, funding acquisition, methodology, and writing—review and editing. WZ: funding acquisition, supervision, and writing—review and editing. LL: investigation and writing—review and editing. MJ: investigation, methodology, and writing—review and editing.

## References

- Behrens, M., Mau-Moeller, A., Wassermann, F., Bader, R., and Bruhn, S. (2015). Effect of balance training on neuromuscular function at rest and during isometric maximum voluntary contraction. *Eur. J. Appl. Physiol.* 115, 1075–1085. doi:10.1007/s00421-014-3089-1
- Booysen, M. J., Gradidge, P. J., and Watson, E. (2015). The relationships of eccentric strength and power with dynamic balance in male footballers. *J. Sports Sci.* 33, 2157–2165. doi:10.1080/02640414.2015.1064152
- Borghuis, A. J., Lemmink, K. A., and Hof, A. L. (2011). Core muscle response times and postural reactions in soccer players and nonplayers. *Med. Sci. Sports Exerc.* 43, 108–114. doi:10.1249/MSS.0b013e3181e93492
- Brough, L. G., Klute, G. K., and Neptune, R. R. (2021). Biomechanical response to mediolateral foot-placement perturbations during walking. *J. Biomech.* 116, 110213. doi:10.1016/j.jbiomech.2020.110213
- Brown, C. N., Bowser, B., and Orellana, A. (2010). Dynamic postural stability in females with chronic ankle instability. *Med. Sci. Sports Exerc.* 42, 2258–2263. doi:10.1249/MSS.0b013e3181e40108
- Frisch, A., Urhausen, A., Seil, R., Croisier, J. L., Windal, T., and Theisen, D. (2011). Association between preseason functional tests and injuries in youth football: a prospective follow-up. *Scand. J. Med. Sci. Sports* 21, e468–e476. doi:10.1111/j.1600-0838.2011.01369.x
- Gatts, S. K., and Woollacott, M. H. (2007). How Tai Chi improves balance: biomechanics of recovery to a walking slip in impaired seniors. *Gait Posture* 25, 205–214. doi:10.1016/j.gaitpost.2006.03.011
- Gribble, P. A., and Robinson, R. H. (2009). Alterations in knee kinematics and dynamic stability associated with chronic ankle instability. *J. Athl. Train.* 44, 350–355. doi:10.4085/1062-6050-44.4.350
- Harput, G., Soyulu, A. R., Ertan, H., and Ergun, N. (2013). Activation of selected ankle muscles during exercises performed on rigid and compliant balance platforms. *J. Orthop. Sports Phys. Ther.* 43, 555–559. doi:10.2519/jospt.2013.4456
- Hof, A. L. (2007). The equations of motion for a standing human reveal three mechanisms for balance. *J. Biomech.* 40, 451–457. doi:10.1016/j.jbiomech.2005.12.016
- Iacono, A. D., Padulo, J., and Ayalon, M. (2016). Core stability training on lower limb balance strength. *J. Sports Sci.* 34, 671–678. doi:10.1080/02640414.2015.1068437
- Kang, H. (2021). Sample size determination and power analysis using the G\* Power software. *J. Educ. Eval. Health P* 18, 17. doi:10.3352/jeehp.2021.18.17
- Kean, C. O., Behm, D. G., and Young, W. B. (2006). Fixed foot balance training increases rectus femoris activation during landing and jump height in recreationally active women. *J. Sport Sci. Med.* 5, 138–148.
- Kibele, A., Granacher, U., Muehlbauer, T., and Behm, D. G. (2015). Stable, unstable and metastable states of equilibrium: definitions and applications to human movement. *J. Sport Sci. Med.* 14, 885–887.
- Kibler, W. B., Press, J., and Sciascia, A. (2006). The role of core stability in athletic function. *Sports Med.* 36, 189–198. doi:10.2165/00007256-200636030-00001
- Krkelj, Z. (2018). Comparison of jump-landing protocols with Biodex Balance System as measures of dynamic postural stability in athletes. *Sports Biomech.* 17, 371–382. doi:10.1080/14763141.2017.1348537

## Funding

The authors declare that financial support was received for the research, authorship, and/or publication of this article. This study was supported by the East Lake Scholars Sponsorship Program of Wuhan Sports University of China; Hubei Provincial Department of Education of China (D20194101); Natural Science Basic Research Program of Shaanxi Province (2022JQ-051); Science and Technology Team Foundation of Wuhan Sports University (21KT02); and 14th Five-Year-Plan Advantageous and Characteristic Disciplines (Groups) of Colleges and Universities in Hubei Province (2021-05).

## Conflict of interest

The authors declare that the research was conducted in the absence of any commercial or financial relationships that could be construed as a potential conflict of interest.

## Publisher's note

All claims expressed in this article are solely those of the authors and do not necessarily represent those of their affiliated organizations or those of the publisher, editors, and reviewers. Any product that may be evaluated in this article or claim that may be made by its manufacturer is not guaranteed or endorsed by the publisher.

## Supplementary material

The Supplementary Material for this article can be found online at: <https://www.frontiersin.org/articles/10.3389/fbioe.2024.1449073/full#supplementary-material>

- Li, Z., Gao, Y., and Lai, Q. (2020). Biomechanical research on the landing control of sheyan jetéin Chinese classical dance. *J. Beijing Dance Acad.*, 129–135. Available at: [https://kns.cnki.net/kcms2/article/abstract?v=yqeyU9EK6jSSZEG1GDarjxfPAeCATltSPD6Zkv6FFkLEt07aZORCDmftj9BGwCj0c7nJ9Ck8whl\\_Reteq4IcBjoira8GeVJRM6mozKtM4QvD-2jCFoCt\\_itoq4Z1KZ-JziDTBmINwFrnbDLsNVkHcg=&uniplatform=NZKPT&language=CHS](https://kns.cnki.net/kcms2/article/abstract?v=yqeyU9EK6jSSZEG1GDarjxfPAeCATltSPD6Zkv6FFkLEt07aZORCDmftj9BGwCj0c7nJ9Ck8whl_Reteq4IcBjoira8GeVJRM6mozKtM4QvD-2jCFoCt_itoq4Z1KZ-JziDTBmINwFrnbDLsNVkHcg=&uniplatform=NZKPT&language=CHS).
- Ma, Q., Zeng, K., and Ding, B. (2016). The characteristics of the lower extremities muscles in landing stage of competitive taiquan 322B + 3. *J. Tianjin Univ. Sport* 31, 292–296. doi:10.13297/j.cnki.issn1005-0000.2016.04.004
- Norris, B., and Trudelle-Jackson, E. (2011). Hip- and thigh-muscle activation during the star excursion balance test. *J. Sport Rehabil.* 20, 428–441. doi:10.1123/jsr.20.4.428
- Prieske, O., Muehlbauer, T., Krueger, T., Kibele, A., Behm, D. G., and Granacher, U. (2015). Role of the trunk during drop jumps on stable and unstable surfaces. *Eur. J. Appl. Physiol.* 115, 139–146. doi:10.1007/s00421-014-3004-9
- Robinson, R., and Gribble, P. (2008). Kinematic predictors of performance on the star excursion balance test. *J. Sport Rehabil.* 17, 347–357. doi:10.1123/jsr.17.4.347
- Salkind, N. J., and Frey, B. B. (2019). *Statistics for people who (think they) hate statistics*. London: Sage Publications.
- Sell, T. C. (2012). An examination, correlation, and comparison of static and dynamic measures of postural stability in healthy, physically active adults. *Phys. Ther. Sport* 13, 80–86. doi:10.1016/j.ptsp.2011.06.006
- Sun, Y. (2023). *Research on the Characteristics of competitive Tai Chi techniques: A case Study of the finalist Athletes of the 14th national games*. Master. Shanghai: Shanghai University of Sport.
- Wang, W., and Qiu, P. (2012). A study of the development of competitive Taijiquan: Conflicts and recognition. *J. Phys. Educ.* 19, 121–124. doi:10.16237/j.cnki.cn44-1404/g8.2012.03.036
- Wikstrom, E. A., Tillman, M. D., Chmielewski, T. L., Cauraugh, J. H., and Borsa, P. A. (2007). Dynamic postural stability deficits in subjects with self-reported ankle instability. *Med. Sci. Sports Exerc* 39, 397–402. doi:10.1249/mss0b013e31802d3460
- Wikstrom, E. A., Tillman, M. D., Smith, A. N., and Borsa, P. A. (2005). A new force-plate technology measure of dynamic postural stability: the dynamic postural stability index. *J. Athl. Train.* 40, 305–309.
- Yang, J., Xu, Y., and Yang, J. (2022). Analysis of core positioning of taijiquan. *J. Wuhan. Sports Univ.* 56, 72–79. doi:10.15930/j.cnki.wtxb.2022.06.007
- Yang, J., and Yang, J. (2017). Historical changes and transitional development of taijiquan. *J. Wuhan. Sports Univ.* 51, 68–73. doi:10.15930/j.cnki.wtxb.2017.07.011
- Yi, P., Wang, F., and Xia, C. (2019). Stability analysis and training method design of one-leg support for difficult movements in competitive taijiquan. *J. Wuhan. Sports Univ.* 53, 76–81. doi:10.15930/j.cnki.wtxb.2019.08.012
- Zhao, P., Ji, Z., Wen, R., Chen, Q., and Jiang, G. (2020). Biomechanical characteristics of lower limbs of yoga posture based on AnyBody simulation. *J. Med. Biomech.* 35, 698–704. doi:10.16156/j.1004-7220.2020.06.008



## OPEN ACCESS

## EDITED BY

Giuseppe De Nisco,  
Polytechnic University of Turin, Italy

## REVIEWED BY

Tinghui Zheng,  
Sichuan University, China  
Carlo Di Donna,  
University of Rome Tor Vergata, Italy

## \*CORRESPONDENCE

Lingling Wei,  
✉ [linglingwei@hfut.edu.cn](mailto:linglingwei@hfut.edu.cn)  
Peng Qiu,  
✉ [hiiigh4@163.com](mailto:hiiigh4@163.com)  
Yanqing Zhan,  
✉ [427751337@qq.com](mailto:427751337@qq.com)

<sup>†</sup>These authors have contributed equally to this work and share first authorship

RECEIVED 15 August 2024

ACCEPTED 12 December 2024

PUBLISHED 06 January 2025

## CITATION

Wei L, Hu K, Wang J, Zhang S, Yang X, Chen Y, Li C, Lu X, Ye K, Qiu P and Zhan Y (2025) Validation of the efficacy of the porous medium model in hemodynamic analysis of iliac vein compression syndrome. *Front. Bioeng. Biotechnol.* 12:1481336. doi: 10.3389/fbioe.2024.1481336

## COPYRIGHT

© 2025 Wei, Hu, Wang, Zhang, Yang, Chen, Li, Lu, Ye, Qiu and Zhan. This is an open-access article distributed under the terms of the [Creative Commons Attribution License \(CC BY\)](https://creativecommons.org/licenses/by/4.0/). The use, distribution or reproduction in other forums is permitted, provided the original author(s) and the copyright owner(s) are credited and that the original publication in this journal is cited, in accordance with accepted academic practice. No use, distribution or reproduction is permitted which does not comply with these terms.

# Validation of the efficacy of the porous medium model in hemodynamic analysis of iliac vein compression syndrome

Lingling Wei<sup>1\*†</sup>, Ke Hu<sup>1†</sup>, Jiaqiu Wang<sup>2</sup>, Shuang Zhang<sup>1</sup>, Xiaoxiao Yang<sup>1</sup>, Yuanli Chen<sup>1</sup>, Chenshu Li<sup>3</sup>, Xinwu Lu<sup>4</sup>, Kaichuang Ye<sup>4</sup>, Peng Qiu<sup>4\*</sup> and Yanqing Zhan<sup>5,6\*</sup>

<sup>1</sup>Key Laboratory of Metabolism and Regulation for Major Diseases of Anhui Higher Education Institutes, Anhui Provincial International Science and Technology Cooperation Base for Major Metabolic Diseases and Nutritional Interventions, School of Food and Biological Engineering, Hefei University of Technology, Hefei, China, <sup>2</sup>School of Engineering, London South Bank University, London, United Kingdom, <sup>3</sup>Department of Vascular Surgery, The Affiliated Chuzhou Hospital of Anhui Medical University, Chuzhou, China, <sup>4</sup>Department of Vascular Surgery, Shanghai Ninth People's Hospital Affiliated to Shanghai Jiao Tong University School of Medicine, Shanghai, China, <sup>5</sup>Department of General Surgery, The First Affiliated Hospital of Anhui Medical University, Hefei, China, <sup>6</sup>Department of General Surgery, Anhui Public Health Clinical Center, Hefei, China

Iliac Vein Compression Syndrome (IVCS) is a common risk factor for deep vein thrombosis in the lower extremities. The objective of this study was to investigate whether employing a porous medium model to simulate the compressed region of an iliac vein could improve the reliability and accuracy of Computational Fluid Dynamics (CFD) analysis outcomes of IVCS. Pre-operative Computed Tomography (CT) scan images of patients with IVCS were utilized to reconstruct models illustrating both the compression and collateral circulation of the iliac vein. A porous medium model was employed to simulate the compressed region of the iliac vein. The agreements of times to peak between discrete phase particles in CFD analysis and contrast agent particles in Digital Subtraction Angiography (DSA) were compared. Furthermore, comparisons were made between the CFD analysis results that incorporated the porous media and those that did not. The results revealed that in the CFD analysis incorporating the porous media model, more than 80% of discrete phase particles reached the inferior vena cava via collateral circulation. Additionally, the concentration variation curve of discrete phase particles demonstrated a high concordance rate of 92.4% compared to that obtained in DSA. In comparison to CFD analysis conducted without the porous medium model, the incorporation of the porous medium model resulted in a substantial decrease in blood flow velocity by 87.5% within the compressed region, a significant increase in pressure gradient of 141 Pa between the inferior vena cava and left iliac vein, and a wider distribution of wall shear stress exceeding 2.0 Pa in collateral vessels rather than in the compressed region. The study suggests that the introduction of a porous medium model improves the hemodynamic analysis of patients with IVCS, resulting in a closer alignment with clinical observations. This provides a novel theoretical framework for the assessment and treatment of patients with IVCS.

## KEYWORDS

iliac vein compression syndrome, porous medium model, computational fluid dynamics, time to peak, clinical validation



# 1 Introduction

Iliac Vein Compression Syndrome (IVCS) is a medical condition caused by the compression of the iliac vein or abnormalities in the vascular structure, resulting in impaired venous return from the lower limbs and pelvis (Poyyamoli et al., 2021). IVCS is a common risk factor for Deep Vein Thrombosis (DVT) in the lower limbs. DVT is characterized by abnormal blood clotting in the deep veins, severely impeding venous return and promoting collateral circulation between the iliac veins. Untreated DVT can lead to severe venous diseases in the lower limbs (Kalu et al., 2013; Virchow, 2024).

Clinical anatomical studies have identified a distinct fibrous structure, known as the venous ridge, in the compressed region of the iliac vein in IVCS patients (Zhou et al., 2022). This structure is primarily composed of collagen and elastin, and obstructs blood flow, contributing to the formation of DVT (Butros et al., 2013; Al-Otaibi et al., 2021). It is nearly invisible in medical imaging.

Collateral circulation refers to the development of alternative blood pathways through newly formed vessels when one iliac vein is blocked or narrowed. This allows blood to bypass the obstruction and return to the inferior vena cava (Chiu and Chien, 2011). The presence of collateral circulation helps maintain blood flow in the lower limbs and alleviate pressure in the narrowed iliac vein trunk. During the reconstruction of the iliac vein model in patients with IVCS, constructing a complete collateral circulation model is beneficial for conducting a comprehensive analysis of venous blood flow, thereby enhancing the accuracy of CFD analysis.

In recent years, there has been an increasing application of CFD in the analysis of venous blood flow. Assi et al. (2023) utilized CFD analysis to identify elevated shear rates in the compressed left iliac vein of IVCS patients. Jiang et al. (2021) investigated the impact of different collateral types and cross-sectional areas on the stenosis of the left iliac vein and distal deep vein thrombosis in IVCS patients, revealing that blood is more likely to stagnate at the site of iliac vein stenosis or its distal end, resulting in reduced flow velocity and volume. These studies suggest that CFD methods contribute to a better understanding of hemodynamic conditions during venous stenosis, by providing quantitative parameters such as velocity and pressure, as well as generating intuitive images and charts. CFD analysis of the iliac vein with established collateral circulation revealed an increase in flow and acceleration in velocity within the narrow vessel, attributed to the reduction in cross-sectional area at the compressed site (Li et al., 2023; Sandeep and Shine, 2021). However, clinical studies have shown that the vein crest and the establishment of collateral circulation result in limited and sluggish blood flow in the compressed area of the iliac vein. Therefore, it is imperative to introduce alternative models to enhance the accuracy of CFD analysis.

A Porous Medium (PM) is a material characterized by a skeletal framework and interconnected pores that facilitate fluid flow, resembling the structure and function of venous sinuses (Wang, 2000). The PM model serves as a mathematical representation of fluid flow and heat transfer within porous materials (Kaviany, 2012). Incorporating a PM model in the compressed region of the iliac vein

in CFD analysis can better simulate the venous ridge structure, reducing blood flow velocity and volume in the compressed area (Bear and Bachmat, 1990). This aligns more closely with clinical scenarios and holds significant clinical relevance.

This study utilized Computed Tomography Venography (CTV) data from IVCS patients to reconstruct models. A PM model was employed to simulate the venous ridge structure and construct a complete collateral circulation pathway. Discrete phase particles were used to simulate the flow of contrast agents, and their times to peak (TTPs) in the inferior vena cava were monitored and compared with DSA to verify the feasibility and accuracy of the PM model in the hemodynamic analysis of IVCS. Additionally, comparing CFD results with and without the PM model explored the significance of the PM model in IVCS analysis, which provides a theoretical basis for clinical evaluation and treatment of IVCS.

# 2 Materials and methods

## 2.1 Data source

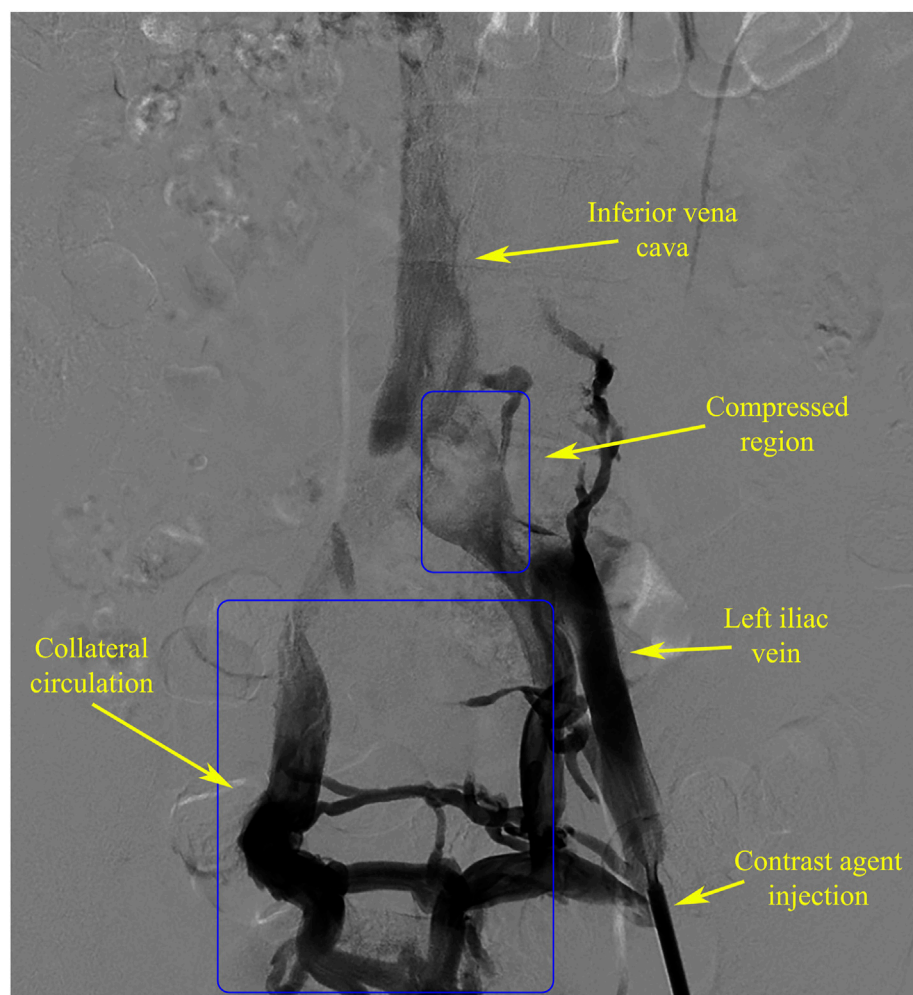
The DSA and CTV image data of an IVCS patient from the North District of the First Affiliated Hospital of Anhui Medical University were selected for analysis. The DSA data (Figure 1) showed severe compression of the left iliac vein, resulting in obstructed blood return and the presence of a well-developed collateral vascular pathway, which met the experimental requirements.

## 2.2 Model construction

The CTV data of the patient was utilized to reconstruct a 3D vascular model. The Mimics software was employed for color segmentation to extract the vessels, create centerlines, and fit the vascular spatial structure. To simplify the calculations, we excluded most of the smaller vessels that are not connected to the main veins during the vessel extraction process. These vessels typically branch off from the iliac vein and gradually diminish, disappearing into the tissue or capillaries, without affecting the primary blood flow of the iliac vein. Additionally, the 3-Matic software was used for segmentation, smoothing, and meshing to ultimately establish a 3D vascular model that included the left and right iliac veins, collateral vessels, and the inferior vena cava (Figure 2). Blood flow entered from both iliac veins, with most of the blood from the left iliac vein flowing through the collateral vessels to reach the right iliac vein before entering the inferior vena cava. Through DSA imaging and in collaboration with clinicians, the identified porous areas were strictly limited to regions characterized by compressed blood vessels.

## 2.3 CFD numerical simulation

The CFD analysis was conducted using ANSYS 22.0 software. The vascular walls were set as rigid and no-slip, with blood flow assumed to be laminar. Blood was modeled as a homogeneous,



**FIGURE 1**  
Clinical DSA images of the patient, indicating clear collateral circulation.

incompressible Newtonian fluid with a viscosity coefficient of  $0.0029 \text{ kg/(m}\cdot\text{s)}$  and a density of  $1,410 \text{ kg/m}^3$ .

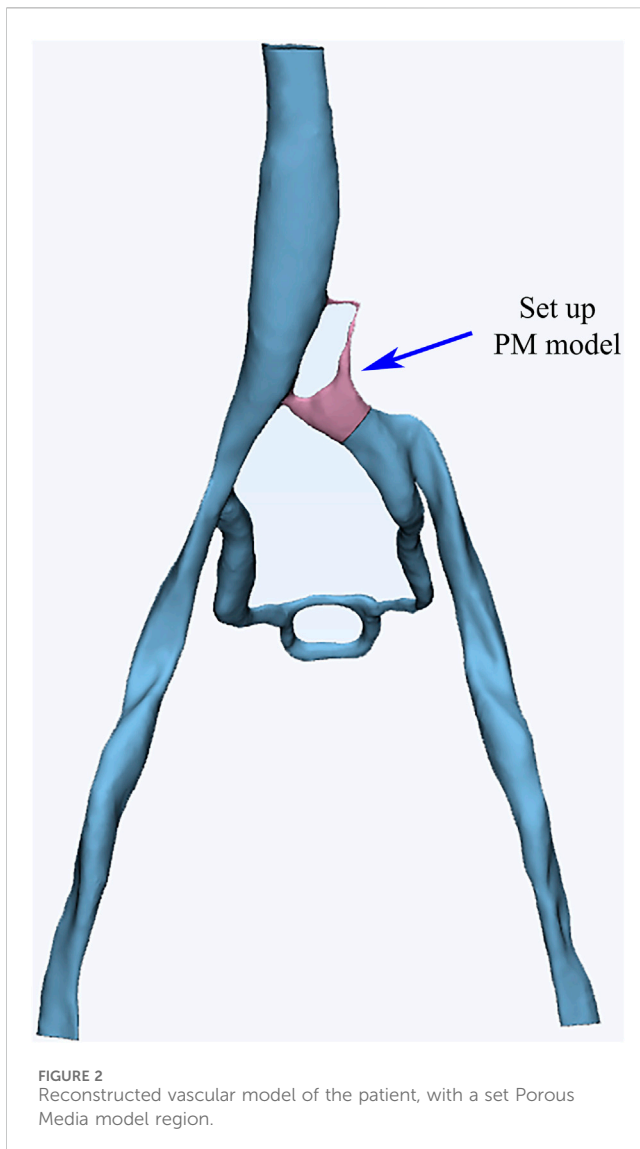
Regarding the boundary condition settings for venous entrances, different approaches were employed for the left and right iliac veins. To simplify the analysis, a constant inlet velocity was assigned to the right iliac vein based on clinically measured averages, resulting in an established flow rate of  $0.099 \text{ m/s}$ . Conversely, the inlet velocity of the left iliac vein was defined as a variable and represented by a sine function that accurately fitted clinical ultrasound spectral data. This led to the following expression for its conditions:  $v = 0.108 + 0.0835 \cdot \sin(1.5t - 1.5) \text{ m/s}$ . The outflow boundary condition was set to  $0 \text{ Pa}$ . For the CFD analysis, the coupled scheme was employed with a time step of  $0.02 \text{ s}$ , and transient calculations were performed for three cycles, totaling  $14 \text{ s}$  (Albadawi et al., 2022; Sikkandar et al., 2019; Taebi, 2022).

The PM model region was calculated using the Brinkman equation, which is suitable for incompressible Newtonian fluids with laminar flow in the pores. This calculation took into account both viscous and inertial resistance. The porosity and relative viscosity of the PM were assumed to be 1, and the viscous

resistance coefficient was adjusted to identify the optimal combination of conditions.

A specific region of the inferior vena cava was chosen from the DSA image data to record the time to peak (TTP) of the contrast agent (Figure 3A). Correspondingly, three planes, spaced  $10 \text{ mm}$  apart, were selected at the appropriate location within the inferior vena cava model (Figure 3B) to calculate the mean values of surface integral velocities and particle counts. These values were utilized for grid independence verification and TTP calculations. TTP was defined as the duration from the start of contrast agent injection to its maximum concentration at a specified location, reflecting the vascular obstruction and collateral circulation condition in the patient.

The iliac vein model was meshed using tetrahedral elements. Mesh independence was verified by setting the triangular edge lengths to  $0.23 \text{ mm}$ ,  $0.30 \text{ mm}$ , and  $0.40 \text{ mm}$ , resulting in 4 million, 2 million, and 1 million mesh elements, respectively. The surface integral of fluid velocity for these different mesh sizes were  $0.02487 \text{ m/s}$ ,  $0.02483 \text{ m/s}$ , and  $0.02495 \text{ m/s}$ , respectively, with differences between each pair being less than 1%. Considering both



mesh accuracy and computational cost, the 2 million-element mesh was selected for CFD analysis.

The Discrete Phase Model (DPM) is a CFD model utilized to simulate the movement of sparsely distributed particles (such as droplets, bubbles, solid particles, etc.) within a continuous phase (such as gas or liquid). It also accounts for the interaction between the discrete and the continuous phases. In this study, DPM was employed to simulate the flow of contrast agent particles in blood. An inert discrete phase model was utilized to simulate the movement and accumulation of the contrast agent within the blood vessels (Brandt and Coletti, 2021). The particle diameter was set to 0.001 mm, and particles were injected from a circular plane with a diameter of 1.5 mm at an injection rate of 0.02133 kg/s and an initial velocity of 0 m/s, following the blood flow. The calculation focused on simulating the flow of discrete phase particles from the left iliac vein inlet through the compressed region (i.e., the PM model region) and collateral vessels into the inferior vena cava. The quantity of discrete phase particles reaching the statistical plane of the inferior vena cava over time was then compared with the TTP of the contrast agent in DSA.

## 3 Results

### 3.1 Viscous resistance coefficient

Various viscous resistance coefficients for the PM model were selected based on a well-established range of parameters identified in the existing literature (Bear and Bachmat, 1990). The CFD analysis was performed using PM models with varying viscous resistance coefficients in order to assess the time of particles reaching the first peak, first valley, and second peak in comparison to results obtained in DSA (Table 1). The results indicated that three sets of data showed a TTP similarity of over 90% compared to DSA, and the viscous resistance coefficients were determined to be  $1.0 \times 10^6$ ,  $5.0 \times 10^7$ , and  $2.5 \times 10^8$ , respectively. Therefore, the PM model and viscous resistance coefficient can be used to evaluate the iliac vein compression in a patient.

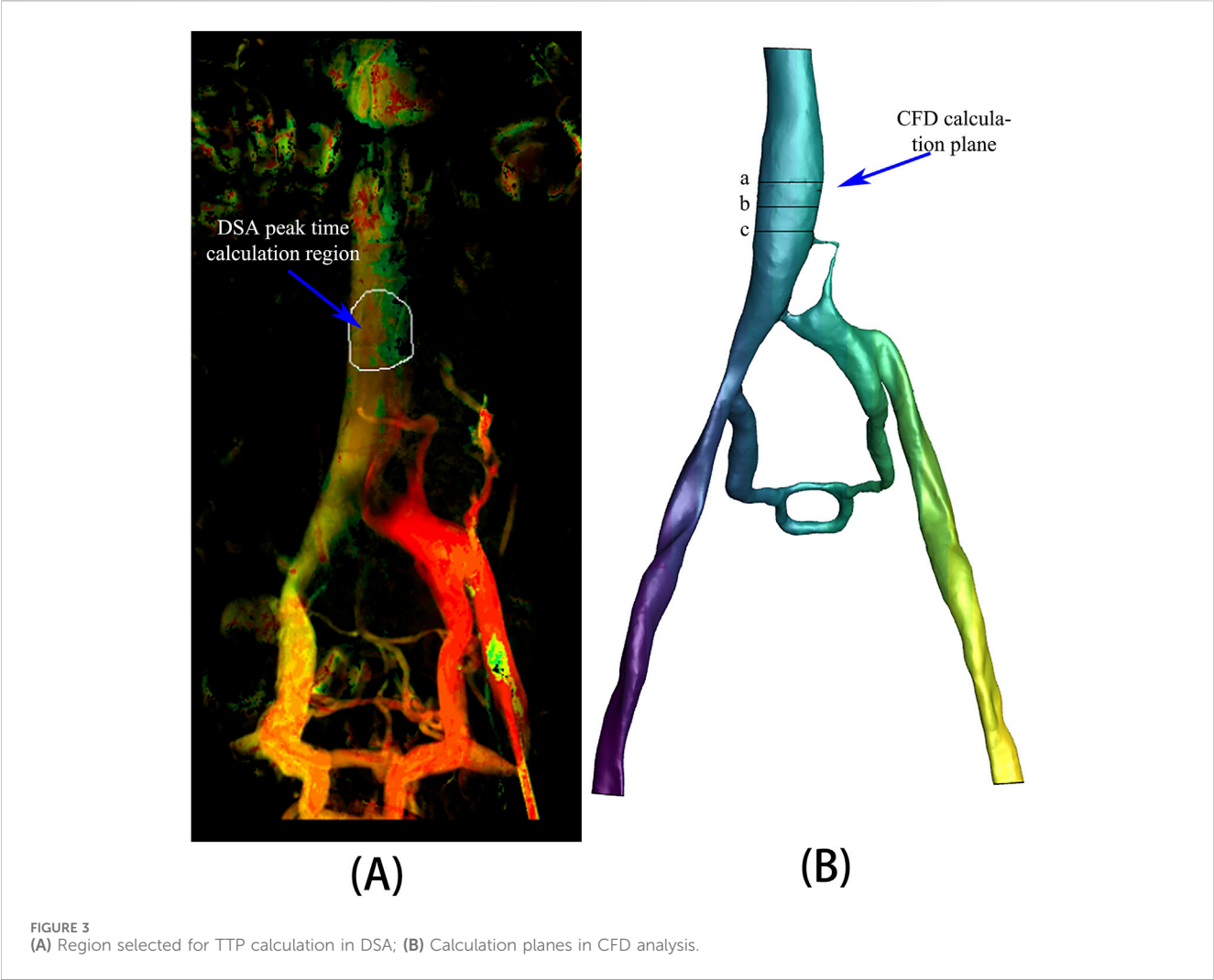
### 3.2 Time to peak (TTP)

The number of discrete phase particles at a specified cross-sectional area of the inferior vena cava (Figure 3B) was counted and compared with the contrast agent particles observed in DSA. The concentration variation curve of discrete phase particles in the CFD analysis with a viscous resistance of  $2.5 \times 10^8$  best matched the concentration variation curve of contrast agent particles in DSA, as depicted in Figure 4. The TTP curve in the DSA was utilized to monitor concentration variations of contrast agent particles as they traveled from the left iliac vein, passed through the compressed region and collateral vessels, and ultimately converged in the inferior vena cava throughout the duration of the procedure. In the CFD analysis incorporating the PM model, the TTP curve was generated by employing discrete phase particles to simulate the behavior of the contrast agents. This approach enabled the simulation of concentration changes of discrete phase particles within a defined plane of the inferior vena cava.

From the graph, it can be observed that the discrete phase particles in the PM model and the contrast agent particles in DSA exhibited similar concentration variation trends. Both curves displayed double peaks, with peak times coinciding. In the PM model, the first TTP of discrete phase particle concentration was 3.465s, while the DSA showed the first TTP at 2.752s, resulting in a difference of 20.58%. The second TTP of concentration was achieved at 5.787s in PM model and at 5.702s in DSA, representing a difference of 1.47%. Additionally, the concentration reached a valley at 4.445s in PM model and at 4.304s in DSA, with a difference of 3.17%.

### 3.3 Velocity distribution of phase discrete particles

A discrete phase particle model was employed to simulate the injection of contrast agents from the left iliac vein. Figure 5 displays the particle distributions in both the non-porous medium (NPM) model and the PM model. The distribution of discrete phase particles in the PM model showed a notable similarity to the

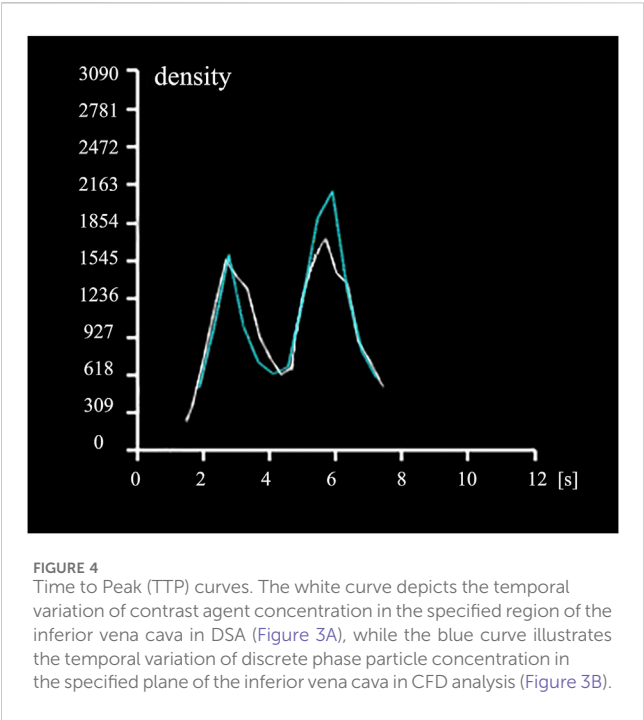


**TABLE 1** Comparison of TTPs among discrete phase particles in CFD analysis with different viscous resistance coefficients and contrast agent concentrations in DSA.

	Viscous resistance coefficient	First TTP (s)	First valley time (s)	Second TTP (s)	Average deviation	TTP similarity
0	DSA data	<b>2.75</b>	<b>4.30</b>	<b>5.70</b>		
1	1.0*10 <sup>6</sup>	3.02	4.69	6.35	10.00%	90.00%
2	2.5*10 <sup>6</sup>	2.88	3.92	10.2	31.03%	68.97%
3	5.0*10 <sup>6</sup>	2.75	3.68	4.18	13.75%	86.25%
4	1.0*10 <sup>7</sup>	3.13	3.95	7.68	18.82%	81.18%
5	2.5*10 <sup>7</sup>	2.70	4.73	6.75	10.12%	89.88%
6	5.0*10 <sup>7</sup>	2.59	4.02	6.36	7.97%	92.03%
7	1.0*10 <sup>8</sup>	4.20	4.92	5.58	22.93%	77.07%
8	2.5*10 <sup>8</sup>	3.47	4.45	5.79	7.57%	92.43%
9	5.0*10 <sup>8</sup>	3.84	4.50	5.88	15.71%	84.29%

The bold values were obtained from DSA image data.





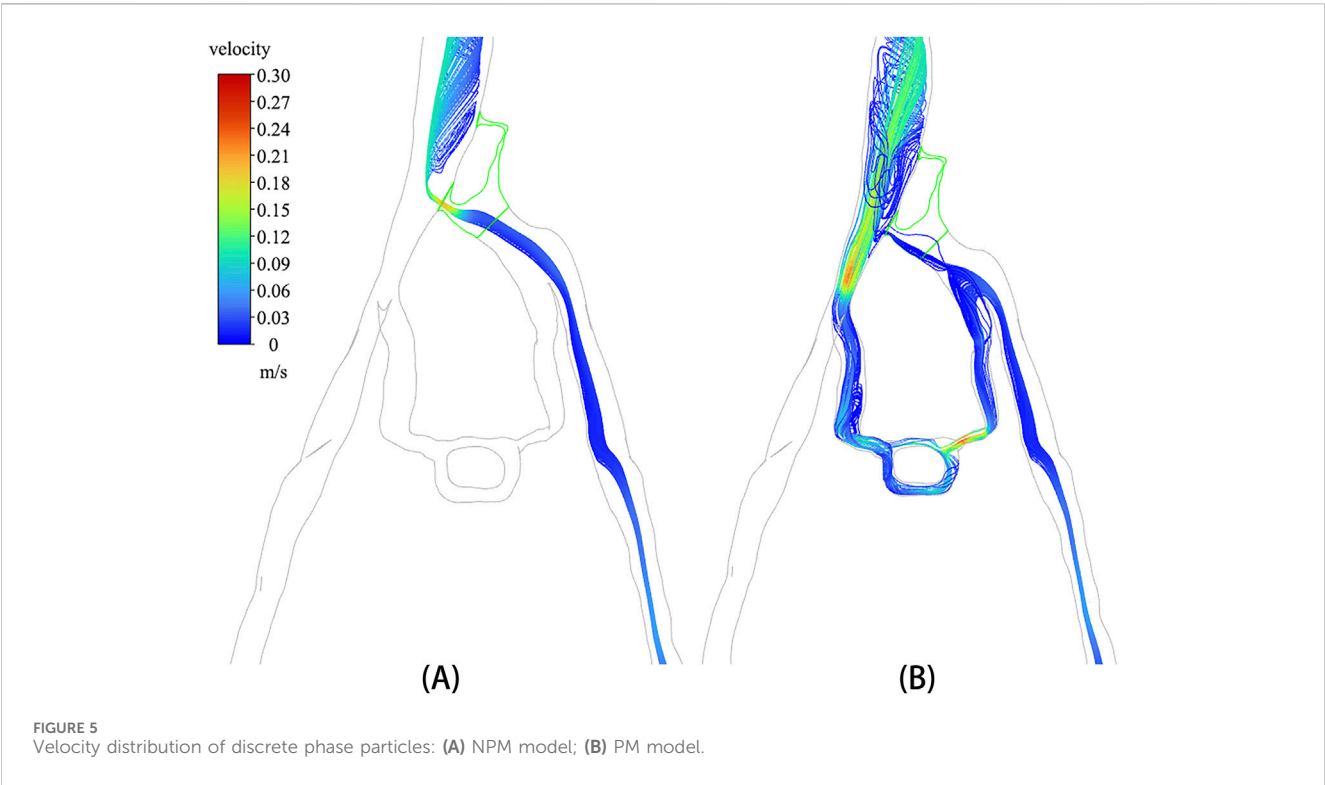
contrast agents in DSA, indicating that the PM model provides a more precise representation of venous flow characteristics in IVCS patients. A significant difference was observed in the velocity and distribution of particles within the compressed region of the iliac vein between the two models. In the NPM model, all discrete phase particles flowed into the inferior vena cava through the compressed

region, displaying a notably increased velocity within this area. Conversely, in the PM model, over 80% of the discrete phase particles entered the inferior vena cava through collateral vessels, with only a small number of particles passing through the compressed region at a slower velocity.

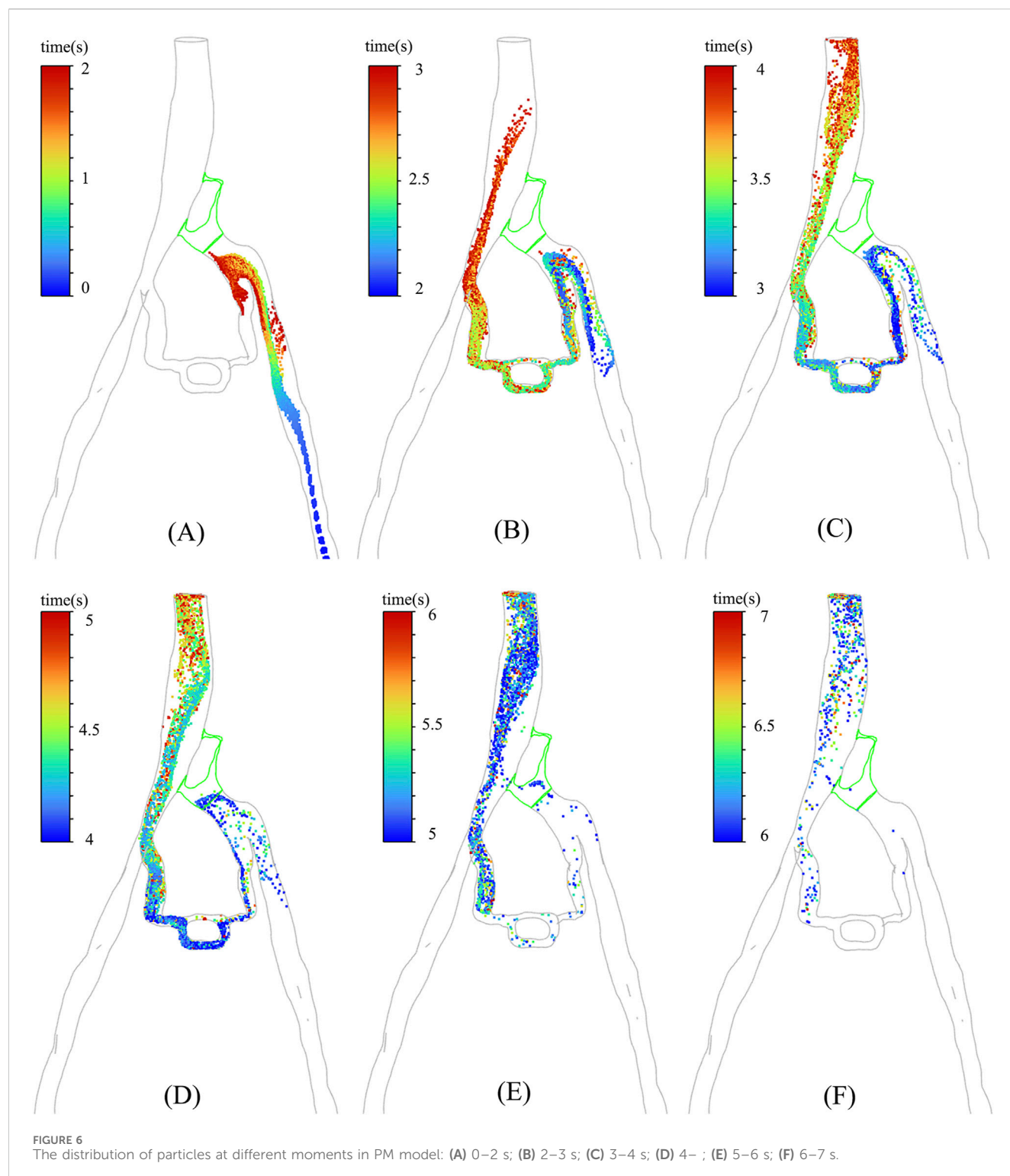
In particular, the temporal distribution of particles in CFD analysis with incorporated PM model is illustrated in Figure 6. It is shown that from 0 s to 7 s, the temporal distribution of particles is well aligned with the TTP curve depicted in Figure 4. Figure 6 revealed that a substantial number of discrete phase particles traveled through the collateral vessels into the inferior vena cava over time, while only a minimal quantity of particles passed through the compressed region. This pattern closely resembled the movement of the contrast agents observed in clinical practice, supporting the notion that both the porous media model and the discrete phase model could effectively simulate the dynamics of the contrast agent within the compromised vascular environment. These findings highlight the potential utility of these modeling approaches in enhancing the understanding of hemodynamics in patients with IVCS.

### 3.4 Pressure gradient

The pressure distribution in the PM and NPM models is depicted in Figure 7. As illustrated, the pressure in the left iliac vein of the NPM model ranged from 20 to 30 Pa, whereas in the PM model, it varied from 160 to 180 Pa, indicating a higher pressure in the left iliac vein. Within the porous medium region (i.e., the stenosis area of the iliac vein), the maximum pressure in the NPM model was 28 Pa, whereas it was 167 Pa in the PM model.



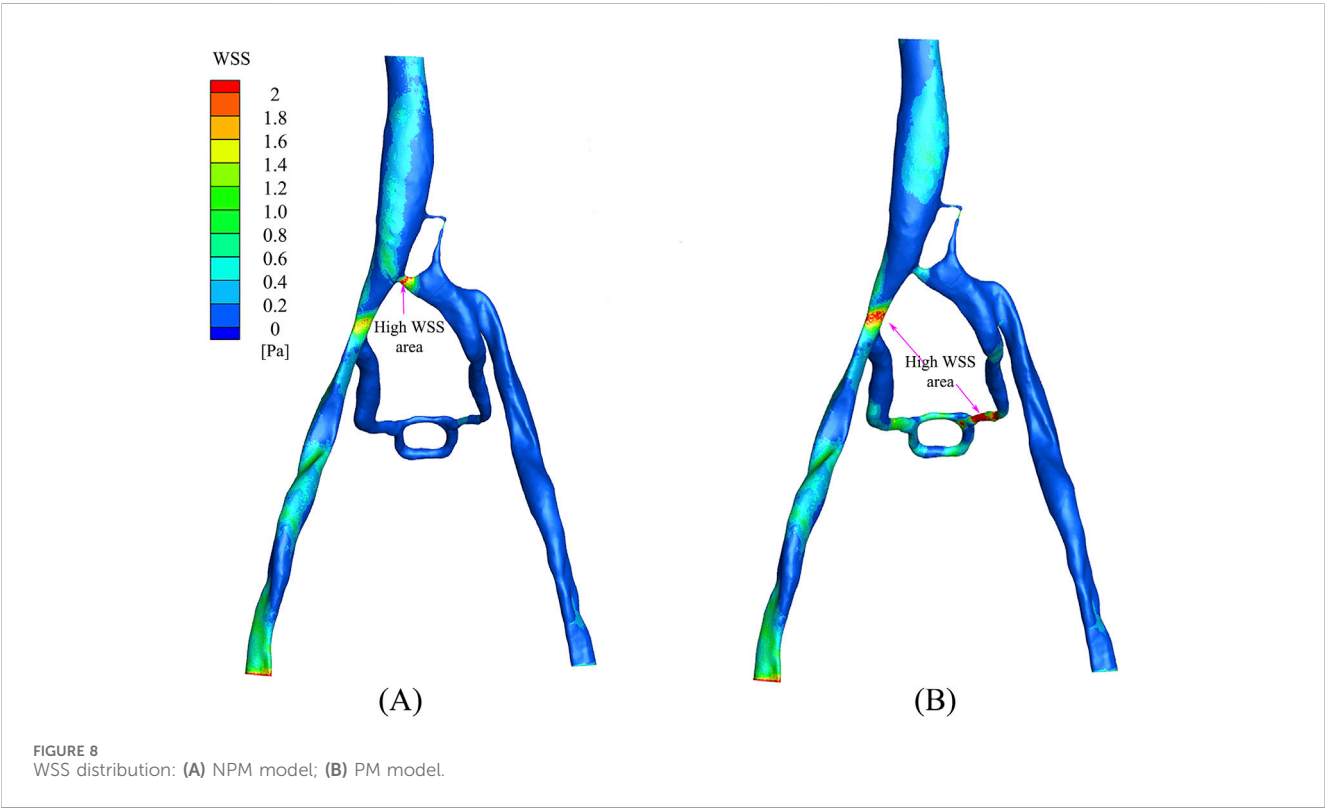
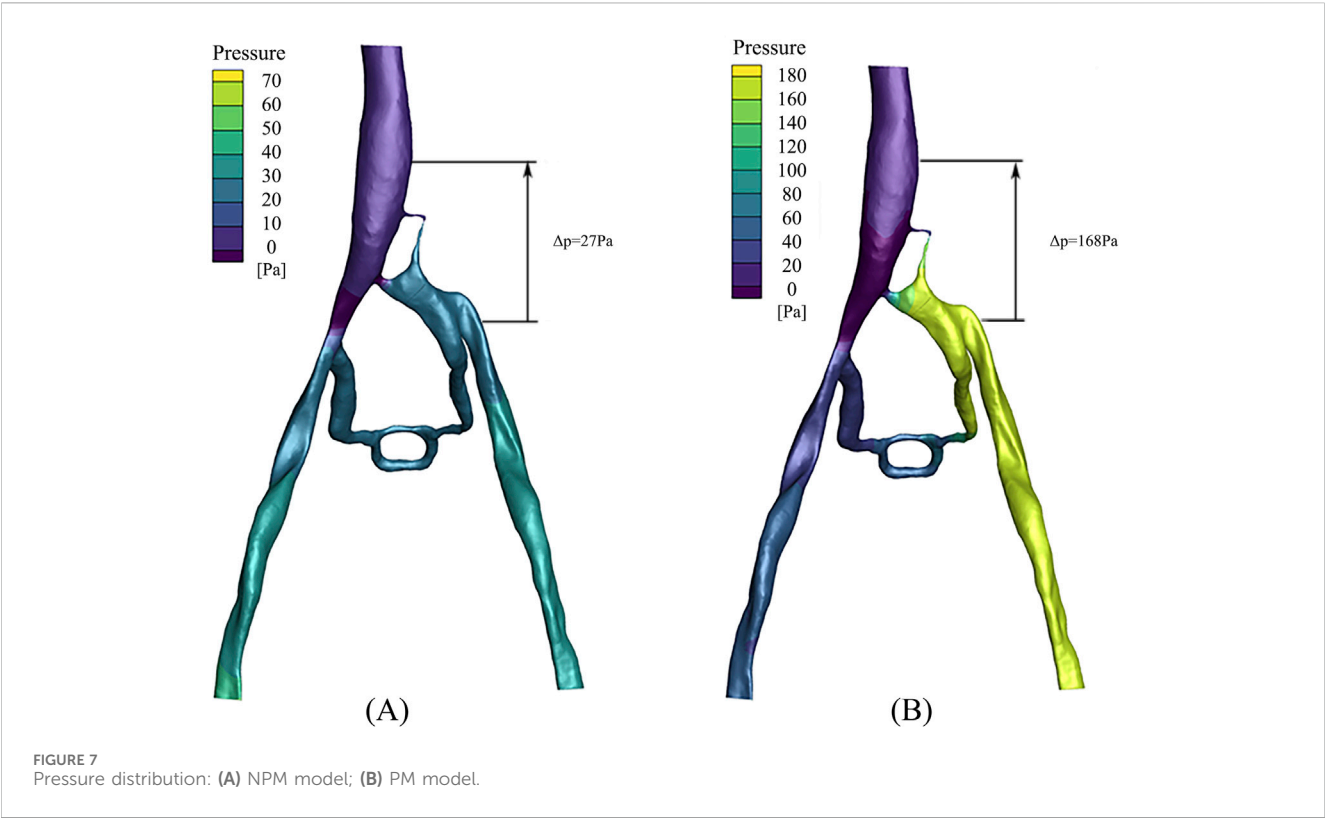




In clinical practice, the pressure gradient is commonly utilized to assess the severity of a patient, which is defined as the pressure difference between the inferior vena cava and the left iliac vein. The data revealed that in the NPM model, the pressure gradient across the compressed region was 27 Pa, whereas it increased to 168 Pa in the PM model. The pressure gradient in the PM model exceeded that of NPM by 141 Pa, demonstrating a closer approximation to clinical reality.

### 3.5 Wall shear stress

The distribution of wall shear stress (WSS) in the PM and NPM models is shown in Figure 8. WSS serves as a crucial parameter that indicates the health status of the vascular wall and blood cells (Candreva et al., 2024). In arterial studies, WSS values above 2.0 Pa are generally deemed to be detrimental to the vessel wall, whereas WSS values below 0.5 Pa are associated with thrombosis



risk (Eshtehardi et al., 2012; Kumar et al., 2018; Samady et al., 2011). In the NPM model, there were limited regions with WSS exceeding 2.0 Pa, predominantly concentrated at the junction of the compressed region and the inferior vena cava. In contrast, the PM model displayed a wider distribution of areas with WSS surpassing 2.0 Pa, primarily situated in the collateral vessels and their junction with the right iliac vein. Furthermore, in the NPM model, regions characterized by low WSS (below 0.5 Pa) were distributed throughout the left iliac vein and collateral vessel regions, while in the PM model, low WSS regions were confined to the vicinity of the left iliac vein.

## 4 Discussion

In the hemodynamic study of the iliac vein, traditional CFD analyses often overlook the structure of venous ridges in patients with iliac vein compression syndrome (IVCS), resulting in discrepancies between computational results and clinical observations. This study employed the PM model to simulate the function and characteristics of venous ridges and validated the feasibility of the PM model in IVCS hemodynamic analysis through TTP.

The TTP of discrete phase particles in CFD analysis incorporating the PM model was found to be highly consistent with that of contrast agents in DSA. This can be attributed to several reasons: firstly, the utilization of the PM model resulted in a reduction of velocity for discrete phase particles within the compressed region, thereby extending the time for particles to reach the inferior vena cava; secondly, the application of the PM model led to an increase of blood flow in collateral circulation, thereby extending the physical distance for particles to travel to the inferior vena cava. The strong resemblance observed between the results of CFD analysis and DSA indicates that the PM model exhibits similar flow characteristics to the compressed iliac vein. Therefore, the PM model can serve as a valuable tool for simulating the venous ridge structure in patients with IVCS. By adjusting the viscosity coefficient of the Porous Media, the PM model can offer a more precise representation of the compressed iliac vein, thereby providing a new theoretical framework for the diagnosis and treatment of IVCS cases.

In comparison to the NPM model, the PM model demonstrated a decrease in the flow and velocity of discrete phase particles within the compressed region, with most particles entering the inferior vena cava through collateral vessels. The reduction in particle velocity within the compressed region in the PM model was primarily attributed to two factors. Firstly, the PM model simulated the compressed region as a porous medium, which increased resistance to particle flow and consequently reduced their velocity. Secondly, the PM model enhanced the blood flow in collateral circulation, resulting in fewer particles entering the inferior vena cava through the compressed region, thereby reducing the velocity of particles within the compressed area. This phenomenon occurs specifically in patients with fully developed collateral circulation. Chen et al. (2023) found that patients with IVCS and without collateral vessels exhibited an increase in blood flow velocity within the compressed region as the severity of iliac vein stenosis progressed. However, Assi et al. (2023) demonstrated that the presence of collateral vessels

significantly reduced blood flow through the left iliac vein to the inferior vena cava by over 50%. These studies suggest that the presence of collateral circulation affects the hemodynamic pattern of the iliac vein in patients with IVCS and can effectively redirect blood flow away from the compressed area towards the inferior vena cava. Compared with the NPM model, the PM model can better simulate this hemodynamic feature. In simulating iliac vein compression with collateral circulation, the PM model can restore real blood flow characteristics by allowing more blood flow into inferior vena cava through the collateral vessels instead of the compressed region, which is more closely aligns with clinical reality.

When comparing the pressure gradient of the left iliac vein and inferior vena cava between PM and NPM models, it was found that the pressure gradient in the PM model was significantly higher than in the NPM model. This finding is consistent with previous research by Li et al. (2023), which demonstrated a notable increase in pressure gradient between these two locations as IVCS progressed. A higher pressure gradient can serve as an indicator of the severity of IVCS, with a pressure gradient exceeding 266 Pa commonly seen as a clinical characteristic of this condition (Liu et al., 2014; O'Sullivan et al., 2000). Although the pressure gradient in PM model did not reach 266 Pa in this study, it is clear that there is a tendency for the PM model to cause a greater pressure gradient difference. The failure to achieve 266 Pa may be attributed to the fact that patients with IVCS in this study were affected by a combination of other factors and pressure gradients. When compared to the NPM model, it is evident that an increased pressure gradient in the PM model aligns more closely with clinical observations.

The comparison of wall shear stress (WSS) between the PM and NPM models revealed that the PM model demonstrated a larger region of high WSS (exceeding 5 Pa). Elevated high WSS regions typically indicate an increased risk of vascular injury in arterial studies (Fallahi et al., 2021; Sandeep and Shine, 2021). A study by Li et al. (2023) demonstrated that an increase in iliac vein stenosis led to a rise in high WSS regions. The higher proportion of high WSS regions in the PM model is more consistent with clinical observations. Conversely, when analyzing low WSS regions, the NPM model showed a larger region with low WSS levels, primarily concentrated in the collateral vessel area. This discrepancy may be attributed to the limited blood flow distribution in the collateral vessels within the NPM model.

This study demonstrates that the incorporation of a porous medium model significantly enhances the hemodynamic analysis of patients with IVCS, leading to a hemodynamic environment that more closely aligns with clinical observations. This improvement is attributed to the effective simulation capabilities of the PM model regarding the obstructive effects posed by venous ridge structures in IVCS. Consequently, when compressed tissues generate ridge-like formations within the constricted region of a vessel, the PM model could accurately replicate the resultant flow disturbances. Therefore, this approach holds considerable promises for conditions such as inferior vena cava compression syndrome or jugular vein compression syndrome.

In this research, a PM model was established in the compressed region of iliac vein, ensuring that parameters such as blood flow velocity, pressure gradient, and wall shear stress in CFD analysis accurately reflected clinical realities. Such approach facilitates a more precise evaluation of both the degree and specific locations

of iliac vein compression. Such insights not only provide robust support for disease diagnosis and treatment, but also play a crucial role in preventing complications, evaluating treatment efficacy, and assessing prognosis. Furthermore, conducting precise CFD analysis of IVCS with the incorporated PM model, could elucidate the relationship between hemodynamic characteristics of IVCS and its onset and progression. This investigation may reveal the pathophysiological mechanisms underlying this condition, thereby providing a theoretical foundation and experimental support for the development of novel therapeutic strategies.

This study has several limitations. Firstly, the sample size was relatively small, which restricts the generalizability of the findings, necessitating further expansion to verify the feasibility of the porous medium model. A larger sample size would not only enhance the statistical power of the study but also facilitate a more nuanced understanding of the performance across diverse patient demographics. This is particularly important given the variability in anatomical and physiological characteristics among individuals with IVCS. Secondly, this study only considered a single porous medium model without investigating the performance differences between various model configurations. Future research could benefit from the selection or design of multiple porous medium models tailored to different patient characteristics, thereby improving both applicability and accuracy of the PM model. Lastly, to further validate the accuracy of the simulation results, it is crucial to conduct *in vitro* or *in vivo* experiments. Such investigations will help confirm validity of the model and provide new theoretical support for the treatment of IVCS patients, ultimately enhancing clinical outcomes.

## 5 Conclusion

In this study, the PM model was utilized to simulate the compressed region of the iliac vein in patients with IVCS, and the feasibility of this model was validated through the hemodynamic analysis of IVCS. The results demonstrated that CFD analysis with the PM model could replicate the hemodynamic environment of IVCS patients. Incorporating the PM model in CFD analysis reduced the flow and velocity in the compressed iliac vein, altered the distribution of blood flow, and directed most of the blood towards the right iliac vein through collateral circulation before returning to the inferior vena cava. Additionally, the pressure gradient value between inferior vena cava and left iliac vein closely approximated to clinical pressure gradient index. Therefore, CFD analysis using PM model has potential applications for evaluating IVCS patient conditions and offering valuable insights for the diagnosis and treatment of IVCS from a fluid mechanics perspective.

## Data availability statement

The original contributions presented in the study are included in the article/supplementary material, further inquiries can be directed to the corresponding authors.

## Ethics statement

Written informed consent was obtained from the individual(s) for the publication of any potentially identifiable images or data included in this article.

## Author contributions

LW: Formal Analysis, Writing–original draft, Writing–review and editing. KH: Writing–original draft, Writing–review and editing, Investigation, Methodology. JW: Writing–review and editing. SZ: Writing–review and editing. XY: Writing–review and editing. YC: Supervision, Writing–review and editing. CL: Writing–review and editing, Data curation. XL: Writing–review and editing. KY: Writing–review and editing. PQ: Conceptualization, Methodology, Writing–review and editing. YZ: Methodology, Writing–review and editing.

## Funding

The author(s) declare that financial support was received for the research, authorship, and/or publication of this article. This work was supported by the Anhui Provincial Natural Science Foundation grant 2308085QA31 and the Fundamental Research Funds for the Central Universities (JZ2022HGTA0314 and JZ2022HGQA0139) to LW.

## Acknowledgments

We would like to express our sincere gratitude to the First Affiliated Hospital of Anhui Medical University and the Shanghai Ninth People's Hospital Affiliated to Shanghai Jiao Tong University School of Medicine for providing clinical medical imaging data and their assistance during the research.

## Conflict of interest

The authors declare that the research was conducted in the absence of any commercial or financial relationships that could be construed as a potential conflict of interest.

## Publisher's note

All claims expressed in this article are solely those of the authors and do not necessarily represent those of their affiliated organizations, or those of the publisher, the editors and the reviewers. Any product that may be evaluated in this article, or claim that may be made by its manufacturer, is not guaranteed or endorsed by the publisher.

## References

- Albadawi, M., Abuouf, Y., Elsaygher, S., Sekiguchi, H., Ookawara, S., and Ahmed, M. (2022). Influence of Rigid-Elastic artery wall of carotid and coronary stenosis on hemodynamics. *Bioeng. (Basel)* 9 (11), 708. doi:10.3390/bioengineering9110708
- Al-Otaibi, M., Vaidy, A., Vaidya, A., Zlotshewer, B., Oliveros, E., Zhao, H., et al. (2021). May-Thurner anatomy in patients with chronic thromboembolic pulmonary hypertension: an important clinical association. *JACC Cardiovasc. Interv.* 14 (17), 1940–1946. doi:10.1016/j.jcin.2021.06.042
- Assi, I. Z., Lynch, S. R., Samulak, K., Williams, D. M., Wakefield, T. W., Obi, A. T., et al. (2023). An ultrasound imaging and computational fluid dynamics protocol to assess hemodynamics in iliac vein compression syndrome. *J. Vasc. Surg. Venous Lymphatic Disord.* 11 (5), 1023–1033.e5. doi:10.1016/j.jvsv.2023.05.017
- Bear, J., and Bachmat, Y. (1990). “Introduction to modeling of transport phenomena in porous media,” Springer Science and Business Media.
- Brandt, L., and Coletti, F. (2021). Particle-laden turbulence: progress and perspectives. *Annu. Rev. Fluid Mech.* 54, 159–189. doi:10.1146/annurev-fluid-030121-021103
- Butros, S. R., Liu, R., Oliveira, G. R., Ganguli, S., and Kalva, S. (2013). Venous compression syndromes: clinical features, imaging findings and management. *Br. J. Radiology* 86 (1030), 20130284. doi:10.1259/bjr.20130284
- Candrea, A., Buongiorno, A. L., Matter, M. A., Rizzini, M. L., Giacobbe, F., Ravetti, E., et al. (2024). Impact of endothelial shear stress on coronary atherosclerotic plaque progression and composition: a meta-analysis and systematic review. *Int. J. Cardiol.* 407, 132061. doi:10.1016/j.ijcard.2024.132061
- Changsheng, L., Haiquan, F., Kun, W., Xiaotian, W., and Yonggang, W. (2023). Influence of the anatomical structure on the hemodynamics of iliac vein stenosis. *J. Biomechanical Eng.* 145 (1), 011013. doi:10.1115/1.4055307
- Chen, H. W., Chen, C. H., Fan, Y. J., Lin, C. Y., Hsu, W. H., Su, I. C., et al. (2023). CFD study of the effect of the angle pattern on iliac vein compression syndrome. *Bioeng. (Basel)* 10 (6), 688. doi:10.3390/bioengineering10060688
- Chiu, J. J., and Chien, S. (2011). Effects of disturbed flow on vascular endothelium: pathophysiological basis and clinical perspectives. *Physiol. Rev.* 91 (1), 327–387. doi:10.1152/physrev.00047.2009
- Eshtehardi, P., McDaniel, M. C., Suo, J., Dhawan, S. S., Timmins, L. H., Binongo, J. N., et al. (2012). Association of coronary wall shear stress with atherosclerotic plaque burden, composition, and distribution in patients with coronary artery disease. *J. Am. Heart Assoc.* 1 (4), e002543. doi:10.1161/JAHA.112.002543
- Fallahi, H., Shirani, E., and Zohravi, E. (2021). Hemodynamic analysis of coronary artery bypass grafting with elastic walls and different stenoses. *Sci. Ironical Trans. B Mech. Eng.* 28, 773–784. doi:10.24200/sci.2020.53378.3211
- Jiang, X., Gu, X., Xu, T., Li, X., Wu, P., and Sun, L. (2021). Patient-specific hemodynamic analysis of IVCS-induced DVT. *Comput. Methods Biomechanics Biomed. Eng.* 25 (11), 1211–1221. doi:10.1080/10255842.2021.2003791
- Kalu, S., Shah, P., Natarajan, A., Nwankwo, N., Mustafa, U., and Hussain, N. (2013). May-thurner syndrome: a case report and review of the literature. *Case Rep. Vasc. Med.* 2013, 1–5. doi:10.1155/2013/740182
- Kaviany, M. (2012). “Principles of heat transfer in porous media,” Springer Science and Business Media. doi:10.1080/10255842.2021.2003791
- Kumar, A., Hung, O. Y., Piccinelli, M., Eshtehardi, P., Corban, M. T., Sternheim, D., et al. (2018). ‘Low coronary wall shear stress is associated with severe endothelial dysfunction in patients with nonobstructive coronary artery disease. *JACC Cardiovasc. Interv.* 11 (20), 2072–2080. doi:10.1016/j.jcin.2018.07.004
- Li, C., Zhan, Y., Wang, Z., Gao, Y., Ye, K., Lu, X., et al. (2023). Effect of stent treatment on hemodynamics in iliac vein compression syndrome with collateral vein. *Med. Eng. and Phys.* 115, 103983. doi:10.1016/j.medengphy.2023.103983
- Liu, Z., Gao, N., Shen, L., Yang, J., Zhu, Y., Li, Z., et al. (2014). Endovascular treatment for symptomatic iliac vein compression syndrome: a prospective consecutive series of 48 patients. *Ann. Vasc. Surg.* 28 (3), 695–704. doi:10.1016/j.avsg.2013.05.019
- O’Sullivan, G. J., Semba, C. P., Bittner, C. A., Kee, S. T., Razavi, M. K., Sze, D. Y., et al. (2000). Endovascular management of iliac vein compression (May-Thurner) syndrome. *J. Vasc. Interventional Radiology* 11 (7), 823–836. doi:10.1016/s1051-0443(07)61796-5
- Poyyamoli, S., Mehta, P., Cherian, M., Anand, R. R., Patil, S. B., Kalva, S., et al. (2021). May-Thurner syndrome. *Cardiovasc. Diagnosis Ther.* 11 (5), 1104–1111. doi:10.21037/cdt.2020.03.07
- Samady, H., Eshtehardi, P., McDaniel, M. C., Suo, J., Dhawan, S. S., Maynard, C., et al. (2011). ‘Coronary artery wall shear stress is associated with progression and transformation of atherosclerotic plaque and arterial remodeling in patients with coronary artery disease. *Circulation* 124 (7), 779–788. doi:10.1161/CIRCULATIONAHA.111.021824
- Sandeep, S., and Shine, S. R. (2021). Effect of stenosis and dilatation on the hemodynamic parameters associated with left coronary artery. *Comput. Methods Programs Biomed.* 204, 106052. doi:10.1016/j.cmpb.2021.106052
- Sikkandar, M. Y., Sudharsan, N. M., Begum, S. S., and Ng, E. Y. (2019). Computational fluid dynamics: a technique to solve complex biomedical engineering problems—a review. *WSEAS Trans. Biol. Biomed.* 16, 121–137.
- Taeibi, A. (2022). Deep learning for computational hemodynamics: a brief review of recent advances. *Fluids* 7, 197. doi:10.3390/fluids7060197
- Virchow, A. A. (2024). Pathological anatomy and histology. *NLM Cat. - NCBI*. Available at: <https://www.ncbi.nlm.nih.gov/nlmcatalog> (Accessed January 11, 2020).
- Wang, H. F. (2000). “Theory of porous media fluid mechanics,” Elsevier.
- Zhao, Y., Li, D., Shi, D., Zhou, T., and Xiong, Z. (2003). Anatomical basis of iliac vein compression syndrome. *Chin. J. Pract. Surg.* 23 (12), 745–746.
- Zhou, Y., Shen, S., and Wu, D. (2022). Hot issues in the interventional treatment of iliac vein diseases. *Chin. J. General Surg.* 37 (3), 227–229. doi:10.3760/cma.j.cn113855-20211223-00739





## OPEN ACCESS

## EDITED BY

Jiaqiu Wang,  
London South Bank University, United Kingdom

## REVIEWED BY

Valeria Graceffa,  
Institute of Technology, Ireland  
Sacha Cavelier,  
Queensland University of Technology, Australia

## \*CORRESPONDENCE

Chuan Ye,  
✉ yechuanchina@hotmail.com

RECEIVED 22 October 2024

ACCEPTED 16 December 2024

PUBLISHED 08 January 2025

## CITATION

Luo J, Zou Z, Zou Q, Luo S, He J and Ye C (2025)  
Effects of different microfracture drilling  
parameters on bone quality: a finite  
element analysis.  
*Front. Bioeng. Biotechnol.* 12:1515136.  
doi: 10.3389/fbioe.2024.1515136

## COPYRIGHT

© 2025 Luo, Zou, Zou, Luo, He and Ye. This is an  
open-access article distributed under the terms  
of the [Creative Commons Attribution License](#)  
(CC BY). The use, distribution or reproduction in  
other forums is permitted, provided the original  
author(s) and the copyright owner(s) are  
credited and that the original publication in this  
journal is cited, in accordance with accepted  
academic practice. No use, distribution or  
reproduction is permitted which does not  
comply with these terms.

# Effects of different microfracture drilling parameters on bone quality: a finite element analysis

Jiayi Luo<sup>1,2</sup>, Zihao Zou<sup>2</sup>, Qiang Zou<sup>1,2</sup>, Siwei Luo<sup>2</sup>, Jialin He<sup>2</sup> and  
Chuan Ye<sup>1,2\*</sup>

<sup>1</sup>Department of Orthopaedics, The Affiliated Hospital of Guizhou Medical University, Guiyang, China,

<sup>2</sup>Center for Tissue Engineering and Stem Cell Research, Guizhou Medical University, Guiyang, China

**Background:** Microfracture drilling is a surgical technique that involves creating multiple perforations in areas of cartilage defects to recruit stem cells from the bone marrow, thereby promoting cartilage regeneration in the knee joint. Increasing the exposed bone marrow surface area (more holes in the same area) can enhance stem cell outflow. However, when the exposed area is large, it may affect the mechanical strength of the bone at the site of the cartilage defect. The purpose of this study is to use the finite element method to analyze the effects of drilling diameter, hole spacing, and drilling depth during microfracture surgery on the stability of the bone structure at the cartilage defect site.

**Methods:** In this study, a normal knee joint model was selected for solid modeling, and a model of a femoral medial condyle cartilage defect was constructed. Microfracture holes with different diameters (1.0 mm, 2.0 mm, 3.0 mm), depths (10 mm, 30 mm), and spacings (1.0 mm, 2.0 mm, 3.0 mm) were created in the femoral medial condyle cartilage defect model. Using Ansys software, the knee joint's loading conditions in the standing position were simulated, and the structural stability of the model was analyzed. The holes in areas of stress concentration were selected for more detailed mechanical analysis.

**Results:** The Von Mises stresses for all the drilling parameters did not exceed the yield strength of the bone. Changes in the drilling parameters did not affect the bone structure around the holes. When smaller diameter drilling tools with closer spacing were used, the average maximum Von Mises stress and the average Von Mises stress on the holes were the lowest.

**Conclusion:** Although the optimal combination of drilling parameters was not determined, this study provides a mechanical reference for the effects of drilling parameters on bone quality. It demonstrates that using smaller diameter drilling tools with closer spacing in areas of the same defect size results in a greater number of holes, with a lesser impact on bone stability. This study provides a mechanical reference for microfracture drilling.

## KEYWORDS

microfracture, finite element analysis, osteoarthritis of the knee (KOA), drilling, kirschner wire

## Background

Knee cartilage injuries can be categorized as acute or chronic. Acute injuries usually manifest as full-thickness cartilage lesions, whereas chronic injuries progress through various stages, eventually leading to subchondral bone proliferation and sclerosis once the cartilage is completely worn away (Lieberthal et al., 2015; Hunziker, 2002). Various clinical treatment methods are currently available, such as microfracture or drilling, autologous chondrocyte implantation, and mosaicplasty (Solheim et al., 2018; Na et al., 2019). Despite recent advances in treatment, microfracture remains the standard surgical technique for cartilage defects due to its cost-effectiveness, simplicity, and studies indicating its effectiveness in larger cartilage defects (Mithoefer et al., 2009). Microfracture or drilling techniques stimulate subchondral bone marrow outflow, promoting cartilage repair by recruiting bone marrow stem cells to the lesion site through the use of awls or Kirschner wires of a certain diameter (Mithoefer et al., 2009).

Numerous studies have shown that the number of mesenchymal stem cells (MSCs) migrating to the cartilage defect after microfracture influences cartilage regeneration outcomes (Na et al., 2019; Mithoefer et al., 2009). The number of MSCs in the lesion area and the therapeutic results vary depending on the size, number, and depth of the holes (Powers et al., 2021). Research has indicated that the spacing between microfracture holes can impact cartilage repair, with denser holes promoting the formation of type II collagen (Orth et al., 2016). Benthien and colleagues found that the depth of microfracture holes affects microcracks and bone compression around the holes, which in turn influences the connectivity of bone marrow around the holes (Benthien and Behrens, 2013). Increasing the surface area of bone marrow stimulation by adjusting the size and number of holes in the subchondral bone plate leads to a greater outflow of MSCs from the microfracture holes. In other words, a larger exposed area is conducive to the release of MSCs. However, since the knee bears the body's weight, too many holes may compromise the structure of the subchondral bone and trabeculae, potentially hindering cartilage regeneration. Currently, most physicians perform microfracture drilling with a hole spacing of 3–4 mm and a depth of 3 mm, based on empirical practice, while the hole diameter is determined by the tools used. However, such microfracture drilling parameters do not adequately meet clinical requirements. Drilling depths of 10 mm or even 30 mm are necessary to effectively penetrate sclerotic bone, facilitate the release of mesenchymal stem cells, and alleviate intramedullary pressure (Benthien and Behrens, 2013). At present, the mechanical interactions among the three key microfracture parameters—holes diameter, spacing, and depth—have not been validated to determine their impact on post-microfracture bone structural stability. Biomechanical studies are needed to investigate the effects of holes diameter, spacing, and depth on bone structure.

To determine the mechanical stability after microfracture, we hypothesized that the distance between holes, the depth, and the hole size in microfracture drilling are associated with the structural stability of the bone in the drilled area. Using MRI-based modeling techniques, we constructed a model of the knee joint, and finite element analysis was applied to examine the mechanical effects of different drilling parameters in microfracture surgery. This allowed us to assess the structural stability of the bone in the drilled area.

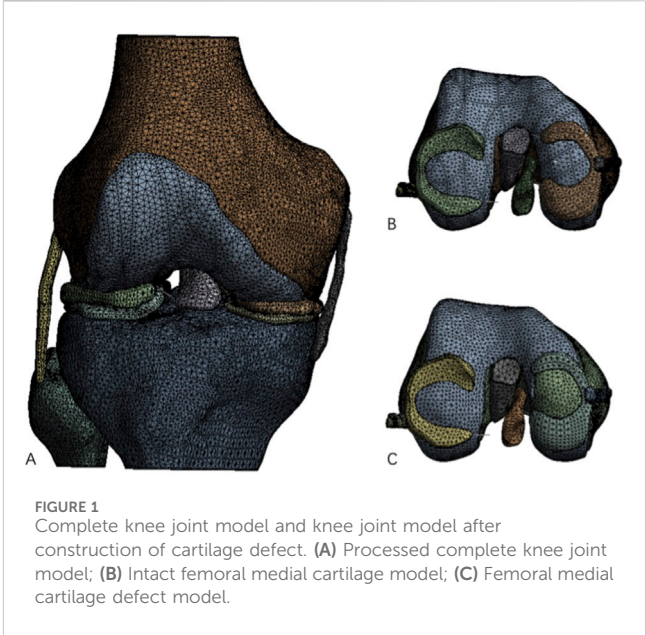


TABLE 1 Microfracture drilling parameters.

Drilling diameter (mm)	1.0	2.0	3.0
Drilling Spacing (mm)	1.0	2.0	3.0
Drilling depth (mm)	10	30	

## Methods

### Construction of knee joint and medial femoral cartilage defect models

In accordance with the standards for finite element analysis model construction, a healthy female volunteer without a history of knee joint diseases was recruited. The participant, aged 50, with a height of 160 cm and a weight of 60 kg, had no history of osteoporosis, lower limb fractures, or malalignment, and provided informed consent for the study. The DICOM format MRI data of the volunteer's knee joint was imported into Mimics 21.0 software, and the right lower limb was selected for model reconstruction. In Mimics 21.0, a new mask was created to perform threshold segmentation of the knee joint, with the threshold set between 198 and 3,071 Hounsfield units (HU). The femur, tibia, and fibula were separated into individual masks using the separation mask tool. Subsequently, the femur, tibia, and fibula models were repaired, sealed, and filled using the add and subtract functions within the mask editing tool.

For soft tissues such as cartilage, menisci, and ligaments, the 3D models were manually extracted. After completing these steps, the extracted 3D models in STL format were imported into Geomagic Wrap 17.0 software for feature removal and smoothing. The models were further refined by adjusting contour lines, surface patches, and constructing grids and NURBS surface fitting, after which the solid 3D models of bone and soft tissues were saved in STEP format.

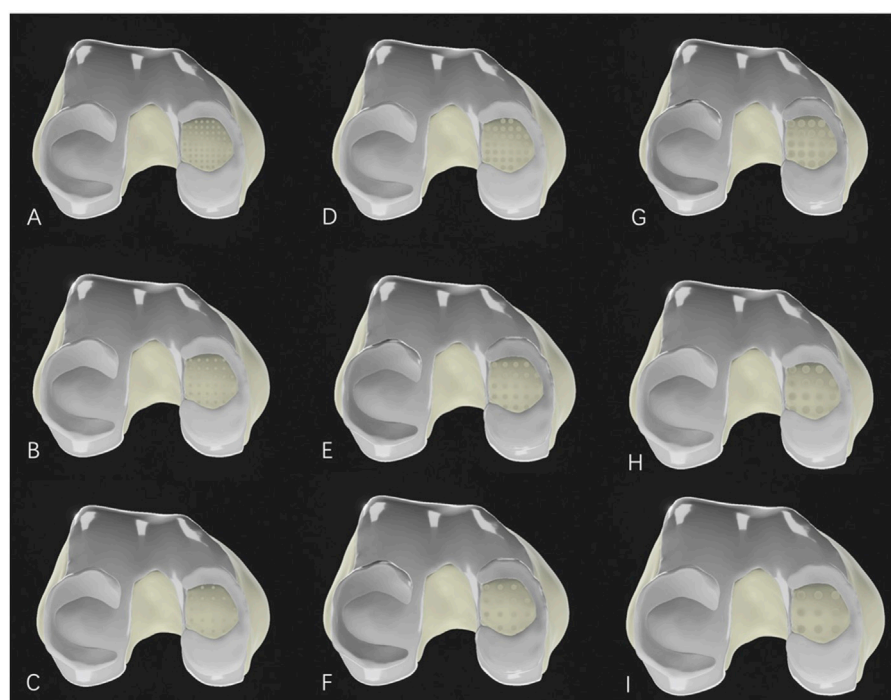


FIGURE 2

Medial femoral cartilage defect model after microfracture drilling. (A–C): Microfracture models with a hole diameter of 1.0 mm; (D–F): Microfracture models with a hole diameter of 2.0 mm; (G–I): Microfracture models with a hole diameter of 3.0 mm. (A, D, G) represent drilling hole spacing of 1.0 mm; (B, E, H) represent drilling hole spacing of 2.0 mm; and (C, F, I) also represent drilling hole spacing of 3.0 mm.

Next, the femoral cartilage solid 3D model was re-imported into Geomagic Wrap 17.0 software, where a model of a full-thickness medial condyle cartilage defect with a diameter of 20 mm was constructed (Figure 1) and saved in STEP format.

The medial condyle cartilage defect model was then combined with the femur, and drilling models with different parameters were constructed in SolidWorks 2021 software (parameters listed in Table 1). These drilling models were assembled with the corresponding bone and soft tissue models for further analysis (Figure 2).

## Finite element section

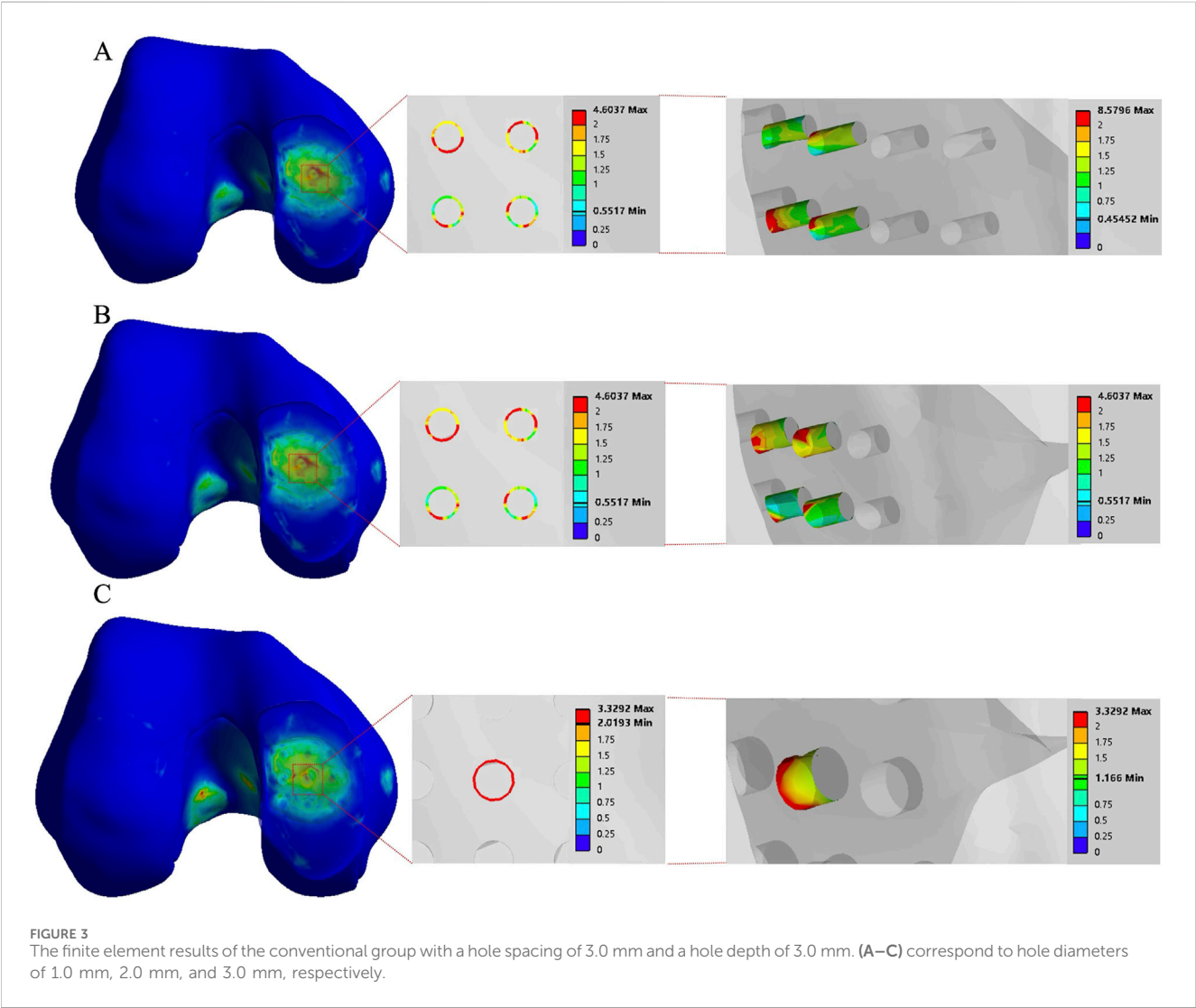
The lower limb cartilage defect model was imported into Ansys Workbench 2021 for meshing. The mesh type used was C3D4 tetrahedral elements, with different mesh sizes applied to various parts of the model. The tibia, fibula, medial and lateral collateral ligaments, as well as the anterior and posterior cruciate ligaments, had a mesh size of 3.0 mm, while the femur, femoral cartilage, medial and lateral tibial cartilage, and medial and lateral menisci had a mesh size of 2.0 mm. It was assumed that all models exhibited homogeneous, isotropic, and linear elastic behavior. For the material properties, the mechanical attributes of the knee joint models were derived from literature reports. Different material properties were assigned according to the stiffness of the bone, cartilage, menisci, and ligaments (Li et al., 2018; Ding et al., 2021) (Table 2), with all models

defined as linear elastic, homogeneous, and isotropic materials. The connections between the menisci and the tibial plateau were replaced by one-dimensional linear spring elements (Koh et al., 2018). One spring element connected the anterior and posterior horns of the menisci to the tibia, with a spring stiffness set to 2000 N/mm.

In the assembled model, there were a total of 20 contact interactions: 8 were defined as “frictionless,” and 14 as “bonded.” The contact area between the femoral medial condyle cartilage and the medial meniscus was defined as Surface 1, the contact area between the femoral lateral condyle cartilage and the lateral meniscus as Surface 2, the contact area between the femoral medial condyle cartilage and the medial tibial cartilage as Surface 3, and the contact area between the femoral lateral condyle cartilage and the lateral tibial cartilage as Surface 4. The contact area between the medial tibial cartilage and the medial meniscus was defined as Surface 5, and between the lateral tibial cartilage and the lateral meniscus as Surface 6. The contact area between the bone tissue at the medial femoral cartilage defect and the medial tibial cartilage was defined as Surface 7, while the contact area between the bone tissue at the medial femoral cartilage defect and the medial meniscus was defined as Surface 8. These contact relationships were set as “hard contact between surfaces,” with the contact surfaces defined as nonlinear, “frictionless finite sliding,” to simulate the limited sliding motion of the knee joint. The remaining bone-to-ligament and bone-to-cartilage contact relationships were set as “bonded.”

TABLE 2 Material properties for all models in this study.

Material	Young's modulus (Mpa)	Poisson's ratio
Bone (Li et al., 2018)	7,300	0.3
Cartilage (Ding et al., 2021)	5	0.46
Meniscus (Ding et al., 2021)	59	0.49
Ligament (Ding et al., 2021)	215	0.46



To simulate the actual loading conditions on the knee joint while standing, an axial compressive load was applied to the entire lower limb. The load was applied along the force line of each model, directed downward from the proximal cross-section of the femur, with a magnitude of 600 N. The distal ends of the tibia and fibula were fixed as support constraints. During the load application, in order to maintain axial load application, the distal ends of the tibia and fibula were fully constrained in all six degrees of freedom, while only the Y-axis of the femur was fixed to prevent flexion.

## Results

### Finite element stress contour maps of knee joint models with different microfracture drilling parameters

In the normal knee joint, the highest von Mises stress in the medial tibial cartilage occurred in the anteromedial region, while the highest von Mises stress in the lateral tibial cartilage was distributed in the central region. The stress distribution in the



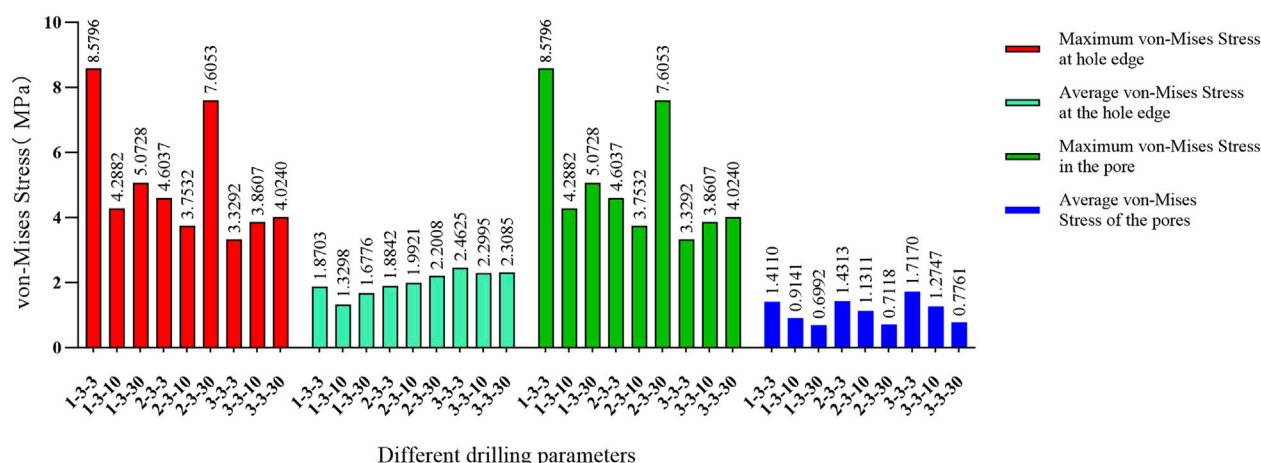


FIGURE 4

Comparison of von Mises forces under different hole diameters: hole spacing of 3.0 mm and depth of 3.0 mm versus hole spacing of 3.0 mm with depths of 10 mm and 30 mm, respectively.

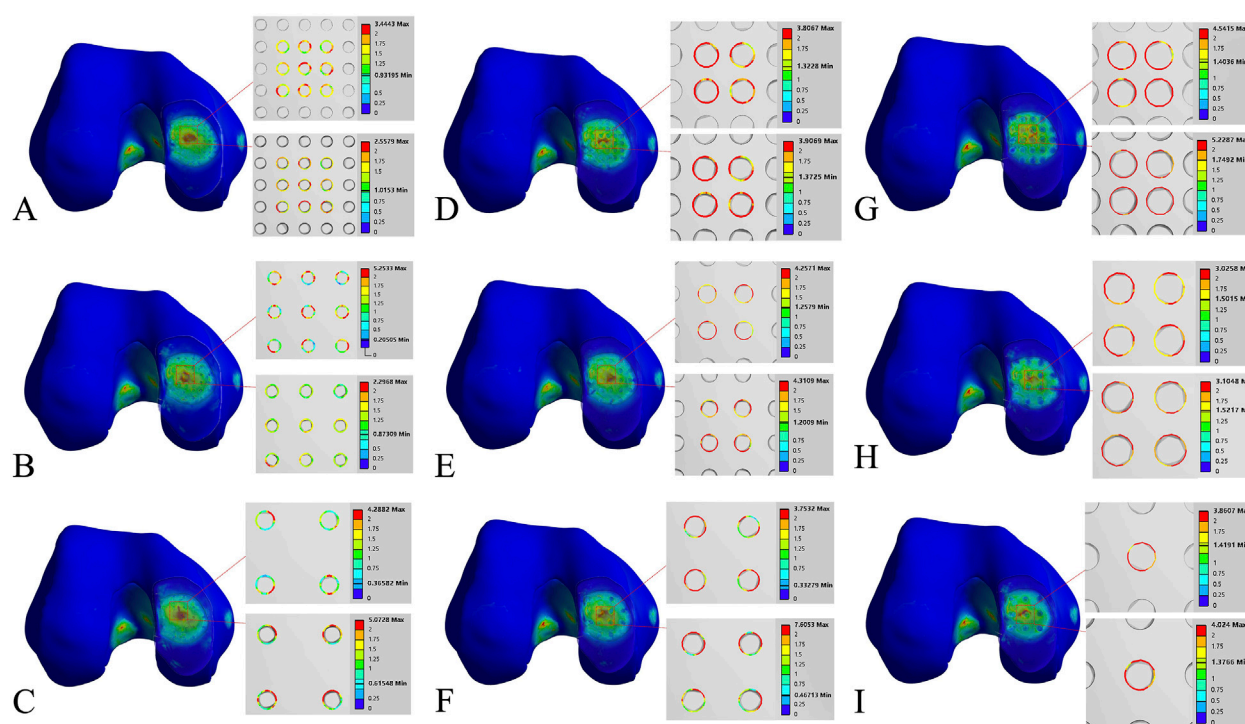


FIGURE 5

Finite element contour maps for different drilling parameters. (A–C): 3D finite element contour maps of the knee joint after microfracture with a hole diameter of 1.0 mm, showing 10 mm hole depth (top) and 30 mm hole depth (bottom); (D–F): 3D finite element contour maps of the knee joint after microfracture with a hole diameter of 2.0 mm, displayed in the same format; (G–I): 3D finite element contour maps of the knee joint after microfracture with a hole diameter of 3.0 mm.

femoral cartilage matched that of the corresponding tibial cartilage, with higher stress on the medial side compared to the lateral side. In the cartilage defect model, the exposed medial femoral condyle was in direct contact with the medial tibial cartilage, causing minor changes in the stress distribution on the lateral femoral cartilage. The average von Mises stress in the

contact area of the lateral femoral cartilage decreased from 0.0427 MPa to 0.0339 MPa. The highest von Mises stress in the medial femoral condyle at the defect site was 1.6563 MPa, with an average von Mises stress of 0.6382 MPa. After microfracture drilling, the average maximum von Mises stress increased to 4.6443 MPa, with an average von Mises stress of 1.2061 MPa.



TABLE 3 Von mises stress data of stress concentration area with different drilling parameters.

Microfracture drilling parameters (mm)	Number of drill holes in the stress concentration area	Maximum von mises stress at the edge of the hole in the stress area (MPa)	Average von mises stress at the edge of the hole in the stress area (MPa)	Maximum von mises stress in the pores of the stress area (MPa)	Average von mises stress in the pores of the stress area (MPa)
1,1,10	9	3.4443	1.686	3.4443	1.2975
1,1,30	9	2.5579	1.7288	2.5579	0.83991
1,2,10	9	5.2533	1.6232	5.2533	1.0648
1,2,30	9	2.2968	1.3881	2.2968	0.68387
1,3,10	4	4.2882	1.3298	4.2882	0.91412
1,3,30	4	5.0728	1.6776	5.0728	0.69922
2,1,10	4	3.8067	2.2081	3.8067	1.5168
2,1,30	4	3.9069	2.269	3.9069	0.9123
2,2,10	4	4.2571	2.0626	4.2571	1.302
2,2,30	4	4.3109	2.1045	4.3109	0.80924
2,3,10	4	3.7532	1.9921	3.7532	1.1311
2,3,30	4	7.6053	2.2008	7.6053	0.71176
3,1,10	4	4.5415	2.5162	4.5415	1.7103
3,1,30	4	5.2287	2.6854	5.2287	1.0673
3,2,10	4	3.0258	1.9985	3.0258	1.2715
3,2,30	4	3.1048	2.0695	3.1048	0.8078
3,3,10	1	3.8607	2.2995	3.8607	1.2747
3,3,30	1	4.024	2.3085	4.024	0.77605

The stress concentration region within the medial compartment of the knee joint was selected for further analysis, focusing on the differences in the number of drilling holes within the stress region caused by variations in hole diameter and spacing. Depending on the drilling parameters, the stress concentration region contained 9 holes, 4 holes, or 1 hole. Due to the sharp edges of the holes, stress concentration is more likely to occur, with the maximum stress location identified for each model. The finite element results of the conventional microfracture model group showed no significant difference compared to the experimental group. However, under the same hole diameter and spacing conditions, the average von Mises stress in the channels exhibited a decreasing trend with increasing hole depth (Figures 3, 4). In the experimental group, the maximum von Mises stress at the drilled holes in the stress concentration region was 7.6053 MPa, with an average maximum von Mises stress of 4.1299 MPa. Different drilling depths resulted in variations in the maximum von Mises stress at the same drilling location (Figure 5).

The maximum von Mises stress for 9 holes was 5.2533 MPa, with an average maximum von Mises stress of 3.3881 MPa. For 4 holes, the maximum von Mises stress was 7.6053 MPa, with an average maximum von Mises stress of 4.3770 MPa. For 1 hole, the maximum von Mises stress was 4.024 MPa, with an average maximum von Mises stress of 3.9424 MPa. The maximum von Mises stress for hole diameters of 1.0 mm, 2.0 mm, and 3.0 mm was 5.2533 MPa, 7.6053 MPa, and 4.024 MPa, respectively, with

corresponding average maximum von Mises stresses of 3.8189 MPa, 4.6067 MPa, and 3.9643 MPa. The maximum von Mises stress for hole spacings of 1.0 mm, 2.0 mm, and 3.0 mm was 5.2287 MPa, 5.2533 MPa, and 7.6053 MPa, respectively, with corresponding average maximum von Mises stresses of 3.9143 MPa, 3.7081 MPa, and 4.7674 MPa (Table 3–6; Figure 6).

The maximum von Mises stress for a hole depth of 10 mm and a hole depth of 30 mm was the same at the hole edge, both occurring at the contact location. Changing the depth did not affect the maximum von Mises stress value but did influence the average stress in the hole channel (Figures 7, 8). The average von Mises stress for a hole depth of 10 mm was 1.2759 MPa, while for a hole depth of 30 mm, it was 0.8583 MPa (Table 7; Figure 9).

## Discussion

Microfracture drilling is a minimally invasive and simple technique that promotes the outflow of bone marrow stem cells to the site of cartilage defects, inducing cartilage repair. Due to its advantages of fewer complications and ease of operation, it has long been the standard treatment for cartilage injuries (Peng et al., 2023). In a follow-up study of patients who underwent microfracture for 5 years, 83% reported pain relief (Kraeutler et al., 2018). Another study reported significant improvements in various knee evaluation

TABLE 4 Von mises stress data in the stress concentration area for different numbers of drill holes (1).

Number of holes in the stress concentration area	Maximum von mises stress at the edge of the hole in the stress area (MPa)	Average von mises stress at the edge of the hole in the stress area (MPa)	Maximum von mises stress in the pores of the stress area (MPa)	Average von mises stress in the pores of the stress area (MPa)
9	3.3881	1.6065	3.3881	0.9715
4	4.4085	2.0928	4.4085	1.0711
1	3.9424	2.304	3.9424	1.0254

TABLE 5 Von mises stress data in the stress concentration area for different numbers of drill holes (2).

Drilling diameter (mm)	Maximum von mises stress at the edge of the hole in the stress area (MPa)	Average von mises stress at the edge of the hole in the stress area (MPa)	Maximum von mises stress in the pores of the stress area (MPa)	Average von mises stress in the pores of the stress area (MPa)
1.0	3.8189	1.5723	3.8189	0.9166
2.0	4.6067	2.1395	4.6067	1.0639
3.0	3.9643	2.3129	3.9643	1.1513

TABLE 6 Von mises stress data in the stress concentration area for different numbers of drill holes (3).

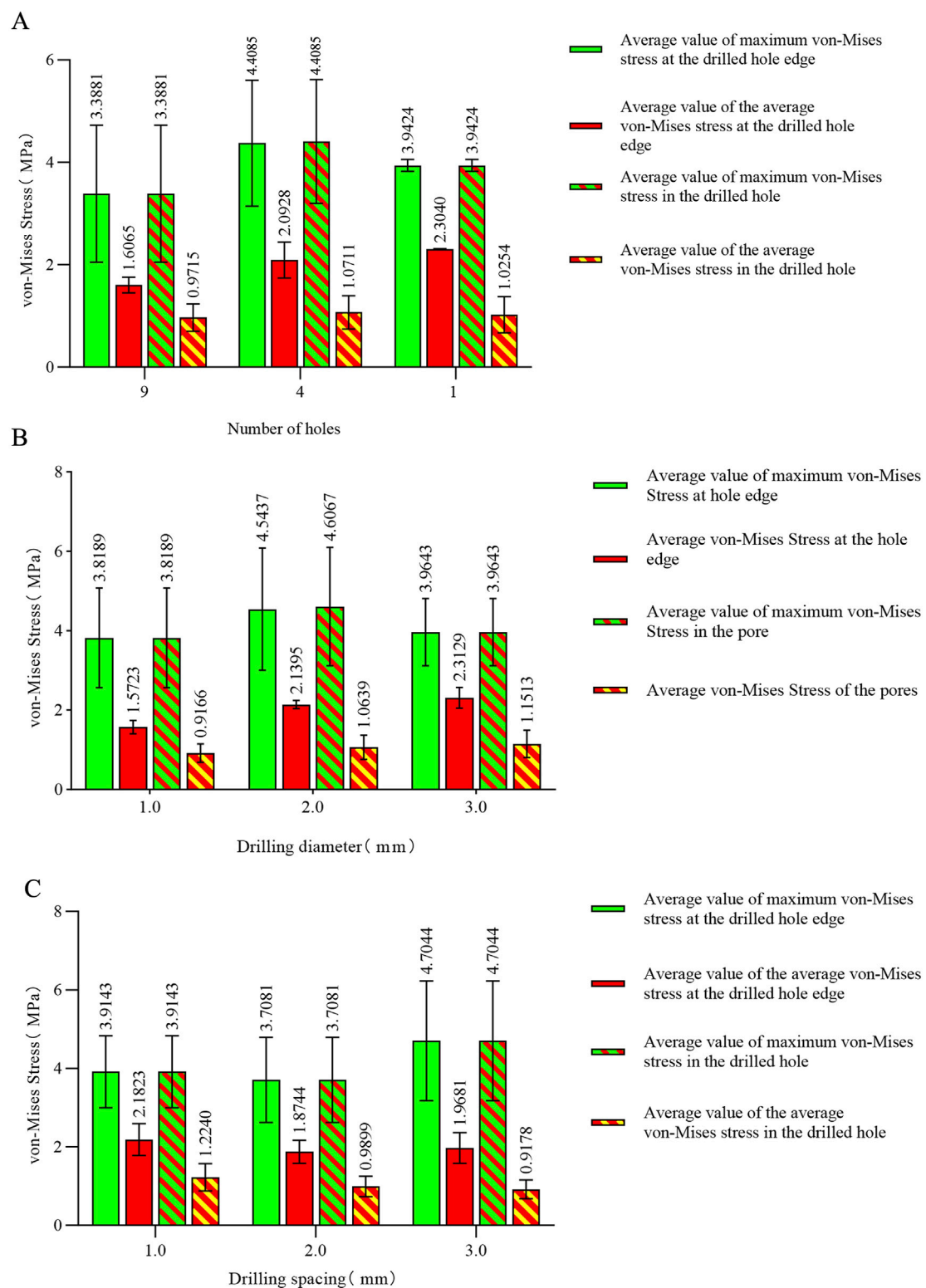
Drilling spacing (mm)	Maximum von mises stress at the edge of the hole in the stress area (MPa)	Average von mises stress at the edge of the hole in the stress area (MPa)	Maximum von mises stress in the pores of the stress area (MPa)	Average von mises stress in the pores of the stress area (MPa)
1.0	3.9143	2.1823	3.9143	1.2240
2.0	3.7081	1.8744	3.7081	0.9899
3.0	4.7674	1.9681	4.7674	0.9178

scores following microfracture. In terms of activity, 86% of patients who underwent microfracture for traumatic osteochondral lesions were able to resume pre-injury levels of physical activity (Steadman et al., 2003).

Although it has advantages, biomechanical studies on microfracture techniques are limited. Current clinical practice typically uses microfracture holes with a diameter of 3 mm, spacing of 3–4 mm, and depth of 3–4 mm, aiming for fat droplets to appear as an endpoint (Gobbi et al., 2005; Hoemann et al., 2013). Some researchers suggest that drilling depths exceeding 10 mm may be more effective for marrow stem cell release and trabecular bone repair (Benthien and Behrens, 2013). However, there is no evidence to confirm whether microfracture drilling causes mechanical structural changes. Chen et al. proposed that drilling in areas of cartilage defects could lead to alterations in the subchondral bone and trabecular structures, potentially modifying the biomechanics of the knee joint and ultimately affecting cartilage repair. Nevertheless, this hypothesis lacks mechanical evidence (Chen et al., 2011). Some researchers have observed in animal studies that microfracture surgery may cause subchondral bone damage and increase the risk of bone cyst formation (Gao et al., 2017). However, we have not encountered any cases of bone cysts resulting from microfracture surgery in clinical practice. The appearance of bone cysts after microfracture in animal models

may be attributed to the smaller skeletal size of animals. When drilling with 0.55 mm or 1.2 mm Kirschner wires, it already constitutes a significant bone defect for small animals, potentially leading to bone cyst formation and poor cartilage repair outcomes. If this is proportionally scaled to the human femoral condyle, it would also represent a substantial bone defect, necessitating autologous cartilage transplantation in such cases. Additionally, some researchers have found in animal studies that simple debridement alone can achieve cartilage repair effects similar to those of microfracture surgery (Sumii et al., 2023). Clinically, we have observed that microfracture not only facilitates cartilage repair but also alleviates subchondral bone sclerosis by releasing intramedullary pressure, thereby further relieving knee joint pain.

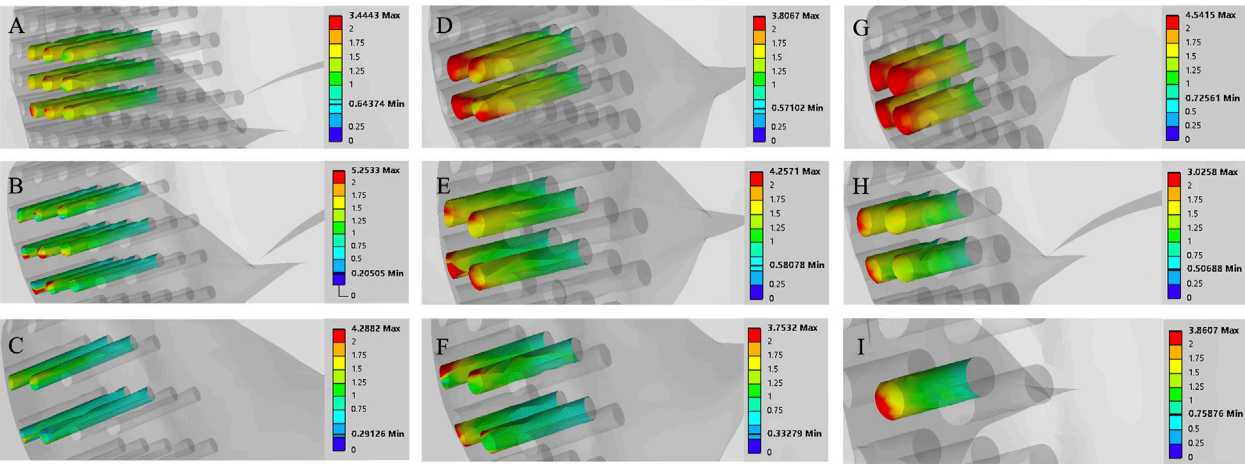
Microfracture is a surgical technique that creates channels in cartilage defects to allow bone marrow outflow, facilitating the aggregation of a large number of cells that promote cartilage regeneration (Kwon et al., 2019; Cooper and Rainbow, 2022). It has been hypothesized that creating larger or more channels for cellular migration could improve cartilage repair, as more mesenchymal stem cells from the bone marrow would be recruited to the lesion area. This concept has been supported by recent studies (Goh et al., 2023; Lin et al., 2017). Biomechanical studies have investigated the relationship between bone stability and



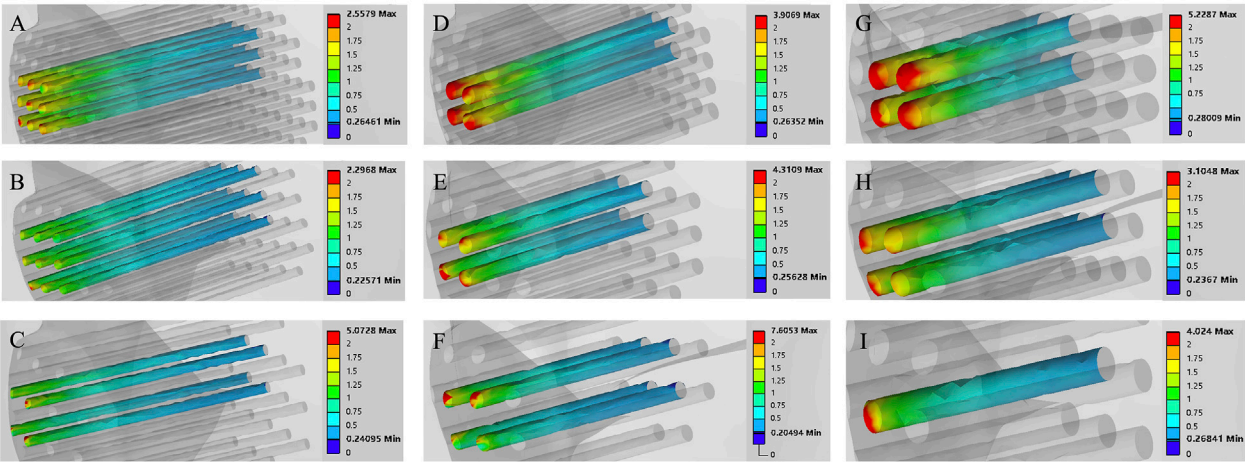
**FIGURE 6**  
**(A)** Von Mises stress data for different numbers of holes in the stress concentration area; **(B)** von Mises stress data for different hole diameters in the stress concentration area; **(C)** von Mises stress data for different hole spacings in the stress concentration area.

microfracture holes. In this study, we used the parameters of microfracture holes as the basis for finite element analysis, grouping the variables of hole diameter, spacing, and depth.

In this study, the von Mises stress varied with changes in the parameters of the holes, but it remained well below the yield stress of bone (135 MPa). Our findings align with those of Yin et al.,



**FIGURE 7**  
Finite element contour maps for different drilling parameters with a hole depth of 10 mm. (A–C): 3D finite element contour maps of the knee joint after microfracture with a hole diameter of 1.0 mm; (D–F): 3D finite element contour maps of the knee joint after microfracture with a hole diameter of 2.0 mm; (G–I): 3D finite element contour maps of the knee joint after microfracture with a hole diameter of 3.0 mm.



**FIGURE 8**  
Finite element contour maps for different drilling parameters with a hole depth of 30 mm. (A–C): 3D finite element contour maps of the knee joint after microfracture with a hole diameter of 1.0 mm; (D–F): 3D finite element contour maps of the knee joint after microfracture with a hole diameter of 2.0 mm; (G–I): 3D finite element contour maps of the knee joint after microfracture with a hole diameter of 3.0 mm.

**TABLE 7** Von mises stress data in the stress concentration area for different numbers of drill holes (4).

Drilling depth (mm)	Maximum von mises stress at the edge of the hole in the stress area (MPa)	Average von mises stress at the edge of the hole in the stress area (MPa)	Maximum von mises stress in the pores of the stress area (MPa)	Average von mises stress in the pores of the stress area (MPa)
10	4.0256	1.9684	4.0256	1.2759
30	4.2342	2.0480	4.2342	0.8119

concluding that while drilling parameters can influence the von Mises stress, they are insufficient to induce changes in the mechanical structure of bone (Yin et al., 2020). However, there are significant differences between our finite element results and theirs, which may be attributed to differences in the models used.

Yin et al. constructed a simplified knee joint stress model that included only the subchondral bone and cancellous bone, resulting in a more idealized representation compared to actual human bone (Yin et al., 2020). In contrast, we developed a complete knee joint model incorporating ligaments, menisci, and cartilage. While their

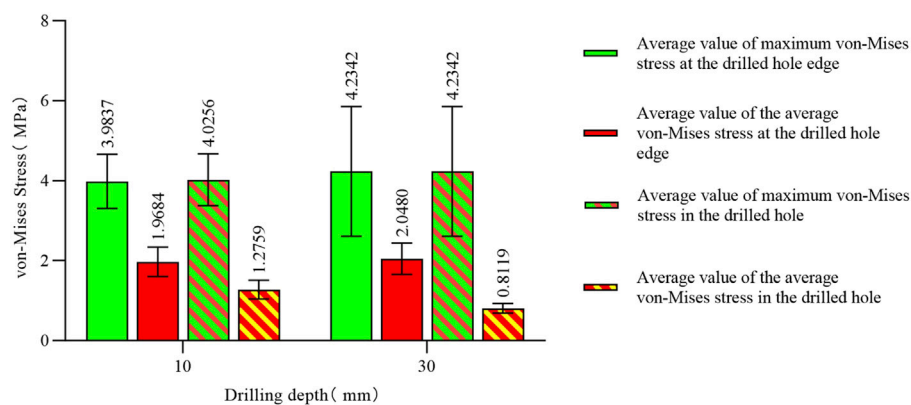


FIGURE 9  
Von Mises stress data for different hole depths in the stress concentration area.

applied force accounted for the effects of cartilage and menisci, we believe that constructing a full knee joint model in finite element analysis provides a more accurate simulation of real-world loading conditions. This is because these additional structures contribute to stress distribution in the mechanical environment. Furthermore, we consider bone to be a complex mechanical structure comprising cortical bone and cancellous bone. The cancellous bone contains an irregular trabecular structure and bone marrow, all of which play a role in stress distribution during loading. Therefore, we believe that analyzing bone stress through a comprehensive model with holistic material property assignments may yield more accurate and clinically relevant results. Analysis of the results revealed that the maximum von Mises stress consistently occurred at the edges of the holes, indicating that sharp edges at the hole boundaries can lead to stress concentration. The average von Mises stress within the hole decreased with increasing hole length, suggesting that longer holes help to distribute stress more effectively. Notably, statistical analysis of the maximum von Mises stress and the average von Mises stress for each parameter showed that a hole diameter of 1.0 mm, a spacing of 2.0 mm, and a depth of 30 mm resulted in the lowest values for both the maximum von Mises stress and the average von Mises stress. We also observed that the maximum von Mises stress for a 2.0 mm hole diameter was higher than that for 1.0 mm and 3.0 mm. This outcome could be explained by the fact that smaller diameter holes (1.0 mm) result in a smaller load-bearing area around the hole. As a result, under applied external forces, the force per unit area is reduced, leading to weaker stress concentration at the hole edges. Additionally, the surrounding bone maintains stronger continuity, distributing the stress more evenly. Typically, stress concentration at the hole edge initially increases with larger diameters but may subsequently decrease as larger holes provide a greater area to disperse the stress (Khechai et al., 2014; Bakhshi and Taheri-Behrooz, 2019; Masrol and Siswanto, 2014). The maximum von Mises stress observed for four holes was higher than that for nine holes and one hole, potentially due to the interaction of stress fields around the holes. With four holes, the distribution may lead to larger overlapping stress field regions, intensifying the interactions and resulting in higher von Mises stress. For a single hole, there is no interaction with other stress fields, resulting in a single stress concentration zone and relatively lower von Mises stress. For

nine holes, the denser distribution might cause more stress field overlap, but the stress concentration around each hole is more evenly distributed, leading to a lower overall von Mises stress (Driscoll, 2014; Zhou et al., 2014). Smaller hole diameters are less likely to cause compression of the surrounding bone. With closer spacing between holes, more holes can be created per unit area, facilitating the release of more mesenchymal stem cells from the bone marrow. Drilling depth should be as deep as possible, as depths of 3–4 mm may not penetrate sclerotic bone in patients with subchondral bone sclerosis. It can be concluded that if the bone structure is adequately protected during microfracture, hole diameter, spacing, and depth are not risk factors within the biomechanical load range. In practical surgical applications, ensuring the strength and operability of the drilling tools, it is recommended to use smaller-diameter drilling tools, denser hole spacing, and the deepest feasible drilling depth. Such parameters not only preserve the mechanical integrity of the drilled region but also enhance the effectiveness of mesenchymal stem cell release from the bone marrow.

The limitations of this study include the lack of validation through dynamic finite element analysis. During walking, the magnitude and angle of the forces exerted on the knee vary across different phases of the gait cycle. In clinical practice, approximately 20 holes are drilled in a 20 mm cartilage defect. However, in this experiment, finite element analysis was only performed on the holes located in the directly loaded region, as the von Mises stresses on the non-contact regions were minimal. The influence of hole arrangement on von Mises stress was not discussed in detail. This study specifically analyzed the biomechanics of a single knee joint in a standing position, chosen as a more extreme and reliable condition.

The aim of this study was to analyze the relationship between bone structural stability and the parameters of microfracture holes. The results indicate that within the parameter ranges used in this study, the hole parameters do not affect structural stability. Based on this finding, using drilling tools with the smallest possible diameter and adopting a drilling approach with small spacing and deeper penetration during microfracture surgery may facilitate the release of more bone marrow-derived mesenchymal stem cells, potentially improving cartilage regeneration. However, it remains unclear whether this would yield superior clinical outcomes. We



hypothesize that smaller hole diameters result in less damage to the bone surrounding the microfracture sites, and greater hole depths facilitate a more efficient release of MSCs. Further studies are required to validate the actual clinical outcomes.

## Conclusion

The limitation of this study is the absence of dynamic finite element analysis for the knee joint, which would provide a more realistic simulation of the mechanical conditions during weight-bearing activities of the knee. However, we constructed a weight-bearing knee joint model in the standing position to simulate the maximum load experienced in this posture. The results demonstrated that various microfracture drilling parameters had no effect on the mechanical structure of the bone. It is equally important to analyze the mechanical effects of microfracture drilling during gait using different lower limb models. This can be achieved by altering bone geometry to create customized lower limb models, allowing finite element analysis of changes in the mechanical conditions at the microfracture sites under varying joint angles.

## Data availability statement

The original contributions presented in the study are included in the article/supplementary material, further inquiries can be directed to the corresponding author.

## Ethics statement

Ethical review and approval was not required for the study on human participants in accordance with the local legislation and institutional requirements. Written informed consent from the patients/ participants or patients/participants legal guardian/next of kin was not required to participate in this study in accordance with the national legislation and the institutional requirements.

## References

- Bakhshi, N., and Taheri-Behrooz, F. (2019). Length effect on the stress concentration factor of a perforated orthotropic composite plate under in-plane loading. *Compos Mater Eng.* 1 (1), 71–90. doi:10.12989/cme.2019.1.1.071
- Benthien, J. P., and Behrens, P. (2013). Reviewing subchondral cartilage surgery: considerations for standardised and outcome predictable cartilage remodelling: a technical note. *Int. Orthop.* 37 (11), 2139–2145. doi:10.1007/s00264-013-2025-z
- Chen, H., Chevrier, A., Hoemann, C. D., Sun, J., Ouyang, W., and Buschmann, M. D. (2011). Characterization of subchondral bone repair for marrow-stimulated chondral defects and its relationship to articular cartilage resurfacing. *Am. J. Sports Med.* 39 (8), 1731–1741. doi:10.1177/0363546511403282
- Cooper, S. M., and Rainbow, R. S. (2022). The developing field of scaffold-free tissue engineering for articular cartilage repair. *Tissue Eng. Part B Rev.* 28 (5), 995–1006. doi:10.1089/ten.teb.2021.0130
- Ding, K., Yang, W., Wang, H., Zhan, S., Hu, P., Bai, J., et al. (2021). Finite element analysis of biomechanical effects of residual varus/valgus malunion after femoral fracture on knee joint. *Int. Orthop.* 45 (7), 1827–1835. doi:10.1007/s00264-021-05039-9
- Driscoll, M. M. (2014). Geometric control of failure behavior in perforated sheets. *Phys. Rev. E* 90 (6), 062404. doi:10.1103/physreve.90.062404
- Gao, L., Orth, P., Müller-Brandt, K., Goebel, L. K., Cucchiari, M., and Madry, H. (2017). Early loss of subchondral bone following microfracture is counteracted by bone marrow aspirate in a translational model of osteochondral repair. *Sci. Rep.* 7, 45189. doi:10.1038/srep45189
- Gobbi, A., Nunag, P., and Malinowski, K. (2005). Treatment of full thickness chondral lesions of the knee with microfracture in a group of athletes. *Knee Surg. Sports Traumatol. Arthrosc.* 13 (3), 213–221. doi:10.1007/s00167-004-0499-3
- Goh, D., Yang, Y., Lee, E. H., Hui, J. H. P., and Yang, Z. (2023). Managing the heterogeneity of mesenchymal stem cells for cartilage regenerative therapy: a review. *Bioeng. (Basel)*. 10 (3), 355. doi:10.3390/bioengineering10030355
- Hoemann, C. D., Gosselin, Y., Chen, H., Sun, J., Hurtig, M. B., Carli, A., et al. (2013). Characterization of initial microfracture defects in human condyles. *J. Knee Surg.* 26 (5), 347–356. doi:10.1055/s-0033-1341580
- Hunziker, E. B. (2002). Articular cartilage repair: basic science and clinical progress. A review of the current status and prospects. *Osteoarthritis Cartil.* 10 (6), 432–463. doi:10.1053/joca.2002.0801
- Khechai, A., Tati, A., and Guettala, A. (2014). Finite element analysis of stress concentrations and failure criteria in composite plates with circular holes. *Front. Mech. Eng.* 9, 281–294. doi:10.1007/s11465-014-0307-9
- Koh, Y. G., Son, J., Kim, H. J., Kwon, S. K., Kwon, O. R., Kim, H. J., et al. (2018). Multi-objective design optimization of high tibial osteotomy for improvement of biomechanical effect by using finite element analysis. *J. Orthop. Res.* 36 (11), 2956–2965. doi:10.1002/jor.24072

## Author contributions

JL: Data curation, Project administration, Validation, Writing—original draft, Writing—review and editing. ZZ: Software, Writing—review and editing. QZ: Methodology, Writing—review and editing. SL: Data curation, Writing—review and editing. JH: Data curation, Software, Writing—review and editing. CY: Conceptualization, Writing—review and editing.

## Funding

The author(s) declare financial support was received for the research, authorship, and/or publication of this article. Guizhou Science and Technology Department ([2020]6013).

## Conflict of interest

The authors declare that the research was conducted in the absence of any commercial or financial relationships that could be construed as a potential conflict of interest.

## Generative AI statement

The authors declare that no Generative AI was used in the creation of this manuscript.

## Publisher's note

All claims expressed in this article are solely those of the authors and do not necessarily represent those of their affiliated organizations, or those of the publisher, the editors and the reviewers. Any product that may be evaluated in this article, or claim that may be made by its manufacturer, is not guaranteed or endorsed by the publisher.

- Kraeutler, M. J., Belk, J. W., Purcell, J. M., and McCarty, E. C. (2018). Microfracture versus autologous chondrocyte implantation for articular cartilage lesions in the knee: a systematic review of 5-year outcomes. *Am. J. Sports Med.* 46 (4), 995–999. doi:10.1177/0363546517701912
- Kwon, H., Brown, W. E., Lee, C. A., Wang, D., Paschos, N., Hu, J. C., et al. (2019). Surgical and tissue engineering strategies for articular cartilage and meniscus repair. *Nat. Rev. Rheumatol.* 15 (9), 550–570. doi:10.1038/s41584-019-0255-1
- Li, L., Yang, L., Yu, F., Shi, J., Zhu, L., Yang, X., et al. (2018). 3D printing individualized heel cup for improving the self-reported pain of plantar fasciitis. *J. Transl. Med.* 16 (1), 167. doi:10.1186/s12967-018-1547-y
- Lieberthal, J., Sambamurthy, N., and Scanzello, C. R. (2015). Inflammation in joint injury and post-traumatic osteoarthritis. *Osteoarthr. Cartil.* 23 (11), 1825–1834. doi:10.1016/j.joca.2015.08.015
- Lin, S., Lee, W. Y. W., Feng, Q., Xu, L., Wang, B., Man, G. C. W., et al. (2017). Synergistic effects on mesenchymal stem cell-based cartilage regeneration by chondrogenic preconditioning and mechanical stimulation. *Stem Cell Res. Ther.* 8 (1), 221. doi:10.1186/s13287-017-0672-5
- Masrol, S. R., and Siswanto, W. A. (2014). Stress concentration analysis of plate with circular hole: elasticity theory and finite element comparison. *Appl. Mech. Mater.* 465–466, 1385–1389. doi:10.4028/www.scientific.net/amm.465-466.1385
- Mithoefer, K., McAdams, T., Williams, R. J., Kreuz, P. C., and Mandelbaum, B. R. (2009). Clinical efficacy of the microfracture technique for articular cartilage repair in the knee: an evidence-based systematic analysis. *Am. J. Sports Med.* 37 (10), 2053–2063. doi:10.1177/0363546508328414
- Na, Y., Shi, Y., Liu, W., Jia, Y., Kong, L., Zhang, T., et al. (2019). Is implantation of autologous chondrocytes superior to microfracture for articular cartilage defects of the knee? A systematic review of 5-year follow-up data. *Int. J. Surg.* 68, 56–62. doi:10.1016/j.ijsu.2019.06.007
- Orth, P., Duffner, J., Zurakowski, D., Cucchiari, M., and Madry, H. (2016). Small-diameter awls improve articular cartilage repair after microfracture treatment in a translational animal model. *Am. J. Sports Med.* 44 (1), 209–219. doi:10.1177/0363546515610507
- Peng, L., Li, H., Deng, H., Gao, T., Li, R., Xu, Z., et al. (2023). Combination of a human articular cartilage-derived extracellular matrix scaffold and microfracture techniques for cartilage regeneration: a proof of concept in a sheep model. *J. Orthop. Transl.* 44, 72–87. doi:10.1016/j.jot.2023.09.004
- Powers, R. T., Dowd, T. C., and Giza, E. (2021). Surgical treatment for osteochondral lesions of the talus. *Arthroscopy* 37 (12), 3393–3396. doi:10.1016/j.arthro.2021.10.002
- Solheim, E., Hegna, J., Strand, T., Harlem, T., and Inderhaug, E. (2018). Randomized study of long-term (15–17 Years) outcome after microfracture versus mosaicplasty in knee articular cartilage defects. *Am. J. Sports Med.* 46 (4), 826–831. doi:10.1177/0363546517745281
- Steadman, J. R., Briggs, K. K., Rodrigo, J. J., Kocher, M. S., Gill, T. J., and Rodkey, W. G. (2003). Outcomes of microfracture for traumatic chondral defects of the knee: average 11-year follow-up. *Arthroscopy* 19 (5), 477–484. doi:10.1053/jars.2003.50112
- Sumii, J., Nakasa, T., Kato, Y., Miyaki, S., and Adachi, N. (2023). The subchondral bone condition during microfracture affects the repair of the osteochondral unit in the cartilage defect in the rat model. *Am. J. Sports Med.* 51 (9), 2472–2479. doi:10.1177/03635465231177586
- Yin, X. Y., Park, D. Y., Kim, Y. J., Ahn, H. J., Yoo, S. H., and Min, B. H. (2020). The effect of distance between holes on the structural stability of subchondral bone in microfracture surgery: a finite element model study. *BMC Musculoskelet. Disord.* 21 (1), 557. doi:10.1186/s12891-020-03467-z
- Zhou, C. P., Cheng, Z. Q., Zhou, X. C., Jiang, J. Y., and Wang, J. Y. (2014). Dynamic stress concentrations in thick plates with two holes based on refined theory. *Appl. Math. Mech.* 35 (12), 1591–1606. doi:10.1007/s10483-014-1883-6



## OPEN ACCESS

## EDITED BY

Chi Wu,  
The University of Sydney, Australia

## REVIEWED BY

Zixiang Gao,  
University of Calgary, Canada  
Ayman El Khatib,  
Beirut Arab University, Lebanon

## \*CORRESPONDENCE

Jia Han,  
✉ jia.han@canberra.edu.au  
Jie Lyu,  
✉ lvj@sumhs.edu.cn

†These authors have contributed equally to this work and share first authorship

RECEIVED 26 October 2024

ACCEPTED 08 January 2025

PUBLISHED 29 January 2025

## CITATION

Wang R, Cao J, Xu H, Guo P, Li Y, Fan Y, Gui Y, Li L, Adams R, Han J and Lyu J (2025) Dynamic balance control in healthy young women during stair descent: a plantar pressure-based study. *Front. Bioeng. Biotechnol.* 13:1517471. doi: 10.3389/fbioe.2025.1517471

## COPYRIGHT

© 2025 Wang, Cao, Xu, Guo, Li, Fan, Gui, Li, Adams, Han and Lyu. This is an open-access article distributed under the terms of the [Creative Commons Attribution License \(CC BY\)](https://creativecommons.org/licenses/by/4.0/). The use, distribution or reproduction in other forums is permitted, provided the original author(s) and the copyright owner(s) are credited and that the original publication in this journal is cited, in accordance with accepted academic practice. No use, distribution or reproduction is permitted which does not comply with these terms.

# Dynamic balance control in healthy young women during stair descent: a plantar pressure-based study

Ruiqin Wang<sup>1,2†</sup>, Jinfeng Cao<sup>3†</sup>, Haoran Xu<sup>2</sup>, Panjing Guo<sup>2</sup>, Yumin Li<sup>2</sup>, Yuyi Fan<sup>2</sup>, Yunfei Gui<sup>2</sup>, Leqi Li<sup>4</sup>, Roger Adams<sup>5</sup>, Jia Han<sup>1,2,5\*</sup> and Jie Lyu<sup>1,2\*</sup>

<sup>1</sup>Department of Orthopedics, Jinshan District Central Hospital Affiliated to Shanghai University of Medicine and Health Sciences, Shanghai, China, <sup>2</sup>College of Rehabilitation Sciences, Shanghai University of Medicine and Health Sciences, Shanghai, China, <sup>3</sup>Periodicals Agency, Shanghai University, Shanghai, China, <sup>4</sup>College of Medical Instruments, Shanghai University of Medicine and Health Sciences, Shanghai, China, <sup>5</sup>Research Institute for Sport and Exercise, University of Canberra, Canberra, ACT, Australia

**Background:** Women are more likely to fall or even die when the ladder falls, which seriously affects the quality of daily life. It is necessary to better understand the plantar mechanism of the ladder falls and put forward reasonable suggestions.

**Method:** Twenty healthy young women volunteered to participate in the experiment. The study used the F-scan plantar pressure to explore the difference in the plantar pressure in the dominance of the leading foot across four step descent height conditions. The landing strategy employed was recorded during the experiment. The Center of Pressure (COP), along with its medial-lateral (ML) and anterior-posterior (AP) adjustment velocities, and the  $V_{COP}$ ,  $R_{COP-ML}$ , and  $R_{COP-AP}$  were analyzed.

**Result:** With an increase in the step height, significant enhancements were observed in the  $V_{COP-ML}$  ( $p < 0.001$ ),  $V_{COP-AP}$  ( $p < 0.001$ ),  $R_{COP-ML}$  ( $p < 0.001$ ), and  $R_{COP-AP}$  ( $p < 0.001$ ) during landing. There was no significant difference in the kinematic parameters of plantar pressure during stair descent, regardless of whether the dominant foot or non-dominant foot was the leading foot.

**Conclusion:** This study found that among young women, an increase in step height during descent significantly affected the plantar pressure and led to greater COP adjustment in the directions of ML and AP, increasing the risk of injury. At a step height of 5 cm, the first choice of the landing strategy for female subjects began to change from the hindfoot to the forefoot. Although there were no significant differences in plantar pressure data and landing strategies between subjects using the dominant side and nondominant side as the forefoot, the dominant side forefoot exhibited better postural balance control than the nondominant side forefoot.

## KEYWORDS

stair descent, females, landing strategy, COP, kinematic parameters, landing strategy

# 1 Introduction

The descent of stairs is one of the most common activities in workplaces, homes, and communities. Falls incurred during stair descent have been reported as the third leading cause of injuries, accompanied by a higher mortality rate compared to other fall types (Ragg et al., 2000; Cai et al., 2023). These falls, in addition to their frequency, often result in ankle sprains, with previous studies indicating that approximately one-quarter of all hospital-treated ankle sprains stem from stair descent (Waterman et al., 2010). Postural balance control, defined as the capacity to swiftly adjust one's center of gravity to maintain posture stability amidst static, dynamic, or sudden external forces, is paramount. Consequently, the purpose of this paper is to explore the underlying mechanisms of postural balance control of human body during stair descent across different environments and to put forward practical recommendations to reduce injuries during stair descent, thereby enhancing both individuals' life quality and community safety.

Stair descent-related falls pose a significant threat to community safety, transcending age boundaries and affecting both the elderly and young alike. Notably, among adults aged 18–24 in the United States, the cumulative cost of fall-related injuries exceeded \$7 billion (Verma et al., 2016). Given their heightened activity levels, young people experience a greater frequency of falls. Furthermore, adult women consistently exhibit a higher propensity for falls than adult men. Research (Talbot et al., 2005) has shown that, among young adults aged 20–45, women experience falls more frequently than men (20% vs. 17%) and suffer injuries more often (81% vs. 61%). Specifically, 48% of falls among young adults are closely related to stair descent (Cho et al., 2021). Compared to men, women were more likely to fall on stairs (15% vs. 10%) (Cho et al., 2021). Additionally, gender disparities are evident in lower limb functional measures, with men typically demonstrating superior muscle strength (Barber-Westin et al., 2006; Danneskiold-Samsøe et al., 2009), muscle activation patterns (Flaxman et al., 2014; Bencke and Zebis, 2011), and joint laxity (Davey et al., 2019). Therefore, exploring gender-specific injury mechanisms during stair descent is imperative.

During stair descent, accidents frequently occur during the transition from stairs to level ground. Research (Francksen et al., 2022; Duckham et al., 2013) has indicated that over 30% of stair-related accidents occur precisely during this transition phase, where even a single step or curb could lead to serious falls. Previous studies (Cluff and Robertson, 2011; Sie et al., 2022) have predominantly focused on lower limb mechanics during continuous stair descent. In light of research (Andriacchi et al., 1980) examining the differences in lower limb mechanics between continuous descent and the transition to level walking, it is evident that the mechanics of continuous stair descent cannot be universally applied to the step-to-level transition. Few studies have explored the biomechanics of the lower extremity in the transition between a single step and a flat surface, but the hazards of falls and injuries occurring during this transition should not be underestimated. Consequently, the step-to-level transition emerges as a pivotal aspect requiring focused attention to understand the mechanisms underlying falls and ankle injuries.

The foot supports the majority of the body weight during human activities and serves as a vital organ of the body. The plantar pressure

distribution varies under different conditions (Razak et al., 2012), providing feedback on the structural composition of the human body and the control of postural balance (Li et al., 2023). Furthermore, analyzing plantar pressure parameters holds significant potential for the development of wearable footwear devices in the future. Plantar pressure measurement is a technique used to capture the distribution of plantar pressure and the center of pressure (COP) data during static and dynamic states. This technique enables the acquisition of key biomechanical parameters related to human kinematics and dynamics, playing a crucial role in gait analysis, clinical diagnosis, and functional assessment of lower limb musculoskeletal disorders.

Two pivotal factors that may influence postural balance control during stair descent are the step height and the dominance of the leading foot (i.e., dominant vs. non-dominant). Postural balance control is facilitated by a cohesive feedback loop involving the interplay of vision, proprioception, and vestibular sense, all contributing to the maintenance of body balance. Impairments in any of the above three parts can affect the balance regulation capability of the human body (Peterka, 2002). As the step height increases, significant changes in lower limb proprioception are observed (Gerstle et al., 2017), potentially compromising posture control during stair descent. Additionally, studies (Gerstle et al., 2017; Gerstle et al., 2018; van Dieën and Pijnappels, 2009) have shown that an increased step height may lead to more complex lower limb muscle activity during stair descent and significantly alter landing strategies and ankle joint kinematics. In addition, use of the dominant or non-dominant side of the lower limbs can have a significant impact on postural balance control. Studies on Body Tracking Tests (BTT) reveal that ankle strategies and balance control in the AP direction were significantly influenced by the choice of leading foot (Yoshida et al., 2013). The dominant lower limb was more crucial for weight support and functional activities, possibly affecting balance (Hoffman et al., 1998; Alonso et al., 2011). Therefore, studying the effects of step height and the dominance of the leading foot during stair descent is valuable for understanding balance control mechanisms.

Accordingly, this study focused on young women to investigate the impact of two factors, i.e., the step height and the dominance of the leading foot (dominant vs. non-dominant), on balance control and landing strategies employed during stair descent. Plantar pressure measurement equipment was utilized to assess biomechanical characteristics and landing strategies across four different heights. Our hypotheses stipulate: 1) An increase in the step height would diminish balance control and affect landing strategies during stair descent; 2) The dominance of the leading foot (dominant or non-dominant) modulates balance and landing strategies during stair descent.

## 2 Materials and methods

### 2.1 Participants

The recruitment period of this experiment was from March 15, 2023 to June 15, 2023. Subjects who met the inclusion and exclusion criteria were selected and signed written informed consent. This study, approved by the Ethics Committee of Shanghai Sport

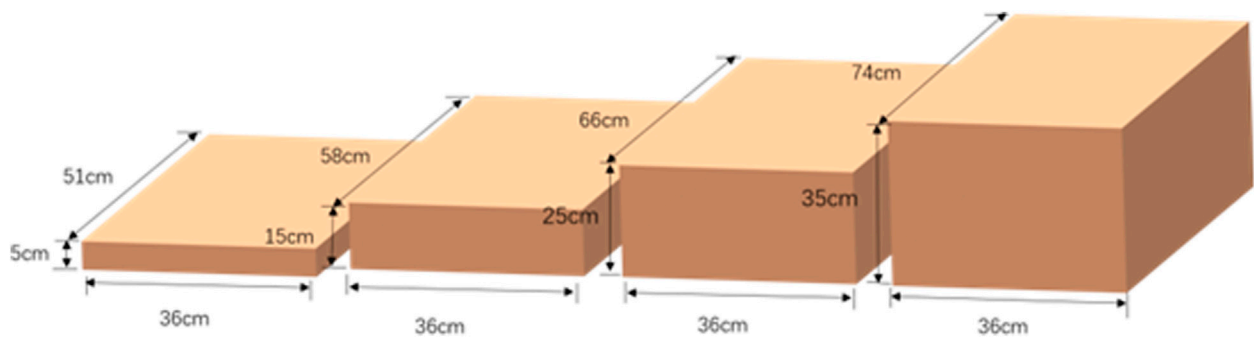


FIGURE 1  
Illustration of step heights of 5 cm, 15 cm, 25 cm, and 35 cm.

University (No.: 102772021RT073), involved 20 young women with a mean age of  $21.30 \pm 0.98$  years, a height of  $164.30 \pm 4.64$  cm, a weight of  $57.18 \pm 11.82$  kg, and a BMI of  $21.17 \pm 4.34$ . Prior to conducting the experiment, the minimum number of subjects required was calculated based on the G-power. The statistical method was a repeated measures ANOVA with a higher effect size set at 0.4 and an efficacy value of 0.8, resulting in a minimum sample size of 13 subjects. All participants possessed shoe sizes ranging from 36 to 39 and were right-footed, as determined by the Chinese version of the Waterloo Footedness Questionnaire (Yang et al., 2018). Informed consent was obtained from all participants after a thorough explanation of the experimental requirements. The research was conducted in accordance with the guidelines outlined in the Declaration of Helsinki. However, a total of 22 female data were taken in our study, with data of 20 subjects ultimately included in the analysis.

Inclusion Criteria: a) women aged between 18 and 25 years, b) no history of musculoskeletal or neurological disorders that may affect postural balance control, and c) ability to walk and descend stairs independently without the aid of assistive devices. Exclusion Criteria: a) persistent pain or a history of surgery in the hip, knee, ankle, or foot within the past 6 months, b) poor compliance, preventing completion of the experiment, and c) allergies to materials involved in the experiment.

## 2.2 Procedure

### 2.2.1 Pre-test preparation

The experiments were conducted in a noise-controlled environment to mitigate auditory disturbances. The primary equipment comprised four steps of varying heights: 5 cm, 15 cm, 25 cm, and 35 cm (dimensions in cm:  $51 \times 36 \times 5$ ,  $58 \times 36 \times 15$ ,  $66 \times 36 \times 25$ , and  $74 \times 36 \times 35$ , respectively). The four types of step heights include the doorstep height of 5 cm, the common residential staircase height of 15 cm, the step height of 25 cm recommended by the U.S. Federal Highway Administration guidelines (Gerstle et al., 2017), and the typical bus pedal height of 35 cm. The height of the four steps is shown in Figure 1. All subjects followed the same step height sequence from low to high. The four step heights are designed to encompass common roadside (5 cm) and building stairs (15 cm) in daily life, as well as the 25 cm step height issued by the US Federal

Highway Administration, and the 35 cm step height to simulate challenging steps encountered by healthy adults

Prior to the testing day, participants were instructed to avoid high-intensity activities and to walk freely with the instrumented insoles inserted for 5 min to ensure a natural gait. For each participant, the F-Scan system was calibrated twice as per the manual to ensure the equipment work properly. Essential details such as name, height, weight, and date were recorded before beginning the experimental briefing and guidance on the tasks.

### 2.2.2 Equipment

The two most commonly used plantar pressure insole systems in the market are the F-Scan system of TEKSCAN (USA) (Chen and Yu, 2005) and the Pedar-X system of Novel (Germany) (Ma, 2002). In this experiment, the F-Scan plantar pressure system of TEKSCAN (United States) was employed. The F-Scan plantar pressure system (Tekscan, Boston, MA, United States) was used to collect data. This system, featuring a customizable insole with four sensors per square centimeter and a sampling rate of 50 Hz, records real-time plantar pressure distribution. In order to minimize the displacement between the shoe and the insole, participants wore standardized cotton socks on bare feet and fixed the insole and cotton socks with double-sided tape (Guo et al., 2023). Figure 2 shows the F-Scan device. This figure depicts the following: ① the plantar pressure insole, ② the CAT5E cable connector, ③ the VersaTek two-port hub, ④ the power cord, ⑤ the fixed ankle bandage, ⑥ the VC-1 VersaTek converter, and ⑦ the USB data connection cable.

### 2.2.3 Testing procedure

Upon completion of the preparatory steps, all participants were instructed to stand in a consistent position at the top of the step, with their feet relaxed and their eyes directed forward for a natural descent. Upon landing with the first foot, the non-first foot followed, and participants remained in a standing position for 5 s to enable the recording of the sole pressure. The experiment encompassed 8 combinations, determined by the step height (5 cm, 15 cm, 25 cm, and 35 cm) and the dominance of the leading foot (dominant or non-dominant) (Guo et al., 2024). This procedure was repeated three times for each condition, with the F-Scan system capturing the data. Upon completion of the experiment, the data were exported into CSV files using the F-Scan plantar pressure system for kinematic data. After each participant



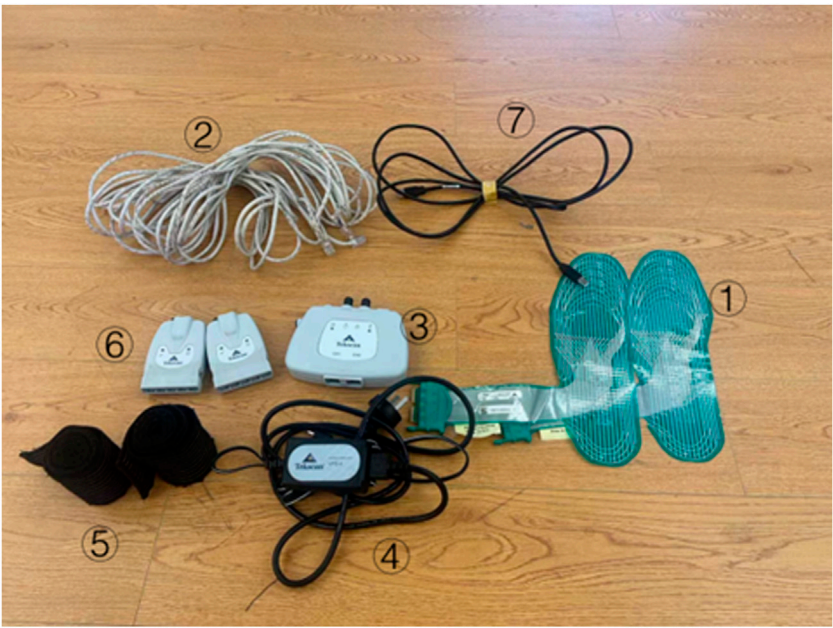


FIGURE 2  
F-Scan plantar pressure system hardware schematic.

TABLE 1 Formulas related to kinematic parameters.

Kinematic parameters	Abbreviation	Formula
COP-ML adjustment velocity	$V_{\text{COP-ML}}$	$\text{COP-ML adjustment velocity (m/s)} = 1/T \sum_{n=1}^{N-1}  ML[n+1] - ML[n] $
COP-AP adjustment velocity	$V_{\text{COP-AP}}$	$\text{COP-AP adjustment velocity (m/s)} = 1/T \sum_{n=1}^{N-1}  AP[n+1] - AP[n] $
COP adjustment velocity	$V_{\text{COP}}$	$\text{COP adjustment velocity (m/s)} = 1/T \sum_{n=1}^{N-1} [(\Delta AP[n])^2 + (\Delta ML[n])^2]^{1/2}$
95% confidence circle area		$\text{Mean Distance} = 1/N \sum_{n=1}^N [AP[n]^2 + ML[n]^2]^{1/2}$
		$\text{RMS Distance} = [1/N \sum_{n=1}^N [AP[n]^2 + ML[n]^2]]^{1/2}$
		$95\% \text{ confidence circle area} = \pi (MDIST^2 + 1.645 [RDIST^2 - MDIST^2]^{1/2})^2$
ML range	$R_{\text{COP-ML}}$	$ML \text{ range} = \max_{1 \leq n \leq m \leq N}  ML[n] - ML[m] $
AP range	$R_{\text{COP-AP}}$	$AP \text{ range} = \max_{1 \leq n \leq m \leq N}  AP[n] - AP[m] $
Maximum swing	$S_{\text{max}}$	$\text{Maximum swing} = \max_{1 \leq n \leq N-1} [(\Delta AP[n])^2 + (\Delta ML[n])^2]^{1/2}$
Minimum swing	$S_{\text{min}}$	$\text{Minimum swing} = \min_{1 \leq n \leq N-1} [(\Delta AP[n])^2 + (\Delta ML[n])^2]^{1/2}$

completes the F-Scan plantar calibration, the calibrated parameters of the left and right feet are compared. If the discrepancy is too large, recalibration is performed. If the discrepancy remains significant after the second calibration, the participant’s experiment is discontinued. Upon completion of each experiment, the researchers verify the completeness of the plantar pressure data and ensure that the foot does not extend beyond the insole’s

boundaries. If such issues are detected, the experiment for that participant is repeated.

2.2.4 Data processing

Plantar pressure data, including the center and distribution, were analyzed to assess postural stability. Python (Pycharm Community Edition 2022.2, JetBrains s.r.o., Prague, Czech

Republic) algorithms were utilized to process the data and extract kinematic parameters. These parameters include the landing strategies across different step heights and a series of parameters related to the center of pressure such as COP-ML adjustment velocity (mm/s), COP-AP adjustment velocity (mm/s), COP adjustment velocity (mm/s), 95% confidence circle area (mm<sup>2</sup>), ML range (mm), and AP range (mm). The 95% confidence circle area represents the area where the sole of the foot oscillates during stair descent. A larger value of this parameter indicates greater variation in the participant's plantar COP, suggesting a higher challenge to postural balance control and an increased risk of falling.

The above measures were obtained through a customized Python program incorporating relevant formulas (Guo et al., 2023), as detailed in Table 1.

Where, it is assumed that the recorded COP trace contains  $N$  data points, sampled at a constant frequency  $F_s$ .  $T$  represents the total duration of the signal in seconds, i.e.:  $T = \frac{N}{F_s}$ . The  $n$  and  $m$  ( $1 \ll n \ll N, 1 \ll m \ll N$ ) in the formula are the coordinates from back to forward on the AP axis and from left to right on the ML axis.

## 2.3 Statistical analysis

Data analysis was performed using SPSS (version 27.0; IBM) and Excel 2016 (Microsoft, Redmond, Washington, United States), with graphics generated by Origin2018 software (Origin Lab Corporation, Northampton, MA, United States). Data that followed a normal distribution were presented as mean  $\pm$  standard deviation (SD). For data confirmed to follow a normal distribution after using the Kolmogorov-Smirnov test, a  $2 \times 4$  repeated measures analysis of variance (ANOVA) was employed. For data deviating from a normal distribution, a generalized linear model was used with Bonferroni corrections for multiple comparisons. The experimental data of the plantar pressure center in this paper shows approximate normality, allowing for the application of the Grubbs criterion to detect outliers in the data. Subsequently, any outliers identified through this method can be removed. The significance level ( $\alpha$ ) was set at 0.05. A P-value of less than 0.05 indicates that the difference is statistically significant, while a P-value of less than 0.001 indicates an extremely significant statistical difference.

## 3 Results

### 3.1 Foot landing strategy

During the experiments, participants were instructed to land on steps of varying heights using either their dominant or non-dominant foot as the leading foot. When the step height was 5 cm, 50% (10 out of 20) of the participants adopted a forefoot landing strategy. As the step height increased to 15 cm, 90% (18 out of 20) of the participants chose to land on the forefoot first. For step heights of 25 cm and 35 cm, all participants (20 out of 20) employed the forefoot landing strategy consistently. Regardless of the height of the step, the probability of selecting the forefoot landing strategy with the dominant foot or non-dominant foot as the leading foot remains the same.

### 3.2 Plantar pressure center during stair descent

This study examined the effects of varying step heights and the dominance of the leading foot on the COP parameters at the plantar pressure center using analysis of variance. Additionally, the interaction between these two factors was explored. The findings revealed no statistically significant interaction between the step height and the dominance of the leading foot. Table 2 presents the results and significance level of all relevant parameters of COP. Only the area of the 95% confidence circle of the dominant foot compared with the non-dominant foot was statistically significant ( $p = 0.013$ ), as the mean value for the non-dominant foot (6,249.01 mm<sup>2</sup>) was greater than that of the dominant foot (5,223.35 mm<sup>2</sup>). No other notable differences emerged due to the leading foot factor. Although the values for the non-dominant foot were greater than those for the dominant foot in the COP adjustment velocity and AP range indicators at 5 cm, 15 cm, and 25 cm step heights, the leading foot factor was not associated with significant differences. Similarly, for the AP adjustment velocity indicator, the non-dominant foot showed marginally higher values across all heights, yet these were not statistically significant.

Analysis of the plantar pressure data across the four different step heights as height increased revealed significant differences ( $p < 0.001$ ) in several parameters:  $V_{COP-ML}$  (mm/s), overall  $V_{COP}$  (mm/s), 95% confidence circle area (mm<sup>2</sup>),  $R_{COP-ML}$  (mm), and  $R_{COP-AP}$  (mm). In contrast, the other two indices,  $S_{max}$  (mm) and  $S_{min}$  (mm) were not significantly affected by the changes in step height.

## 4 Discussion

This study investigated changes in the biomechanical attributes of the plantar surface of the dominant and non-dominant feet in young women during stair descent across varying step heights and under different leading foot conditions. The kinematic data revealed that both the landing strategy and the plantar pressure center during stair descent were closely associated with the step height. However, no significant effects on the landing strategy were discernible when comparing the use of dominant versus non-dominant foot as the landing foot.

### 4.1 Landing strategy

In normal flat gait, where the step height difference is 0, the contact between the sole and the ground during each step typically involves the back-foot touch strategy (Freedman and Kent, 1987). When the height difference increased from 0 to 5 cm, the subjects' bodies faced few challenges of potential energy and balance control due to the minor drop. However, the results of this paper showed that 50% of female subjects still opt for the forefoot touch strategy to manage body potential energy and maintain body balance. Studies have shown (van Dieën et al., 2008; Van Der Linden et al., 2007) that even with a 5 cm height difference, subjects tend to choose the toe touch strategy when they cannot observe the height difference during step descent. During the experiment, the subjects could not see the height difference when looking ahead, which was consistent with the results of this study. Compared with the flat-

TABLE 2 Comparison of COP parameters of plantar pressure during stair descent across different step heights and the dominance factor of the leading foot.

	5 cm step		15 cm step		25 cm step		35 cm step		P (height)	P (leading foot)
	N	D	N	D	N	D	N	D		
$V_{COP-ML}$ (mm/s)	9.77 ± 1.89	10.90 ± 2.14	12.03 ± 1.84	13.51 ± 3.40	14.85 ± 2.82	14.13 ± 3.73	16.70 ± 2.73	17.32 ± 5.13	<0.001	0.206
$V_{COP-AP}$ (mm/s)	55.12 ± 11.64	50.09 ± 8.93	60.23 ± 13.03	55.15 ± 12.04	66.04 ± 12.30	63.22 ± 10.54	77.63 ± 11.98	75.99 ± 14.6	<0.001	0.057
$V_{COP}$ (mm/s)	57.55 ± 11.42	53.29 ± 8.86	63.79 ± 12.95	59.58 ± 12.54	70.74 ± 12.43	67.39 ± 10.36	82.23 ± 11.7	81.07 ± 15.14	<0.001	0.091
95% confidence circle area (mm <sup>2</sup> )	4,546.70 ± 2,531.80	3,673.98 ± 1895.43	5,366.30 ± 1794.34	4,451.46 ± 2,165.48	7,043.09 ± 3,420.52	5,619.20 ± 1930.27	8,039.93 ± 3,737.14	7,148.78 ± 2,194.9	<0.001	0.013
$R_{COP-ML}$ (mm)	18.11 ± 6.60	18.85 ± 4.90	21.64 ± 6.52	23.80 ± 6.11	27.05 ± 9.22	23.40 ± 5.78	28.53 ± 5.96	28.21 ± 7.56	<0.001	0.802
$R_{COP-AP}$ (mm)	116.06 ± 18.30	109.13 ± 18.38	118.33 ± 21.93	110.84 ± 21.52	123.27 ± 17.46	121.86 ± 19.84	132.52 ± 19.64	137.13 ± 17.8	<0.001	0.362
$S_{max}$ (mm)	43.50 ± 16.02	47.43 ± 20.36	41.35 ± 18.93	36.96 ± 10.33	43.01 ± 10.396	43.26 ± 14.7	47.93 ± 15.61	46.68 ± 14.95	0.682	0.890
$S_{min}$ (mm)	9.90E-03 ± 4.74E-03	1.09E-02 ± 5.27E-03	1.12E-02 ± 6.08E-03	1.17E-02 ± 3.92E-03	1.02E-02 ± 7.74E-03	1.29E-02 ± 4.35E-03	1.19E-02 ± 5.45E-03	1.36E-02 ± 8.23E-03	0.010	0.116

N: Non-Dominant, D: dominant.

bottom gait strategy, when the step descent height was 5 cm, the female subjects began to change from the back-foot approach to the front-foot approach.

At a step height of 15 cm, 90% of the participants opted for a forefoot landing strategy (Freedman and Kent, 1987). When the step height was increased to 25 cm and 35 cm, all participants switched their landing strategy from hindfoot to forefoot contacting the ground. When descending high steps, a forefoot landing augments the load on the ankle joint, potentially surpassing safe thresholds and predisposing individuals to ankle sprains or falls. Descending a step increases the potential energy due to the COM, and significantly raises the torque on the knees and ankles (Silverman et al., 2014). It has been noted that (Jeon et al., 2021) regardless of the landing strategy, joints, ligaments, and muscles have to absorb the potential energy caused by the COM changes. The process of descending a step can be divided into three phases: weight acceptance, forward continuation, and controlled descent (Zachazewski et al., 1993). During both weight acceptance and forward progression, ankle torque is higher with the forefoot strategy compared to the hindfoot strategy (Demers et al., 2021). Research has indicated that during the transition from a step to a flat surface, the potential energy absorbed by the ankle joint (van Dieën et al., 2008) is three times greater with the forefoot landing than with the heel landing. Therefore, choosing a forefoot landing strategy for higher step descents would allow subjects to better manage the balance challenges posed by height descents but would also increase ankle loading, with the risk of ankle sprains or falls when the tolerance threshold is exceeded. Importantly, all participants in this study were healthy individuals without any pre-existing lower limb injuries. Although the ankle joints of healthy individuals may be able to withstand the load brought by the forefoot touching the ground during descent from high steps, preventing unstable posture control or falls, the potential for accidents remains unmitigated.

As the height escalates to 20 cm, the adoption of the forefoot strategy during stair descent becomes increasingly prevalent (Freedman and Kent, 1987; van Dieën et al., 2008). In this paper, the proportion of participants using the forefoot strategy increased from 50% at 5 cm to 90% at 15 cm. Initially, we speculated that the reason for choosing the forefoot strategy at a lower height might be related to the height and leg length of the participants, and those with shorter height and leg length might change from the hindfoot strategy to the forefoot strategy at a lower step, so as to better control their postural balance and absorb the kinetic energy brought by the descent. However, it was found that there was no significant relationship between landing mode and anthropometric factors. This observation could be attributed to the experiment setup, where the participants gazed ahead, deprived of the ability to visually assess the step heights, potentially eliciting a degree of anxiety. Consistent with our findings, researchers in a previous study (Van Der Linden et al., 2007) hypothesized that the participants who could not see the difference in height would use a forefoot strategy when descending the steps, even for steps as low as 5 cm.

## 4.2 Plantar pressure parameter

The results presented herein indicated that COP-related parameters such as  $V_{COP-ML}$ ,  $V_{COP-AP}$ , overall  $V_{COP}$ ,  $R_{COP-ML}$ , and  $R_{COP-AP}$  all increased with the step height during stair descent. Compared to walking on flat ground, actions such as descending stairs and stepping off curbs involve a vertical descent of the center of mass (COM) because the body's center of gravity shifts downward relative to the support surface, facilitating the smooth transfer of the COM. During stair descent, the COM is adjusted horizontally by leaning the body forward or backward to maintain balance, particularly at higher steps where the body tends to lean forward more to mitigate the impact of

descent (Gosine et al., 2021). The COP, being the projection of the COM onto the support surface (Kilby et al., 2016), exhibits analogous patterns of variation. Consequently, as step height increased, participants adjusted the COM forward or backward tilt, as reflected in the COP, leading to increased COP adjustment velocities and ranges in the AP and ML directions. This aligns with our findings and previous studies indicating that the range of foot posture swings in the ML direction was associated with an increased risk of falling (Eckardt and Rosenblatt, 2018; Krishnan et al., 2013). During challenging daily activities, foot control was more prone to sway in the ML direction, affecting postural balance control. High  $V_{COP}$  and the swing range of COP are regarded as important indicators of balance instability and risk when falling, and the greater the COP value, the greater the postural swing, and thus the lower postural stability (Maki et al., 1994; Fernie et al., 1982). This study found that the increase in step height made the postural control of steps more challenging, augmenting the range of postural swing in the ML direction and increasing the risk of falling due to postural instability. These findings support hypothesis 1 of this paper, which states that heightened step heights diminish lower limb stability and balance when touching the ground. Walking down steps or stairs, as a common dynamic activity in daily life, may offer a more insightful glimpse into balance mechanisms than conventional balance tests such as bipedal standing, unipedal standing, or horizontal ground walking. From a kinematic perspective, as step height rises, the forward distance of the COM on the stairs becomes longer, accelerating the COP in the ML and AP directions, which reflects the instability of the step descent and increases the risk of injury and falling.

Comparing the plantar pressure parameters with the dominant and the non-dominant sides as the leading foot, the results of this study underscore a significant difference exclusively in the 95% confidence circle area parameters. Specifically, the 95% confidence circle area value of the dominant side as the leading foot was significantly lower than that of the non-dominant side as the leading foot. According to the index formula used in this paper, the 95% confidence circle area represents the plantar swaying area when walking down the steps. The smaller the value, the more stable the posture (Maki et al., 1994). The results also showed that the  $V_{COP}$ ,  $R_{COP-ML}$ , and  $V_{COP-AP}$  of the dominant foot were lower than those of the non-dominant foot at 5 cm, 15 cm, and 25 cm step heights, although there was no significant difference in other COP-related indexes. According to the previous description, the higher the COP parameter value, the worse the postural stability. Comparing the dominant lower limb side with the non-dominant side as the leading foot during stair descent is important for understanding postural balance control. The results here support hypothesis 2: “The dominance of the leading foot (dominant or non-dominant) modulates balance and landing strategies during stair descent.” which is consistent with previous research (Hoffman et al., 1998; Alonso et al., 2011).

### 4.3 Limitations and future directions

This study focused exclusively on healthy young women, thus necessitating caution in generalizing the results to broader populations. Our research team plans to explore the stair descending characteristics of women across the entire age spectrum in future work, with the aim of further determining whether the findings of this study are applicable to other age groups or populations with balance disorders. Additionally, this experiment primarily investigated the influence of step height and

foot dominance on biomechanics during stair descent. Other factors that may affect the descent strategy, such as participant height, lower limb strength, and environmental conditions, were not considered in this study. We intend to incorporate them into our subsequent research.

## 5 Conclusion

The results of this study indicate that among young female participants, the height factor during stair descent significantly influences the plantar pressure data of the subjects, with the increase in step height leading to notably larger adjustment speed and swing amplitude of the subjects' COP in the ML and AP directions, thereby elevating the risk of injury and falls. At a step height of 5 cm, the first choice of the landing strategy for female subjects changed from the hindfoot to the forefoot. Although there was no significant difference in the plane pressure data of the two groups of subjects during stair descent, the postural balance control of the leading foot on the dominant side was stronger than the leading foot on the non-dominant side, and this factor had no influence on the choice of landing strategy.

It is suggested that young women choose the dominant side as the leading foot during stair descent to have a better control of postural balance control. As the step height increases, the risk of falling also rises. Therefore, it is recommended that the design height of daily stairs be kept within a reasonable range and minimized as much as possible. It is also recommended that the female population optimize ankle flexibility to reduce the risk of ankle sprains and falls associated with choosing a forefoot touchdown strategy.

## Data availability statement

The raw data supporting the conclusions of this article will be made available by the authors, without undue reservation.

## Ethics statement

The studies involving humans were approved by the Ethics Committee of Shanghai Sport University (No.: 102772021RT073). The studies were conducted in accordance with the local legislation and institutional requirements. The participants provided their written informed consent to participate in this study. Written informed consent was obtained from the individual(s) for the publication of any potentially identifiable images or data included in this article.

## Author contributions

RW: Conceptualization, Data curation, Formal Analysis, Supervision, Validation, Visualization, Writing—original draft, Writing—review and editing. JC: Conceptualization, Writing—review and editing, Writing—original draft. HX: Conceptualization, Investigation, Software, Writing—review and editing. PG: Conceptualization, Investigation, Methodology, Supervision, Writing—review and editing. YL: Data curation, Investigation, Writing—review and editing. YF: Formal Analysis,



Investigation, Software, Writing–review and editing. YG: Conceptualization, Data curation, Formal Analysis, Methodology, Writing–review and editing. LL: Conceptualization, Supervision, Writing–review and editing. RA: Data curation, Formal Analysis, Methodology, Project administration, Supervision, Writing–review and editing. JH: Conceptualization, Data curation, Formal Analysis, Investigation, Writing–review and editing. JL: Conceptualization, Investigation, Methodology, Project administration, Supervision, Validation, Writing–review and editing.

## Funding

The author(s) declare that no financial support was received for the research, authorship, and/or publication of this article.

## Acknowledgments

We extend our sincere gratitude to all the participants for their invaluable contribution to our study. Additionally, we are deeply thankful to JL and JH for their guidance in the experiment design and manuscript preparation.

## References

- Alonso, A. C., Brech, G. C., Bourquin, A. M., and Greve, J. M. D. (2011). The influence of lower-limb dominance on postural balance. *Sao Paulo Med. J.* 129, 410–413. doi:10.1590/s1516-31802011000600007
- Andriacchi, T. P., Andersson, G. B., Fermier, R. W., Stern, D., and Galante, J. O. (1980). A study of lower-limb mechanics during stair-climbing. *JBS* 62 (5), 749–757. doi:10.2106/00004623-198062050-00008
- Barber-Westin, S. D., Noyes, F. R., and Galloway, M. (2006). Jump-land characteristics and muscle strength development in young athletes: a gender Comparison of 1140 athletes 9 to 17 Years of age. *Am. J. Sports Med.* 34 (3), 375–384. doi:10.1177/0363546505281242
- Bencke, J., and Zebis, M. K. (2011). The influence of gender on neuromuscular pre-activity during side-cutting. *J. Electromyogr. Kinesiol* 21 (2), 371–375. doi:10.1016/j.jelekin.2010.10.008
- Cai, Y., Leveille, S. G., Andreeva, O., Shi, L., Chen, P., and You, T. (2023). Characterizing fall circumstances in community-dwelling older adults: a mixed methods approach. *J. Gerontol. Ser. A* 78 (9), 1683–1691. doi:10.1093/gerona/glad130
- Chen, Y. X., and Yu, G. R. (2005). Current status of clinical application of F-Scan plantar pressure gait analyzer. *Overseas Med. Orthop.* (3), 187–189+192.
- Cho, H., Heijnen, M. J., Craig, B. A., and Rietdyk, S. (2021). Falls in young adults: the effect of sex, physical activity, and prescription medications. *PLoS One* 16 (4), e0250360. doi:10.1371/journal.pone.0250360
- Cluff, T., and Robertson, D. G. E. (2011). Kinetic analysis of stair descent: Part 1. Forwards step-over-step descent. *Gait Posture* 33 (3), 423–428. doi:10.1016/j.gaitpost.2010.12.016
- Danneskiold-Samsøe, B., Bartels, E. M., Bülow, P. M., Lund, H., Stockmarr, A., Holm, C. C., et al. (2009). Isokinetic and isometric muscle strength in a healthy population with special reference to age and gender. *Acta Physiol.* 197 (s673), 1–68. doi:10.1111/j.1748-1716.2009.02022.x
- Davey, A. P., Vacek, P. M., Caldwell, R. A., Slauterbeck, J. R., Gardner-Morse, M. G., Tourville, T. W., et al. (2019). Risk factors associated with a noncontact anterior cruciate ligament injury to the contralateral knee after unilateral anterior cruciate ligament injury in high school and college female athletes: a prospective study. *Am. J. Sports Med.* 47 (14), 3347–3355. doi:10.1177/0363546519886260
- Demers, T., Bednarz, N., Mitchell, K., Gerstle, E., and Almonroeder, T. G. (2021). The influence of step-down technique on lower extremity mechanics during curb descent. *J. Electromyogr. Kinesiol* 61, 102590. doi:10.1016/j.jelekin.2021.102590
- Duckham, R. L., Procter-Gray, E., Hannan, M. T., Leveille, S. G., Lipsitz, L. A., and Li, W. (2013). Sex differences in circumstances and consequences of outdoor and indoor falls in older adults in the MOBILIZE Boston cohort study. *BMC Geriatr.* 13 (1), 133. doi:10.1186/1471-2318-13-133
- Eckardt, N., and Rosenblatt, N. J. (2018). Healthy aging does not impair lower extremity motor flexibility while walking across an uneven surface. *Hum. Mov. Sci.* 62, 67–80. doi:10.1016/j.humov.2018.09.008
- Fernie, G. R., Gryfe, C. I., Holliday, P. J., and Llewellyn, A. (1982). The relationship of postural sway in standing to the incidence of falls in geriatric subjects. *Age Ageing* 11 (1), 11–16. doi:10.1093/ageing/11.1.11
- Flaxman, T. E., Smith, A. J. J., and Benoit, D. L. (2014). Sex-related differences in neuromuscular control: implications for injury mechanisms or healthy stabilisation strategies? *J. Orthop. Res.* 32 (2), 310–317. doi:10.1002/jor.22510
- Francksen, N., Ackermans, T., Holzer, D., Maganaris, C., Hollands, M., Roys, M., et al. (2022). Underlying mechanisms of fall risk on stairs with inconsistent going size. *Appl. Ergon.* 101, 103678. doi:10.1016/j.apergo.2022.103678
- Freedman, W., and Kent, L. (1987). Selection of movement patterns during functional tasks in humans. *J. Mot. Behav.* 19 (2), 214–226. doi:10.1080/00222895.1987.10735408
- Gerstle, E. E., Keenan, K. G., O'Connor, K., and Cobb, S. C. (2018). Lower extremity muscle activity during descent from varying step heights. *J. Electromyogr. Kinesiol* 42, 57–65. doi:10.1016/j.jelekin.2018.06.006
- Gerstle, E. E., O'Connor, K., Keenan, K. G., and Cobb, S. C. (2017). Foot and ankle kinematics during descent from varying step heights. *J. Appl. Biomech.* 33 (6), 453–459. doi:10.1123/jab.2016-0301
- Gosine, P., Komisar, V., and Novak, A. C. (2021). A kinematic analysis of balance recovery following an unexpected forward balance loss during stair descent. *Appl. Ergon.* 92, 103317. doi:10.1016/j.apergo.2020.103317
- Guo, P., Wang, D., Li, Y., Wang, R., Xu, H., Han, J., et al. (2023). Do visual and step height factors cause imbalance during bipedal and unipedal stances? A plantar pressure perspective. *Front. Bioeng. Biotechnol.* 11, 1253056. doi:10.3389/fbioe.2023.1253056
- Guo, P., Zhang, X., Xu, H., Wang, R., Li, Y., Xu, C., et al. (2024). Evaluating plantar biomechanics while descending a single step with different heights. *Front. Bioeng. Biotechnol.* 12, 1431988. doi:10.3389/fbioe.2024.1431988
- Hoffman, M., Schrader, J., Applegate, T., and Kocaja, D. (1998). Unilateral postural control of the functionally dominant and nondominant extremities of healthy subjects. *J. Athl. Train.* 33 (4), 319–322.
- Jeon, H. M., Lee, K. K., Lee, J. Y., Shin, J. H., and Eom, G. M. (2021). Energy absorption at lower limb joints in different foot contact strategies while descending stairs. *Technol. Health Care* 29 (S1), 433–440. doi:10.3233/thc-218041
- Kilby, M. C., Slobounov, S. M., and Newell, K. M. (2016). Augmented feedback of COM and COP modulates the regulation of quiet human standing relative to the stability boundary. *Gait Posture* 47, 18–23. doi:10.1016/j.gaitpost.2016.03.021

## Conflict of interest

The authors declare that the research was conducted in the absence of any commercial or financial relationships that could be construed as a potential conflict of interest.

The author(s) declared that they were an editorial board member of Frontiers, at the time of submission. This had no impact on the peer review process and the final decision.

## Generative AI statement

The authors declare that no Generative AI was used in the creation of this manuscript.

## Publisher's note

All claims expressed in this article are solely those of the authors and do not necessarily represent those of their affiliated organizations, or those of the publisher, the editors and the reviewers. Any product that may be evaluated in this article, or claim that may be made by its manufacturer, is not guaranteed or endorsed by the publisher.



- Krishnan, V., Rosenblatt, N. J., Latash, M. L., and Grabiner, M. D. (2013). The effects of age on stabilization of the mediolateral trajectory of the swing foot. *Gait Posture* 38 (4), 923–928. doi:10.1016/j.gaitpost.2013.04.023
- Li, S., Wang, Z., Pang, Z., Gao, M., and Duan, Z. (2023). “Design and analysis of a hemispherical parallel mechanism for forearm–wrist rehabilitation,” in *Appl bionics biomech.* Editor W. M. Chen, 1–14.
- Ma, J. Y. (2002). Preliminary development of Novel pedar plantar pressure distribution measurement system. *China Sports Sci. Technol.* (7), 24–26.
- Maki, B. E., Holliday, P. J., and Topper, A. K. (1994). A prospective study of postural balance and risk of falling in an ambulatory and independent elderly population. *J. Gerontol.* 49 (2), M72–M84. doi:10.1093/geronj/49.2.m72
- Peterka, R. J. (2002). Sensorimotor integration in human postural control. *J. Neurophysiol.* 88 (3), 1097–1118. doi:10.1152/jn.2002.88.3.1097
- Ragg, M., Hwang, S., and Steinhart, B. (2000). Analysis of serious injuries caused by stairway falls. *Emerg. Med.* 12 (1), 45–49. doi:10.1046/j.1442-2026.2000.00090.x
- Razak, A. H. A., Zayegh, A., Begg, R. K., and Wahab, Y. (2012). Foot plantar pressure measurement system: a review. *Sensors* 12 (7), 9884–9912. doi:10.3390/s120709884
- Sie, A., Karrenbach, M., Fisher, C., Fisher, S., Wieck, N., Caraballo, C., et al. (2022). Descending 13 real world steps: a dataset and analysis of stair descent. *Gait Posture* 92, 383–393. doi:10.1016/j.gaitpost.2021.10.039
- Silverman, A. K., Neptune, R. R., Sinitski, E. H., and Wilken, J. M. (2014). Whole-body angular momentum during stair ascent and descent. *Gait Posture* 39 (4), 1109–1114. doi:10.1016/j.gaitpost.2014.01.025
- Talbot, L. A., Musiol, R. J., Witham, E. K., and Metter, E. J. (2005). Falls in young, middle-aged and older community dwelling adults: perceived cause, environmental factors and injury. *BMC Public Health* 5, 86–89. doi:10.1186/1471-2458-5-86
- Van Der Linden, M. H., Marigold, D. S., Gabreëls, F. J. M., and Duysens, J. (2007). Muscle reflexes and synergies triggered by an unexpected support surface height during walking. *J. Neurophysiol.* 97 (5), 3639–3650. doi:10.1152/jn.01272.2006
- van Dieën, J. H., and Pijnappels, M. (2009). Effects of conflicting constraints and age on strategy choice in stepping down during gait. *Gait Posture* 29 (2), 343–345. doi:10.1016/j.gaitpost.2008.08.010
- van Dieën, J. H., Spanjaard, M., Könemann, R., Bron, L., and Pijnappels, M. (2008). Mechanics of toe and heel landing in stepping down in ongoing gait. *J. Biomech.* 41 (11), 2417–2421. doi:10.1016/j.jbiomech.2008.05.022
- Verma, S. K., Willetts, J. L., Corns, H. L., Marucci-Wellman, H. R., Lombardi, D. A., and Courtney, T. K. (2016). Falls and fall-related injuries among community-dwelling adults in the United States. *PLoS One* 11 (3), e0150939. doi:10.1371/journal.pone.0150939
- Waterman, B. R., Owens, B. D., Davey, S., Zaccilli, M. A., and Belmont, P. J. (2010). The epidemiology of ankle sprains in the United States. *Jbjs* 92 (13), 2279–2284. doi:10.2106/jbjs.i.01537
- Yang, N., Waddington, G., Adams, R., and Han, J. (2018). Translation, cultural adaption, and test–retest reliability of Chinese versions of the Edinburgh Handedness Inventory and Waterloo Footedness Questionnaire. *Laterality Asymmetries Body Brain Cogn.* 23 (3), 255–273. doi:10.1080/1357650x.2017.1357728
- Yoshida, T., Ikemiyagi, F., Ikemiyagi, Y., Tanaka, T., Takanami, T., Tamura, Y., et al. (2013). The tracking Axis of the body tracking test. *Nihon Jibiinkoka Gakkai Kaiho.* 116 (12), 1308–1314. doi:10.3950/jibiinkoka.116.1308
- Zachazewski, J. E., Riley, P. O., and Krebs, D. E. (1993). Biomechanical analysis of body mass transfer during stair ascent and descent of healthy subjects. *J. Rehabil. Res. Dev.* 30, 412–422.



## OPEN ACCESS

## EDITED BY

Liguo Zhao,  
Nanjing University of Aeronautics and  
Astronautics, China

## REVIEWED BY

Qiang Chen,  
Southeast University, China  
Jingwen Zhang,  
Loughborough University, United Kingdom

## \*CORRESPONDENCE

Ahmed Sewify,  
✉ sewify@qut.edu.au

RECEIVED 21 October 2024

ACCEPTED 20 January 2025

PUBLISHED 06 February 2025

## CITATION

Sewify A, Lavaill M, O'Rourke D, Antico M,  
Pivonka P, Fontanarosa D and Martelli S (2025)  
Non-contact tracking of shoulder bones using  
ultrasound and stereophotogrammetry.  
*Front. Bioeng. Biotechnol.* 13:1514568.  
doi: 10.3389/fbioe.2025.1514568

## COPYRIGHT

© 2025 Sewify, Lavaill, O'Rourke, Antico,  
Pivonka, Fontanarosa and Martelli. This is an  
open-access article distributed under the terms  
of the [Creative Commons Attribution License](#)  
(CC BY). The use, distribution or reproduction in  
other forums is permitted, provided the original  
author(s) and the copyright owner(s) are  
credited and that the original publication in this  
journal is cited, in accordance with accepted  
academic practice. No use, distribution or  
reproduction is permitted which does not  
comply with these terms.

# Non-contact tracking of shoulder bones using ultrasound and stereophotogrammetry

Ahmed Sewify<sup>1,2\*</sup>, Maxence Lavaill<sup>2,3</sup>, Dermot O'Rourke<sup>2,3</sup>,  
Maria Antico<sup>1,4</sup>, Peter Pivonka<sup>2,3</sup>, Davide Fontanarosa<sup>1,2</sup> and  
Saulo Martelli<sup>2,3</sup>

<sup>1</sup>School of Clinical Sciences, Queensland University of Technology, Gardens Point Campus, Brisbane, QLD, Australia, <sup>2</sup>Centre for Biomedical Technologies, Queensland University of Technology, Brisbane, QLD, Australia, <sup>3</sup>School of Mechanical Medical and Process Engineering, Faculty of Engineering, Queensland University of Technology, Gardens Point Campus, Brisbane, QLD, Australia, <sup>4</sup>Australian e-Health Research Centre, The Commonwealth Scientific and Industrial Research Organisation (CSIRO), Brisbane, QLD, Australia

**Purpose:** We explored the integration of 3D ultrasound (US) imaging with motion capture technology for non-invasively tracking bones of the shoulder district during normal activity. Our study aimed to demonstrate *ex-vivo* the proposed 3D US method's feasibility and accuracy of tracking shoulder bones in a controlled cadaveric shoulder positioned in various arm elevations (low, mid and high).

**Method:** We registered previously acquired full bone shapes to spatially small bony surface patches segmented from 3D US. The bone registration approach used was based on *in silico* analyses that investigated the effects of different — 1) registration algorithms (Iterative-Closest-Point-ICP, and Coherent Point Drift-CPD) and 2) initial estimate levels of the bone model pose relative to the targeted final bone pose—on the overall registration efficiency and accuracy in a controlled environment.

**Results:** CPD provided the highest accuracy in the simulation at the cost of 8x longer computation compared to ICP. The RMSE errors were <1 mm for the humerus and scapula at all elevations. *Ex-vivo*, the CPD registration errors were (Humerus = 2 mm and Scapula = 13.9 mm) (Humerus = 7.2 mm and Scapula = 16.8 mm) and (Humerus = 14.28 mm and Scapula = 27.5 mm), for low, medium and high elevations respectively.

**Conclusion:** In summary, we demonstrated the feasibility and accuracy of tracking shoulder bones with 3D US in a simulation and a cadaveric experiment. We discovered that CPD may be a more suitable registration method for the task than ICP. We also discussed that 3D US with motion capture technology is very promising for dynamic bone tracking, but the US technology may not be ready for the task yet.

## KEYWORDS

bone tracking, ultrasound, 3D-ultrasound, bone registration, *ex-vivo*, stereophotogrammetry, iterative closest point (ICP) algorithm, Shoulder

# 1 Introduction

Skin-mounted markers and stereophotogrammetry enable kinematic analysis of the human body during physical activity. However, the relative motion between the skin and the underlying skeleton causes measurement kinematic errors (Charbonnier et al., 2014; Akbarshahi et al., 2010; Andersen et al., 2010a). When the application requires millimetre accuracy or below, invasive methods are typically preferred. For example, fluoroscopy (Gray et al., 2019; Vogl et al., 2022) and intracortical bone pins (Hajizadeh et al., 2019) are employed, complicating the procedure and exposing the patients to additional risk. The combination of stereophotogrammetry and ultrasound (US) methods has shown promising results for improving the tracking accuracy of current stereophotogrammetry methods by bypassing the skin-motion artefact problem via the US transducer (Fieten et al., 2009; Barber et al., 2009). This advancement may be critical for many fields including sports performance (Zhu et al., 2024), clinical diagnosis, surgery and rehabilitation (Charbonnier et al., 2014; Niu, 2018) and work ergonomics (Salisu et al., 2023).

The combined US-stereophotogrammetry approach has been previously demonstrated for the lower extremity during normal and highly dynamic tasks (Niu et al., 2018b; Niu et al., 2018a; Niu et al., 2018c; Niu et al., 2024; Niu et al., 2018a; Niu et al., 2018b). Niu et al. used several A-mode US transducers to localize in space the knee bone geometry segmented from CT scan. This was done using Iterative-Closest-Point (ICP) registration for minimizing the distance between the CT-based geometry and the US-based bone position (Magnusson et al., 2009). Overall, Niu et al. achieved translational root mean square error (RMSE) that ranged from 2.52 to 5.84 mm and rotational errors between 0.88° and 3.44°. Studies that focused on the upper extremity are very limited (Vicini and Sabick, 2021). Vicini and Sabick (2021) applied Niu et al.'s technique using B-mode US and ICP to a scapula phantom, achieving a similar RMSE equal to 2.5 mm. Despite being limited to lower extremity and phantom studies, these studies demonstrated improved accuracy over traditional stereophotogrammetry only approaches (Andersen et al., 2010b) demonstrating their potential for no-invasive precision tracking methods of complex joints like the shoulder (Sewify et al., 2024).

The literature mainly focused on A-mode US because it can simultaneously cover several anatomical areas using multiple transducers. Studies have shown that the number of registration points is proportional to the tracking accuracy (Niu et al., 2018b; Niu et al., 2018a; Niu et al., 2018c; Niu et al., 2024; Niu et al., 2018d). This is because the spatial distribution of the points provides more geometrical constraints to contribute to the registration results (Niu et al., 2018b). To date, up to 25 A-mode transducers have been used while studies suggested that a further increase of the number of sensors may further improve the registration accuracy (Niu et al., 2018a). Nevertheless, ICP is commonly adopted for being less computationally expensive than other methods (Magnusson et al., 2009), although its sensitivity to local minima can prevent reducing the accuracy of the registration down to sub-millimetre levels (Niu et al., 2018b). Another possibility resides in the use of higher dimensional US transducers (3D US), which can provide a patch of the bone surface as opposed to the single point provided by A-mode sensors, and advanced registration algorithm less

susceptible to local minimum might help improving the bone tracking accuracy (Niu et al., 2024).

This pilot study aimed to integrate 3D US imaging and stereophotogrammetry technologies into a non-invasive precision tracking method. The underlying hypothesis of this study was that combined 3D ultrasound and stereophotogrammetry allow a direct measurement of the instantaneous 3D bone pose during motion. The aim of the present pilot study was to combine 3D ultrasound and stereophotogrammetry and quantify the method's tracking efficacy of the shoulder bones at intermediate static poses in a single cadaveric specimen. The scapula and humerus geometries were segmented from CT images of the donor. The bones position of reference was measured using bone-fixed pins. 3D-ultrasound patches were obtained at relevant bony landmarks locations. The 3D-ultrasound position was obtained by registering the whole bone surface (CT-based) to the 3D-ultrasound patches using different alternative registration algorithms publicly available. The efficacy of the method was quantified by comparing the 3D bone pose reconstructed from the 3D-ultrasound patched and the corresponding measurements obtained *via* bone-fixed pins.

## 2 Materials and methods

### 2.1 Experimental setup

This section outlines the setup of the experimental procedure, detailing protocols employed for setting up the cadaveric specimen, preparing and calibrating the acquisition systems (US, motion capture and CT), selecting and US imaging, the cadaveric bony landmarks.

#### 2.1.1 Cadaveric setup

Here we detail the cadaveric specimen and its setup, the intracortical bone pin insertion protocol and the CT acquisition procedure.

The cadaveric specimen used was the whole thorax and right arm of a female donor (72-year-old, 62 kg, 1.68 m height) which was sourced from the Body Bequest Program of the Queensland University of Technology. The donor died due to natural causes and had no history of shoulder pathology and surgeries. The study was conducted according to the requirements of the National Statement on Ethical Conduct in Human Research and approved by the Institutional Human Research Ethics Committee under approval number LR 20236773-13156.

The specimen was sat in a beach chair position with their right upper arm clamped on an elevation control mechanism. The whole body was covered, except for the right shoulder. Stainless steel intracortical pins and orthopaedic reference frames (Rosa, Zimmer Biomet, Warsaw, IN, United States) were implanted by an experienced shoulder orthopaedic surgeon into the middle aspect of the cadaver's right scapular spine and lateral aspect of their right humerus. The scapula frame had three reflective markers and the humeral frame had four reflective markers. The fourth marker was added to account for potential occlusions of a marker from the motion capture device's field of vision. All markers were 14 mm in size. The stability of the bone-pin construct was manually inspected

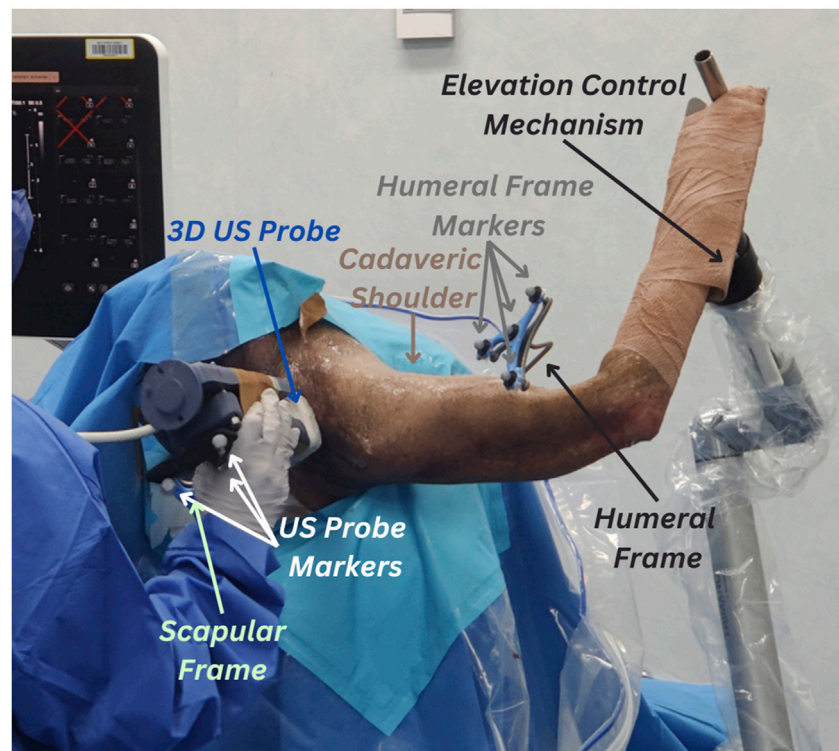


FIGURE 1

Experimental setup for 3D ultrasound (US) tracking of the shoulder bones. Cadaveric shoulder is secured in a beach chair setup and arm elevation is set to high using the elevation control mechanism. The protocol uses retroreflective marker clusters tracked via the VICON motion capture system. The first cluster is attached to the humeral reference frames, the second cluster (partly concealed in the figure) is attached to the scapular frame and the third cluster is attached to the 3D US probe.

by the surgeon. A summary of the experimental setup is depicted in Figure 1.

The whole upper body was subsequently scanned using CT (Toshiba Aquilion Lightning scanner) with a routine clinical shoulder CT imaging protocol (pitch 0.0, increment 2.0 mm, voltage 120 kV, amperage 150A) and the application of a Single Energy Metal Artefact Reduction (SEMAR) (Jabas et al., 2023). The in-plane pixel size was 0.93 mm. The size of the image volume was  $476.16 \times 476.16 \times 556.50$  mm, using a 0.50 mm spacing. The bone geometry was segmented from the images using a uniform threshold value equal to 180 HU (Mimics 25.0, Materialise, Leuven, Belgium). Reflective markers' locations (centre of the ball) were obtained from the segmentation. The 3D humeral and scapular bone models were extracted and exported as stereolithography files with 18,079 humeral vertices/36,154 humeral faces and 22,603 scapular vertices/45,210 scapular faces, respectively. We refer to the segmented CT-based whole bone geometry as *bone CT*.

### 2.1.2 VICON and US probe calibrations

This subsection describes the hardware used for the US and VICON acquisition during the experiment along with how they were calibrated.

Stereophotogrammetry data were captured using a VICON motion capture system consisting of three Vero 2.2 cameras (VICON, Oxford, United Kingdom) fixed on a single tripod and pointing towards the posterior aspect of the specimen. We optimised

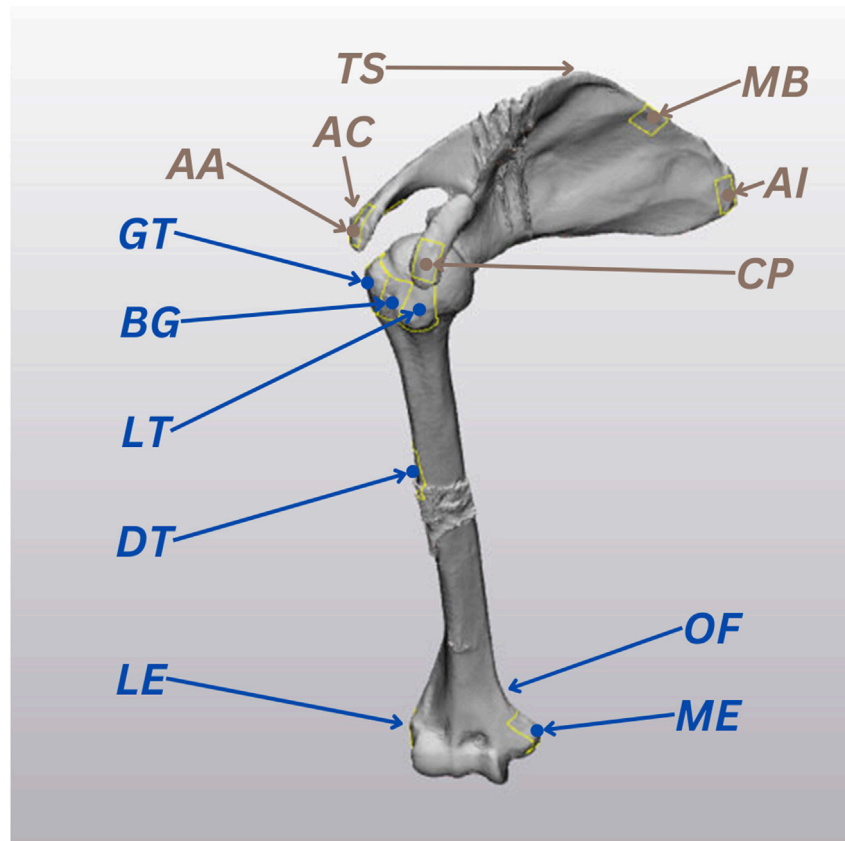
the pose of the camera to maximize the portion of the cadaveric shoulder visible by all three cameras while avoiding any camera view obstructions.

The US system consisted of a VL13-5 3D US probe (Philips Medical Systems, Andover, MA, United States), a mechanically swept 3D linear probe, attached to a Philips EPIQ7 US system (Philips Medical Systems, Andover, MA, United States). The probe was instrumented with a cluster of four reflective markers (Figure 1) to provide the US probe pose in the stereophotogrammetry space.

The transformation from the US probe space and the VICON space was determined using the calibration method proposed by Lange and Eulenstein (2002), which is based on a Blue Phantom MSK Knee US Training Model (Elevate Healthcare, Sarasota, Florida, US) imaged with sixty US volumes captured from different angles. The pose of the probe markers was recorded simultaneously with the US data. Motion capture US probe poses within each 5-second sweep were averaged for each landmark scan, as suggested by Vicini and Sabick (2021). Then, the alignment of the US volumes was manually conducted in ImFusion (ImFusion GmbH, München, Bayern, Germany). The US volumes were calibrated into the VICON space using the equation:

$$v_v = {}^w X_I^P X v_I$$

where  $v_I$  is the US volume location in volume space,  ${}^P X_I$  is the transformation from the US volume space to the US probe space,



**FIGURE 2**  
The 13 ultrasound (US) landmarks selected for the study, based on the International Society of Biomechanics recommendations (Wu et al., 2005). Humeral landmarks are highlighted in blue and scapular landmarks are represented in brown.

${}^wX_p$  is the transformation from the US probe space to the VICON space and  $v_v$  is the desired US volume location in the VICON space.

### 2.1.3 Landmark selection and US imaging

Here we describe the protocol for selecting and acquiring bony landmarks using US from the cadaveric shoulder specimen.

The scapular and humeral bony landmarks were selected according to the International Society of Biomechanics recommendations, and they were all accessible to US imaging (Wu et al., 2005). The 7 humeral landmarks included: Greater Tuberosity (GT), Lesser Tuberosity (LT), Bicipital Groove (BG), Deltoid Tuberosity (DT), Lateral Epicondyle (LE), Medial Epicondyle (ME), Olecranon Fossa (OF). The 6 scapular landmarks were: Angulus Acromialis (AA), Terminus Spinae (TS), Angulus Inferior (AI), Medial Border (MB), Coracoid Process (CP), Acromioclavicular joint (AC) (Figure 2).

The specimen's right arm was sequentially placed and clamped at low ( $\sim 30^\circ$ ), medium ( $\sim 90^\circ$ ) and high ( $\sim 120^\circ$ ) elevation angles. Then, for each elevation trial, the selected landmarks of the specimen's right arm were sequentially imaged by a registered musculoskeletal sonographer using the 3D US system. Care was taken to avoid movements of the specimen for the entire duration of the experiment. The probe was kept still for a period of 5 s for each landmark. The US volume resolution was  $512 \times 403 \times 256$  voxels with spacings of  $0.123 \times 0.110 \times 0.240$  mm. The position of the

reflective markers on the probe and those attached to the intracortical pins fixed to the cadaver were continuously recorded at 50 Hz throughout the experiment. The average pose of the US probe within each 5-second sweep was used for the following analyses. Bone frame and probe movements during the US scans are further discussed and analyzed in the displacement errors section of error quantification.

## 2.2 Bone registration procedure

This section details the registration procedure performed to test our hypothesis that we can localize the cadaveric *bone CT* by aligning it to corresponding US-based bone position in the same VICON space. The US-based bone position was determined in two ways, *in silico* - by directly extracting the landmarks from the surface of the *bone CT* itself - and *ex-vivo* - by segmenting the selected landmarks from the scapular and humeral US acquisitions. The whole registration procedure was conducted separately for the humerus and scapula *bone CT*.

### 2.2.1 In-silico registration

The purpose of the *in silico* registration was to develop the bone registration procedure by considering alternative registration algorithms, compared in terms of accuracy and sensitivity to



TABLE 1 Summary of the registration methods used in the study.

Registration method	Registration type	Description	Performance characteristics	Details
ICP	-Local approach -Iteratively minimizes the distance between the closest corresponding points	Dependent on the initial transform estimate	-Fast -Consistent/Predictable -Highly susceptible to local minima	Magnusson et al. (2009)
CPD	Global, probabilistic density estimation approach	Does not rely on an initial transformation estimate	-Slow -More robust to noise, outliers and missing points than ICP	Myronenko and Song (2010)

initial pose estimate. These factors were analyzed numerically independent of other potential sources of error like segmentation errors and probe-sensor calibration. The optimal registration algorithms and factors determined from the *in silico* analyses were then employed for the *ex-vivo* registration. This subsection describes the: 1) extraction of the *in silico* patches that simulate the US bone segmentations. 2) bone registration setup. 3) registration methods considered. 4) registration scenarios examined.

To simulate US bone segmentations, we extracted  $40 \times 40$  mm surfaces (*patches*) from the *bone CT* surfaces centred around the 13 selected landmarks using 3-Matic (Materialise, Leuven, BE). The centroid locations of the *patches* were measured and recorded as *landmarks*, the blue and brown point locations marked in Figure 2. The 13 *patches* were then converted into point clouds, normalized to the size of the smallest point cloud (196 points), and divided into 7 humerus *patches* and 6 scapula *patches*.

The bone registration setup involved three different sets of point clouds per bone: *moving CT*, *target CT* and *target patches*, duplicated from the *bone CT* and corresponding *patches*. The *target* set referred to the *bone CT* and its extracted *patches* fixed in a reference pose (true pose). The *moving* set referred to the corresponding mispositioned set that is to be registered to align with the fixed *target* set. The accuracy of our method in determining the bone poses was based on the best fit of the *moving CT* with the *target patches* using various registration methods. The registration accuracy was based on the distance minimization between the *moving CT* and *target CT*.

Our study considered multiple registration methods, including ICP, Normal Distributions Transform (NDT) (Magnusson et al., 2009), Lidar Odometry and Mapping (LOAM) (Zhang and Singh, 2014), Fast Global Registration (FGR) (Osipov et al., 2023) and CPD. We opted to undertake a comparative analysis between 2 registration methods, ICP and CPD, as summarized in Table 1. We selected ICP since, as previously discussed, it is possibly the most commonly employed registration method in previous studies. Given the distinct characteristics of CPD, as shown in Table 1, we opted to investigate if it may resolve the drawbacks experienced by previous studies that have employed ICP. The performance characteristics in Table 1 are reported relative to other registration methods, as further discussed in the *Details* column of the table.

The *in silico* bone registration was conducted on three scenarios considering extreme levels of knowledge of the initial pose prior to the bone registration performed using ICP and CPD. The three initial pose estimate scenarios considered were *perfect initial estimate*, without pre-registration (*without Pre-Reg*) and with pre-registration (*with Pre-Reg*):

- 1) *Perfect initial estimate*: the *moving CT* was already positioned in the true pose (i.e., same as *target CT*).
- 2) *Without Pre-Reg*: the *moving CT* was initially transformed to a random pose. The random pose of the *moving CT*'s three translations and rotations values followed uniform distributions of  $[-50; 50]$  mm and  $[-15; 15]^\circ$ , respectively, across 1,000 randomly simulated iterations. These values were wisely selected to represent a random, credible initial guess, which can realistically be obtained from stereophotogrammetry.
- 3) *With Pre-Reg*: the initial pose was defined using an initial coarse registration (Horn, 1987), which offers the best possible transformation between 2 sets of corresponding points (A and B) in a single step, without iteration (Horn, 1987). Only the ISB *landmarks* were used for this initial pose estimate.

The entire registration protocol conducted in the *With Pre-Reg* scenario using the scapula as an example is depicted in Figure 3.

## 2.2.2 Data analyses and ex-vivo registration

After analysing the results obtained from the *in silico* experiment, the registration procedure was replicated *ex-vivo* using the best-performing registration method and initial estimate scenario obtained numerically, as described in section 2.3.1 - Registration errors. For the cadaveric experiment, the *target patches* were the actual 3D US imaged landmarks after they had been segmented from the US volumes in 3D Slicer (Texas, United States), and the true poses of the *target CT* were determined using the VICON-tracked bone frames.

## 2.3 Error quantification

### 2.3.1 Registration errors

The feasibility of integrating 3D US imaging and stereophotogrammetry technologies as a non-invasive shoulder bone tracking method was evaluated by assessing the alignment between the pose estimated *moving CT* and the true positioned *target CT* (registration error/accuracy). *In-silico*, the registration error was determined by calculating the RMSE (averaged point-to-point location errors) between the *moving CT* and *target CT* point clouds, after registering the *moving CT* to the *target patches*. This was determined for each registration method in each of the three previously discussed scenarios, and the time taken for each registration was also recorded. These two metrics allowed comparing the accuracy and efficiency of the registration methods as well as their sensitivity to initial pose estimates. For

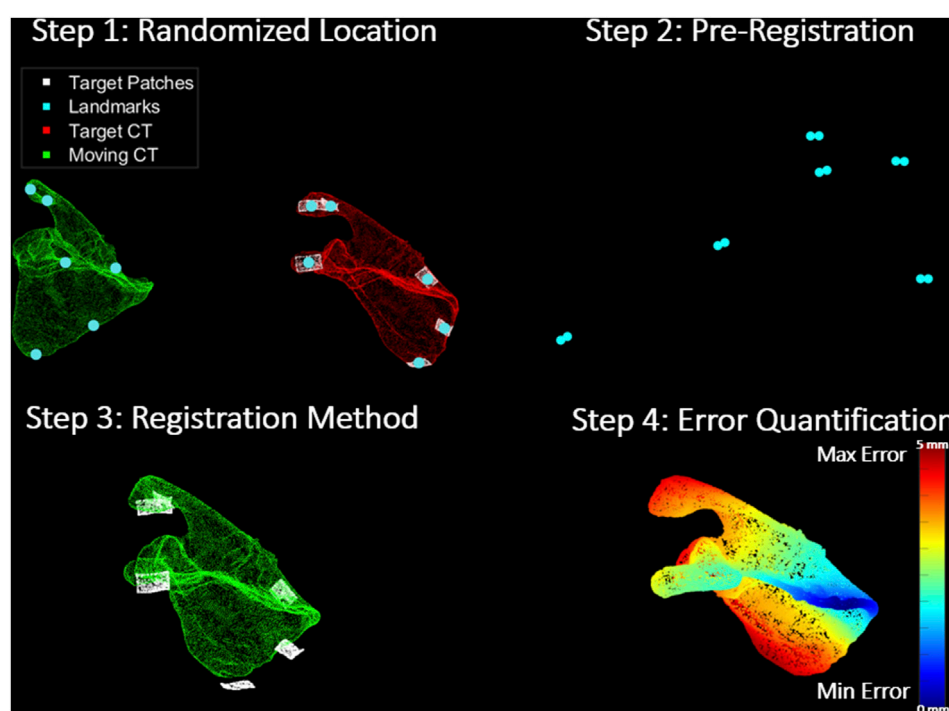


FIGURE 3

Registration Protocol: Step 1 shows the moving CT (green) transformed to an arbitrary location away from their true pose, target CT (red) and its corresponding target patches (white). It also shows the corresponding landmarks (turquoise) on the surface of each set. Step 2 depicts the pre-registration approach (coarse registration) utilized to obtain a positional initial estimate of the moving CT with respect to the target patches through the alignment of the corresponding landmarks from both sets. In step 3, the registration methods (ICP and CPD) are applied to register the moving CT to the target patches. Finally, step 4 shows the error quantification procedure which calculates the RMSE between the target and estimated moving CT pose in a point-by-point manner. The scapula in the figure is colour-coded based on how far each point in the moving CT of the scapula is from its corresponding true pose in the target CT.

the *ex-vivo* experiment, the RMSE was based on the difference between the registered pose of the *moving CT* compared to their corresponding *target CT* identified by the VICON-tracked bone frames.

### 2.3.2 Calibration errors

To further analyze our results and enable more comprehensive conclusions, we recorded sources of errors that could arise from our presented experimental setup. Errors in the motion capture device calibration were obtained from the VICON software provided by the manufacturer following the active wand calibration procedure (VICON, 2024). The US calibration error was quantified using the reconstruction accuracy metric suggested by Lange and Eulenstein (2002) by mapping test points in the US volumes to the VICON space and computing the RMS error between the corresponding points in the true (manually aligned) poses and transformed poses.

### 2.3.3 Displacement errors

Two other experiment setup error metrics related to the imaging stability inter and intra-trials were analyzed during the cadaveric experiment, i.e., bone frame marker displacement (inter-trials) and US probe displacement (intra-trials). As with the registration, the displacement errors were separately analyzed for the humerus and scapula.

Displacement of the bone frame relative to the shoulder bone was manually checked as in Ludewig et al. (2009) and Dal Maso et al. (2014). We quantified the deviation of the humeral and scapular bone frames during each US landmark acquisition relative to the first US acquisition in the trial. These deviations are what we refer to as bone frame displacement errors in this study, and they were obtained by tracking the centre marker of the bone frames. The errors were measured across X, Y and Z-axes, considering a posterior view of the cadaveric shoulder, X was directed medially, Y was directed inferiorly and Z was in the posterior direction.

The US probe displacement error measured the fluctuation of the probe marker poses during the 5 s sweeps required by the 3D mechanically swept probe to image the US landmarks.

## 3 Results

### 3.1 Registration errors

#### 3.1.1 *In-silico* registration accuracy

Table 2 shows the average registration accuracy results (*moving CT* alignment with *target CT*) of the humerus and scapula across 1,000 iterations of a randomized starting location from true pose using ICP and CPD and for all 3 initial pose estimate scenarios (*Perfect Initial estimate*, *Without Pre-Reg* and *With Pre-Reg*).

**TABLE 2** Average *in-silico* registration accuracy results of ICP and CPD for the humerus and scapula at all 3 initial estimate levels (coarse registration only as a pre-registration step, directly applying registration method from the perfect initial estimate and directly applying the registration method without coarse registration from a random location, up to 1 m afar).

Anatomy			ICP			CPD		
	(mm)	Pre-reg only	Perfect initial estimate	Without pre-reg	With pre-reg	Perfect initial estimate	Without pre-reg	With pre-reg
Humerus	mean	2.73	2.30	9.66	2.30	0.04	0.04	0.04
	min	2.73		2.30	2.30		0.04	0.04
	max	2.73		89.77	2.30		0.04	0.04
Scapula	mean	15.80	21.44	37.46	21.44	0.03	0.03	0.03
	min	6.40		21.26	21.44		0.03	0.03
	max	37.37		99.90	21.44		0.03	0.03

**TABLE 3** *Ex-vivo* registration accuracy results of ICP and CPD for the humerus and scapula across all 3 trials (low, mid and high) using coarse registration alone and using coarse registration as a pre-registration step, combined with CPD.

Shoulder elevation	Anatomy	Pre-reg only (mm)	CPD with pre-reg (mm)
Low	Humerus	103.1	2.0
	Scapula	115.4	15.1
Mid	Humerus	89.2	7.2
	Scapula	117.9	16.8
High	Humerus	61.3	14.1
	Scapula	96.5	27.5

CPD outperformed ICP in every condition investigated, yielding consistent registration results for the humerus and scapula, 0.4 and 0.3 mm, respectively. As for the ICP, incorporating it with pre-registration to support the registration method by providing an initial estimate, significantly improved its registration accuracy from (Humerus RMSE = 9.7 mm and Scapula = 37.5 mm) to (Humerus RMSE = 2.3 mm and scapula = 21.4 mm), with the scapula registration error remaining beyond 20 mm.

Interestingly, coarse registration alone yielded better accuracy than ICP alone when registering both the humerus (2.7 mm vs. 9.6 mm, respectively) and scapula (15.8 mm vs. 37.46 mm, respectively).

The average computation times taken by the pre-registration only, ICP and CPD for registering the humerus were 0.0002, 1.96 and 6.11 s, respectively. For the scapula, the average time taken was 0.0001, 1.02 and 6.18, seconds respectively. Therefore, despite being approximately 4–5 s slower, CPD was the best-performing registration method, yielding overall registration errors close to 0 mm for both anatomies.

### 3.1.2 Ex-Vivo registration accuracy

Table 3 shows the results of the registration procedure that was replicated on the cadaveric shoulder using the best-performing *in silico* registration method, i.e., CPD, and the incorporation of pre-registration.

In general, registration accuracy was best in the low elevation trial (Humerus = 2 mm and Scapula = 15.1 mm) and worst in the

high elevation trial (Humerus = 14.1 mm and Scapula = 27.5 mm). Moreover, all humeral registration results (Low = 2 mm, Mid = 7.2 mm and High = 14.1 mm) were better than the scapular results (Low = 15.1 mm, Mid = 16.8 mm and High = 27.5 mm).

Pre-registration alone minimized the distance between *moving CT* and *target CT* (identified from true bone frame-tracked poses) with an RMSE between 61.3 and 103.1 mm, performing slightly better than for the scapula (RMSE between 96.5 and 117.9 mm). Leveraging CPD significantly reduced the registration error range between 2 and 27.5 mm.

## 3.2 Calibration errors

The computed calibration error for each of the 3 cameras of the motion capture device was <0.02 mm. The hand-eye calibration between the markers attached to the US probe and the US probe transducer led to an average error of  $2.9 \pm 1.6$  mm (max error = 6 mm).

## 3.3 Displacement errors

### 3.3.1 Bone frame displacement

The positional deviation of the VICON-tracked humeral and scapular bone frames in each trial is shown in Figure 4.



**FIGURE 4**  
Humeral (blue) and scapular (red) bone frame markers position deviation during the US capture for each of the 13 landmarks across the low, mid and high elevation trials respectively. The X-axis of the plots refers to the 13 US landmark volume acquisitions, and the Y-axis refers to the positional deviation of the bone frame markers as recorded by VICON during the acquisition of each of the 13 landmarks and relative to the acquisition of the first landmark.

As depicted in the figure, overall, the humeral frame displaced more than the scapular frame across all trials, deviating by less than 3 mm on average. However, during the US acquisition of the ME and LE landmarks in the low elevation trial, the humeral frame exhibited deviations of 5 mm and 10 mm along the Z and Y-axes, respectively.

In the case of the scapular frame, while the deviations were kept approximately below 4 mm along the Y and Z-axes for all trials, significant scapular frame deviations were experienced along the X-axis. Deviations larger than 10 mm (and up to 28 mm) occurred during the acquisition of the following landmarks: AA (Low); AA, MB and AC (Mid); and AA, TS, AI and MB (High).

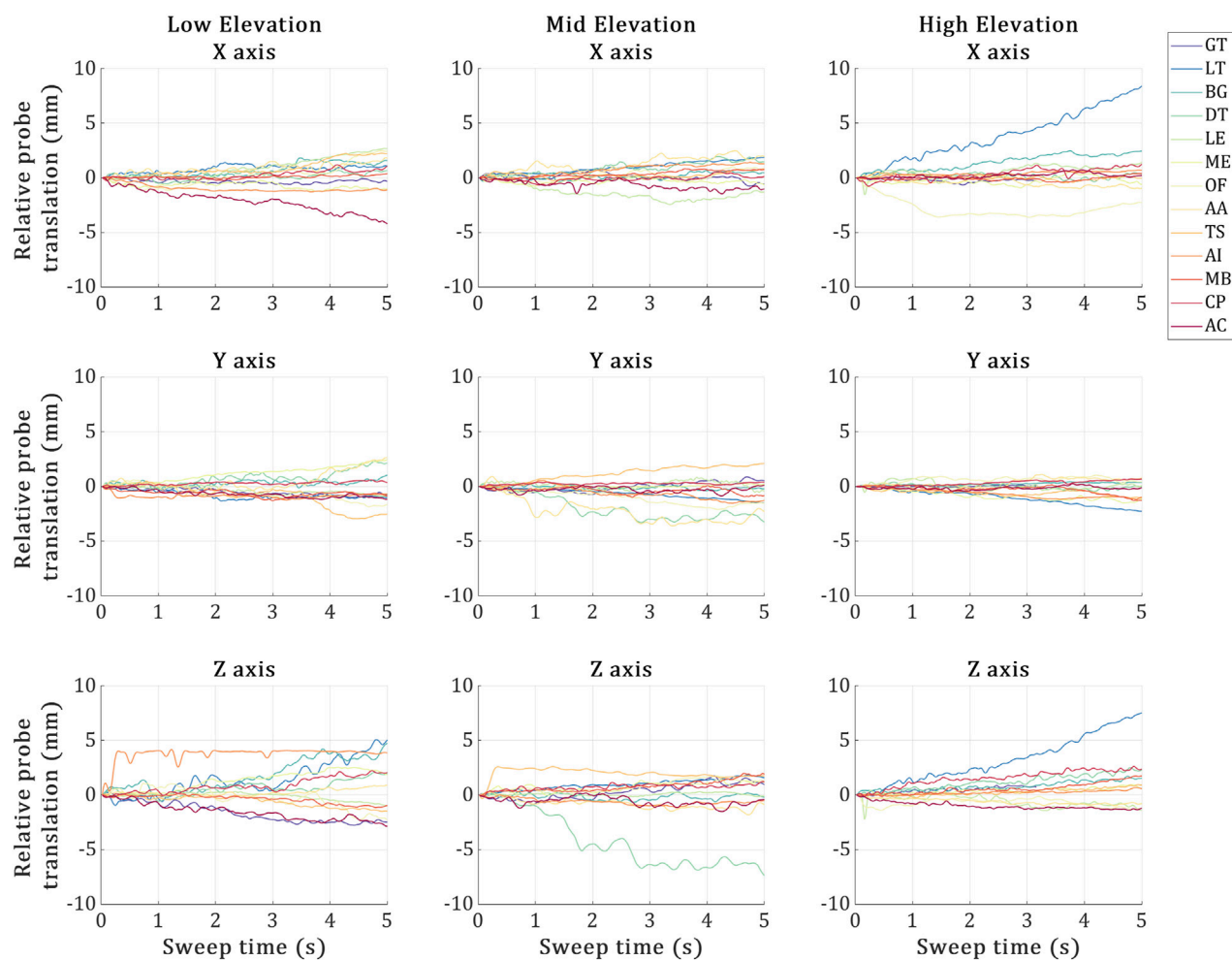
### 3.3.2 Probe displacement

The probe displacement for each trial is illustrated in Figure 5. Overall, the probe was stable during the US landmark acquisitions in all trials, deviating by around 3 mm on average across all directions. In terms of probe deviations reaching past 5 mm, (Low) no such deviations, (Mid) during the US imaging of the DT and (High) during the US imaging of the LT. The high elevation trial's LT was

the most erroneous landmark, experiencing a maximum deviation of ~7 mm during the US acquisition along two axes at once (X and Z).

## 4 Discussion

The primary focus of this study was to demonstrate the feasibility of integrating 3D US and motion capture systems to track the shoulder bones in space. The bone shapes segmented from CT scan were registered to a set of segmented bone surfaces obtained using 3D US and registered in space using stereophotogrammetry (Vicon, Oxford, United Kingdom). We found the combination of CPD with coarse registration to be the most accurate registration approach. The accuracy of the bone pose obtained using 3D US and stereophotogrammetry combined was in line with earlier studies based on A-mode sensors and different anatomical regions and better than the pose estimate based on stereophotogrammetry alone. Therefore, the present pilot study demonstrates the viability of 3D



**FIGURE 5**  
Probe displacement during the 5-second sweeps required by the 3D probe to image each US landmark at the low, mid and high elevation trials. X-axis represents the 5-second sweep time interval, and the Y-axis represents the US probe marker displacements recorded via VICON during the sweep time. The 13 coloured plot lines refer to each landmark acquisition.

US for precision tracking in space of shoulder bones, potentially mitigating the drawback of current studies based on A-mode US sensors.

The simulation analyses in our study assessed the effects of two factors on the overall registration accuracy, the level of initial pose estimate and the specific registration algorithm employed. Despite being 4–5 times slower, CPD outperformed ICP in every condition investigated across all iterations, aligning both the humerus and scapula to their true pose with an RMSE of  $\sim 0.4$  mm. CPD was also insensitive to initial estimates, being a global registration method; nevertheless, registration error never reached 0 mm error even under ideal conditions. For ICP, it was very sensitive to initial estimates and yielded worse registration results than employing coarse registration for both the humerus (*Pre-Reg* alone RMSE = 2.7 mm vs. ICP RMSE = 9.6 mm) and scapula (*Pre-Reg* alone RMSE = 15.8 mm vs. ICP RMSE = 37.46 mm). Combining coarse registration and ICP achieved the same registration results as supplying ICP with the true pose as the initial pose estimate, 2.3 and 21.44 mm, for the humerus and scapula respectively. This may demonstrate the effectiveness of the pre-employing

coarse registration with initial local registration methods. Results may imply that standard ICP is not suitable for the task since it could not approach sub-mm results even under ideal conditions. ICP may be more accurate when registering point clouds with the same number of nodes and representing the same, entire shape, instead of patches (sub-samples of the entire shape). Anatomically, with initial estimates, ICP registration errors were nine times better for the registering humerus than registering the scapula, suggesting that the scapula is a more challenging registration target, being a unique, non-convex geometry. Indeed, ICP minimizes the distance between corresponding points in point clouds until a minimum is reached (Magnusson et al., 2009), complex shapes may offer more local minima than relatively simpler shapes, making the solution sensitive to the initial position. This may explain the lower performance of the ICP algorithm for the scapula over that for the humerus. CPD, being less sensitive to the initial pose, appears more suitable for this type of registration problem, particularly for the scapula.

Our cadaveric experiment was conducted on 3 different static arm elevations, low, mid and high ( $\sim 30^\circ$ ,  $90^\circ$  and  $120^\circ$ ). The



registration accuracy for aligning the humerus across all three trials (Low = 2 mm, Mid = 7.2 mm and High = 14.1 mm) to its true bone frame position in the VICON coordinates was significantly better than the scapula registration results (Low = 15.1 mm, Mid = 16.8 mm and High = 27.5 mm). *Ex-vivo*, coarse registration was no longer a viable solution for registering the humerus, with its registration accuracy dropping from 2.73 mm *in silico* to a minimum error of 61.3 mm in the low elevation trial of the cadaveric experiment. Registration accuracy of CPD with *Pre-Reg* also dropped from ~0.4 mm across 1,000 iterations for both the scapula and humerus to a minimum of 15.1 and 2 mm, respectively, in the low elevation trial of the cadaveric experiment. Our best registration accuracy achieved in the low elevation trial for the humerus using CPD and coarse registration (RMSE = 2 mm) was lower than the lowest error reported in the cadaveric literature on the lower extremity (RMSE = 2.81 mm) (Niu et al., 2018b; Niu et al., 2018a; Niu et al., 2018c; Niu et al., 2024; Niu et al., 2018). Our maximum registration error recorded across all trials (High Elevation Scapula RMSE = 27.5 mm) was still lower than standard skin-mounted marker tracking results (~30 mm) (Akbarshahi et al., 2010; Andersen et al., 2010a; Lavaill et al., 2022), yet much higher than the highest error reported error by Niu et al. (27.5 mm vs. 5.88 mm). These *ex-vivo* results show the potential for our proposed approach in tracking the shoulder bones.

The large difference between our simulation results (CPD with *Pre-Reg* range = 0.03 mm–0.04 mm) and the cadaveric experiment results (CPD with *Pre-Reg* range = 2 mm–27.5 mm) is attributed to the fact that in the former experiment, the only source of error is the registration error. In the latter experiment, however, errors came from multiple sources, each one adding on top of the other. This includes inter-trial bone frame displacement (up to 28 mm), inter-trial US probe displacement (up to 7 mm), US calibration (up to 6 mm), bone-pin construct rigidity (not quantified, likely <1 mm), Vicon calibration (0.02 mm) and eventually the registration errors (<1 mm). The *ex-vivo* registration results we reported reflect the sum of these errors in addition to the registration error, implying the collective impact of the setup errors on the registration accuracy. The primary error contributor in our experiment is that our assumption, that the cadaver did not move during and between the different trials, is false as depicted by the inter-trial bone frame displacement and the intra-trial US probe displacement, likely due to the action of the sonographer pressing against the cadaveric specimen during each US landmark acquisition, resulting in unwanted specimen and probe displacements.

It is important to note that the bone frame and US probe displacements concern the control of the experiment and the underlying assumption of static pose, rather than the localization accuracy of the method analysed. Future studies may either improve the control of experiment or account for the movement of the bone tracked with submillimeter error by the bone-fixed pin. These analyses, however, were out of the scope for the present pilot study. The more controlled *in-vitro* experiment by Vicini and Sabick (2021) that used a fixed scapula phantom, proved that removing inter-trial bone frame displacement and intra-trial US probe displacement reduced the registration error to 2.5 mm for the scapula. It appears essential to minimise these experimental errors for a more accurate tracking *in-vivo*.

The bone localization error reported in the present study were larger than what similar studies reported earlier in Niu et al. (2018b). This is evident when we compare the gap in our *in silico* and *ex-vivo* experiments to theirs (1.71 vs. [2.81–5.84] mm, respectively). Such differences are likely attributable to the different anatomical regions, experimental procedure and analyses, complicating a direct comparison of the results. However, our experimental procedure shows both potential limitations and strengths compared to their approach, which might explain the differences in results. In terms of limitations, our protocol introduced experimental setup errors which may not have been relevant to Niu et al. (2018b); in particular, our discussed sonographer displacement and subject displacement between probing. Simultaneously imaging multiple bone landmarks using distributed synchronized A-mode US transducers completely dismisses these errors. This imaging protocol capability is not plausible using a single 3D US probe. Another limitation may be due to the US calibration protocol. Higher calibration errors may arise when a relatively large, heavy US transducer presses against a phantom, proning movement between the calibration acquisitions. Unfortunately, none of the similar A-mode or 2D US studies have reported their calibration protocols or errors for direct comparison (Vicini and Sabick, 2021; Niu et al., 2018a; Niu et al., 2018b; Niu et al., 2018c; Niu et al., 2024; Niu et al., 2018). The way these experimental setup errors impacted our experiment was by generating outliers which either skewed the results or had to be discarded, ultimately compromising the registration outcomes. However, in terms of our approach's strengths, our 3D US imaging protocol dismisses experimental setup limitations experienced by the similar A-mode studies reported by Niu et al. These included the US transducers missing the target landmark approximately 30% of the time, challenge in retaining perpendicular line of sight between the US transducers and reflecting bone surface which may not be visible due to overlaying soft tissue, and limited number of registration points. Additionally, their protocol required significantly more US transducers as the A-mode devices are only capable of obtaining a single registration point on the bone surface per transducer. These experimental procedure differences highlight strengths and limitations of both experimental protocols and explain the differences in the bone localization errors obtained.

Despite not being the main aim of our study, there are some interesting discoveries when we compare the results achieved in our numerical analyses to literature. Our randomized location with pre-registration scenario closely resembles the US Point Localization Error scenario in Niu et al. (2018b), and structural similarities between the humerus and tibia are valid. Notably, overall, our proposed CPD approach was 0.22 mm more accurate for the humerus than their proposed four-stage ICP was for the tibia. Interestingly, in the same scenario, standard ICP with *Pre-Reg* achieved slightly better accuracy on their tibia than it did on our humerus, with an accuracy of around 1.71 mm (Niu et al., 2018b) compared to 2.3 mm in the present study. This was observed despite the similar conditions and the extra abundance of registration points provided by our 3D registration approach. Their tibia registration relied on 25 registration points compared to our 1,372 points (7 humeral patches–196 points each). While they did not share the exact number of landmarks/locations these points covered, from their protocol's image, we may assume that their points are roughly

three times more spread out than our humerus points. Their investigation on the relationship between the number of registration points utilized and the registration accuracy concluded a proportional relationship as long as the added points are not relatively more erroneous. Given that they managed to reach 0 mm registration error in 80/100 cases using 25 points under ideal conditions, we could revise their conclusion to the following: the registration accuracy is indeed proportional to the number of registration points as long as the added points are sufficiently far enough from existing points, i.e., add more dispersity. Future work shall investigate the sensitivity of the registration accuracy to the patch locations and numbers to confirm this.

This study does have some limitations. Firstly, this was a pilot study conducted on a single cadaveric specimen and only one trial per arm elevation because of time and resource limitations, preventing further analyses to reinforce the reliability of our RMSE data across trials. Secondly, the study assumed that the humeral and scapular bone frames were stable relative to their respective bones throughout the experiment. This assumption may prove to be a limitation, especially due to the challenging insertion of the scapular frame through the scapula spine. The challenge posed was not only anatomical but also due to the old age of the donor and the low bone mineral density of the scapula. Future works may investigate the most stable insertion techniques for scapular bone frames, quantify the instability of the bone frames relative to bone and investigate the impact of the instabilities on the registration results. Thirdly, only one US probe was used forcing the assumption that the specimen did not move between landmark imaging, despite the displacement results showing otherwise. Current commercial US technologies may not allow us to proceed to the next step with the employment of multiple 3D US probes at the same time, especially for dynamic motion. However, promising distributed, wearable US research devices using capacitive micromachined technologies are currently being developed by member of our team for achieving dynamic bone registrations using real-time 3D US motion capture (CSIRO, QUT, 2024).

## 5 Conclusion

In conclusion, this study demonstrated the feasibility of integrating 3D US and stereophotogrammetry for tracking shoulder bones through both a simulation and a cadaveric shoulder experiment. *In-silico* results showed that the CPD registration algorithm provided more accurate and repeatable results than standard ICP, achieving sub-mm accuracies in the numerical analyses regardless initial estimates. The cadaveric experiment showed that the proposed approach can successfully track the humerus and scapula at different arm elevations by comparing results against the established intracortical bone pin tracking method as well as results obtained from previous literature. The humerus tracking accuracy was comparable to previous reports of motion capture tracked A-mode US on lower extremities, while scapula tracking exhibited higher errors, likely due to experimental setup challenges such as bone frame displacement and calibration inaccuracies. These findings highlight the potential of combining motion capture technologies

and 3D US for non-invasive, safe, real-time shoulder tracking. Future research will focus on the employment of multiple US transducers for dynamic tracking of the shoulder joint using real-time 3D US motion capture.

## Data availability statement

The original contributions presented in the study are included in the article/supplementary material, further inquiries can be directed to the corresponding author.

## Ethics statement

The studies involving humans were approved by the QUT Human Research Ethics Committee. The studies were conducted in accordance with the local legislation and institutional requirements. Written informed consent for participation was not required from the participants or the participants' legal guardians/next of kin because it is a cadaveric study. Written informed consent was not obtained from the individual(s) for the publication of any potentially identifiable images or data included in this article because it was a cadaveric study.

## Author contributions

AS: Data curation, Formal Analysis, Investigation, Methodology, Software, Validation, Visualization, Writing—original draft, Writing—review and editing. ML: Conceptualization, Data curation, Formal Analysis, Methodology, Project administration, Software, Validation, Visualization, Writing—review and editing. DO'R: Conceptualization, Formal Analysis, Funding acquisition, Methodology, Project administration, Software, Visualization, Writing—review and editing. MA: Conceptualization, Methodology, Supervision, Writing—review and editing. PP: Conceptualization, Funding acquisition, Resources, Supervision, Writing—review and editing. DF: Conceptualization, Funding acquisition, Methodology, Resources, Supervision, Writing—review and editing. SM: Conceptualization, Funding acquisition, Methodology, Project administration, Resources, Supervision, Writing—review and editing.

## Funding

The author(s) declare that financial support was received for the research, authorship, and/or publication of this article. This research was supported by funding schemes of the Australian Government: ARC Industrial Transformation Training Centre (ITTC) for Joint Biomechanics under grant IC190100020 and FT180100338.

## Acknowledgments

The authors would like to acknowledge Professor Glen Lichtwark for his guidance and support concerning the overall

project and US probe calibration. We also acknowledge the sonographer Jacqueline Roots for performing 3D US imaging in this study and QUT Medical Engineering Research Facility for facilitating the equipment and venue needed for the project.

## Conflict of interest

The authors declare that the research was conducted in the absence of any commercial or financial relationships that could be construed as a potential conflict of interest.

## References

- Akbarshahi, M., Schache, A. G., Fernandez, J. W., Baker, R., Banks, S., and Pandey, M. G. (2010). Non-invasive assessment of soft-tissue artifact and its effect on knee joint kinematics during functional activity. *J. Biomechanics* 43 (7), 1292–1301. doi:10.1016/j.jbiomech.2010.01.002
- Andersen, M. S., Benoit, D. L., Damsgaard, M., Ramsey, D. K., and Rasmussen, J. (2010a). Do kinematic models reduce the effects of soft tissue artefacts in skin marker-based motion analysis? An *in vivo* study of knee kinematics. *J. Biomechanics* 43 (2), 268–273. doi:10.1016/j.jbiomech.2009.08.034
- Andersen, M. S., Benoit, D. L., Damsgaard, M., Ramsey, D. K., and Rasmussen, J. (2010b). Do kinematic models reduce the effects of soft tissue artefacts in skin marker-based motion analysis? An *in vivo* study of knee kinematics. *J. Biomechanics* 43 (2), 268–273. doi:10.1016/j.jbiomech.2009.08.034
- Barber, L., Barrett, R., and Lichtwark, G. (2009). Validation of a freehand 3D ultrasound system for morphological measures of the medial gastrocnemius muscle. *J. Biomechanics* 42 (9), 1313–1319. doi:10.1016/j.jbiomech.2009.03.005
- Charbonnier, C., Chagué, S., Kolo, F. C., Chow, J. C. K., and Lädermann, A. (2014). A patient-specific measurement technique to model shoulder joint kinematics. *Orthop. and Traumatology Surg. and Res.* 100 (7), 715–719. doi:10.1016/j.OTSRS.2014.06.015
- CSIRO, QUT (2024). *Sonography Device*. Australia Provisional Patent 2024902640, filed August 23, 2024. <https://ipsearch.ipaustralia.gov.au/patents/2024902640>. 18, 1353257. doi:10.3389/fnins.2024.1353257
- Dal Maso, F., Raison, M., Lundberg, A., Arndt, A., and Begon, M. (2014). Coupling between 3D displacements and rotations at the glenohumeral joint during dynamic tasks in healthy participants. *J. Biomech.* 29 (9), 1048–1055. doi:10.1016/j.clinbiomech.2014.08.006
- Fieten, L., Schmieder, K., Engelhardt, M., Pasalic, L., Radermacher, K., and Heger, S. (2009). Fast and accurate registration of cranial CT images with A-mode ultrasound. *Int. J. Comput. Assisted Radiology Surg.* 4 (3), 225–237. doi:10.1007/S11548-009-0288-Z
- Gray, H. A., Guan, S., Thomeer, L. T., Schache, A. G., de Steiger, R., and Pandey, M. G. (2019). Three-dimensional motion of the knee-joint complex during normal walking revealed by mobile biplane x-ray imaging. *J. Orthop. Res. Official Publ. Orthop. Res. Soc.* 37 (3), 615–630. doi:10.1002/JOR.24226
- Hajizadeh, M., Michaud, B., and Begon, M. (2019). The effect of intracortical bone pin on shoulder kinematics during dynamic activities. *Int. Biomech.* 6 (1), 47–53. doi:10.1080/23335432.2019.1633958
- Horn, B. K. P. (1987). Closed-form solution of absolute orientation using unit quaternions. *J. Opt. Soc. Am. A* 4 (4), 629. doi:10.1364/JOSAA.4.000629
- Jabas, A., Abello Mercado, M. A., Altmann, S., Ringel, F., Booz, C., Kronfeld, A., et al. (2023). Single-energy metal artifact reduction (SEMAR) in ultra-high-resolution CT angiography of patients with intracranial implants. *Diagnostics* 13 (4), 620. doi:10.3390/DIAGNOSTICS13040620
- Lange, T., and Eulenstein, S. (2001). “Calibration of swept-volume 3-D ultrasound,” in *Calibration and motion. Proceedings of Medical Image Understanding and Analysis*. Editors A. Houston and R. Zwigelaar (Cosham, United Kingdom: University of Portsmouth), 3, 29–32.
- Lavall, M., Martelli, S., Kerr, G. K., and Pivonka, P. (2022). Statistical quantification of the effects of marker misplacement and soft-tissue artifact on shoulder kinematics and kinetics. *Life* 12 (6), 819–911. doi:10.3390/life12060819
- Ludewig, P. M., Phadke, V., Braman, J. P., Hassett, D. R., Cierniak, C. J., and LaPrade, R. F. (2024). Motion of the shoulder complex during multiplanar humeral elevation. *J. Bone Joint Surg. Am.* 91 (2), 378–389. doi:10.2106/JBJS.G.01483
- Magnusson, M., Nüchter, A., Lörken, C., Lilienthal, A. J., and Hertzberg, J. (2009). Evaluation of 3D registration reliability and speed-A comparison of ICP and NDT. *Proc. - IEEE Int. Conf. Robotics Automation*, 3907–3912. doi:10.1109/ROBOT.2009.5152538
- Myronenko, A., and Song, X. (2010). Point set registration: coherent point drift. *IEEE Trans. Pattern Analysis Mach. Intell.* 32 (12), 2262–2275. doi:10.1109/TPAMI.2010.46
- Niu, K. (2018). *Ultrasound based skeletal motion capture - the development and validation of a non-invasive knee joint motion tracking method - transducer focus*.
- Niu, K., Anijs, T., Sluiter, V., Homminga, J., Sprengers, A., Marra, M. A., et al. (2018a). *In situ* comparison of A-mode ultrasound tracking system and skin-mounted markers for measuring kinematics of the lower extremity. *J. Biomechanics* 72, 134–143. doi:10.1016/j.jbiomech.2018.03.007
- Niu, K., Homminga, J., Sluiter, V., Sprengers, A., and Verdonchot, N. (2018c). Measuring relative positions and orientations of the tibia with respect to the femur using one-channel 3D-tracked A-mode ultrasound tracking system: a cadaveric study. *Med. Eng. and Phys.* 57, 61–68. doi:10.1016/j.medengphys.2018.04.015
- Niu, K., Homminga, J., Sluiter, V. I., Sprengers, A., and Verdonchot, N. (2018b). Feasibility of A-mode ultrasound based intraoperative registration in computer-aided orthopedic surgery: a simulation and experimental study. *PLOS ONE* 13 (6), e0199136. doi:10.1371/JOURNAL.PONE.0199136
- Niu, K., Sluiter, V., Homminga, J., Sprengers, A., and Verdonchot, N. (2018d). A novel ultrasound-based lower extremity motion tracking system. *Adv. Exp. Med. Biol.* 1093, 131–142. doi:10.1007/978-981-13-1396-7\_11
- Niu, K., Sluiter, V., Lan, B., Homminga, J., Sprengers, A., and Verdonchot, N. (2024). A method to track 3D knee kinematics by multi-channel 3D-tracked A-mode ultrasound. *Sensors* 24 (8), 2439. doi:10.3390/S24082439
- Osipov, A., Ostanin, M., and Klimchik, A. (2023). Comparison of point cloud registration algorithms for mixed-reality cross-device global localization. *Information* 14 (3), 149. doi:10.3390/INFO14030149
- Salisu, S., Ruhaiyem, N. I. R., Eisa, T. A. E., Nasser, M., Saeed, F., and Younis, H. A. (2023). Motion capture technologies for ergonomics: a systematic literature review. *Diagnostics* 13 (15), 2593. doi:10.3390/DIAGNOSTICS13152593
- Sewify, A., Antico, M., Steffens, M., Roots, J., Gupta, A., Cutbush, K., et al. (2024). 3D ultrasound mosaic of the whole shoulder: a feasibility study. *Appl. Sci. Switz.* 14 (5), 2152. doi:10.3390/AP14052152
- Vicini, A., and Sabick, M. (2021). Use of motion capture-coupled ultrasound sensors to determine scapular position. *Comput. Methods Biomechanics Biomed. Eng. Imaging and Vis.* 9 (6), 717–723. doi:10.1080/21681163.2021.1958258
- VICON (2024). Motion capture calibration with the Vicon active wand. Available at: <https://www.vicon.com/hardware/devices/calibration/> (Accessed January 30, 2025).
- Vogl, F., Schutz, P., Postolka, B., List, R., and Taylor, W. (2022). Personalised pose estimation from single-plane moving fluoroscope images using deep convolutional neural networks. *PLOS ONE* 17 (6), e0270596. doi:10.1371/JOURNAL.PONE.0270596
- Wu, G., Van Der Helm, F. C. T., Veeger, H. E. J., Makhsous, M., Van Roy, P., Anglin, C., et al. (2005). ISB recommendation on definitions of joint coordinate systems of various joints for the reporting of human joint motion--Part II: shoulder, elbow, wrist and hand. *J. Biomechanics* 38 (5), 981–992. doi:10.1016/j.jbiomech.2004.05.042
- Zhang, J., and Singh, S. (2014). LOAM: lidar Odometry and mapping in real-time. *Robotics Sci. Syst.* doi:10.15607/RSS.2014.X.007
- Zhu, J., Ye, Z., Ren, M., and Ma, G. (2024). Transformative skeletal motion analysis: optimization of exercise training and injury prevention through graph neural networks. *Front. Neurosci.* 18, 1353257. doi:10.3389/fnins.2024.1353257

## Generative AI statement

The author(s) declare that no Generative AI was used in the creation of this manuscript.

## Publisher's note

All claims expressed in this article are solely those of the authors and do not necessarily represent those of their affiliated organizations, or those of the publisher, the editors and the reviewers. Any product that may be evaluated in this article, or claim that may be made by its manufacturer, is not guaranteed or endorsed by the publisher.



## OPEN ACCESS

## EDITED BY

Zhiyong Li,  
Queensland University of Technology, Australia

## REVIEWED BY

Paolo Di Achille,  
Google, United States  
Ying He,  
Dalian University of Technology, China

## \*CORRESPONDENCE

Daniela Mazzaccaro,  
✉ daniela.mazzaccaro@grupposandonato.it

<sup>†</sup>These authors have contributed equally to this work and share last authorship

RECEIVED 09 August 2024

ACCEPTED 13 February 2025

PUBLISHED 07 March 2025

## CITATION

Curcio N, Conti M, Cardani R, Renna LV, Dell'Antonio G, Bari V, Nano G, Matrone G and Mazzaccaro D (2025) Biomechanical assessment of vulnerable plaque: from histological evidence to ultrasound elastography and image-based computational patient-specific modelling.  
*Front. Bioeng. Biotechnol.* 13:1478408.  
doi: 10.3389/fbioe.2025.1478408

## COPYRIGHT

© 2025 Curcio, Conti, Cardani, Renna, Dell'Antonio, Bari, Nano, Matrone and Mazzaccaro. This is an open-access article distributed under the terms of the [Creative Commons Attribution License \(CC BY\)](#). The use, distribution or reproduction in other forums is permitted, provided the original author(s) and the copyright owner(s) are credited and that the original publication in this journal is cited, in accordance with accepted academic practice. No use, distribution or reproduction is permitted which does not comply with these terms.

# Biomechanical assessment of vulnerable plaque: from histological evidence to ultrasound elastography and image-based computational patient-specific modelling

Nicoletta Curcio<sup>1</sup>, Michele Conti<sup>1,2</sup>, Rosanna Cardani<sup>3</sup>, Laura Valentina Renna<sup>3</sup>, Giacomo Dell'Antonio<sup>4</sup>, Vlasta Bari<sup>5,6</sup>, Giovanni Nano<sup>6,7</sup>, Giulia Matrone<sup>8†</sup> and Daniela Mazzaccaro<sup>7\*†</sup>

<sup>1</sup>3D and Computer Simulation Laboratory, IRCCS Policlinico San Donato, San Donato Milanese, Italy, <sup>2</sup>Department of Civil Engineering and Architecture, University of Pavia, Pavia, Italy, <sup>3</sup>Biobank BioCor, IRCCS Policlinico San Donato, San Donato Milanese, Italy, <sup>4</sup>Unit of Pathology, Cerba Healthcare Laboratories, Limena, Italy, <sup>5</sup>Department of Cardiothoracic, Vascular Anesthesia and Intensive Care, IRCCS Policlinico San Donato, San Donato Milanese, Milan, Italy, <sup>6</sup>Department of Biomedical Sciences for Health, University of Milan, Milan, Italy, <sup>7</sup>Operative Unit of Vascular Surgery, IRCCS Policlinico San Donato, San Donato Milanese, Italy, <sup>8</sup>Department of Electrical, Computer and Biomedical Engineering, University of Pavia, Pavia, Italy

The assessment of carotid plaque vulnerability is a relevant clinical information that can help prevent adverse cerebrovascular events. To this aim, in this work we study the ability of different non-invasive methods for assessing plaque vulnerability in patients undergoing carotid endarterectomy (CEA). Histological examinations of patients' plaque samples were conducted after CEA while ultrasound (US) and computed tomography angiography (CTA) acquisitions were performed preoperatively. US acquisition included point shear wave elastography (p-SWE) and a radio frequency echo-based wall tracking mode for the evaluation of arterial wall stiffness. CTA images were segmented, and the results were used for an *ad hoc* procedure that semi-automatically reconstructed the atherosclerotic wall providing a 3D model of the different plaque components to perform patient-specific finite element analysis (FEA) of stress distributions. One hundred patients were involved in the study and a macroscopic assessment of the surgeon was used to classify carotid atherosclerotic plaques as vulnerable or stable. The data derived from histological analysis, US acquisitions and FEA were correlated with the outcome of the classification. Indeed, histological features differentiated between vulnerable and stable plaques, confirming the surgeon's classification. From p-SWE, the measurement of Young's Modulus (YM) in stable plaques was significantly higher than in vulnerable plaques. Also stress indexes related to the Von Mises and Max Principal stresses from FEAs showed statistically significant differences between plaque groups. These results demonstrate that both stiffness-related US measurements and stress parameters derived preoperatively from computational analyses were able to differentiate patients with vulnerable plaques from ones with stable plaques.



Thus, the development and application of new methods for a non-invasive biomechanical assessment of atherosclerotic artery walls could give valuable information for plaque vulnerability evaluation.

#### KEYWORDS

carotid plaque vulnerability, biomechanical assessment, non-invasive imaging, elastography, patient-specific plaque modelling, finite element analysis

## 1 Introduction

Stroke is the main cause of long-term disability and the third leading cause of death (Kolos et al., 2015), and carotid artery (CA) stenosis due to atherosclerosis accounts for a major cause of all ischemic strokes (Banerjee and Chimowitz, 2017). Atherosclerosis is a pathological condition characterized by the accumulation of inflammatory cells, lipids, extracellular matrix, and other materials within the inner layers of artery walls, which leads to the development of an atherosclerotic plaque and the consequent narrowing of the arterial lumen. Plaques that cause a severe narrowing of the lumen increase the risk of having cerebrovascular events. In such cases, current guidelines recommend surgical intervention to prevent stroke (Spence, 2016). Carotid endarterectomy (CEA) has been reported as a safe and effective procedure to reduce stroke risk by removing the atherosclerotic plaque from the CA, especially for symptomatic patients.

Nevertheless, some studies highlighted that plaques can cause severe cardiovascular events regardless of the degree of stenosis (Kashiwazaki et al., 2019; Truijman et al., 2014). Clinical practice, in fact, suggests that the type of plaque is a crucial determinant of stroke risk for the same degree of stenosis, as certain plaques are more susceptible to inflammation and rupture and, therefore, more likely to cause cerebrovascular events (Mughal et al., 2011). Such plaques are defined “vulnerable.” From the histopathological point of view, they are characterized by active inflammation, a large lipid core, thin fibrous cap and may have features of intraplaque haemorrhage, neovascularization, necrosis, small calcification and surface ulceration. Currently, the identification of plaque vulnerability features can only be performed through histological examination after the plaque has been surgically removed (Gerosa et al., 2023).

Since modern literature questions the benefit of CEA in asymptomatic patients with optimal medical treatment (Spence, 2016), it appears crucial to identify a method suitable for the preoperative phase to offer plaque information as accurately as the histological analysis performed after CEA. Indeed, preoperative identification of vulnerable plaques would enable the identification of a high-risk subgroup of patients who could mostly benefit from a surgical procedure, thereby allowing for *in vivo* risk stratification.

The underlying mechanism for plaque rupture has not been fully understood yet. Biomechanical factors, such as structural and hemodynamic stresses on the atherosclerotic vessel wall, are among risk factors that promote the progression and compositional changes of atherosclerotic plaques (Brown et al., 2016). Furthermore, it has been hypothesized that sudden rupture is triggered by local stress concentrations, when

structural stress exceeds the plaque strength (Teng et al., 2015). Consequently, biomechanical features can be considered crucial in plaque vulnerability assessment.

Several different medical imaging modalities, such as computed tomography angiography (CTA), magnetic resonance angiography (MRA), ultrasonography and positron emission tomography (PET), were employed to assess morphological characteristics of CA wall and plaque in a three-dimensional (3D) way. However, these methods neither detect and distinguish all the different plaque components nor provide information related to biomechanical assessment of tissues.

Recently, ultrasound (US) elastography has been increasingly used as a non-invasive imaging technique, that could help to obtain additional information on carotid artery stiffness and thus on its composition, possibly improving the assessment of plaque rupture (Bulum et al., 2022). Different US elastography techniques exist, based on the type of physical quantity measured or on the type of force applied to deform the underlying tissues. Quasi-static methods (also called strain elastography) use a manual compression on the skin and quantify the percentage of tissue strain, which produces a deformation map. Dynamic methods instead use an acoustic radiation force impulse (ARFI) or a mechanical vibrator to generate shear waves which propagate through the tissues; thus, they are also known as shear wave elastography (SWE). Since the velocity of the shear waves is measurable and proportional to tissue elasticity, quantitative values of tissue stiffness can be determined in terms of Young’s modulus (YM). A specific modality of SWE is the point-SWE, which provides an averaged YM measure within a predefined region of interest (ROI). Since the stiffer the tissue, the higher the YM, vulnerable plaques exhibit lower YM, reflecting changes in deformation and stress/strain characteristics.

Another promising method for noninvasively studying plaque biomechanical characteristics is the use of computational simulation models and finite element analysis (FEA). Computational simulations allow for the computation of 3D stress/strain distributions in patient-specific diseased arteries of various types and morphologies, which could be used to estimate the risk of plaque rupture.

The assessment of plaque vulnerability has been considered in several previous works that studied different vessel types, stress values, and material models by performing computational analyses integrating different imaging techniques (Holzapfel, 2014). The principal findings from FEA studies regard: (i) the association between stress and plaque rupture (Leach et al., 2010; Teng et al., 2015; Costopoulos et al., 2017; Warren et al., 2022) or cerebrovascular events (Sadat et al., 2010); (ii) the factors that impact on the stress distribution (Gao and Long, 2008; Gao



et al., 2009; Akyildiz et al., 2011); (iii) the influence of mechanical forces on the progression of the lesions (Tang et al., 2013; Timmins et al., 2016; Kang et al., 2016; Liu et al., 2017).

In this paper, we aimed to evaluate the role of ultrasound point SWE (pSWE) and of computational FEA in assessing the biomechanical features of vulnerable and stable plaques in a group of asymptomatic patients submitted to CEA for a significant carotid stenosis, correlating the results obtained from these methods to those of the macroscopic and microscopic analysis of the excised plaques.

The paper is organized as follows: in Section 2 we illustrate the procedures for clinical data acquisitions, histological analyses and 3D FEAs of patient-specific models derived from CTA images; in Section 3 we report the outcomes of analyses on the collected data; in Section 4 the results are discussed and compared to previous works, the potentialities and limitations of our study are illustrated, as well as possible future developments; Section 5 finally provides the conclusions.

## 2 Materials and methods

### 2.1 Patients' recruitment and data acquisition

This prospective monocentric study was approved by the Ethics Committee of San Raffaele Hospital on 20 June 2019 (110/int/2019) and registered on [ClinicalTrials.gov](https://clinicaltrials.gov) (ClinicalTrials.gov Identifier: NCT05566080). All patients enrolled in the study at IRCCS Policlinico San Donato gave written informed consent. The study involved the enrolment of 100 patients who underwent CEA at the Vascular Surgery Unit of IRCCS Policlinico San Donato due to the presence of atherosclerotic plaques, causing asymptomatic critical stenosis, according to the current guidelines. For each enrolled patient, demographic data such as sex, age, body mass index (BMI), and cardiovascular risk factors including the presence of dyslipidaemia, coronary artery disease (CAD), chronic obstructive pulmonary disease (COPD) history, diabetes and history of previous cerebrovascular events were collected.

All patients underwent a preoperative evaluation of carotid stenosis using US imaging and CTA.

The vascular surgeon (DM) also provided a visual macroscopic assessment of the removed plaques of the enrolled patients, in order to classify them as vulnerable or stable plaques. Plaques with prevalence of calcifications were classified as stable plaques; meanwhile, plaques with soft components were classified as vulnerable.

### 2.2 Histology analysis

All carotid plaques were removed in one piece. Immediately after removal, collected plaques were transferred to the Biobank BioCor where a tissue sample approximately 5 mm thick, obtained by a cross-sectioning of a representative part of the plaque was fixed with 10% buffered formaldehyde. Samples were then processed using a routine paraffin technique, some of them were decalcified by a hydrochloric acid solution. Five-micron-thick parallel sections

were cut, deparaffinised in xylene and hydrated in graded alcohol. Sections were stained with haematoxylin and eosin or by an indirect immunohistologic method to detect macrophages (CONFIRM anti-CD68 (KP-1) mouse primary antibody and CD163 (MRQ-26) mouse monoclonal primary antibody; Roche Diagnostic).

An experienced pathologist (GDA) evaluated the histological slides using a bright-field optical microscope Olympus BX43.

Since atherosclerosis was defined as the presence of intimal plaques composed by deposits of lipids and proliferating spindle cells, fragmentation of elastic lamina, degeneration of smooth muscle, medial calcification, adventitial fibrosis, and chronic inflammatory infiltration, these different features were considered and classified by the pathologist using a semi-quantitative grade scale, as recommended by (Lovett et al., 2004). More specifically, in our study the following features were considered: the presence of a necrotic/haemorrhagic core, the fibrous cap thickness, the presence of inflammatory infiltrate, the composition of the atheroma and positivity for CD68 and CD163. The corresponding scores were calculated by the pathologist as follows:

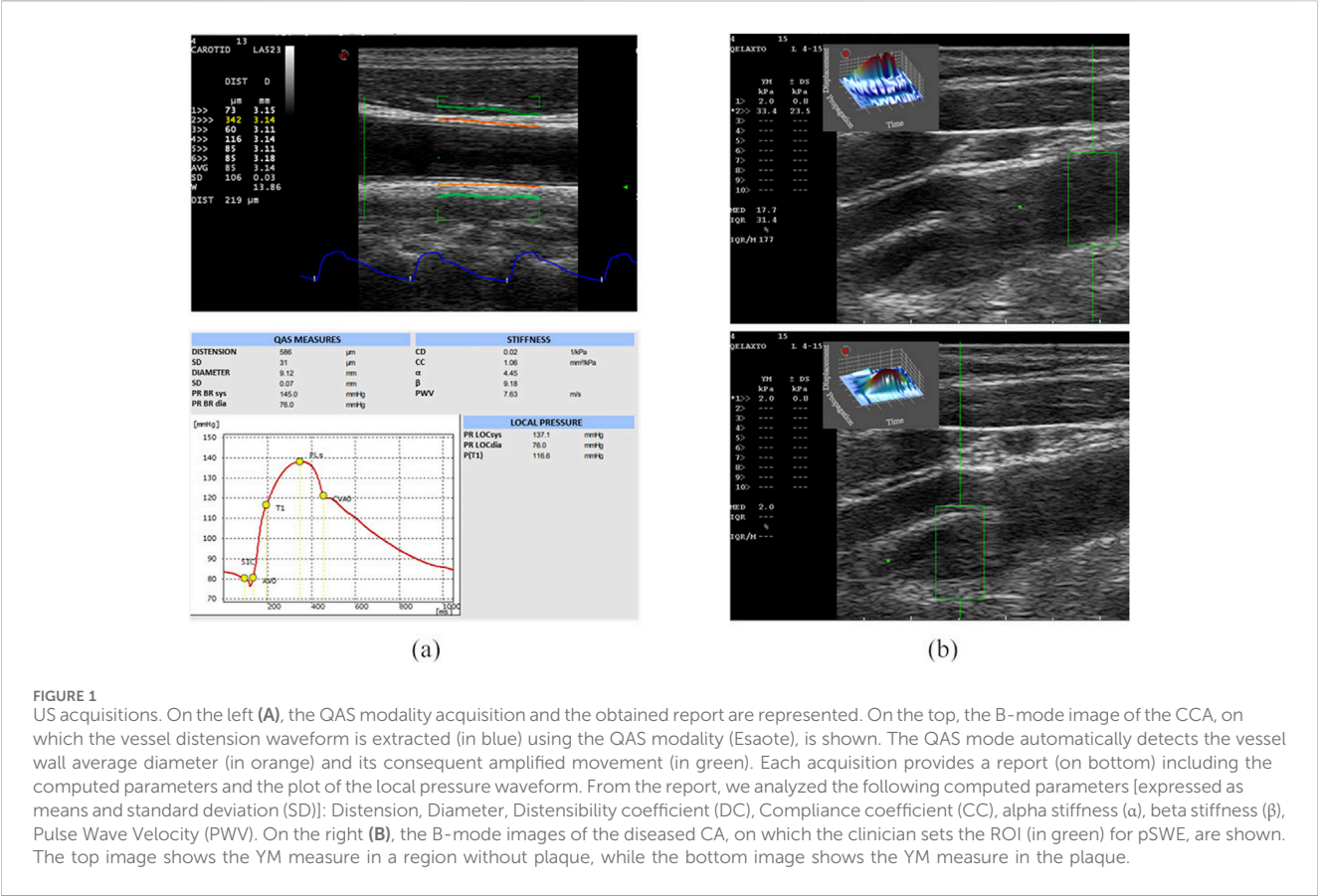
- presence of atheroma/necrosis: score = 0 if less than 10%, score = 1 if between 10% and 50%, score = 2 if greater than 50%;
- fibrous cap thickness: score = 3 if < 200  $\mu$ m, score = 2 if in the range 200–400  $\mu$ m, score = 1 if in the range 400–800  $\mu$ m, score = 0 if > 800  $\mu$ m;
- presence or absence of inflammation: score = 1 for inflamed plaque, score = 0 for non-inflamed plaque;
- presence (score = 1) or absence (score = 0) of cholesterol;
- immunohistochemical response to CD163 and CD68: score = 0 if there is no response, score = 1 if the positive response was up to 5% of the plaque area, score = 2 if between 5% and 10%, and score = 3 if greater than 10%.

In all cases, a lower score indicated a more stable plaque, whereas a higher score indicated a more vulnerable plaque. About 10% of cases were blind revised or underwent further sections.

### 2.3 Ultrasound image acquisition

The patients were scanned before undergoing CEA for asymptomatic stenosis. In particular, the US acquisitions were conducted by experienced vascular surgeons using a MyLab Eight scanner and a 7.5 MHz linear probe, model L4-15 (both from Esaote S.p.A., Genova, Italy). The acquisitions were performed with the patients in a supine position and with a slight neck extension, on the side of the carotid stenosis. The device was equipped with two different software packages, i.e., Quality Arterial Stiffness (QAS) and q-Elaxto modalities.

QAS derives carotid pressure waveforms by implementing a radiofrequency (RF) echo-based tracking of arterial wall distension (Meinders and Hoeks, 2004; Vermeersch et al., 2008; Esaote, 2018). In this case, the linear probe was placed along a longitudinal axis at 1 cm down from the common carotid artery (CCA) bifurcation, strictly perpendicular to the ultrasound beam, with both walls clearly visualized. An automatic real-time measurement of the change in diameter of the vessel walls



between the systolic and diastolic phases was performed, plotting the instantaneous distension waveform (see Figure 1A). The local CA pressure waveform was calculated from the patient's diastolic and systolic brachial pressure values and arterial cross-section values derived from the distension waveform. Therefore, the software automatically calculated the following measurements, starting from distension and pressure waveforms, which were then provided in a report (Figure 1A):

- Distension (the average of six successive measurements);
- Diameter (the average of six successive measurements);
- Distensibility coefficient (DC), i.e., the absolute change in vessel diameter during systole for a given pressure change;
- Compliance coefficient (CC), i.e., the relative change in vessel diameter during systole for a given pressure change;
- Alpha stiffness ( $\alpha$ ), which is the elastic coefficient of the vessel;
- Beta stiffness ( $\beta$ ), which is the elastic coefficient normalized on the diameter;
- Pulse-wave Velocity (PWV).

The same probe was also used in the q-Elaxto modality, which performs a pSWE acquisition, creating a localized perturbation in the ROI around the focused US beam. This "pushing" phase is followed by a tracking phase, which provides a quantitative estimate of stiffness inside the ROI, i.e., the tissue's average YM, in kPa, in the selected region. The linear probe was placed longitudinally on the side of the carotid and the acquisitions were performed on the distal and proximal part of the plaque region, obtaining a measure of the

YM of the plaque and two measure of the YM of the CCA and internal carotid artery (ICA) walls, as shown in Figure 1B.

## 2.4 Computational analysis

The following sections explain the workflow used to quantify the stress distribution of an atherosclerotic CA by means of 3D patient-specific vessel modelling and structural simulations derived from CTA scans. The developed 3D geometric modelling methodology and the simulation settings are described in detail in Curcio et al. (2023).

### 2.4.1 3D patient-specific modelling of the vessel and plaque

The segmentation of the DICOM sequences of CTA scans was performed by using a semi-automatic method implemented in ITK-Snap ([www.itksnap.org](http://www.itksnap.org)), or by manual reconstruction when plaque components were not easily detectable in the images.

CTA segmentation allows to obtain the CA lumen and calcific or lipidic plaque component geometries. The CA wall and the plaque fibrous component, instead, are usually not clearly distinguishable in CTA images, and, for this reason, they were automatically reconstructed after image segmentation. The detailed description of the developed reconstruction procedure can be found in our previous study (Curcio et al., 2023) and is illustrated in the Supplementary Material too. This method allows reconstructing the patients' atherosclerotic carotid walls, starting from lumen and

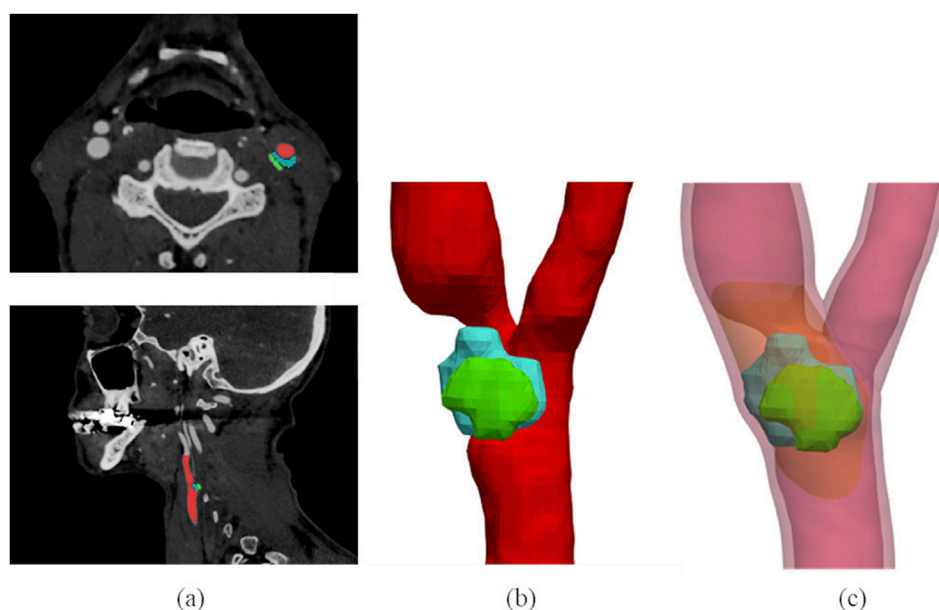


FIGURE 2

3D plaque model reconstruction from CTA images. CTA axial and sagittal views (A), and corresponding segmentation results (B): the lumen is labelled in red, the lipid content of the plaque is represented in blue and the calcific content in green. Final atherosclerotic wall geometry (C) obtained from the corresponding segmentation, by enlarging the lumen sections to include calcific and lipid components of the plaque in the CA walls, and by filling the stenotic region (where other components of plaque are not present) with the fibrous content. The healthy wall is labelled in light red, the fibrous content of the plaque is represented in orange. The figure is adapted from (Curcio et al. 2023).

TABLE 1 Material properties set in FEAs.

Material	Young's modulus (kPa)
Plaque calcific component	20,000
Plaque lipid component	4
Plaque fibrous component	400
CA healthy wall	550

plaque segmentations, with an *ad hoc* developed semi-automatic procedure, while it automatically generates the model of the plaque fibrous component. In this way, it is possible to model more accurately an atherosclerotic vessel by considering different plaque compositions, as illustrated in Figure 2.

Thanks to 3D modelling of the plaque different contents, the volume of each component was computed to perform the morphological analysis. Both absolute and relative volumes were evaluated.

## 2.4.2 Simulation settings

Finite element simulations based on models generated from CTA images and geometrical reconstructions were performed using Abaqus CAE (Simulia, Providence, RI, United States). Models were simulated as static analyses. The optimum mesh density was obtained by means of a previous convergence analysis. The plaque and arterial wall were assumed to be nearly incompressible, isotropic, linear elastic, with a 0.49 Poisson's ratio; instead, a different Young's Modulus was considered for each of them. The used material properties are reported in

Table 1 and were obtained as an average of values available in the literature (Lee et al., 1991; Holzapfel et al., 2004; Barrett et al., 2009; Gao et al., 2009; Leach et al., 2010; Mahmoud, Hassan, and Mahmoud, 2019; Djukic et al., 2020; Benitez et al., 2021; Bennati et al., 2021).

Blood pressure was considered as uniformly applied to the lumen surface, setting the patient-specific differential carotid pressure obtained from QAS US modality as the blood vessel load. Boundary conditions were applied to fully constrain the distal ends of the bifurcation and the proximal end of the CCA.

## 2.4.3 Post-processing of simulation results

For each analysed patient, different values of simulated stresses were calculated from the structural simulations of the vessel. Specifically, von Mises stress (VM) and Max Principal stress (MPS) were evaluated, as done in similar computational studies (Gao et al., 2009; Leach et al., 2010; Mahmoud, Hassan, and Mahmoud, 2019; Djukic et al., 2020; Benitez et al., 2021; Bennati et al., 2021), in each component of the plaque. In both cases, the stress value corresponding to 99% of the cumulative volume of the respective plaque component (denoted as  $VM_{99}$  and  $MPS_{99}$ , respectively) and the average stress value within each component (denoted as  $VM_{mean}$  and  $MPS_{mean}$ , respectively) were calculated.

Additionally, these stress values associated with each single component were used to calculate an overall plaque stress index. This index was obtained by linearly combining the corresponding stress values of the three different components, considering the relative volume of each component as a weight. For example, the  $VM_{99}$  index is the weighted average of the  $VM_{99}$  values in each plaque component, based on their relative volumes.

TABLE 2 Preoperative characteristics of the analysed cohort of patients.

Demographic data	Vulnerable plaque (N = 43p)	Stable plaque (N = 57p)	p-value
Female sex	10p (23%)	23p (40%)	0.072
Age [years]	74.00 (10.00)	75.00 (11.00)	0.286
BMI	25.88 (6.04)	25.45 (5.11)	0.786
Dyslipidemia	36p (84%)	49p (85%)	0.972
CAD	10p (23%)	12p (21%)	0.792
COPD	1p (2%)	3p (5%)	0.458
Diabetes	14p (33%)	18p (32%)	0.935
Cerebrovascular event	6p (14%)	7p (12%)	0.805

p = patients; N stands for the considered sample size. Categorical data are presented as numbers with the corresponding percentages. Continuous data are presented as median (IQR).

## 2.5 Statical analysis

Data were analysed using the statistical software SPSS (IBM Corp., Armonk, NY, United States). The Shapiro-Wilk test tested the normality of the distribution of values, and the variables sample was defined as non-normally distributed. The Mann-Whitney U test was used to evaluate the differences in results between the group of patients with a vulnerable plaque and the ones with a stable plaque, as defined by the surgeon. P-values < 0.05 were considered statistically significant.

## 3 Results

In this section, results from statistical analyses on the previously presented parameters are presented. In all tables presented in this section, continuous data values are properly summarized as median with interquartile range (IQR); categorical data are instead presented as numbers with the corresponding percentages.

Demographic data were collected from all 100 patients enrolled in the clinical study, as well as US imaging data. On the other hand, 11 patients had to be excluded from histological analysis because of not complete lumen or wall presence or cutting problems due mainly to artifacts or calcifications. Besides, the CTA segmentation of lumen and plaque components was not performed on four patients' acquisitions. This was due to the exclusion of one patient for whom CTA images were unavailable and three patients due to image artifacts. Seven patients were also excluded because the proposed semi-automatic reconstruction method was not applicable due to the tortuous geometry of their vessels. Finally, FEAs were performed on data from 89 patients.

### 3.1 Clinical data analysis

We first analysed demographic data in patients with vulnerable plaque compared to patients with stable plaque (Table 1). The macroscopic assessment provided by the surgeon revealed the presence of vulnerable plaques in 43 patients; 10 of them are females, and the median age is 74 years. The clinical

characteristics of both groups of patients, as reported in Table 2, showed a similar representation of cardiovascular risk factors between the two groups, with no statistically significant differences, except for a prevalence of higher female patients in the group with stable plaques.

### 3.2 Histological data analysis

The univariate analysis of histological features identified some statistically significant predictors for vulnerable plaques, as reported in Table 3. Vulnerable plaques had a greater necrotic core compared to stable plaques (p-value = 0.018).

Atherosclerotic plaques classified as vulnerable were also associated with higher presence of cholesterol in the atheroma (p-value = 0.011). Then, the statistical analysis showed that CD163 and CD68 markers were more expressed in vulnerable than in stable plaques (p-value < 0.001). Specifically, vulnerable plaques tended to have higher scores for these markers compared to stable ones.

### 3.3 US data analysis

All US measurements, derived from both QAS and pSWE (q-Elaxto) modalities, are reported in Table 4. Although no one of the QAS parameters reaches statistical significance in group comparison, the distension values tend to be lower in stable plaques (302.00 (173.00)  $\mu\text{m}$  vs. 281.00 (210.50)  $\mu\text{m}$ , p-value = 0.382). Both the  $\alpha$  the  $\beta$  index, defined as stiffness indexes, tend to be higher in stable plaques. Also DC and CC tend to be slightly higher in patients with vulnerable plaques than in those with stable plaque, even if differences are not statistically significant. Finally, the PWV values are instead very similar in the two groups.

Concerning q-Elaxto measurements, the YM values show a significant difference between the vulnerable and stable plaque groups when measurements are acquired in the plaque region (12.40 (34.50) kPa vs. 34.70 (82.15) kPa, p-value = 0.008). Instead, the other two measurements performed in regions without plaques (i.e.,  $YM_{ICA}$  and  $YM_{CCA}$ ) do not show significant differences between the two groups.

TABLE 3 Comparison of the data derived from the histological analysis between the group of patients with vulnerable plaque and those with stable plaque.

Histological features	Score	Vulnerable plaque (N = 38p)	Stable plaque (N = 51p)	p-value
Atheroma/necrosis	0	1p (3%)	8p (16%)	<b>0.018</b>
	1	19p (50%)	29p (56%)	
	2	18p (47%)	14p (28%)	
Fibrous cap thickness	0	6p (16%)	6p (12%)	0.179
	1	11p (29%)	14p (28%)	
	2	10p (26%)	5p (10%)	
	3	11p (29%)	25p (50%)	
Inflammation	0	20p (53%)	35p (69%)	0.124
	1	18p (47%)	16p (31%)	
Cholesterol	0	8p (21%)	24p (47%)	<b>0.011</b>
	1	30p (79%)	27p (53%)	
CD68	0	0p (0%)	16p (31%)	< <b>0.001</b>
	1	12p (31%)	15p (30%)	
	2	17p (45%)	16p (31%)	
	3	9p (24%)	4p (8%)	
CD163	0	0p (0%)	15p (29%)	< <b>0.001</b>
	1	17p (45%)	24p (47%)	
	2	13p (35%)	7p (14%)	
	3	7p (19%)	5p (10%)	

p = patients. N stands for the considered sample size. Data are presented as numbers with the corresponding percentages. Significant p-values are highlighted in bold.

TABLE 4 Comparison of the data derived from the preoperative US imaging (QAS wall-tracking modality and pSWE) between the group of patients with a vulnerable plaque and those with a stable plaque.

QAS and pSWE parameters	Vulnerable plaque (N = 43)	Stable plaque (N = 57)	p-value
Distension [μm]	302.00 (173.00)	281.00 (210.50)	0.382
Diameter [mm]	9.17 (1.63)	8.46 (1.89)	0.064
DC [kPa <sup>-1</sup> ]	0.01 (0.00)	0.01 (0.01)	0.930
CC [mm <sup>2</sup> /kPa]	0.55 (0.38)	0.48 (0.54)	0.304
α	8.67 (4.12)	8.50 (10.30)	0.694
β	17.61 (8.17)	17.32 (20.68)	0.699
PWV [m/s]	10.54 (3.54)	10.64 (6.07)	0.704
YM <sub>plaque</sub> [kPa]	12.40 (34.50)	34.70 (82.15)	<b>0.008</b>
YM <sub>I<sub>CA</sub></sub> [kPa]	6.5 (29.90)	6.00 (39.90)	0.709
YM <sub>CCA</sub> [kPa]	11.90 (38.40)	5.80 (42.25)	0.335

N stands for the considered sample size. Significant p-values are highlighted in bold.

### 3.4 Morphological analysis

Results obtained considering the volumes of the different plaque components are listed in Table 5. The patients with stable plaques show the lower presence of calcium components as compared to the vulnerable plaque group (10.47 (12.61) % vs. 25.94 (46.56) %,

p-value = 0.003 for relative volumes; 42.41 (65.66) mm<sup>3</sup> vs. 101.62 (200.41) mm<sup>3</sup>, p-value = 0.013 for absolute volumes) and a higher presence of lipidic components (6.06 (14.96) % vs. 0.96 (6.81) %, p-value = 0.005 for relative volumes; 20.50 (69.78) mm<sup>3</sup> vs. 2.09 (21.15) mm<sup>3</sup>, p-value = 0.005 for absolute volumes). Also the volume of the fibrous content shows significant differences between



TABLE 5 Comparison of volumes (both percentage and absolute values) between the group of patients with vulnerable plaque and those with stable plaque.

Volume	Vulnerable plaque (N = 40)	Stable plaque (N = 49)	p-value
Calcific content [%]	10.47 (12.61)	25.94 (46.56)	<b>0.003</b>
Lipid content [%]	6.06 (14.96)	0.96 (6.81)	<b>0.005</b>
Fibrous content [%]	73.78 (26.42)	63.35 (39.472)	<b>0.015</b>
Calcific content [mm <sup>3</sup> ]	42.41 (65.66)	101.62 (200.41)	<b>0.013</b>
Lipid content [mm <sup>3</sup> ]	20.50 (69.78)	2.09 (21.15)	<b>0.005</b>
Fibrous content [mm <sup>3</sup> ]	264.09 (489.66)	197.47 (251.83)	0.147
Total plaque [mm <sup>3</sup> ]	397.44 (566.09)	376.10 (370.49)	0.692

N stands for the considered sample size. Data are presented as median (IQR). Significant p-values are highlighted in bold.

TABLE 6 Comparison of stress parameters in each plaque component and global stress indexes between the group of patients with vulnerable plaque and those with stable plaque.

Plaque component	Stress parameter [kPa]	Vulnerable plaque (N = 40)	Stable plaque (N = 49)	p-value
Calcific component	VM <sub>99</sub>	100.51 (77.79)	97.92 (130.63)	0.314
	MPS <sub>99</sub>	177.47 (179.02)	191.36 (235.26)	0.228
	VM <sub>mean</sub>	25.06 (20.24)	28.03 (36.99)	0.306
	MPS <sub>mean</sub>	18.94 (16.48)	18.76 (27.11)	0.314
Lipid component	VM <sub>99</sub>	0.32 (0.47)	0.16 (0.33)	<b>0.021</b>
	MPS <sub>99</sub>	0.94 (1.25)	0.62 (1.57)	0.224
	VM <sub>mean</sub>	1.13 (0.16)	0.06 (0.17)	0.062
	MPS <sub>mean</sub>	-0.01 (0.67)	0.00 (0.124)	0.100
Fibrous component	VM <sub>99</sub>	36.21 (19.52)	36.21 (17.07)	0.882
	MPS <sub>99</sub>	73.57 (45.29)	91.33 (49.52)	0.242
	VM <sub>mean</sub>	12.46 (6.38)	11.96 (8.94)	0.547
	MPS <sub>mean</sub>	12.03 (6.21)	11.65 (7.86)	0.711
Stress index [kPa]		Vulnerable plaque (N = 40)	Stable plaque (N = 49)	p-value
VM <sub>99</sub>		42.55 (25.30)	54.89 (45.89)	0.034
MPS <sub>99</sub>		90.92 (43.90)	113.06 (88.25)	0.011
VM <sub>mean</sub>		13.03 (8.87)	16.48 (14.53)	0.063
MPS <sub>mean</sub>		11.64 (8.31)	13.45 (11.23)	0.094

N stands for the considered sample size. Data are presented as median (IQR). Significant p-values are highlighted in bold.

the two groups. The total volume of the plaque is the only volume variable that does not show a significant p-value.

### 3.5 Biomechanical analysis

As illustrated in Section 2.4.3, VM<sub>99</sub>, VM<sub>mean</sub>, MPS<sub>99</sub>, and MPS<sub>mean</sub> stress parameters were computed in each plaque component. Thus, Table 6 reports the statistical analysis results showing possible differences for these parameters (evaluated in each component) between the two groups of patients. Particularly, only the VM<sub>99</sub> stress calculated in the lipid component is statistically significant (0.32 (0.47) kPa vs.

0.16 (0.33) kPa, p-value = 0.021) among the simulated stress variables in each component of the plaque.

Each stress parameter computed in the single plaque components was characterized by different values. Indeed, the stress associated to calcific components had significantly higher values, while intermediate and lower values were shown by the fibrous and lipid components, respectively.

Moreover, we calculated some global stress indexes relative to the whole plaque, as reported in Section 2.3.3. Only 99-percentile stress indexes showed a statistically significant difference between groups (42.55 (25.30) kPa vs 54.89 (45.89) kPa, p-value = 0.034 for VM<sub>99</sub>; 90.92 (43.90) kPa vs 113.06 (88.25) kPa, p-value = 0.011 for MPS<sub>99</sub>), while mean index values did not.

## 4 Discussion

Our study recruited 100 patients, with carotid plaque stenosis greater than 70%, who were scheduled to undergo CEA. Ultrasound imaging and CTA scans were performed preoperatively; demographic and clinical data were also collected to evaluate the presence of risk factors for plaque vulnerability.

After surgery, the vascular surgeon visually assessed the removed plaques and classified them as either vulnerable or stable.

While no demographic differences were observed between patient groups, it is important to note that there is a prevalence of stable plaques in the female group. Other studies have also indicated gender differences in atherosclerotic populations. Specifically, there are differences for the presence of calcifications, lipid content, and hemorrhages, with a higher prevalence of these components in men compared to women (van Dam-Nolen et al., 2023). Furthermore, the incidence of ischemic stroke varies between men and women, with substantially higher rates in men (van Dam-Nolen et al., 2022).

In addition, histological analysis was performed on post-surgical plaque samples confirming the surgeon's classification of vulnerable/stable plaques.

Nevertheless, the principal limitation of histological analysis is its invasive nature, as it requires tissue samples that are obtained post-surgery, thereby limiting its applicability in predicting plaque vulnerability during routine clinical practice but could open or be confirmatory to new CTA or US predictive valuations.

Thus, the aim of this study was also to evaluate non-invasive imaging methods (i.e., CTA, US), combined with structural simulations based on FEA, to consider morphological, compositional and also biomechanical aspects of the plaque rupture, in order to have more information for preoperatively identifying patients with plaques that are likely to be vulnerable.

It is worth pointing out that our study uses patient-specific clinical data from different imaging techniques: CTA images were employed for the 3D vessel model creation used for FEA, while US wall tracking modality and elastography were used to analyse other biomechanical factors that could be useful for the assessment of plaque vulnerability.

Specifically, in the comparison of preoperative QAS evaluation data between the two groups, patients with stable, calcified plaques exhibited distension and stiffness-related index values suggesting a tendency towards greater stiffness as compared with those with vulnerable, soft plaques. However, p-values showed no statistically significant differences between QAS data in the two groups. There were instead significant differences in patients' classification in terms of YM of the CA plaque region. According to other studies (Garrard et al., 2015; Mazzaccaro et al., 2023), a higher YM would indicate the presence of a non-vulnerable plaque.

For what concerns the plaque morphological and stress analyses, we expanded our previous work (Curcio et al., 2023) by involving a greater number of patients. For each patient, the reconstructed atherosclerotic CA model include the three main components of an atheromatous plaque: the calcific and lipid plaque components were segmented from *in vivo* CTA images, whereas the fibrous component and the surrounding healthy wall were reconstructed by means of an *ad hoc* developed procedure (see [Supplementary Material](#)).

From our results, the volumes of all three components of the plaque result to be statistically significantly different in the comparison between patients with stable and vulnerable plaques.

In agreement with other studies (Ylä-Herttuala et al., 2013; Shi et al., 2020; Sakamoto et al., 2021), a mostly calcified plaque content is usually associated with plaque stability, while mostly lipidic plaques are usually vulnerable. We also analysed the plaque total volume, but it did not show significant differences between the two groups. According to this finding, compared with plaques that cause severe luminal stenosis, vulnerable plaques may cause relatively minor stenosis, although they account for more cases of rupture and thrombosis (Shah, 2003).

After biomechanical simulations were performed for all patients, we analysed the obtained stress distributions within subsets representing each plaque component, for a quantitative evaluation. VM stress and MPS were considered in these analyses, since they are used in several other works in the literature (Gao and Long, 2008; Gao et al., 2009; Leach et al., 2010; Holzapfel, 2014; Mahmoud et al., 2019; Benitez et al., 2021; Bennati et al., 2021). For each plaque component, the maximum stresses were computed by excluding 1% of all elements containing the highest stresses, as done in (Speelman et al., 2008); in addition, also mean stresses were included in our analysis. Furthermore, we investigated the potential of using alternative stress indexes that combine the computed stress parameters and plaque component volumes to distinguish patients with different types of plaque. In our findings, particularly 99-percentile stress indexes can differentiate groups of vulnerable and stable plaques. More specifically, the obtained results show that the VM<sub>99</sub> and MPS<sub>99</sub> stresses are higher in stable plaques, according to the material properties assigned to the different structures in the simulations.

Integrating computed stress indices (e.g., VM<sub>99</sub>, MPS<sub>99</sub>) with imaging-derived parameters (e.g., component volumes and stiffness metrics) could indeed enhance the predictive capability of plaque assessment. The YM values, particularly in the plaque region, were significantly lower in vulnerable plaques compared to stable ones. This finding aligns with the lower stiffness of vulnerable plaques due to their compositional differences, including a reduced calcific and fibrous content and increased lipidic components. Similarly, CTA-derived volumetric analyses showed that stable plaques exhibited a greater calcific content, correlating with the increased stiffness, whereas vulnerable plaques demonstrated a higher proportion of lipidic components. Furthermore, biomechanical simulations provided additional evidence by revealing differences in stress distributions across plaque components. Stress indices, such as VM<sub>99</sub> and MPS<sub>99</sub>, were higher in stable plaques, that had a higher calcific component and stiffness. Thus, these insights on the relationship between biomechanical and imaging-derived data reveal the potential for new non-invasive indices to aid in plaque classification.

The methods employed in this study also show some limitations. First, US acquisitions could present shadowing and reverberation artefacts. Moreover, blood and subcutaneous fat can attenuate wave propagation, which may render the measurements invalid. Additionally, other problems could include the variability introduced by the subjective selection of the ROI for point shear wave elastography and the assumptions about the material under examination to simplify the analysis and the calculated averaged value (Sigrist et al., 2017).

The proposed computational analysis had some limitations too. These included a non-automatic methodology for reconstructing

and simulating patient-specific vessel geometries, simplifying assumptions about material properties and residual stresses, as well as the absence of a fluid domain and time-dependent pressure load. Although it is well established that arterial soft tissues are non-linear anisotropic hyperelastic materials, we chose to set the material properties as linear elastic and isotropic in line with other studies in the literature (Gao et al., 2009; Kelly-Arnold et al., 2013; Mahmoud, Hassan, and Mahmoud, 2019; Benitez et al., 2021; Bennati et al., 2021). Additionally, we did not have access to the specific moment in the cardiac cycle of the lumen configuration in CTA scans. This led us to reconstruct CA geometries undefining particular loading conditions such as blood pressure, residual stresses, and axial pre-stretch. However, there are several works that do not account for residual arterial stresses too (Gao et al., 2009; Creane et al., 2010; Leach et al., 2010; Kelly-Arnold et al., 2013; Mahmoud, Hassan, and Mahmoud, 2019; Benitez et al., 2021; Bennati et al., 2021). Although these simplifications could affect the accuracy of our stress simulation results, we aimed to compare computational results from different types of plaques across different patients under the same conditions. Such limitations will be the object of future developments of this work.

Future advancements of our study could also include the development of composite indices that integrate biomechanical and imaging-derived variables for the non-invasive classification of plaques. For example, combining stress parameters obtained from finite element analysis (FEA) with component volumes derived from computed tomography angiography (CTA) and stiffness metrics from ultrasound could provide a more thorough assessment of plaque vulnerability.

In conclusion, the biomechanical variables obtained from US imaging evaluation and FEA, which show significant differences between the two groups with different types of plaque, have the potential to represent indicators of plaque vulnerability. This information can aid in developing a non-invasive risk assessment method for predicting plaque rupture before any potential cerebrovascular event occurs.

## 5 Conclusion

In this work we evaluate the potential of different measures relative to the morphology and composition of CA plaques that are considered promising for preoperatively predicting their vulnerability. Identifying patients with plaques that are likely to be vulnerable represents a crucial step for the risk stratification of patients requiring surgical intervention, as well as for detecting the early stages of unstable plaques, which continues to be a significant challenge. Among the methods analysed, preoperative elastosonography, 3D modelling of the plaque different components and structural biomechanical analysis are valid means to confirm differences between subgroups of patients with vulnerable and stable plaques.

## Data availability statement

The raw data supporting the conclusions of this article will be made available by the authors, without undue reservation.

## Ethics statement

The studies involving humans were approved by the Ethics Committee of San Raffaele's Hospital (110/int/2019). The studies were conducted in accordance with the local legislation and institutional requirements. The participants provided their written informed consent to participate in this study.

## Author contributions

NC: Data curation, Formal Analysis, Investigation, Software, Writing—original draft. MC: Data curation, Investigation, Software, Supervision, Writing—review and editing. RC: Investigation, Writing—review and editing. LR: Investigation, Writing—review and editing. GD: Data curation, Writing—review and editing. VB: Data curation, Investigation, Writing—review and editing. GN: Data curation, Investigation, Writing—review and editing. GM: Data curation, Investigation, Software, Supervision, Writing—original draft. DM: Conceptualization, Funding acquisition, Investigation, Project administration, Supervision, Validation, Writing—review and editing.

## Funding

The author(s) declare that financial support was received for the research, authorship, and/or publication of this article. This study was supported by Italian Ministry of Health Grant (GR-2018-12366862) to Daniela Mazzaccaro.

## Conflict of interest

The authors declare that the research was conducted in the absence of any commercial or financial relationships that could be construed as a potential conflict of interest.

## Publisher's note

All claims expressed in this article are solely those of the authors and do not necessarily represent those of their affiliated organizations, or those of the publisher, the editors and the reviewers. Any product that may be evaluated in this article, or claim that may be made by its manufacturer, is not guaranteed or endorsed by the publisher.

## Supplementary material

The Supplementary Material for this article can be found online at: <https://www.frontiersin.org/articles/10.3389/fbioe.2025.1478408/full#supplementary-material>

## References

- Akyildiz, A. C., Speelman, L., van Brummelen, H., Gutiérrez, M. A., Virmani, R., Lugt, A. van der, et al. (2011). Effects of intima stiffness and plaque morphology on peak cap stress. *Biomed. Eng. OnLine* 10 (1), 25. doi:10.1186/1475-925X-10-25
- Banerjee, C., and Chimowitz, M. I. (2017). Stroke caused by atherosclerosis of the major intracranial arteries. *Circulation Res.* 120 (3), 502–513. doi:10.1161/CIRCRESAHA.116.308441
- Barrett, S. R. H., Sutcliffe, M. P. F., Howarth, S., Li, Z.-Y., and Gillard, J. H. (2009). Experimental measurement of the mechanical properties of carotid atherothrombotic plaque fibrous cap. *J. Biomech.* 42, 1650–1655. doi:10.1016/j.jbiomech.2009.04.025
- Benitez, J., Fontanarosa, D., Wang, J., Kumari Paritala, P., McGahan, T., Lloyd, T., et al. (2021). Evaluating the impact of calcification on plaque vulnerability from the aspect of mechanical interaction between blood flow and artery based on MRI. *Ann. Biomed. Eng.* 49 (4), 1169–1182. doi:10.1007/s10439-020-02655-1
- Bennati, L., Vergara, C., Domanin, M., Malloggi, C., Bissacco, D., Trimarchi, S., et al. (2021). A computational fluid–structure interaction study for carotids with different atherosclerotic plaques. *J. Biomechanical Eng.* 143 (9), 091002. doi:10.1115/1.4050910
- Brown, A. J., Teng, Z., Evans, P. C., Gillard, J. H., Habib, S., and Bennett, M. R. (2016). Role of biomechanical forces in the natural history of coronary atherosclerosis. *Nat. Rev. Cardiol.* 13 (4), 210–220. doi:10.1038/nrcardio.2015.203
- Bulum, A., Ivanac, G., Mandurić, F., Pfeifer, L., Bulum, M., Divjak, E., et al. (2022). Contribution of UltraFast™ ultrasound and shear wave elastography in the imaging of carotid artery disease. *Diagnostics* 12 (5), 1168. doi:10.3390/diagnostics12051168
- Costopoulos, C., Huang, Y., Brown, A. J., Calvert, P. A., Hoole, S. P., West, N. E. J., et al. (2017). Plaque rupture in coronary atherosclerosis is associated with increased plaque structural stress. *JACC. Cardiovasc. Imaging* 10 (12), 1472–1483. doi:10.1016/j.jcmg.2017.04.017
- Creane, A., Maher, E., Sultan, S., Hynes, N., Kelly, D. J., and Lally, C. (2010). Finite element modelling of diseased carotid bifurcations generated from *in vivo* computerised tomographic angiography. *Comput. Biol. Med.* 40, 419–429. doi:10.1016/j.combiomed.2010.02.006
- Curcio, N., Rosato, A., Mazzaccaro, D., Nano, G., Conti, M., and Matrone, G. (2023). 3D patient-specific modeling and structural finite element analysis of atherosclerotic carotid artery based on computed tomography angiography. *Sci. Rep.* 13 (1), 19911. doi:10.1038/s41598-023-46949-5
- Djukic, T., Arsic, B., Djorovic, S., Filipovic, N., and Koncar, I. (2020). “Validation of the machine learning approach for 3D reconstruction of carotid artery from ultrasound imaging,” in *2020 IEEE 20th international conference on bioinformatics and bioengineering (BIBE)*, 789–794. doi:10.1109/BIBE50027.2020.00134
- Esaote. (2018). MyLab advanced operations QAS section. Available at: [https://eifu.esaote.com/fileadmin/Manuals/F100100/english/optional\\_sections/QASSection\\_E\\_R03.pdf](https://eifu.esaote.com/fileadmin/Manuals/F100100/english/optional_sections/QASSection_E_R03.pdf).
- Gao, H., and Long, Q. (2008). Effects of varied lipid core volume and fibrous cap thickness on stress distribution in carotid arterial plaques. *J. Biomechanics* 41 (14), 3053–3059. doi:10.1016/j.jbiomech.2008.07.011
- Gao, H., Long, Q., Graves, M., Gillard, J. H., and Li, Z.-Y. (2009). Carotid arterial plaque stress analysis using fluid–structure interactive simulation based on *in-vivo* magnetic resonance images of four patients. *J. Biomechanics* 42 (10), 1416–1423. doi:10.1016/j.jbiomech.2009.04.010
- Garrard, J. W., Ummur, P., Nduwayo, S., Kanber, B., Hartshorne, T. C., West, K. P., et al. (2015). Shear wave elastography may be superior to greyscale median for the identification of carotid plaque vulnerability: a comparison with histology. *Ultraschall Der Medizin (Stuttgart, Ger. 1980)* 36 (4), 386–390. doi:10.1055/s-0034-1399676
- Gerosa, C., Cerrone, G., Suri, J., Aimola, V., Cau, F., Coni, P., et al. (2023). The human carotid atherosclerotic plaque: an observational review of histological scoring systems. *Eur. Rev. Med. Pharmacol. Sci.* 27 (April), 3784–3792. doi:10.26355/eurrev\_202304\_32179
- Holzappel, G. A., Mulvihill, J. J., Cunnane, E. M., and Walsh, M. T. (2014). Computational approaches for analyzing the mechanics of atherosclerotic plaques: a review. *J. Biomech.* 47, 859–869. doi:10.1016/j.jbiomech.2014.01.011
- Holzappel, G. A., Sommer, G., and Regitnig, P. (2004). Anisotropic mechanical properties of tissue components in human atherosclerotic plaques. *J. Biomech. Eng.* 126, 657–665. doi:10.1115/1.1800557
- Kang, S.-J., Ha, H., Lee, J.-G., Han, S.-B., Mintz, G. S., Kweon, J., et al. (2016). Plaque structural stress assessed by virtual histology-intravascular ultrasound predicts dynamic changes in phenotype and composition of untreated coronary artery lesions. *Atherosclerosis* 254 (November), 85–92. doi:10.1016/j.atherosclerosis.2016.09.072
- Kashiwazaki, D., Shiraishi, K., Yamamoto, S., Kamo, T., Uchino, H., Saito, H., et al. (2019). Efficacy of carotid endarterectomy for mild (<50%) symptomatic carotid stenosis with unstable plaque. *World Neurosurg.* 121 (January), e60–e69. doi:10.1016/j.wneu.2018.09.013
- Kelly-Arnold, A., Maldonado, N., Laudier, D., Aikawa, E., Cardoso, L., and Weinbaum, S. (2013). Revised microcalcification hypothesis for fibrous cap rupture in human coronary arteries. *Proc. Natl. Acad. Sci. U. S. A.* 110, 10741–10746. doi:10.1073/pnas.1308814110
- Kolos, I., Troitskiy, A., Balakhonova, T., Shariya, M., Skrypnik, D., Tvorogova, T., et al. (2015). Modern medical treatment with or without carotid endarterectomy for severe asymptomatic carotid atherosclerosis. *J. Vasc. Surg.* 62 (4), 914–922. doi:10.1016/j.jvs.2015.05.005
- Leach, J. R., Rayz, V. L., Soares, B., Wintermark, M., Mofrad, M. R. K., and Saloner, D. (2010). Carotid atheroma rupture observed *in vivo* and FSI-predicted stress distribution based on pre-rupture imaging. *Ann. Biomed. Eng.* 38 (8), 2748–2765. doi:10.1007/s10439-010-0004-8
- Lee, R. T., Grodzinsky, A. J., Frank, E. H., Kamm, R. D., and Schoen, F. J. (1991). Structure-dependent dynamic mechanical behavior of fibrous caps from human atherosclerotic plaques. *Circulation* 83, 1764–1770. doi:10.1161/01.cir.83.5.1764
- Liu, X., Wu, G., Xu, C., He, Y., Shu, L., Liu, Y., et al. (2017). Prediction of coronary plaque progression using biomechanical factors and vascular characteristics based on computed tomography angiography. *Comput. Assist. Surg. Abingdon, Engl.* 22 (Suppl. 1), 286–294. doi:10.1080/24699322.2017.1389407
- Lovett, J. K., Gallagher, P. J., Hands, L. J., Walton, J., and Rothwell, P. M. (2004). Histological correlates of carotid plaque surface morphology on lumen contrast imaging. *Circulation* 110 (15), 2190–2197. doi:10.1161/01.CIR.0000144307.82502.32
- Mahmoud, A. H., Hassan, N., and Ahmed, M. M. (2019). “Three dimensional fluid structure interaction analysis of carotid artery models with different calcification patterns,” in *Annual international Conference of the IEEE Engineering in Medicine and biology society. IEEE Engineering in Medicine and biology society. Annual international conference 2019 (july)*, 7019–7022. doi:10.1109/EMBC.2019.8856813
- Mazzaccaro, D., Giannetta, M., Fancoli, F., Matrone, G., Curcio, N., Conti, M., et al. (2023). Role of preoperative ultrasound shear-wave elastography and radiofrequency-based arterial wall tracking in assessing the vulnerability of carotid plaques: Preliminary results. *Diagn. Basel, Switz.* 13 (4), 805. doi:10.3390/diagnostics13040805
- Meinders, J. M., and Hoeks, A. P. G. (2004). Simultaneous assessment of diameter and pressure waveforms in the carotid artery. *Ultrasound Med. and Biol.* 30 (2), 147–154. doi:10.1016/j.ultrasmedbio.2003.10.014
- Mughal, M. M., Khan, M. K., DeMarco, J. K., Majid, A., Shamoun, F., and Abela, G. S. (2011). Symptomatic and asymptomatic carotid artery plaque. *Expert Rev. Cardiovasc. Ther.* 9 (10), 1315–1330. doi:10.1586/erc.11.120
- Sadat, U., Teng, Z., Young, V. E., Walsh, S. R., Li, Z. Y., Graves, M. J., et al. (2010). Association between biomechanical structural stresses of atherosclerotic carotid plaques and subsequent ischaemic cerebrovascular events – a longitudinal *in vivo* magnetic resonance imaging-based finite element study. *Eur. J. Vasc. Endovascular Surg.* 40 (4), 485–491. doi:10.1016/j.ejvs.2010.07.015
- Sakamoto, A., Cornelissen, A., Sato, Yu, Mori, M., Kawakami, R., Kawai, K., et al. (2021). Vulnerable plaque in patients with acute coronary syndrome: identification, importance, and management, October. Available at: <https://www.uscjournal.com/articles/vulnerable-plaque-patients-acute-coronary-syndrome-identification-importance-and>.
- Shah, P. K. (2003). Mechanisms of plaque vulnerability and rupture. *J. Am. Coll. Cardiol.* 41 (4), S15–S22. doi:10.1016/S0735-1097(02)02834-6
- Shi, X., Gao, J., Lv, Q., Cai, H., Wang, F., Ye, R., et al. (2020). Calcification in atherosclerotic plaque vulnerability: friend or foe? *Front. Physiology* 11 (February), 56. doi:10.3389/fphys.2020.00056
- Sigrist, R. M. S., Liao, J., Ahmed, El K., Chammas, M. C., and Willmann, J. K. (2017). Ultrasound elastography: review of techniques and clinical applications. *Theranostics* 7 (5), 1303–1329. doi:10.7150/thno.18650
- Speelman, L., Bosboom, E. M. H., Schurink, G. W. H., Hellenenthal, F. A. M. V. I., Buth, J., Breeuwer, M., et al. (2008). Patient-specific AAA wall stress analysis: 99-percentile versus peak stress. *Eur. J. Vasc. Endovascular Surg. Official J. Eur. Soc. Vasc. Surg.* 36 (6), 668–676. doi:10.1016/j.ejvs.2008.09.007
- Spence, J. D. (2016). Endarterectomy vs. Stenting vs. Medical therapy. *Int. J. Stroke Official J. Int. Stroke Soc.* 11 (5), 500–501. doi:10.1177/1747493016643552
- Tang, D., Yang, C., Canton, G., Wu, Z., Hatsukami, T., and Chun, Y. (2013). Correlations between carotid plaque progression and mechanical stresses change sign over time: a patient follow up study using MRI and 3D FSI models. *Biomed. Eng. OnLine* 12 (1), 105. doi:10.1186/1475-925X-12-105
- Teng, Z., Feng, J., Zhang, Y., Sutcliffe, M. P. F., Huang, Y., Brown, A. J., et al. (2015). A uni-extension study on the ultimate material strength and extreme extensibility of atherosclerotic tissue in human carotid plaques. *J. Biomechanics* 48 (14), 3859–3867. doi:10.1016/j.jbiomech.2015.09.037
- Timmins, L. H., Suo, J., Eshtehardi, P., Molony, D. S., McDaniel, M. C., Oshinski, J. N., et al. (2016). Comparison of angiographic and IVUS derived coronary geometric reconstructions for evaluation of the association of hemodynamics with coronary artery disease progression. *Int. J. Cardiovasc. Imaging* 32 (9), 1327–1336. doi:10.1007/s10554-016-0918-9
- Truijman, M. T. B., de Rotte, A. A. J., Aaslid, R., van Dijk, A. C., Steinbuch, J., Liem, M. I., et al. (2014). Intraplaque hemorrhage, fibrous cap status, and microembolic signals in symptomatic patients with mild to moderate carotid artery stenosis. *Stroke* 45 (11), 3423–3426. doi:10.1161/STROKEAHA.114.006800

- van Dam-Nolen, D. H. K., van Egmond, N. C. M., Dilba, K., Kelly, N., van der Kolk, A. G., Liem, M. I., et al. (2022). Sex differences in plaque composition and morphology among symptomatic patients with mild-to-moderate carotid artery stenosis. *Stroke* 53 (2), 370–378. doi:10.1161/STROKEAHA.121.036564
- van Dam-Nolen, D. H. K., van Egmond, N. C. M., Koudstaal, P. J., van der Lugt, A., and Bos, D. (2023). Sex differences in carotid atherosclerosis: a systematic review and meta-analysis. *Stroke* 54 (2), 315–326. doi:10.1161/STROKEAHA.122.041046
- Vermeersch, S. J., Rietzschel, E. R., De Buyzere, M. L., De Bacquer, D., De Backer, G., Van Bortel, L. M., et al. (2008). Determining carotid artery pressure from scaled diameter waveforms: comparison and validation of calibration techniques in 2026 subjects. *Physiol. Meas.* 29 (11), 1267–1280. doi:10.1088/0967-3334/29/11/003
- Warren, J. L., Yoo, J. E., Meyer, C. A., Molony, D. S., Habib, S., and Hayenga, H. N. (2022). Automated finite element approach to generate anatomical patient-specific biomechanical models of atherosclerotic arteries from virtual histology-intravascular ultrasound. *Front. Med. Technol.* 4, 1008540. doi:10.3389/fmedt.2022.1008540
- Ylä-Herttuala, S., Jacob, F. B., Daemen, M., Falk, E., Garcia-Garcia, H. M., Herrmann, J., et al. (2013). Stabilization of atherosclerotic plaques: an update. *Eur. Heart J.* 34 (42), 3251–3258. doi:10.1093/eurheartj/eh301





## OPEN ACCESS

## EDITED BY

Jiaqiu Wang,  
London South Bank University, United Kingdom

## REVIEWED BY

Z. Xiao,  
China Institute of Sport Science, China  
Runxin Fang,  
Jiangsu Institute of Metrology, China

## \*CORRESPONDENCE

Cheng Wang,  
✉ chengwang2013@foxmail.com  
Zhun Xu,  
✉ xuzhun2012@163.com

RECEIVED 24 November 2024

ACCEPTED 19 March 2025

PUBLISHED 27 March 2025

## CITATION

Luo B, Li Y, Wang C and Xu Z (2025) Finite element analysis of the biomechanical effects of manipulation of lower limb hyperextension on the sacroiliac joint.  
*Front. Bioeng. Biotechnol.* 13:1533585.  
doi: 10.3389/fbioe.2025.1533585

## COPYRIGHT

© 2025 Luo, Li, Wang and Xu. This is an open-access article distributed under the terms of the [Creative Commons Attribution License \(CC BY\)](https://creativecommons.org/licenses/by/4.0/). The use, distribution or reproduction in other forums is permitted, provided the original author(s) and the copyright owner(s) are credited and that the original publication in this journal is cited, in accordance with accepted academic practice. No use, distribution or reproduction is permitted which does not comply with these terms.

# Finite element analysis of the biomechanical effects of manipulation of lower limb hyperextension on the sacroiliac joint

Bangmin Luo<sup>1</sup>, Yikai Li<sup>2</sup>, Cheng Wang<sup>1\*</sup> and Zhun Xu<sup>1\*</sup>

<sup>1</sup>Department of Spine Surgery, The First Affiliated Hospital, Hengyang Medical School, University of South China, Hengyang, Hunan, China, <sup>2</sup>School of Traditional Chinese Medicine, Southern Medical University, Guangzhou, Guangdong, China

**Objective:** The objective of this study was to explore the effects of four Manipulations of lower limb hyperextension (MLLHs) on the sacroiliac joint (SIJ) and surrounding ligaments.

**Methods:** A three-dimensional finite element model of the pelvis was built. Four MLLHs were simulated. The stresses on the pelvis and SIJ were calculated. The SIJ displacements and ligament strains were analyzed.

**Results:** Under MLLH-F1, -F2, -F3 and -F4, the maximum stresses on the pelvis were 49.2, 50.5, 48.6 and 54.0 MPa, and the maximum stresses on the left SIJ were 3.1, 3.2, 3.0 and 3.4 MPa, respectively. The total SIJ displacements were 0.129, 0.164, 0.080 and 0.154 mm under MLLH-F1, -F2, -F3 and -F4, respectively. The four MLLHs all caused different degrees of ligament strain, MLLH-F2 the greatest.

**Conclusion:** MLLH-F2 and -F4 caused greater stresses on the pelvis and the SIJ surface. The four MLLHs all produced small SIJ displacements. MLLH-F2 produced the largest SIJ displacement and the greatest ligament strain. These findings can guide the choice of therapy.

## KEYWORDS

manipulation, biomechanical, sacroiliac joint, finite element analysis, stress, strain

## 1 Introduction

The sacroiliac joint (SIJ) is the largest axial joint in human body. It connects the spine to the pelvis and transfers weight from the upper body to the lower extremities (Cohen, 2005; Joukar et al., 2018). The articular surface is composed of the ligament part and the synovial part. The ligament part maintains the stability of the SIJ, and the synovial part provides a certain range of motion of the SIJ (Al-Subahi et al., 2017; Poilliot et al., 2019). One side of the SIJ bears more weight because of the abnormal gait and is likely to degenerate (DonTigny, 1990; Vanelderen et al., 2010). Long-term incorrect standing or sitting posture can cause strain on the SIJ joints and surrounding ligaments, which can lead to lower back pain (Sacroiliac joint dysfunction: pathophysiology, diagnosis, and treatment, 2021). Recent studies have found that SIJ diseases can also cause low back pain, accounting for approximately 14.5%–22.5% of cases (Lindsey et al., 2014).

Commonly, abnormal gait and long-term strain cause high pressure in the SIJ and surrounding ligaments, resulting in the SIJ and ligament damage. Inflammation damages the SIJ. The range of motion of the SIJ increases abnormally after lumbar fusion surgery with fixation of the sacrum, which aggravates the strain of the joint. These factors may cause SIJ pain without specific causes (Schuit et al., 1989). The mechanism may include the following processes: these pathogenic factors acting on the auricular surface of the sacrum and ilium may cause injury to the ligaments or muscles around the SIJ, which will result in slight movement of the SIJ, making the joints difficult to reduce. The mechanical environment of the joints may ultimately be imbalanced, and the soft tissues will be damaged. This condition is one of the causes of SIJ dysfunction (Hing et al., 2015).

Clinically, SIJ dysfunction without specific cause is usually treated by manipulation (Farazdaghi et al., 2018; Kamali et al., 2019; Nejati et al., 2019; García-Peñalver et al., 2020). Many studies have reported that the manipulation of lower limb hyperextension (MLLH) could significantly relieve lower back pain in patients with SIJ dysfunction, and the treatment efficacy rate was 90%–95% (Xie, 2017; Liu et al., 2020; Fan and Wu, 2021). Manipulations have the characteristics of no trauma and a quick effect, so they are widely accepted by patients. In a previous study, a finite element pelvic model was built, and it was found that MLLH could produce small SIJ displacement and different degrees of ligament strain (Xu et al., 2020). However, the point and direction of the manipulative force were different among therapists. It is not known whether the MLLH with different points and directions will produce different effects on the SIJ. Thus, the purpose of this study is to explore the biomechanical characteristics of four MLLHs through a three-dimensional finite element model, so as to provide a reference for clinical manipulation.

## 2 Materials and methods

### 2.1 Model construction

A healthy male volunteer (34 years old, 170 cm in height, and 65 kg in weight) was recruited. The volunteer signed the informed consent form, and the study protocol was approved by the ethics committee. Computed tomography (CT) of the pelvis and femur with axial slices 0.5 mm thick was performed. CT data were imported into Mimics 20.0 (Materialise Company, Leuven, Belgium), and the cortical and cancellous regions of the bones were identified. The surfaces of the model were meshed using Geomagic 2013 (Raindrop Company, Marble Hill, USA). The SIJ consists of articular cartilage, the endplate of the sacrum and the ilium, and the surrounding ligaments. The sacral and

iliac cartilage of the SIJ were built with uniform thicknesses of 2 mm and 1 mm, respectively. The ranges of the articular surfaces were derived from CT data. The thicknesses of the sacral and the ilial endplates were set at 0.23 mm and 0.36 mm, respectively. The gap width between the two cartilages was assumed to be 0.3 mm. (McLauchlan and Gardner, 2002; Kim et al., 2014). The hip joints were set to be fully constrained. The material properties, based on previous studies (Kim et al., 2014; Lee et al., 2017), are listed in Table 1.

The anterior sacroiliac ligament (ASL), short posterior sacroiliac ligament (SPSL), long posterior sacroiliac ligament (LPSL), sacrospinous ligament (SS), interosseous sacroiliac ligament (ISL), and sacrotuberous ligament (ST) complexes were established as 3D tension-only truss elements. The attachment ranges were based on previous literature (Kim et al., 2014). The ASL is made up of numerous thin bands that span the ventral surface of the SIJ, connecting the lateral aspect of the sacrum to the margin of the auricular surface of the ilium. The LPSL extends from the posterior superior iliac spine to the third and fourth transverse tubercles of the back of the sacrum. The SPSL lies deep relative to the LPSL and consists of large fibers attaching the lateral aspect of the dorsal sacral surface to the tuberosity of the ilium. The ISL lies in the intra-articular space and is composed of a series of short, strong fibers connecting the tuberosities of the sacrum and ilium. The SS is a thin triangular ligament that connects the ischial spine to the lateral border of the sacrum. The ST is behind the sacrospinous ligament, which attaches the ischial tuberosity to the lateral border of the sacrum. The material properties of each ligament were obtained from the literature (Lee et al., 2017). In the end, the pelvis-femur model included 727,474 elements and 275,399 nodes.

### 2.2 Simulation of MLLHs

The patient lay in a prone position, and the leg treated was hyperextended at the hip so that the anterior superior spine could just lift off the bed. Then, the therapist applied a downward force to the treated iliac crest. The procedure is shown in Figure 1A.

The MLLH simulation was as follows: The magnitudes of the forces were determined by determining the manipulative power of five therapists using a biomechanical testing machine. Their average manipulative force was 600 N (Xu et al., 2020). In this manner, the right lateral region of the ilium and the right pubic tubercle were fixed. Then, a pushing force of 600 N along the dorsal-ventral direction was applied at the left iliac crest or posterior superior iliac spine (PSIS). PSIS is a bony prominence on the posterior aspect of the ilium, which facilitates the application of manipulative force by physiotherapists. The iliac crest is closer to the synovial portion of the SIJ, making it more likely to induce SIJ micromotion (Zhang et al., 2019; Xiao et al., 2022). Therefore, the PSIS and the midpoint between the highest point of the ilium and the PSIS were selected as the points of manipulative force. The articular surface of the SIJ forms an angle of approximately 30° with the sagittal plane of the human body (Zhang et al., 2019; Xiao et al., 2022). Based on the structure, two orientations were selected: one at a 30-degree angle relative to the sagittal plane to align with articular surface, and the

**Abbreviations:** MLLHs, Manipulations of lower limb hyperextension; SIJ, sacroiliac joint; ASL, anterior sacroiliac ligament; SPSL, short posterior sacroiliac ligament; LPSL, long posterior sacroiliac ligament; SS, sacrospinous ligament; ISL, interosseous sacroiliac ligament; ST, sacrotuberous ligament; PSIS, posterior superior iliac spine; AP, anterior-posterior; SI, superior-inferior; MI: medial-lateral.

TABLE 1 Material properties of the sacrum, ilium, femur, pubic symphysis and endplate.

Material		Young's modulus (MPa)	Poisson's ratio
Sacrum	Cortical	12,000	0.3
	Cancellous	100	0.2
Ilium	Cortical	12,000	0.3
	Cancellous	100	0.2
Femur	Cortical	15,000	0.3
	Cancellous	100	0.2
Pubic symphysis		5	0.45
Articular cartilage		100	0.3
Endplate		1,000	0.4

other parallel to the sagittal plane. Additionally, the two points and orientations of manipulative force were determined based on the consensus of senior physiotherapists (Zhong et al., 2025; Huang et al., 2019; Fan and Wu, 2021). The two force points are described in Figure 1B.

Four MLLHs were tested. MLLH-F1: The force was applied at the left iliac crest (Point 3, Figure 1B) at an angle of 30° from the sagittal plane, which was roughly parallel to the SIJ surface. MLLH-F2: The force was applied at the left iliac crest (Point 3, Figure 1B), parallel to the sagittal plane. MLLH-F3: The force was applied at the left PSIS (Point 1, Figure 1B) at an angle of 30° from the sagittal plane. MLLH-F4: The force was applied at the left PSIS (Point 1, Figure 1B), parallel to the sagittal plane. The detailed loading and boundary conditions, as well as the x-, y-, and z-axes, are described in Figure 1C. The compressive stresses and displacements of the SIJ and the strains of the ligaments with the four MLLHs were then investigated using Abaqus 2018 (Dassault Systemes SA, Massachusetts, USA).

## 2.3 Mesh convergence study

To assess the accuracy of the pelvic model, a convergence analysis was performed through systematic mesh refinement. Four finite element models with progressively decreasing element sizes were constructed, with corresponding element and node counts detailed in Table 2. The models incorporated boundary conditions, material properties, loading configurations, and constraint definitions as previously described in the abovementioned section. Each mesh configuration was subjected to four loading conditions (MLLH-F1, -F2, -F3 and -F4). Subsequently, the maximum stresses and displacements observed on the left SIJ articular surface of the sacrum were comparatively analyzed across all model variants under the four loading scenarios.

## 2.4 Model validation

Two tests were performed to validate the model. For the pelvic model, the distribution of the principal strain of the pelvis was compared with that indicated by Zhang et al. (2010). Zhang et al.

analyzed the distribution of principal strain on the cortical bone of the pelvis in a single-legged stance. In this model, the distribution of the principal strain of the pelvis was observed under the same loading and boundary conditions.

For the sacrum model, the relationship between load and displacement was compared with that reported in cadaveric (Miller et al., 1987) and computational studies (Eichenseer et al., 2011; Kim et al., 2014). In the cadaveric experiment, the bilateral ilia were fixed. Five translational forces (anterior, posterior, superior, inferior, and mediolateral) of 294 N and three moments (flexion, extension, and axial rotation) of 42 Nm were applied separately to the center of the sacrum. Under these stimuli, the displacements of a node lying in the mid-sagittal plane between the inferior S1 and superior S2 vertebral endplates were calculated. In this model, the displacement was estimated under the same loading.

## 3 Results

### 3.1 Mesh convergence study

Quantitative evaluation of maximum stresses and maximum displacements on the left SIJ surface of the sacrum was performed across all mesh configurations under four loading conditions (MLLH-F1, -F2, -F3 and -F4), which are shown in Figure 2. Comparative analysis revealed less than 5% variation in maximum stress and maximum displacement between Mesh 3 and Mesh 4 across all loading scenarios, falling within acceptable convergence thresholds ( $\leq 5\%$ ). Based on these findings, Mesh 3 (727,474 elements) demonstrating optimal balance between computational efficiency and solution accuracy was subsequently adopted for subsequent biomechanical analyses.

### 3.2 Model validation

The principal stresses were distributed mainly in the upper and posterior areas of the acetabulum and extended to the iliac crest, the incisura ischiadica major, and the rear acetabulum. The distribution and maximum value of stress were consistent with those reported in

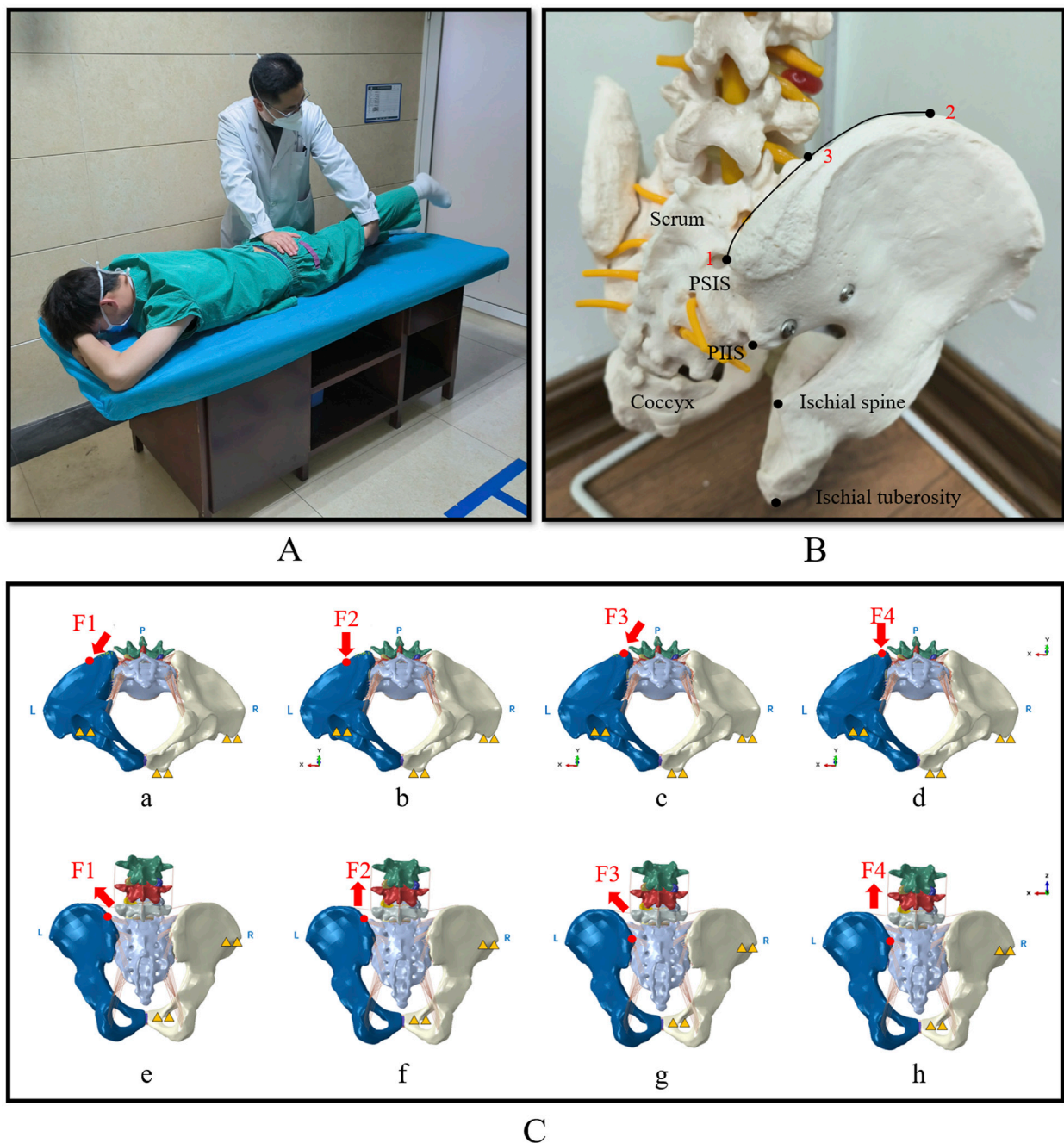


FIGURE 1

The picture showing MLLH, pelvic force application point and biomechanical modelling of the four loading conditions. (A) Showed that the therapist performed MLLH on the patient. (B) Showed the two force points in a pelvic model. Point 1 was the PSIS, which was the force point of MLLH-F3 and -F4. Point 2 was the highest point of the iliac crest. Point 3 was the mid-point between the highest point of the iliac crest and the PSIS, which was the force point of MLLH-F1 and -F2. (C) Showed the loading and boundary conditions for four MLLHs. The yellow triangles represent the fixed sites of pelvic model. The inferior view (a–d) and posterior view (e–h) of pelvis are shown. (a, e) MLLH-F1; (b, f) MLLH-F2; (c, g) MLLH-F3; (d, h) MLLH-F4. MLLH, manipulation of lower limb hyperextension; PSIS, posterior superior iliac spine; PIIS: posterior inferior iliac spine.

a previous study (Zhang et al., 2010). The displacements under the eight loading conditions agreed not only with those in an experimental study but also with those in some computational studies, which are shown in Figure 3 (Miller et al., 1987; Eichenseer et al., 2011; Kim et al., 2014).

The validation results of this model were consistent with those of previous studies, indicating that it was a valid model.

### 3.3 Pelvic and SIJ stress

The stress distributions of the pelvis under the four MLLHs are shown in Figure 4. In the ventral pelvis, the areas of high stress were located at the left SIJ, arcuate line, and left acetabulum under MLLH-F3 and -F4, while the highly stressed areas extended to the left wing of the ilium under MLLH-F1 and -F2. In the dorsal pelvis, the areas



TABLE 2 Element and node numbers for four different mesh resolutions.

Model	Element number	Node number
Mesh 1	204094	75352
Mesh 2	378199	133863
Mesh 3	727474	275399
Mesh 4	1590376	589032

of high stress were located at the left greater ischial notch and left acetabulum under MLLH-F3 and -F4, while these areas extended to the posterior inferior iliac spine under MLLH-F1 and -F2. The maximum stress values produced by MLLH-F1, -F2, -F3 and -F4 were 49.2, 50.5, 48.6 and 54.0 MPa, respectively.

The stress distributions on the sacrum surface of the SIJ are shown in Figure 5. Under all four MLLHs, the areas of high stress were located at the anterior and inferior parts of the SIJ. The stresses on the left SIJ were higher than those on the right SIJ. The maximum stress values produced by MLLH-F1, -F2, -F3 and -F4 were 3.1, 3.2, 3.0 and 3.4 MPa, respectively.

These results indicated that different MLLH techniques had a significant impact on the stress distribution of the pelvis and SIJ, with MLLH-F4 producing the highest stress value.

### 3.4 Displacement of SIJ

Under MLLH-F1, the displacements of the left SIJ were 0.114, 0.013 and 0.060 mm in the anterior-posterior (AP), superior-inferior (SI) and medial-lateral (MI) directions, respectively. In MLLH-F2, the displacements were 0.134, 0.078 and 0.054 mm in the AP, SI and MI directions, respectively. In MLLH-F3, the displacements were 0.042, 0.020 and 0.065 mm in the AP, SI and MI directions, respectively. In MLLH-F4, the displacements were 0.078, 0.116 and 0.066 mm in the AP, SI and MI directions, respectively. The total displacements of the SIJ were 0.129, 0.164, 0.080 and 0.154 mm under MLLH-F1, -F2, -F3 and -F4, respectively. The displacements of the left SIJ are shown in Figure 6A.

These results indicated that different MLLH techniques had a significant impact on the displacement of left SIJ. The MLLH-F2 produced the maximum displacement in AP, as well as the greatest total displacement. The MLLH-F4 produced the maximum displacement in SI and MI.

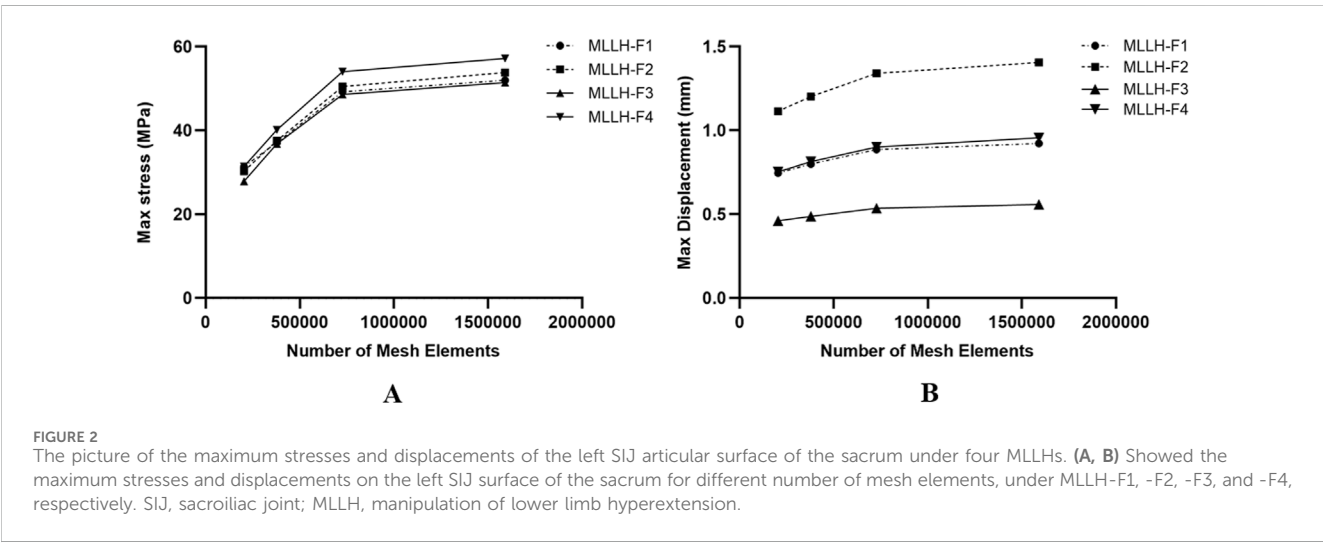


FIGURE 2 The picture of the maximum stresses and displacements of the left SIJ articular surface of the sacrum under four MLLHs. (A, B) Showed the maximum stresses and displacements on the left SIJ surface of the sacrum for different number of mesh elements, under MLLH-F1, -F2, -F3, and -F4, respectively. SIJ, sacroiliac joint; MLLH, manipulation of lower limb hyperextension.

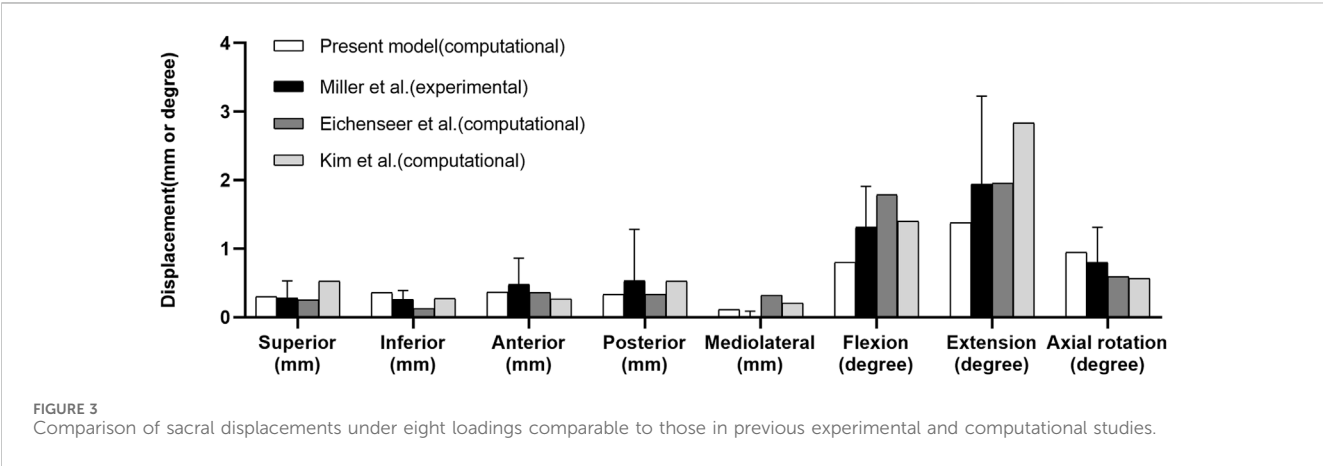
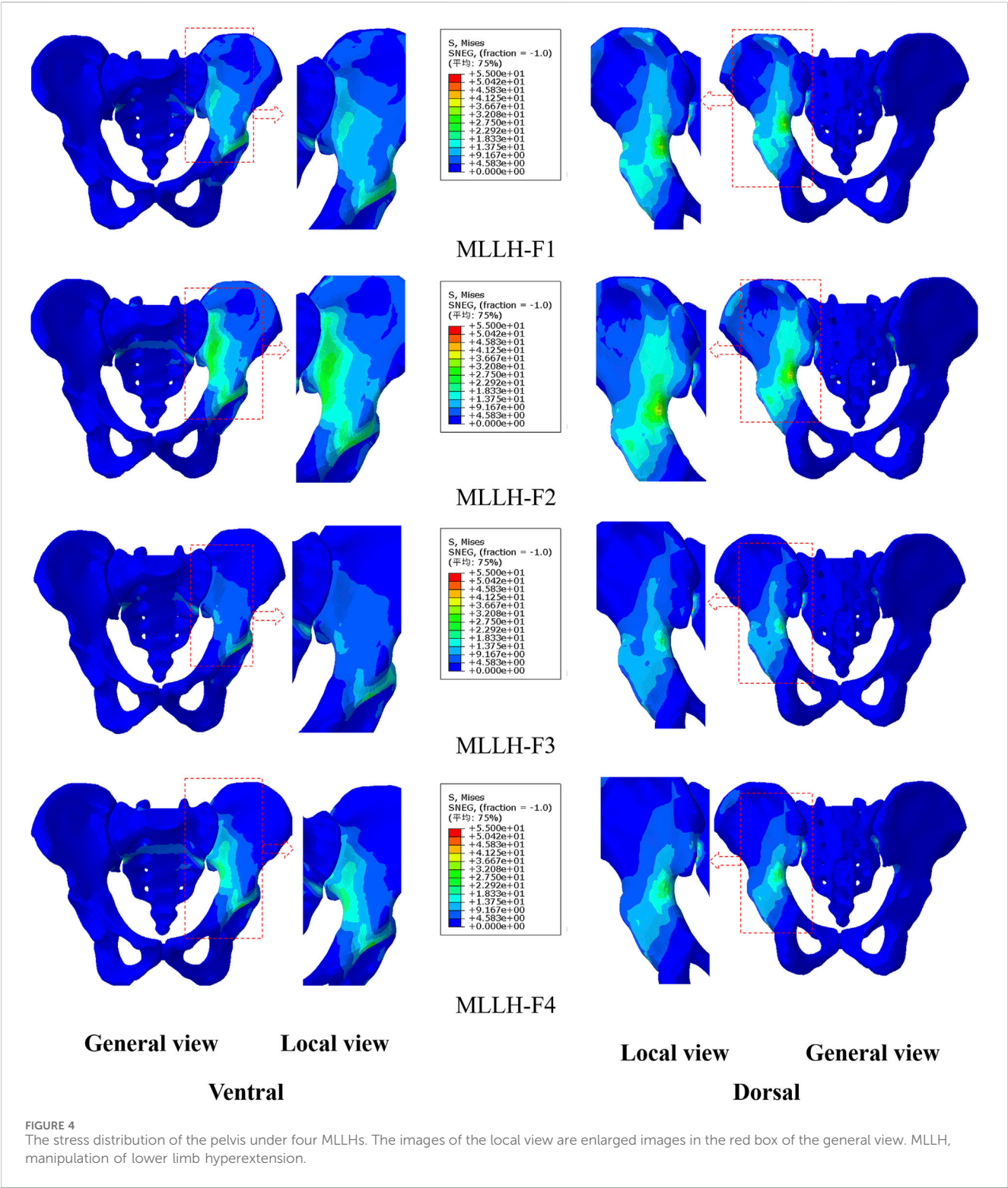


FIGURE 3 Comparison of sacral displacements under eight loadings comparable to those in previous experimental and computational studies.





3.5 Strain of ligaments

The ligament strains under the four MLLHs are shown in Figure 6B. In most ligaments, the left ligament strain was greater under each MLLH. With MLLH-F1, the left ISL, LPSL and SPSL were the ligaments with the highest strain values, at 0.78%, 0.29%

and 0.25%, respectively. With MLLH-F2, the left ISL, SPSL and ASL had the highest strain values, at 3.56%, 1.28% and 1.14%, respectively. Under MLLH-F3, the left ISL, ASL and LPSL had the highest strain values, at 0.33%, 0.20% and 0.18%, respectively. Under MLLH-F4, the left ISL, SPSL and ASL had the highest strain values, at 2.04%, 1.12% and 1.04%, respectively.

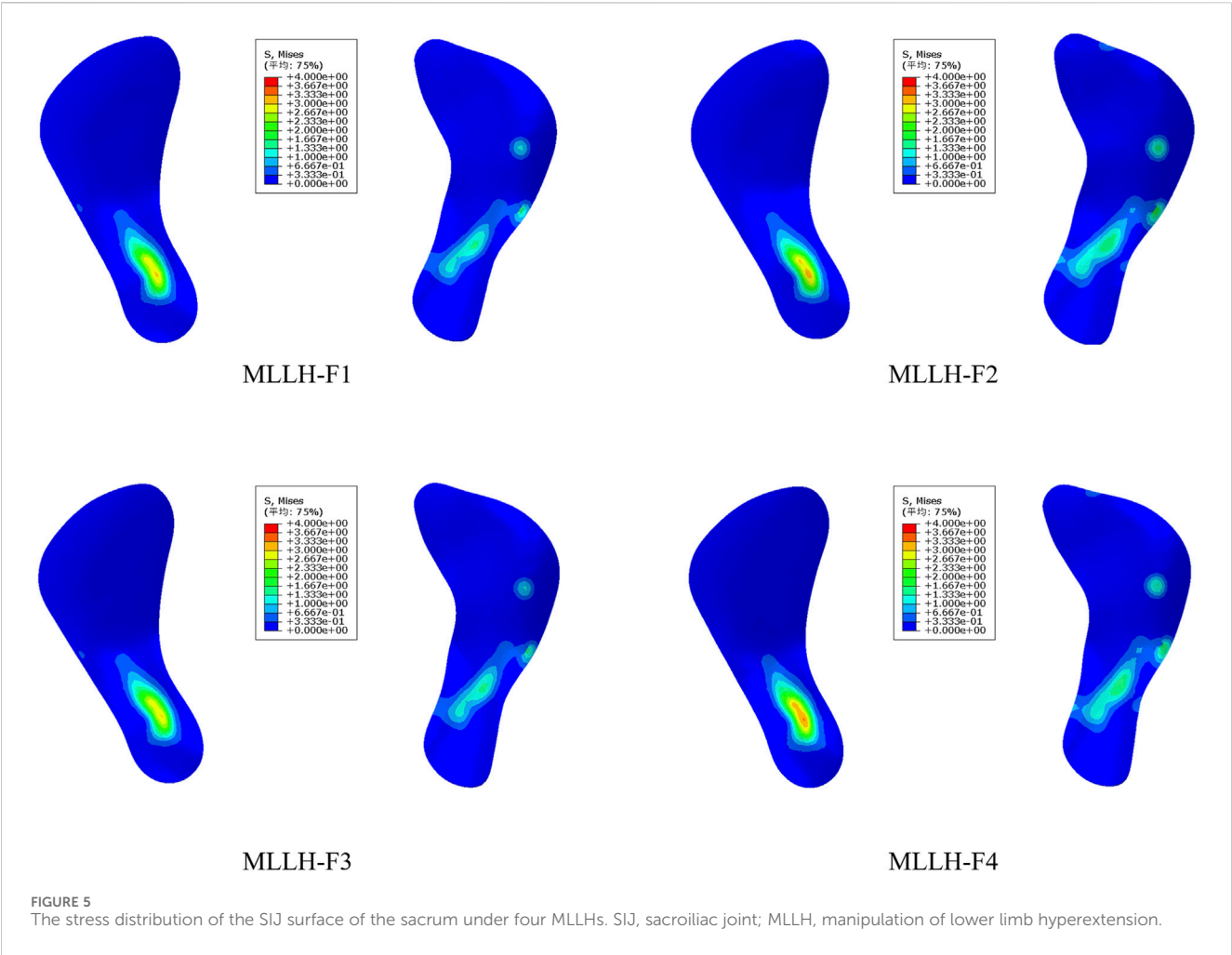


FIGURE 5 The stress distribution of the SIJ surface of the sacrum under four MLLHs. SIJ, sacroiliac joint; MLLH, manipulation of lower limb hyperextension.

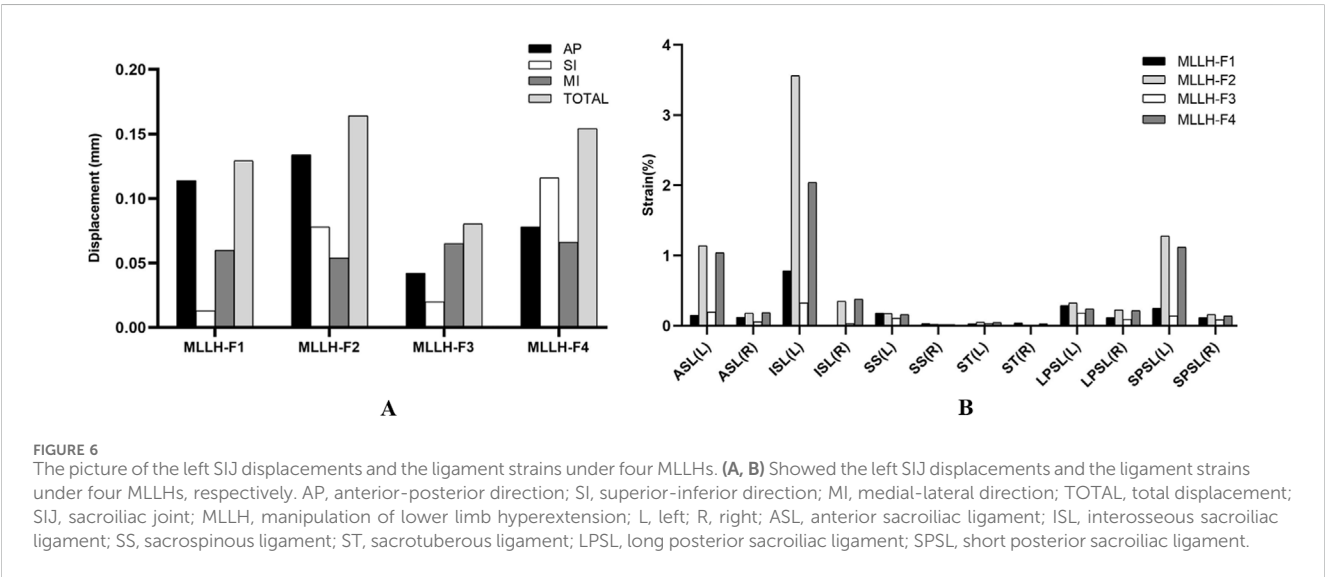


FIGURE 6 The picture of the left SIJ displacements and the ligament strains under four MLLHs. (A, B) Showed the left SIJ displacements and the ligament strains under four MLLHs, respectively. AP, anterior-posterior direction; SI, superior-inferior direction; MI, medial-lateral direction; TOTAL, total displacement; SIJ, sacroiliac joint; MLLH, manipulation of lower limb hyperextension; L, left; R, right; ASL, anterior sacroiliac ligament; ISL, interosseous sacroiliac ligament; SS, sacrospinous ligament; ST, sacrotuberous ligament; LPSL, long posterior sacroiliac ligament; SPSL, short posterior sacroiliac ligament.

These results indicated that different MLLH techniques had a significant impact on the ligament strains. The MLLH-F2 and -F4 produced the higher ligament strains. The ISL, SPSL, ASL had higher strain values.

#### 4 Discussion

SIJ pain is a common disease, affecting 90% of adults throughout their lives (Joukar et al., 2018). SIJ dysfunction is

one of the primary etiological factors contributing to SIJ pain. The main causes include:

1. Acute trauma and chronic strain: injuries from accidents, falls, or repetitive stress can lead to joint misalignment or ligament damage.
2. Pregnancy and childbirth: hormonal changes, such as increased relaxin levels, and the physical stress of childbirth can reduce joint stability.
3. Degenerative changes and arthritis: conditions such as osteoarthritis or ankylosing spondylitis can cause inflammation and degenerative changes in the SIJ.
4. Leg length discrepancy and scoliosis.
5. Infectious sacroiliitis: bacterial or viral infections can lead to inflammation of the SIJ.
6. Pelvic or spinal surgery: surgical interventions may alter pelvic mechanics, affecting SIJ function.
7. Other factors: obesity and aging can exacerbate joint degeneration and increase the risk of dysfunction. These factors highlight the multifactorial nature of SIJ dysfunction and its role in the development of SIJ pain. MLLH is a common treatment for SIJ dysfunction without specific causes. However, the best point and direction of the manipulative force are currently disputed. Thus, this work intended to study the four MLLHs based on the finite element model to provide a theoretical basis for the manipulation.

Since the force point of MLLH was on the dorsal side of the pelvis, the maximum pelvic stresses produced by the four MLLHs were all on the dorsal side of the pelvis. The area of high stress was mainly located at the greater ischial notch, which was related to the structure of the pelvis. The greater ischial notch is the transition area of the broad iliac wing to the narrow ischial spine and acetabulum. The area of high stresses caused by MLLH-F1 and -F2 extended to the iliac crest, which was related to the fact that the force points of MLLH-F1 and -F2 were on the iliac crest. The maximum pelvic stresses caused by MLLH-F1 and -F3 were smaller than those caused by MLLH-F2 and -F4. This difference was related to the direction of manipulative force, which was roughly parallel to the SIJ surface in the former.

It is difficult to measure the stress on the surface of the SIJ in the human body. Shi et al. (2014) built a pelvic model and found that the stresses of the SIJ surface of the sacrum and ilium were 16.5 and 31.4 MPa under the double-support standing posture. Zhang et al. (2022) observed that the stresses of the right SIJ surface of the sacrum ranged from 15 to 21 MPa, 18–19 MPa and 17–20 MPa under flexion and extension, lateral bending and rotation motions, respectively. Kiapour et al. (2012) studied the relationship between the load distribution on the SIJ surface and the limb length discrepancy. For flexion and extension, lateral bending and rotation motions, the respective stresses of the SIJ surface ranged from 3.6 to 6.9 MPa, 4.5–53.1 MPa and 24.7–83.5 MPa under various leg length discrepancies (0, 1, and 2 cm). In this study, the stress on the left SIJ surface was greater than that on the right, which was related to the manipulative force on the left ilium. MLLH-F4 produced the highest stress, at 3.4 MPa, while MLLH-F3 produced the lowest stress, at 3.0 MPa. The stresses on the SIJ were less than those of normal activity of humans, so the MLLH would not cause damage to the SIJ. The SIJ surface of the ilium was behind, outside and below the SIJ surface of the

sacrum. MLLH-F4 made the ilium nearer to the sacrum. MLLH-F3 caused the ilium to move nearer to the sacrum parallel to it. Therefore, the stress produced by MLLH-F4 was higher than that produced by MLLH-F3. The anterior and inferior parts of the SIJ surface were the synovial structure, and the posterior part was the ligament structure, so the stress on the SIJ was concentrated on the anterior and inferior parts. This result was consistent with that of Kim's study (Kim et al., 2014).

Walker (1992) found that SIJ displacements were no more than 3 mm and rotation was less than 2° when SIJ underwent rotation or flexion-extension in a standing and sitting position. Klima et al. (2018) performed a cadaveric study and found that the SIJ displacements were 0.1, 0.0, and 0.3 mm in the AP, MI, and SI directions under 100% body weight loading. Jacob and Kissling (1995) performed an *in vivo* study using a cam k-wire device. The results showed that SIJ displacements were 0.4, 0.7, and 0.5 mm in the AP, MI, and SI directions when the SIJ underwent flexion-extension in a one-legged stance in an upright position. Kibsgård et al. (2012) observed that the SIJ displacements were 0.5, 0.4, and 0.3 mm in the AP, MI, and SI directions using Roentgen stereophotogrammetry analysis when the SIJ underwent flexion-extension, lateral bending and rotation. In this study, it was found that the SIJ displacements were less than 0.2 mm under all four MLLHs, which was consistent with previous studies (Walker, 1992; Jacob and Kissling, 1995; Kibsgård et al., 2012; Klima et al., 2018). These small displacements are within the normal range of motion and are not harmful to the SIJ. The SIJ is an incomplete sagittal and coronal joint, so its motion is complex. Under MLLH-F1 and -F2, the displacement in the AP direction was the largest. Under MLLH-F3, the displacement in the MI direction was the largest. Under MLLH-F4, the displacement in the SI direction was the largest. Thus, the point and direction of the manipulative force had clear influences on the SIJ movement. In addition, MLLH-F2 produced the largest total displacement among the four MLLHs. This might be related to the greater torque of SIJ rotation caused by MLLH-F2.

Hammer et al. (2013) built a finite element model and indicated that an increase in SIJ cartilage and ligament material stiffnesses decreased pelvic motion. Enix and Mayer (2019) suggested that hypermobility of the SIJ could be caused by ligamentous instability or be secondary to adaptive biomechanical changes and increased stresses affecting the joints of the pelvis. Hammer et al. (2019) found that the SS and ST played an important role in maintaining SIJ stability in the two-leg stance. The instability resulting from partial or complete SS and ST injury merits consideration when choosing and designing treatment strategies. Ligaments play an important role in maintaining pelvic stability. Our results indicated that the strains of the ISL, SPSTL, and ASL were larger than those of the other three ligaments under all four MLLHs. The ISL and SPSTL are located at the posterior and upper parts of the SIJ. When the MLLHs were performed, the ISL and SPSTL were the first to withstand the force. The force point of the MLLH-F2 was closer to the synovial portion of the SIJ, resulting in a shorter lever arm, which made it easier to produce ligament strain. Additionally, the direction of the manipulative force was parallel to the sagittal plane of body and intersected with the orientation of the ISL, SPSTL and ASL, further facilitating the induction of ligament strain. This biomechanical advantage may enhance the effectiveness of the manipulation in restoring joint alignment and improving ligament function.

Low back pain caused by SIJ dysfunction primarily attributes to minor joint subluxation and abnormal strain in the surrounding

ligaments. Manipulation aims to alleviate pain and restore function by realigning the joint surfaces and normalizing the mechanical state of the ligaments, which forms the biomechanical basis for its effectiveness. This study found that among four MLLHs, MLLH-F2 resulted in the greatest displacement of the SIJ and induced the maximum strain in the ligaments. These findings suggested that MLLH-F2 was highly effective in restoring joint alignment and improving the mechanical state of the ligaments. In clinical, when applying the MLLH, the midpoint between the highest point of the iliac crest and the PSIS should be selected as the manipulative force point. The direction of manipulative force should be parallel to the sagittal plane of the body. This approach can optimize the therapeutic effect of MLLH by ensuring precise force transmission to the SIJ, and improve clinical outcomes in the treatment of SIJ dysfunction.

There are some limitations to this experiment. First, the data used in this model were derived from a young male individual, which may not be applicable to female or elderly populations. Therefore, the findings of this study may have limited generalizability to these groups. Future research should focus on investigating the characteristics of other populations. Second, in this model, ligaments were typically simplified as linear elements, despite the fact that ligaments exhibited nonlinear characteristics in reality. This simplification might result in the model's inability to accurately reflect the true mechanical behavior of ligaments. Furthermore, the model did not account for muscle factors, which represented a significant deviation from actual conditions. The manipulation in the model was relatively simplistic, whereas clinical manipulative procedures were far more complex, involving greater detail and dynamic adjustments. Therefore, although the model held certain values in research and prediction, the findings must be interpreted with caution and validated against clinical practice. Future improvements to the model could consider incorporating nonlinear ligament models and muscle factors to more accurately simulate real-world conditions. Finally, the SIJs in this model were normal joint structures, but MLLH was applied to subluxated SIJs clinically. The results might not fully reflect the mechanical characteristics of MLLH.

## 5 Conclusion

This study analyzed the effects of four MLLHs on the SIJ. MLLH-F2 and -F4 caused greater stresses on the pelvis and the SIJ surface. The high stress areas of the SIJ were located at the anterior and inferior parts of the SIJ. The four MLLHs all produced small SIJ displacements. Among them, MLLH-F2 and -F4 produced greater total displacements. MLLH-F1 and -F2 mainly produced displacement in the AP direction. MLLH-F3 mainly produced displacement in the MI direction. MLLH-F4 mainly produced displacement in the SI direction. In addition, the four MLLHs all caused different degrees of ligament strain, MLLH-F2 the greatest.

## Data availability statement

The original contributions presented in the study are included in the article/supplementary material, further inquiries can be directed to the corresponding authors.

## Ethics statement

The studies involving humans were approved by the Clinical Research Ethics Committee of the First Affiliated Hospital, Hengyang Medical School, University of South China (No. 2023LL0206001). The study was conducted in accordance with the principles of the Declaration of Helsinki. The studies were conducted in accordance with the local legislation and institutional requirements. The participants provided their written informed consent to participate in this study. Written informed consent was obtained from the individual(s) for the publication of any potentially identifiable images or data included in this article.

## Author contributions

BL: Data curation, Investigation, Methodology, Writing-review and editing, Formal Analysis, Software, Visualization, Writing-original draft. YL: Methodology, Writing-review and editing, Conceptualization, Supervision. CW: Methodology, Writing-review and editing, Data curation, Formal Analysis, Investigation, Project administration, Validation, Writing-original draft. ZX: Conceptualization, Data curation, Funding acquisition, Investigation, Methodology, Project administration, Resources, Supervision, Validation, Writing-review and editing.

## Funding

The author(s) declare that financial support was received for the research and/or publication of this article. The study was supported by Clinical Medical Technology Innovation Guidance Project of Hunan Province, China (grant number 2021SK51803).

## Conflict of interest

The authors declare that the research was conducted in the absence of any commercial or financial relationships that could be construed as a potential conflict of interest.

## Generative AI statement

The author(s) declare that no Generative AI was used in the creation of this manuscript.

## Publisher's note

All claims expressed in this article are solely those of the authors and do not necessarily represent those of their affiliated organizations, or those of the publisher, the editors and the reviewers. Any product that may be evaluated in this article, or claim that may be made by its manufacturer, is not guaranteed or endorsed by the publisher.



## References

- Al-Subahi, M., Alayati, M., Alshehri, M. A., Helal, O., Alhasan, H., Alalawi, A., et al. (2017). The effectiveness of physiotherapy interventions for sacroiliac joint dysfunction: a systematic review. *J. Phys. Ther. Sci.* 29, 1689–1694. doi:10.1589/jpts.29.1689
- Cohen, S. P. (2005). Sacroiliac joint pain: a comprehensive review of anatomy, diagnosis, and treatment. *Anesth. Analgesia* 101, 1440–1453. doi:10.1213/01.ane.0000180831.60169.ea
- Dontigny, R. L. (1990). Anterior dysfunction of the sacroiliac joint as a major factor in the etiology of idiopathic low back pain syndrome. *Phys. Ther.* 70, 250–262. doi:10.1093/ptj/70.4.250
- Eichenseer, P. H., Sybert, D. R., and Cotton, J. R. (2011). A finite element analysis of sacroiliac joint ligaments in response to different loading conditions. *Spine* 36, E1446–E1452. doi:10.1097/brs.0b013e31820bc705
- Enix, D. E., and Mayer, J. M. (2019). Sacroiliac joint hypermobility biomechanics and what it means for health care providers and patients. *PM and R J. Inj. Funct. Rehabilitation* 11 (Suppl. 1), S32–S39. doi:10.1002/pmrj.12176
- Fan, Z., and Wu, S. (2021). Based on the theory of 'bone staggered suture and sinew grooving', the characteristics of Lin's bone-setting manipulation in the treatment of sacroiliac joint dysfunction. *J. Trad. Chin. Orthop. Trauma* 33, 47–49.
- Farazdaghi, M. R., Motealleh, A., Abtahi, F., Panjan, A., Šarabon, N., and Ghaffarinejad, F. (2018). Effect of sacroiliac manipulation on postural sway in quiet standing: a randomized controlled trial. *Braz. J. Phys. Ther.* 22, 120–126. doi:10.1016/j.bjpt.2017.09.002
- García-Peñalver, U. J., Palop-Montoro, M. V., and Manzano-Sánchez, D. (2020). Effectiveness of the muscle energy technique versus osteopathic manipulation in the treatment of sacroiliac joint dysfunction in athletes. *Int. J. Environ. Res. Public Health* 17, 4490. doi:10.3390/ijerph17124490
- Hammer, N., Höch, A., Klima, S., Le Joncour, J.-B., Rouquette, C., and Ramezani, M. (2019). Effects of cutting the sacrospinous and sacrotuberous ligaments. *Clin. Anat. (New York, N.Y.)* 32, 231–237. doi:10.1002/ca.23291
- Hammer, N., Steinke, H., Lingslebe, U., Bechmann, I., Josten, C., Slowik, V., et al. (2013). Ligamentous influence in pelvic load distribution. *Spine J. Official J. North Am. Spine Soc.* 13, 1321–1330. doi:10.1016/j.spinee.2013.03.050
- Hing, W., Hall, T., Rivett, D., and Vicenzino, B. (2015). *The mulligan concept of manual therapy: textbook of techniques*. Elsevier Health Sciences.
- Huang, J., He, Y., Liu, H., He, Z., Wu, B., and Zhao, X. (2019). Advances in the diagnosis, treatment and research of sacroiliac joint misalignment. *Tissue Eng. Res. China* 23, 3201–3206.
- Jacob, H. A.C., and Kissling, R. O. (1995). The mobility of the sacroiliac joints in healthy volunteers between 20 and 50 years of age. *Clin. Biomech. (Bristol, Avon)* 10, 352–361. doi:10.1016/0268-0033(95)00003-4
- Joukar, A., Shah, A., Kiapour, A., Vosoughi, A. S., Duhon, B., Agarwal, A. K., et al. (2018). Sex specific sacroiliac joint biomechanics during standing upright: a finite element study. *Spine* 43, E1053–E1060. doi:10.1097/brs.0000000000002623
- Kamali, F., Zamanlou, M., Ghanbari, A., Alipour, A., and Bervis, S. (2019). Comparison of manipulation and stabilization exercises in patients with sacroiliac joint dysfunction patients: a randomized clinical trial. *J. Bodyw. Mov. Ther.* 23, 177–182. doi:10.1016/j.jbmt.2018.01.014
- Kiapour, A., Abdelgawad, A. A., Goel, V. K., Souccar, A., Terai, T., and Ebraheim, N. A. (2012). Relationship between limb length discrepancy and load distribution across the sacroiliac joint—a finite element study. *J. Orthop. Res.* 30, 1577–1580. doi:10.1002/jor.22119
- Kibsgård, T. J., Røise, O., Stuge, B., and Röhrli, S. M. (2012). Precision and accuracy measurement of radiostereometric analysis applied to movement of the sacroiliac joint. *Clin. Orthop. Relat. Res.* 470, 3187–3194. doi:10.1007/s11999-012-2413-5
- Kim, Y. H., Yao, Z., Kim, K., and Park, W. M. (2014). Quantitative investigation of ligament strains during physical tests for sacroiliac joint pain using finite element analysis. *Man. Ther.* 19, 235–241. doi:10.1016/j.math.2013.11.003
- Klima, S., Grunert, R., Ondruschka, B., Scholze, M., Seidel, T., Werner, M., et al. (2018). Pelvic orthosis effects on posterior pelvis kinematics an *in-vitro* biomechanical study. *Sci. Rep.* 8, 15980. doi:10.1038/s41598-018-34387-7
- Lee, C.-H., Hsu, C.-C., and Huang, P.-Y. (2017). Biomechanical study of different fixation techniques for the treatment of sacroiliac joint injuries using finite element analyses and biomechanical tests. *Comput. Biol. Med.* 87, 250–257. doi:10.1016/j.combiomed.2017.06.007
- Lindsey, D. P., Perez-Orribo, L., Rodriguez-Martinez, N., Reyes, P. M., Newcomb, A., Cable, A., et al. (2014). Evaluation of a minimally invasive procedure for sacroiliac joint fusion – an *in vitro* biomechanical analysis of initial and cycled properties. *Med. Devices Auckl. N.Z.* 7, 131–137. doi:10.2147/meder.s63499
- Liu, G., Feng, W., and Mak, F.-W. (2020). Clinical observation of Lin's manipulation combined with musculoskeletal ultrasound in the treatment of postpartum sacro-iliac articulation malposition. *J. Pract. traditional Chin. Med.* 36, 1065–1067.
- McLauchlan, G. J., and Gardner, D. L. (2002). Sacral and iliac articular cartilage thickness and cellularity: relationship to subchondral bone end-plate thickness and cancellous bone density. *Rheumatol. Oxf. Engl.* 41, 375–380. doi:10.1093/rheumatology/41.4.375
- Miller, J. A., Schultz, A. B., and Andersson, G. B. (1987). Load-displacement behavior of sacroiliac joints. *J. Orthop. Res.* 5, 92–101. doi:10.1002/jor.1100050112
- Nejati, P., Safarcherati, A., and Karimi, F. (2019). Effectiveness of exercise therapy and manipulation on sacroiliac joint dysfunction: a randomized controlled trial. *Pain Physician* 22, 53–61.
- Poilliot, A. J., Zwirner, J., Doyle, T., and Hammer, N. (2019). A systematic review of the normal sacroiliac joint anatomy and adjacent tissues for pain physicians. *Pain Physician* 22, E247–E274.
- Schuit, D., Mcpoil, T. G., and Mulesa, P. (1989). Incidence of sacroiliac joint malalignment in leg length discrepancies. *J. Am. Podiatric Med. Assoc.* 79, 380–383. doi:10.7547/87507315-79-8-380
- Shi, D., Wang, F., Wang, D., Li, X., and Wang, Q. (2014). 3-D finite element analysis of the influence of synovial condition in sacroiliac joint on the load transmission in human pelvic system. *Med. Eng. and Phys.* 36, 745–753. doi:10.1016/j.medengphy.2014.01.002
- Vanelderen, P., Szadek, K., Cohen, S. P., De Witte, J., Lataster, A., Patijn, J., et al. (2010). 13. Sacroiliac joint pain. *Pain Pract. Official J. World Inst. Pain* 10, 470–478. doi:10.1111/j.1533-2500.2010.00394.x
- Walker, J. M. (1992). The sacroiliac joint: a critical review. *Phys. Ther.* 72, 903–916. doi:10.1093/ptj/72.12.903
- Xiao, P., Li, Y., Yan, Y., Hou, D., Zhang, K., Xu, Z., et al. (2022). CT imaging anatomical observations of the sacroiliac joint space in normal people of different ages. *Chin. J. Clin. Anat.* 40, 143–149. doi:10.13418/j.issn.1001-165x.2022.2.05
- Xie, H. (2017). Clinical study on sacroiliac joint dysfunction treated by manipulation. *world Clin. Med.* 11, 140–142.
- Xu, Z., Li, Y., Zhang, S., Liao, L., Wu, K., Feng, Z., et al. (2020). A finite element analysis of sacroiliac joint displacements and ligament strains in response to three manipulations. *BMC Musculoskelet. Disord.* 21, 709. doi:10.1186/s12891-020-03735-y
- Zhang, Q.-H., Wang, J.-Y., Lupton, C., Heaton-Adegbile, P., Guo, Z.-X., Liu, Q., et al. (2010). A subject-specific pelvic bone model and its application to cemented acetabular replacements. *J. Biomechanics* 43, 2722–2727. doi:10.1016/j.jbiomech.2010.06.023
- Zhang, S., Chen, Y., Ren, R., Jiang, S., Cao, Y., and Li, Y. (2022). Quantitative study on the biomechanical mechanism of sacroiliac joint subluxation: a finite element study. *J. Orthop. Res. Official Publ. Orthop. Res. Soc.* 40, 1223–1235. doi:10.1002/jor.25132
- Zhang, S., Feng, Z., Chen, Y., Zhang, L., Qi, J., and Li, Y. (2019). CT imaging anatomical observations of the normal sacroiliac joint space in adults and its clinical significance. *Chin. J. Clin. Anat.* 37, 14–19. doi:10.13418/j.issn.1001-165x.2019.01.004
- Zhong, Z., Liao, L., Li, Z., Xu, X., Miao, X., and Zhang, K. (2025). Clinical study on the treatment of sacroiliac joint subluxation by tuina manipulation combined with pelvic floor biofeedback. *Mod. Chin. Med. Clin.*, 1–12.





## OPEN ACCESS

## EDITED BY

Jiaqiu Wang,  
London South Bank University, United Kingdom

## REVIEWED BY

Hans Korfage,  
Academic Centre for Dentistry Amsterdam, VU  
Amsterdam, Netherlands  
Luping Wang,  
China Jiliang University, China

## \*CORRESPONDENCE

Przemysław Stróżyk,  
✉ przemyslaw.strozyk@pwr.edu.pl

RECEIVED 13 January 2025

ACCEPTED 06 March 2025

PUBLISHED 01 April 2025

## CITATION

Stróżyk P and Bałchanowski J (2025) Unilateral  
chewing of foods. Analysis of energy balance  
and peak power of the mandibular  
elevator muscles.  
*Front. Bioeng. Biotechnol.* 13:1559555.  
doi: 10.3389/fbioe.2025.1559555

## COPYRIGHT

© 2025 Stróżyk and Bałchanowski. This is an  
open-access article distributed under the terms  
of the [Creative Commons Attribution License](#)  
(CC BY). The use, distribution or reproduction in  
other forums is permitted, provided the original  
author(s) and the copyright owner(s) are  
credited and that the original publication in this  
journal is cited, in accordance with accepted  
academic practice. No use, distribution or  
reproduction is permitted which does not  
comply with these terms.

# Unilateral chewing of foods. Analysis of energy balance and peak power of the mandibular elevator muscles

Przemysław Stróżyk<sup>1\*</sup> and Jacek Bałchanowski<sup>2</sup>

<sup>1</sup>Department of Mechanics, Materials and Biomedical Engineering, Faculty of Mechanical Engineering, Wrocław University of Science and Technology, Wrocław, Poland, <sup>2</sup>Department of Fundamentals of Machine Design and Mechatronic Systems, Faculty of Mechanical Engineering, Wrocław University of Science and Technology, Wrocław, Poland

**Introduction:** The paper presents the results concerning the energy (work) and peak power generated by the elevator muscles of the mandible (the masseter, medial pterygoid, and temporalis muscles) during unilateral chewing of selected food products in vitro. Since the act of chewing is a very complex issue in the biomechanics of the masticatory system, the research and analysis of the obtained results were therefore limited to the first cycle.

**Methods:** Determination of the peak energy and power of the muscles required: (1) preparation of food patterns, in the form of the function  $F = f(\Delta h)$  (force ( $F$ ) vs displacement ( $\Delta h$ )), based on experimental studies and (2) conducting numerical simulations using a 3D kinematic-dynamic model of the human masticatory system.

**Results and Discussion:** Based on the results, the peak energy and power of the muscles were determined based on food patterns. A comparative analysis was also performed to evaluate the energy and peak power generated by the aforementioned muscles during symmetrical incisal biting vs unilateral chewing of the same food products. The results indicate that (1) food height and texture significantly affect muscle energy and (2) the masticatory and medial pterygoid muscles generate more incredible energy and peak power on the working side than on the non working side, while the opposite was observed for the temporalis muscle and (3) comparative analysis showed that food position on the dental arch has a more significant effect on muscle peak power for foods with high texture heterogeneity than for foods with low texture heterogeneity.

## KEYWORDS

mastication, mandibular elevator muscles, numerical simulation, muscle energy, peak muscle power

## 1 Introduction

Energy (work) produced by muscles and their power are critical parameters associated with the functioning of organisms, enabling movement, postural stabilization, and interaction with the environment. In the context of humans, understanding the mechanisms governing muscle energy and power is crucial not only for biomechanics but also for sports medicine, rehabilitation, and the design of biomechanical systems.

Generally, analyzing the energy (work) and power generated by muscles can provide valuable insights into humans' evolution and motor adaptations in various environments.

Determining muscle work, the amount of energy expended by muscles during contraction is a complex process involving both mechanical and biochemical aspects. Muscles generate force, which translates into motion by applying moments of force to joints, a process can be modelled using dynamics equations. Muscle power can be determined based on knowledge of (1) muscle force, muscle contraction, and contraction time or (2) muscle force and contraction velocity.

Given this information, it is evident that the key parameter related to studies on muscle energy and power is muscle force. In general, the fundamental method for determining muscle forces relies on (1) analyzing motion dynamics and (2) biomechanical modelling, in which muscle forces are calculated based on balancing the moments of forces generated by muscles with external moments acting on selected body segments. Furthermore, studies (Kjær, 2004; Narici and Maganaris, 2006) indicate that muscles adapt to varying external loads through muscle fibres' structure and mechanical properties changes.

In the case of the muscles of the human masticatory system, it has been shown that the adaptation of the muscular system is primarily associated with the mechanical properties of food (Agrawal et al., 1998; Hiimeae et al., 1996; Koolstra, 2002; Mathevon et al., 1995; Shimada et al., 2012), which play a significant role in the act of chewing. Additionally, studies (Mioche et al., 1999; Stróżyk and Bałchanowski, 2018, Stróżyk and Bałchanowski, 2023) indicate that food patterns (typical mechanical characteristics in the form of force vs. displacement) impose individual muscle activity patterns (muscle force vs. muscle contraction), which must adapt to various functional requirements (Fitts et al., 1991) during the act of chewing.

The muscles playing a key role in the mechanical processing of food are the muscles of mastication, which enable its fragmentation and mixing with saliva, ultimately preparing the bolus of food. From a mechanical perspective, this process requires the coordinated activity of muscles, especially the masseter, temporalis, medial, lateral pterygoid, and suprahyoid and infrahyoid muscles.

Determining muscle forces in the masticatory muscles can be achieved using several methods, each with advantages and limitations. The most commonly used methods include (1) electromyography (EMG) (Ferrario and Sforza, 1996; Itoh et al., 1997; Mioche et al., 1999; Murray et al., 1999; Pruim et al., 1980; Ferrario et al., 2006; Castroflorio et al., 2008) and (2) biomechanical modeling, primarily based on numerical models (Stróżyk and Bałchanowski, 2016; Stróżyk and Bałchanowski, 2018; Stróżyk and Bałchanowski, 2023; Pachnicz and Stróżyk, 2021; Griffin et al., 1998; Wang et al., 2023; Pinheiro et al., 2021; Antic et al., 2016; Ackland et al., 2015).

Many publications over the past 30 years suggest that EMG measurements are most frequently conducted for the masseter and temporalis muscles, as these measurements do not present significant difficulties (Blanksma and van Eijden, 1995; Mioche et al., 1999; Plesh et al., 1996; Roark et al., 2003). In contrast, measuring the lateral and medial pterygoid muscles is challenging due to the intraoral placement of electrodes (Koole et al., 1990;

Murray et al., 1999; Wood et al., 1986), which may interfere with the natural chewing pattern of food.

In the context of muscle energy and power, electromyography does not allow the determination of a fundamental parameter such as muscle contraction. Therefore, the data obtained from EMG measurements will make determining muscle energy and power impossible. However, an important advantage of EMG is that measurements can be made *in vivo*.

An analysis of the act of chewing in terms of muscle energy and power reveals that a solution enabling the simultaneous determination of parameters needed to calculate these values is biomechanical modelling. This approach, however, requires the development of advanced numerical models utilizing principles of solid mechanics or deformable body mechanics. In the first case, muscles are modeled using vectors (Pachnicz and Stróżyk, 2021; Stróżyk and Bałchanowski, 2016, Stróżyk and Bałchanowski, 2018, Stróżyk and Bałchanowski, 2023; Gross et al., 2001; Gröning et al., 2012; Langenbach and Hannam, 1999), while in the second case, muscle models are based on Hill's model or volumetric models (Zajac, 1989; Winters, 1990; Sagl et al., 2019; De Zee et al., 2007; Röhrle and Pullan, 2007).

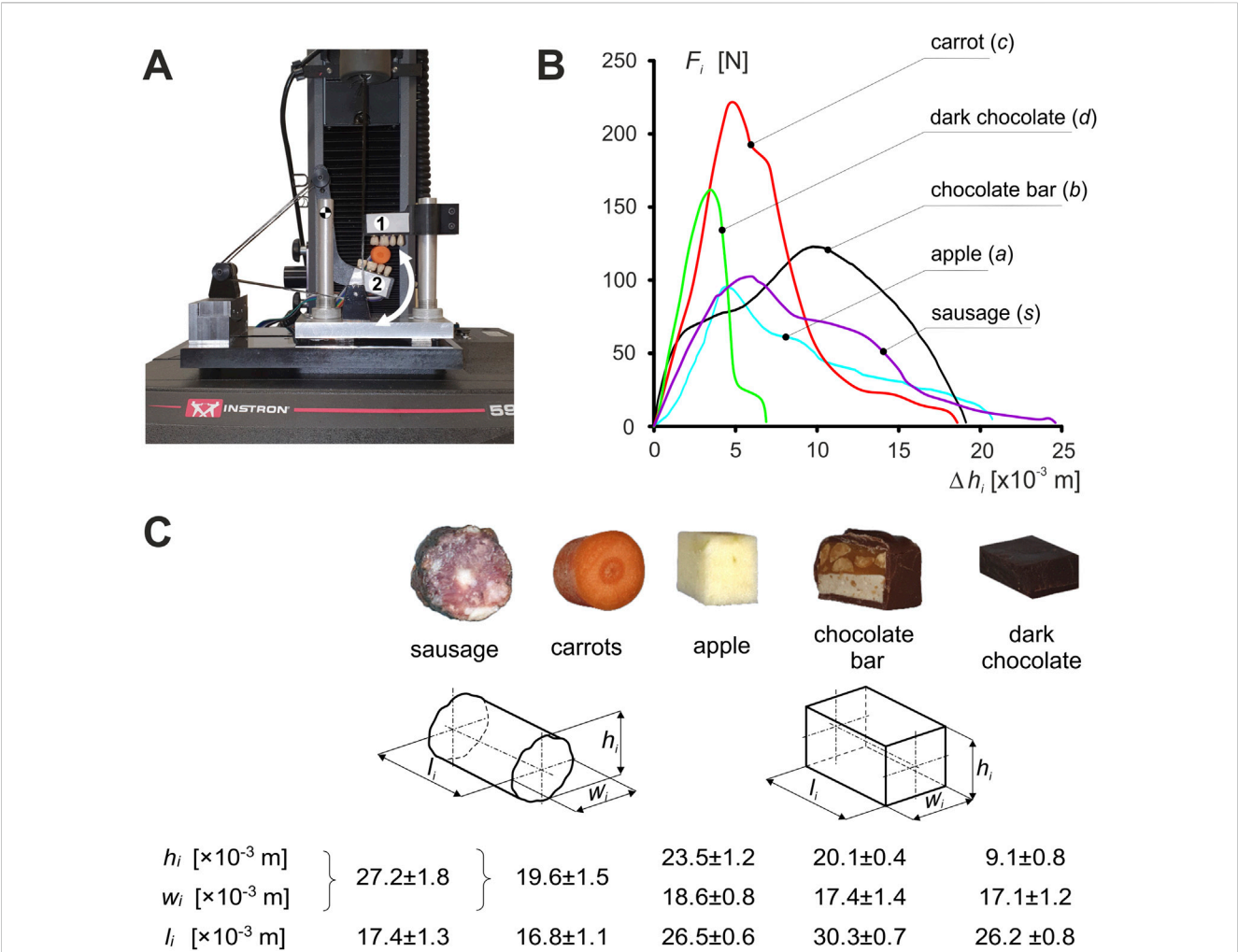
Literature analysis indicates that the kinematic-dynamic model is an optimal model enabling the simultaneous determination of muscle force, contraction, and contraction velocity and, thus, muscle energy and power as a function of food texture. However, its application requires preparing appropriate boundary conditions based on the dynamic characteristics of food (Stróżyk and Bałchanowski, 2018, Stróżyk and Bałchanowski, 2023) and incisal point paths (trajectory) (Stróżyk and Bałchanowski, 2023; Bhatka et al., 2004; Buschang et al., 2007; Nishigawa et al., 1997; Piacino et al., 2012; Slavicek, 2010).

An interesting solution involves integrating computational models (e.g., kinematic-dynamic models) with EMG data and imaging techniques (e.g., magnetic resonance imaging (MRI) and computed tomography (CT)), allowing for more precise determination of muscle forces and analysis of various factors influencing their values, such as changes in maxilla and mandible geometry or malocclusion (Tanne et al., 1995; van Eijden et al., 2003).

The primary aim of this study was to determine the energy and peak power generated by the elevator muscles of the mandible (the masseter, medial pterygoid, and temporalis muscles) for the working and non-working sides during unilateral chewing as a function of selected foods.

Numerical simulations were based on inverse kinematic and dynamic analysis (Lenton et al., 2018; Neptune and van den Bogert, 1998), where the variables were food patterns (classical characteristics in the form of force vs. displacement functions) and kinematic inputs in the form of incisal point paths (trajectory) corresponding to selected foods (Stróżyk and Bałchanowski, 2016, Stróżyk and Bałchanowski, 2018, Stróżyk and Bałchanowski, 2023).

For this study, a proprietary kinematic-dynamic model (Stróżyk and Bałchanowski, 2016, Stróżyk and Bałchanowski, 2018, Stróżyk and Bałchanowski 2023) was developed and utilized to conduct simulations that determined muscle energy and power depending on the food. Additionally, a comparative analysis was conducted to compare the energy and peak power generated by the elevator



**FIGURE 1** Experimental studies: **(A)** unilateral chewing simulator - one upper grip (maxilla), two lower grip (mandible)) [developed based on a patent application - Stróżyk, 2021], **(B)** characteristics of foods ( $i$ ) and **(C)** mean values of the dimensions of food samples  $\pm$ SD. ( $i$  = c, s, a, b, d).

muscles of the mandible during unilateral chewing (Stróżyk and Bałchanowski, 2020) and the symmetrical incisal biting of the same foods.

During the act of chewing, the kinematic-dynamic parameters of the masticatory system adapt to changing boundary conditions related to variations in (1) the mechanical properties and geometric dimensions of food and (2) the food's position on the dental arches. Consequently, the study and analysis of results were limited to the first cycle for both unilateral chewing and symmetrical incisal biting.

Mechanical analysis of the masticatory system indicates that it is an advanced biomechanical system used for dynamic food processing (Stokes et al., 2013). Thus, determining the energy (work) and peak power produced by the elevator muscles of the mandible may be helpful for (1) understanding the functioning of the masticatory system and (2) diagnosing and treating disorders of the stomatognathic system. Furthermore, the presented results can also be utilized in designing mechatronic systems inspired by the mechanical functioning of the masticatory system.

## 2 Material and methods

Determination of energy (work) and peak power for the elevator muscles of the mandible (masseter muscle (M), medial pterygoid muscle (P) and temporalis muscle (T)) during unilateral mastication required (1): preparation of a numerical model of the human masticatory system (Stróżyk and Bałchanowski, 2023), (2) development of external loading patterns.

The computational model of the human masticatory system consisted of two members, i.e., a stationary skull and a movable mandible. The external load of the model was the characteristics of the food ( $i$ ) in the form of the function  $F_i = f(\Delta h_i)$  - force ( $F_i$ ) vs displacement ( $\Delta h_i$ ), determined from experimental studies of unilateral chewing of food. On the other hand, the initial positions of the model were determined based on the prepared chewing loops individually for each food (Stróżyk and Bałchanowski, 2023). The computational model developed based on the aforementioned guidelines was used to conduct simulation studies of unilateral chewing of selected foods to determine the

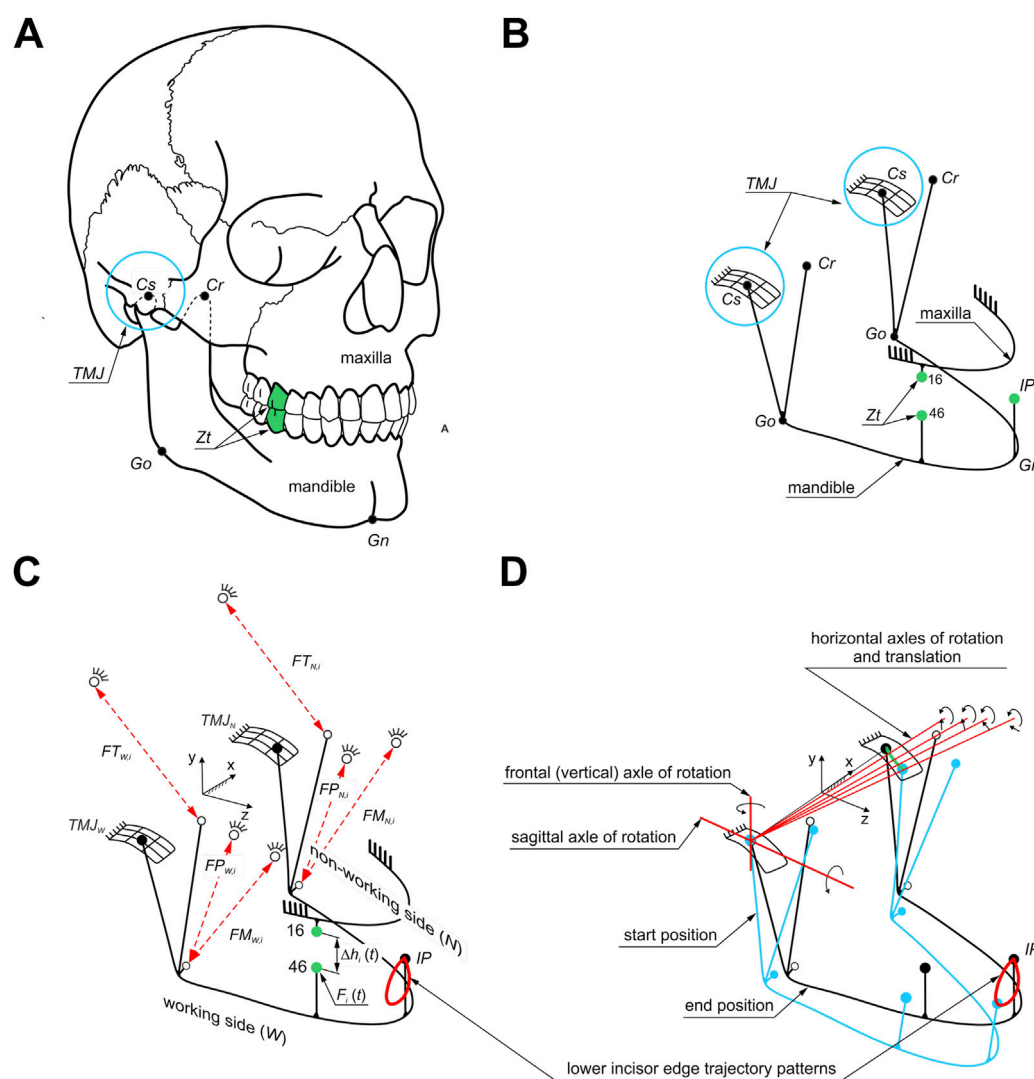


FIGURE 2

Model of the masticatory system: (A) location of selected anthropometric points ( $Go$ ,  $Gn$ ,  $Cr$ ,  $Cs$ ) on the mandible and a pair of corresponding molars ( $Zt$ ), (B) geometric model, (C) computational model of unilateral chewing. Symbols (1): anthropometric points:  $Go$  - location of the junction of the mandibular branch and mandibular body,  $Gn$  - the lowest point on the mandible,  $Cr$  - the highest point on the beak process of the mandible,  $Cs$  - the highest point on the mandibular condyle (2), points corresponding to the selected pair of molars ( $Zt$ ) (teeth 46-16) (3), muscle forces: masseter muscle ( $F_{MW,i}$ ,  $F_{MN,i}$ ), medial pterygoid muscle ( $F_{PW,i}$ ,  $F_{PN,i}$ ) and temporalis muscle ( $F_{TW,i}$ ,  $F_{TN,i}$ ) and (4) incisal point ( $IP$ ) including the masticatory loop, and (D) kinematics of the masticatory system during unilateral biting.

kinematic and dynamic parameters necessary to determine the energy and peak power of the muscles.

The present work continues the article on unilateral biting (Stróżyk and Bałchanowski, 2023). Therefore, selected aspects of food testing and numerical simulations are described in an abbreviated form compared to the article.

## 2.1 Determination of model load and food characteristics

The general algorithm for determining the characteristics of foods corresponding to unilateral chewing, as well as incisal biting, is described in detail in Stróżyk and Bałchanowski

(2016), Stróżyk and Bałchanowski (2018), and Stróżyk and Bałchanowski (2023); Stróżyk et al. 2018. An in-house designed test rig (Figure 1A) (developed based on a patent application (Stróżyk, 2021) was used in the experimental study to determine the characteristics of foods corresponding to the first cycle of unilateral chewing.

The measuring system consisted of two grips (holding grips), i.e., the upper (maxilla) and lower (mandible), imitating fragments of dental arches. To make the tests similar, mechanically, to natural unilateral chewing, acrylic dental prostheses (premolars and molars) were attached to each holder. During testing, the stand was mounted on an Instron 5944 test machine. All foods were tested at the same chewing velocity of  $V = 0.02$  m/s (Stróżyk and Bałchanowski, 2023).



Five foods were used in the study ( $i = c$  (carrot),  $a$  (apple),  $d$  (dark chocolate),  $b$  (chocolate bar),  $s$  (sausage)) (Stróżyk and Bałchanowski, 2016, Stróżyk and Bałchanowski, 2018, and Stróżyk and Bałchanowski, 2023). The samples in terms of dimensions (height ( $h_i$ ), width ( $w_i$ ) and length ( $l_i$ )) were similar to a typical bite of food, while the shape was product-dependent (Figure 1C).

Based on the results, the characteristics (patterns) of the selected foods were determined in the form of the classical function  $F_i = f(\Delta h_i)$  (Figure 1B).

## 2.2 Numerical model of the human masticatory system

Determination of the energy (work) and peak power of the elevator muscle of the mandible required a dynamic analysis of unilateral chewing of selected foods. For this purpose, a computational model was prepared (Stróżyk and Bałchanowski, 2023), the geometry of which was prepared based on anatomical models (skull 8,500 and mandible 8,596) from Synbone (SYNBONE AG, Tardisstrasse 199, 7,205 Zizers, Switzerland). Then, based on the geometric model (Figure 2A), the anthropometric points of the mandible (Phuntsho et al., 2018; Saini et al., 2021) were introduced based on which its model was prepared as a rigid solid (Figure 2B). The maxilla, on the other hand, was modelled in the form of stationary support correlated with corresponding points on the mandible, which in effect made it possible to model a pair of corresponding teeth between which an occlusal force ( $F_i$ ) acts as a function  $F_i = f(\Delta h_i)$ . The force was applied at a point on the occlusal surface of the first molar (Stróżyk and Bałchanowski, 2023). The muscles were modelled using linear kinematic forcing, which allows the mandible to move relative to the maxilla during chewing (Stróżyk and Bałchanowski, 2023). A schematic of the geometric and computational model is shown in Figure 2.

The mandibular model at baseline is fixed at the *TMJ* and the initial attachment points of the masseter muscle, medial pterygoid muscle and temporalis muscle (Figure 2C).

In addition, the numerical simulation assumed that the mandibular condyle on the working side would have a fixed centre of rotation through which the instantaneous axes of rotation would pass. In contrast, the condyle on the non-working side would be able to rotate and translate (Figure 2D).

Based on the developed chewing loops (Stróżyk and Bałchanowski, 2023), there are contact kinematic pairs with five degrees of freedom (three rotations and two displacements) in the *TMJ* on the working ( $W$ ) and non-working ( $N$ ) sides. The mandible's movement model relative to the skull during unilateral chewing is based on the function describing the chewing loops specified for foods. The functions of the chewing loops describing the movement of the *IP* point (Figure 2C) on the mandibular incisor during unilateral chewing of food allowed us to determine the functions of changes in the elongation of individual muscles during chewing (Figure 2; Stróżyk and Bałchanowski, 2023). The

proposed way of fixing the model allowed for the simulation of the complex movement of the lower incisors during chewing (Figure 2). A detailed description of the model can be found in Stróżyk and Bałchanowski (2023).

## 3 Results

The kinematic and dynamic parameters necessary to determine the energy (work) and peak power of the elevator muscles of the mandible were determined in two stages: in the first stage, experimental studies were carried out to determine food patterns (Figure 1), while in the second stage, numerical simulations of unilateral chewing were carried out, based on which muscle forces, muscle contractions and muscle contraction time were determined on the working ( $W$ ) and non-working ( $N$ ) sides, respectively, depending on the food pattern.

Since the calculations and analyses were comparative, the simulation assumed an identical chewing velocity with the molars, i.e.,  $V = 0.02$  m/s (Stróżyk and Bałchanowski, 2023). The energy (work) required to bite ( $E_{Xi}$ ) the selected foods was determined from the characteristics of the foods (Figure 1) based on Equation 1.

$$E_{Xi} = \int_0^{h_{max,i}} F_i d(\Delta h_i) \quad (1)$$

Based on the data obtained, after numerical simulations, the characteristics were first determined in the form of a function  $q_{jki} = q_{jki}(t_{ji})$  i.e., muscle length ( $q_{jki}$ ) vs time ( $t_{ji}$ ) (Figure 3), and muscle contraction  $\Delta q_{jki}$  (Equation 2), both for the working side ( $W$ ) and non-working side ( $N$ ), for the masseter muscle, medial pterygoid muscle and temporalis muscle, respectively.

$$\Delta q_{jki} = |q_{jki}(t_{ji}) - q_{jki}(0)| \quad (2)$$

where:

- $q_{jki}(0)$ —initial muscle length for time  $t = 0$ s—open mouth,
- $q_{jki}(t_{ji})$ —muscle length determined for time ( $t_{ji}$ ) from the interval  $0 \div t$ ,
- $j = M, P, T$ ,
- $k = W, N$ .

The contraction velocity  $V_{jkmax,i}$  corresponding to the maximum muscle force  $F_{jkmax,i}$  was determined from Equation 3, for both the working side ( $W$ ) and non-working side ( $N$ ), for the masseter muscle, medial pterygoid muscle and temporalis muscle, respectively.

$$V_{jkmax,i} = \Delta q_{jkmax,i} / t_{jmax,i} \quad (3)$$

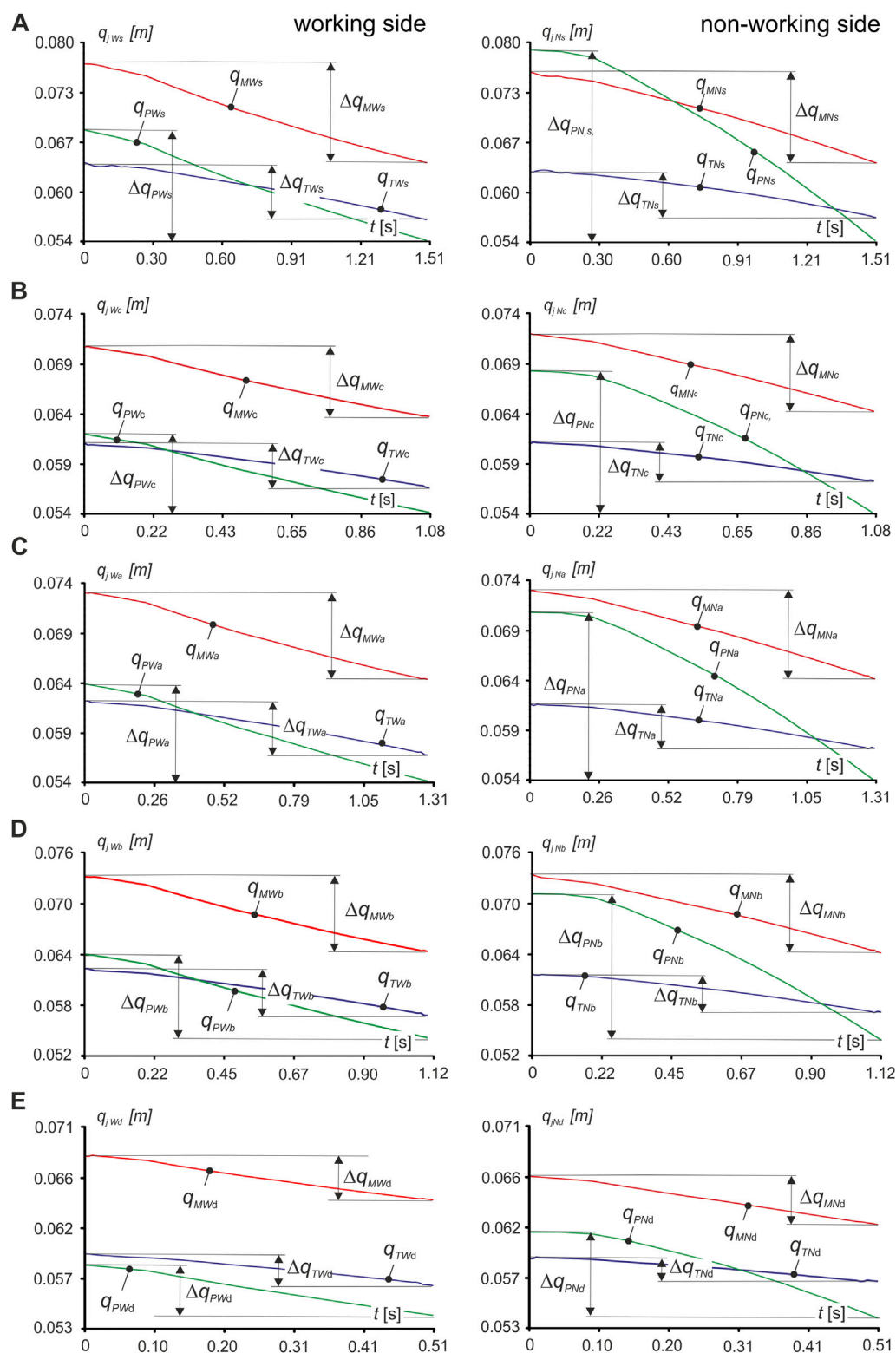
where:

$\Delta q_{jkmax,i}$  - muscle contraction corresponding to maximum muscle force for time  $t_{jmax,i}$ ,  $t_{jmax,i}$  - contraction time corresponding to maximum muscle force,

- $j = M, P, T$ ,
- $k = W, N$ .

Based on the data above, dynamic muscle patterns (muscle force  $F_{jk,max,i}$  vs. muscle contraction  $\Delta q_{jki}$ ) were developed





**FIGURE 3**  
Runs of functions describing the change in muscle length  $q_{jki}$  lying on the right side with molars: on the working side (W) and on the non-working side (N) when unilateral chewing food: (A) sausage s, (B) carrot c, (C) apple a, (D) chocolate bar b, (E) dark chocolate d. ( $j = M, P, T$ ;  $k = N, W$ ;  $i = c, s, a, b, d$ ).

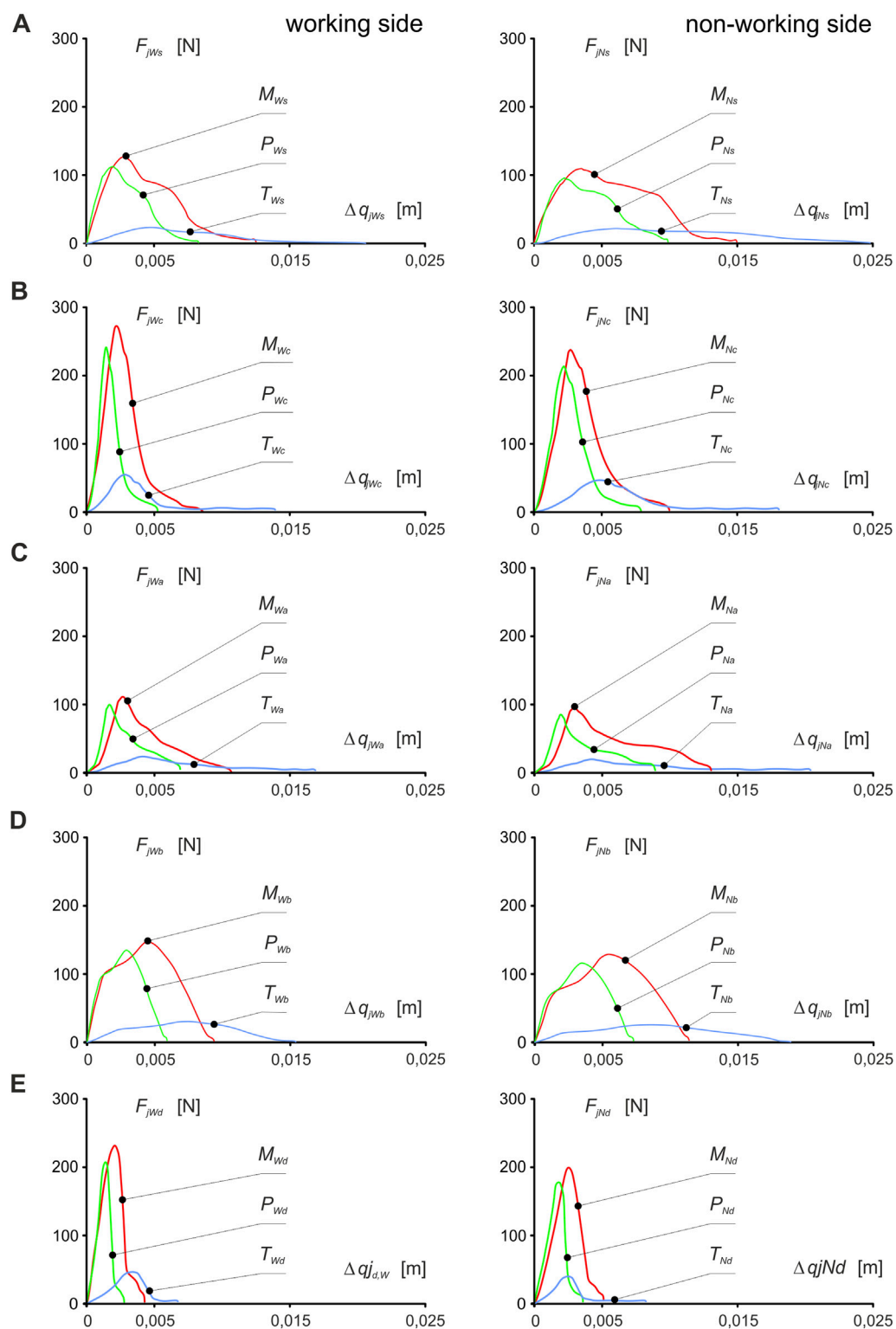


FIGURE 4

Dynamic patterns of mandibular elevator muscle forces (muscle force vs muscle contraction) about food: (A) sausage s, (B) carrot c, (C) apple a, (D) chocolate bar b, (E) dark chocolate d and the side of the mandible, i.e. working (W) and non-working (N) sides, respectively, for the masseter muscle ( $F_{MWi}$  vs  $\Delta q_{MWi}$ ,  $F_{MNi}$  vs  $\Delta q_{MNi}$ ), medial pterygoid muscle ( $F_{PW_i}$  vs  $\Delta q_{PW_i}$ ,  $F_{PNi}$  vs  $\Delta q_{PNi}$ ) and temporalis muscle ( $F_{TW_i}$  vs  $\Delta q_{TW_i}$ ,  $F_{TNi}$  vs  $\Delta q_{TNi}$ ). .  $i = M, P, T$ ;  $i = c, s, a, b, d$  - [Stróżyk and Bałchanowski, 2023].

**TABLE 1** Kinematic-dynamic parameters (energy  $E_{jki}$ , contraction velocity  $V_{jki}$  corresponding to maximum unilateral chewing force, maximum muscle force  $F_{jkmax,i}$  and peak power  $PP_{jki}$  of the dynamic patterns of elevator muscles of mandible forces (muscle force vs muscle contraction) about food and mandibular side, i.e. working side ( $W$ ) and non-working side ( $N$ ), respectively, for the masseter (masseter muscle ( $M$ ), medial pterygoid muscle ( $P$ ), temporalis muscle ( $T$ )) depending on food ( $i$ ) and sides of the mandible i.e. working side ( $W$ ) and non-working side ( $N$ ) ( $j = M, P, T$ ;  $k = W, N$ ) - The maximum values of muscle forces ( $F_{jkmax,i}$ ) were determined based on the results presented in Stróżyk and Bałchanowski (2023).

Side	Kinematic and dynamic parameters	Sausage (s)	Carrot (c)	Apple (a)	Chocolate bar (b)	Chocolate (d)
Masseter ( $M$ )						
Working	$E_{MWi}$ [J]	0.62	0.49	0.33	0.56	0.18
	$PP_{MWi}$ [W]	1.90	2.80	0.40	0.95	0.73
	$F_{MWmax,i}$ [N]	126.9	274.3	112.2	233.2	149.4
	$V_{MWi}$ [m/s]	0.0162	0.0139	0.0049	0.0091	0.0053
Non-working	$E_{MNi}$ [J]	0.45	0.36	0.24	0.41	0.13
	$PP_{MNi}$ [W]	0.85	1.82	0.28	0.78	0.64
	$F_{MNmax,i}$ [N]	108.8	235.5	96.2	200.3	127.8
	$V_{MNi}$ [m/s]	0.0116	0.0118	0.0049	0.0088	0.005
Medial pterygoid ( $P$ )						
Working	$E_{PW_i}$ [J]	0.35	0.24	0.17	0.27	0.08
	$PP_{PW_i}$ [W]	0.81	1.55	0.19	0.49	0.28
	$F_{PWmax,i}$ [N]	113.5	244.7	100.6	209.3	134.5
	$V_{PW_i}$ [m/s]	0.0074	0.0101	0.0026	0.0053	0.0023
Non-working	$E_{PNi}$ [J]	0.26	0.18	0.13	0.20	0.15
	$PP_{PNi}$ [W]	0.35	1.42	0.11	0.35	0.25
	$F_{PNmax,i}$ [N]	97.3	209.8	86.2	179.2	115.4
	$V_{PNi}$ [m/s]	0.0052	0.0084	0.0022	0.0045	0.0022
Temporalis ( $T$ )						
Working	$E_{TW_i}$ [J]	0.14	0.11	0.07	0.12	0.04
	$PP_{TW_i}$ [W]	0.41	0.40	0.09	0.20	0.15
	$F_{TWmax,i}$ [N]	24.4	53.4	22.7	46.1	29.3
	$V_{TW_i}$ [m/s]	0.0176	0.01	0.0053	0.0099	0.0056
Non-working	$E_{TNi}$ [J]	0.18	0.14	0.09	0.15	0.05
	$PP_{TNi}$ [W]	0.39	0.44	0.08	0.32	0.14
	$F_{TNmax,i}$ [N]	20.9	45.9	19.4	39.4	25.0
	$V_{TNi}$ [m/s]	0.0254	0.0141	0.0074	0.0181	0.0057

(Figure 4) from which the energy values  $E_{jki}$  from Equation 4 and the peak power value  $PP_{jki}$  from Equation 5 generated by a single muscle, after working side and non-working side were calculated (Table 1).

$$E_{jki} = \int_0^{\Delta q_{jki}} F_{jki} d(\Delta q_{jki}) \quad (4)$$

$$PP_{jki} = F_{jkmax,i} \times V_{jkmax,i} \quad (5)$$

Where:

$$j = M, P, T, \\ k = W, N.$$

## 4 Discussion

The analysis of the results obtained from numerical simulations demonstrated that work (energy) and peak power are parameters that can be utilized for qualitative and quantitative assessment of the effect of food (characterized by the function  $F_i = f(\Delta h_i)$ -force ( $F_i$ ) vs. displacement ( $\Delta h_i$ )) on the functioning of the masticatory system during unilateral chewing.

Detailed analysis also revealed that obtaining the same energy value for two foods with differing textures is possible. The results showed no explicit relationship between muscle force and muscle energy, such as a

high force value = high energy value. For example, In the study (Stróżyk and Bałchanowski, 2023), the maximum muscle forces during unilateral chewing were reported, demonstrating that the masseter muscle generates the most significant force, e.g., for sausage 126.9N and 108.8N and chocolate 233.2N and 200.3N, for the working and non-working sides respectively. In Table 1, the energy values for the masseter muscle for sausage and chocolate were 0.62J and 0.18J for the working side and 0.45J and 0.13J for the non-working side, respectively. The obtained energy values are attributed to differences in the height of sausage and chocolate—the difference was 18.1 mm. This finding indicates that the height of the food significantly affects the contraction of the elevator muscles of the mandible and their energy. A similar relationship to energy was also observed for the muscle's peak power (Table 1).

The results were analyzed using the percentage difference ( $|\Delta|$ ) between values A and B, determined based on the general Equation 6.

$$|\Delta| = 2(A-B) / (A + B) \times 100\% \quad (6)$$

## 4.1 Limitations of the model

The model's limitations include two factors (1): the measurement setup used in experimental studies to determine food characteristics (patterns) in the form of the function  $F_i = f(\Delta h_i)$ , and (2) the numerical model. In the experimental studies, a unilateral chewing simulator replicates a section of the mandibular and maxillary dental arch (Figure 1). The measurement setup allowed rotation about the hinge axis but not the vertical axis. Due to these limitations, food characteristics were determined during the crushing phase for the first cycle of unilateral chewing.

Another limitation is the numerical model of the masticatory system (Figure 2), which included only the elevator muscles of the mandible (masseter, medial pterygoid, and temporalis muscles) (Stróżyk and Bałchanowski, 2016; Stróżyk and Bałchanowski, 2018; Stróżyk and Bałchanowski, 2023; Pachnicz and Stróżyk, 2021) modelled as single vectors (Kashi et al., 2010; Tuijt et al., 2010; Pinheiro et al., 2021). Only one geometric model of the masticatory system was used in the numerical simulations.

The temporomandibular joint was modelled as a contact kinematic pair with five degrees of freedom (three rotations and two displacements) without considering the soft tissues (joint capsule, ligaments and articular disc). In contrast, the connection between the tooth and the body of the mandible did not consider the periodontal ligament with its receptors.

Despite these limitations, the model satisfies the fundamental criteria of solid body mechanics and conditions corresponding to unilateral chewing [boundary conditions (Stróżyk and Bałchanowski, 2018; Stróżyk and Bałchanowski, 2023)]. Thus, it can be used in numerical simulations to identify differences in the functioning of the elevator muscles of the mandible depending on the food texture during unilateral chewing.

## 4.2 Energy of a single muscle

The analysis of the data in Table 1 shows that during unilateral chewing, the masseter muscle (*M*) has the most

significant influence on the energy (work) of the muscular system (elevator muscles of the mandible), while the temporalis muscle (*T*) has the least influence, regardless of food type or mandibular side. The average percentage difference between them is  $\Delta_{MTW} = 127.9\%$  for the working side (*W*) and  $\Delta_{MTN} = 89.3\%$  for the non-working side (*N*). However, the average percentage difference (regardless of food type) between the medial pterygoid muscle (*P*) and the masseter (*M*) and temporalis (*T*) muscles for the working and non-working sides is  $\Delta_{PMW} = 67.0\%$  and  $\Delta_{PTW} = 77.4$  and  $\Delta_{PMN} = 64.4\%$  and  $\Delta_{PTN} = 28.9\%$ , respectively.

As expected, the results indicate that the masseter and medial pterygoid muscles generate more incredible energy (work) on the working side than on the non-working side. The average percentage difference between sides is  $\Delta_{MWN} = 31.8\%$  for the masseter muscle and  $\Delta_{PWN} = 29.5\%$  for the medial pterygoid muscle. In contrast, the temporalis muscle generates more energy on the non-working side than on the working side, which is the opposite of the behaviour observed for the masseter and medial pterygoid muscles. Regardless of food texture, the average difference between sides is  $\Delta_{TWN} = 25.0\%$ .

These relationships can be interpreted in terms of solid body mechanics, considering the numerical model of the masticatory system (Figure 2C) and the boundary conditions. During unilateral chewing, the masseter and medial pterygoid muscles on the working side overcome the vertical resistance associated with crushing the food. The temporalis muscle on the working side stabilizes and assists (via its anterior portion) the masseter and medial pterygoid muscles in pressing the mandibular teeth against the maxillary teeth. This stabilization is due to the temporalis muscle's role in maintaining the temporary centre of mandibular rotation in the TMJ during elevation (Figure 2D). On the non-working side, the masseter and medial pterygoid muscles stabilize the mandible, preventing rotation around the sagittal axis during elevation. Meanwhile, the temporalis muscle retracts the mandible and rotates it about the vertical axis due to the oblique positioning of the mandible relative to the maxilla. Consequently, the temporalis muscle performs work associated with mandibular displacement and rotation, as well as overcoming horizontal resistance of the food linked to the imposed trajectory of the lower incisors (Figure 2D).

## 4.3 Energy of the muscular system

### 4.3.1 Unilateral chewing

The analysis of total energy ( $E_{TUi}$ ) determined from numerical simulations (Table 2) indicates that during unilateral chewing, the elevator muscles of the mandible generate the highest energy for sausage (*s*) and the lowest for chocolate (*d*), with respective values of 2.00J and 0.54J. The percentage difference ( $\Delta_{ii}$ ) between the above foods is as high as  $\Delta_{sd} = 115\%$ . For other foods (Table 2), including a chocolate bar (*b*), apple (*a*), and carrot (*c*), the percentage differences relative to sausage are significantly more minor, amounting to  $\Delta_{sb} = 16\%$ ,  $\Delta_{sa} = 64\%$ , and  $\Delta_{sc} = 27\%$ , respectively.

Table 2 also presents the energy values required to destroy the food samples, determined through experimental studies (Stróżyk and Bałchanowski, 2023). A comparative analysis of the energy for selected products (*i*) shows that the percentage difference ( $\Delta E_{UXi}$ )

TABLE 2 Total energy values obtained from numerical simulations ( $E_{TUi}$ ) and experimental studies ( $E_{TXi}$ ), and the percentage differences ( $\Delta E_{UXi}$ ) between them for selected foods ( $i$ ).

Foodstuff ( $i$ ) <sup>a</sup>	Total energy [J]		Percentage difference [%]
	Numerical simulation ( $U$ )	Experimental studies ( $X$ )	
	$E_{TUi}$ <sup>b</sup>	$E_{TXi}$	$\Delta E_{UXi}$
Sausage ( $s$ )	2.00	1.93	3.6
Carrot ( $c$ )	1.52	1.48	2.7
Apple ( $a$ )	1.03	0.98	5.0
Chocolate bar ( $b$ )	1.71	1.74	1.7
Chocolate ( $d$ )	0.54	0.53	1.9

<sup>a</sup> $i = s, c, a, b$  and  $d$ .  
<sup>b</sup> $E_{TUi} = E_{MWi} + E_{PWi} + E_{TWi} + E_{MNi} + E_{PNi} + E_{TNi}$  (Table 1).

TABLE 3 Percentage differences between: (1) energy determined for unilateral chewing ( $E_{WUi}$ ;  $E_{Wli}$ ) and symmetrical incisal biting ( $E_{NUi}$ ;  $E_{Nli}$ ), for the working side ( $\Delta E_{WUi}$ ) and non-working side ( $\Delta E_{NUi}$ ) and (2) total energy ( $\Delta E_{Ui}$ ) for unilateral chewing ( $E_{TUi}$ ) and symmetrical incisal biting ( $E_{Tli}$ ), depending on the food type ( $i$ ).

Working side ( <i>W</i> )			Non-working side ( <i>N</i> )			Total Energy [J]		Percentage difference [%]
Energy [J]		Percentage difference [%]	Energy [J]		Percentage difference [%]			
Unilateral chewing	Symmetric incisal biting		Unilateral chewing	Symmetric incisal biting				
$E_{WUi}$ <sup>b</sup>	$E_{Wli}$ <sup>c</sup>	$\Delta E_{WUli}$	$E_{NUi}$ <sup>b</sup>	$E_{Nli}$ <sup>c</sup>	$\Delta E_{NUli}$	$E_{TUi}$ <sup>d</sup>	$E_{Tli}$ <sup>e</sup>	$\Delta E_{Uli}$
Sausage ( <i>s</i> )								
1.11	0.36	102.0	0.89	0.36	84.8	2.00	0.72	94.1
Carrot ( <i>c</i> )								
0.84	0.56	40.0	0.68	0.56	19.41	1.52	1.12	30.3
Apple ( <i>a</i> )								
0.57	0.20	96.1	0.46	0.20	78.8	1.03	0.40	88.1
Chocolate bar ( <i>b</i> )								
0.95	0.24	119.3	0.76	0.24	104.0	1.71	0.48	112.3
Chocolate ( <i>d</i> )								
0.30	0.19	44.9	0.24	0.19	23.33	0.54	0.38	34.8

<sup>a</sup> $i = s, c, a, b$  and  $d$ .  
<sup>b</sup> $E_{WUi} = E_{MWi} + E_{PWi} + E_{TWi}$  and  $E_{NUi} = E_{MNi} + E_{PNi} + E_{TNi}$  (Table 1).  
<sup>c</sup>Stróżyk and Bałchanowski (2020).  
<sup>d</sup> $E_{TUi} = E_{WUi} + E_{NUi}$ .  
<sup>e</sup> $E_{Tli} = E_{Wli} + E_{Nli}$ .

between the experimental and numerical results is  $\Delta E_{UXi} \leq 5.0\%$ . The highest percentage difference was observed for the apple  $\Delta E_{UXa} = 5.0\%$ , while the lowest was for the chocolate bar  $\Delta E_{UXb} = 1.7\%$ . The percentage differences for sausage, carrot, and chocolate were  $\Delta E_{UXs} = 3.6\%$ ,  $\Delta E_{UXc} = 2.7\%$ , and  $\Delta E_{UXd} = 1.9\%$ , respectively. These results ( $\Delta E_{UXi}$ ) indicate good agreement between experimental studies and numerical calculations. The differences are primarily attributed to the limitations of the simulator used in the experimental studies and the constraints of the numerical model.

4.3.2 Unilateral chewing vs symmetrical incisal biting

Based on the energy values (Table 3), it can be observed that on the working side, the highest percentage differences ( $\Delta E_{WUi}$ ) between unilateral chewing and symmetrical incisal biting were noted for the chocolate bar ( $\Delta E_{WUlb} = 119.3\%$ ), and the smallest for carrot ( $\Delta E_{WUlc} = 40.0\%$ ). In contrast, for sausage and apple, the values are comparable and amount to  $\Delta E_{WUIS} = 102.0\%$  and  $\Delta E_{WUIa} = 96.1\%$ , respectively. For chocolate, the percentage difference value ( $\Delta E_{WUID} = 44.9\%$ ) is almost identical to the value obtained for carrot ( $\Delta E_{WUlc} = 40.0\%$ ). On the non-



TABLE 4 Peak power for the working side ( $PP_{WUi}$ ) and non-working side ( $PP_{NUi}$ ), percentage differences ( $\Delta PP_{WNUi}$ ) between them, and total peak power ( $PP_{TUi}$ ) of the masticatory system, depending on the food type ( $i$ ).

Foodstuff <sup>a</sup>	Power (PP) [W]			
	Working side (W)	Non-working side (N)	Percentage difference [%]	Total power
	$PP_{WUi}^b$	$PP_{NUi}^c$	$\Delta PP_{WNUi}$	$PP_{TUi}^d$
Sausage ( <i>s</i> )	3.33	2.30	36.5	5.63
Carrot ( <i>c</i> )	6.82	5.19	27.1	12.01
Apple ( <i>a</i> )	0.93	0.80	14.6	1.73
Chocolate bar ( <i>b</i> )	2.36	2.10	11.9	4.46
Chocolate ( <i>d</i> )	1.98	1.62	19.2	3.60

<sup>a</sup> $i = s, c, a, b,$  and  $d$ .

<sup>b</sup> $PP_{WUi} = PP_{MWUi} + PP_{PWUi} + PP_{TWUi}$  (Table 1).

<sup>c</sup> $PP_{NUi} = PP_{MNUi} + PP_{PNUi} + PP_{TNUi}$  (Table 1).

<sup>d</sup> $PP_{TUi} = PP_{WUi} + PP_{NUi}$ .

working side, the percentage differences are lower than on the working side, with an average of 16% for sausage, apple, and chocolate bars and 50% for carrots and chocolate.

The results of the total energy of the masticatory system ( $E_{TUi}$ ) for unilateral chewing (Table 2) enable comparison with those for symmetrical incisal biting (Stróżyk and Bałchanowski, 2020). For a detailed comparative analysis, it was first established that the energy ( $E_{TUi}$ ) can be divided in a 55.4/44.6% ratio (Table 2) between the working side ( $E_{WUi}$ ) and the non-working side ( $E_{NUi}$ ) (Table 3). Meanwhile, the total energy of symmetrical incisal biting ( $E_{Ti}$ ), as per the assumptions in Stróżyk and Bałchanowski (2020), is divided equally (50.0/50.0%) between the working side ( $E_{Wi}$ ) and the non-working side ( $E_{Ni}$ ) (Table 3).

An analysis of the percentage differences ( $\Delta E_{Ui}$ ) between the total energy of unilateral chewing ( $E_{TUi}$ ) and symmetrical incisal biting ( $E_{Ti}$ ) indicates that the highest percentage differences are observed for the chocolate bar ( $\Delta E_{Uib} = 112.3$ ), sausage ( $\Delta E_{Uis} = 94.1\%$ ) and apple ( $\Delta E_{Uia} = 88.1\%$ ), while the most minor differences are for chocolate ( $\Delta E_{Uid} = 34.8\%$ ) and carrot ( $\Delta E_{Uic} = 30.3\%$ ) (Table 3).

The results presented in Table 3 demonstrate that energy differences primarily depend on (1) the food texture and (2) the food's position on the dental arch, i.e., the mechanisms of food damage.

Based on solid mechanics, it can be shown that the internal structure of materials significantly influences their mechanical parameters. Similar relationships can be observed when analyzing the biting and/or chewing of foods with different textures. Results reported in the literature (Agrawal et al., 1998; Fitts et al., 1991; Hiiemae et al., 1996; Koolstra, 2002; Mathevon et al., 1995; Mioche et al., 1999; Shimada et al., 2012; Stróżyk and Bałchanowski, 2018; Stróżyk and Bałchanowski, 2023), indicate that the mechanical properties of food have a significant effect on muscle activity patterns and muscle force values during the act of chewing. A second important parameter that significantly impacts muscle characteristics will be the position of the food on the dental arch, on which the opening of the mouth - and thus the contraction of the muscle - depends at a fixed food height.

For example, by analyzing a particular food during symmetrical incisor biting and unilateral chewing, assuming a fixed height, it can be shown that during symmetrical incisor biting, the mouth opening

is less than during chewing, i.e., the muscles will have different initial lengths, resulting in different contractions. Furthermore, as mentioned, the position of the food also forces the activation of other mechanisms of food damage.

When comparing symmetrical incisal biting and unilateral chewing, it becomes apparent that these are two distinct processes in terms of solid mechanics and deformable body mechanics. Specifically, symmetrical incisal biting involves a single cycle in which the incisors cut the food into two parts and transport it to the molars for substantial dimensional reduction and concurrent modification of their internal structure (texture). The mandibular movements primarily occur in the sagittal plane, with slight lateral deviations in the frontal plane. Consequently, the support and loading conditions are quasi-symmetrical. Therefore, it can be assumed that during mandibular movement, the condyle trajectories, left and right, are identical (Stróżyk and Bałchanowski, 2016). Furthermore, the position of the food bite on the incisors, its loading along the line, and the wedge-shaped structure of the incisors indicate that the biting process is analogous to typical shearing.

Unlike symmetrical incisal biting, unilateral chewing is a multi-cycle process where the number of cycles depends on the changing mechanical parameters, food texture, and individual characteristics. The food damage process primarily involves crushing and grinding food between surfaces formed by two pairs of corresponding molars or one pair of premolars and one pair of molars, depending on individual characteristics.

The above shows that the damage process (food positioning on the dental arch) significantly affects bite force, mouth opening, and muscle contraction. Considering the information above, it is evident that during chewing, muscle energy and/or the energy of the masticatory system depends on the food stiffness.

## 4.4 Peak power of the elevator muscles of the mandible

### 4.4.1 Unilateral chewing

An analysis of peak power values for the mandibular elevator muscles indicates that the masseter muscle generates the highest power

TABLE 5 Percentage differences between (1) peak power values obtained for unilateral chewing ( $PP_{WUi}$ ,  $PP_{Nui}$ ) and symmetrical incisal biting ( $PP_{Wli}$ ,  $PP_{Nli}$ ), on the working side ( $\Delta PP_{WUii}$ ) and non-working side ( $\Delta PP_{NUii}$ ) and (2) total peak power ( $\Delta PP_{Uii}$ ) obtained for unilateral chewing ( $PP_{TUi}$ ) and symmetrical incisal biting ( $PP_{Tli}$ ), depending on the food type ( $i$ ).

Working side (W)			Non-working side (N)			Total Power [W]		Percentage difference [%]
Power [W]		Percentage difference [%]	Power [W]		Percentage difference [%]			
Unilateral chewing	Symmetric incisal biting		Unilateral chewing	Symmetric incisal biting				
$PP_{WUi}^b$	$PP_{Wli}^c$	$\Delta PP_{WUii}$	$PP_{Nui}^b$	$PP_{Nli}^c$	$\Delta PP_{NUii}$	$PP_{TUi}^d$	$PP_{Tli}^e$	$\Delta PP_{Uii}$
Sausage ( <i>s</i> )								
3.33	0.72	128.8	2.30	0.72	104.6	5.62	1.44	118.5
Carrot ( <i>c</i> )								
6.82	1.39	132.3	5.19	1.39	115.5	12.01	2.78	124.8
Apple ( <i>a</i> )								
0.93	0.44	71.7	0.80	0.44	58.6	1.74	0.88	65.5
Chocolate bar ( <i>b</i> )								
2.36	0.60	119.0	2.10	0.60	111.0	4.46	1.20	115.2
Chocolate ( <i>d</i> )								
1.98	1.05	61.2	1.62	1.05	42.7	3.60	2.10	52.5

<sup>a</sup>*i* = *s*, *c*, *a*, *b* and *d*.

<sup>b</sup>(Table 1).

<sup>c</sup>The authors' own unpublished data for this paper.

<sup>d</sup> $PP_{TUi} = PP_{WUi} + PP_{Nui}$ .

<sup>e</sup> $PP_{Tli} = PP_{Wli} + PP_{Nli}$ .

during unilateral chewing. In contrast, the temporalis muscle generates the lowest, regardless of the side of the mandible and the food type (Table 1). The average percentage difference between the masseter and temporalis muscles for the working and non-working sides amounts to 134.1% and 104.9%, respectively. The medial pterygoid muscle generates less power than the masseter but more than the temporalis muscle (Table 1). The average percentage difference between the medial pterygoid and the masseter and temporalis muscles for the working side is 69.6% and 82.4%, respectively, and for the non-working side, it is 75.2% and 36.8%.

Analysis of peak power values in relationship to the mandibular side indicates that the elevator muscles of the mandible generate greater power on the working side than on the non-working side (Table 4). Calculations indicate that the highest percentage difference between the sides ( $\Delta PP_{WNUi}$ ) was observed for sausage ( $\Delta PP_{WNUs} = 36.5\%$ ), while the smallest was for the chocolate bar ( $\Delta PP_{WNUb} = 11.9\%$ ). The carrot, chocolate, and apple values are  $\Delta PP_{WNUc} = 27.1\%$ ,  $\Delta PP_{WNUd} = 19.8\%$ , and  $\Delta PP_{WNUa} = 14.6\%$ , respectively.

Analyzing the masticatory system in terms of total peak power ( $PP_{TUi}$ ), it was found that the elevator muscles of the mandible must generate the highest power for carrot ( $PP_{TUC} = 12.01W$ ) and the lowest for apple ( $PP_{TUA} = 1.73W$ ) (Table 4). For the remaining foods, the total peak power is ranked as follows: sausage ( $PP_{TUs} = 5.63W$ ), chocolate bar ( $PP_{TUb} = 4.46W$ ), and chocolate ( $PP_{TUD} = 3.60W$ ). Interestingly, three foods (carrot, chocolate bar, and apple) of similar heights (Figure 1) require the muscular system to generate different power values (Table 4). The results indicate that food texture significantly affects the power generated by the muscular system, which depends on the muscular force and contraction velocity of individual foods (Table 1).

Additionally, the masseter and medial pterygoid muscles generate higher peak power on the working side than on the non-working side (Table 1). In contrast, the temporalis muscle generates higher peak power on the non-working side than on the working side. This results from the fact that the muscle must achieve a more significant contraction (Stróżyk and Bałchanowski, 2023) on the non-working side than on the working side. Consequently, to meet the demands of a simple mechanical model (e.g., simultaneous increase in contraction and muscle force values and reaching their maxima at the same time), the muscles must contract at different velocities, i.e., the contraction velocity on the non-working side must be higher than on the working side (Table 1). As a result, despite lower maximum force values on the non-working side, the temporalis muscle generates higher peak power.

#### 4.4.2 Unilateral chewing vs. symmetrical incisal biting

The peak power values (Table 5) show that percentage differences can be divided into two groups, regardless of the mandibular side, i.e., above and below 100%. The first group includes carrots, sausages, and chocolate bars, while the second group comprises apples and chocolate.

The percentage differences between unilateral biting and biting in the first group indicate that the highest value for the working side is observed for carrot, followed by sausage and the lowest value for chocolate bar  $\Delta PP_{WUic} = 132.3\%$ ,  $\Delta PP_{WUIS} = 128.8\%$  and  $\Delta PP_{WUIb} = 119.0\%$ , respectively, while for the non-working side the highest values are also for carrot ( $\Delta PP_{NUic} = 115.5\%$ ), and the lowest for sausage ( $\Delta PP_{NUis} = 104.6\%$ ). For chocolate bars, the percentage difference value is  $\Delta PP_{NUib} = 111.0\%$ .

In the second group, the highest value was observed for apple and the lowest for chocolate, respectively, on the working side:  $\Delta PP_{WUIa} = 71.7\%$  and  $\Delta PP_{WUID} = 61.2\%$  and on the non-working side:  $\Delta PP_{NUia} = 58.6\%$  and  $\Delta PP_{NUid} = 42.7\%$ .

The results obtained for chocolate are surprising. However, considering (1) its small height relative to other foods (Table 1; Figure 1) and (2) its brittle material properties, the results obtained at this stage of the research should be regarded as highly probable.

Analysis of the percentage differences ( $\Delta PP_{Ui}$ ) between total peak power during unilateral chewing ( $PP_{TUi}$ ) and symmetrical incisal biting ( $PP_{Ti}$ ) indicates that the most significant differences occur for carrot ( $\Delta PP_{Uic} = 124.8\%$ ), and the smallest for chocolate ( $\Delta PP_{UID} = 52.5\%$ ). The values for sausage and chocolate bar are almost identical, amounting to  $\Delta PP_{Uis} = 118.5\%$  and  $\Delta PP_{UIb} = 115.3\%$ , respectively. For apple, the percentage difference ( $\Delta PP_{UIa} = 65.5\%$ ) is 13% higher than that for chocolate.

Analyzing these results for individual foods reveals that the power of the muscle system is strongly dependent on the food's location on the dental arch. This dependency is most pronounced for carrot, sausage, and chocolate bar, with an average percentage difference of 119.5%. Differences between apple and chocolate are also apparent but not as significant as for the aforementioned foods - the average difference is 59.0%.

Considering the results in Tables 4 and 5, it can be concluded that differences in muscular system forces depend primarily on (1) the texture of the food and (2) the position of the food on the dental arch, i.e., the mechanism of food destruction (biting and unilateral chewing).

Furthermore, based on the percentage differences between peak power during unilateral chewing and symmetrical incisal biting, the following hypothesis can be proposed: the mechanism of food damage has a significantly more significant impact on the peak power of the muscle system for foods with high texture heterogeneity than for foods with low texture heterogeneity.

## 5 Conclusion

Analysis of the results showed that energy and peak power can be used to quantitatively and qualitatively assess the elevator muscle of the mandible during the first cycle of unilateral chewing of foods with different textures (Stróżyk and Bałchanowski, 2023). Furthermore, the study showed that these parameters can also be used to compare two kinematically and dynamically different stages of the chewing act, i.e., incisal biting and unilateral chewing.

Additionally, it should be noted that muscle-generated energy depends on two parameters (1): muscle force and (2) contraction, which in turn depend on bite force (food texture) and food height (mouth opening), respectively. Bite force and mouth opening are influenced by the food's position on the dental arch. Regarding peak muscle power, the contraction velocity during symmetrical incisal biting and/or unilateral chewing must also be considered. This velocity, in turn, depends on time, food height, position on the dental arch, food texture, and individual characteristics.

A method to determine which of these parameters significantly affects energy and peak power patterns is dimensional analysis (Buckingham's Pi theorem) (Gibbings, 2011).

Since experimental studies and numerical simulations were carried out for only five food products (Figure 1), the results and

conclusions must be verified for products with different internal textures and heights.

In addition, a complete understanding of the function of the masticatory system during the act of chewing requires *in vivo* studies, which should take into account the effects of age, dental status, masticatory dysfunction and dietary habits (type of diet) on the velocity of chewing, and thus on the contraction velocity of the mandibular elevator muscles.

The results obtained can be used in (I) clinical practice, e.g., for the evaluation of temporomandibular joint disorders, planning of orthodontic and prosthetic treatment, i.e., design of braces, prostheses and implants of the masticatory system, maxillofacial surgery, i.e., planning of mandibular reconstruction, therapy after fractures and after Bilateral Sagittal Split Osteotomy-BSSO), (II) rehabilitation, e.g., development of exercise programs for patients after injury, surgery and those suffering from muscle weakness, optimization of therapy for bruxism, development of muscle monitoring devices, (III) bionic systems of the masticatory system, e.g., design of mandibular and maxillary prostheses taking into account the natural loads and functioning of the muscular system, development of robots to assist in masticatory therapy and rehabilitation of the masticatory system after injuries, development of nerve impulse-controlled muscle implants that mimic their natural functions, (IV) biomechanical research, e.g., primarily, development of numerical dynamic models of the masticatory system based on finite element methods-FEM and carrying out simulations and analyses for selected boundary conditions - muscle characteristics, position of the mandible.

## Data availability statement

The original contributions presented in the study are included in the article/Supplementary Material, further inquiries can be directed to the corresponding author.

## References

- Ackland, D. C., Moskaljuk, A., Hart, C., Vee Sin Lee, P., and Dimitroulis, G. (2015). Prosthesis loading after temporomandibular joint replacement surgery: a musculoskeletal modeling study. *J. Biomech. Eng.* 137 (4), 041001. doi:10.1115/1.4029503
- Agrawal, K. R., Lucas, P. W., Bruce, I. C., and Prinz, J. F. (1998). Food properties that influence neuromuscular activity during human mastication. *J. Dent. Res.* 77, 1931–1938. doi:10.1177/00220345980770111101
- Antic, S., Saveljic, I., Nikolic, D., Jovicic, G., Filipovic, N., Rakocevic, Z., et al. (2016). Does the presence of an unerupted lower third molar influence the risk of mandibular angle and condylar fractures? *Int. J. Oral Maxillofac. Surg.* 45 (5), 588–592. doi:10.1016/j.ijom.2014.09.018
- Bhatka, R., Throckmorton, G. S., Wintergerst, A. M., Hutchins, B., and Buschang, P. H. (2004). Bolus size and unilateral chewing cycle kinematics. *Arch. Oral Biol.* 49, 559–566. doi:10.1016/j.archoralbio.2004.01.014
- Blanksma, N. G., and van Eijden, T. M. G. J. (1995). Electromyographic heterogeneity in the human temporalis and masseter muscles during static biting, open/close excursions, and chewing. *J. Dent. Res.* 74, 1318–1327. doi:10.1177/00220345950740061201
- Buschang, P. H., Throckmorton, G. S., Austin, D., and Wintergerst, A. M. (2007). Chewing cycle kinematics of subjects with deepbite malocclusion. *Am. J. Orthod. Dentofac. Orthop.* 131, 627–634. doi:10.1016/j.ajodo.2005.06.037
- Castroflorio, T., Bracco, P., and Farina, D. (2008). Surface electromyography in the assessment of jaw elevator muscles. *J. Oral Rehabil.* 35 (8), 638–645. doi:10.1111/j.1365-2842.2008.01864.x
- De Zee, M., Dalstra, M., Cattaneo, P. M., Rasmussen, J., Svensson, P., and Melsen, B. (2007). Validation of a musculo-skeletal model of the mandible and its application to mandibular distraction osteogenesis. *J. Biomech.* 40 (6), 1192–1201. doi:10.1016/j.jbiomech.2006.06.024
- Ferrario, V. F., and Sforza, C. (1996). Coordinated electromyographic activity of the human masseter and temporalis anterior muscles during mastication. *Eur. J. Oral. Sci.* 104, 511–517. doi:10.1111/j.1600-0722.1996.tb00134.x
- Ferrario, V. F., Sforza, C., Serrao, G., Dellavia, C., and Tartaglia, G. M. (2006). Single tooth bite forces in healthy young adults. *J. Oral Rehabil.* 31 (1), 18–22. doi:10.1046/j.0305-182x.2003.01179.x
- Fitts, R. H., McDonald, K. S., and Schluter, J. M. (1991). The determinants of skeletal muscle force and power: their adaptability with changes in activity pattern. *J. Biomech.* 24, 111–122. doi:10.1016/0021-9290(91)90382-W
- Gibbings, J. C. (2011). Dimensional analysis. London: Springer. doi:10.1007/978-1-84996-317-6
- Griffin, T. M., Tolani, N. A., and Kram, R. (1998). Walking in simulated reduced gravity: mechanical energy fluctuations and exchange. *J. Appl. Physiol.* 85 (1), 680–689. doi:10.1152/jappl.1998.85.1.680
- Gröning, F., Fagan, M., and O'higgins, P. (2012). Modeling the human mandible under masticatory loads: which input variables are important? *Anat. Rec.* 295 (5), 853–863. doi:10.1002/ar.22455
- Gross, M. D., Arbel, G., and HersHKovitz, I. (2001). Three-dimensional finite element analysis of the facial skeleton on simulated occlusal loading. *J. Oral Rehabil.* 28 (7), 684–694. doi:10.1046/j.1365-2842.2001.00711.x
- Hiimeae, K., Heath, M. R., Heath, G., Kazazoglu, E., Murray, J., Sapper, D., et al. (1996). Natural bites, food consistency and feeding behaviour in man. *Arch. Oral Biol.* 41, 175–189. doi:10.1016/0003-9969(95)00112-3
- Itoh, K., Hayashi, T., and Miyakawa, M. (1997). Controllability of temporomandibular joint loading by coordinative activities of masticatory muscles: a two-dimensional static analysis. *Front. Med. Biol. Eng.* 8, 123–138. doi:10.1109/IEMBS.1996.651895

## Author contributions

PS: writing–original draft, writing–review and editing, conceptualization, data curation, formal analysis, investigation, methodology, software, supervision, visualization. JB: writing–original draft, writing–review and editing, conceptualization, data curation, funding acquisition, investigation, methodology, software, supervision.

## Funding

The author(s) declare that financial support was received for the research and/or publication of this article. This paper was supported by Grants-in-Aid from the Wrocław University of Science and Technology, Faculty of Mechanical Engineering, Poland; (K58 and K61 - No. 825 1050 500).

## Conflict of interest

The authors declare that the research was conducted in the absence of any commercial or financial relationships that could be construed as a potential conflict of interest.

## Publisher's note

All claims expressed in this article are solely those of the authors and do not necessarily represent those of their affiliated organizations, or those of the publisher, the editors and the reviewers. Any product that may be evaluated in this article, or claim that may be made by its manufacturer, is not guaranteed or endorsed by the publisher.

- Kashi, A., Roy Chowdhury, A., and Saha, S. (2010). Finite element analysis of a TMJ implant. *J. Dent. Res.* 89, 241–245. doi:10.1177/0022034509357716
- Kjær, M. (2004). Role of extracellular matrix in adaptation of tendon and skeletal muscle to mechanical loading. *Physiol. Rev.* 84 (2), 649–698. doi:10.1152/physrev.00031.2003
- Koole, P., Beenhakker, F., de Jongh, H. J., and Boering, G. (1990). A standardized technique for the placement of electrodes in the two heads of the lateral pterygoid muscle. *J. Craniomandib. Pract.* 8, 154–162. doi:10.1080/08869634.1990.11678309
- Koolstra, J. H. (2002). Dynamics of the human masticatory system. *Crit. Rev. Oral Biol. Med.* 13, 366–376. doi:10.1177/154411130201300406
- Langenbach, G. E., and Hannam, A. (1999). The role of passive muscle tensions in a three-dimensional dynamic model of the human jaw. *Arch. Oral Biol.* 44 (7), 557–573. doi:10.1016/s0003-9969(99)00034-5
- Lenton, G. K., Doyle, T. L. A., Lloyd, D. G., Higgs, J., Billing, D., and Saxby, D. J. (2018). Lower-limb joint work and power are modulated during load carriage based on load configuration and walking speed. *J. Biomech.* 83, 174–180. doi:10.1016/j.jbiomech.2018.11.036
- Mathevon, E., Mioche, L., Brown, W. E., and Culioli, J. (1995). Texture analysis of beef cooked at various temperatures by mechanical measurements, sensory assessments and electromyography. *J. Text. Stud.* 26, 175–192. doi:10.1111/j.1745-4603.1995.tb00792.x
- Mioche, L., Bourdiol, P., Martin, J. F., and Noël, Y. (1999). Variations in human masseter and temporalis muscle activity related to food texture during free and side imposed mastication. *Arch. Oral Biol.* 44, 1005–1012. doi:10.1016/s0003-9969(99)00103-x
- Murray, G. M., Orfanos, T., Chan, J. Y., Wanigaratne, K., and Klineberg, I. J. (1999). Electromyographic activity of the human lateral pterygoid muscle during contralateral and protrusive jaw, movements. *Arch. Oral Biol.* 44, 269–285. doi:10.1016/s0003-9969(98)00117-4
- Narici, M. V., and Maganaris, C. N. (2006). Adaptability of elderly human muscles and tendons to increased loading. *J. Anat.* 208 (4), 433–443. doi:10.1111/j.1469-7580.2006.00548.x
- Neptune, R. R., and van den Bogert, A. J. (1998). Standard mechanical energy analyses do not correlate with muscle work in cycling. *J. Biomech.* 31, 239–245. doi:10.1016/s0021-9290(97)00129-2
- Nishigawa, K., Nakano, M., and Bando, E. (1997). Study of jaw movement and masticatory muscle activity during unilateral chewing with and without balancing side molar contacts. *J. Oral Rehabil.* 24, 691–696. doi:10.1046/j.1365-2842.1997.00553.x
- Pachnicz, D., and Stróżyk, P. (2021). A biomechanical analysis of muscle force changes after bilateral sagittal split osteotomy. *Front. Physiol.* 12, 679644. doi:10.3389/fphys.2021.679644
- Phuntsho, U., Komoltri, J., and Viwattanatipa, N. (2018). Comparison of skull dimension and geometric formulas method to solve projection errors in 2D cephalometric radiographs. *Biomed. J. Sci. Tech. Res.* 12, 8982–8993. doi:10.26717/BJSTR.2018.12.002201
- Piancino, M. G., Isola, G., Merlo, A., Dalessandri, D., Debernardi, C., and Bracco, P. (2012). Chewing pattern and muscular activation in open bite patients. *J. Electromyogr. Kinesiol.* 22, 273–279. doi:10.1016/j.jelekin.2011.12.003
- Pinheiro, M., Willaert, R., Khan, A., and Van Paepegem, W. (2021). Biomechanical evaluation of the human mandible after temporomandibular joint replacement under different biting conditions. *Sci. Rep.* 11, 14034. doi:10.1038/s41598-021-93564-3
- Plesh, O., Bishop, B., and McCall, W. D. (1996). Patterns of jaw muscle activity during voluntary chewing. *J. Oral Rehabil.* 23, 262–269. doi:10.1111/j.1365-2842.1996.tb00851.x
- Pruim, G. J., de Jongh, H. J., and ten Bosch, J. J. (1980). Forces acting on the mandible during bilateral static bite at different bite force levels. *J. Biomech.* 13, 755–763. doi:10.1016/0021-9290(80)90237-7
- Roark, A. L., Glaros, A. G., and O'Mahony, A. M. (2003). Effects of interocclusal appliances on EMG activity during parafunctional tooth contact. *J. Oral Rehabil.* 30, 573–577. doi:10.1046/j.1365-2842.2003.01139.x
- Röhrle, O., and Pullan, A. J. (2007). Three-dimensional finite element modelling of muscle forces during mastication. *J. Biomech.* 40 (15), 3363–3372. doi:10.1016/j.jbiomech.2007.05.011
- Sagl, B., Schmid-Schwap, M., Piehslinger, E., Kundi, M., and Stavness, I. (2019). A dynamic jaw model with a finite-element temporomandibular joint. *Front. Physiol.* 10, 1156. doi:10.3389/fphys.2019.01156
- Saini, V., Chowdhry, A., and Mehta, M. (2021). Sexual dimorphism and population variation in mandibular variables: a study on a contemporary Indian population. *Anthropol. Sci.* 130 (1), 59–70. doi:10.1537/ase.2108282
- Shimada, A., Yamabe, Y., Torisu, T., Baad-Hansen, L., Murata, H., and Svensson, P. (2012). Measurement of dynamic bite force during mastication. *J. Oral Rehabil.* 39, 349–356. doi:10.1111/j.1365-2842.2011.02278.x
- Slavicek, G. (2010). Human mastication. *Int. J. Stomatol. Occlusion Med.* 3, 29–41. doi:10.1007/s12548-010-0044-6
- Stokes, J. R., Boehm, M. W., and Baier, S. K. (2013). Oral processing, texture and mouthfeel: from rheology to tribology and beyond. *Curr. Opin. Colloid Interface Sci.* 18, 349–359. doi:10.1016/j.cocis.2013.04.010
- Stróżyk, P. (2021). The patent Pat.242091 (System for measuring the loads acting on the dental arch for selected states of dentition) Patent Office of the Republic of Poland.
- Stróżyk, P., and Bałchanowski, J. (2016). Effect of foodstuff on muscle forces during biting off. *Acta Bioeng. Biomech.* 18, 81–91. doi:10.5277/ABB-00305-2015-03
- Stróżyk, P., and Bałchanowski, J. (2018). Modelling of the forces acting on the human stomatognathic system during dynamic symmetric incisal biting of foodstuffs. *J. Biomech.* 79, 58–66. doi:10.1016/j.jbiomech.2018.07.046
- Stróżyk, P., and Bałchanowski, J. (2020). Effect of foods on selected dynamic parameters of mandibular elevator muscles during symmetric incisal biting. *J. Biomech.* 106, 109800. doi:10.1016/j.jbiomech.2020.109800
- Stróżyk, P., and Bałchanowski, J. (2023). Application of numerical simulation studies to determine dynamic loads acting on the human masticatory system during unilateral chewing of selected foods. *Front. Bioeng. Biotechnol.* 11, 993274. doi:10.3389/fbioe.2023.993274
- Stróżyk, P., Bałchanowski, J., and Szrek, J. (2018). “Modelling of the dynamic loads of the human stomatognathic system during biting off,” in *24th international conference engineering mechanics. Institute of theoretical and applied mechanics of the Czech academy of sciences* (Svratka, Czech Republic), 825–828. May 14–17, paper 145. doi:10.21495/91-8-825
- Tanne, K., Tanaka, E., and Sakuda, M. (1995). Stress distribution in the TMJ during clenching in patients with vertical discrepancies of the craniofacial skeleton. *J. Orofac. Pain* 9 (2), 171–177. doi:10.1080/000163594428860
- Tuijt, M., Koolstra, J. H., Lobbezoo, F., and Naeije, M. (2010). Differences in loading of the temporomandibular joint during opening and closing of the jaw. *J. Biomech.* 43, 1048–1054. doi:10.1016/j.jbiomech.2009.12.013
- Van Eijden, T. M., Korfage, J. A., and Brugman, P. (2003). Architecture of the human jaw-closing and jaw-opening muscles. *Anat. Rec.* 248 (4), 464–474. doi:10.1002/(sici)1097-0185(199707)248:3<464::aid-ar20>3.3.co;2-4
- Wang, C. F., Liu, S., Hu, L. H., Yu, Y., Peng, X., and Zhang, W. B. (2023). Biomechanical behavior of the three-dimensionally printed surgical plates for mandibular defect reconstruction: a finite element analysis. *Comput. Aided Surg.* 28 (1), 2286181. doi:10.1080/24699322.2023.2286181
- Winters, J. M. (1990). “Hill-based muscle models: a system engineering perspective,” in *Multiple muscle systems: biomechanics and movement organization*. Editors J. M. Winters and S. L. J. Woo (New York: Springer), 69–93.
- Wood, W. W., Takada, K., and Hannam, A. G. (1986). The electromyographic activity of the inferior part of the human lateral pterygoid muscle during clenching and chewing. *Arch. Oral Biol.* 31, 245–253. doi:10.1016/0003-9969(86)90056-7
- Zajac, F. E. (1989). Muscle and tendon: properties, models, scaling, and application to biomechanics and motor control. *Crit. Rev. Biomed. Eng.* 17 (4), 359–411.





## OPEN ACCESS

## EDITED BY

Zhiyong Li,  
Queensland University of Technology, Australia

## REVIEWED BY

Valeria Graceffa,  
Institute of Technology, Ireland  
Z. Xiao,  
China Institute of Sport Science, China

## \*CORRESPONDENCE

Tao Zhang,  
✉ gzlupus@126.com  
Xiaona Wu,  
✉ 13889904009@139.com  
Wu Wu,  
✉ gzyswuwu@163.com

<sup>†</sup>These authors share first authorship

RECEIVED 06 February 2025

ACCEPTED 10 April 2025

PUBLISHED 23 April 2025

## CITATION

Kong L, Lai H, Zeng X, Gao P, Liang W, Gao Q, Kong Z, Wu W, Wu X and Zhang T (2025) The evolution of three-dimensional knee kinematics after ACL reconstruction within one year. *Front. Bioeng. Biotechnol.* 13:1572160. doi: 10.3389/fbioe.2025.1572160

## COPYRIGHT

© 2025 Kong, Lai, Zeng, Gao, Liang, Gao, Kong, Wu, Wu and Zhang. This is an open-access article distributed under the terms of the [Creative Commons Attribution License \(CC BY\)](https://creativecommons.org/licenses/by/4.0/). The use, distribution or reproduction in other forums is permitted, provided the original author(s) and the copyright owner(s) are credited and that the original publication in this journal is cited, in accordance with accepted academic practice. No use, distribution or reproduction is permitted which does not comply with these terms.

# The evolution of three-dimensional knee kinematics after ACL reconstruction within one year

Lingchuang Kong<sup>1†</sup>, Huahao Lai<sup>2†</sup>, Xiaolong Zeng<sup>3</sup>, Peng Gao<sup>1,4</sup>, Wenhao Liang<sup>1</sup>, Qi Gao<sup>1,4</sup>, Zhiyuan Kong<sup>1</sup>, Wu Wu<sup>2\*</sup>, Xiaona Wu<sup>5\*</sup> and Tao Zhang<sup>1\*</sup>

<sup>1</sup>Department of Orthopedics, General Hospital of Southern Theatre Command of People's Liberation Army, Guangzhou, China, <sup>2</sup>Department of Bone and Joint Rehabilitation, Guangdong Work Injury Rehabilitation Hospital, Guangzhou, Guangdong, China, <sup>3</sup>Department of Orthopedics, Guangdong Provincial Hospital of Chinese Medicine, Guangzhou, China, <sup>4</sup>Department of Graduate School, Guangzhou University of Chinese Medicine, Guangzhou, China, <sup>5</sup>Department of Neurosurgery, General Hospital of Southern Theatre Command of People's Liberation Army, Guangzhou, China

**Introduction:** This study aims to explore the dynamic changes in the six degrees of freedom (6DOF) kinematics of the knee joint in patients within one year after anterior cruciate ligament reconstruction (ACLR), combined with clinical scoring systems to analyze functional recovery characteristics, providing scientific evidence for optimizing postoperative rehabilitation strategies.

**Methods:** The study enrolled 49 patients followed up at 3 months postoperatively, 33 patients at 6 months, and 35 patients at 12 months. Twenty-nine healthy controls were recruited. A three-dimensional motion capture system was used to collect 6DOF knee kinematic data at 3, 6, and 12 months after surgery, including flexion-extension, internal-external rotation, adduction-abduction angles, and anterior-posterior, distal-proximal, medial-lateral translation data. Clinical function was assessed using the IKDC and KOOS scores. One Way ANOVA of one-dimensional statistical parametric mapping (SPM1D) was used to assess the changes in gait kinematics and differences compared to healthy controls.

**Results:** After ACLR, the IKDC and KOOS scores of patients significantly improved between 3 and 12 months postoperatively, showing good subjective functional recovery. Over the course of one year, the knee kinematic data of gait has gradually recovered. However, abnormalities in knee joint kinematics still exist. In the coronal plane, the adduction angle of the knee joint during motion is relatively large ( $p < 0.05$ ); In the sagittal plane, the flexion angle increased during the standing phase ( $p < 0.05$ ); In the transverse plane, the internal rotation angle of the knee joint increased compared to the controls ( $p < 0.05$ ). The range of motion of flexion and rotational angles decreased compared to the controls ( $p < 0.05$ ).

**Discussion:** The kinematic recovery of the knee joint in ACLR patients presents multidimensional characteristics and dynamic changes. The recovery rates and patterns differ significantly across dimensions, with some abnormalities not fully corrected within one-year post-surgery. These findings provide scientific evidence for individualized rehabilitation strategies, emphasizing the need for strengthening joint stability and range of motion recovery in the early

postoperative phase (0–6 months) and focusing on correcting rotational and flexion–extension function during the later phase (6–12 months) to further improve knee function and prevent long-term adverse outcomes.

#### KEYWORDS

anterior cruciate ligament reconstruction, knee kinematics, gait analysis, postoperative rehabilitation, knee

## 1 Introduction

Anterior cruciate ligament reconstruction (ACLR) is a common surgical procedure to restore knee stability and function following ACL injury (Lohmander et al., 2007; Rodriguez-Merchan and Encinas-Ullan, 2022). Despite advancements in surgical techniques, achieving optimal postoperative recovery remains challenging, as it involves complex rehabilitation to restore not only static stability but also dynamic functional movements. A critical aspect of ACLR rehabilitation is understanding the recovery trajectory of knee joint kinematics, particularly in terms of the six degrees of freedom (6DOF), including flexion–extension, internal–external rotation, adduction–abduction, and translation across the anterior–posterior, medial–lateral, and distal–proximal axes (Zhang et al., 2015). These kinematic changes are essential for assessing the progression of functional recovery and the restoration of normal joint motion.

Previous studies have predominantly focused on clinical outcomes and static measurements (Elabd et al., 2024; Hamido et al., 2021; Herbst, et al., 2023), often neglecting the dynamic kinematic behavior of the knee during functional movements, such as walking or running. However, dynamic kinematic analysis provides crucial insights into the joint's functional performance, which is not fully captured by traditional clinical scoring systems like the International Knee Documentation Committee (IKDC) or the Knee injury and Osteoarthritis Outcome Score (KOOS) (Holsgaard-Larsen et al., 2014; Kaiser et al., 2017; Lepley and Kuenze, 2018). Static measurements, such as clinical scores or radiographic evaluations, primarily assess joint stability at rest but fail to capture transient kinematic changes during functional movements like gait. In contrast, dynamic analysis enables the identification of phase-specific abnormalities that correlate with functional deficits, offering insights into compensatory mechanisms and targeted rehabilitation needs (Yang et al., 2019; Zhang et al., 2016), underscoring the need for kinematic monitoring. Understanding how kinematic parameters evolve over time after surgery is vital for optimizing rehabilitation strategies that are both individualized and comprehensive.

This study aims to fill this gap by investigating the dynamic changes in knee joint kinematics across 1 year post-ACLR surgery, using a three-dimensional motion capture system to evaluate 6DOF knee motion. The study also integrates clinical scoring systems (IKDC and KOOS) to assess functional recovery, thus offering a multidimensional view of post-surgical knee rehabilitation. By analyzing the kinematic patterns at multiple time points (3, 6, and 12 months) and comparing them to healthy controls, this research seeks to provide valuable insights into the recovery process and inform more targeted, evidence-based rehabilitation strategies for ACLR patients.

## 2 Materials and methods

### 2.1 Subjects recruitment

This study recruited 49 ACLR patients followed up at 3 months postoperatively, 33 ACLR patients at 6 months, and 35 ACLR patients at 12 months. All the subjects underwent single-bundle anatomical ACLR by the orthopedic team of the hospital under the same technical standards and received standard rehabilitation treatment within 1-year post-surgery. Subjects were required to be aged between 18 and 50 years, and able to complete all research-related tests and follow-up visits. Exclusion criteria included severe postoperative complications such as infection, fractures, or the need for reoperation, the presence of other knee joint diseases such as meniscal tears or knee osteoarthritis, any other lower limb-related injuries within 1-year post-surgery, undergoing other interventions that may affect knee function, and neurological diseases or other major health issues that could interfere with the study.

This study enrolled 29 control subjects. Participants in the control group were required to be aged between 18 and 50 years, with no history of lower limb-related injuries or surgeries, no history of chronic pain or long-term medication use, and the ability to complete all research-related tests and follow-up visits. Exclusion criteria included any acute or chronic diseases affecting muscle function, undergoing medication treatments that could influence muscle size or function, any lower limb-related injuries in the past 6 months, and neurological disorders or conditions affecting joint movement. All the subjects were consented to participate by signing the informed consent form.

### 2.2 Rehabilitation protocol

ACLR patients began their rehabilitation procedure after surgery. Therapists followed a standardized protocol, but blinding was not feasible due to the nature of postoperative rehabilitation. Variability in technique was minimized through regular team training. The specific rehabilitation phases are as follows: Early Phase (0–1 week): The primary focus is on swelling control, pain management, and neuromuscular activation. Ice therapy should be applied every 2 h for 15 min within the first 48 h, followed by 3–5 sessions daily. Ankle pumping exercises (500–1,000 repetitions/day, 5-s holds for dorsiflexion and plantarflexion) are critical for venous return and thrombosis prevention. Passive range of motion (ROM) training begins on postoperative day 1, with heel-supported knee extension (3–5 sessions/day) and bedside leg-dangling flexion (60°–90°, 5 sets of 10 repetitions/day). Quadriceps isometric contractions (10-s holds, 500 repetitions/day) and straight-leg

raises (15° elevation, 3 sets of 20 repetitions/day) are initiated to prevent muscle atrophy. A brace locked at 0° is mandatory during ambulation to protect the graft; Initial Phase (2–4 weeks): This phase emphasizes partial weight-bearing transition and balance re-education. Wall-sliding exercises (90°–100° flexion, 6–8 sets of 10 repetitions/day) and patellar mobilization (5 min/session, 5 sessions/day) optimize joint mobility. Strength training includes wall sits (30° knee flexion, 30-s holds, 3 sets of 20 repetitions/day) and lateral step-ups with resistance bands (10 steps/set, 3 sets/day). Weight-bearing progresses from 25% body weight at week 2 to full weight-bearing by week 4. Balance training involves split-leg standing (30 cm apart, 1-min holds, 5 sets/day) and soft-tilt board exercises (15 min cumulative/day); Middle Phase (5 weeks to 3 months): Full ROM restoration ( $\geq 120^\circ$  flexion) and dynamic stability are prioritized. Slide-board-assisted flexion (5° incremental increases/day) and lunge stretches (4–6 breaths/hold, 6 sets/day) enhance terminal ROM. Eccentric hamstring training (Nordic curls: 0°–60° controlled lowering, 3 sets of 15 repetitions/day) reduces anterior tibial shear forces. Advanced proprioception drills include BOSU ball squats with ball throws (20 min/day) and 20-cm step-ups (10 repetitions/set, 3 sets/day). Low-resistance cycling (70–90 rpm, 20–30 min/day) and aquatic walking (chest-deep water, 15 min/day) improve cardiovascular endurance; Late Phase (4–12 months): This phase prepares for sports-specific demands. Stair training (8–25 cm step height, 2 sets of 15 repetitions/day) and weighted squats (kettlebell-loaded, 90° depth, 3 sets of 10 repetitions/day) build functional strength. Light jogging begins at 6 months (10–15 min/session, 2–3 sessions/week), progressing to 30 min. Agility drills (two-cone figure-eight pattern runs, lateral cross-steps) and sport-specific simulations (jump landings, pivoting) are introduced at 20 min/session, 3 times/week. Functional milestones include  $\geq 85\%$  limb symmetry in single-leg hop tests and  $< 4$  cm discrepancy in Y-balance anterior reach (Kotsifaki et al., 2023). We conducted regular follow-up visits and collected gait data and clinical scores at postoperative 3 months, 6 months, and 12 months. Therapists adhered to a standardized protocol, but blinding was infeasible due to the nature of postoperative rehabilitation. Variability in technique was minimized through regular team training.

## 2.3 Knee kinematic data collection

We used a 3D motion capture gait system, Opti\_Knee (developed by Innomotion, Shanghai), to collect knee kinematic data. This system uses surgical navigation infrared tracking devices (NDI Polaris Spectra, Northern Digital Inc., Canada), markers, high-speed optical cameras, and handheld digital probes, with a data sampling frequency of 60 Hz. The system has been validated for high accuracy and repeatability (Elfring et al., 2010; Wang et al., 2021; Zhang et al., 2016). Marker clusters were securely attached to the distal thigh and proximal calf using elastic bands to prevent motion artifacts. A handheld probe was used to digitize bony landmarks, including the greater trochanter of the femur, medial/lateral femoral condyles, and medial/lateral malleoli (Zhang et al., 2015). By attaching a set of markers on the patient's thigh and calf, the system can precisely track the movement of the knee joint. The kinematic data calculation is done by dedicated software (Opti\_Knee,

developed by Innomotion, Shanghai). The markers identify bony landmarks such as the greater trochanter of the femur, the medial and lateral femoral condyles, and the medial and lateral malleoli, allowing precise recording of the three-dimensional spatial relationship between the femur and tibia. The femur is used as the reference frame, and changes in the tibia's coordinate system relative to the femoral coordinate system are calculated, with the femur-tibia trajectory collected. Ultimately, we obtained 6DOF knee kinematic data, including flexion-extension (degree), adduction/abduction (degree), femoral internal/external rotation (degree), anterior-posterior translation (mm), proximal/distal translation (mm), and medial/lateral translation (mm) of the knee joint.

Before data collection, all participants underwent an adaptive gait test on a treadmill. The patients were instructed to walk at a comfortable speed, simulating ground walking. Finally, we recorded 15 s of gait data. Averaging 15-s gait data minimizes noise while preserving cycle trends, as validated in prior gait studies (Wang et al., 2021). The total test time for each participant was controlled within 10 min. The gait cycle began when one heel touched the ground and ended when the same heel touched the ground again. In this study, we divided and averaged the gait data for each participant within 15 s to form a complete gait cycle (0%–100% of the gait cycle phase). The gait cycle was divided into the stance phase (0%–62%) and swing phase (62%–100%) (Di Gregorio and Vocenas, 2021).

## 2.4 Clinical scores assessment

We assessed patients using the International Knee Documentation Committee (IKDC) Subjective Knee Evaluation Form and the Knee injury and Osteoarthritis Outcome Score (KOOS) system (Irrgang et al., 2001; Monticone et al., 2012). The assessments were conducted in a quiet clinic environment by researchers who were trained and familiar with the scoring systems. During the assessment, the purpose of the scoring was explained to the patients, and consent was obtained. The researchers then asked the relevant questions and summarized the responses to calculate the total IKDC and KOOS scores.

## 2.5 Statistical analysis

The normality of demographic data (age, height, weight, and body mass index) and clinical scores between groups was assessed using the One-Way ANOVA test with Dunnett's correction for post-hoc comparisons, setting the control group as the reference. Normality (Shapiro-Wilk test) and homogeneity of variance (Levene's test) were confirmed ( $p > 0.05$ ). Non-parametric tests were applied to non-normal data. The gender difference was assessed with a Chi-Squared test. Statistical analysis was conducted in SPSS version 24.0 (IBM Corp., Armonk, NY, United States), with the significance level set at 0.05. Analysts were blinded to group allocation during data processing to reduce measurement bias.

The range of motion of knee kinematics across groups was similarly compared using the One-Way ANOVA test with Dunnett's correction. Kinematic curve data were analyzed using the One-Way ANOVA test implemented in the one-dimensional statistical

TABLE 1 Demographic Data of ACLR groups and control group.

Variables	3 months	6 months	12 months	Control group	P Value
Male: Female	24:25	16:17	18:17	29:29	0.995
Age (years)	27.7 ± 6.4	26.5 ± 5.8	27.3 ± 6.6	25.7 ± 2.8	0.245
Height (cm)	169.2 ± 7.4	169.8 ± 7.1	169.2 ± 5.9	167.1 ± 8.0	0.283
Weight (kg)	58.5 ± 10.2	59.5 ± 12.5	59.3 ± 11.4	58.2 ± 9.0	0.926
BMI	20.3 ± 2.6	20.6 ± 3.9	20.6 ± 3.1	20.7 ± 2.0	0.916

TABLE 2 Knee clinical function scores.

Clinical scores	3 Months	6 Months	12 Months	P Value
IKDC	48.8 ± 5.8	66.0 ± 4.7 <sup>a</sup>	88.2 ± 5.9 <sup>b</sup>	<0.001
KOOS pain	49.0 ± 6.0	67.6 ± 5.6 <sup>a</sup>	92.0 ± 4.5 <sup>a</sup>	<0.001
KOOS symptom	57.6 ± 4.7	67.4 ± 4.6 <sup>a</sup>	86.7 ± 4.3 <sup>a</sup>	<0.001
KOOS ADL	60.5 ± 6.0	76.9 ± 5.7 <sup>a</sup>	90.5 ± 3.9 <sup>a</sup>	<0.001
KOOS sport	30.4 ± 6.1	50.3 ± 6.5 <sup>a</sup>	85.0 ± 5.9 <sup>a</sup>	<0.001
KOOS QOL	40.6 ± 6.6	55.3 ± 9.1 <sup>a</sup>	87.3 ± 4.9 <sup>a</sup>	<0.001

<sup>a</sup>significant different compared to 3 months.

<sup>b</sup>significant different compared to 3 months.

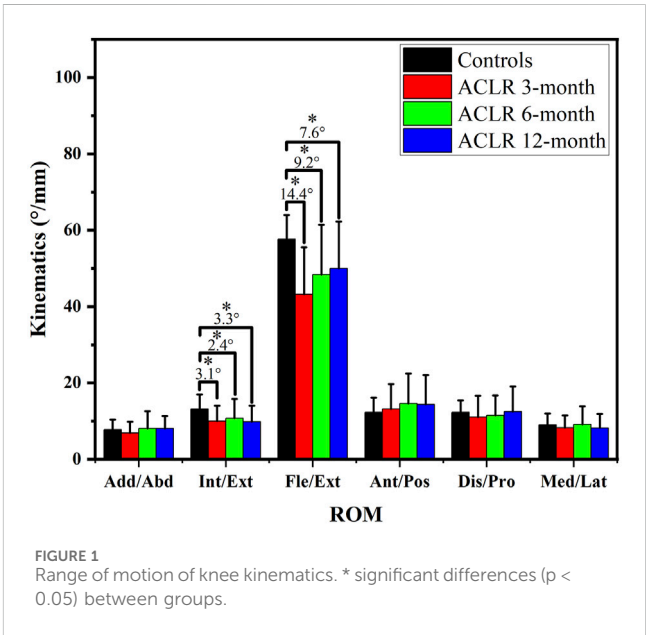
parametric mapping (SPM1D) software package (<http://spm1d.org>). This method applies random field theory and one-dimensional Gaussian smoothing to perform statistical inference on one-dimensional data. SPM1D analysis used cluster-level correction ( $\alpha = 0.0166$ ) to control for multiple comparisons. For these analyses, the significance level ( $\alpha$ ) was adjusted to 0.0166 (accounting for three comparisons) based on Dunnett's correction, with the control group set as the reference.

### 3 Results

#### 3.1 Demographic data and clinical scores assessment

At 3 months after ACLR, the group consisted of 24 males and 25 females. At 6 months, there were 16 males and 17 females, and at 12 months, 18 males and 17 females. The control group included 29 males and 29 females. All the demographic characteristics between groups were not significantly different (Table 1).

The knee joint clinical function scores indicated significant improvements in patient function at all postoperative follow-up time points ( $p < 0.05$ ). The IKDC score significantly increased from  $48.8 \pm 5.8$  at 3 months post-surgery to  $66.0 \pm 4.7$  at 6 months and further improved to  $88.2 \pm 5.9$  at 12 months. The KOOS scores also showed a continuous improvement trend, such as the KOOS Pain score, which increased from  $49.0 \pm 6.0$  at 3 months to  $67.6 \pm 5.6$  at 6 months, and reached  $92.0 \pm 4.5$  at 12 months. These results suggest that the subjective knee joint function and quality of life of ACLR patients significantly improved over time (Table 2).



#### 3.2 Knee kinematic analysis

Throughout the follow-up time points, there were varying degrees of significant differences in the kinematic characteristics of the ACLR knee joint compared to the control group. The range of motion (ROM) of knee kinematics (Figure 1) showed significant differences in internal/external rotation and Flexion/Extension between the control and ACLR groups across the gait cycle. The ROM of internal/external rotation and flexion/extension angles of

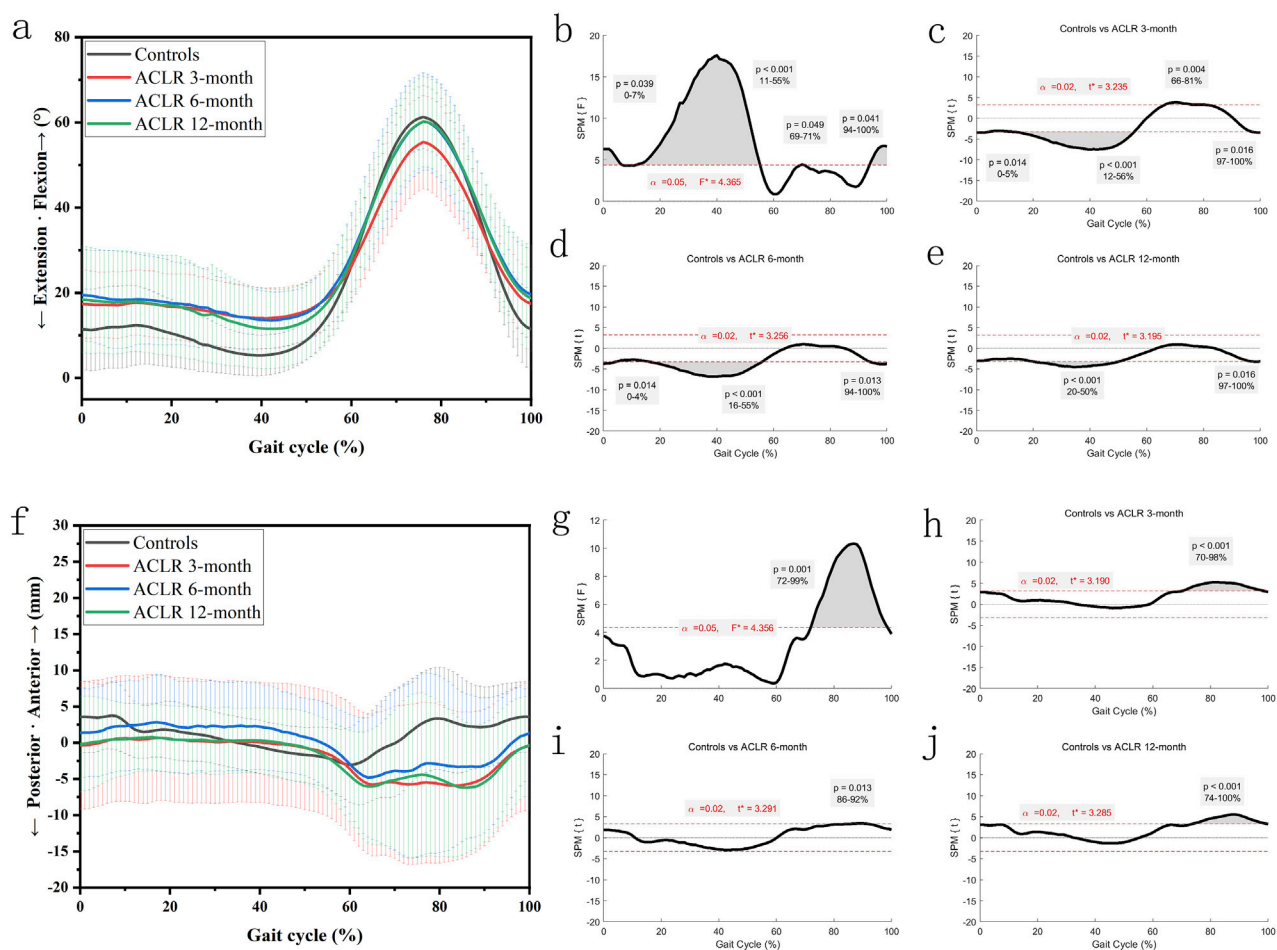


FIGURE 2

Knee kinematics of the sagittal plane in a gait cycle. Chart (a), flexion/extension angles in a gait cycle; chart (b), F value of flexion/extension using SPM1D method (One Way ANOVA section) in a gait cycle; chart (c), posthoc statistical comparison of flexion/extension between the control group and ACLR patients at 3 months; chart (d), posthoc statistical comparison of flexion/extension between the control group and ACLR patients at 6 months; chart (e), posthoc statistical comparison of flexion/extension between the control group and ACLR patients at 12 months; Chart (f), anterior/posterior tibial translation in a gait cycle; chart (g), F value of anterior/posterior tibial translation using SPM1D method (One Way ANOVA section) in a gait cycle; chart (h), posthoc statistical comparison of anterior/posterior tibial translation between the control group and ACLR patients at 3 months; chart (i), posthoc statistical comparison of anterior/posterior tibial translation between the control group and ACLR patients at 6 months; chart (j), posthoc statistical comparison of anterior/posterior tibial translation between the control group and ACLR patients at 12 months; the posthoc comparison of SPM1D method was based on Dunnett tests.

ACLR groups at different time points were smaller than the control groups ( $p < 0.05$ ). However, as rehabilitation progressed, at the 12-month follow-up time point, the difference in ACLR kinematics compared to the control group was minimal. Flexion ROM at 12 months differed significantly from 3 months ( $p = 0.003$ ) but not from 6 months ( $p = 0.12$ ), indicating a plateau in recovery.

### 3.3 Knee kinematics of the sagittal plane

The knee extension-flexion angles (Figures 2a–e) showed significant differences between the control and ACLR groups across the gait cycle. SPM analysis (Figures 2b–e) revealed significant differences at 3 months ( $p < 0.001$  from 12% to 56% and  $p = 0.004$  from 66% to 81%, Figure 2c), at 6 months ( $p < 0.001$  from 16% to 55% and  $p = 0.013$  from 94% to 100%, Figure 2d), and at 12 months ( $p < 0.001$  from 20% to 50% and  $p = 0.016$  from 97% to

100%, Figure 2e). These findings suggest partial recovery of knee extension-flexion kinematics by 12 months post-ACLR.

The anterior tibial translation (Figures 2f–j) showed significant differences between the control and ACLR groups across the gait cycle. SPM analysis (Figures 2g–j) revealed significant differences at 3 months ( $p < 0.001$  from 70% to 98%, Figure 2h), at 6 months ( $p = 0.013$  from 86% to 92%, Figure 2i), and at 12 months ( $p < 0.001$  from 74% to 100%, Figure 2j). These findings suggest no significant extra-changes of anterior tibial translation by 12 months post-ACLR. Increased anterior translation at 12 months may reflect graft laxity or delayed neuromuscular fatigue, necessitating biomechanical imaging for validation.

### 3.4 Knee kinematics of the transverse plane

The knee internal-external rotation angles (Figures 3a–e) showed significant differences between the control and ACLR



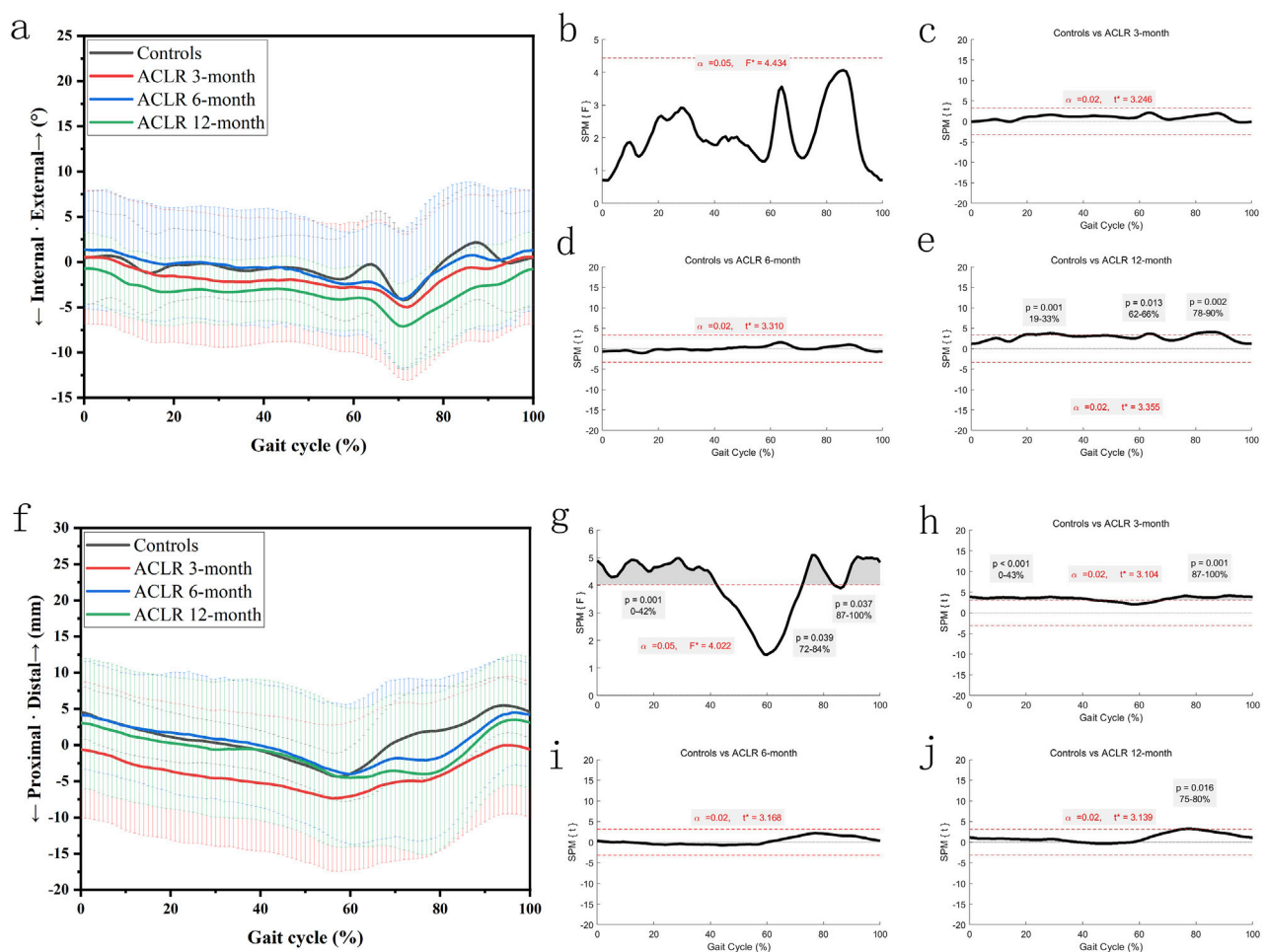


FIGURE 3

Knee kinematics of the transverse plane in a gait cycle. Chart (a), internal/external rotation angles in a gait cycle; chart (b), F value of internal/external rotation using SPM1D method (One Way ANOVA section) in a gait cycle; chart (c), posthoc statistical comparison of internal/external rotation between the control group and ACLR patients at 3 months; chart (d), posthoc statistical comparison of internal/external rotation between the control group and ACLR patients at 6 months; chart (e), posthoc statistical comparison of internal/external rotation between the control group and ACLR patients at 12 months; Chart (f), distal/proximal tibial translation in a gait cycle; chart (g), F value of distal/proximal tibial translation using SPM1D method (One Way ANOVA section) in a gait cycle; chart (h), posthoc statistical comparison of distal/proximal tibial translation between the control group and ACLR patients at 3 months; chart (i), posthoc statistical comparison of distal/proximal tibial translation between the control group and ACLR patients at 6 months; chart (j), posthoc statistical comparison of distal/proximal tibial translation between the control group and ACLR patients at 12 months; the posthoc comparison of SPM1D method was based on Dunnett tests.

groups across the gait cycle. SPM analysis (Figures 3b–e) revealed differences at all recovery stages, with  $p = 0.001$  for the entire gait cycle at 3 months (Figure 3c). At 6 months, significant differences (Figure 3d) were observed from 19% to 33% ( $p = 0.001$ ) and 62%–66% ( $p = 0.013$ ). At 12 months, differences (Figure 3e) were significant from 19% to 33% ( $p = 0.001$ ), 62%–66% ( $p = 0.013$ ), and 78%–90% ( $p = 0.002$ ). These findings suggest partial normalization of knee rotation by 12 months post-ACLR.

The distal tibial translation (Figures 3f–j) showed significant differences between the control and ACLR groups across the gait cycle. SPM analysis (Figures 3g–j) revealed significant differences at 3 months ( $p < 0.001$  from 0% to 43% and  $p = 0.001$  from 87% to 100%, Figure 3h). There was little significant difference at 6 months and 12 months ( $p = 0.016$  from 75% to 80%, Figure 3j). These findings suggest great recovery of distal tibial translation kinematics by 12 months post-ACLR.

### 3.5 Knee kinematics of the coronal plane

Figure 4 showed significant differences in knee adduction-abduction angles and distal tibial translation between the control and ACLR groups across the gait cycle. SPM analysis (Figures 4a–e) revealed significant deviations of knee adduction-abduction angles at all recovery stages (3, 6, and 12 months), with  $p$ -values  $< 0.001$  for the 0%–100% gait cycle at 3 months (Figure 4c). At 6 months, differences (Figure 4d) were significant from 0% to 63% ( $p < 0.001$ ) and 86%–100% ( $p = 0.004$ ), while at 12 months, differences (Figure 4e) were significant from 0% to 61% ( $p < 0.001$ ) and 86%–100% ( $p = 0.005$ ).

SPM analysis (Figures 4f–j) revealed significant differences in medial tibial translation at 3 months ( $p < 0.001$  from 0% to 60% and  $p < 0.001$  from 70% to 100%, Figure 4h), at 6 months ( $p = 0.009$  from 0% to 6%,  $p < 0.001$  from 7% to 52%, and  $p = 0.007$  from 93% to

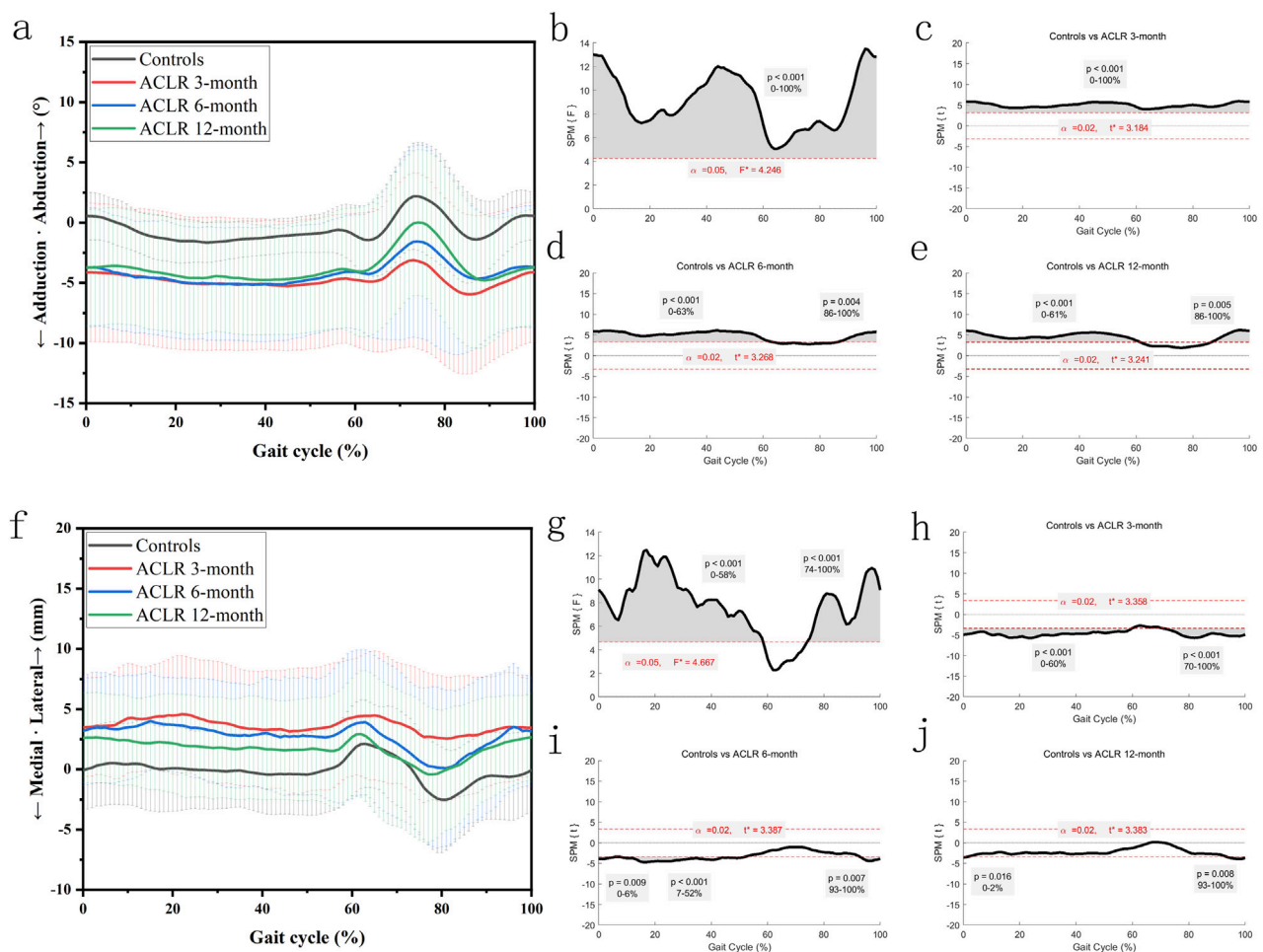


FIGURE 4

Knee kinematics of the coronal plane in a gait cycle. Chart (a), adduction/abduction angles in a gait cycle; chart (b), F value of adduction/abduction using SPM1D method (One Way ANOVA section) in a gait cycle; chart (c), posthoc statistical comparison of adduction/abduction between the control group and ACLR patients at 3 months; chart (d), posthoc statistical comparison of adduction/abduction between the control group and ACLR patients at 6 months; chart (e), posthoc statistical comparison of adduction/abduction between the control group and ACLR patients at 12 months; Chart (f), medial/lateral tibial translation in a gait cycle; chart (g), F value of medial/lateral tibial translation using SPM1D method (One Way ANOVA section) in a gait cycle; chart (h), posthoc statistical comparison of medial/lateral tibial translation between the control group and ACLR patients at 3 months; chart (i), posthoc statistical comparison of medial/lateral tibial translation between the control group and ACLR patients at 6 months; chart (j), posthoc statistical comparison of medial/lateral tibial translation between the control group and ACLR patients at 12 months; the posthoc comparison of SPM1D method was based on Dunnett tests.

100%, Figure 4i), and at 12 months ( $p = 0.016$  from 0% to 2% and  $p = 0.008$  from 93% to 100%, Figure 4j). These findings suggest recovery of distal tibial translation kinematics by 12 months post-ACLR. These differences diminished as recovery progressed, with partial normalization by 12 months post-ACLR.

## 4 Discussion

This study demonstrates that the IKDC and KOOS scores of ACLR patients significantly improved between 3 and 12 months post-surgery, which is consistent with the findings of Everhart et al. (2022). Their 20-year follow-up study on ACLR patients found that the IKDC scores were generally close to or at normal levels, indicating that ACLR surgery has a significant effect on improving patients' quality of life and subjective evaluations

(Everhart et al., 2022). However, despite the significant improvement, other studies have indicated that objective knee function recovery, particularly the restoration of knee biomechanics, still presents challenges within the first year post-surgery (Knurr et al., 2021; Zhou et al., 2022). This suggests that although clinical scores improve, the recovery of knee biomechanics in patients may still be far from ideal, reflecting the complexity and variability of postoperative rehabilitation.

ACLR patients demonstrated significantly smaller adduction angles compared to healthy controls at 6 months postoperatively, potentially indicating transient biomechanical overcorrection during early rehabilitation. However, these differences resolved by 12 months, suggesting gradual normalization of gait patterns. Previous studies have shown that changes in the peak pressure within the medial knee compartment are closely related to increases in the adduction angle after ACLR (Wellsandt et al., 2016). This

result suggests that the abnormal adduction angle in ACLR patients may be a potential risk factor for early knee joint degeneration or the development of osteoarthritis. Therefore, adjustments and monitoring of the adduction angle in the early postoperative stage, especially within 6 months, are crucial. This discrepancy may be attributed to progressive neuromuscular compensatory mechanisms—early deviations (e.g., internal rotation asymmetry) could be gradually mitigated through reconstructed quadriceps-hamstrings co-activation patterns, restored proprioception, and adaptive gait strategies.

In addition, ACLR patients exhibited notable changes in the internal/external rotation angles between 6 and 12 months, particularly an increase in the internal rotation angle. Literature has already pointed out that abnormal internal rotation angles after ACLR may be closely related to the onset of knee joint degeneration, such as knee osteoarthritis (Rodriguez-Merchan and Encinas-Ullan, 2022; Scanlan et al., 2010). This abnormal internal rotation angle may cause uneven loading on the knee joint during the gait cycle, thus increasing the risk of cartilage degeneration. Therefore, early identification and correction of these internal rotation abnormalities are of great significance in preventing the development of postoperative knee osteoarthritis.

During the stance phase of the gait cycle, ACLR patients showed significant impairment in knee extension, which was particularly prominent at 6 months post-surgery. Although some improvement was observed at 12 months, full recovery was not achieved. Restoration of knee extensor strength is one of the key goals in ACLR rehabilitation. Studies have shown that deficits in knee extensor strength are closely related to decreased knee function, increased risk of osteoarthritis, and recurrence of sports injuries (Buckthorpe et al., 2019; Hart et al., 2016; Lisee et al., 2022). Therefore, early strengthening exercises for the knee extensors can not only improve function but may also play a key role in preventing the progression of knee osteoarthritis.

On the other hand, ACLR patients exhibited significant increased posterior tibial displacement during the swing phase of the gait cycle. Although this abnormality improved at 6 months, it reappeared at 12 months post-surgery. The transient increase in anterior translation at 12 months could represent physiological graft maturation rather than pathological laxity. The tibial displacement difference (1.2 mm) is close to the system error ( $\pm 1$  mm), so the results should be interpreted with caution. Additionally, the abnormal medial-lateral displacement of the knee persisted until 12 months post-surgery, with gradual improvement over time, but still presenting challenges for full recovery. Recurrent displacement at 12 months may reflect graft creep or delayed neuromuscular control (Sherman et al., 2021). Abnormal knee kinematics may alter the distribution of cartilage load, increasing the risk of cartilage wear and knee joint degeneration.

It is worth noting that the recovery of distal-proximal displacement in ACLR patients was nearly complete within 3 months post-surgery, and the recovery of quadriceps strength was closely related to improvements in knee joint space (Pietrosimone et al., 2019). This finding suggests that postoperative quadriceps strengthening exercises can effectively improve the biomechanical performance of the knee joint,

especially in restoring joint space, providing important intervention support for postoperative rehabilitation.

The following is our correction plan for improving the abnormal biomechanical parameters after ACLR. Real-time biofeedback training (threshold: adduction angle  $\leq 3^\circ$ ) within 6 months postoperatively. Eccentric quadriceps strengthening (initiated at 4 weeks postoperatively): Single-leg eccentric squats performed twice weekly with progressive loading. Functional electrical stimulation for patients with Vastus Medialis Oblique activation deficits. This strategy aims to correct abnormal mechanical loading and reduce osteoarthritis risk.

In conclusion, this study demonstrates that the recovery of knee joint function in ACLR patients shows stage-dependent differences, with varying recovery patterns across different biomechanical parameters. While this study identified persistent kinematic abnormalities during the first 12 months following ACL reconstruction, a 20-year longitudinal follow-up study demonstrated normalized IKDC scores in long-term outcomes (Everhart et al., 2022), implying potential temporal resolution of initial movement impairments. This apparent contradiction between short-term observations and long-term functional recovery highlights the need for extended longitudinal monitoring to elucidate the trajectory of kinematic recovery and validate the neuromuscular compensation hypothesis.

To advance these insights, future investigations should: (1) Implement longitudinal designs with extended 5-year follow-ups to map OA progression against residual kinematic deficits; (2) Employ within-subject comparisons (operative vs. contralateral limbs) to detect individualized recovery patterns; (3) Integrate biplanar fluoroscopy for precise graft biomechanics analysis during functional movements; (4) Validate real-time biofeedback protocols targeting persistent rotational abnormalities. Such methodological enhancements will improve causal inference while informing personalized rehabilitation frameworks.

## 5 Conclusion

This study reveals the dynamic changes and recovery patterns of knee joint six degrees of freedom kinematics within 1 year after ACL reconstruction. Clinical function scores of patients significantly improved between 3 and 12 months post-surgery, but gait kinematics exhibited abnormalities in several degrees of freedom, with significant differences in the recovery process. Specifically, the adduction-abduction angle and anterior-posterior displacement showed significant improvement within 6 months post-surgery, stabilizing afterward but not fully recovering. Abnormalities in internal-external rotation and flexion-extension angles worsened or showed no significant improvement between 6 and 12 months post-surgery, suggesting that later-stage rehabilitation should focus on optimizing rotational control and flexion-extension function. Additionally, distal-proximal displacement was nearly fully recovered within 3 months post-surgery, while abnormal lateral displacement persisted until 12 months but gradually improved. The findings provide scientific evidence for the optimization of individualized rehabilitation strategies and emphasize the importance of correcting key kinematic abnormalities for functional recovery in later-stage rehabilitation.

## Data availability statement

The data analyzed in this study is subject to the following licenses/restrictions: Because of patient privacy restrictions, the data in this report will not be made public. Requests for the data presented in this study are available from the corresponding authors. Requests to access these datasets should be directed to TZ, gzlupus@126.com.

## Ethics statement

The studies involving humans were approved by the Ethics committee of Guangdong Provincial People's Hospital. The studies were conducted in accordance with the local legislation and institutional requirements. The participants provided their written informed consent to participate in this study.

## Author contributions

LK: Data curation, Investigation, Project administration, Supervision, Writing – original draft. HL: Data curation, Visualization, Writing – original draft, Writing – review and editing. XZ: Conceptualization, Data curation, Methodology, Project administration, Visualization, Writing – review and editing. PG: Data curation, Project administration, Resources, Writing – original draft. WL: Data curation, Investigation, Project administration, Writing – original draft. QG: Methodology, Project administration, Writing – original draft. ZK: Project administration, Resources, Supervision, Writing – original draft. WW: Conceptualization, Data curation, Investigation, Project administration, Resources, Writing – original draft, Writing – review and editing. XW: Conceptualization, Data curation, Investigation, Methodology, Project administration, Resources, Writing – original draft, Writing – review and editing. TZ: Conceptualization, Data curation, Formal Analysis, Funding acquisition, Investigation, Methodology, Project administration,

Resources, Supervision, Writing – original draft, Writing – review and editing.

## Funding

The author(s) declare that no financial support was received for the research and/or publication of this article.

## Conflict of interest

The authors declare that the research was conducted in the absence of any commercial or financial relationships that could be construed as a potential conflict of interest.

## Generative AI statement

The authors declare that no Generative AI was used in the creation of this manuscript.

## Publisher's note

All claims expressed in this article are solely those of the authors and do not necessarily represent those of their affiliated organizations, or those of the publisher, the editors and the reviewers. Any product that may be evaluated in this article, or claim that may be made by its manufacturer, is not guaranteed or endorsed by the publisher.

## Supplementary material

The Supplementary Material for this article can be found online at: <https://www.frontiersin.org/articles/10.3389/fbioe.2025.1572160/full#supplementary-material>

## References

- Buckthorpe, M., La Rosa, G., and Villa, F. D. (2019). Restoring knee extensor strength after anterior cruciate ligament reconstruction: a clinical commentary. *Int. J. Sports Phys. Ther.* 14 (1), 159–172. doi:10.26603/ijspst20190159
- Di Gregorio, R., and Vocenas, L. (2021). Identification of gait-cycle phases for prosthesis control. *Biomimetics (Basel)* 6 (2), 22. doi:10.3390/biomimetics6020022
- Elabd, O. M., Alghadir, A. H., Ibrahim, A. R., Hasan, S., Rizvi, M. R., Sharma, A., et al. (2024). Functional outcomes of accelerated rehabilitation protocol for anterior cruciate ligament reconstruction in amateur athletes: a randomized clinical trial. *J. Rehabil. Med.* 56, jrm12296. doi:10.2340/jrm.v56.12296
- Elfring, R., de la Fuente, M., and Radermacher, K. (2010). Assessment of optical localizer accuracy for computer aided surgery systems. *Comput. Aided Surg.* 15 (1-3), 1–12. doi:10.3109/10929081003647239
- Everhart, J. S., Yalcin, S., and Spindler, K. P. (2022). Twenty-year outcomes after anterior cruciate ligament reconstruction: a systematic review of prospectively collected data. *Am. J. Sports Med.* 50 (10), 2842–2852. doi:10.1177/03635465211027302
- Hamido, F., Habiba, A. A., Marwan, Y., Soliman, A. S. I., Elkhadrawe, T. A., Morsi, M. G., et al. (2021). Anterolateral ligament reconstruction improves the clinical and functional outcomes of anterior cruciate ligament reconstruction in athletes. *Knee Surg. Sports Traumatol. Arthrosc.* 29 (4), 1173–1180. doi:10.1007/s00167-020-06119-w
- Hart, H. F., Culvenor, A. G., Collins, N. J., Ackland, D. C., Cowan, S. M., Machotka, Z., et al. (2016). Knee kinematics and joint moments during gait following anterior cruciate ligament reconstruction: a systematic review and meta-analysis. *Br. J. Sports Med.* 50 (10), 597–612. doi:10.1136/bjsports-2015-094797
- Herbst, E., Costello, J., Popchak, A. J., Tashman, S., Irrgang, J. J., Fu, F. H., et al. (2023). Untreated injuries to the anterolateral capsular structures do not affect outcomes and kinematics after anatomic anterior cruciate ligament reconstruction. *J. Clin. Med.* 12 (13), 4408. doi:10.3390/jcm12134408
- Holsgaard-Larsen, A., Jensen, C., and Aagaard, P. (2014). Subjective vs objective predictors of functional knee joint performance in anterior cruciate ligament-reconstructed patients--do we need both? *Knee* 21 (6), 1139–1144. doi:10.1016/j.knee.2014.09.004
- Irrgang, J. J., Anderson, A. F., Boland, A. L., Harner, C. D., Kurosaka, M., Neyret, P., et al. (2001). Development and validation of the international knee documentation committee subjective knee form. *Am. J. Sports Med.* 29 (5), 600–613. doi:10.1177/03635465010290051301
- Kaiser, J. M., Vignos, M. F., Kijowski, R., Baer, G., and Thelen, D. G. (2017). Effect of loading on *in vivo* tibiofemoral and patellofemoral kinematics of healthy and ACL-reconstructed knees. *Am. J. Sports Med.* 45 (14), 3272–3279. doi:10.1177/0363546517724417
- Knurr, K. A., Kliethermes, S. A., Stiffler-Joachim, M. R., Cobian, D. G., Baer, G. S., and Heiderscheit, B. C. (2021). Running biomechanics before injury and 1 Year after



anterior cruciate ligament reconstruction in division I collegiate athletes. *Am. J. Sports Med.* 49 (10), 2607–2614. doi:10.1177/03635465211026665

Kotsifaki, R., Korakakis, V., King, E., Barbosa, O., Maree, D., Pantouveris, M., et al. (2023). Aspetar clinical practice guideline on rehabilitation after anterior cruciate ligament reconstruction. *Br. J. Sports Med.* 57 (9), 500–514. doi:10.1136/bjsports-2022-106158

Lepley, A. S., and Kuenze, C. M. (2018). Hip and knee kinematics and kinetics during landing tasks after anterior cruciate ligament reconstruction: a systematic review and meta-analysis. *J. Athl. Train.* 53 (2), 144–159. doi:10.4085/1062-6050-334-16

Lisee, C., Davis-Wilson, H. C., Evans-Pickett, A., Horton, W. Z., Blackburn, J. T., Franz, J. R., et al. (2022). Linking gait biomechanics and daily steps after ACL reconstruction. *Med. Sci. Sports Exerc.* 54 (5), 709–716. doi:10.1249/mss.0000000000002860

Lohmander, L. S., Englund, P. M., Dahl, L. L., and Roos, E. M. (2007). The long-term consequence of anterior cruciate ligament and meniscus injuries: osteoarthritis. *Am. J. Sports Med.* 35 (10), 1756–1769. doi:10.1177/0363546507307396

Monticone, M., Ferrante, S., Salvaderi, S., Rocca, B., Totti, V., Foti, C., et al. (2012). Development of the Italian version of the knee injury and osteoarthritis outcome score for patients with knee injuries: cross-cultural adaptation, dimensionality, reliability, and validity. *Osteoarthr. Cartil.* 20 (4), 330–335. doi:10.1016/j.joca.2012.01.001

Pietrosimone, B., Pfeiffer, S. J., Harkey, M. S., Wallace, K., Hunt, C., Blackburn, J. T., et al. (2019). Quadriceps weakness associates with greater T1ρ relaxation time in the medial femoral articular cartilage 6 months following anterior cruciate ligament reconstruction. *Knee Surg. Sports Traumatol. Arthrosc.* 27 (8), 2632–2642. doi:10.1007/s00167-018-5290-y

Rodriguez-Merchan, E. C., and Encinas-Ullan, C. A. (2022). Knee osteoarthritis following anterior cruciate ligament reconstruction: frequency, contributory elements,

and recent interventions to modify the route of degeneration. *Arch. Bone Jt. Surg.* 10 (11), 951–958. doi:10.22038/ABJS.2021.52790.2616

Scanlan, S. F., Chaudhari, A. M., Dyrby, C. O., and Andriacchi, T. P. (2010). Differences in tibial rotation during walking in ACL reconstructed and healthy contralateral knees. *J. Biomech.* 43 (9), 1817–1822. doi:10.1016/j.jbiomech.2010.02.010

Sherman, D. A., Glaviano, N. R., and Norte, G. E. (2021). Hamstrings neuromuscular function after anterior cruciate ligament reconstruction: a systematic review and meta-analysis. *Sports Med.* 51 (8), 1751–1769. doi:10.1007/s40279-021-01433-w

Wang, S., Zeng, X., Huangfu, L., Xie, Z., Ma, L., Huang, W., et al. (2021). Validation of a portable marker-based motion analysis system. *J. Orthop. Surg. Res.* 16 (1), 425. doi:10.1186/s13018-021-02576-2

Wellsandt, E., Gardinier, E. S., Manal, K., Axe, M. J., Buchanan, T. S., and Snyder-Mackler, L. (2016). Decreased knee joint loading associated with early knee osteoarthritis after anterior cruciate ligament injury. *Am. J. Sports Med.* 44 (1), 143–151. doi:10.1177/0363546515608475

Yang, X. G., Feng, J. t., He, X., Wang, F., and Hu, Y. c. (2019). The effect of knee bracing on the knee function and stability following anterior cruciate ligament reconstruction: a systematic review and meta-analysis of randomized controlled trials. *Orthop. Traumatol. Surg. Res.* 105 (6), 1107–1114. doi:10.1016/j.otsr.2019.04.015

Zhang, Y., Huang, W., Yao, Z., Ma, L., Lin, Z., Wang, S., et al. (2016). Anterior cruciate ligament injuries alter the kinematics of knees with or without meniscal deficiency. *Am. J. Sports Med.* 44 (12), 3132–3139. doi:10.1177/0363546516658026

Zhang, Y., Yao, Z., Wang, S., Huang, W., Ma, L., Huang, H., et al. (2015). Motion analysis of Chinese normal knees during gait based on a novel portable system. *Gait Posture* 41 (3), 763–768. doi:10.1016/j.gaitpost.2015.01.020

Zhou, L., Xu, Y., Zhang, J., Guo, L., Zhou, T., Wang, S., et al. (2022). Multiplanar knee kinematics-based test battery helpfully guide return-to-sports decision-making after anterior cruciate ligament reconstruction. *Front. Bioeng. Biotechnol.* 10, 974724. doi:10.3389/fbioe.2022.974724



# Frontiers in Bioengineering and Biotechnology

Accelerates the development of therapies,  
devices, and technologies to improve our lives

A multidisciplinary journal that accelerates the  
development of biological therapies, devices,  
processes and technologies to improve our lives  
by bridging the gap between discoveries and their  
application.

## Discover the latest Research Topics

[See more →](#)

### Frontiers

Avenue du Tribunal-Fédéral 34  
1005 Lausanne, Switzerland  
[frontiersin.org](https://frontiersin.org)

### Contact us

+41 (0)21 510 17 00  
[frontiersin.org/about/contact](https://frontiersin.org/about/contact)



Frontiers in  
Bioengineering  
and Biotechnology

